STABILITY OF RIPRAP SIDE SLOPES IN OPEN CHANNELS

By

AHMED FAHMY AHMED

A thesis submitted for the degree of
DOCTOR OF PHILOSOPHY

in the Faculty of Engineering and Applied Science

University of Southampton

Under the Supervision of

The Late Dr.K.V.H. Smith, M.Sc., Ph.D., M.ASCE, M.I.C.E., M.I. Struct.E.
and
Mr.N.B. Webber, B.Sc.(Eng.), F.I.C.E., M.ASCE, M.I.W.E.M., M.I.Struct.E.

UNIVERSITY OF SOUTHAMPTON

ABSTRACT

FACULTY OF ENGINEERING AND APPLIED SCIENCE
CIVIL ENGINEERING

Doctor of Philosophy

STABILITY OF RIPRAP SIDE SLOPES IN OPEN CHANNELS

by
AHMED FAHMY AHMED

The present design techniques for the sizing of rock in riprap side slopes give results that differ appreciably. In previous researches both deterministic and probabilistic methods have been applied, but the assumptions made have been based on inadequate experimental and field data.

In this investigation, experiments were conducted in 10m long channels having a $1\frac{1}{2}$: 1 side slope protected with a rock layer of $1\frac{1}{2}$ diameter equivalent thickness. Both an outdoor flume and an indoor tilting flume were utilised and, in all, six models were tested, including two bed widths (0.4 and 0.5m), two filter types, and a uniform and a graded rock.

In the case of the first three models, increasing the discharges up to the maximum pumping capacity did not produce any more than minor rock displacement, although failure was predicted by all of the recognised methods.

In the last three models, where the bed slope was increased, failure did occur. The mode of failure was assessed and, in one case, a more detailed examination was made with the aid of coloured rock particles.

It was found that the riprap was more stable than predicted by any of the recognised approaches. Consequently, with the aim of obtaining a more fundamental appreciation of the incipient motion and the forces acting, a special force measuring apparatus was devised whereby the lift and drag forces acting on a spherical particle placed in the riprap slope could be measured simultaneously. Preliminary experiments were conducted to establish the appropriate sphere diameter and its location at the level of maximum wall shear.

Advantage was taken of the data obtained in the force measurements to devise modified deterministic and probabilistic techniques affording greater conformity with the experimental results.

The effect of particle shape and orientation was investigated experimentally by measuring the forces acting on four different shaped non-spherical particles as well as on the spherical particle.

Recommendations for further research on this important topic have been made.

ACKNOWLEDGEMENTS

In the Name of Allah, Most Gracious, Most Merciful. Praise be to Allah, Lord of the Worlds.

The research topic was decided upon in consultation with Dr.K.V.H. Smith who was initially the supervisor. Regretably, Dr.Smith developed a serious illness from which he did not recover. The writer gratefully acknowledges his sound advice and encouragement in these early stages.

The writer would like to express his sincere gratitude to Mr.N.B. Webber for his invaluable guidance and keen supervision throughout the subsequent stages as well as critical reading of the manuscript and the preparation of this thesis.

The writer wishes also to acknowledge and thank Dr.P.Tosswell for many stimulating discussions and his encouragement during this study.

Mr. L.Williams, senior technician in the Chilworth Laboratory, has been of great assistance in the experimental work; the writer is also grateful to Mr.E.J. Meech and Mr.K. Yeates for the skilful fabrication and maintenance of the measurement apparatus.

The manuscript was typed by Mrs. P.A. Dawson with commendable speed and accuracy, for which the writer is grateful.

Special thanks are due to the Water Research Centre and the Hydraulic and Sediment Research Institute, Cairo-Egypt for affording me this research opportunity. Many thanks are also due to the United Nations and Egyptian Education Bureau - Ministry of Higher Education for their financial support without which my study would not have been possible.

Lastly, but not least, the writer is especially indebted to his family for their continuous support and encouragement throughout three arduous but rewarding years. He also wishes to express his highest gratitude and respect to his father and mother who have encouraged him, over the years, to pursue higher education.

CONTENTS

PAGE NO.

SYMBOLS AND NOTATIONS

Symbols	Description	Dimension
A	Flow cross-section area	(L^2)
A_1	Cross-section area associated with the channel bed	(L^2)
A_2	Cross-section area associated with the channel side slopes	(L^2)
A_B	Wetted roughness cross-section area	(L^2)
A_L	Projected area of the particle related to lift force	(L^2)
a	Coefficient	-
a	Inner radius of Preston tube	(L)
B	$= f(C_u)$ as in Eq. (2.28)	-
B	Channel bed width	(L)
B	Width of the approach channel	(L)
b	Weir width	(L)
b_e	Effective width of weir	(L)
C	Chezy resistance coefficient	$(L^{\frac{1}{2}}T^{-1})$
C	Coefficient relating the piezometric-head gradient to the effective seepage force at channel bed as in Eq. (2.7)	-
C	Izbach's turbulence coefficient	-
C_D	Drag coefficient	-
C_e	Discharge coefficient	-
C_L	Lift coefficient	-
C_s	Shape correction as in Eq. (4.42)	-
C_T	Tractive stress coefficient	-
C_u	Uniformity coefficient	-
C_w	Particle shape coefficient	-
D	Representative particle size	(L)
DI	Drag intensity	-
D_i	Particle size for which i percent by weight is finer	(L)
D_m	Volume weighted effective grain size	(L)
d	Pipe diameter	(L)
d	Flow depth	(L)

Symbols	Description	Dimension
E	Modulus of elasticity	(ML^{-2})
e	Void ratio	-
e	Traverse spacing of roughness element	(L)
F_c	Critical drag force	(MLT^{-2})
F_D	Drag force	(MLT^{-2})
F_{DF}	Form drag force	(MLT^{-2})
F_{DR}	Driving force	(MLT^{-2})
F_g	Gravity force	(MLT^{-2})
F_L	Lift force	(MLT^{-2})
F_n	Resultant force normal to the plane containing the particle	(MLT^{-2})
F_r	Resisting force	(MLT^{-2})
F_{RE}	Resisting force	(MLT^{-2})
F_r	Froude number	-
F_s	Cutoff frequency	(T^{-1})
F_s	Seepage force	(MLT^{-2})
F_{se}	Seepage force per unit volume	$(ML^{-2}T^{-2})$
F_t	Resultant force parallel to the plane containing the particle	(MLT^{-2})
F_w	Gravity force	(MLT^{-2})
f_i	Functions	-
f	Darcy-Weisbach friction factor	-
f_c	Sampling interval	(T)
G	Ratio of γ_s/γ_w	-
G	Constant parameter as in Eq. (4.38)	-
g	Gravitational acceleration	(LT^{-2})
H_w	Water head difference	(L)
h	Measured head difference above weir	(L)
h	Height of centre of stagnation tube from zero datum	(L)
h_e	Effective head over weir	(L)
h_L	Friction losses associated with flow in pipes	(L)

Symbols	Description	Dimension
I	Piezometric-head gradient	-
i	Seepage flow hydraulic gradient	-
j	Square root of (-1)	-
K	Reduction factor	-
k_b	Empirical adjustment for weir head	(L)
k_h	Empirical adjustment for flow head	(L)
K_p	Seepage coefficient of laminar flow	-
K_s	Equivalent sand roughness of Nikuradse	(L)
L	Pipe length	(L)
L	Horizontal distance between two control sections	(L)
LI	Lift intensity	-
ℓ	Characteristic length known as the mixing length	(L)
m	Constant parameter as in Eq. (4.37)	-
N	Number of revolutions per second	(T^{-1})
N	Number of data values	-
n	Porosity	-
n	Manning coefficient	$(TL^{-\frac{1}{3}})$
n_{eff}	Equivalent Manning roughness coefficient	$(TL^{-\frac{1}{3}})$
n_1	Manning roughness associated with the channel bed	$(TL^{-\frac{1}{3}})$
n_2	Manning roughness associated with the side walls	$(TL^{-\frac{1}{3}})$
O_e	Effective fabric pore size of the cloth filter	(L)
p	Height of the weir crest	(L)
P	Wetted perimeter	(L)

Symbols	Description	Dimension
P	Cumulative probability of riprap adequacy	-
P_a	Probability of adequacy	-
P_c	Critical dynamic lift pressure	$(ML^{-1}T^{-2})$
P_c	Volumetric packing factor as in Eq. (2.29)	-
P_L	Dynamic lift pressure	$(ML^{-1}T^{-2})$
P_1	Wetted perimeter associated with channel bed	(L)
P_2	Wetted perimeter associated with channel side slopes	(L)
P_o	Static pressure	$(ML^{-1}T^{-2})$
P_t	Total pressure recorded by Preston tube	$(ML^{-1}T^{-2})$
Q	Flow rate	(L^3T^{-1})
q_n	qth quantile point of standard normal	-
R	Hydraulic radius	(L)
R_e	Reynolds number	-
R_*	Boundary Reynolds number	-
S_o	Channel bed slope	-
S_e	Slope of the energy gradient	-
S_f	Shape factor of the particle	-
SF	Factor of safety	-
S_n	Size of short axis of the particle	(L)
S_m	Safety factor for riprap on a side slope with no flow	-
S_s	Specific gravity	-
S_w	Slope of water surface	-
T	Water temperature in degrees centigrade	-
T	Sampling interval	(T)
T_c	Function of the grain Reynolds number as in Eq. (2.21)	-
u	Flow velocity	(LT^{-1})
u_*	Shear velocity	(LT^{-1})

Symbols	Description	Dimension
u_r	Reference velocity	(LT^{-1})
u_{*c}	Shear velocity at the threshold condition	(LT^{-1})
u_{35}	Velocity at a distance 0.35 D_{35} above the theoretical bed	(LT^{-1})
V	Displayed voltage	-
V_s	Volume of the solid material	(L^3)
V_v	Volume of voids	(L^3)
V_T	$= V_s + V_v$	(L^3)
V_w	The fall velocity	(LT^{-1})
W	Particle weight	(MLT^{-2})
W	Surface width of flow	(L)
X	Distance	(L)
X	Roughness parameter	(L)
y	Flow depth	(L)
y_o	Constant of integration	-
y_m	Depth of the maximum wall shear	(L)
Z	Elastic modulus	(L^3)
α	Slope angle of the plane bed	-
α	Velocity head coefficient	-
β	Angle between the resultant vector and the downstream component of submerged weight vector	-
β	Ratio of lift to drag	-
γ or γ_w	Specific weight of water	$(ML^{-2}T^{-2})$
γ_s	Specific weight of the particle	$(ML^{-2}T^{-2})$
γ_s'	Specific weight of the submerged particle	$(ML^{-2}T^{-2})$
ρ or ρ_w	Water density	(ML^{-3})
ρ_s	Particle density	(ML^{-3})

Symbols	Description	Dimension
ϕ	Angle of repose	-
μ	Dynamic viscosity	$(ML^{-1}T^{-1})$
μ	Mean value	-
ν	Kinematic viscosity	(L^2T^{-1})
κ	Von-Karman constant	-
δ	Thickness of turbulent boundary layer	(L)
δ	Stability parameter	(L^2)
δ	Angle between the resultant vector and the drag vector	-
ε	Ratio of seepage force to submerged weight	-
ε	Strain gauge reading	-
η	Stability number	-
η'	Particle stability factor modified for side slope	-
τ or τ_o	Mean tractive force (shear force) per unit wetted area	$(ML^{-1}T^{-2})$
τ_{oB}	Tractive stress on the side slope	$(ML^{-1}T^{-2})$
τ_s	Permissible tractive stress on channel bed	$(ML^{-1}T^{-2})$
τ_{sB}	Permissible tractive stress on channel side slope	$(ML^{-1}T^{-2})$
τ_c	Critical boundary shear stress	$(ML^{-1}T^{-2})$
$\tau*$	Shields entrainment function	$(ML^{-1}T^{-2})$
τ_c'	Critical shear stress on side slope	$(ML^{-1}T^{-2}$
ΔP	Pressure difference between top and bottom of the particle as in Eq. (2.31)	$(ML^{-1}T^{-2})$
ΔB	Bed width correction	(L)
ΔY	Depth correction	(L)
Δ	Relative density	-

Symbols	Description	Dimension
σ	Geometric standard deviation of the graded mixture	-
σ	Standard deviation	-

CHAPTER ONE

INTRODUCTION

1.1 THE PROBLEM

Riprap may be defined as a layer consisting of discrete rock particles placed on stream banks, slopes of dams and highway embankments to prevent erosion or scour of structure due to flowing water. Rock material, which can be successfully employed as riprap, needs to meet certain requirements such as sufficient weight for stability, porosity for drainage, roughness for energy dissipation, availability in even the most remote areas, and finally low cost compared with manufactured materials such as concrete.

Some rivers, more than others, have side slopes that are subject to scour and serious erosion due to high velocities of flow. Under these circumstances not only is the agricultural land bordering the river diminished, but also the river morphology is changed. This situation is particularly occurring along the River Nile in Egypt. For these reasons the stability of riprap side slopes in open channels is considered and comprehensively investigated during this study.

A large number of design criteria for sizing riprap have been recently developed, see Lane, E.W. (1955), Stevens, M.A. and Simons, D.B. (1971 and 1976), Ruh-Ming, L. et al. (1976 and 1979), and Samad, M.A. (1978). Some of these methods have been derived from the viewpoint of equilibrium of a single particle in a flowing water and referred to as the deterministic approach. Whilst in the case of the others, which are referred to as the probabilistic approach, the fluctuating nature of the hydrodynamic forces acting on an individual particle has been considered.

In order to investigate the applicability of these methods, a preliminary study was carried out involving representative discharges and riprap conditions. It was found that the results differed materially from those predicted by the various recognised

methods and that the predictions themselves covered a wide range. It demonstrated that these deterministic methods are principally based on theoretical considerations and have not been confirmed by real measurements.

As a result of this, it was felt that the establishment of stability criteria for sizing riprap either deterministically or probabililstically should be based on measurement of the actual hydrodynamic forces acting on an individual roughness element. Then, utilizing laboratory data, a number of experiments to check the applicability of the criteria developed should be conducted so as to indicate their validity and relative merits.

Measurements of forces on roughness elements have been made on a bed particle under idealized uniform flow conditions over either uniform spherical or hemispherical particles, see Einstein, H.A. and El-Samni, E. (1949), Chepil, W.S. (1958), Coleman, N.L. (1971), and Cheng, E.D. and Clyde, C.G. (1972). This revealed that to the best of the Author's knowledge no attempt has hitherto been made to measure such forces acting on side slope particles.

Consequently, several methods were considered to determine the lift and drag forces on an individual particle on a side slope. To avoid the complication of mechanical problems, a load beam cell has been devised to measure lift and drag forces indirectly by measuring the stresses on the load beam. These stresses can be transformed into simultaneous values of lift and drag forces, which can then form the basis of reliable formulae having a wide range of application. This obviously necessitates locating the point of maximum wall shear in the side slope, which increases the scope of the problem.

The availability of the hydraulics laboratory facility at Chilworth allowed the problem to be investigated at fairly large scale and under controlled conditions. A series of tests was devised in which the factors affecting riprap stability could be investigated, and the various stages of failure identified.

1.2 OUTLINE OF RESEARCH

The current investigation is planned to provide more information on the problem of stability of riprap side slopes in open channels with a view to establishing a better understanding of the failure process and the hydrodynamic forces acting on the rock particles.

Unlike the flow characteristics in unlined or smooth lined open channels in which the flow resistance is primarily due to the geometry of the section, the flow in rough lined channels is usually associated with the large scale roughness elements which directly influence the flow behaviour. In this case, the velocity distribution, degree of turbulence and the characteristics of the flow will be somewhat different from those in the more commonly encountered channels.

Hitherto, knowledge of the hydrodynamic lift and drag forces acting on a side slope riprap particle has been inadequate for the purposes of developing a suitable design criterion for side slope protection. This has been due to the numerous factors that influence the stability, and the difficulties of acquiring data concerning the problem.

With the above in mind, the experimental work planned in this study was as follows:

1 - Visualization study to identify the hydraulic parameters at the threshold and failure conditions. This study was also to include an investigation of the factors affecting the riprap stability and mode of failure.

2 - Investigation of the hydraulic resistance and flow characteristics of the large scale rough channels.

3 - An investigation of the applicability of the existing approaches for sizing riprap either deterministically or probabilistically. This would be carried out by utilizing the data obtained from the various failure tests.

4 - Since the forces acting on a side slope particle would be measured, it was necessary to establish the location of the point of maximum shear. This was to be achieved by conducting an experimental study involving the Preston tube as a means of determining boundary shear stress.

5 - Determination of the best size of roughness element that can be employed in the forces measurements. This test to be conducted experimentally by taking into account the real particle configuration.

6 - Design and manufacture of a measuring device that could be used to obtain simultaneous values of lift and drag forces for various flow conditions.

7 - As a result of the data obtained in item 6, the formulation of the stability criteria could be established, and then a deterministic method for sizing riprap and another auxiliary probabilistic method could be derived. These new methods could then be examined with the existing methods in the light of the results obtained from the failure tests carried out in item 1.

8 - An assessment of the effect of particle shape and orientation on the stability of the riprap layer. This could be achieved by measuring the forces acting on four non-spherical particles under uniform flow conditions. The results could then be compared with that obtained on a spherical particle under similar flow conditions.

These were the objectives in the study and the following chapters describe the detailed procedures and the results.

CHAPTER TWO

HYDRODYNAMIC FORCES AND STABILITY CONCEPT

2.1 INTRODUCTION

Rock protecting the banks of a river or canal is exposed not only to the drag force acting in the direction of fluid flow, but also to a component of weight acting down the side slope, and lift force acting perpendicular to the side slope plane. The resultant force acting on the particle under consideration is a combination of these forces which tend to dislodge the particle out of the riprap layer. This situation makes it necessary to determine the characteristics of a non-cohesive discrete particle that would not be moved under the specified forces in a stream of a designated shape and flow condition.

In fact, stability of the particle is not only influenced by the aforementioned hydrodynamic forces, but also there are numerous other factors which should be taken into account in the development of an effective design procedure for riprap protection. These factors are:

(a) Magnitude and direction of the flow
(b) Fluid properties (density and viscosity)
(c) Rock characteristics (size, shape, size distribution and specific weight)
(d) Magnitude and direction of the seepage force
(e) Thickness of the protective layer
(f) Type and thickness of the under layer filter
(g) Packing factor (which depends on the manner of placing the protective layer).

In this chapter, forces acting on a typical single particle as well as the factors affecting its stability are identified. Then a general review of previous experimental and analytical work carried out in this field is presented.

2.2 FORCES ACTING ON A SINGLE PARTICLE

Whenever there is relative motion between a flowing fluid and an immersed body, a certain force is exerted on the body. The component parallel to the direction of fluid motion is known as the drag force, F_D, and the component perpendicular to the direction of motion is known as the lift force, F_L. In addition to these hydrodynamic force components, there are two more forces which should be involved in the stability concept of the immersed body. These forces are seepage and gravity forces, and are independent of fluid impact.

The forces acting on a typical particle on the channel bed and side slope are illustrated in Fig. (2.1) and can be described as:

2.2.1 Drag Force

The drag force is one of the most important factors causing motion of riprap particles. As the flow passes the particle, a drag force is exerted on the particle parallel to the flow direction which is composed of the following:

I - Form drag force

The form drag force is caused by the pressure difference between upstream and downstream forces acting on the particle. This force is parallel to the flow direction and can be evaluated by considering a particle with a representative diameter D, immersed in a viscous incompressible flow with velocity u; the fluid density and viscosity are ρ and μ respectively. The form drag F_{DF} can be written in the functional form

$$F_{DF} = f_1(D,u,\mu,\rho) \qquad (2.1)$$

Applying the Buckingham Pi theorem in two dimensionless π parameters, so that

$$\frac{F_{DF}}{\rho u^2 D^2} = f_2\left(\frac{\rho u D}{\mu}\right) = f_2(R_e) \qquad (2.2)$$

in which

R_e is the Reynolds number

Note that D^2 term is proportional to the projected area subjected to the form drag and the characteristic length employed in the Reynolds number depends on the particle shape. The form drag is defined as

$$F_{DF} = C_D \tfrac{1}{2} \rho u^2 D^2 \qquad (2.3)$$

in which

C_D is the drag coefficient.

II - Skin friction force

Part of the force exerted by the fluid on the particles is caused by shear stress between the fluid and the particle surface. This portion is known as skin-friction force and its magnitude depends on the surface area of contact between the particle and the flow, and the relative roughness of the particle surface.

For a large particle in the turbulent flow condition, the skin friction force is insignificant compared to the form drag. Therefore, the effect of skin shear stress could be neglected in the stability analysis and then the drag force F_D would be only due to the form drag as

$$F_D = C_D \tfrac{1}{2} \rho u^2 D^2 \qquad (2.4)$$

2.2.2 Lift Force

Due to the difference in flow velocity around the upper and lower parts of the particle, the pressure on the upper side is reduced below the static pressure and approaches to static pressure on the lower side. This pressure difference between upper and lower

sides produces the hydrodynamic lift force, which acts perpendicular to the flow direction and the protective layer plane.

The variables used to derive the drag formula can be utilized to obtain the lift force equation, and applying the same procedure used to obtain Eq. (2.4), the lift force F_L can be expressed as

$$F_L = C_L \tfrac{1}{2} \rho u^2 D^2 \qquad (2.5)$$

in which C_L is the lift coefficient.

2.2.3 Gravity Force

The gravity force represented by the submerged weight of the particle is the only resisting force in the case of the bed particle. But when a similar particle is situated on the side slope, there will be a component acting downwards parallel to the side slope plane which causes the particle to move down the sloping side of the channel.

Generally, the gravity force can be evaluated as a force acting vertically downwards and equivalent to the submerged weight of the particle which can be expressed as

$$F_W = C_W (\gamma_S - \gamma_W) D^3 \qquad (2.6)$$

in which

C_W is the particle shape coefficient;
γ_S is the particle specific weight;
and γ_W is the fluid specific weight.

2.2.4 Seepage Force

There is no doubt that the effect of seepage cannot be neglected in studying the stability of a riprap layer. The seepage

force may be defined as the resultant force due to the water movement through a permeable soil. This force is usually associated with the piezometric head gradient, which is necessary for the flow movement in any stream or irrigation canal. But due to the different water level between the upstream and downstream portions of any hydraulic structure, the negative piezometric head might be magnified which consequently generates a significant seepage force and endangers the protective layer within this area.

On the other hand, Martin, C.S. (1966) suggested that the magnitude of the effective seepage force per unit volume acting on the top layer of bed particles is proportional to the piezometric-head gradient normal to the plane of the bed, and can be defined as

$$F_S = C \gamma I \qquad (2.7)$$

in which

F_S is the seepage force per unit volume of the soil mass;
C is the coefficient relating the piezometric-head gradient to the effective seepage force at the bed;
and I is the piezometric-head gradient evaluated at the bed from measured results or from theory.

2.3 CONCEPT OF INCIPIENT MOTION

When the resultant force acting on a non-cohesive particle is less than some critical value, the particle remains motionless and the condition can be considered stable. But if the resultant force increases to a value such that the particle moves even slightly, the critical or threshold condition is said to have been reached. Under this condition the hydrodynamic forces acting on the particle under consideration are just balanced by the resisting force due to its submerged weight.

The critical condition has usually been defined by visual observations in laboratory flumes in which the movement of an arbitrary selected number of particles has been taken to define the

critical condition. Obviously this definition is not definitive, giving rise to numerous factors affecting the stability, which explains the diversity of experimental results.

2.3.1 Dimensional Analysis

The solution of any fluid flow problem usually comprises numerous variables. Normally, in order to establish such relationship between those variables, the tool of the dimensional analysis should be utilized. From this viewpoint it may be stated that the threshold condition of particles subjected to a flow field depends on: D, R, ρ_s, ρ_w, ν, u_{*c}, S_f, θ, ϕ and σ, in which

R is the hydraulic radius;
ρ_s is the particle density;
ν is the kinematic viscosity of the water;
g is the gravitational acceleration;
θ is the side slope angle;
ϕ is the angle of repose;
S_f is the shape factor of the particle;
u_{*c} is the shear velocity at the threshold condition;
and σ is the geometric standard deviation of the particles.

Considering the above variables, a general expression for the beginning of motion can be obtained as

$$f_1(D,R,\rho_s,\rho_w,\nu,g,u_{*c},\theta,\phi,\sigma,S_f) = 0 \qquad (2.8)$$

Since the flow is uniform and the beginning of motion is basically a question of static equilibrium, neither g or ρ_s can be relevant as independent characteristic parameters. But they can only occur in the combination $g(\rho_s - \rho_w)$. Therefore, the derived form becomes

$$f_2(D,R,\rho_w,\nu,u_{*c},\gamma'_s,\theta,\phi,\sigma,S_f) = 0 \qquad (2.9)$$

in which

$$\gamma_s' = g(\rho_s - \rho_w) \tag{2.10}$$

where γ_s' is the specific weight of the submerged particle.

Choosing D, ρ_w and u_{*c} as repeating variables, the Buckingham's Pi-theorm yields

$$f_3\left(\frac{\rho_w u_{*c}^2}{D\gamma_s'}, \frac{D\, u_{*c}}{\nu}, \frac{R}{D}, \theta, \phi, \sigma, S_f\right) = 0 \tag{2.11}$$

Noting that, $\tau_c = \rho u_{*c}^2$, where τ_c is the critical boundary shear stress, Eq. (2.11) yields

$$f_3\left(\frac{\tau_c}{D\gamma_s'}, \frac{D\, u_{*c}}{\nu}, \frac{R}{D}, \theta, \phi, \sigma, S_f\right) = 0 \tag{2.12}$$

where

$\frac{\tau_c}{D\gamma_s'}$ is the Shields parameter, τ_{*c} which is the ratio between the drag force to the gravitational force;

$\frac{D\, u_{*c}}{\nu}$ is the critical boundary Reynolds number R_{*c};

and $\frac{R}{D}$ is the relative roughness.

It was suggested that, when the boundary is completely rough, the Shields parameter would be independent of viscous effect which is represented by R_{*c}. Then Eq. (2.12) can be written as

$$\frac{\tau_c}{D\gamma_s'} = f_4\left(\frac{R}{D}, \theta, \phi, \sigma, S_f\right) \tag{2.13}$$

In general, it is possible to state that Eq. (2.13) can be treated only if sets of family curves would be carried out to identify the influence of the variables θ, ϕ, σ and S_f on the beginning of motion. Therefore, the final relationship takes the form

$$\frac{\tau_c}{D\gamma_s'} = f\left(\frac{R}{D}\right) \tag{2.14}$$

2.3.2 Literature Review

In fact many researchers have attempted to identify the criteria of the initiation of motion and still the exact solution continues to defy theoretical analysis. Among the earliest and most frequently quoted research was that conducted by Kramer, H. (1935), in which three types of motion near the critical condition were defined as

1) Weak movement - indicates that only a few particles are in motion on the bed so that those moving particles on one square centimetre of the bed can be counted.

2) Medium movement - indicates that the grains of mean diameter begin to move. The motion is not local in character but the bed continues to be plane.

3) General movement - indicates that all the grains are in motion, that is the movement is occurring in all parts of the bed at all times.

In fact the definition of the critical condition is rather indefinite which can explain the variation in results of different workers. However, the critical shear stress was determined by Shields, A. (1936). Using a uniform sand grain size and plane bed, the value of the stress for zero sediment discharge was obtained by extrapolating a graph of observed sediment discharge versus shear stress and does not depend on a quantitative criterion. In this study, a number of relevant parameters were chosen and assembled into two dimensionless numbers; the first is known as the Shields entrainment function and the second is called the particle Reynolds number. These two numbers were related to experimental results in a graphical form known as the Shields diagram.

The critical shear stress from Shields entrainment function can then be calculated as

$$\tau_c = \tau_* (\gamma_s - \gamma_w) D \qquad (2.15)$$

in which

τ_c is the critical average shear stress exerted by the fluid on the boundary at the flow stage when bed particles begin to move;

and τ_* is the Shields entrainment function.

In his experiments, Shields was unable to obtain a single value for the critical shear stress, so the relationship between the Shields function τ_* and the particle Reynolds number R_*, was graphically indicated by the upper and lower limits. This diagram was modified later into a single curve after adding the results obtained by other investigators as shown in Fig. (2.2).

It is indicated in this figure that for the hydrodynamically rough boundary ($R_* > 400$) the τ_* value is independent of R_* and is equal to

$$\tau_* = \frac{\tau_c}{(\gamma_s - \gamma_w)D} = 0.06 \qquad (2.16)$$

Further research was carried out by White, C.M. (1939) in which the critical shear stress required to move a particular grain in a horizontal bed was expressed as

$$\tau_c = 0.18(\gamma_s - \gamma_w)D \tan \phi \qquad (2.17)$$

in which the constant is obtained from the experiments with laminar flow; ϕ is the angle of repose of the particles.

Considerable field data was used by Lane, E.W. (1952) to establish the limiting tractive force diagram, in which the critical shear stress for clear water was considerably lower than for water with a low or high content of sediment as shown in Fig. (2.3). It was found that for coarse noncohesive material, the permissible tractive force in pounds per square foot can be expressed as

$$\tau_c = 0.4\ D_{75} \qquad (2.18)$$

in which D_{75} is the rock size (in inches) for which 75% of the material is finer.

Using the metric system units, Eq. (2.18) can be written as

$$\tau_c = 0.049(\gamma_s - \gamma_w) D_{75} \qquad (2.19)$$

which is similar to Shields equation for the hydraulically rough boundary.

Chien, N. (1954) studied the variation of the critical shear stress as a function of mean particle diameter by utilizing the available shear stress formulae. This comparison is reproduced in Fig. (2.4), which shows the diversity of the experimental and theoretical results obtained by different investigators.

As a result of the closer review of the formulae by Chien, it was revealed that the so-called critical value in some cases is the practical value indicating zero transport. But in some other cases, it is some constant value. These two are so different in nature that one should not be astonished by the apparent spread of the critical value.

Gessler, J. (1965) studied the beginning of motion theoretically and experimentally on channel beds formed by non-cohesive sediment mixtures with a large grain size distribution curve. In order to make a theoretically approachable treatment to the problem, it was assumed that the turbulent fluctuations of the bed shear stress are distributed according to the normal error law, and the movement will occur when the effective eroding bed shear stress on the grain exceeds a critical value which is a function of the grain size and Reynolds number of the grain. According to this, the movement condition can be written as

$$\frac{\tau}{(\gamma_s - \gamma_w)D} > T_c \qquad (2.20)$$

in which T_c is a function of the Reynolds number of the grain and is equal to

$$T_c = \frac{\tau_c}{(\gamma_s - \gamma_w)D} \qquad (2.21)$$

Similar results were reported by Grass, A.J. (1970) in which the frequency distribution of the bed shear stress in flow over a hydraulically smooth boundary was related to sediment transport. Using a hydrogen bubble technique the instantaneous longitudinal velocity profiles were photographed and the velocity gradients were then utilized to calculate the instantaneous bed shear stresses. These were found to be slightly skew-normally distributed.

Similarly to the other formulae, Gessler obtained the limiting value of $T_c = 0.047$ for fully developed rough turbulent flow to give

$$\frac{\tau_c}{(\gamma_s - \gamma_w)D} = 0.047 \qquad (2.22)$$

which is identical to that used by Meyer-Peter in his bed load formula and obtained by the same method as Shields.

Another modification of Shields diagram was given by Gessler, J. (1971) in which he regrouped dimensionless variables and developed a dimensionless graphical relation as shown in Fig. (2.5). This figure is based on Shields diagram that includes the dependent variable in only one of the two dimensionless parameters.

2.3.3 Discussion

The literature review presented in this section reveals that one of the main reasons for the appreciable scatter in the data for initiation of motion of non-cohesive materials stems from the difficulty encountered in consistently defining critical flow conditions. The difficulty arises because no flow stage exists at which the particles are suddenly placed in motion in mass, as

movement takes place gradually over a wide range of average shear stress when the flow velocity increases. Many researchers have simply defined the critical condition as some arbitrary point in the initial movement process which has led to wide variation in their results.

2.4 STABILITY OF A SINGLE PARTICLE

Consideration is now given to study the stability of a single particle either on the stream bed or side slope. As a particle is subjected to fluid motion, its stability will be governed by the applied lift and drag. These forces grow regularly as the flow rate increases until a certain stage is reached. During this stage the particle starts oscillating and rocking irregularly without being displaced which would thus indicate the beginning of particle movement well in advance. A certain stage is reached when if the hydrodynamic forces are increased even slightly, the movement of the particle occurs which is substantially a displacement threshold.

Because of the possible variation in the magnitude of the generated hydrodynamic forces, and due to the wide variety in particle shapes and orientations, the way in which the instant movement will occur is rather indeterminate. Therefore, the movement of a particle may occur in one of the following ways:

2.4.1 Movement By Rolling

For each particle in the upper layer, either on the channel bed or side slope, there is a chance of having a point-support on the particle underneath it. If the resultant moment due to the lift and drag about the point of contact, in case of the bed particles, is greater than the moment due to the gravity force about the same point, the particle will move to some other point downstream by rolling. Whereas, the particle will roll down the sloping side, in the case of the side slope particles, if the resultant moment due to the lift and the component of the gravity force in the side slope plane is greater than that due to the component of the gravity force down the slope.

2.4.2 Movement By Sliding

When the angle between the resultant of the forces acting on the particle under consideration and the normal to the plane containing this particle is equal to the angle of repose of the material, the motion is initiated by sliding on the surface. Therefore, one may conclude that the incipient movement will occur by sliding when the following condition is fulfilled:

$$F_t > F_n \tan \phi \qquad (2.23)$$

where

F_t and F_n are the resultant forces parallel and normal to the plane containing the particle; and ϕ is the angle of repose.

2.5 OTHER FACTORS AFFECTING RIPRAP STABILITY

In addition to the hydrodynamic forces which are generated by the flowing fluid on the particles, there are some other factors governing the stability of riprap layer, which can be described as follows:

2.5.1 Rock Shape

The effect of rock shape on the riprap stability is easy to recognize if the present particle irregularities are considered. The rock shape may be classified into five general categories as depicted in Fig. (2.6). Each of them, due to numerous factors, has a certain resistance against the hydrodynamic forces which vary from one particle to another.

However, the influence of particle shape is taken into account by the angle of repose of the riprap, although an immense variety of shapes may be represented. Hence the degree of exposure to the fluid forces and consequently the rock stability would not be identical over the whole riprap blanket which makes the problem of determining the particle movement very complex.

2.5.2 Rock Grading

In the design procedure, the riprap material is characterized by its geometric size D_{50} without regard to its grading. However, in practice, as is shown in Fig. (2.7), for the same geometric size one might have a mixture covering a rather wide range of grading which possibly affects the riprap stability.

The effect of riprap grading was studied experimentally by Anderson, A.G. et al. (1970). They pointed out that in the case of grading riprap, as the smaller particles tend to fill the interstices between the larger particles, the layer thickness required to prevent the attack on the base material tends to be appreciably less than for uniform riprap material.

On the other hand, Simons, D.B. and Senturk, F. (1977) suggested that with a well distributed size range, the interstices formed by the larger particles are filled with the smaller sizes preventing formation of open pockets which affect the stability of the riprap layer.

2.5.3 Layer Thickness

It is suggested that the minimum layer thickness should be sufficient to accommodate the largest particles in the riprap layer. On the other hand, as the layer thickness increases, the particles tend to overlap and close the interstices between the particles through which the base may be exposed by the secondary action of the water. This simply means that the protective layer will be increasingly stable as the layer thickness increases which confirms the relationship between riprap stability and thickness of riprap layer.

2.5.4 Filter Properties

According to practices carried out by many engineers today, the necessity of using appropriate filters between a riprap layer and the underlying permeable soil is accepted. The filter has been

viewed primarily as a device to prevent leaching of the permeable soil through the riprap interstices. This phenomenon was demonstrated by Herman, J.K. (1984) in which the scour due to improper filter underneath the riprap downstream of the hydraulic structures was investigated. It was proved in this study that piping and leaching are sometimes the common cause of failure which would be likely to occur before any riprap erosion occurs.

The filter could be sheet cloth, graded aggregate or other suitable materials. Each of these types has its own design specifications relative to the underlying permeable soil and rock layer properties as follows:

2.5.4.1 Conventional (Inverted) filter

In order to prevent leaching of permeable soil through the riprap interstices, a protective layer must be designed to act as an inverted filter; this is called the conventional filter. This layer consists of either one or successively coarser layers of well-graded gravel, and designed according to the size of riprap particles and underlying finer soil and their gradings.

Criteria for such filters to prevent leaching as well as piping failure of dams on alluvium have been formulated by Terzaghi, K. and Peck, P. (1948). On the basis of the tests, the Terzaghi criteria were slightly modified by the U.S. Army Waterways Experiment Station at Vicksburg, Mississippi, for application in dam design as reported by Posey, C.J. (1969). Those modified formulae can be described as follows:

2.5.4.1-A Piping criteria

To prevent washing of the underlying material through the filter, the smaller particles in the filter should be small enough to trap the underlying materials. Therefore, for uneven-shaped riprap particles, the criterion is satisfied if

$$\frac{D_{15}\ (\text{filter})}{D_{85}\ (\text{base})} \quad < 4 \text{ to } 5 \qquad (2.24)$$

in which

D_i is the grain size for which i percentage of the material by weight is finer.

2.4.4.1-B Segregation criterion

To ensure that the fine particles are not separated from the filter mixture and washed out of one layer into the one beneath, the particle size distribution curve for both layers should be approximately parallel and not too far apart. This criterion is

$$\frac{D_{50}\ (\text{filter})}{D_{50}\ (\text{base})} \quad < 25 \qquad (2.25)$$

2.5.4.1-C Permeability criterion

The permeability of the filter should be sufficient for the hydraulic gradient through it to be negligible compared with that through the underlying material. The size D_{15} was selected to represent the permeability of both filter and base material and the criterion is

$$\frac{D_{15}\ (\text{filter})}{D_{15}\ (\text{base})} \quad > 4 \text{ to } 5 \qquad (2.26)$$

It was reported by Posey, C.J. (1969), that the U.S. Army Waterways Experiment Station tested the modified criteria and found it satisfactory for a sand of 0.045mm D_{50} size, and would be satisfactory for any finer sand. Therefore, to confirm these filter specifications, more tests were conducted by Posey, C.J. (1953, 1957 and 1969), in which the applicability of these criteria for a coarser sand was investigated.

On the other hand, to ensure the efficiency of a filter blanket when riprap is placed on it, Simons, D.B., and Senturk, F. (1977), recommended that the total filter thickness should be at least equal to one half of the thickness of the protective layer. Whereas Herman, J.K. (1984) concluded that the filter thickness should be at least five times the size of the largest particle contained in the filter. Furthermore, according to the investigation carried out by Thanikachalam, V. and Sakthivadivel, R. (1975), it was concluded that a thickness of two to three times the maximum filter grain diameter would be sufficient to establish a continuous layer.

2.5.4.2 Cloth (Fabric) filter

This type of filter is made from either woven or random-packed continuous plastic filter cloth which is replacing the granular filter to meet the diverse demands of the civil engineering industry. The filter requirements vary, depending upon the problem, but in almost any ground engineering application, the need to counter both permeability and piping is important.

On the basis of the filter characteristics, Stephenson, D. (1979) suggested that the maximum opening size should be not less than about 0.25mm whereas to fulfil the permeability condition, the opening between the filters should be between 5 to 30 percent of filter area. An attempt has been made by Schober, W. and Teindl, H. (1979) to extend the scope of fabric filter design rules by considering the design criteria of the granular filter. In this study, the effective pore size, O_e (taken as O_{90}) was linked to the mean particle size, D_{50}, by the following expression:

$$O_e = B \times D_{50} \qquad (2.27)$$

in which

$$B = f(C_u) \qquad (2.28)$$

C_u is the uniformity coefficient = D_{60}/D_{10}

O_e is the particular pore diameter which may be taken as effectively controlling the filtration behaviour of the fabric.

To obtain the value of B in Eq. (2.28), Schober and Teindl developed design curves incorporating a factor of safety against soil migration.

Hoare, D.J. (1982) presented a general review of the fundamentals of fabric filters and their design and pointed out the importance of the cloth filter having sufficient tensile strength to maintain separation of the various soil/granular materials involved.

Cloth filters have several advantages over granular filters. In general, the cloth filter is economical, quick and easy to install, less labour-demanding and resistant to puncturing, but some care should be taken when placing the riprap over it.

2.5.5 Manner of Placement

Riprap placement is usually carried out either by dumping directly from trucks or by hand. As a comparison between both types, Searcy, J.K. (1967) showed that the hand-placed riprap is not as satisfactory as an equivalent thickness of dumped riprap, and the percentage of failures in hand-placed riprap for slope protection is six times that of dumped riprap. This simply means that using both types with similar flow conditions, the behaviour of the protective layer will not be identical. This shows how inconsistent will be the expected results if both types are compared.

In the author's opinion, it is essential to introduce this factor in the stability criterion which could be represented by either one of the following methods:

A) Including the porosity of the protective layer which reflects the volume of voids per unit volume of riprap layer

or

B) Including the volumetric packing factor P_c which was defined by Olivier, H. (1967) as a factor relating the number of particles of a given size contained within a given volume of riprap layer as

$$P_c = \frac{\text{Unit volume}}{\text{Number of stones per unit volume x average rock volume}} \qquad (2.29)$$

On the assumption that the stones are spheres, the packing factor can be written as

$$P_c = \frac{6}{\pi N D^3} \qquad (2.30)$$

2.6 PREVIOUS EXPERIMENTAL WORK

2.6.1 Hydrodynamic Forces

Many investigations have been carried out to establish a proper criterion for treating the hydrodynamic forces acting on a non-cohesive grain lying in a bed of similar particles, over which a fluid is flowing. Among the earliest studies on the lift force in sediment motion was that reported by Jeffreys, H. (1929). In this study, the case of a cylinder lying on a plane bed with its long axis perpendicular to the flow was treated theoretically. Also, Milne-Thomson, L.M. (1968), studied the same problem analytically.

Further study of the incipient motion in turbulent flow was carried out analytically by White, C.M. (1939). However, in this study, the effect of lift force was neglected on the basis of a brief laboratory experiment.

The first quantitative observation for the hydrodynamic forces acting on a stream bed consisting of non-cohesive particles

was achieved by Einstein, H.A., and El-Samni, E. (1949). Their experiments were conducted in a laboratory channel with a bed of closely packed plastic hemispheres 68.6mm (0.225 ft) diameter which were glued to the bottom of a 0.3m wide flume in a hexagonal pattern. In this study, the lift force was measured as a pressure difference between the top and the bottom of the hemispheres. It was found that the lift force could be divided into a constant average value plus a random fluctuation superimposed over the average as shown in Fig. (2.8). The measured pressure difference between the top and the bottom of the particle, which is represented by the lift force, was expressed as

$$\Delta P = 0.178 \rho \frac{u_{35}^2}{2} \qquad (2.31)$$

where

u_{35} is the measured velocity at distance equal to 0.35 times the grain diameter above the theoretical bed level

To verify the applicability of the results obtained from the idealized bed by hemispheres to natural sediment, another series of experiments was conducted on gravel having particle diameters (D_{50}) varying between 20 and 75mm. This verification was restricted to the measurement of average values of the shear force and the lift pressure which was found from Eq. (2.31).

Chepil, W.S. (1958) carried out a series of laboratory studies in a wind tunnel to evaluate the lift and drag forces on hemispherical particles arranged in a hexagonal pattern three diameters apart centre to centre. In this study, the effective pressure distribution on hemispherical roughness element, ranging from 0.16 to 5.08 cm in height, was measured by means of a straight tube alcohol manometer. The average drag and lift forces were determined directly as a resultant pressure difference between the upstream and downstream and the top and the bottom of the hemisphere, respectively. The lift and drag were then determined analytically by integrating the measured pressure distributions.

The results revealed that the pressure on the lower portion of the hemisphere was always substantially higher than the pressure on a considerable area around the top. The pressure distribution was almost identical for nearly all sizes of hemispheres and velocities used, this is shown in Fig. (2.9). The ratio of lift to drag was essentially constant with an average value of 0.85 for all sizes and shear velocities within the Reynolds number range of 47 to 5000.

Further measurements in a wind tunnel were conducted by Chepil, W.S. (1961) to determine the relative magnitude of lift and drag on small spheres similar to soil grains. In this study, the aerodynamic pressure difference on three different sizes of spheres ranging from 3 to 51mm in diameter were determined in a like manner for different elevations of the sphere above the ground surface and for different drag velocities of the wind. The average lift force obtained was equal to only about 0.75 of the drag on a sphere resting on the bed surface.

As a result of this study, it was concluded that the lift force was at its greatest only when the sphere is on the bed surface and diminishes rapidly with height and ceases to be measurable at a short distance above the bed surface. On the other hand, the measured drag force is least when the sphere is on the ground and increases rapidly with height as long as the wind velocity increases with the height, as shown in Fig. (2.10).

The effective lift force on a small sphere in a low flow velocity was analytically studied by Saffman, P.G. (1965) in which no negative lift force was determined at low Reynolds number.

In order to establish the state of knowledge concerning sediment erosion, Vanoni, V.A. (1966) reviewed the results of several workers in this field. To identify the importance of the lift force in entraining sediment, Vanoni compared the lift pressure difference ΔP given by Einstein and El-Samni, Eq. (2.31), with the boundary shear stress τ_o which was found approximately to be 2.5 times for sediment with geometric mean standard deviation equal to 1.4.

The earliest measurements of lift force in hydraulically smooth boundary conditions (Reynolds number $R_e<5$) and transition flow conditions ($5<R_e<70$) were carried out by Coleman, N.L. (1967). He measured the drag force on 12.5mm diameter steel and plastic balls resting on top of a hypothetical bed comprising closely packed hemispheres of similar size glued to the floor of a water circulating tunnel of rectangular section.

Using a strain gauge, the effective drag was measured and the lift force was then inferred as a fraction of the particle submerged weight. It was concluded from this study that the lift force decreased through zero to become negative as R_e decreased to a value of about 15, and increased to become a positive value at large R_e.

Similar results were obtained by Watters, G.Z. and Rao, M.V. (1971) in which the lift and drag forces, acting on a 95.0mm diameter plastic sphere resting on top of several layers of identical spheres, were measured simultaneously by a parallel-link strain gauge dynamometer. The results revealed that the ratio of lift to drag, when there is no seepage, varies from 4.5 to 0.5 within the Reynolds number range of 25 to 100.

Based on the potential flow theory, Bendict, B.A. and Cristensen, B.A. (1972) obtained an analytical solution for lift forces on idealized beds composed of identical hemispheres laid in a closely-packed hexagonal pattern.

In order to verify the obtained solution, the method was applied to data from Einstein and El-Samni (1949) and Chepil (1958) which have shown acceptable agreement between theoretical and experimental results as shown in Fig. (2.11). These results imply a possible increased capability in analytical development as well as in planning experimental programmes on initiation of sediment motion.

Further experimental measurements were carried out by Cheng, E.D. and Clyde, C.G. (1972) to obtain the instantaneous fluctuation of the hydrodynamic lift and drag forces acting on an individual instrumented spherical roughness element 30 cm in diameter placed

in a 15m long, 2.45m wide flume. The roughened bed was formed by hollow plastic spheres and hemispheres 30cm diameter. Firstly, the hemispheres with the closest packing possible were attached to the bed, then a layer of spheres, in the most densely packed arrangement, was embedded on the top of the hemispheres and held in place by screws. The instrumented sphere, which contained a set of strain gauges, was placed at approximately three-quarters of the channel bed length downstream from the upper end. A cavity was left in the bed a short distance downstream from the instrumented sphere to allow the placement of a variable density sphere which was free to move for the purpose of observing the critical condition. Steel blocks of different sizes were used to vary the specific gravity of the instrumented sphere from 1.1 to 1.5.

In this study, the discharge was slowly increased until the instrumented sphere moved out of its cavity. When such incipient motion was established, the instantaneous drag and lift forces were recorded. A simple record is shown in Fig. (2.12).

As a result of the experiments, it was concluded that the probability density of the fluctuating lift and drag forces at the initiation of motion were approximately normal distributions as may be concluded from Fig.(2.12). The relative intensity of the lift force was found to be independent of the depth of flow and slope of the channel bed.

Using basic principles of fluid mechanics, Aksoy, S. (1973) reported an experimental study on forces acting on a sphere near a solid boundary. The simultaneous values of drag and lift forces acting on an instrumented sphere were directly measured by using a specially designed transducer. The instrumented sphere was made of plexiglass with a diameter of 2cm which was placed on the bottom of the flume. The lift and drag forces were transferred to two springs on each of which a strain gauge was mounted. As a result, it was found that the simultaneously measured drag and lift forces are fluctuating about mean values over a range of Reynolds number of 2700 to 6600 as shown in Fig. (2.13). The mean values of measured

lift forces were not as large as expected and they were approximately one-seventh of the drag force. The variation in the calculated drag and lift coefficients were not completely determined due to the limited range of experiments.

Davies, T.R. and Samad, M.F. (1978), performed an experimental study to measure the lift force in hydraulically smooth and transitional flow regions to investigate the flow condition under which negative lift force occurs. In order to generate such measurable lift force 25.4mm diameter spheres were used. The upper flow boundary consisted of a fixed layer of spheres, and the test sphere was attached to a rigid rod passed through a 5mm diameter hole in the fixed layer in a way that it could freely move. The end of this rod was attached to a null deflection type balance from which the lift force could be read.

As a result of the experimental work, it was concluded that the resultant lift force on exposed bed particles changes from strongly negative to strongly positive as the value of the grain size Reynolds number increases through a value of about 5.

In order to determine the upward driving force that a particle experiences as it begins to travel upwards from a location near the bottom, Sumer, B.M. and Oguz, B. (1978), and Sumer, B.M. and Deigaard, R. (1981) carried out a visualization study concerned with the three-dimensional motions of small heavy particles with diameter less than 4.0mm and specific gravity slightly heavier than that of water. Using a stereo-photo-grammetric technique, the particle motions close to the bottom of a turbulent open channel flow were recorded.

Sumer, M.B. (1985) utilized the path data recor ed previously to calculate the lift force on the moving particle at the instant when the particle is lifted up from near the bottom. As a result of this study, it was found that in the smooth wall case, the lift force appears to reach a weak maximum, and then decreases with the distance from the wall, while in the rough wall case, it decreases appreciably with the distance from the wall.

2.6.2 Seepage Effect

Seepage is a common occurrence in rivers and canals and is a consequence of the difference in water levels. Therefore it is worthwhile to study the effects of seepage on the non-cohesive particles of the uppermost layer to determine whether or not seepage can play an important role in the stability of particles contained in this layer, which is obviously relevant to the current study.

Few experimental studies have been carried out to determine the magnitude of the seepage force on the interfacial bed particles. Martin, C.S. (1966 and 1971) performed an experiment on the determination of the magnitude of seepage force on the uppermost bed particles for the case of seepage flow only with no effect of channel flow. From the results of the instability and erosion tests performed by Martin, it was concluded that the seepage force per unit volume on the top grains is given by

$$(1/3)\ \gamma I < F_{se} < \tfrac{1}{2}\ \gamma I \qquad (2.32)$$

Further laboratory tests were conducted by Martin, C.S. (1970) to study the incipient motion due to flow into and out of a permeable bed. It was concluded from this study that the seepage out of the bed does not affect incipient motion measurably because the seepage force may become insignificant once a bed particle rocks slightly out of its position. On the other hand, seepage into the bed may either enhance or hinder incipient motion, depending upon the relative effect of the boundary shear stress and the seepage force, both of which depend on the seepage flow.

The effects of seepage on the hydrodynamic lift and drag forces acting on an idealized bed of spherical particles of 95.0mm diameter were described by Watters, G.Z. and Rao, M.V. (1971). In this study, the measurements carried out with and without seepage revealed that the effect of seepage is to modify the velocity profile near the channel bed which consequently affects the stability of the particles. It was also found that effluent seepage

decreases the drag regardless of the position of the particle, and the effect of seepage is to increase or decrease the lift force depending upon whether the seepage is respectively upward or downward through the bed.

The effect of seepage on non-cohesive materials placed on an alluvial channel immediately downstream from a hydraulic structure was clarified by Herman, J.K. (1984). In this study, it was shown how a properly designed filter is needed to eliminate the erosive effect of the influent seepage when the negative piezometric gradient occurs.

2.6.3 Discussion

It has been shown throughout this part of the study that particles comprising a protective layer are experiencing many type of forces, and their stability, and ultimately the stability of the whole structure, is not only influenced by the hydrodynamic forces, but also there are numerous other factors to be considered.

Some attempts have been made to measure the hydrodynamic forces, which were mostly carried out on stream beds consisting of closely packed hemispheres. In other words this means none of these measurements was conducted to investigate the forces acting on side slopes. This situation made it necessary to measure the forces acting on side slope particles, which will be discussed later through the following chapters.

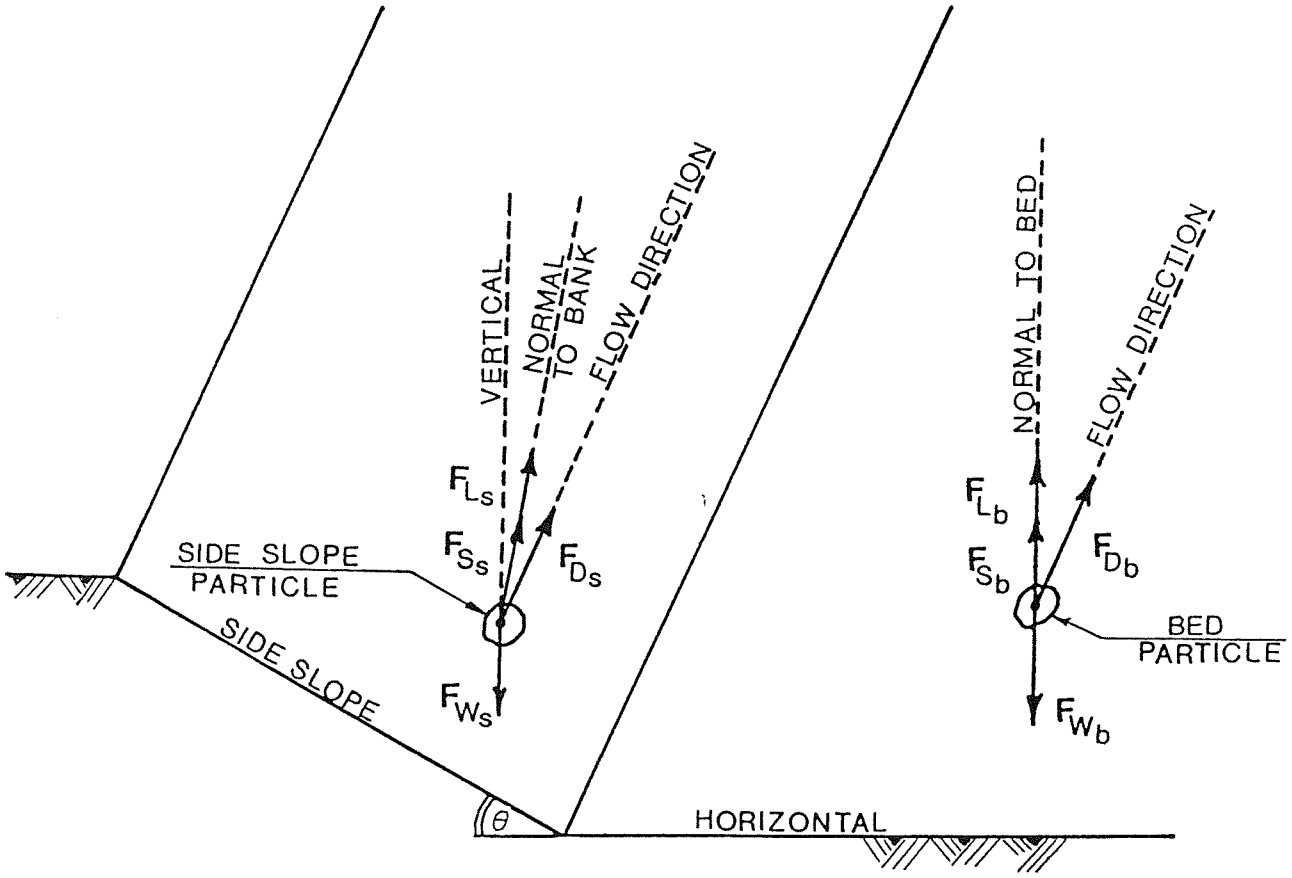

FIG. 2-1 : FORCES ACTING ON BED AND SIDE SLOPE PARTICLES

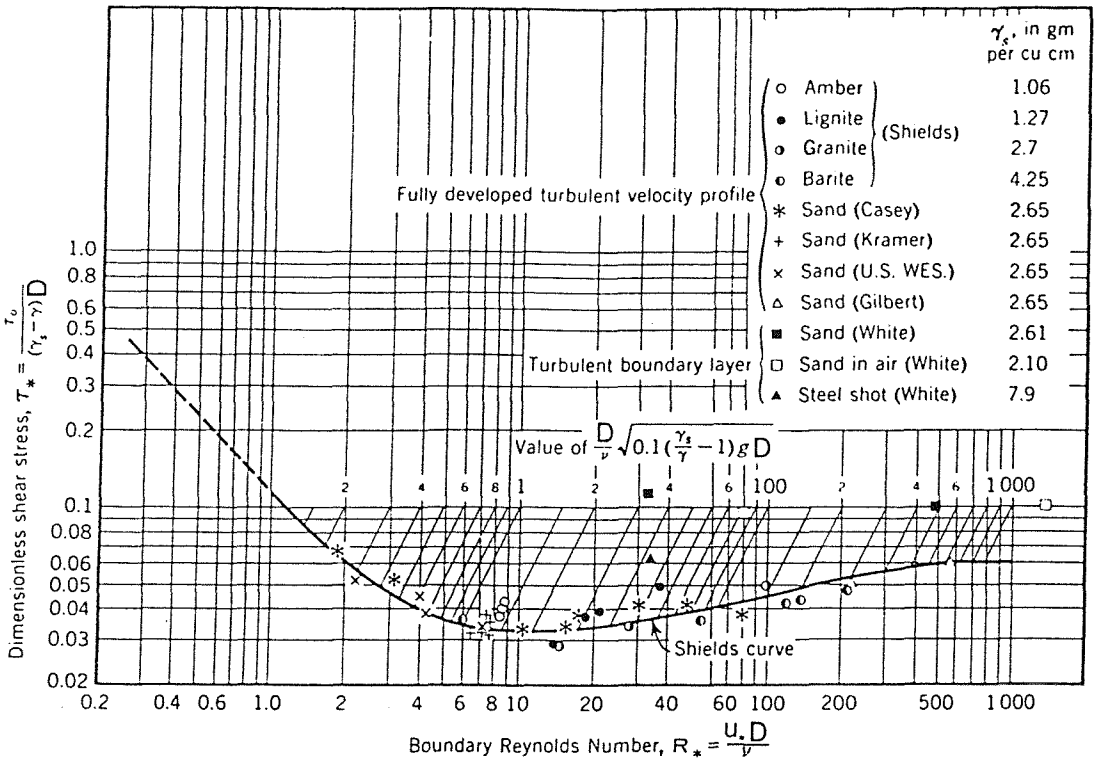

FIG. 2-2 : SHIELDS DIAGRAM WITH SOME OTHER DATA ADDED AFTER VANONI, 1966

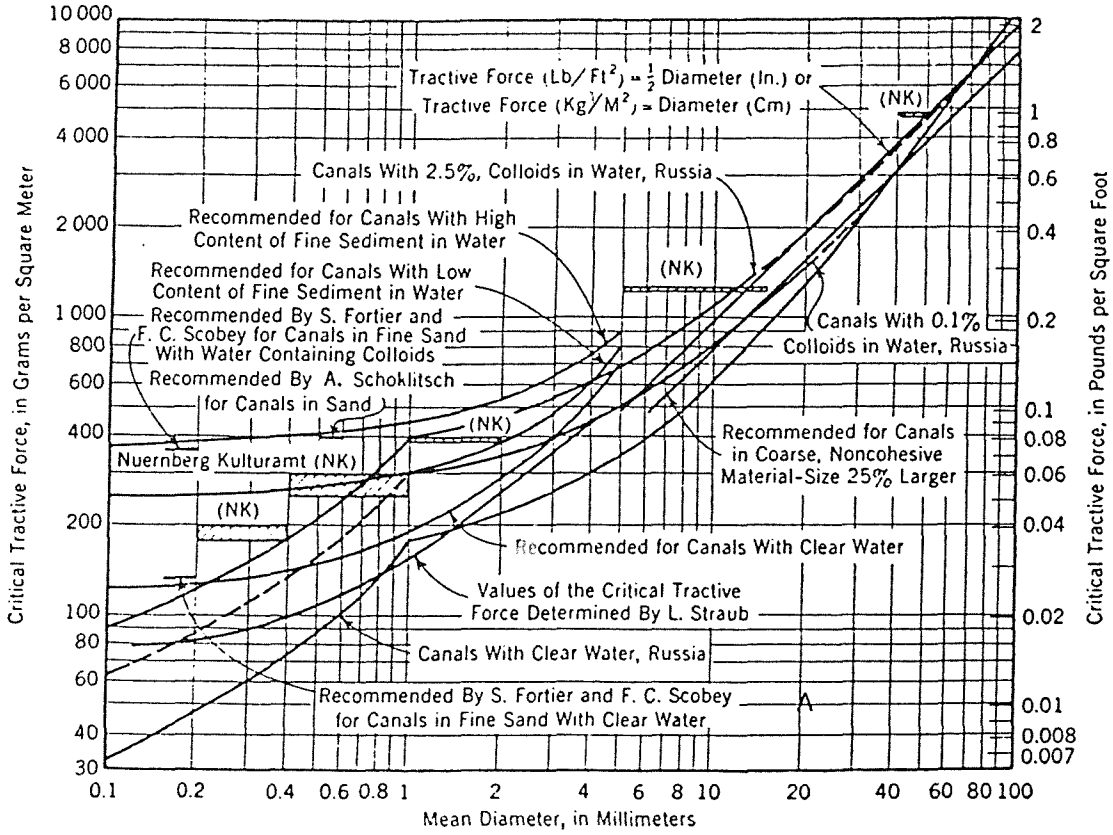

FIG. 2-3 : CRITICAL TRACTIVE FORCE AS A FUNCTION OF GRAIN DIAMETER (AFTER LANE, 1953)

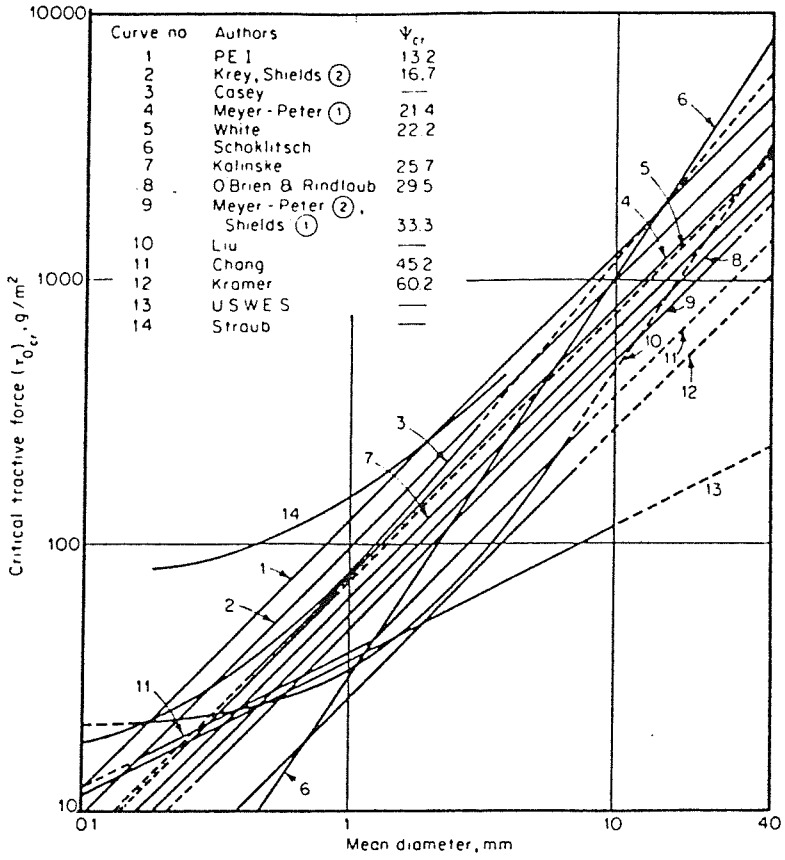

FIG. 2-4 CRITICAL TRACTIVE FORCE VS PARTICLE SIZE AFTER CHIEN 1954

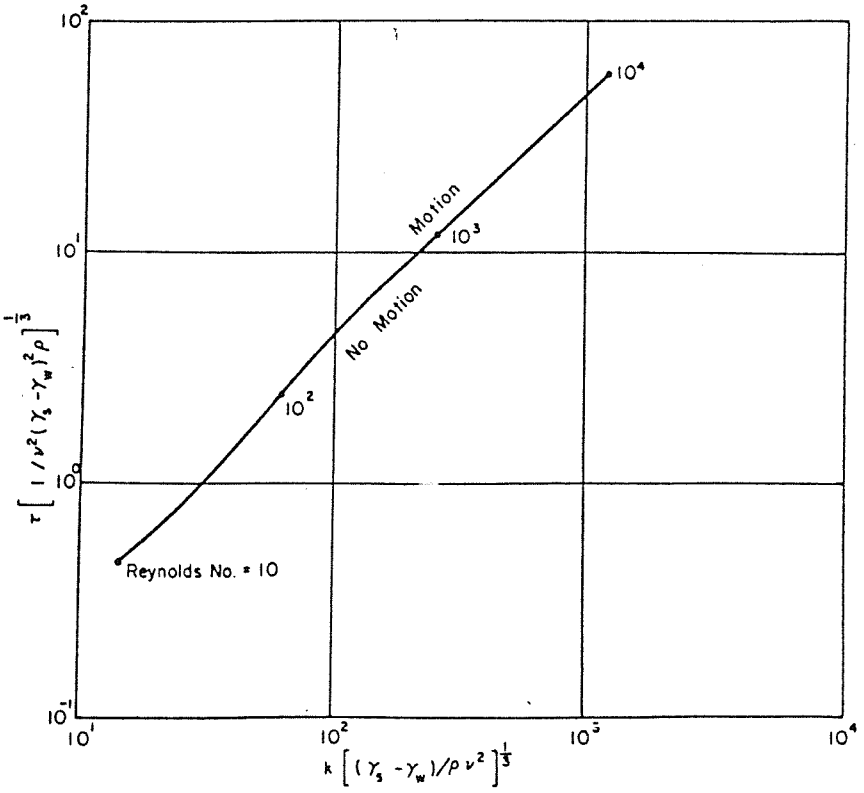

FIG. 2-5 MODIFIED SHIELDS DIAGRAM AFTER GESSLER 1971

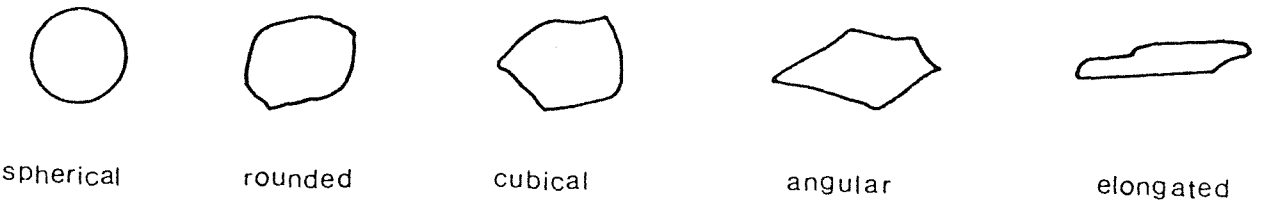

FIG. 2-6 ROCK SHAPES

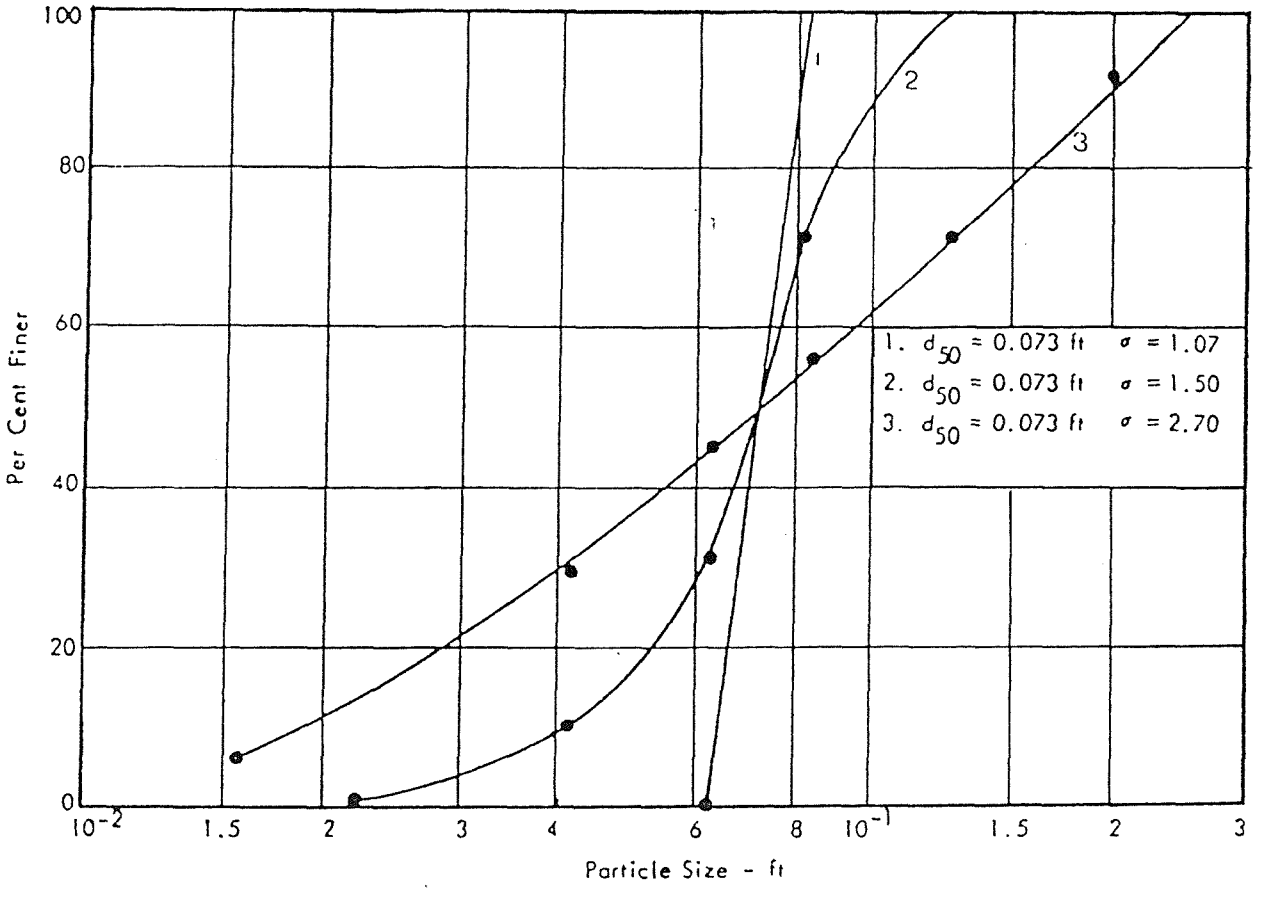

FIG. 2-7 DIFFERENT ROCK MIXTURES HAVING THE SAME MEAN DIAMETER AFTER ANDERSON, 1970

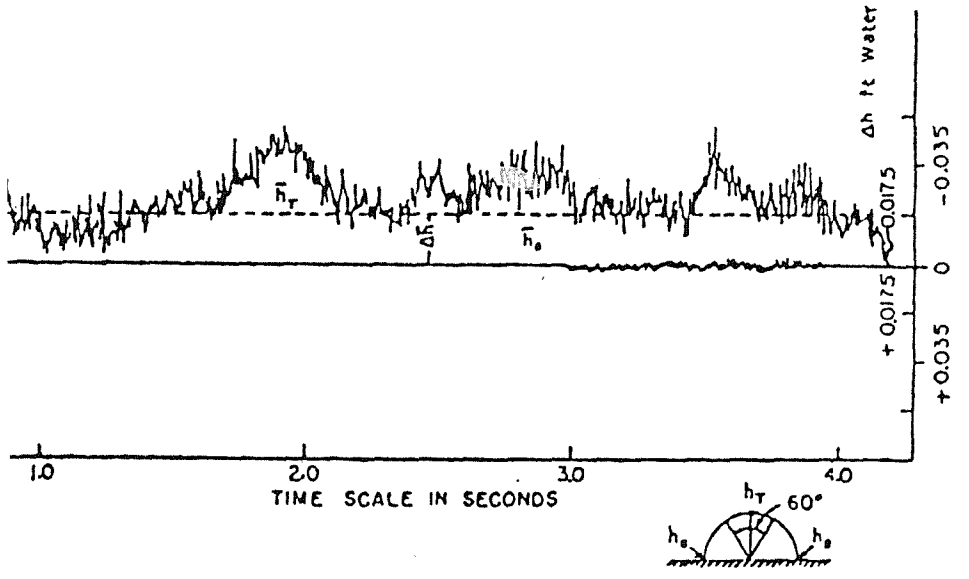

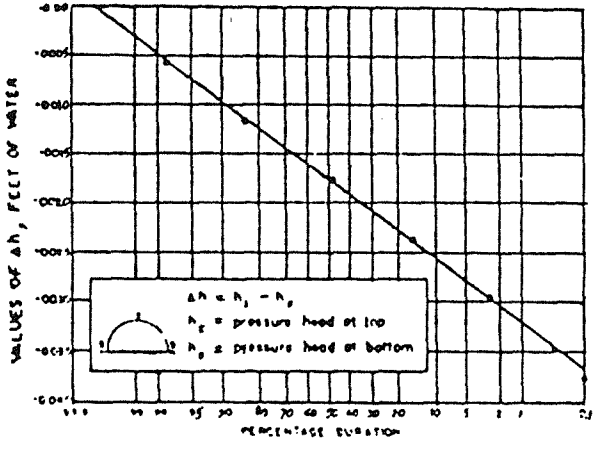

Duration of lift pressures.

FIG. 2-8 EINSTEIN AND EL-SAMNI RESULTS (1949)

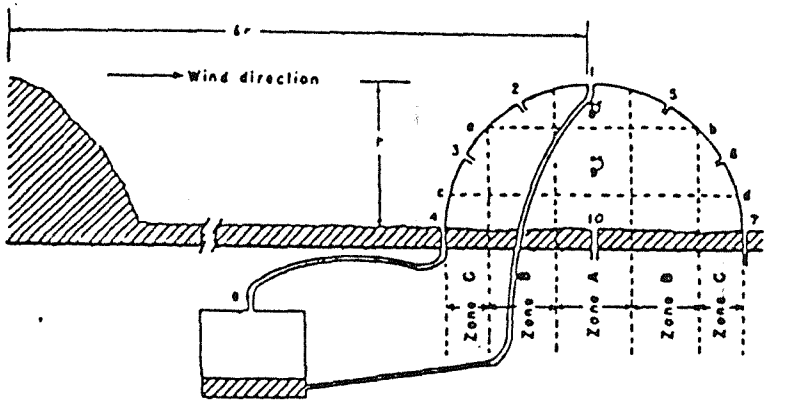

pressure measurement setup

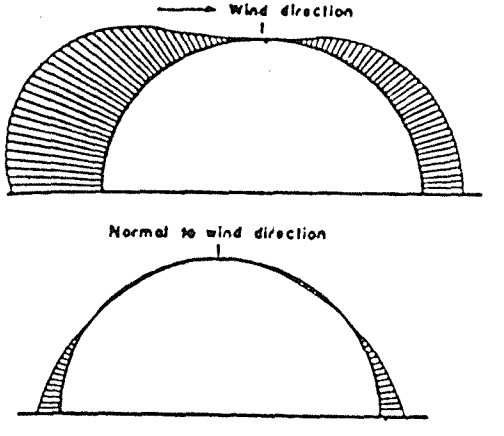

measured pressure differences

FIG. 2-9 CHEPIL'S SETUP AND RESULTS (1958)

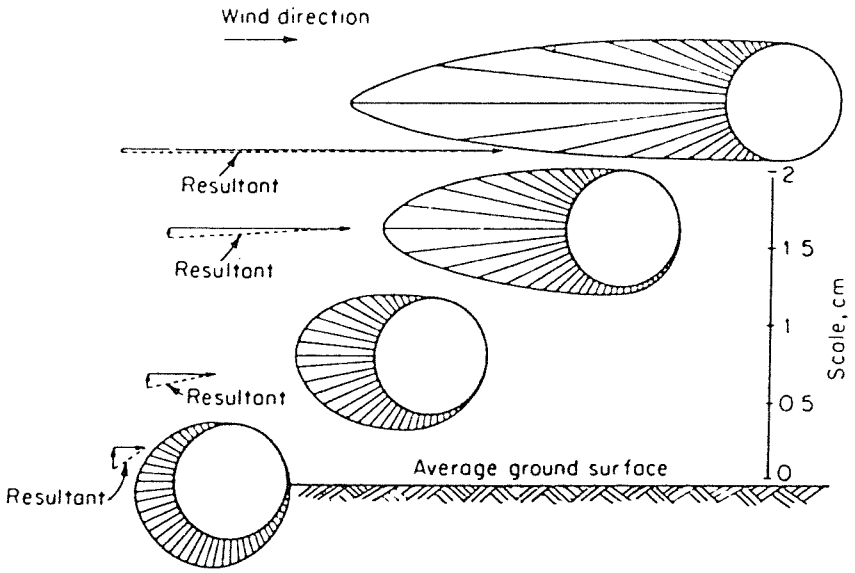

Fig.2–10: Change of pressure pattern of a grain in a windstream at various positions above the ground. [*After* CHEPIL (*1961*).]

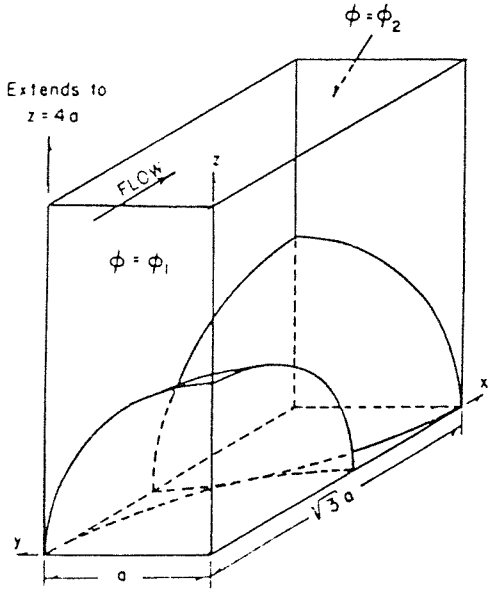

Solution Space for Closely-Packed Hemispheres

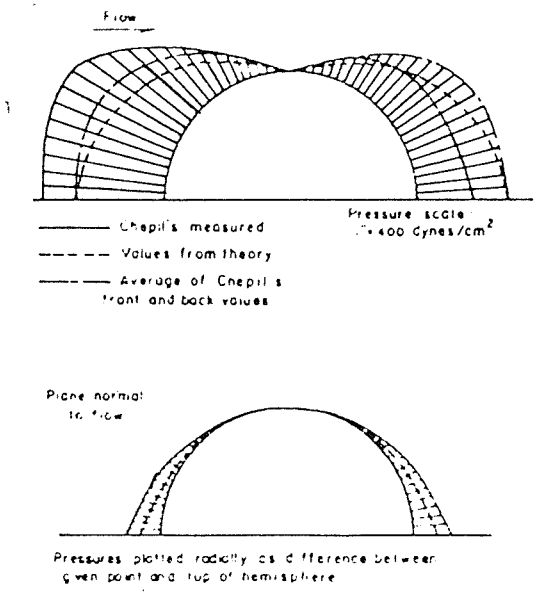

theoretical and measured pressure distribution for Chepil's hemisphere

FIG 2–11 : BENEDICT AND CHRISTENSEN RESULTS , 1972

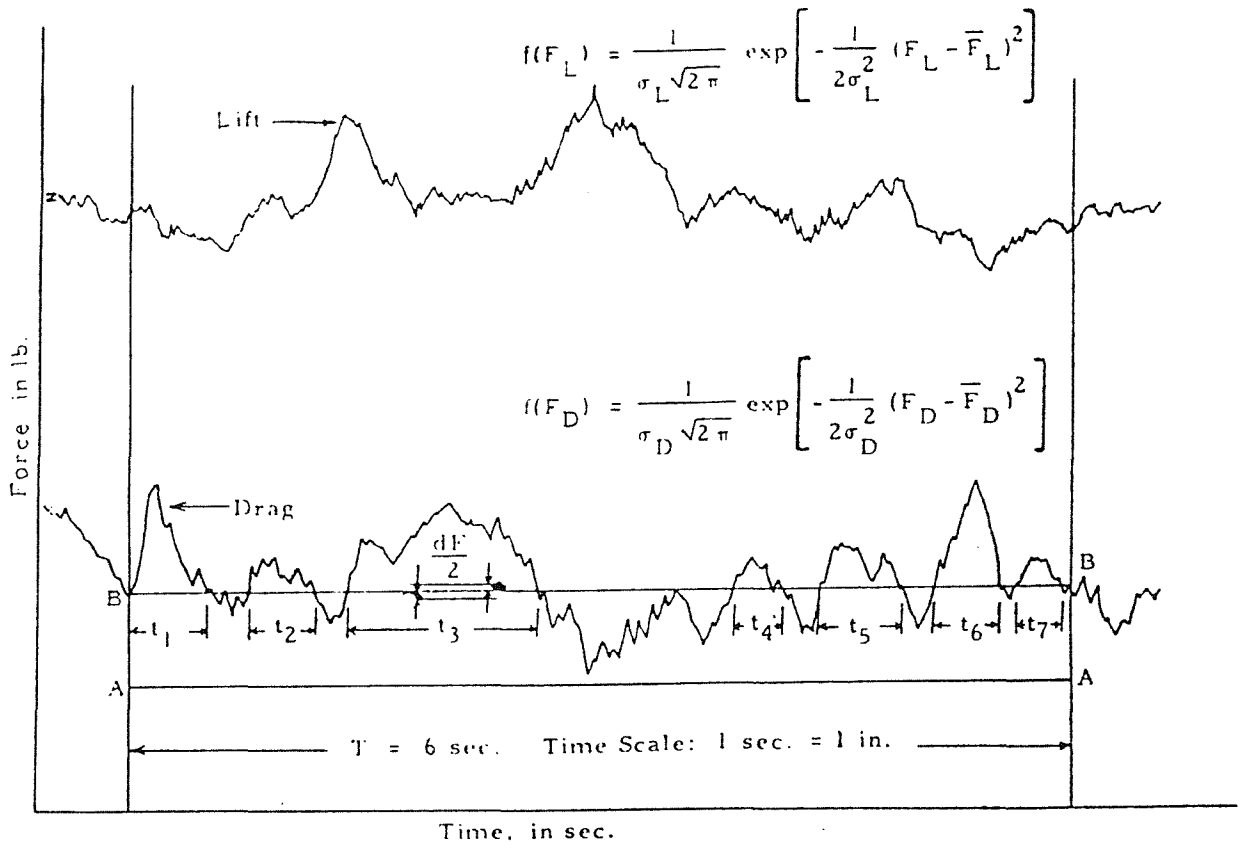

A Sample of the Counting Method in Analysis of the Instantaneous Lift and Drag Forces

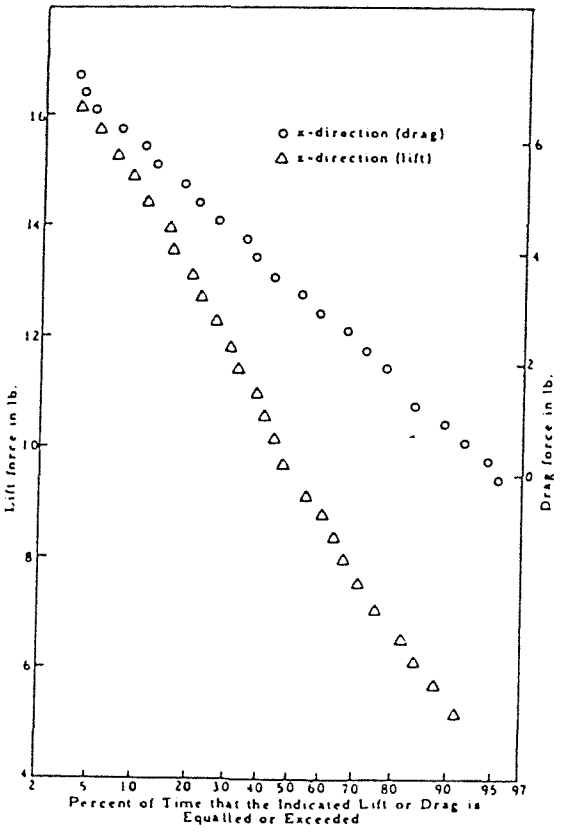

Distribution of Instantaneous Force

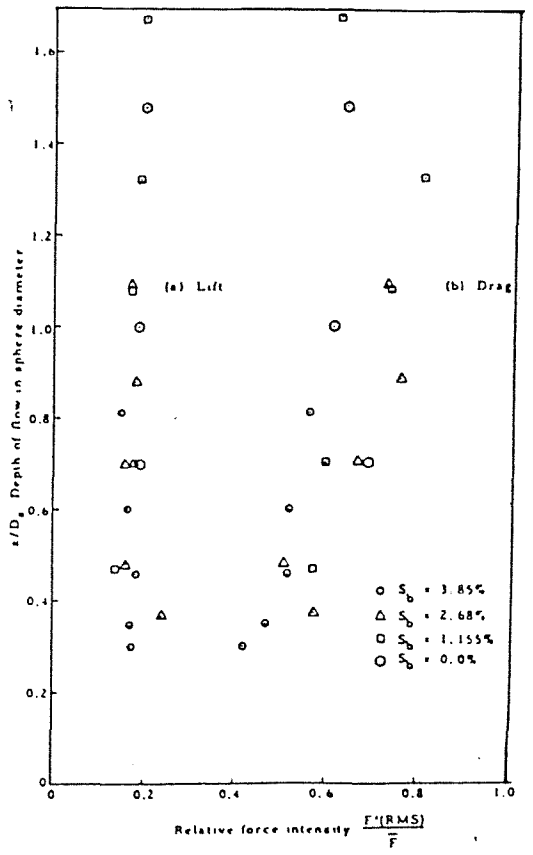

Comparison of the Relative Force Intensity

FIG.2-12:CHENG AND CLYDE RESULTS (1972)

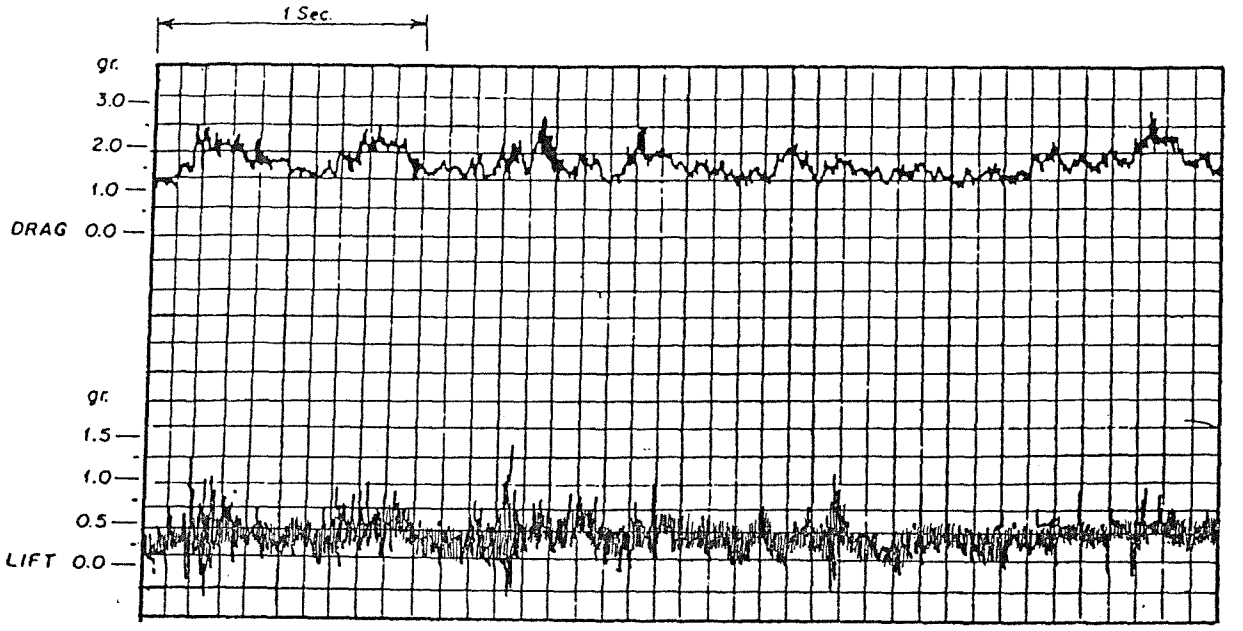

RECORDED VALUES OF LIFT AND DRAG FORCES ON A TEST RUN

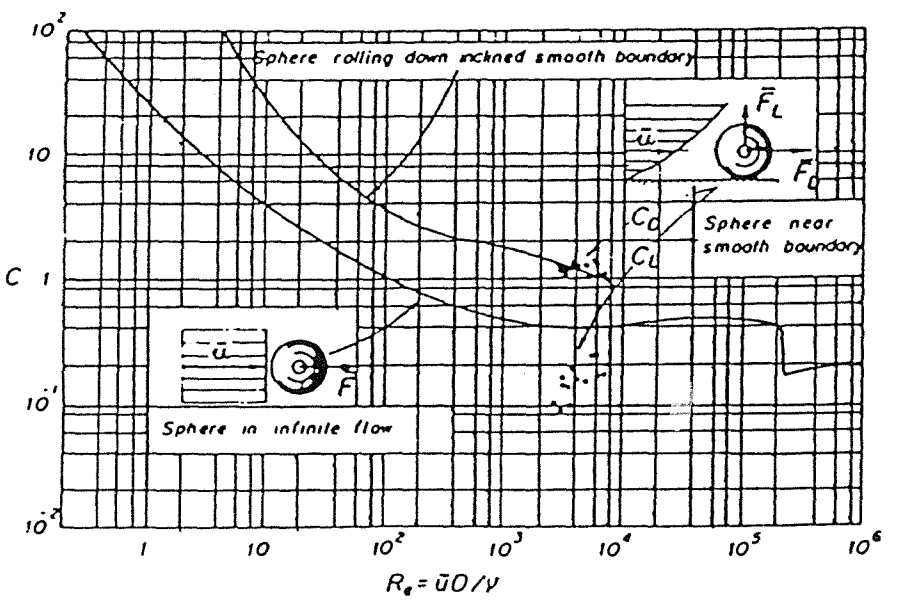

VARIATION OF C WITH REYNOLDS NUMBER

FIG. 2-13 THE RESULTS OBTAINED BY AKSOY (1973)

CHAPTER THREE

RIPRAP PROTECTION SIZING METHODS

3.1 INTRODUCTION

Riprap has been defined as a protective layer, randomly placed, to resist the erosive power of flowing water. Stone or rock fragments of different sizes are widely used and are found to be the most economical and satisfactory material. Efficient design, of such riprap protection, demands that a suitable size should be provided with full consideration given to the stability criteria achieved in the previous chapter.

In fact, many empirical relationships have been proposed for sizing riprap, most of which were developed for overflow rockfilled dams as well as protection of the upstream slope of earth dams. These relationships are referred to in this study as the empirical methods or approaches. Also a large number of design criteria for sizing riprap have been recently developed. These methods have generally been derived from the viewpoint of the equilibrium of a single particle in a flowing stream, and will be referred to as deterministic methods.

On the other hand, considering the stability of riprap protection in relation to the probability of movement of individual rocks forming the protective layer, a significant contribution has been recently made by demonstrating how such probabilistic models can be developed so as to establish the adequacy of the protective layer. These are referred to as probabilistic methods.

As previously stated, the objective of the current study is to achieve a design criterion for side slope riprap protection, on the basis of the results obtained from experimental measurements. Therefore, it is worthwhile to review all the methods for sizing riprap that are relevant to this study.

A complete summary of the work carried out on the problem of sizing riprap for either stream bed or side slopes is presented in this chapter.

3.2 THE EMPIRICAL METHODS

These methods were developed as a result of a constant search for a rational method for sizing riprap for different purposes as protection of highway embankments, overflow embankments, stream banks and slopes of dams. Most of these empirical relationships were derived individually as well as by different sources. Some attempts were made to generalize these empirical relationships, but due to the difficulty of the problem as well as the limited knowledge on the nature of the hydrodynamic forces acting on the particles, some gross assumptions have been made in some of them. A brief review of these methods follows:

3.2.1 Bureau of Public Roads

The summary of (1948) by the ASCE sub-committee on slope protection of earth dams was utilized by Searcy, J.K. (1967) to prepare the Bureau of Public Roads, Hydraulic Engineering Circular, No. 11, in which two graphic relationships were developed. Fig. (3.1) is employed to convert the mean flow velocity u into a corresponding velocity against the stone u_s which can be then used to interpolate the equivalent spherical diameter of the rock by using Fig. (3.2).

The Bureau recommended a grading specification for riprap patterned after the grading recommended by Murphy, T.E. and Grace, J.L. (1963). These gradings were called the A-rock for which ($\frac{D}{D_{50}}$ = 1.08), and B-rock for which ($\frac{D}{D_{50}}$ = 1.36) where D is the representative grain size; and D_{50} is the mean particle size.

A factor of safety analysis of the above method was carried out by Stevens, M.A. and Simons, D.B. (1976). This analysis proved that the safety factors for the sizing curves in Fig. (3.2) are always less than unity.

3.2.2 U.S. Bureau of Reclamation

Comprehensive research was conducted by the U.S. Bureau of Reclamation to investigate the hydraulic design of stilling basins and energy dissipators, in which Fig. (3.3) was developed to determine the maximum stone size in a riprap mixture downstream of stilling basins.

3.2.3 U.S. Army Corps of Engineers

In order to determine the effective rock size, Campbell, F.B. (1966) formulated a design criterion by making a stability analysis of an idealized cubical element resting on a channel bed and side slope. In this study, Campbell used an equation for the construction of dams by depositing rock in running water, which was developed by Izbash (1936) to formulate the relation

$$W = 1.22 \times 10^{-5} u_r^6 \qquad (3.1)$$

where

$$u_r = 8.5\, u_* \qquad (3.2)$$

in which

W is the weight of stone in pounds;
u_* is the shear velocity;
and u_r is the reference velocity.

Further research was carried out by the Corps of Engineers (1970), in which the following Izbash's formula for movement of stones in flowing water was adopted.

$$u = C\,[2g(S_s-1)]^{\frac{1}{2}}\, D^{\frac{1}{2}} \qquad (3.3)$$

in which

u is the velocity (ft/sec);

g is the acceleration due to gravity;

S_s is the specific gravity of the stone;

D is the stone diameter;

and C is the Izbash's turbulent coefficient which was taken equal to 0.86 for high turbulent level flow and 1.20 for low turbulent level flow.

3.2.4 California Division of Highways

An empirical expression for sizing stream bank protection was used by the California Division of Highways (1970) as follows:

$$W = \frac{2 \times 10^{-5} \times S_s \, u^6}{(S_s - 1)^3 \sin^3 (70^o - \theta)} \qquad (3.4)$$

in which

θ is the angle of side slope in degrees;

and W is the minimum weight of the outside stones in pounds.

Assuming S_s = 2.65 and the particles are spheres with average diameter D_{50}, Eq. (3.4) for horizontal flow on side slopes might be written as

$$\frac{0.27 \, u^2}{(S_s - 1) g \, D_{50}} = \sin (70 - \theta) \qquad (3.5)$$

For flow on level beds, substitute θ = zero in Eq. (3.5) which reduces to

$$\frac{0.29 \, u^2}{(S_s - 1) g \, D_{50}} = 1 \qquad (3.6)$$

3.2.5 ASCE Task Committee on Preparation of a Sedimentation Manual

This Committee in (1972) recommended the formula proposed by Izbash (1936) for the construction of dams by depositing rock in running water. The formula was modified to take into account the slope of the bank and can be written as follows

$$W = \frac{4.1 \times 10^{-5} S_s u^6}{(S_s-1)^3 \cos^3 \theta} \qquad (3.7)$$

in which

W is the weight of the stone in pounds;
u is the flow velocity (ft/sec);
and S_s is the specific gravity of the stone.

3.2.6 University of Minnesota

A method to determine size of riprap to line an entire channel section has been proposed by Anderson, A.G., et al. (1970). The method applied to channels that are trapezoidal or triangular in shape that are essentially straight in alignment. The proposed equation relating size of riprap to the discharge and channel geometry is

$$Q = \frac{1}{118} \frac{D_{50}^{5/2}}{S_e^{13/6}} \frac{P}{R} \qquad (3.8)$$

in which

P is the wetted perimeter (ft);
S_e is the slope of the energy gradient;
and R is the hydraulic radius (ft).

Eq.(3.8) is based on the maximum shear stress related to rock diameter and Manning's equation of flow. It can be seen that for a fixed channel size, P/R, the riprap size are a function of Q and S_e so that a family of design curves can be made for fixed P/R values.

3.3 DETERMINISTIC APPROACH

To assess the relative importance of factors affecting the riprap stability of coarse non-cohesive particles, and to make it possible to predict the adequacy of the protective layer against the hydrodynamic forces due to the flowing water, the deterministic approach was introduced. According to this method, the stability of a side slope is represented by a safety factor computed from equations relating the flow characteristics as well as the other geometric factors to the stability of individual particles.

In view of the fact that prediction of the side slope safety factor, using the deterministic approaches, involved many factors such as magnitude and direction of the mean velocity, angle of side slope, size and angle of repose of the material, one may conclude that the deterministic method is more reliable than the empirical which is restricted to specific conditions.

A discussion of the different available approaches for determining riprap size follows:

3.3.1 Lane's Method

The first attempt to establish the hydrodynamic force under which either a channel side or a bed will be in a state of incipient motion was developed by Lane, E.W. and Carlson, E.J. (1953), and Lane, E.W. (1955). In this method for designing a stable channel, Lane identified the forces that caused the erosion of a coarse non-cohensive material in a steady uniform condition, as depicted in Fig. (3.4). These forces are

1) The force F due to the action of flowing water which acts in the flow direction and tends to dislodge the particle.

2) The force G due to the weight of the particle which acts vertically downward to resist the movement in the case of the bed particles; whereas in the case of the side slope particles, the force G acts to roll the particles down the sloping side.

The movement of the particle will begin when the resultant of these two forces is large enough to initiate the threshold condition. In Lane's study the tractive force was defined as the force which the flowing water exerts on a channel boundary. This force was evaluated by equating the boundary roughness with the component of the water weight in the flow direction to obtain

$$\tau_o = \rho g R S_e \tag{3.9}$$

in which

τ_o is the mean value of tractive force per unit wetted area;
ρ is the water density;
R is the channel hydraulic radius;
and S_e is the energy slope.

It was suggested by Lane that in most canals of the shape used for irrigation, the tractive stress near the middle of the bottom closely approaches that in an infinitely wide channel. Hence Eq. (3.9) can be written as

$$\tau_o = \rho g y S_e \tag{3.10}$$

in which y is the flow depth.

Using membrane analogy and finite-difference methods, the shear stress distribution, for trapezoidal, triangular and rectangular channels, was obtained in terms of the maximum bed stress as given in Fig. (3.5). These results indicate that within the limits of the usual proportions of a typical canal section, the maximum shear stress is about equal to $\rho g y S_e$ and $0.75\ \rho g y S_e$ for the bed and sides of the channel respectively, and zero shear stress exists in the corners.

Therefore, to determine the maximum tractive stress on the side slope, Eq. (3.10) can be utilized as

$$\tau_{oB} = C_T \rho g y S_e \qquad (3.11)$$

in which

C_T is the tractive stress coefficient determined from Fig. (3.5) for the given values of side slope ratio and bed width to flow depth ratio.

As a result of the considerable field data studied by Lane, he defined the permissible tractive force as "the maximum unit tractive force (shear force) that will not cause serious erosion of channel bed or side slopes". From a study of the extensive field data, he proposed the following expression for the tractive stress exerted on a canal bed of rock with S_s equal to 2.56.

$$\tau_s = 0.75\ D_{75} \qquad (3.12)$$

in which

D_{75} is the rock size (in mm), for which 75 percent of the material by weight is finer.

To apply Eq. (3.12) for different specific gravities, it might be modified to

$$\tau_s = 0.49 \times 10^{-4}(S_s - 1)\ \rho g\ D_{75} \qquad (3.13)$$

To relate the stability of side slope materials to those on a horizontal bed, Lane and Carlson (1953) formulated a reduction factor which is defined as "the ratio of the tractive force required to start motion on the sloping sides to that force required, in the same material, to start motion on a level surface". This factor was expressed as

$$K = \cos\theta \sqrt{1 - \frac{\tan^2\theta}{\tan^2\phi}} \qquad (3.14)$$

in which

ϕ is the angle of repose of the material.

Fig. (3.6) shows the value of K for different values of ϕ and θ. Using the reduction factor K, the permissible tractive stress for a side slope can be evaluated as

$$\tau_{sB} = \tau_s \times K \tag{3.15}$$

or

$$\tau_{sB} = 0.49 \times 10^{-4} \; K(S_s-1) \rho g D_{75} \tag{3.16}$$

To assess the side slope stability, using Lane (USBR) approach and a given flow condition, the terms τ_{oB} and τ_{sB} should be calculated and then the side slope adequacy established according to the following criteria:

$\tau_{sB} > \tau_{oB}$ no movement will occur

$\tau_{sB} = \tau_{oB}$ the side slope is in incipient condition

$\tau_{sB} < \tau_{oB}$ the failure will occur

The safety factor, SF, for the side slope adequacy can be defined as the ratio of the permissible tractive stress, τ_{sB} to the actual tractive stress τ_{oB}. If SF is greater than unity, the riprap is safe and no movement will occur; if SF is unity, the riprap is at the condition of incipient motion; and if SF is less than unity, the riprap will fail.

3.3.2 Stevens and Simons' Methods

Comprehensive stability hypotheses for sizing riprap for stream bank and bed protection were formulated by Stevens, M.A. and

Simons, D.B. (1971 and 1976). On the basis of stability of a single particle as a function of the magnitude and direction of the stream velocity, angle of repose and the side slope angle, the forces acting on it, under uniform turbulent flow conditions and in the absence of seepage and wave forces, were identified as the lift force, F_L, the drag force, F_D and the submerged weight of the particle, W.

The safety factor SF was defined as "the ratio of the moments of forces resisting rotation of the rock particle out of the riprap blanket to the moments tending to dislodge the particle out of the riprap layer into the flow". At the critical condition, the riprap particles have a safety factor of unity; if the safety factor is greater than one, the riprap is considered safe from failure; if the safety factor is less than one, rocks are washed from the riprap layer and failure of protection may occur. To assess the adequacy of either stream bed or side slopes, Stevens and Simons developed three different methods for sizing riprap which can be described as follows:

3.3.2.1 First method

3.3.2.1-A Stability on plane beds

Referring to Fig. (3.7), where α is the bed slope on which the particle is resting, the forces that act on the particle lying on the plane bed are

1) The resultant of the hydrodynamic drag F_D acting parallel to the flow motion.

2) The hydrodynamic lift F_L acting upward and perpendicular to the bed slope.

3) The submerged weight of the particle W acting vertically downwards.

For the purpose of deriving an expression for the incipient motion, Stevens and Simons (1971) adopted Shields parameter τ_* for the fully rough turbulent flow with a numerical value of 0.047 which was obtained by Gessler, J. (1965) (see Eq. (2.22)). Then the final stability criterion for two dimensional, uniform steady flow on plane sloping beds was derived as

$$SF = \frac{\cos\alpha \tan\phi}{\eta \tan\phi + \sin\alpha} \tag{3.17}$$

in which

$$\eta = \frac{0.4\ u^2}{(S_s-1)gD_m} \left(\frac{D}{y}\right)^{1/3} \tag{3.18}$$

where

α is the slope angle (in degrees) of the plane bed;
D_m is the volume weighted effective grain size;
y is the local depth of the flow;
η is the stability number;
and SF is the particle safety factor.

Considering the effect of seepage, the modified stability equation was obtained as

$$SF = \frac{\cos\alpha \tan\phi}{(\eta+\varepsilon)\tan\phi + \sin\alpha} \tag{3.19}$$

in which

$$\varepsilon = \frac{i(1+e)}{(G-1)} \tag{3.20}$$

where

ε is the ratio of the seepage force to the submerged weight;

i is the seepage flow hydraulic gradient;

e is the void ratio;

and G is the ratio γ_s/γ_w.

3.3.2.1-B Stability on side slope

Assuming the bed slope angle α = 0 and θ is the side slope angle in degrees, the forces that affect the stability of a single particle placed on the side slope are illustrated in Fig. (3.8). These are

1) The resultant of the hydrodynamic drag F_D which acts parallel to the flow direction.

2) The resultant of the hydrodynamic lift force F_L acts perpendicular to the side slope plane.

3) The submerged weight W acts vertically downwards.

The formula for the safety factor with no seepage effect is then:

$$SF = \frac{\cos\theta\tan\phi}{\eta'\tan\phi+\sin\theta\cos\beta} \qquad (3.21)$$

in which

$$\eta' = \frac{1 + \cos\delta}{2}\,\eta \qquad (3.22)$$

$$\eta = \frac{0.4u^2}{(S_s-1)gD_m}\left(\frac{D}{y}\right)^{1/3} \qquad (3.23)$$

$$\delta = 90 - \lambda - \beta \qquad (3.24)$$

$$\tan \beta = \frac{\cos \lambda}{\frac{2\sin\theta}{\eta \tan\phi} + \sin \lambda} \qquad (3.25)$$

where

β is the angle (degrees) between the resultant vector R and the downstream component of submerged weight vector;

λ is the angle (degrees) between the horizontal and the velocity vector in the plane of the side slope;

θ is the side slope angle (degrees);

η' is the particle stability factor modified for side slope;

and δ is the angle (degrees) between the resultant vector R and the drag vector.

It was assumed in this study that for both banks the velocity vectors are parallel to the bed, i.e., $\lambda = 0$, so Eq. (3.25) can be written as

$$\tan \beta = \frac{\eta \tan\phi}{2 \sin\theta} \qquad (3.26)$$

To include the effect of the seepage force which acts normal to the side slope plane, Eq. (3.21) was modified as

$$SF = \frac{\cos\theta \tan\phi}{(\eta' + \varepsilon)\tan\phi + \sin\theta\cos\beta} \qquad (3.27)$$

Other equations are the same as before.

3.3.2.2 Second method

Considering the boundary shear stress as a design parameter,

and based on the Shields criterion for the incipient movement condition, Stevens, M.A. and Simons, D.B. (1976), studied the stability of individual particles from the viewpoint of interaction between two particles either on a stream bed or side slope as follows:

3.3.2.2-A Stability on plane beds

For flow on a plane bed sloping α degrees to the horizontal, the following stability formula was developed.

$$SF = \frac{\cos\alpha \tan\phi}{\eta\tan\phi + \sin\alpha} \tag{3.28}$$

in which

$$\eta = \frac{21\tau_s}{(S_s-1)\gamma D} \tag{3.29}$$

$$\tau_s = \rho\, g\, R\, S_e \tag{3.30}$$

3.3.2.2-B Stability on side slopes

The safety factor for an individual particle placed on a stream bank was determined as follows:

$$SF = \frac{S_m}{2}\left[(\xi^2+4)^{\frac{1}{2}}-\xi\right] \tag{3.31}$$

in which

$$\xi = S_m\, \eta\, \sec\theta \tag{3.32}$$

$$S_m = \frac{\tan\phi}{\tan\theta} \tag{3.33}$$

$$\eta = \frac{21\tau_s'}{(S_s-1)\gamma D} \tag{3.34}$$

$$\tau_s' = K\tau_s \tag{3.35}$$

$$\tau_s = \rho\, g\, R\, S_e \tag{3.36}$$

$$K = \cos\theta \sqrt{1 - \frac{\tan^2\theta}{\tan^2\phi}} \tag{3.37}$$

where

τ_s' is the side slope tractive stress;

K is the Lane reduction factor;

and other symbols are as defined before.

3.3.2.3 Third method

In order to compare the equations presented in the previous section with those employed by others for sizing riprap, Stevens and Simons (1976) found it necessary to relate the tractive stress acting on the riprap particles to the fluid velocity in the vicinity of the particles. Using the velocity distribution equation derived by Keulegan, G.H. (1938), another expression for the stability factor, η, in terms of the reference velocity, was derived which can be used to formulate a sizing riprap method as follows:

3.3.2.3-A Stability of plane beds

The stability criterion for the plane bed is

$$SF = \frac{\cos\alpha\tan\phi}{\eta\tan\phi+\sin\alpha} \tag{3.38}$$

in which

$$\eta = \frac{0.3\,u_r^2}{(S_s-1)gD} \tag{3.39}$$

$$u_r = \frac{3.4\,u}{\ell n(12.3\,\frac{y}{D})} \tag{3.40}$$

where

u_r is the reference velocity;

y is the flow depth;

and u is the depth average velocity.

In the case of a narrow channel, the flow depth y must be replaced by the hydraulic radius R, so Eq. (3.40) can be written as

$$u_r = \frac{3.4\,u}{\ell n(12.3\,\frac{R}{D})} \tag{3.41}$$

3.3.2.3-B Stability on side slope

Using the reference velocity as a known quantity, the following equation can be used:

$$SF = \frac{\cos\theta\tan\phi}{\eta'\tan\phi+\sin\theta\ \cos\alpha} \tag{3.42}$$

in which

$$\eta' = \eta\,(\frac{1+\sin(\lambda+\alpha)}{2}) \tag{3.43}$$

$$\alpha = \tan^{-1}\left[\frac{\cos\lambda}{\frac{2\sin\theta}{\eta\tan\phi}+\sin\lambda}\right] \tag{3.44}$$

$$\eta = \frac{0.3\,u_r^2}{(S_s-1)gD} \tag{3.45}$$

$$u_r = \frac{3.4u}{\ell n(12.3\frac{R}{D})} \qquad (3.46)$$

where

λ is the angle between the horizontal and the velocity vector;

and η' is the stability number for particle on side slope.

In the case of horizontal flow, the angle λ is very small, then Eqs. (3.43) and (3.44) can be reduced to

$$\eta' = \eta\ (\frac{1+\sin\alpha}{2}) \qquad (3.47)$$

$$\alpha = \tan^{-1}\ \frac{\eta\tan\phi}{2\sin\theta} \qquad (3.48)$$

3.3.3 Ruh-Ming's Methods

On the basis of the stability of an individual particle, Ruh-Ming, L., et al.(1976), then Ruh-Ming, L., and Simons, D.B. (1979), developed two different methods for sizing riprap for river bank protection. To make it possible to treat the hydrodynamic forces realistically, the safety factor was defined as the ratio of the force resisting the movement of a single particle to the force acting to dislodge the particle out of the riprap layer. The forces acting on a single particle resting on the side slope are shown in Fig. (3.9).

In order to compare the applicability of those approaches for sizing riprap with the previous methods, a summary of the two approaches follows:

3.3.3.1 First method

The safety factor of an individual particle placed on a stream bank was formulated by Ruh-Ming, L., et al. (1976) as

$$SF = \frac{(W\cos\theta - \beta\delta\tau)\tan\phi}{[(W\sin\theta)^2 + \delta^2\tau^2]^{\frac{1}{2}}} \qquad (3.49)$$

in which

$$\tau = \rho \left[\frac{u}{2.5\ell n\ (12.3\frac{R}{D})} \right]^2 \qquad (3.50)$$

$$W = \frac{1}{6}\pi D^3(\gamma_s - \gamma_w) \qquad (3.51)$$

$$\delta = \frac{11.14\ D^2}{\beta + \cot\phi} \qquad (3.52)$$

where

W is the submerged weight of the particle;

δ is the stability parameter;

and β is the ratio of the lift to drag force which was considered as a constant value equal to 0.85.

To determine the factor of safety for a particle placed on a horizontal bed, $\theta = 0$ is substituted in Eq. (3.49) to obtain

$$SF = \frac{(W - \beta\delta\tau)\tan\phi}{\delta\tau} \qquad (3.53)$$

then the other equations can be used.

3.3.3.2 Second method

Using a different constant value for the ratio of lift to drag, Ruh-Ming, L. and Simons, D.B. (1979) presented another approach for sizing riprap for bank protection. The value of β equal to 2.85 was used as adopted by Samad, M.A. (1978). Hence the stability parameter δ was expressed as

$$\delta = \frac{9.52\ D^2}{\beta + \cot\phi} \tag{3.54}$$

Then the other Eqs. (3.49), (3.50) and (3.51), remain as previously.

3.3.4 Samad's Methods

Samad, M.A. (1978) put forward two different approaches for riprap sizing. The first approach was based on the pressure concept and utilized the Einstein and El-Samni's lift coefficient, the second approach was based on the shear concept and utilized the extended Shields diagram for large particles. In both theoretical approaches, the forces that act on a single particle were treated similarly to the one presented by Ruh-Ming et al. (1976).

On the basis of the experimental data for the lift to drag ratio which were obtained by Coleman, N.L. (1967) and Cheng, E.D. and Clyde, C.G. (1972), Samad developed a graphic relationship between the ratio β and the boundary Reynolds number as depicted in Fig. (3.10).

These methods for sizing riprap can be summarized as follows:

3.3.4.1 First method

The mean safety factor of a riprap with uniform particles placed on a side slope was formulated as follows:

$$SF = \frac{(W\cos\theta - P_L A_L)\tan\phi}{\left[W^2\sin^2\theta + \left(\frac{P_L A_L}{\beta}\right)^2\right]^{\frac{1}{2}}} \tag{3.55}$$

in which

$$A_L = \frac{\pi}{4} D^2 \tag{3.56}$$

$$P_L = 0.178\ \rho \frac{u_{35}^2}{2} \tag{3.57}$$

$$u_{35} = 5.9\ u_* \tag{3.58}$$

$$u_* = \frac{u}{2.5\ell n(12.3\frac{R}{D})} \tag{3.59}$$

$$\beta = f(R_*) \tag{3.60}$$

$$R_* = \frac{u_* D}{\nu} \tag{3.61}$$

where

A_L is the projected area of the particle related to lift;
P_L is the dynamic lift pressure;
R_* is the particle Reynolds number;
ν is the kinematic viscosity;
u_{35} is the flow velocity at a distance of 0.35 D_{35} above the theoretical bed;
u_* is the shear velocity;
and D_{35} is the particle size for which 35 percent is finer.

In this method, knowing the particle Reynolds number, the value of β can be determined from Fig. (3.10). On the other hand, in the case of using non-uniform riprap materials, Eqs. (3.58 and 3.59) are given as

$$u_{35} = 5.502\ u_* \tag{3.62}$$

$$u_* = \frac{u}{2.5\ell n(11.172\frac{R}{D})} \tag{3.63}$$

This approach can also be utilized for the stream bed by substituting $\theta = 0$ in Eq. (3.55) to obtain

$$SF = \frac{(W - P_L A_L)\beta \tan\phi}{A_L P_L} \tag{3.64}$$

3.3.4.2 Second method

On the basis of the shear concept, Samad developed another approach to determine the side slope safety factor. This method is similar to the one presented by Ruh-Ming, L. and Simons, D.B. (1979) except that β does not have a constant value, but is treated as a function of the particle Reynolds number as:

$$\beta = f(R_*) \tag{3.65}$$

which can be evaluated from Fig. (3.10).

3.4 PROBABILISTIC APPROACH

Taking into account the fluctuating nature of the hydrodynamic lift and drag forces and accordingly the boundary shear stress, and knowing the probability distribution of these forces as well as its relation with the flow conditions, a probabilistic model for sizing riprap has been formulated. This model enables the designer to interpret the stability of riprap by checking its probability of adequacy under design conditions rather than indicating a factor of safety.

As a result of comprehensive researches carried out primarily in the USA on the design of rock riprap for highways and river bank protection, four different probabilistic approaches have been developed. In these models, the probability of adequacy for the riprap particles at the critical condition (SF=1) is considered equal to 0.5. This implies that there is a 50 percent chance of adequacy if the riprap is designed according to the conventional safety factor of 1.0. These approaches can be summarized as follows:

3.4.1 Ruh-Ming's First Method

On the basis of the experimental measurements carried out by Blinco, P.B. and Simons, D.B. (1974) for the smooth boundary turbulent open channel flow, it was found that the boundary shear stress

can be approximated by a lognormal distribution. Assuming that these results are applicable to a rough boundary and using the derived formula of the safety factor, Ruh-Ming, L. et al. (1976), developed a probabilistic model based on the exceedance of shear stress value above a certain critical value.

The relations that define the probability of adequacy of the riprap particles placed on a stream bank are:

$$\delta = \frac{11.14\ D^2}{\beta + \cot\phi} \tag{3.66}$$

$$W = \frac{\pi}{6} D^3(\gamma_s - \gamma_w) \tag{3.67}$$

$$A1 = \beta W \cos\theta \tan^2\phi \tag{3.68}$$

$$A2 = 1 - \beta^2 \tan^2\phi \tag{3.69}$$

$$A3 = \cos^2\theta \tan^2\phi - \sin^2\theta \tag{3.70}$$

$$\tau_c = \frac{(A1^2 + W^2 A2 A3)^{\frac{1}{2}} - A1}{A2\delta} \tag{3.71}$$

$$f = 8/[2.5 \ell n(12.5\frac{R}{D})] \tag{3.72}$$

$$\frac{\sigma}{\bar{\tau}} = 137.67\ f^{1.536} \tag{3.73}$$

$$\bar{\tau} = \rho\left[\frac{u}{2.5\,\ell n(12.3\frac{R}{D})}\right]^2 \tag{3.74}$$

$$\sigma_n = \sqrt{1 + (\frac{\sigma}{\bar{\tau}})^2} \tag{3.75}$$

$$\mu_n = \frac{\ell n\ \bar{\tau}}{2} - \frac{\sigma_n^2}{4} \tag{3.76}$$

$$q_n = \frac{\ell n\ \tau_c - \mu_n}{\sigma_n} \tag{3.77}$$

$$P = \phi (q_n) \tag{3.78}$$

in which

τ_c is the critical boundary shear stress;
σ is the standard deviation of the boundary shear stress;
μ_n, σ_n are the mean and standard deviation of the lognormal distribution respectively;
q_n is the qth quantile point of standard normal;
and P is the cumulative probability of riprap adequency.

In this method the value β was considered as a constant parameter equal to 0.85.

3.4.2 Ruh-Ming's Second Method

Considering the exceedance of the drag force above a certain critical value as a design parameter, a probabilistic approach, for the probability of adequacy of a riprap structure for particular design condition, was formulated by Ruh-Ming, L. and Simons, D.B. (1979). The probability density function of the drag force was assumed normally distributed, then a relationship between the drag force and the shear velocity was developed.

To determine the probability that the individual particles placed on the side slope is adequate, the following procedure should be used:

$$\delta = \frac{0.25D^2}{\beta+\cot\phi} \tag{3.79}$$

$$W = \frac{\pi}{6} D^3(\gamma_s - \gamma_w) \tag{3.80}$$

$$A1 = \beta W \cos\theta \tan^2\phi \tag{3.81}$$

$$A2 = 1-\beta^2\tan^2\phi \tag{3.82}$$

$$A3 = \cos^2\theta\tan^2\phi - \sin^2\theta \tag{3.83}$$

$$F_c = \frac{(A1^2 + W^2 A2A3)^{\frac{1}{2}} - A1}{A2} \tag{3.84}$$

$$u_* = \frac{u}{2.5\ell n(12.3\frac{R}{D})} \tag{3.85}$$

$$\mu_d = 74.8\delta u_*^2 \tag{3.86}$$

$$\sigma_d = 27.6\delta u_*^2 \tag{3.87}$$

$$q_n = \frac{F_c - \mu_d}{\sigma_d} \tag{3.88}$$

$$P = \phi\ (q_n) \tag{3.89}$$

in which

μ_d and σ_d are the mean and standard deviation of the drag force respectively;
F_c is the critical drag force;
q_n is the qth quantile point of a standard normal
P is the probability of adequacy for individual particle.

In this method, the ratio of lift to drag was also considered as a constant value equal to 2.85.

3.4.3 Samad's First Method

To evaluate the probability that the individual particles placed on the side slope is adequate, Samad, M.A. (1978) utilized the available information on hydrodynamic forces, acting on a riprap particle in a turbulent flow condition, to formulate a probabilistic model. In this method, the mean value of lift pressure P_L in Eq. (3.55) was considered as a random quantity; then, setting $P_L = P_c$ when SF = 1, Eq. (3.55) was modified to

$$P_c = \frac{w\cos\theta}{A_L} \left[\frac{1-\sqrt{1-P1xP2}}{P1}\right] \tag{3.90}$$

in which

$$P1 = 1-(1/\beta^2\tan^2\phi) \tag{3.91}$$

$$P2 = 1-(\tan^2\theta/\tan^2\phi) \tag{3.92}$$

where

P_L is the mean value of the dynamic lift pressure;
P_c is the critical dynamic lift pressure;
and SF is the factor of safety.

Therefore, using Eqs. (3.56) to (3.61), the probability of adequacy can then be determined as

$$\sigma = 0.36\ P_L \tag{3.93}$$

$$q_n = \frac{P_c - P_L}{\sigma} \tag{3.94}$$

$$P = \phi(q_n) \tag{3.95}$$

3.4.4 Samad's Second Method

This approach was developed by Samad (1978), on the basis of the statistical properties of lift pressure by using Eq. (3.49) and setting SF=1 when $\bar{\tau} = \tau_c$, thus

$$\tau'_c = \frac{[C1^2 + W^2 C_2 C_3]^{\frac{1}{2}} - C1}{\delta C2} \tag{3.96}$$

in which

$$C1 = \beta W \cos\theta \tan^2\phi \quad (3.97)$$

$$C2 = 1-\beta^2\tan^2\phi \quad (3.98)$$

$$C3 = \cos^2\theta\tan^2\phi-\sin^2\theta \quad (3.99)$$

where

τ is the mean boundary shear stress

τ_c' is the critical boundary shear stress on a side slope

To evaluate the probability of adequacy, the following equations should be used:

$$u_* = \frac{u}{2.5\ell n\ (12.3\frac{R}{D})} \quad (3.100)$$

$$R_* = \frac{u_*D}{\nu} \quad (3.101)$$

$$\beta = f(R_*) \quad (3.102)$$

$$\delta = \frac{9.51\ D^2}{\beta+\cot\phi} \quad (3.103)$$

$$\bar{\tau} = \rho u_*^2 \quad (3.104)$$

$$A_L = \frac{\pi}{4} D^2 \quad (3.105)$$

$$\overline{P_L} = \frac{\beta\ \delta\ \bar{\tau}}{A_L} \quad (3.106)$$

$$P_c = \frac{\beta\ \delta\ \tau_c}{A_L} \quad (3.107)$$

$$\sigma = \overline{P_L} \times 0.36 \quad (3.108)$$

$$q_n = \frac{P_c-\bar{P}_L}{\sigma} \quad (3.109)$$

$$P = \phi\ (q_n) \quad (3.110)$$

The definitiion of these symbols is the same as before.

3.5 DISCUSSION

In fact, the sizing methods presented in this study are a useful advance in an area where present knowledge is inadequate. But in order to ascertain the merits of these approaches, they need to be examined in the light of laboratory and field observations. The experiments conducted by the Author help to serve this purpose.

According to the riprap sizing methods presented herein, Lane's design criterion suggests that the particles will be in motion if the actual tractive stress is more than the permissible stress. But no conclusive proof has been produced that lift should be disregarded in the stability concept.

In the methods developed by Stevens and Simons, the stability criterion was based on the moment tending to rotate a particle out of the riprap blanket and the moment resisting particle motion. In their analysis of forces acting on a riprap particle, it was assumed that the ratio e_2/e_1 [Fig. (3.7)], which is the moment arm of the normal component of the submerged weight divided by the moment arm of the downslope component of the submerged weight, is equal to $\tan\phi$ (where ϕ is the angle of repose). However, this assumption was not supported by real measurements.

On seeking a relationship between lift and drag, they assumed that the moments of lift and drag about the point of rotation are equal. This assumption also was not substantiated by experimental data and must be taken on trust.

They also assumed that the projected area to drag, A_D is equal to that area subjected to lift A_L, which is valid only in the case of spherical particles.

In the two deterministic approaches developed by Ruh-Ming, L. et al. (1976 and 1979), the stability formulae were based on forces acting to resist the movement and forces acting to dislodge the particle. In those methods a constant value for the lift to drag

ratio, equal to 0.85 in the first approach and 2.85 in the second approach, was recommended which is not in agreement with the available information on the fluctuating nature of the boundary shear stress.

To check the probability of adequacy of an individual particle resting on a side slope, Ruh-Ming, L. et al. (1976) developed the first probabilistic approach. This model was based on the assumption that the information obtained on the shear stress process in a smooth boundary is applicable to the rough boundary case. However, this assumption was not supported by experimental evidence for rough boundaries.

In addition, the examination of the deterministic and the probabilistic methods by the Author showed that nearly all the methods were based on the equilibrium of an individual particle. But, during the course of the experimental work, it was observed that movement of one or some particles does not usually cause failure of the whole protective layer.

Finally, to the best of the Author's knowledge there is insufficient laboratory and field data available to indicate their validity and relative merits.

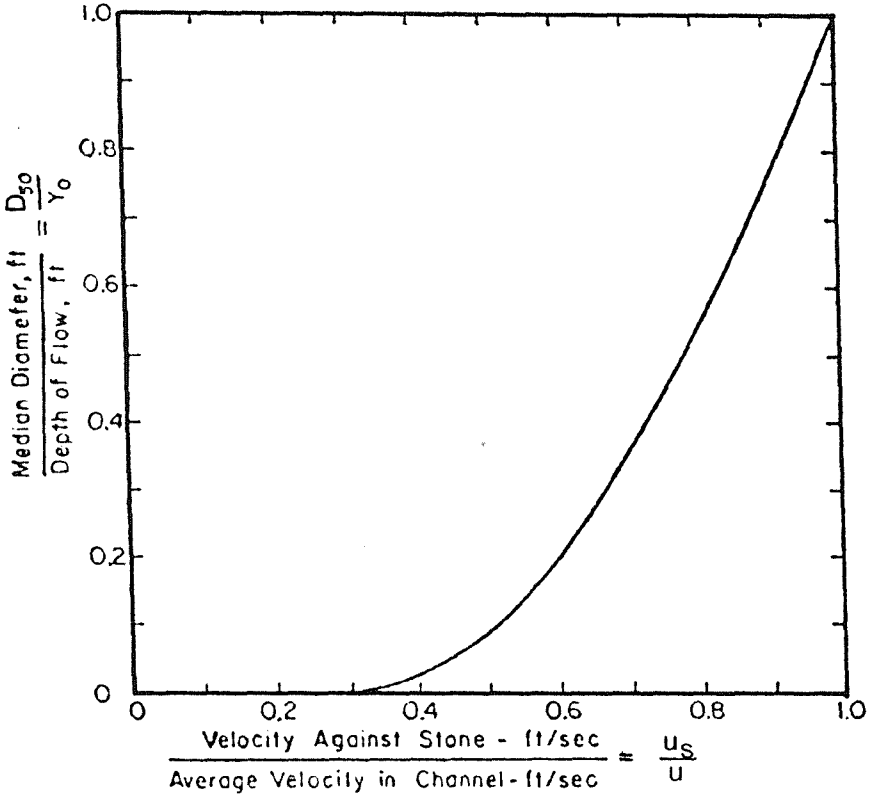

FIG. 3–1 : VELOCITY AGAINST STONE ON CHANNEL BOTTOM (AFTER SEARCY, 1967)

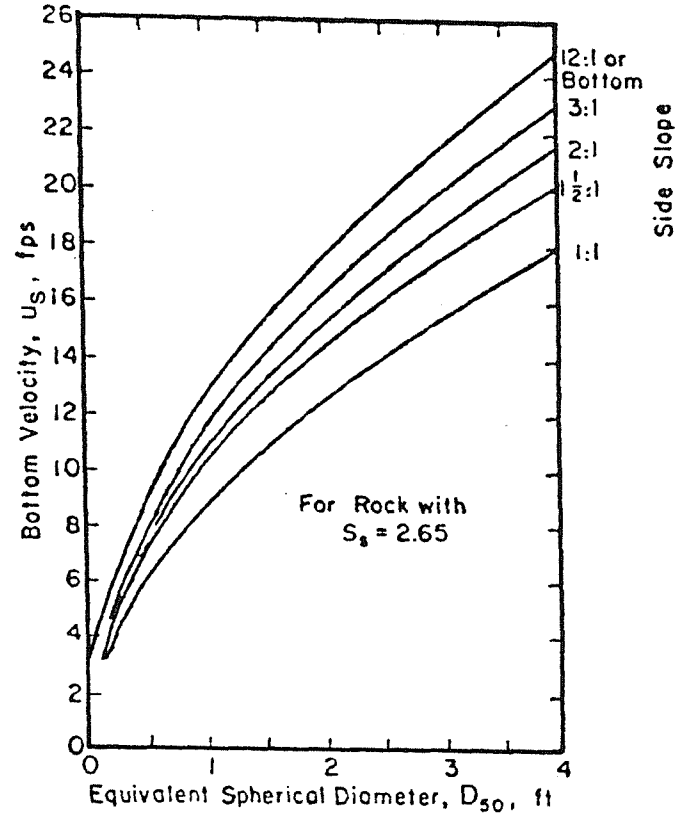

FIG. 3–2 : ROCK SIZE FOR THE BUREAU OF PUBLIC ROADS DESIGN METHOD (AFTER SEARCY, 1967)

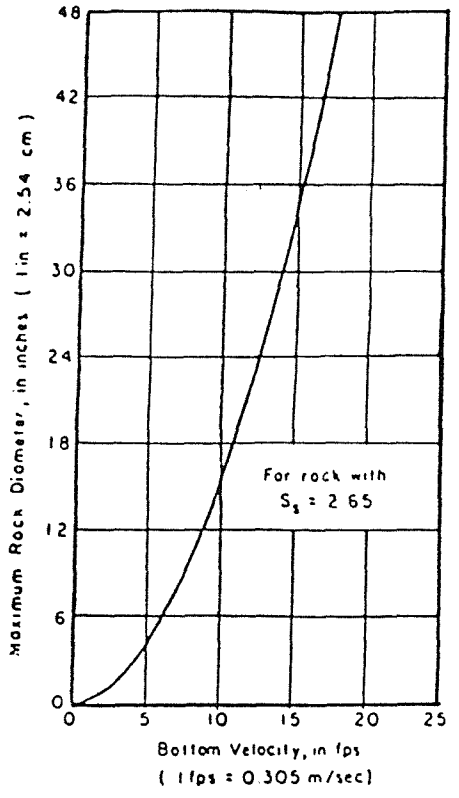

FIG 3-3 ROCK SIZE FOR THE BUREAU OF RECLAMATION DESIGN

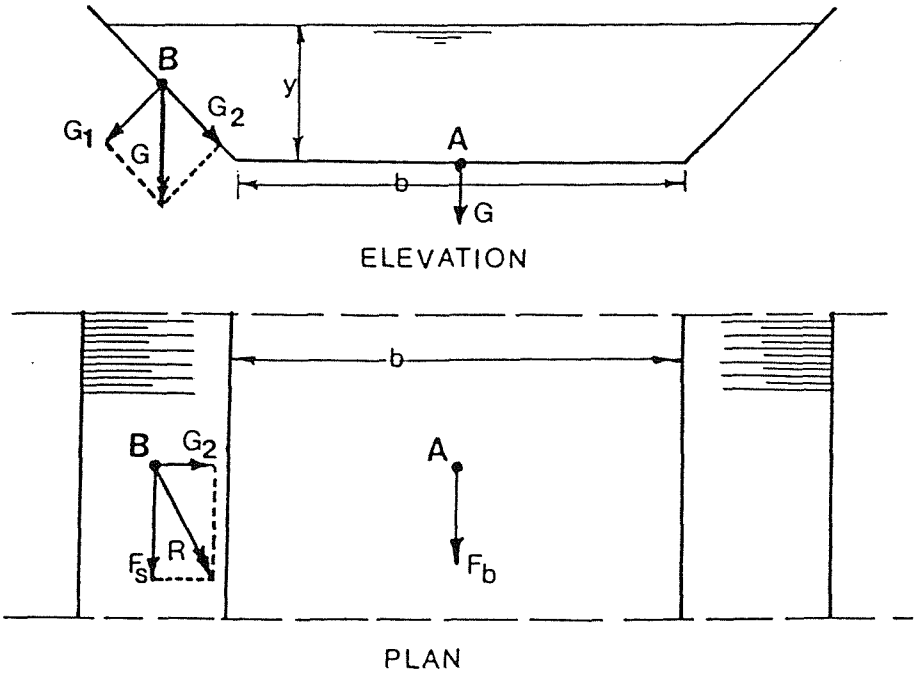

FIG. 3-4 TRACTIVE AND GRAVITY FORCE DEFINITION (AFTER LANE 1953)

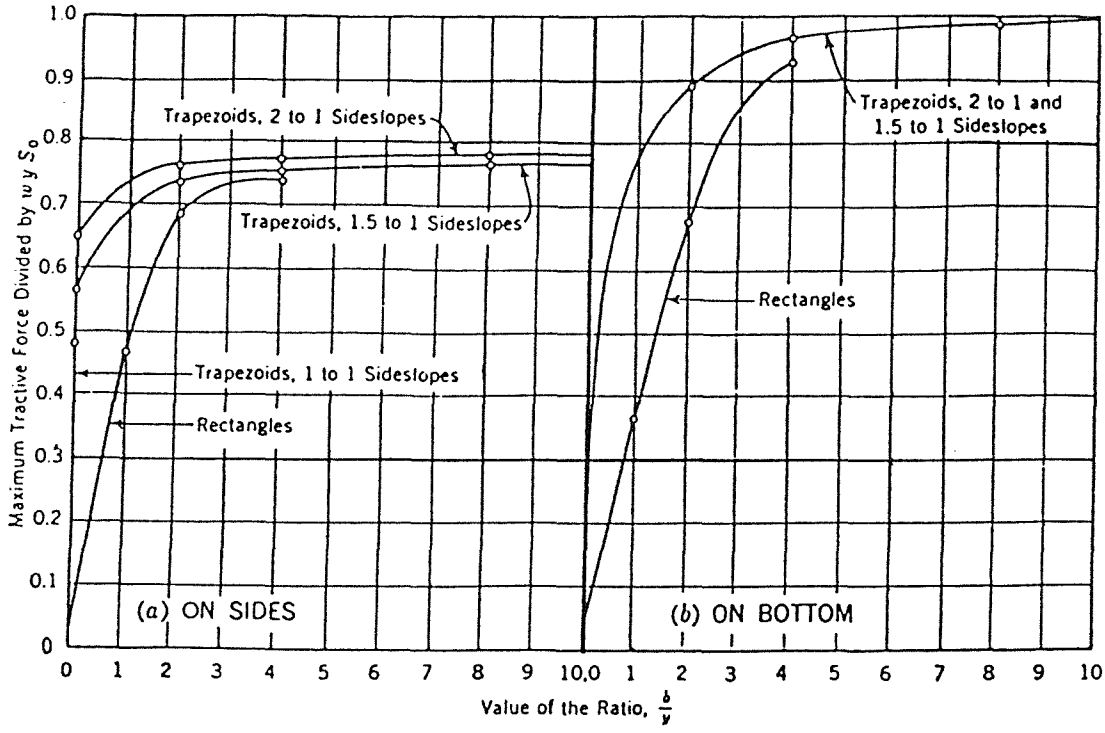

FIG. 3–5: VARIATION OF THE MAXIMUM UNIT TRACTIVE FORCE (AFTER LANE 1955)

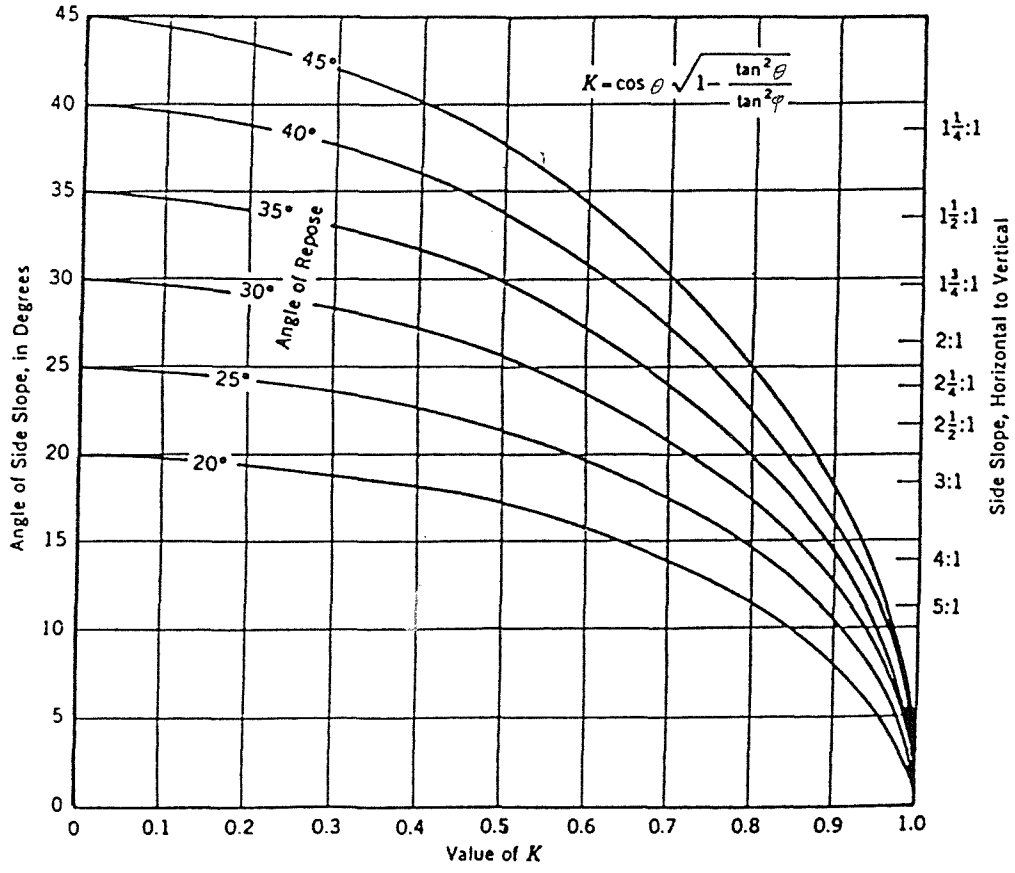

FIG. 3–6: RELATIONSHIP BETWEEN SIDE SLOPE ANGLE OF REPOSE AND K VALUE (AFTER LANE, 1953)

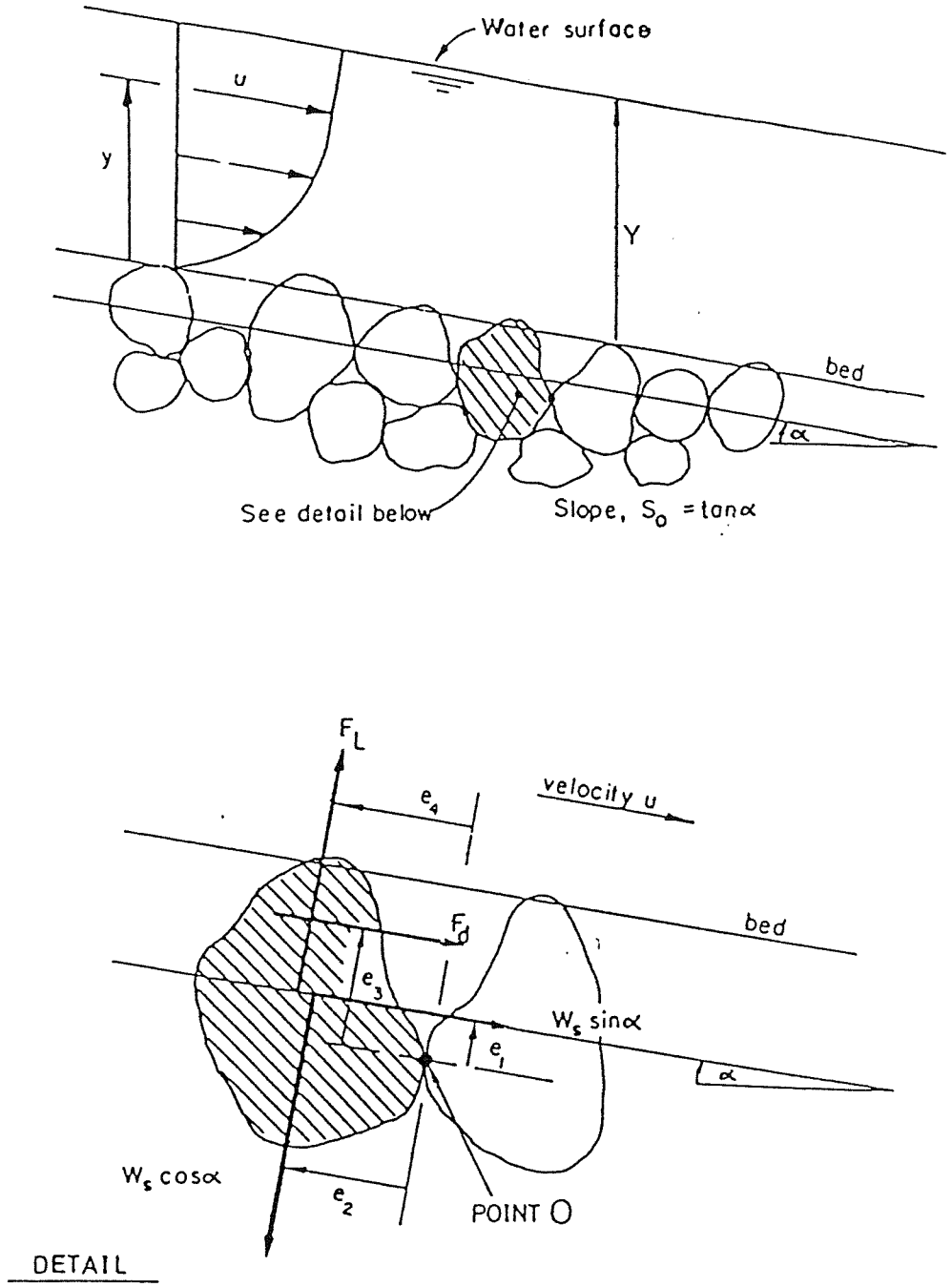

FIG. 3–7 : FORCES ACTING ON A SUBMERGED PARTICLE ON CHANNEL BED

(AFTER STEVENS, 1971)

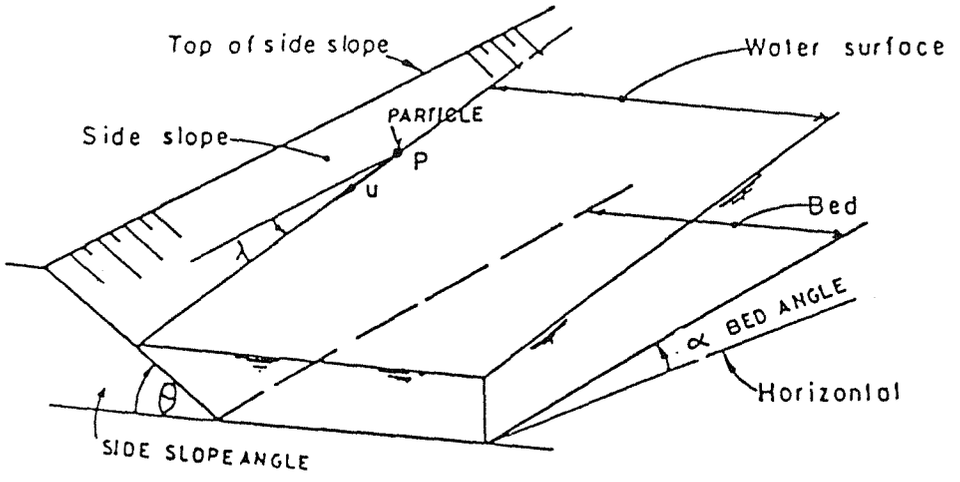

General View

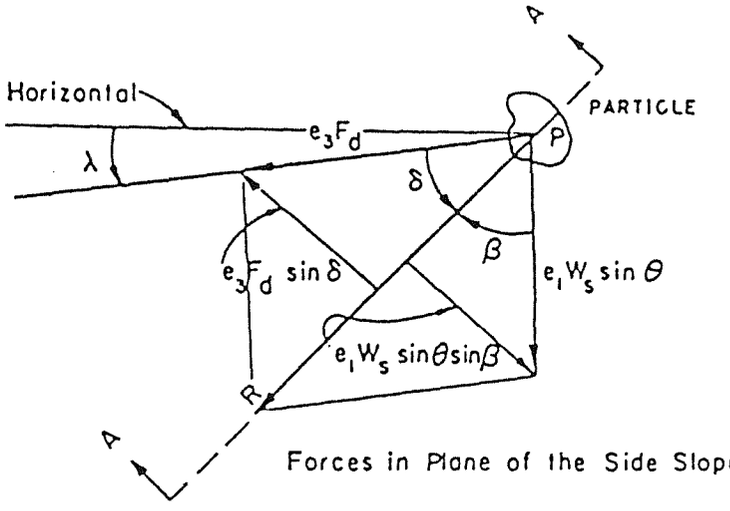

Forces in Plane of the Side Slope

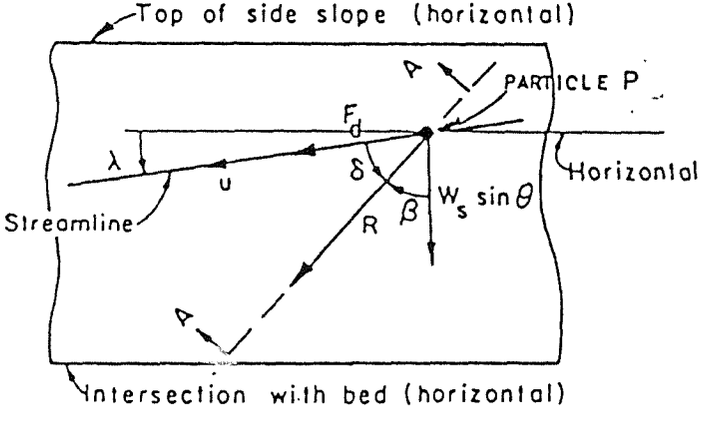

View Normal to Side Slope

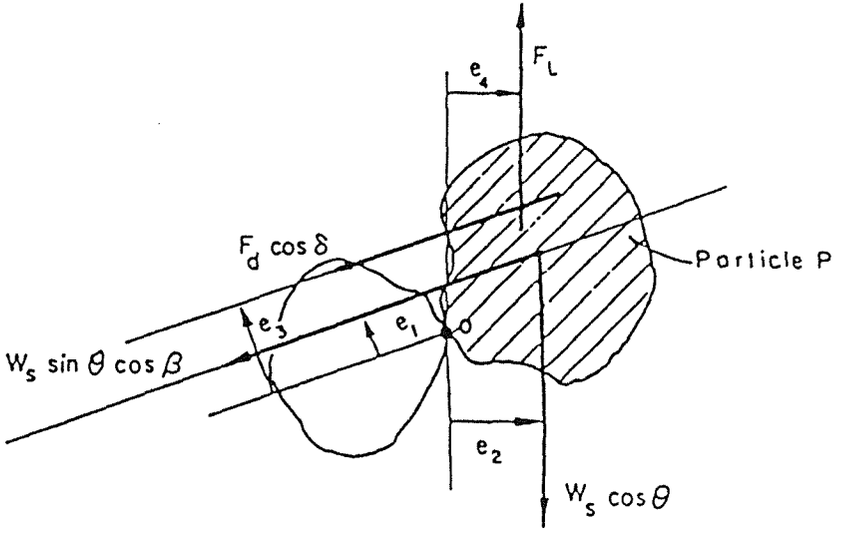

Section A-A

FIG. 3-8 FORCES ACTING ON A SIDE SLOPE PARTICLE

(AFTER STEVENS,1971)

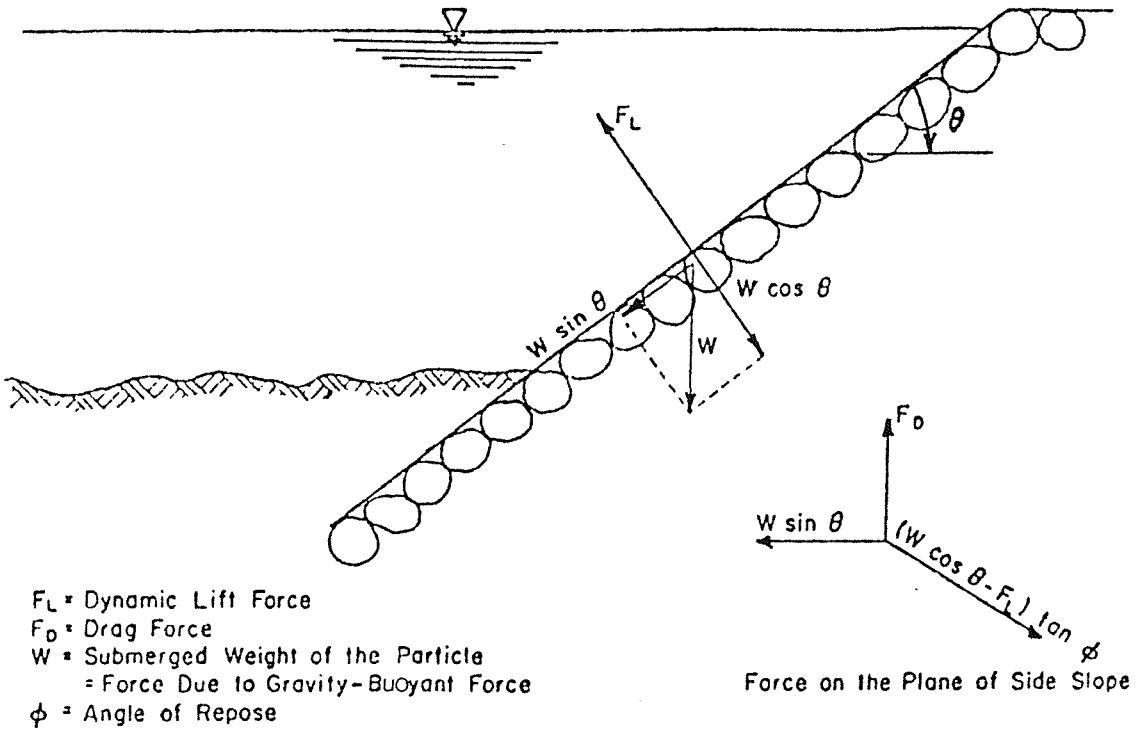

FIG. 3–9 : FORCES ON A SUBMERGED PARTICLE ON THE SIDE OF A CHANNEL (AFTER RUH-MING,1976)

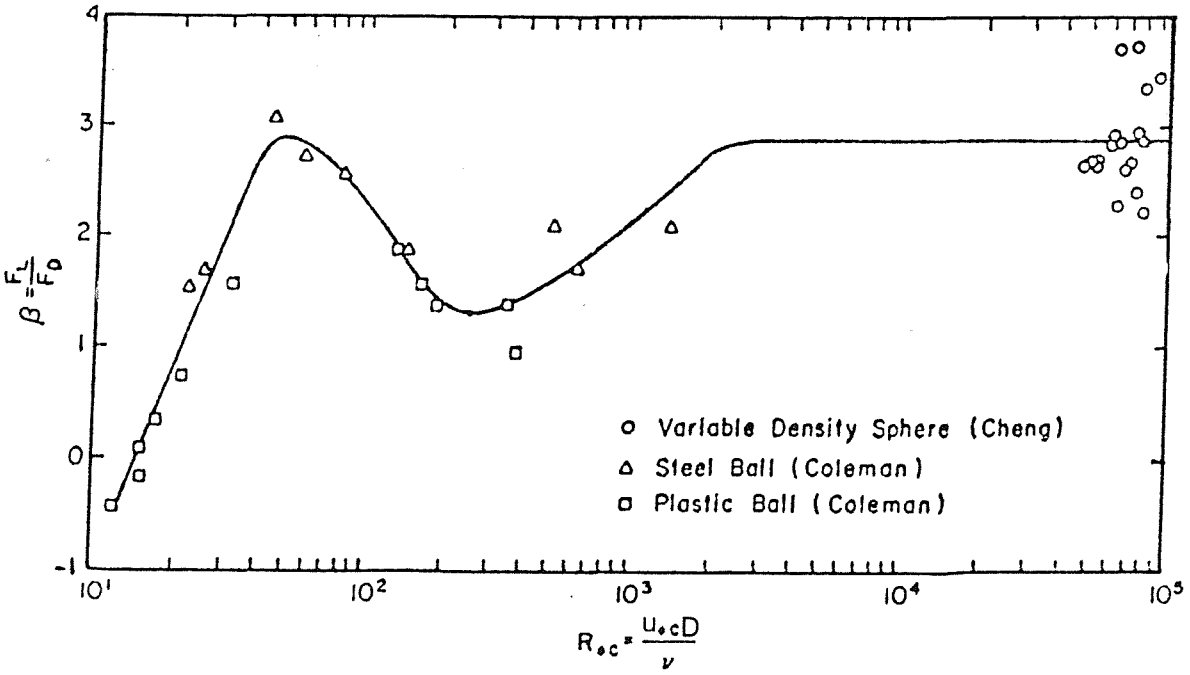

FIG. 3–10 : RATIO OF THE LIFT TO DRAG FORCE VERSUS THE BOUNDARY REYNOLDS NUMBER (AFTER SAMAD,1978)

CHAPTER FOUR

FLOW RESISTANCE OF CHANNELS

4.1 INTRODUCTION

When a fluid flows past a boundary, the fluid molecules in immediate contact with the perimeter, according to the existing boundary conditions, have zero velocity. As a result of that a shear is set up within the fluid and also at the boundary. This boundary shear results in a drag force transmitted from the fluid to the boundary, and the boundary in turn transmits to the fluid a force equal in magnitude but opposite in direction, which offers resistance to flow.

In brief, one may conclude that both the drag and flow resistance are associated with the flow movement. But, in fact, drag direction is the same as the direction of flow motion, while the total surface resistance of the boundary is in the opposite direction and equivalent to the component of fluid weight in the flow direction.

On the other hand, the resistance to flow in a fully rough open channel was classified according to Leopold, L.B., et al. (1964), Burkham, D.E. and Dawdy, D.R. (1976), and Griffiths, G.A. (1981), into the following three elements:

1) Skin resistance produced by the boundary surface, this depends on the depth of flow relative to size of roughness element along the boundary surface.

2) Form resistance caused by discrete boundary features that set up eddies and secondary circulations.

3) Spill resistance occurs locally at particular places in open channels under some conditions and its effect can usually be neglected.

On the basis of the theoretical investigations of the phenomenon of turbulent flow by Prandtl and by Karman, corresponding formulae for estimating the resistance to flow in rigid channels have been derived by Keulegan, G.H. (1938). The extensive studies carried out recently by different investigators have indicated similar formulae but with different coefficients. However, some investigators like Powell, R.W. (1950) found that the Keulegan's formulae are not accurate because they are based entirely on experiments with pipes neglecting the effect of free surface and of the angles between walls and bottom of the channel.

Due to the diversity of the factors governing the case under consideration, several empirical relationships for estimating the resistance to flow have been developed, which are set forth in this chapter.

4.2 DIMENSIONAL ANALYSIS

As an attempt to develop a formula for estimating the resistance to flow in a straight, rigid channel, the dimensional analysis technique should be utilized. The variables governing the flow characteristics can be expressed in the general flow formula

$$f_1(u,R,S_e,\rho_w,\mu,g,D,\sigma,B,S_f,\tau) = 0 \qquad (4.1)$$

in which

- u is the mean flow velocity;
- R is the hydraulic radius;
- S_e is the slope of the energy gradient;
- ρ_w is the water density;
- μ is the flow dynamic viscosity;
- g is the acceleration due to gravity;
- D is the representative diameter of the particle;
- σ is the standard deviation of the size distribution of the bed material;

B is the channel width;

S_f is the particle shape factor;

and τ is the boundary shear stress

Choosing R, ρ_w and u as repeating variables, the Buckingham's Pi-theorem yields

$$f_2\left(\frac{R}{D},\frac{R}{B},\frac{u}{\sqrt{\frac{\tau}{\rho}}},\frac{u\,R\,\rho_w}{\mu},\frac{u}{\sqrt{gR}},\ S_e,\ S_f,\sigma\ \right) = 0 \qquad (4.2)$$

Substituting $u_* = \sqrt{\frac{\tau}{\rho_w}}$ where u_* is the shear velocity, and $\nu = \frac{\mu}{\rho_w}$ where ν is the kinematic viscosity, Eq.(4.2) can be rewritten as

$$\frac{u}{u_*} = f_3\left(\frac{R}{D},\frac{R}{B},\frac{uR}{\nu},\frac{u}{\sqrt{gR}},\ S_e,\ S_f,\sigma\right) \qquad (4.3)$$

where

$\frac{R}{D}$ is the relative roughness parameter;

$\frac{u}{\sqrt{gR}}$ is the Froude number F_r;

$\frac{uR}{\nu}$ is the flow Reynolds number R_e;

$\frac{u}{u_*}$ is a parameter of the resistance;

and $\frac{R}{B}$ is the aspect ratio of the cross section.

Therefore, Eq. (4.3) may be transformed into

$$\frac{u}{u_*} = f_3\left(\frac{R}{D},\ \frac{R}{B},R_e,F_r,S_e,S_f,\sigma\right) \qquad (4.4)$$

The influence of the terms S_e, S_f and σ are undoubtedly known but because each of them has no dimension they could be eliminated. Whereas for fully turbulent flows over rough boundaries the boundary Reynolds number R_e and the Froude number F_r may be neglected because viscosity effects are likely to be unimportant. Considering the aforementioned conditions, Eq. (4.4) finally reduces to

$$\frac{u}{u_*} = f_4 \left(\frac{R}{D}, \frac{R}{B}\right) \qquad (4.5)$$

4.3 RESISTANCE TO FLOW IN RIGID BED CHANNEL

Various equations have been proposed over the last two centuries to relate the mean flow velocity in open channels to flow resistance. Among the earliest and most frequently quoted equation is the uniform-flow formula developed by Chezy in 1769 which is usually used to determine the mean flow velocity as

$$u = C \sqrt{RS_e} \qquad (4.6)$$

where

C is called Chezy's coefficient of resistance which has the dimensions

$$C = \left[\frac{L^{\frac{1}{2}}}{T}\right] \qquad (4.7)$$

The Chezy formula as given by Eq. (4.6) is applicable to open channel flow in the absence of bedforms and bed material transport.

In 1857 Darcy modified Chezy's formula to use it for flow in pipes by inserting $h_L/L = S_e$, and $d = 4R$ and solving for h_L as

$$h_L = f \frac{L}{d} \frac{u^2}{2g} \qquad (4.8)$$

in which

h_L is the friction loss associated with flow in pipes;
f is the Darcy-Weisbach friction factor;
L is the pipe length;
and d is the pipe diameter.

For open channel flow Eq. (4.8) can be written in terms of the Darcy-Weisbach friction coefficient as

$$f = \frac{8gRS_e}{u^2} \tag{4.9}$$

Noting that $u_*^2 = gRS_e$, Eq.(4.9) yields

$$\frac{u}{u_*} = \sqrt{\frac{8}{f}} \tag{4.10}$$

Also Darcy-Weisbach coefficient f can be expressed as a function of the Chezy resistance coefficient C by elminating u from Eqs. (4.6) and (4.9) to obtain

$$\frac{C}{\sqrt{g}} = \sqrt{\frac{8}{f}} \tag{4.11}$$

In 1889 Manning presented his well-known formula to estimate the mean flow velocity as

$$u = \frac{1.49}{n} R^{2/3} S_e^{\frac{1}{2}} \tag{4.12}$$

in English units, this can be written as

$$u = \frac{1}{n} R^{2/3} S_e^{\frac{1}{2}} \tag{4.13}$$

in metric units in which n is the Manning's coefficient of roughness and has the dimensions

$$n = \left[\frac{T}{L^{1/3}} \right] \tag{4.14}$$

Dividing both sides of Eq. (4.13) by u_*, Manning's formula can be transformed to

$$\frac{u}{u_*} = \frac{R^{1/6}}{n\sqrt{g}} \tag{4.15}$$

Also Manning's Roughness Coefficient n can be expressed as a function of Dracy-Weisbach's f and Chezy's C as follows:

$$n = \frac{R^{1/6}}{C} \tag{4.16}$$

$$n = \frac{R^{1/6}\sqrt{f}}{\sqrt{8g}} \tag{4.17}$$

The Manning formula as presented in Eq. (4.13) has become the most widely used of all uniform-flow formulae for open channel flow computations, and many attempts have been made to evaluate the coefficient n either numerically or as a function of the bed material size as follows:

In order to give guidance in the proper determination of the roughness coefficient n, Chow, V.T. (1959) tabulated n values for various channel conditions in what seems to be a most comprehensive list.

Strickler (1923) defined Manning's n as a function of the particle size as

$$n = \frac{D_{50}^{1/6}}{21.1} \tag{4.18}$$

in which D_{50} is the median size of the bed material in m. Keulegan, G.H. (1938) proposed a formula similar to that presented by Strickler in which n was expressed as

$$n = \frac{D_{50}^{1/6}}{46.9} \tag{4.19}$$

where D_{50} is in ft

Another attempt was made by Meyer-Peter, E. and Muller, R. (1948) in which the following formula was developed

$$n = \frac{D_{90}^{1/6}}{26} \tag{4.20}$$

where D_{90} is the particle size (in mm) in which 90 percent is finer. Lane, E.W. and Carlson, E.J. (1953) in their comprehensive study of

the design of stable channels in San Luis Valley suggested the following formula to determine the Manning's n

$$n = \frac{D_{75}^{1/6}}{39} \qquad (4.21)$$

where D_{75} is the particle size (in inches) in which 75 percent is finer.

Limerinos, J.T. (1970) used data from gravel-bed rivers in California to develop an expression of the following form

$$n = \frac{0.113\ R^{1/6}}{1.16+2.01\ \log(\frac{R}{D_{84}})} \qquad (4.22)$$

in which D_{84} is the characteristic bed material size for the reach in metres.

It was found by Bray, D.I. (1979) that Limerinos Eq. (4.22) is the most acceptable expression for quantitatively determining the value of Manning's n.

On the other hand, in a comprehensive review of the various uniform-flow formulae, the ASCE task force committee on friction factors in open channels (1963) recommended the use of the Darcy-Weisbach Eq. (4.9). This is simply because, unlike the empirical Manning type of equation, the Darcy-Weisbach formula is dimensionally correct, and the relative roughness does not influence the exponents of hydraulic radius and slope as shown by Liu, H.K. and Hwang, S.Y. (1959).

4.4 DEVELOPMENT OF THE FLOW RESISTANCE EQUATIONS

Among the various formulae of resistance equations proposed for fully turbulent open channel flow over rigid boundaries, two types were denoted as the logarithmic and the exponential (monomial) and frequently used by hydraulic engineers. A brief review of the development of each type can be presented as follows:

4.4.1 Logarithmic Type Formula

It is suggested that in uniform channel flow, the velocity distribution will be stable as long as the turbulent boundary layer is fully developed. This implies that the velocity distribution can be shown to be approximately logarithmic. Accordingly the shear stress at any point in a turbulent flow moving over a solid surface was given by Prandtl as

$$\tau = \rho \ell^2 \left(\frac{du}{dy}\right)^2 \qquad (4.23)$$

in which

ℓ is a characteristic length known as the mixing length;

$\frac{du}{dy}$ is the velocity gradient at a normal distance y from the solid surface;

and u is the average velocity at distance y from the solid surface.

Eq.(4.23) leads to an expression for the mean flow velocity at any point with the aid of two simplifying assumptions as follows:

First, Prandtl assumed that the mixing length is proportional to the distance from the wall, i.e.

$$\ell = \kappa y \qquad (4.24)$$

where

κ is known as the Von-Karman constant for the proportionality between ℓ and y.

Thus Eq. (4.23) becomes

$$\tau = \rho \kappa^2 y^2 \left(\frac{du}{dy}\right)^2 \qquad (4.25)$$

Prandtl next made the second assumption that the shear stress is everywhere the same as at the wall, i.e. $\tau = \tau_o$, so that

$$u_*^2 = \kappa^2 y^2 \left(\frac{du}{dy}\right)^2 \qquad (4.26)$$

where

$$u_* = \sqrt{\frac{\tau_o}{\rho}} = \sqrt{gRS_e} \qquad (4.27)$$

in which u_* is a quantity has the dimension of velocity. Since it varies with the boundary friction τ_o, so it is known as the friction velocity or the shear velocity. Thus Eq. (4.21) may be written as

$$du = \frac{1}{\kappa} u_* \frac{dy}{y} \qquad (4.28)$$

Integrating Eq. (4.28) leads to

$$\frac{u}{u_*} = \frac{1}{\kappa} \ln y + \text{constant} \qquad (4.29)$$

The constant of integration can be expressed as the point on the y axis where $u = 0$, whereas κ has been found experimentally (by Nikuradse and others) to be 0.4. Thus Eq. (4.29) yields

$$\frac{u}{u_*} = 2.5 \ln \frac{y}{y_o} \qquad (4.30)$$

Eq. (4.30) indicates that the velocity in the turbulent region is a logarithmic function of the distance y from the boundary. It is commonly known as the Prandtl-Von Karman universal velocity distribution law. In the case of turbulent flow over a rough boundary, the value of y_o is a function of a roughness size.

For pipes with sand grains glued to the wall, Nikuradse found that

$$y_o = \frac{k_s}{30} \qquad (4.31)$$

where

K_s is the diameter of Nikuradse's sand grains known as the "Equivalent Sand Roughness" which was found to apply well to natural roughness, and to open channel flow.

Substituting Eq. (4.31) into Eq. (4.30) and changing to common logarithms gives

$$\frac{u}{u_*} = 5.75 \log \frac{y}{K_s} + 8.5 \qquad (4.32)$$

Eq. (4.32) expresses the resistance to flow of a pipe with a rough wall in a turbulent regime, and it can be integrated for different shapes of cross-section to obtain the following general theoretical formula.

$$\frac{u}{u_*} = A_o + 5.75 \log \frac{R}{K_s} \qquad (4.33)$$

Keulegan, G.H. (1938) studied Bazin's data and found that the parameter A_o reflects the shape of the cross section which has a wide range varying from 3.23 to 16.92, and it may be used as a mean value equal to6.25. It was also found that the theoretical uniform flow equation for rough channels is of the form

$$\frac{u}{u_*} = 6.25 + 5.75 \log \frac{R}{K_s} \qquad (4.34)$$

which yields

$$\frac{1}{\sqrt{f}} = 2.21 + 2.03 \log \frac{R}{K_s} \qquad (4.35)$$

Substituting Eq. (4.11) into Eq. (4.35), the Chezy's C for rough channel can be expressed as

$$C = 18 \log 12.21 \frac{R}{K_s} \qquad (4.36)$$

4.4.2 Power (Monomial) Type Formula

When a fully developed turbulent flow takes place over a hydrodynamically rough boundary, the friction factor parameter represented by $1/\sqrt{f}$, or u/u_*, will be directly related to the relative roughness parameter, $R/_D$. In this case the resistance equation may be expressed in the following power form.

$$\frac{1}{\sqrt{f}} = G \left(\frac{R}{D}\right)^m \qquad (4.37)$$

in which

G and m are parameters that may be determined for each particular case

It was also suggested by Nikuradse that over a limited range of $y/_D$, a power law will give an adequate approximation of the flow resistance, but that the exponent, m, and hence the coefficient, G, will vary with the channel geometry and the particle size.

In addition, Keulegan, G.H. (1938) developed a power type resistance equation as

$$\frac{u}{u*} = G\left(\frac{R}{D_{90}}\right)^m \qquad (4.38)$$

in which the value of, m, using the Karman form of the law of resistance for sand-coated pipes, was found equal to 1/6.

Simons, D.B., and Santurk, F. (1977) eliminated u/u* between the Keulegan's Eqs. (4.34 and 4.38) then by setting the exponent 1/6, the mean value of the coefficient, G, was derived as equal to 8.12, so Eq. (4.38) yields

$$\frac{u}{u*} = 8.12\left(\frac{R}{K_s}\right)^{1/6} \qquad (4.39)$$

which can be used to estimate the flow resistance in natural channels.

4.5 INVESTIGATIONS OF CHANNEL ROUGHNESS

Many investigations concerning the resistance to flow in natural rough channels have been carried out in the past. Einstein, H.A., and El-Samni, E.S. (1949) carried out a laboratory study on hemispherical roughness elements arranged in a hexagonal pattern and glued to the bottom of the flume. The objective of this study was to measure the hydrodynamic lift force acting on the roughness elements. The velocity profiles were also measured and the derived equation was found as

$$\frac{u}{u*} = 8.5 + 5.75 \log\left(\frac{y}{K_s}\right) \qquad (4.40)$$

in which

y is the flow depth above the theoretical bed datum which was deemed to be at 0.2D below the top of the hemispheres.

Also Mirajgaoker, A.G. and Charlu, K.L. (1963) conducted an experimental study to investigate the effects of large natural roughness in open channel flow. In an attempt to create such boulder stream conditions, they fixed natural stones from 65 to 75mm in diameter to the bed of a 0.9m wide rigid bed flume. Six different patterns of stone placements were tried during which the roughness densities varied from 15 to 114 stones per square yard.

As a result of this study, it was reported that Chezy's resistance factor and the relative roughness parameter are related by a logarithmic formula as

$$\frac{C}{\sqrt{g}} = 0.24 + 5.64 \log \frac{y}{K} \qquad (4.41)$$

in which

K is the roughness parameter dependent on the size, shape and spacing of the roughness elements.

Another type of artificial roughness was used by Powell, R.W. (1946) to study the effect of definite wall roughness upon the resistance to flow. The experiment was conducted in a rectangular flume in which eleven different arrangements of square steel strips and four different slopes were studied. This study indicated that Chezy's C could be expressed as

$$C = 40 \log \frac{R}{D} + C_s \qquad (4.42)$$

in which

C_s is a small shape correction equal to 2.74 for the case of rough channel when the depth is half of the width.

Leopold, L.B. et al. (1964) developed an equation to represent the resistance to flow in channels with beds of coarse materials as

$$\frac{1}{\sqrt{f}} = 1.0 + 2.03 \log \frac{y}{D_{84}} \tag{4.43}$$

which yields

$$\frac{u}{u_*} = 2.83 + 5.75 \log \frac{y}{D_{84}} \tag{4.44}$$

in which

D_{84} is the particle size referred to as the diameter which equals or exceeds 84 percent of the bed particle by count.

On the basis of experimental study in a channel with coarse bed material, Limerinos, J.T. (1970) developed the following resistance equation

$$\frac{n}{R^{1/6}} = \frac{0.0926}{1.16+2.03 \log \left(\frac{R}{D_{84}}\right)} \tag{4.45}$$

in which

D_{84} is the particle size for which 84 percent is finer. Noting that the measured roughness was obtained by Limerinos as

$$\frac{1}{\sqrt{f}} = 0.0926/(n/R^{1/6}) \tag{4.46}$$

Therefore Eq. (4.45) can be changed to

$$\frac{1}{\sqrt{f}} = 1.16 + 2.03 \log \frac{R}{D_{84}} \tag{4.47}$$

which can be also written as

$$\frac{u}{u_*} = 3.28 + 5.75 \log \frac{R}{D_{84}} \tag{4.48}$$

It can be seen that Eq. (4.48), which results from the empirical fit to Limerinos data, differs slightly from Eq. (4.44) which also results from an empirical fit to Leopold et al's data.

Limerinos has also used D_{50} to represent the roughness height, K, and the equation was

$$\frac{1}{\sqrt{f}} = 0.35 + 2.03 \log \frac{R}{D_{50}} \qquad (4.49)$$

or

$$\frac{u}{u_*} = 0.99 + 5.75 \log \frac{R}{D_{50}} \qquad (4.50)$$

On the basis of the assumption that the theory used to develop resistance equations for flow in pipes may be used to develop resistance equations for flow in rigid and movable boundary channels; Burkham, D.E. and Dawdy, D.R. (1976) utilized data from different sources to evaluate the applicability of some resistance formulae. Using Limerinos data, in which the mean of the ratios, D_{84}/D_{16}, is 7.3, Burkham and Dawdy replaced D_{84} in Eq. (4.48) with $7.3\ D_{16}$, and developed the following formula

$$\frac{u}{u_*} = -1.68 + 5.75 \log \frac{R}{D_{16}} \qquad (4.51)$$

The preceding equation leads to the conclusion that the average relation between, $(1/\sqrt{f})$, and, (R/D_{84}), apparently is reasonably well presented by Limerinos Eq. (4.47) as shown in Fig. (4.1). Also Burkham and Dawdy applied Keulegan's Eq. (4.34) to turbulent flow of channels of fairly rigid beds of boulders and gravels and concluded that using $K_s = D_{90}$ is reasonably accurate and better than using $K_s = D_{50}$ or $K_s = D_{65}$. This is also found to be in agreement wi .1 the work carried out by Bray, D.I. (1979).

The characteristics of the free surface flow over a bed consisting of hemispherical roughness elements of 23mm diameter were studied experimentally by Bayazit, M. (1976). It was found in this study that for large values of relative roughness (K/y>0.3) where K

is the hemisphere radius (the absolute roughness), the Darcy-Weisbach friction factor can be represented by the following equation

$$\frac{1}{\sqrt{f}} = 0.74 + 0.85 \ln \frac{y}{K} \qquad (4.52)$$

Bayazit also determined the location of the theoretical bed, with respect to which the depth can be measured, at distance 0.35D from the top of the roughness elements. He obtained the value of Von-Karman K = 0.41 and Nikuradse sand roughness K_s = 5D. The results obtained by Bayazit are shown in Fig. (4.2). These results were confirmed by Thompson, S.M. and Campbell, P.L. (1979) in their experimental study which was carried out on a large channel paved with boulders. Using a 41m wide by 308m long, open channel constructed of loose boulders and through which flows up to 140 m^3/s are passed, the Nikuradse's sand roughness K_s = 4.5D was obtained, in which D is the median boulder diameter by counting sample. In this study, a new expression for the Darcy-Weisbach coefficient was proposed as

$$\frac{1}{\sqrt{f}} = \left(1 - \frac{0.1K_s}{R}\right) 2 \log \left(\frac{12y}{K_s}\right) \qquad (4.53)$$

Zagni, A.F. and Smith, K.V.H. (1976) conducted extensive experiments on the flow over permeable beds of graded spheres placed in two laboratory flumes. They investigated the extent of the interchange between the flow in the channel and in the upper layers of the bed, and the effect of the permeable bed on the velocity distribution and on the boundary resistance using spherical particles of lead shot and steel balls; because of their high density these were capable of resisting erosion under relatively high tractive forces. With these materials, 20 different permeable beds were investigated using 4 different gradings. They have fitted the following equation for the whole population of the measured data.

$$\frac{u}{u_*} = 9.09 + 2.5 \ln \left(\frac{y}{D_{50}} + 0.68\right) \qquad (4.54)$$

The friction factor for fully rough flow is found

$$\frac{1}{\sqrt{f}} = 2.03 \log\left(\frac{2.74R}{e}\right) \tag{4.55}$$

$$e = (D_{65} K_p^{\frac{1}{2}})^{\frac{1}{2}} \tag{4.56}$$

in which

e is the permeable bed roughness parameter;

and K_p is the seepage coefficient of laminar flow.

The flow resistance of large-scale roughness on three locations at the upper River Tees in England was studied by Bathurst, J.C. (1978). It was suggested that the resistance to flow in a very rough channel depends mainly on the roughness geometry and varies with channel geometry. Bathurst concluded that the resistance coefficient should vary with the relative roughness, roughness shape, size, distribution, and spacing, and channel geometry. He suggested the following resistance equation

$$\frac{u}{u_*} = \left(\frac{R}{0.365 D_{84}}\right)^{2.34} \left(\frac{W}{y}\right)^{7(\lambda-0.08)} \tag{4.57}$$

in which

W is the surface width of flow;

and λ is the frontal concentration of the roughness elements which could be calculated as

$$\lambda = 0.139 \log\left(1.91 \frac{D_{84}}{R}\right) \tag{4.58}$$

Bathurst stated that the applicability of Eqs. (4.57) and (4.58) are only limited to the flow conditions for which they were developed.

In order to assess the effect of cross-sectional shape on the resistance to uniform flow in straight gravel-bed rivers, Hey, R.D. (1979) standardized the roughness height of the banks to that of the bed material. This was achieved by reducing the effective hydraulic length of the bank, if the bed is rougher than the bank, and the reverse if the bank is rougher than the bed.

Using data from 21 sites in four rivers in the U.K., Hey demonstrated the influence of cross-section geometry on the flow resistance which is represented by the coefficient, α, in the Colebrook, C.F. and White, C.M. (1937) formula as

$$\frac{1}{\sqrt{f}} = 2.03 \log \frac{\alpha R}{D_s} \qquad (4.59)$$

in which

D_s is the roughness height.

The value of, α in Eq. (4.59) was defined as a function of the ratio, R/y, as shown in Fig. (4.3) in which y is the perpendicular distance from the perimeter to the point of maximum velocity which is normally the maximum flow depth unless flow width-depth ratio is very small. This was explained by transforming a variety of channel cross-sections to their equivalent plane surface as indicated in Fig. (4.4).

Hey found that the roughness height of non-uniform gravel material was equal to $3.5\ D_{84}$, thus Eq. (4.59) may be modified to

$$\frac{1}{\sqrt{f}} = 2.03 \log \left(\frac{\alpha R}{3.5 D_{84}}\right) \qquad (4.60)$$

It was concluded from this study that the coefficient, α, in the Colebrook-White Eq. (4.59) must lie between the limits 11.1, for infinitely wide channels, and 13.46 for circular pipes. This small range implies that the influence of wide channel cross-section shape on friction factors is minor.

In conformity with this conclusion, Kazemipour, A.K. and Apelt, C.J. (1979), presented an analysis in which a new method for dealing with shape effect was developed based on a consideration of dimensional analysis and using experimental data.

The shape factor was derived as $\psi = \psi_1/\psi_2$, where, ψ_1, reflects

the effect of non-uniform distribution of the boundary shear stress and equals $\sqrt{P/B}$ where P is the wetted perimeter, and ψ_2 is a function of the width-average depth ratio and can be obtained from Fig. (4.5).

Griffiths, G.A. (1981) used 136 field data sets obtained from 72 reaches on 46 New Zealand gravel bed rivers for deriving flow resistance equations for both rigid and mobile beds. When the channel boundary is rigid the resistance to fully turbulent flow, in fairly straight and regular reaches, was found dependent largely on the relative roughness provided that the bed and bank roughness are the same and the surface bed material is described by the median size.

A theoretically based equation calibrated by the comprehensive data is found applicable to a rigid bed and defined as

$$\frac{1}{\sqrt{f}} = 0.76 + 1.98 \log \frac{R}{D_{50}} \qquad (4.61)$$

Also on the grounds of the correlation between the friction factor parameter, $1/\sqrt{f}$, and shape factor, P/R, the acceptable result of the statistical analysis was given by Griffiths as shown in Fig. (4.6) which yields

$$\frac{1}{\sqrt{f}} = 1.33 \left(\frac{R}{D_{50}} \right)^{0.287} \qquad (4.62)$$

A further contribution to the investigation of the resistance of boulder-bed channels with large scale roughness, was made by Bathurst, J.C. et al. (1981). The object of the study was to identify the processes affecting the flow hydraulics, and testing the based theory by using the flume data to develop a theoretical flow resistance equation. In order to permit a theoretical qualification of the developed equation, a variety of mathematical relationships between flow resistance and its determining factors were separately specified. Consequently, combinations between those relationships were analysed. Utilizing this technique and based on the experimental data, the combinations of the derived relationships which formed the flow resistance equation was given as:

$$\frac{u}{u_*} = \left(\frac{0.28Fr}{b}\right)^{A1} \times \left[13.434\left(\frac{B}{Y_{50}}\right)^{0.492} b^{A2}\right] \times \frac{A_B}{Bd'} \qquad (4.63)$$

in which

$$b = a\left(\frac{y}{S_{50}}\right)^{c} \qquad (4.64)$$

$$A1 = \log \frac{0.755}{b} \qquad (4.65)$$

$$A2 = 1.025\left(\frac{B}{Y_{50}}\right)^{0.118} \qquad (4.66)$$

$$Bd' = A + Aw \qquad (4.67)$$

$$Y_{50} = \frac{L_{50}+D_{50}}{2} \qquad (4.68)$$

where

S_n is the size of the short axis of the particle, which is bigger than or equal to n percent of the short axis;

d' is the depth from the free surface to the bed datum level;

A_B is the wetted roughness cross-sectional area;

A is the flow cross-section area;

a and c are constants varying with bed material properties;

L_{50} is long axis of the particle;

and Y_{50} is the cross-stream axis of the particle.

Based on the river data of Bathurst, J.C. (1978), as well as the data obtained for five different fixed roughness beds, a comparison between the observed values of $\frac{u}{u*}$ and values prediced by Eq. (4.63), and the results obtained by Thompson, S.M. and Campbell P.L. (1979), and Kellerhals, R. (1970), Hey, R.D. (1979), was carried out. In this comparison test, Eq. (4.63) compared favourably although its predictions were a little low.

4.6 BOUNDARY LAYER DEVELOPMENT

The major part of the current study was conducted in a trapezoidal channel having a certain degree of bed roughness which was

distinctly different from that of the side slopes. Also it was necessary to carry out the laboratory measurements in the full developed boundary layer zone. Therefore it is important to examine establishment of the boundary layer.

When water enters a channel from a quiescent area the flow at the boundary is laminar and the velocity distribution in the boundary layer is approximately parabolic. As the water travels farther along the channel, the flow in the boundary layer will eventually change to turbulent and the velocity distribution will eventually reach a definite pattern that can be shown to be approximately logarithmic. If the conditions for uniform flow exist throughout the channel, the turbulent boundary layer will be fully developed and the velocity profiles at various sections along the channel will be identical. This condition implies that the flow is established.

For the development of the boundary layer in wide channels, an approximate but practical method of computation was proposed by Bauer, W.J. (1954) (see Chow, V.T. 1959). The study of boundary layer development was made on concrete overflow spillways, but it has been found applicable also to channels of small slopes. From the results of Bauer's investigation, the following equation may be written

$$\frac{\delta}{x} = \frac{0.024}{(x/k)^{0.13}} \qquad (4.69)$$

where δ is the thickness of the turbulent boundary layer at distance x from upstream end of the channel.

The boundary layer development for the case of steady flow in a horizontal open channel was created theoretically by Delleur, J.W. (1957). The problem was also solved for a wide channel in terms of the two-dimensional equation and subsequently verified experimentally. It was shown by Delleur that the layer develops more slowly than for a flat plate in an infinite fluid under similar flow conditions. This implies that in the presence of a rough side wall the turbulent boundary layer would grow rapidly until it reaches the surface.

In addition, Chow, T.V. (1959) reported that in a laboratory channel the laminar boundary layer can be eliminated easily by placing roughness elements at the entrance. Thus the boundary layer may reach complete establishment at the very beginning of the channel.

As a result of this, one may conclude that the development of the boundary layer in open channels of finite width has received little attention. Since the present investigation was conducted in a channel having a bed roughness distinctly different from that of the side slopes, it was necessary to measure the velocity distribution along the channel centre line for different flow conditions to ascertain the flow establishment.

4.7 COMPOSITE ROUGHNESS : EFFECTIVE MANNINGS'S n

In ordinary open channels, the boundary roughness may be distinctly different from part to part of the perimeter, but the mean velocity can still be computed by uniform-flow formula without sub-dividing the section. But to apply these formulae to such a channel having more than one degree of roughness along its wetted perimeter, it is necessary to compute an equivalent (effective) roughness coefficient for the entire perimeter which can be then used for the determination of the flow in the whole section.

Using the Manning formula given by Eq. (4.13), four different approaches, to determine the effective roughness coefficient, for channels having bed roughness different from bank roughness, were developed. In each approach, the effective n value was evaluated as a function of the bed and bank roughness and their respective segments of the wetted perimeter or flow area. These approaches, which are reported by Chow, V.T. (1959), can be described as follows:

A - Los Angeles District Formula

$$n_{eff} = \frac{\Sigma nA}{\Sigma A} \qquad (4.70)$$

which can be written for the rectangular or trapezoidal cross-section channel as

$$n_{eff} = \frac{2A_2 n_2 + A_1 n_1}{2A_2 + A_1} \qquad (4.71)$$

where

n_{eff} is the equivalent (effective) roughness coefficient;

A_2 and A_1 are the cross-sectional areas associated with the channel side walls and bed, respectively;

and n_2 and n_1 are the roughness coefficients associated with the channel side walls and bed, respectively.

B - Horton or Einstein Formula

$$n_{eff} = \left[\frac{\Sigma(n^{3/2} P)}{P}\right]^{2/3} \qquad (4.72)$$

This equation can be written as

$$n_{eff} = \left[\frac{2P_2 n_2^{3/2} + P_1 n_1^{3/2}}{2P_2 + P_1}\right]^{2/3} \qquad (4.73)$$

in which

P_2 and P_1 are the wetted perimeters associated with the channel side walls and bed respectively

C - Colebach Formula

$$n_{eff} = \left[\frac{\Sigma A\, n^{3/2}}{\Sigma A}\right]^{2/3} \qquad (4.74)$$

which can be written as

$$n_{eff} = \left[\frac{2A_2 n_2^{3/2} + A_1 n_1^{3/2}}{2A_2 + A_1}\right]^{2/3} \qquad (4.75)$$

D - Chow Formula

On the basis of the Einstein, H.A. and Banks, R.B. (1950) assumption that the total force resisting the flow can be expressed as the sum of the forces resisting the flow developed in the sub-divided areas, Chow, V.T. (1959) derived the following formula

$$n_{eff} = \left[\frac{\Sigma\, Pn^2}{\Sigma P} \right]^{\frac{1}{2}} \qquad (4.76)$$

which can be written for the rectangular cross-section channel as

$$n_{eff} = \left[\frac{2P_2 n_2^2 + P_1 n_1^2}{2P_2 + P_1} \right]^{\frac{1}{2}} \qquad (4.77)$$

Further research was carried out by the U.S. Army Engineers (1970), in which the effective roughness coefficient according to the Horton-Einstein formula Eq. (4.73) was found to be more conservative than that computed by the other methods. Accordingly, they recommended the Horton-Einstein approach and developed two charts to provide a rapid graphical solution. The first chart, which is shown in Fig. (4.7A), is used to obtain the required wetted perimeter ratio as a function of the channel geometry. This ratio can then be entered to the second chart depicted in Fig. (4.7B) to the intersection with an imaginary line connecting n_1 and n_2. The value of n_{eff} at this point is read on the right side of the chart.

To justify the applicability of the preceding formulae, Cox, R.G. (1973) carried out an experimental study using a composite roughened rectangular channel. It was reported from this study that extensive laboratory and field investigations are needed for a complete evaluation.

4.8 DISCUSSION

From the extensive literature survey presented in this chapter, one may conclude that several best-fit relations were developed and calibrated utilizing comprehensive field and model data. But due to the complexity of the phenomenon under consideration, there is no unique empirical formula which can be said to be

applicable for the various conditions. In addition, on the basis of the theory introduced by Prandtl-Von Karman, which is explained earlier in Section (4.4.1), Keulegan developed his universal resistance formula Eq. (4.34) for turbulent flow in a rigid boundary. Other investigators using different types of roughness elements as well as different cross-section geometries presented several formulae, as Eqs. (4.40), (4.44), (4.48), (4.50), (4.51) and (4.54), but with different coefficients.

Additionally, to the best of the Author's knowledge no investigation has been carried out on channels having bed roughness distinctly different from that of side slope as used during the current study. This implies the difficulty of comparing the results obtained from the laboratory tests with that reviewed in this chapter.

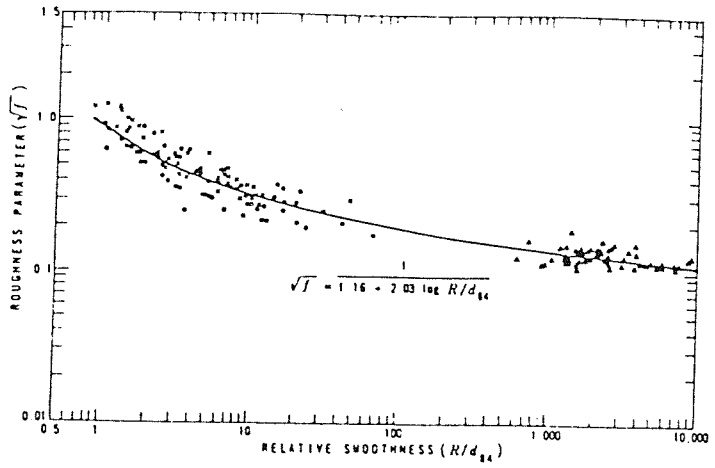

Fig. 4-1 : Relation of Roughness Parameter to Relative Smoothness

(LIMERINOS, 1970)

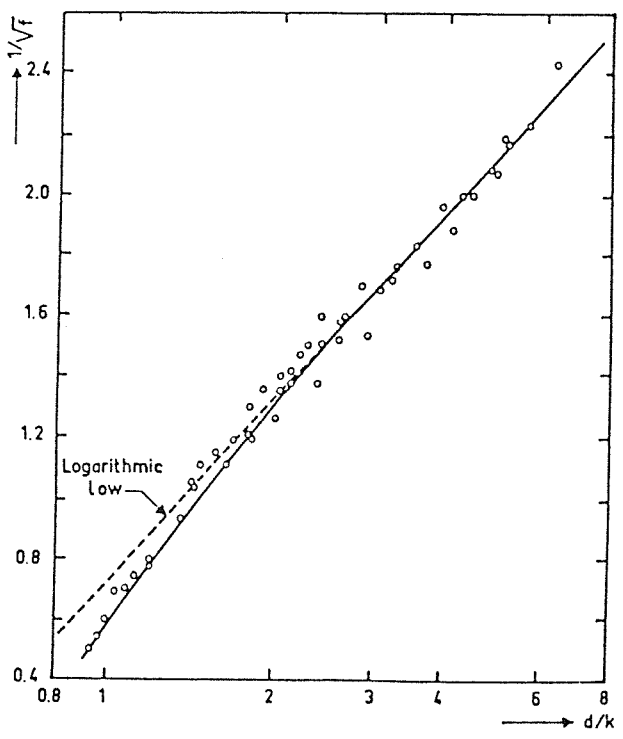

Variation of Darcy's friction factor f with relative roughness.

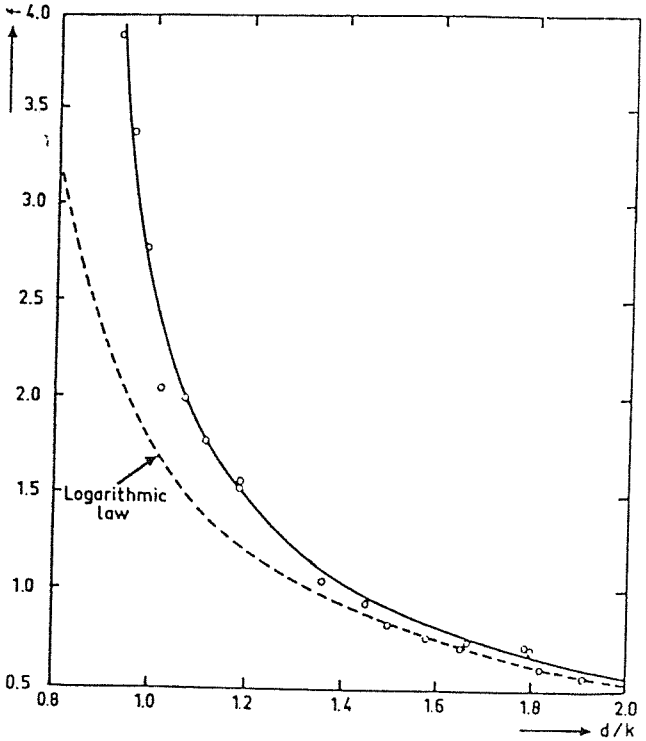

Deviation of friction factor from logarithmic law at large values of relative roughness.

FIG. 4-2 : THE RESULTS OBTAINED BY BAYAZIT, 1975

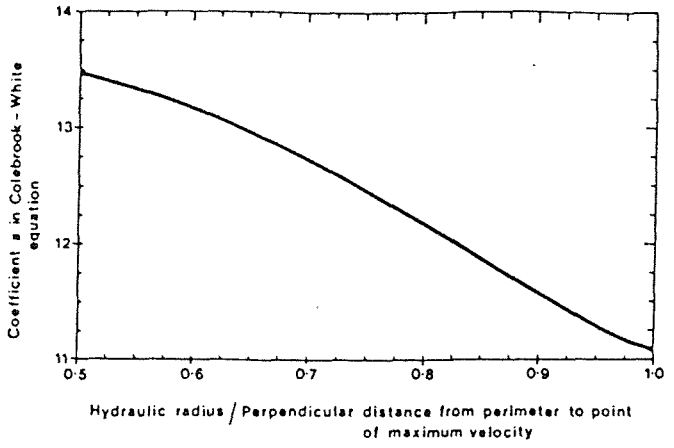

FIG. 4–3: General Relation between Value of Coefficient a in Colebrook-White Flow Resistance Equation and Hydraulic Shape of Channel (R/y)

(HEY, 1979)

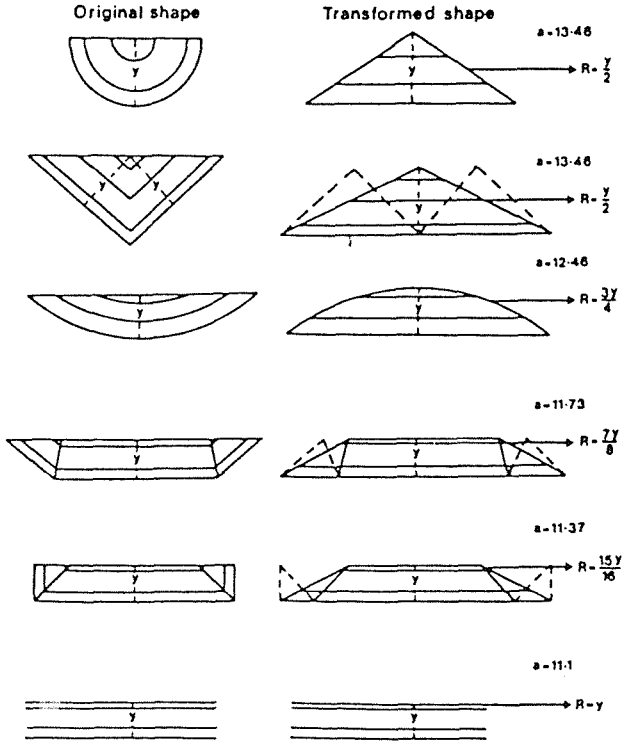

FIG. 4–4: Influence of Cross-Sectional Shape on Coefficient a in Colebrook-White Flow Resistance Equation for Given Value of Hydraulic Radius (Uniform Bed and Bank Material)

(HEY, 1979)

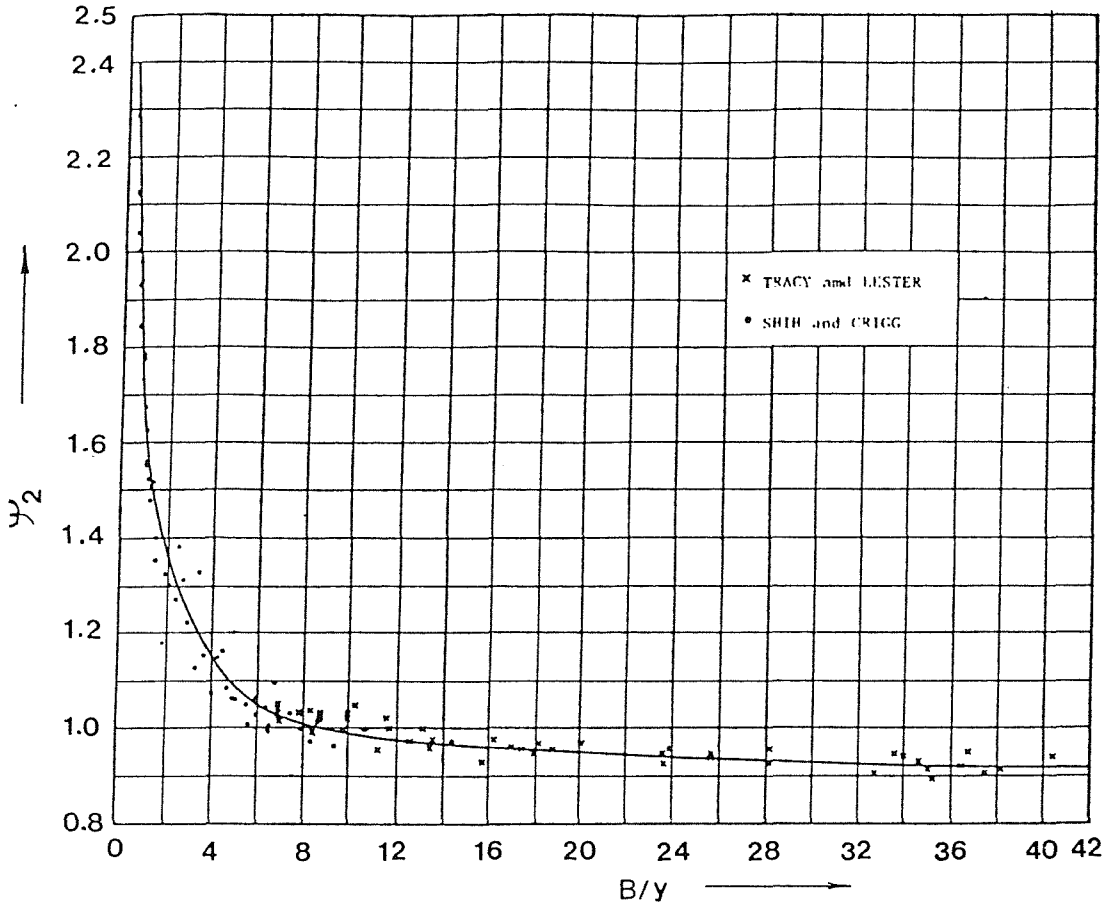

FIG. 4-5 : THE EFFECT OF THE WIDTH/ DEPTH RATIO ON Ψ_2

(KAZEMIPOUR, 1979)

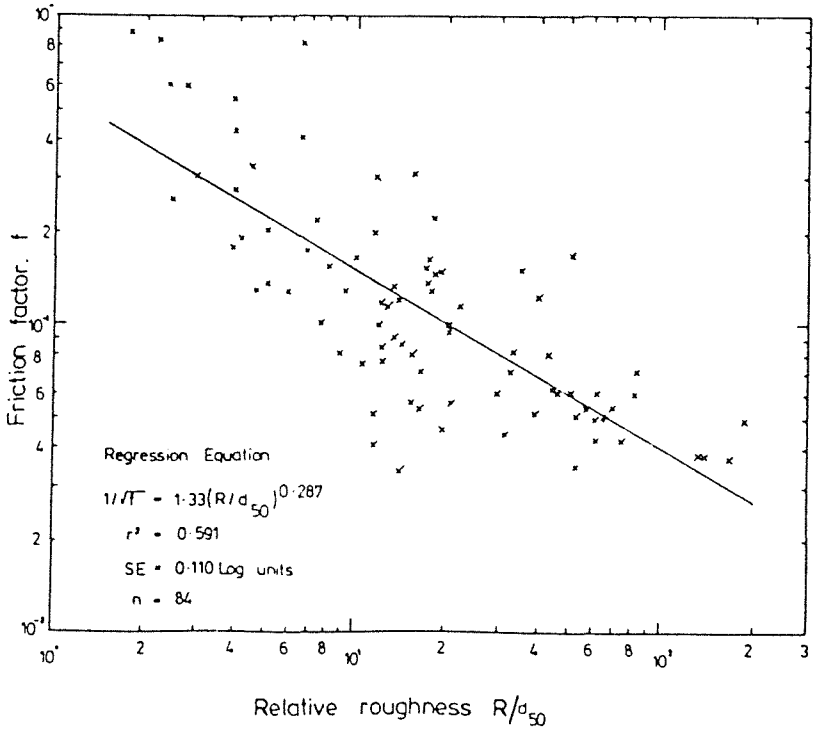

FIG.4-6:Friction Factor vs Relative Roughness for Rigid Boundary Conditions in Coarse Gravel Bed Rivers

(GRIFFITHS, 1981)

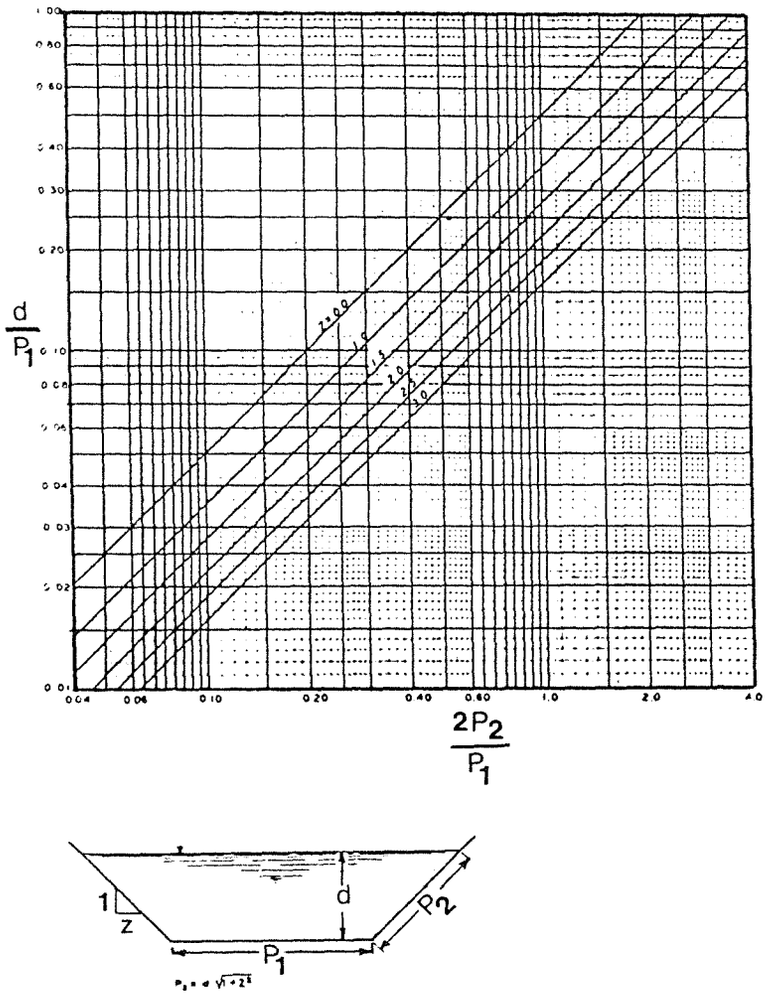

FIG. 4-7A–WETTED PERIMETER RELATION

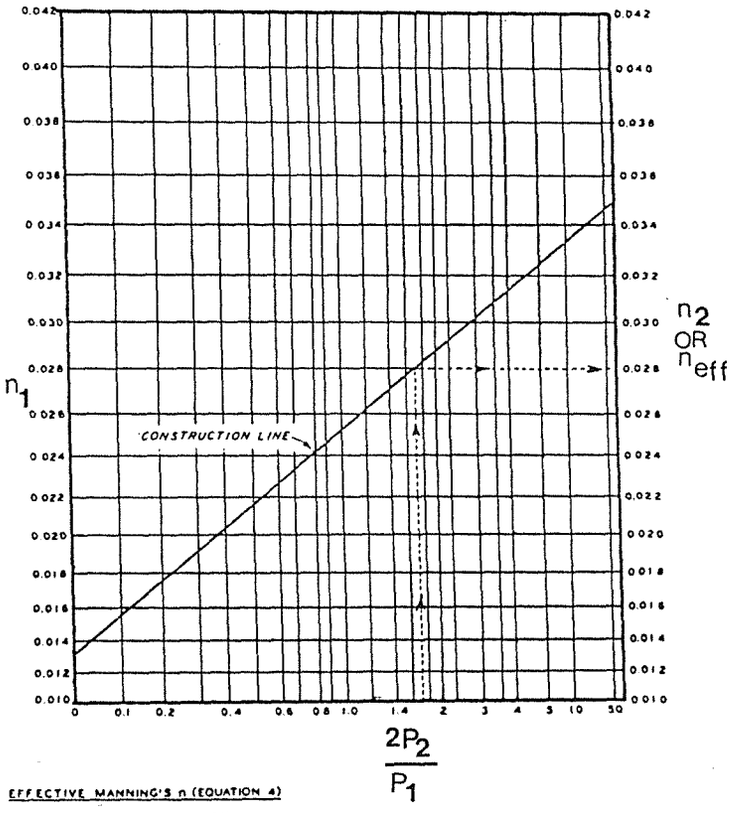

EFFECTIVE MANNING'S n (EQUATION 4)

$$n_{eff} = \left(\frac{n_1^{3/2} P_1 + 2 n_2^{3/2} P_2}{P_1 + 2P_2} \right)^{2/3}$$

WHERE:

n_1 = BED ROUGHNESS

n_2 = SIDE SLOPE ROUGHNESS

n_{eff} = EFFECTIVE ROUGHNESS

P_2 = SIDE SLOPE WALL LENGTH

P_1 = BOTTOM WIDTH

FIG. 4-7B– EFFECTIVE MANNING'S n

(U.S. ARMY ENGINEERS, 1970)

CHAPTER FIVE

EXPERIMENTAL EQUIPMENT AND PROCEDURES

5.1 INTRODUCTION

The current investigation was carried out in the hydraulic laboratory of Southampton University at Chilworth. Three series of testing programmes were conducted in modelled channels of trapezoidal cross-section. These are summarized as follows:

1) The first series was carried out in a concrete-lined outdoor flume to investigate the failure mode of the protective layer, and to identify the hydraulic parameters at the threshold and failure flow conditions as well as to study the flow resistance of the roughened channels. Four different designs were tested, in which the protective layer consisted of uniform riprap material of mean size 20.7mm.

2) The second series was conducted in a large recirculating indoor flume to investigate the effect of some major factors influencing failure. In this series, two different models were tested to assess the use of a sheet cloth filter as well as a graded material.

3) Finally, the third series was also conducted in the large indoor flume to record the hydrodynamic lift and drag forces on instrumented spherical and non-spherical particles. To achieve these results, the following three studies were conducted:

   a) Location of the point of maximum shear
   b) Determination of the representative spherical particle
   c) Theoretical approach to convert the recorded signals into lift and drag forces.

In this chapter, the facilities utilized during the course of the first two series, namely the flumes, equipment, instrumentation, as well as calibration of the measuring devices are described in detail. Also the testing programme, including the design, operation and working procedure of all the constructed models is described.

5.2 THE FLUMES

5.2.1 The Concrete Flume

The first series of the experimental work was conducted in a 55m long concrete flume which has a trapezoidal cross-section 2.07m bed width, 0.53m depth and 1H:1V side slopes. To control the flow rate a manually operated sluice gate was installed at the upstream end of the flume, whereas a 1.002m width movable rectangular thin plate weir was constructed at the downstream end for measuring the discharge. The flume was provided with an upstream deep concrete reservoir, downstream tank and pumping station consisting of three vertical axial flow pumps (capacity 150 l/s) each and the whole system was located in the open air outside the laboratory building.

Referring to the flow process, water is pumped from the upstream reservoir to an upstream distribution tank where it enters the concrete flume by gravity feed through the upstream gate. The water collected at the downstream tank then returned to the upstream reservoir by gravity through an underground concrete tunnel. The layout and details of the system are shown in Fig. (5.1).

5.2.2 The Large Flume

The second and third series of the study were conducted in a large recirculating flume which has a working length of 21.4m with a rectangular cross-section 1.37m width and 0.61m depth. The general layout of the flume is schematically shown in Fig. (5.2), whereas a cross-section is depicted in Fig. (5.3). The walls were of toughened glass and the bed was made of 6mm steel plate. Along the top of the side walls, brass rails were mounted for the purpose of

supporting a movable instrument carriage containing a point gauge which can measure vertical elevations relative to the flume to 0.1mm accuracy.

To control the water surface slope, the flume was provided with a radially movable steel weir which could be adjusted manually. The entire flume was mounted on a steel truss and provided with an electrical actuator to adjust the truss and hence the slope of the flume. The flume was also equipped with three electrically driven centrifugal pumps providing a total flow capacity of 0.47 m^3/s. Each pump was provided with suction and delivery pipes, a system of control valves and a "Kent Commander" flow gauge connected to a Dall tube inserted within the pipeline to measure the flow rate.

Water enters the flume from two 0.3m diameter delivery pipes discharging into a steel inlet tank. At the downstream end of the flume, a short steel exit tank was provided from which the flow passes via the sump to the suction pipes of the three pumps. A schematic arrangement of the system is shown in Fig. (5.4).

5.3 DISCHARGE MEASURING EQUIPMENT

5.3.1 The Concrete Flume

To measure the flow discharge accurately in the concrete flume, a movable thin plate weir was installed at the downstream end of the lined channel. The weir was made of stainless steel plate 12mm thick manufactured according to the specifications set by the British Standards Institution, BS No. 3680: Part 4A: (1981), as illustrated in Fig. (5.5). In order to establish steady uniform flow in the upstream portion of the weir, which is necessary for measuring the flow head accurately, a short approach channel was constructed upstream from the weir. This approach was of rectangular cross-section 2.2m in length, 1.8m bed width and 0.53m height. A long point gauge with a vernier reading to 0.1mm was mounted upstream from the weir for measuring the head over the thin plate weir.

One of the accepted discharge formulae for the rectangular thin plate weir is that proposed by Kindsvater-Carter, which is reported by BS. (1981) as:

$$Q = \frac{2}{3}\sqrt{2g}\ C_e\ b_e\ h_e^{3/2} \qquad (5.1)$$

in which

Q is the flow rate;
b_e is the effective width;
h_e is the effective head;
g is the acceleration due to gravity;
and C_e is the coefficient of the discharge which can be determined as:

$$C_e = f\left(\frac{b}{B}, \frac{h}{p}\right) \qquad (5.2)$$

in which

b is the width of the weir;
B is the width of the approach channel;
h is the measured head;
and p is the height of the weir crest.

For the case under consideration, the ratio b/B was found equal to 0.556. Therefore to obtain the, C_e, value in Eq. (5.2), a graphical chart, which is provided by BS for the relation between, C_e, and, h/b, for various values of, b/B, was used as depicted in Fig. (5.6). As a result of this the interpolated value of, C_e, for, $b/B = 0.556$, was determined as:

$$C_e = 0.592 + 0.0152\frac{h}{p} \qquad (5.3)$$

To obtain the values b_e and h_e in Eq. (5.1), such relationships were given by BS as:

$$b_e = b + k_{b1} \qquad (5.4)$$

$$h_e = h + k_h \qquad (5.5)$$

in which

k_h is an empirical adjustment for the head which can be taken as a constant value of 0.001m for the weirs constructed according to BS;

and k_{b1} is an empirical adjustment for the bed width and can be obtained by using Fig. (5.7), which gives the value of k_{b1} equal to 3.4mm.

5.3.2 The Large Flume

As has been mentioned previously, the large flume was equipped with a rotating tail gate as well as the facility for measuring the flow by means of three "Kent Commander" flow gauges. But because precise measurements were required, it was decided to use the thin plate weir as a convenient and accurate method for measuring the flow rate.

A rectangular thin plate weir was designed, manufactured and installed by the Author according to the specifications set in the British Standards No. 3680 : Part 4A : 1981. The weir was made of 12mm thick perspex plate with p = 0.20m and ratio b/B = 0.8. The crest was cut and shaped with reasonable care and skill to meet the BS specifications. The discharge formula specified by Eq. (5.1) was also used, in which C_e was found equal to

$$C_e = 0.596 + 0.045 \frac{h}{p} \qquad (5.6)$$

Using Fig. (5.7), as before, for b/B = 0.8, the empirical correction, k_{b2}, was obtained equal to 4.25mm. Fig. (5.8), shows the calibration curve of the rectangular thin plate weir.

To install the fabricated weir, a frame consisting of channel section was screwed firmly in the vertical position into the flume 2m upstream of the rotating tail gate and perpendicular to the flow direction. At the beginning of each run, the gate was placed at a

horizontal position, then the rectangular weir was set up. Using the mounted point gauge, the actual flow head could be recorded and hence the flow rate could be determined. At this stage, the weir could be removed and the tail gate was raised or lowered according to the requirement for uniform flow conditions in the modelled channel. Plate (5.1), shows the rectangular weir used in the large flume.

5.4 DEPTH MEASUREMENTS

5.4.1 The Concrete Flume

Since the study conducted in this flume was mainly concerned with the visualization of the particle movement, a new technique was established for measuring the flow depth. Five side wells were installed along the right bank of the constructed models. Each side well consisted of a horizontal steel pipe 15mm diameter and 0.62m length connected to another vertical steel pipe 175mm diameter and 375mm height with a steel base. The connection between the two pipes was arranged in such a way as to provide a dead water zone of 20mm height serving as a stilling well at the bed of the vertical pipe. The side well details and its locations in the model are shown in Fig. (5.9) and Plate (5.2).

The side wells were located 0.8m apart starting at distance 3.7m downstream of the constructed channel. Each side well was cemented firmly in the vertical position with its horizontal pipe perpendicular to the flow direction, and equipped with a point gauge and a vernier scale reading to 0.1mm.

In each run using the movable end gate, the flow depth along the channel was adjusted so as to be approximately constant. The flow depth opposite to each side well station was obtained as the difference between the water level in each side well and its corresponding bed level. The mean flow depth could then be obtained as the average of the measured depth in the five side well stations.

5.4.2 The Large Flume

To measure the flow depth in the large flume, a constant flow depth was arbitrarily obtained by using the downstream gate. Then the water surface elevation along the constructed model was measured. The mean flow depth was defined as the average difference between the water surface level and the corresponding bed level.

The water surface slope was measured by a series of eight piezometer tappings distributed 70 cm apart along the lower part of the right bank. Each piezometer mouth consists of a 15 mm diameter plastic tube connected from the other side to an especially manufactured metallic tube which was firmly screwed through the flume bed. Another eight plastic piezometer tappings 15 mm diameter were connected to the metallic tubes from outside of the flume. These tappings were then extended underneath the flume and connected from the other side to eight piezometer glass tubes 15 mm diameter and 60 cm length. The glass tubes were attached side by side vertically against a wooden board which was fixed on the left side wall of the flume from outside as shown in Plate (5.3). A cathetometer reading to 0.01 mm was used to measure the water surface elevations inside the glass tubes, from which the mean flow depth could be worked out.

5.4.3 Flow Depth and Bed Width Corrections

In the case of a channel riprap lined either on the bed or side slopes, as water flows in the channel a certain amount of water will flow through the interstices between the particles. Accordingly, the measured flow depth will not be the same as that in a similar channel without rock protection as illustrated in Fig. (5.10). Moreover, the measured flow depth in the riprap lined channel will depend on the voids contained within the protective layer which are respectively dependent on either the degree of compaction or the manner of placement of the protective layer. Therefore, it was decided to correct the designed cross-section area by adding certain increments to the measured bed width and flow depth equivalent to the voids contained within the unit area of the protective layer.

This test was carried out experimentally on both types of rock materials used during the course of the experimental work according to the procedure mentioned by Vickers, B. (1978), as follows:

A square wooden frame with inside area 60 x 60 cm and height equal to 31 mm which represents the thickness of riprap layer used in the investigation, was made. A random sample of the protective layer was taken. The frame was laid on a horizontal desk then filled with the particles in the same manner as applied during the model construction. This test was carried out 20 times for each riprap type; for each test the weight of the tested layer was worked out then the following procedure was applied.

Knowing the specific weight of the particles, the volume of the solid tested material was determined as V_s. Subtracting V_s from the volume of the layer, the contained volume of voids within the tested layer can be worked out as V_v. The mean value of V_v for each riprap type was calculated, then converted into an imaginary constant thickness which covers the whole area of the tested layer. This thickness was then calculated in the vertical and horizontal directions, as shown in Fig. (5.10), as empirical corrections for the measured flow depth and designed bed width, respectively. The results obtained from this test are:

No.	Description	Uniform material	Non-Uniform material
1	void ratio $e = \frac{V_v}{V_s}$	0.718	0.579
2	porosity $n = \frac{V_v}{V_T}$	0.418	0.367
3	depth correction ΔY (m)	0.013	0.011
4	bed width correction ΔB(m)	0.047	0.04

in which

V_T is the whole layer volume = $V_V + V_S$

It is easy to conclude from this test that the voids content in the case of graded material is less than that in the uniform material case which is due to the tendency of smaller particles to fill the interstices between the larger particles. Hence the correction factors for non-uniform material were less than those for uniform material.

On the other hand, the depth correction, ΔY, was added only during the first two models, where the channel bed was protected, whereas the bed width correction, ΔB, was added for each run of all the constructed models.

5.5 DETERMINATION OF THE ENERGY SLOPE

As mentioned earlier, the surface water elevation along the constructed models was recorded by utilizing the point gauges in the case of the concrete flume and the cathetometer in the case of the large flume. Using these measurements, the water surface slope and hence the energy slope could be precisely determined.

Since an accurate evaluation of the energy slope was required, a full discussion of two approaches for determining the energy slope is presented, and the selection of the appropriate method would be then justified by a comparison between the results obtained by applying both methods. These methods can be described as follows in the sub-sections.

5.5.A The Energy Approach

This approach utilizes the energy conservation concept, according to which the total energy head at the upstream control section should be equal to that at the downstream control section plus the energy loss due to friction.

From the geometry of Fig. (5.11), the following expression can be derived:

$$S_o L + d_1 + \alpha_1 \frac{u_1^2}{2g} = LS_e + d_2 + \alpha_2 \frac{u_2^2}{2g} \qquad (5.7)$$

in which

d_1 and d_2 are the flow depths at the upstream and downstream control section respectively;

u_1 and u_2 are the mean velocities at the two control sections;

α_1 and α_2 are the velocity head coefficients at the two control sections;

S_o is the bed slope;

S_e is the slope of the energy line;-

and L is the horizontal distance between both control sections.

Eq. (5.7) is the well-known Bernoulli energy equation. On the other hand, in evaluating the values α_1 and α_2, Webber, N.B. (1971), reported that for normal turbulent flow the velocity head is only a small proportion of the total head and the error which results from assuming the coefficients α_1 and α_2 to be unity is negligible. In addition, Chow, V.T. (1959) suggested that for a channel of small slope, the velocity head coefficients may be taken equal to unity. Therefore, Eq. (5.7) may be written as

$$S_o L + d_1 + \frac{u_1^2}{2g} = LS_e + d_2 + \frac{u_2^2}{2g} \qquad (5.8)$$

Knowing the flow parameters at both sections and the distance between both of them, the S_e value can be determined.

5.5-B The O'Brien Approach

Since most of the experiments were conducted in steady and near-uniform flow conditions, the formula for near-uniform flow developed by O'Brien, M.P. and Hickox, G.H. (1937), and recommended by Simons, D.B. and Senturk, F. (1977), can be used in the determination of the energy slope as

$$S_e = S_w - F_r^2 (S_w - S_o) \qquad (5.9)$$

in which

$$F_r^2 = \frac{u^2}{gR} \qquad (5.10)$$

where

S_w is the slope of the water surface;
F_r is the Froude number;
and R is the hydraulic radius.

To justify the applicability of the aforementioned formulae given by Eqs. (5.8 and 5.9), the energy slope of each run of the first model (40 runs) was calculated by both methods. The comparison between the results obtained from this test, which are plotted in Fig. (5.12), indicated that the relationship between the results obtained by both approaches yields

$$S_{e1} = 0.00022 + 0.954\ S_{e2} \qquad (5.11)$$

in which

S_{e1} is the energy slope resulting from applying O'Brien's Eq. (5.9);
and S_{e2} is the energy slope resulting from applying the energy Eq. (5.8).

Equation (5.11) was obtained with correlation coefficient of 0.9996 and standard error of estimate 0.0042. This implies that O'Brien's formula gives an appreciably conservative result with a negligible difference comparable to that obtained by the other formula. Therefore, it was decided to use the O'Brien's equation because it reflects more accurately the state of flow.

5.6 MODEL DESIGNS

In order to describe the various designs used during the course of the experimental tests, consideration should be firstly directed to state the reasons for which these designs were selected. It is obvious that stability of a protected side slope is dependent upon numerous factors such as:

1) Dimension of the channel cross-section
2) Side slope value
3) Particle size
4) Thickness of the protective layer.

On the other hand, there are also considerations that should be taken into account associated with the experiment requirements such as:

1) The attainable flow rate in the laboratory
2) The available space needed for the model construction
3) The instrumentation needed for measuring the hydrodynamic forces.

Therefore, taking into account that the available approaches for sizing riprap for side slope protection were mainly derived on the basis of the theoretical considerations, a preliminary study was carried out by the Author involving the various possibilities of the required design, and the optimum design which fulfils all the requirements was then established.

The design of the models will now be explained. Six models were constructed during the first two series of the experimental work as indicated in Table (5.1). These models were designed, as mentioned earlier, to investigate the flow characteristics at the threshold and failure conditions, to study the mode of failure, to evaluate the factors affecting the side slope stability and to study the flow resistance of the roughened channel. Those models can be described as follows:

5.6.1 Models Constructed in the Concrete Flume

Four models of trapezoidal cross-section channel of 10.0m length were designed and constructed in the concrete flume. These models, as seen in Plate (5.4) were mainly constructed with a sand base, a conventional filter composed of two aggregate layers 1.5 cm thick each and a rock protective layer consisting of a uniform rock

particle of mean size 20.7 mm and equivalent to 1.5 particle diameter thick. In the first two models, the channel bed and side slopes were protected, whereas in the case of the other two models, the side slopes only were protected and the beds were lined with a cloth sheet filter. The bed width of the first three models was 0.4m, and 0.5m in the case of the fourth model.

Considering the model alignments, the following portions can be distinguished:

1) 1.0m of two converging side slopes act as a smooth transition zone between the exterior cross-section of the flume and the designed channel.

2) 8.0m long channel of trapezoidal cross-section with two protected side slopes 1.5H:1.0V each.

3) 1.0m of two diverging side slopes act as a transition zone leading to the flume cross-section. General layout of those models are shown in Fig. (5.13).

In general, the mean difference between these models may be summarized as:

Model No. (1). The channel bed and side slopes were protected with a free uniform rock layer equivalent to 1.5 mean particle size thickness. The bed slope was 0.005 and forty runs were carried out.

Model No. (2). The channel bed and side slopes were protected as that in model No. (1), and the bed slope was steepened to 0.008 and twenty-one runs were carried out.

Model No. (3). the bed slope was 0.008 as that in the previous model, but the channel cross-section was composed of two protected side slopes and a sand bed covered with a cloth sheet filter. Twenty-two runs were conducted with this model.

Model No. (4). The channel protection was the same as that in model No. (3), but the bed slope was steepened to 0.0125, and the bed width enlarged to 0.5m. Thirty three runs were conducted on this model.

The details of these models are shown in Figs. (5.14 to 5.16) and Table (5.1), whilst Plate (5.5) shows model No. (4) during the experimental tests.

Consideration is now given to provide more details about the model alignments, facilities and construction of those models. To improve the flow condition as well as to obtain accurate results from the experimental work, these models were provided with the following facilities:

I) Inlet and exit sills

Two timber sills 100mm width each were installed at the inlet and exit of the models perpendicular to the flow direction. Using a survey level, these sills were adjusted horizontally to the designed levels of the channel bed at both ends. The purpose of constructing these sills was to use them as the reference levels to adjust the channel bed slope during the model construction.

II) Feed pipeline

Since stability is the purpose of the current investigation, it was decided to adjust the flow rate in such a way as to prevent any possible disturbance to the protective layer, due to the difference between upstream and downstream water surface levels at the beginning of each run. To achieve this goal, a steel pipeline 12m length and 50mm diameter was positioned along the right corner of the flume cross-section and underneath the model construction. This pipeline was cemented at a gentle slope to the downstream direction and provided with sluice valves at both ends.

At the beginning of each run, the pipeline was used as a by-pass to deliver the flow directly into the downstream portion of the

model in such a way as to maintain the upstream and downstream water surfaces at almost the level. As the flow rate was approximately adjusted, the pipeline was then closed to pass the total flow through the channel.

II) Upstream and downstream ramps

Several methods were tried to improve the flow conditions at the channel entrance and exit. A simple and successful method was established.

Two ramps were constructed as a transition zone between the bed level of the channel and that of the flume. The ramps consisted of a mixture of coarse gravel and cobbles which allowed seepage flow through the permeable bed material. The purpose of the ramp constructions was to divert the flow smoothly into the channel cross-section without creating any local disturbance. On the other hand, placing roughness elements at the channel entrance would eliminate the laminar boundary layer. Consequently, the turbulent boundary layer would be developed at the very beginning of the channel.

These models were constructed according to the following procedure:

The feed pipeline was firstly positioned and cemented to the flume bed, then both the sills were installed and adjusted horizontally to their designed levels. The side wells, in the case of the concrete flume, or the piezometer tappings, in the case of the large flume, were carefully located and adjusted, then the sand base material was put into the flume, and using a special timber template representing the sand base cross-section profile, the base material was formed along the channel. Two layers each 1.5 cm thick of properly designed granular material filter were introduced in between the sand base and the protective layer. Then a rock layer of 31mm was applied manually with a uniform thickness over the whole filter layers by using a square frame of 31mm thick. Finally the ramp materials were placed and compacted gently to a mild slope.

5.6.2 Models Constructed in the Large Flume

Two models were constructed in the large flume to investigate the effect of utilizing sheet cloth filter and graded material on the side slope riprap stability, and also to study the failure process quantitatively. The construction of these models, which are shown in Fig. (5.17) and Plate (5.6) can be summarized as:

Model No. (5). This was constructed to assess the effect of using sheet filter on the stability of the riprap layer. The model was similar to Model No. (4) except that instead of using a conventional filter underneath the protective layer, a synthetic cloth filter was used. Thirty-six runs were carried out on this model.

Model No. (6). This was constructed similar to that of Model No. (5), except that the protective layer consisted of graded material. Twenty-two runs were conducted on this model to study the flow characteristics and the failure discharge.

These two models were constructed similar to the procedure applied in the case of the first four models discussed previously.

Considering the particle size distribution of the riprap layer, and in order to compare the results obtained from various models, the following conditions were established:

1) D_{50} of the graded material should be the same as that of uniform material used in the previous models.

2) The thickness of the protective layer should also be the same.

3) To prevent segregation of the small particles, the size distribution curve of the graded material should cover a wide range of particle sizes.

To establish the appropriate particle sized distribution, the recommended gradation curve by Simons, D.B. and Senturk, F. (1977), which is shown in Fig. (5.18), was modified by the Author to satisfy the aforementioned three conditions. According to the gradation criteria, which are depicted in Fig. (5.19), the ratio of maximum size to the median should be about 1.5, and the ratio between median size and the 20 percent size should also be about 1.5. Plate (5.7) shows the riprap materials used in the investigations and Plate (5.8) shows the various particle sizes used in the mixture.

In order to define the failure of the protective layer quantitatively, a specially designed study was conducted on the Model No. (6). In this study the protective layer, of one metre length along the right side slope at 2.0 m upstream of the channel exit, was marked with eight different coloured compartments, 20 x 25 cm each. The particle mixture content of each compartment was composed separately by weight then coloured with a permanent colour. Using a timber frame with thickness 31 mm and divided into eight areas 20 x 25 each, the mixture materials were applied with uniform thickness on the side slope.

This test was conducted to distinguish the particle movement at the failure flow condition and also to work out some statistical relationships to analyse this criterion quantitatively.

5.7 THE EXPERIMENTAL PROCEDURE

To enable the side slope stability as well as the flow characteristics to be studied, a comprehensive testing programme was carried out on all the constructed models. This testing programme consisted of numerous runs which covered a wide range of flow rates. For each run the uniform steady flow was firstly established then the flow rate and the corresponding uniform depth were measured according to the following procedure:

Using the end gate, in the case of the concrete flume, the uniform flow was approximately established. Then utilizing the mounted point gauges, the water surface elevations and hence the

water surface slope was determined. This procedure was repeated until the measured water surface slope became nearly equal to the bed slope which means the establishment of the uniform flow. When the observed readings had settled for at least half an hour, the levels were recorded again at the five side well stations, and the corresponding water surface slope as well as the mean flow depth were worked out. To determine the flow rate, the head over the rectangular thin plate weir was recorded by means of the mounted point gauge on the approach channel.

In the case of the large flume, the same procedure was carried out in each run except that the flow rate was measured firstly by means of the perspex weir, whilst the water surface levels were measured at the piezometer glass tubes by using the cathetometer.

5.8 FILTER DESIGN

Two filter types were used during the current investigation. A conventional filter layer composed of two aggregate layers 1.5 cm thick each was used for the first four models, whereas in the last two models a layer of synthetic cloth filter was utilized. The design procedure of both types was as follows:

5.8.1 Conventional Filter

According to the design criteria explained in Chapter Two, filter design would be satisfied if the following conditons are fulfilled:

$$\frac{D_{15}\ (\text{filter})}{D_{85}\ (\text{base})} < 4 \text{ to } 5 \qquad (5.12)$$

$$\frac{D_{50}\ (\text{filter})}{D_{50}\ (\text{base})} < 25 \qquad (5.13)$$

$$\frac{D_{15}\ (\text{filter})}{D_{15}\ (\text{base})} > 4 \text{ to } 5 \qquad (5.14)$$

in which D_i is the particle size for which i percent of the material, by weight, is finer.

From the grading curves for filter and sand base materials used in the first four models, which are shown in Fig. (5.20),one may obtain the following results:

	Sand base	Filter (1)	Filter (2)	Rock layer
D_{15} mm	0.205	0.83	4.32	19.23
D_{50} mm	0.27	1.12	6.57	20.8
D_{85} mm	0.4	1.30	9.0	21.92
$\frac{D_{15}(\text{filter})}{D_{85}(\text{base})}$	<4.5	$\frac{0.83}{0.4} = 2.075$	$\frac{4.32}{1.30} = 3.32$	$\frac{19.23}{9.0} = 2.136$
$\frac{D_{50}(\text{filter})}{D_{50}(\text{base})}$	<25	$\frac{1.12}{0.27} = 4.148$	$\frac{6.57}{1.12} = 5.86$	$\frac{20.8}{6.57} = 3.165$
$\frac{D_{15}(\text{filter})}{D_{15}(\text{base})}$	>4.5	$\frac{0.83}{0.205} = 4.04$	$\frac{4.32}{0.83} = 5.204$	$\frac{19.23}{4.32} = 4.451$

As a result of the above calculations one may conclude that the size distribution curves of both the filter layers shown in Fig. (5.20), satisfied successfully all the criteria mentioned beforehand.

It was also realized that the filter thickness is an important factor that needs careful consideration and has to be designed to prevent excessive flow of soil fines from the base layer into the flow. Accordingly, and on the basis of the literature review presented in section (2.5.4.1), two filter layers 1.5 cm each were used.

5.8.2 Filter Cloth

This filter was selected from the manufacturer's (ICI) catalogue to suit the sand base grading satisfying both piping and permeability requirements so as to prevent particles from being washed through the filter layer and to permit seepage water to escape freely and thus prevent building up of hydrostatic pressure behind the filter layer and hence prevent uplifting.

5.9 ROCK SPECIFICATIONS

The stone used in the experimental work was subangular crushed limestone which had the following specifications:

5.9.1 Size and Specific Gravity

During the course of the experimental work, two types of protective layers were utilized. The selected uniform size passed a sieve opening of 22.4mm and was retained on sieve opening of 19.0mm which gives mean size of 20.7mm. This was selected as a result of the preliminary study discussed in Section (5.6) earlier. The graded material was prepared according to the depicted size distribution curve in Fig. (5.19), so as to have the same mean value of D_{50} as that of uniform material.

On the other hand, applying the specifications set by the British Standards Institution, BS No. 1377: (1975), the specific gravity test was carried out on representative particles of the rip-rap material. This test was conducted in soil laboratories at Southampton University and the specific gravity was found equal to 2.66.

5.9.2 Angle of Repose

In conjunction with designing the riprap lining of canal banks, it is necessary to define the angle of repose of the riprap material. The angle of repose of loose sand was defined by Terzaghi, K. and Peck, R.B. (1948), as the direct proportionality between the shear stress and the relative displacement, which was found also equal to the coefficient of the internal friction. It was also reported by Glanville, W.H. (1951), that the angle of repose for dry loose sand and granular material is equal to the angle of internal friction. This simply means that the angle of repose can be defined experimentally by applying one of the known tests.

Among the first attempts to determine the angle of repose for non-cohesive materials is that reported by Lane, E.W. (1952), in which a figure relating angle of repose, median diameter of the material and shape of the particle was developed. Subsequent investigation was carried out by Simons, D.B. and Albertson, M.L. (1960) to establish another diagram to define the angle of repose. In their diagram, the reported values for the angle of repose for very angular material have been somewhat arbitrarily ranged between 31.5 and 42.0 degrees.

Since a precise evaluation for the angle of repose was needed, it was decided to determine it experimentally. The experiment was conducted by analogy with the case of similar particles resting on an inclined plane. A layer of riprap material was glued on a wooden board 50 x 30 cms, another free layer of the same material was laid randomly on the glued layer, the board was then tilted on a horizontal desk until the free layer started to move; in this position the angle between the horizontal desk and the board is the angle of repose.

Two boards were utilized as shown in Plate (5.9); one for each riprap material. Twenty tests were carried out for each riprap material and the average value for the angle of repose was found equal to 36.5 degrees in the case of uniform riprap material and 38.24 degrees in the case of non-uniform material.

5.10 VELOCITY MEASURING EQUIPMENT

As a result of the study reported in Section (4.6), it was concluded that it was necessary to measure the velocity distribution along the channel centre line, for different flow conditions, so as to ascertain the flow establishment. To fulfil this purpose, a laboratory type Ott current meter, shown in Plate (5.10), was used as a simple and accurate device.

This investigation was conducted on model No. (5) as a preliminary study to select a suitable place for force measurements.

Seven vertical velocity profiles at distances 0.75 to 1.1m apart were recorded. For each profile the velocity was measured at a distance 0.2, 0.4, 0.6 and 0.8 of the flow depth. This procedure was carried out on three different flow rates by using propeller No. (2.3/13659) which had the calibration equations

$$u = 0.2886N + 0.226 \qquad \text{for } N < 1.9 \qquad (5.15)$$

$$u = 0.3388N + 0.131 \qquad \text{for } N > 1.9 \qquad (5.16)$$

where

u is the measured flow velocity in ft/sec
N is the number of revolutions per second

5.11 WATER DENSITY AND VISCOSITY

As it was necessary to establish the water density, ρ, and kinematic viscosity, ν, during the current investigations, two relationships to obtain the both properties were developed as a function of the flow temperature. Using hydraulic tables provided by HSRI, (1966), (the Hydraulic and Sediment Research Institute at Delta Barrages, Egypt), two fitting equations were developed as

$$\rho = 999.883 + 0.0585T - 0.0078T^2 + 4.029E\text{-}5T^3 \qquad (5.17)$$

$$\nu = 1.785E\text{-}6 - 5.813E\text{-}8T + 1.156E\text{-}9T^2 - 1.02E\text{-}11T^3 \qquad (5.18)$$

in which

T is the water temperature in degrees centrigrade.

Eqs. (5.17 and 5.18) were obtained with correlation coefficient 0.9994 and 0.9996 respectively, and standard error of estimate 2.85E-2 and 3.12E-9 respectively. Additionally, to show the variation of ρ and ν with, T, the developed relationships were plotted as shown in Fig. (5.21).

TABLE 5-1: SUMMARY OF THE CONSTRUCTED MODELS

Model No.	Flume	Bed Width (m)	Bed Slope	Bed Material	Filter Type	Riprap Material	Max. Flow (m^3/s)	Threshold Flow (m^3/s)	Failure Flow (m^3/s)	No. Of Tests
1	Concrete Flume	0.4	0.005	Free Particles	Conventional	Uniform	0.2191	—	—	40
2		0.4	0.008	"	"	"	0.2157	—	—	21
3		0.4	0.008	Cloth Filter	"	"	0.2216	—	—	22
4		0.5	0.0125	"	"	"	0.1794	0.1488	0.1794	33
5	Large Flume	0.5	0.0125	"	Cloth Filter	"	0.1424	0.1295	0.1424	36
6		0.5	0.0125	"	"	Non-Uniform	0.1296	0.1038	0.1296	22

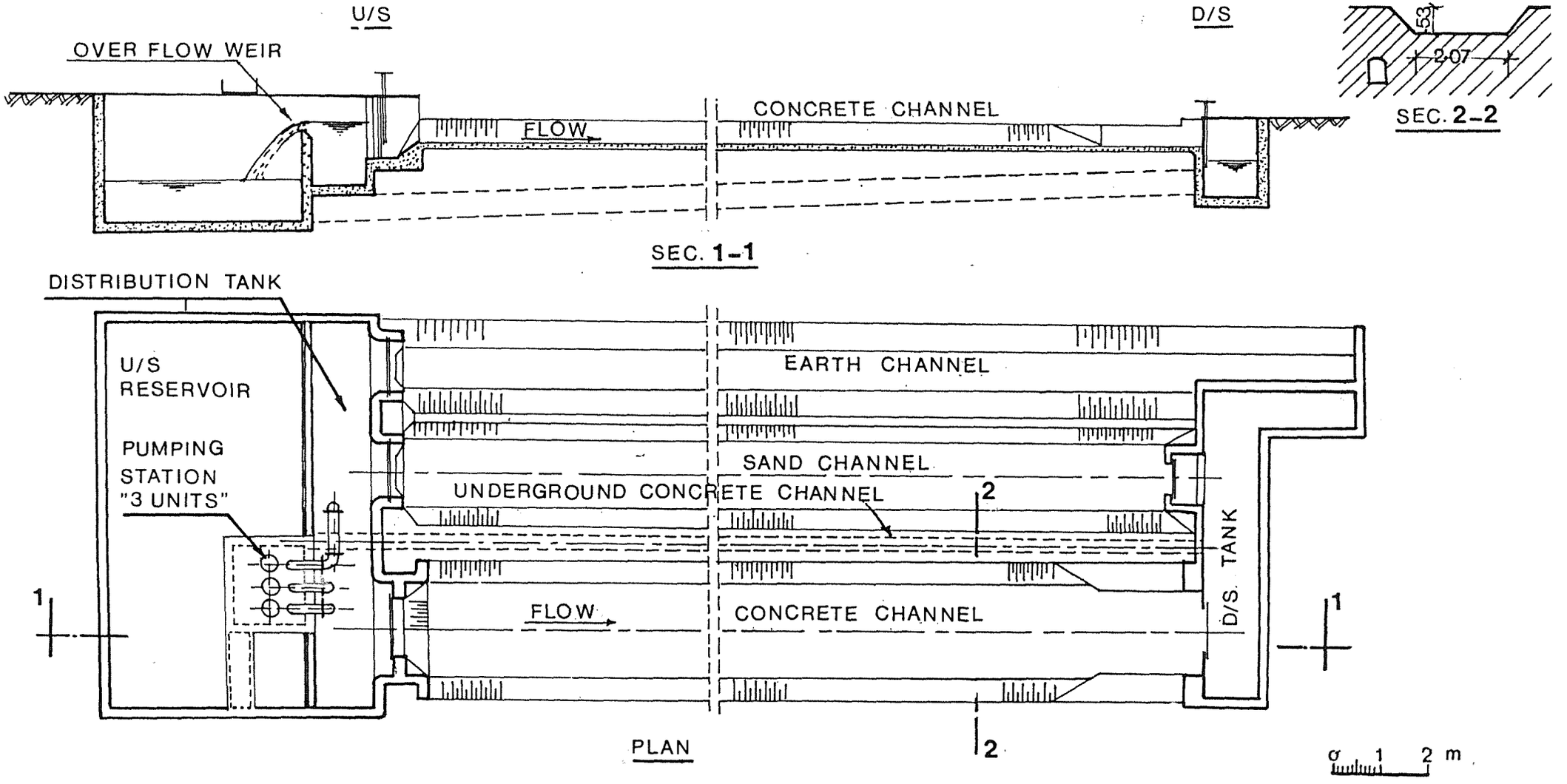

FIG. 5-1: GENERAL LAYOUT OF THE CONCRETE FLUME

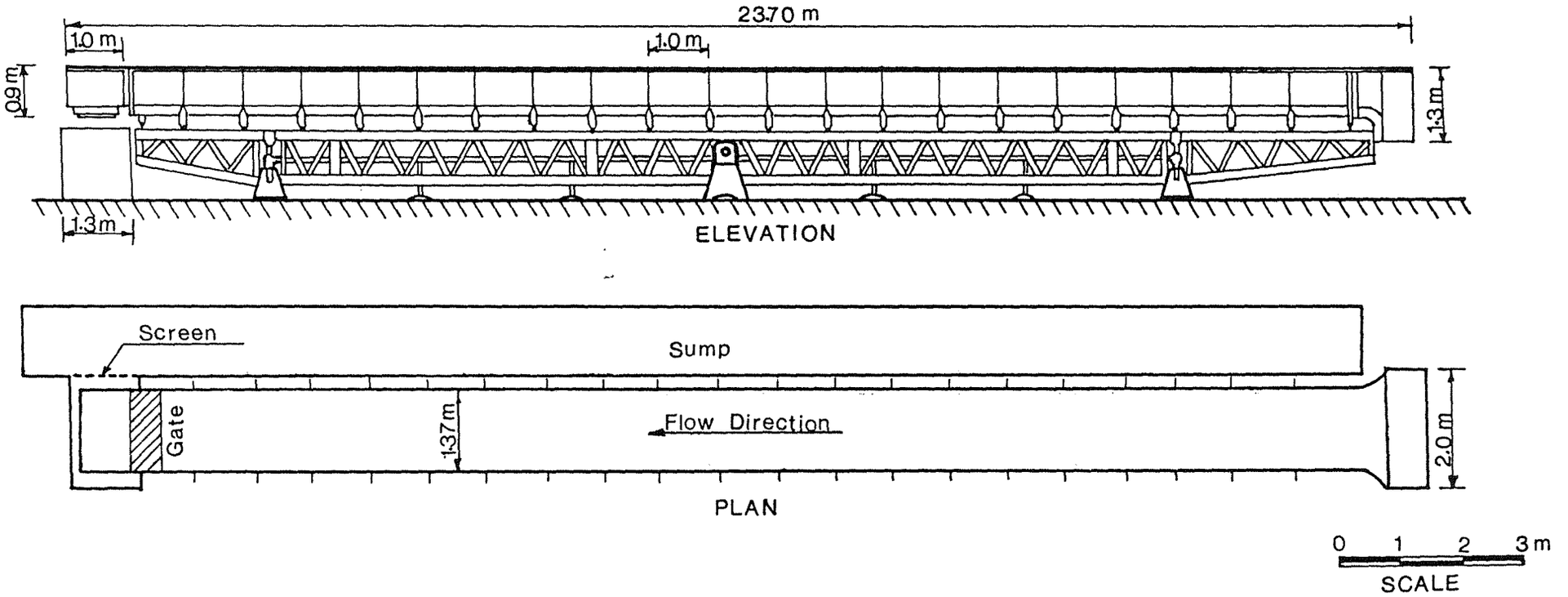

FIG. 5-2: GENERAL ELEVATION AND PLAN OF THE LARGE FLUME

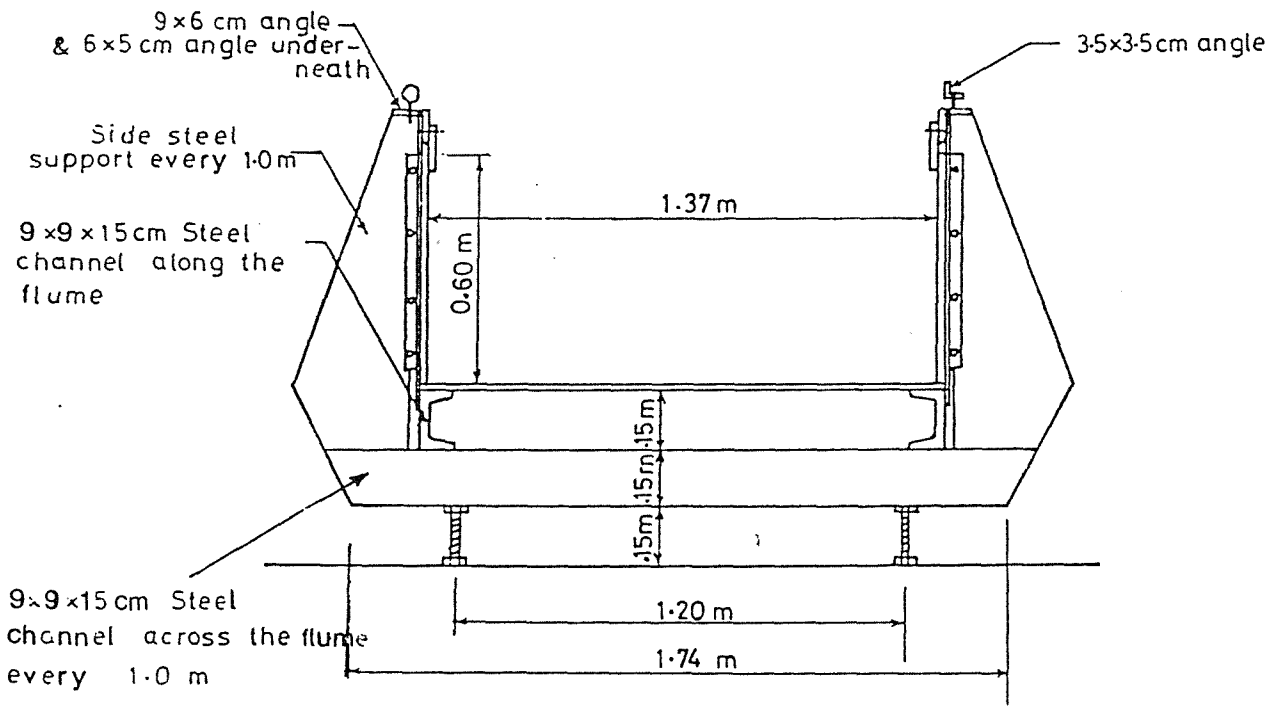

FIG. 5-3 : CROSS SECTION OF THE LARGE FLUME

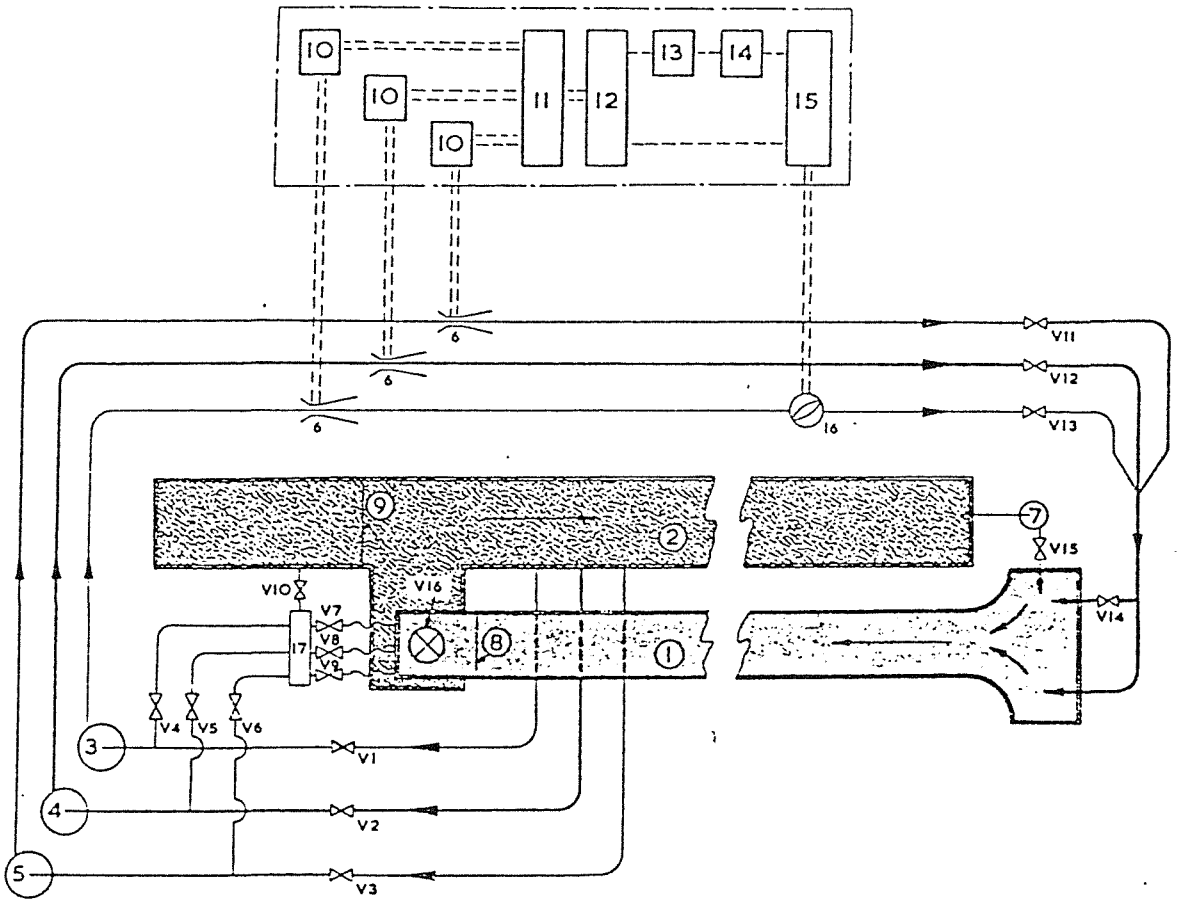

1 GLASS SIDED ADJUSTABLE SLOPE CHANNEL.
2 RESERVOIR OR SUMP RETURN.
3 CENTRIFUGAL PUMP 90 L / SEC.
4 CENTRIFUGAL PUMP 150 L / SEC.
5 CENTRIFUGAL PUMP 230 L / SEC.
6 VENTURI TUBES.
7 AXIAL FLOW TRANSFER PUMP 300 IMP. G.P.M.
8 CHANNEL END WEIR.
9 SEDIMENT RETAINING WEIR.
10 FLOW INDICATOR AND SIGNAL GENERATORS.
11 AMPLIFIER.
12 INTEGRATOR.
13 TOTAL FLOW RECORDER.
14 AUTOMATIC FLOW CONTROL SELECTOR.
15 CONTROLLER.
16 ELECTRICALLY OPERATED BUTTERFLY VALVE AND FEEDBACK SIGNAL GENERATOR.
17 MANIFOLD.
VI TO V16 MANUALLY OPERATED VALVES FOR ISOLATION OR TRIMMING.

FIG. 5-4 : A SCHEMATIC ARRANGEMENT OF THE FLUME AND PUMPS

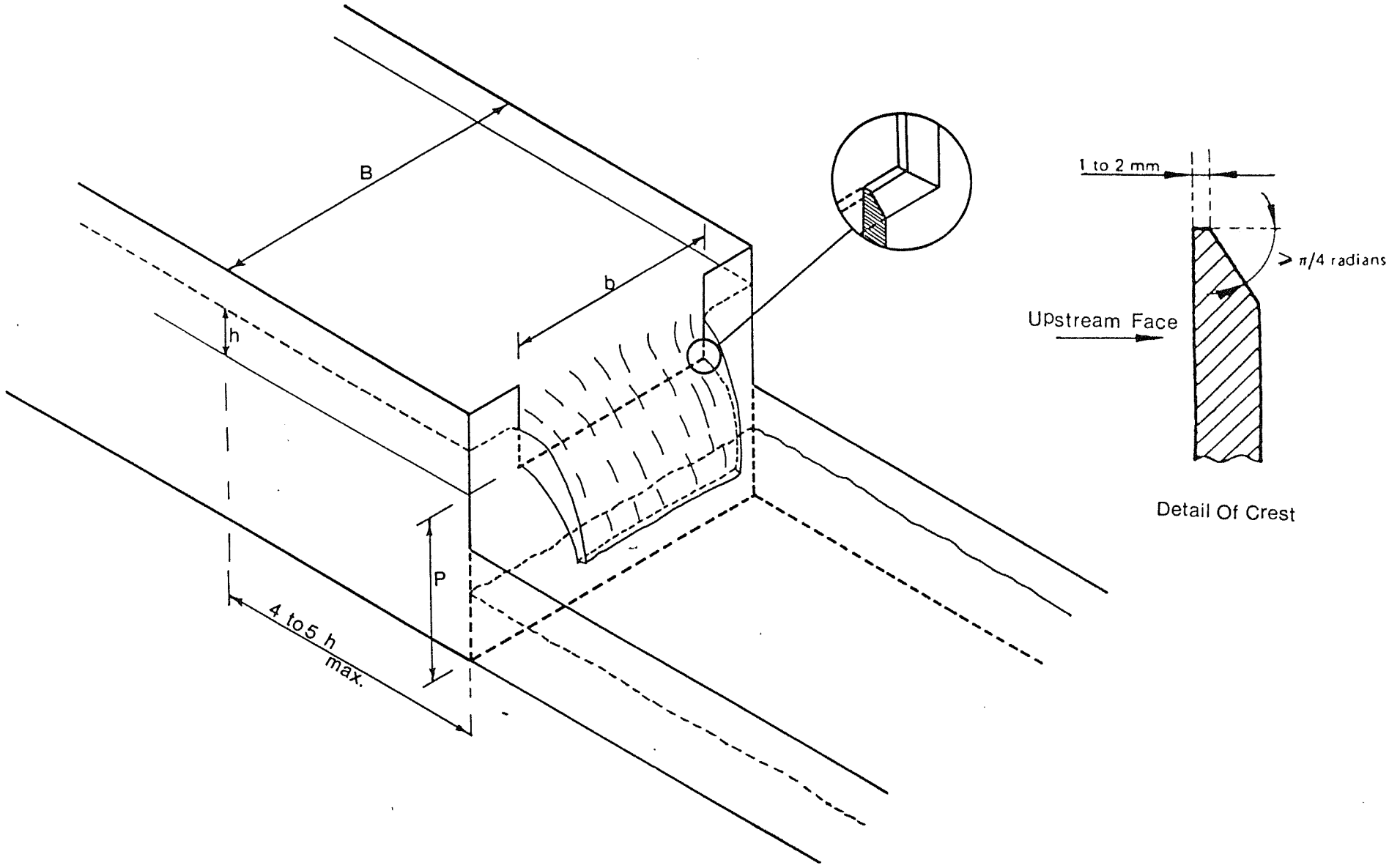

FIG. 5-5 : THE RECTANGULAR THIN-PLATE WEIR

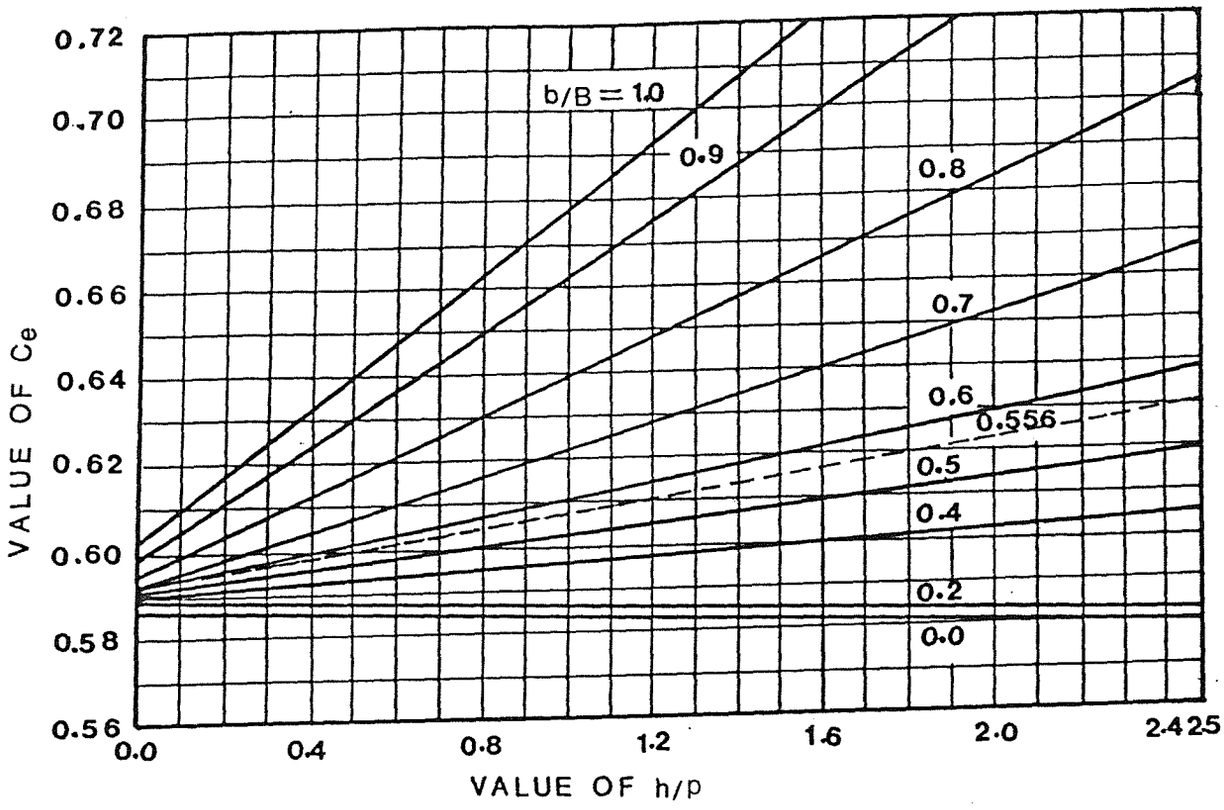

FIG.5-6 : VARIATION OF C_e WITH h/p AND b/B FOR A RECTANGULAR WEIR

« BS No.3680:1981 »

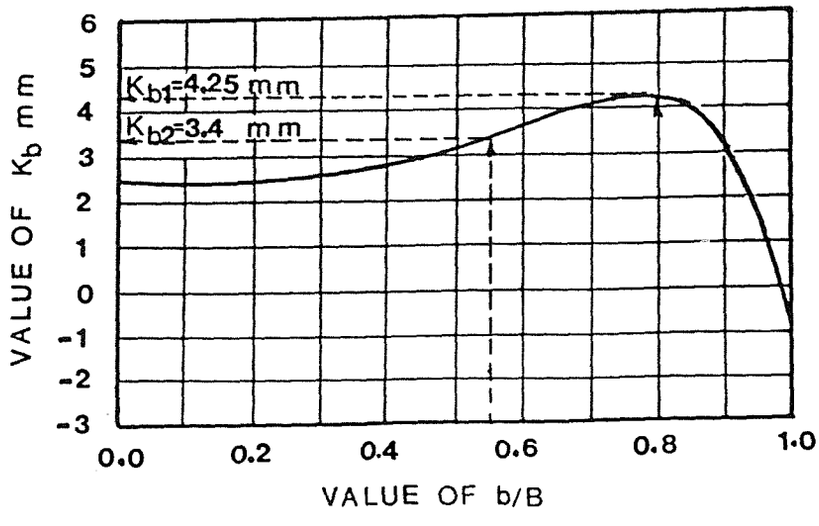

FIG.5-7: VALUE OF K_b RELATED TO b/B

« BS No. 3680:1981 »

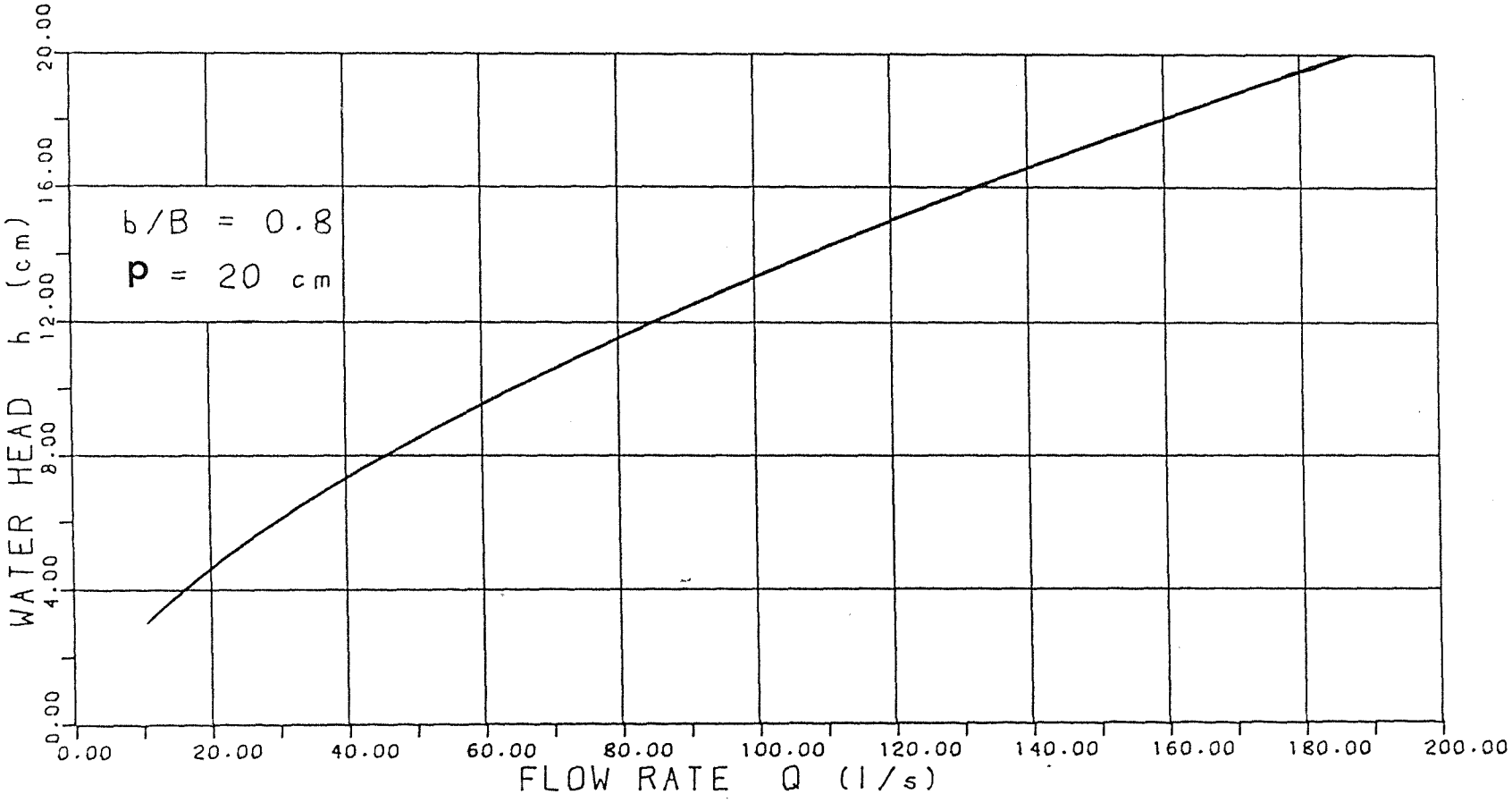

FIG. 5-8: CALIBRATION CURVE OF THE RECTANGULAR (THIN PLATE) WEIR USED IN THE LARGE FLUME

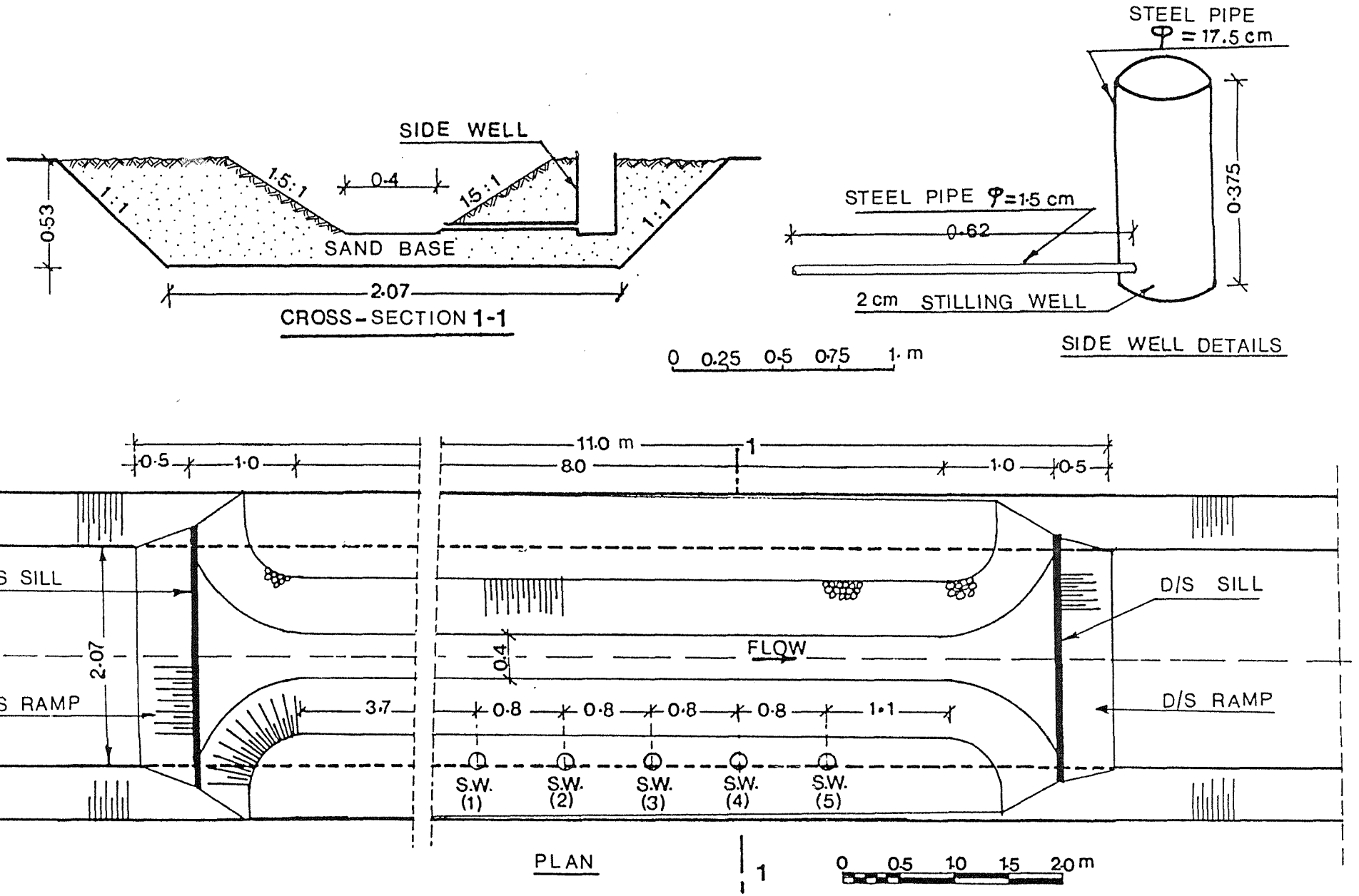

FIG. 5-9 : DETAILS OF THE SIDE WELLS

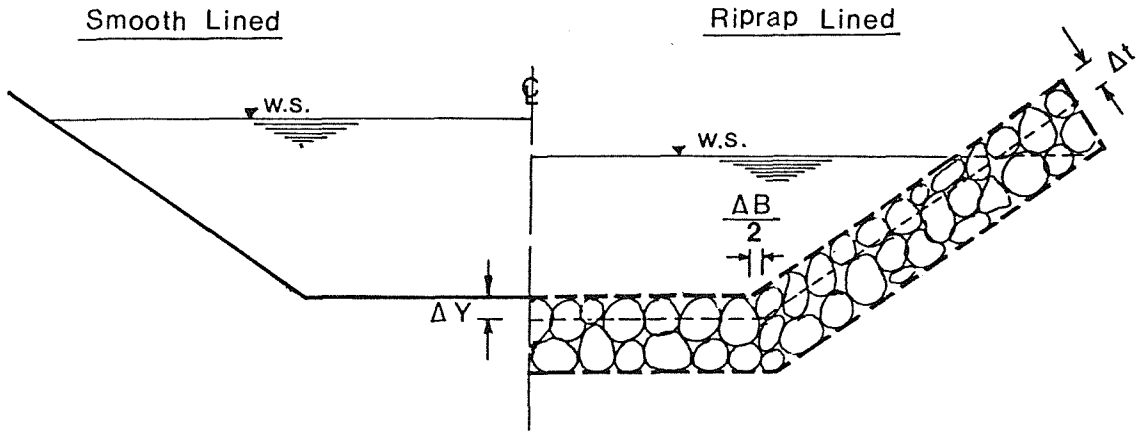

FIG. 5-10 DEFINITION SKETCH OF THE FLOW DEPTH AND BED WIDTH CORRECTIONS

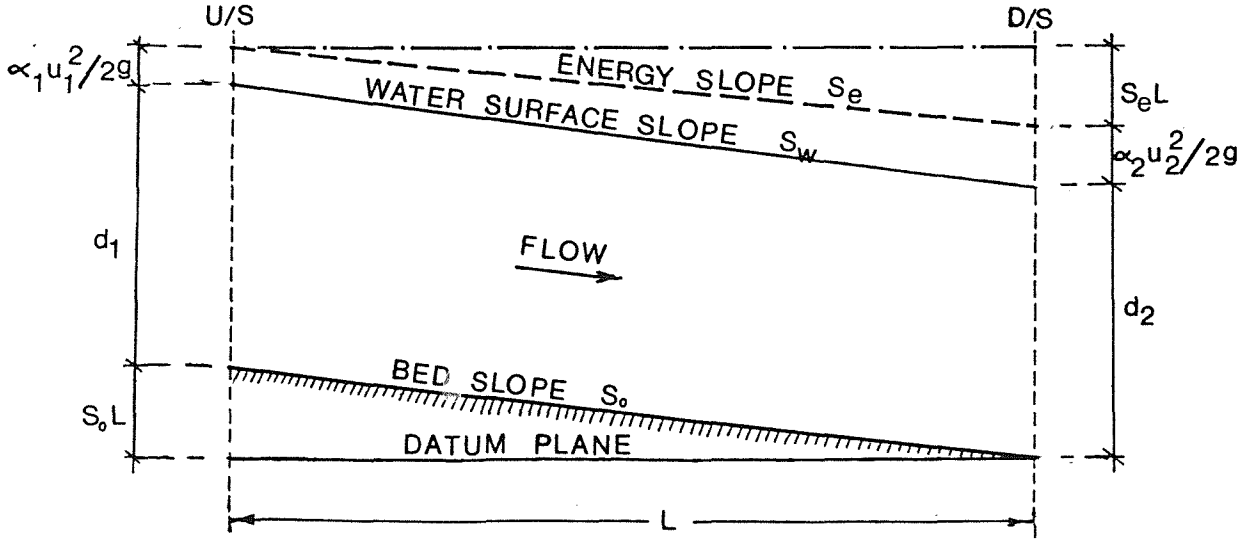

FIG. 5-11-ENERGY RELATIONSHIPS IN OPEN CHANNELS

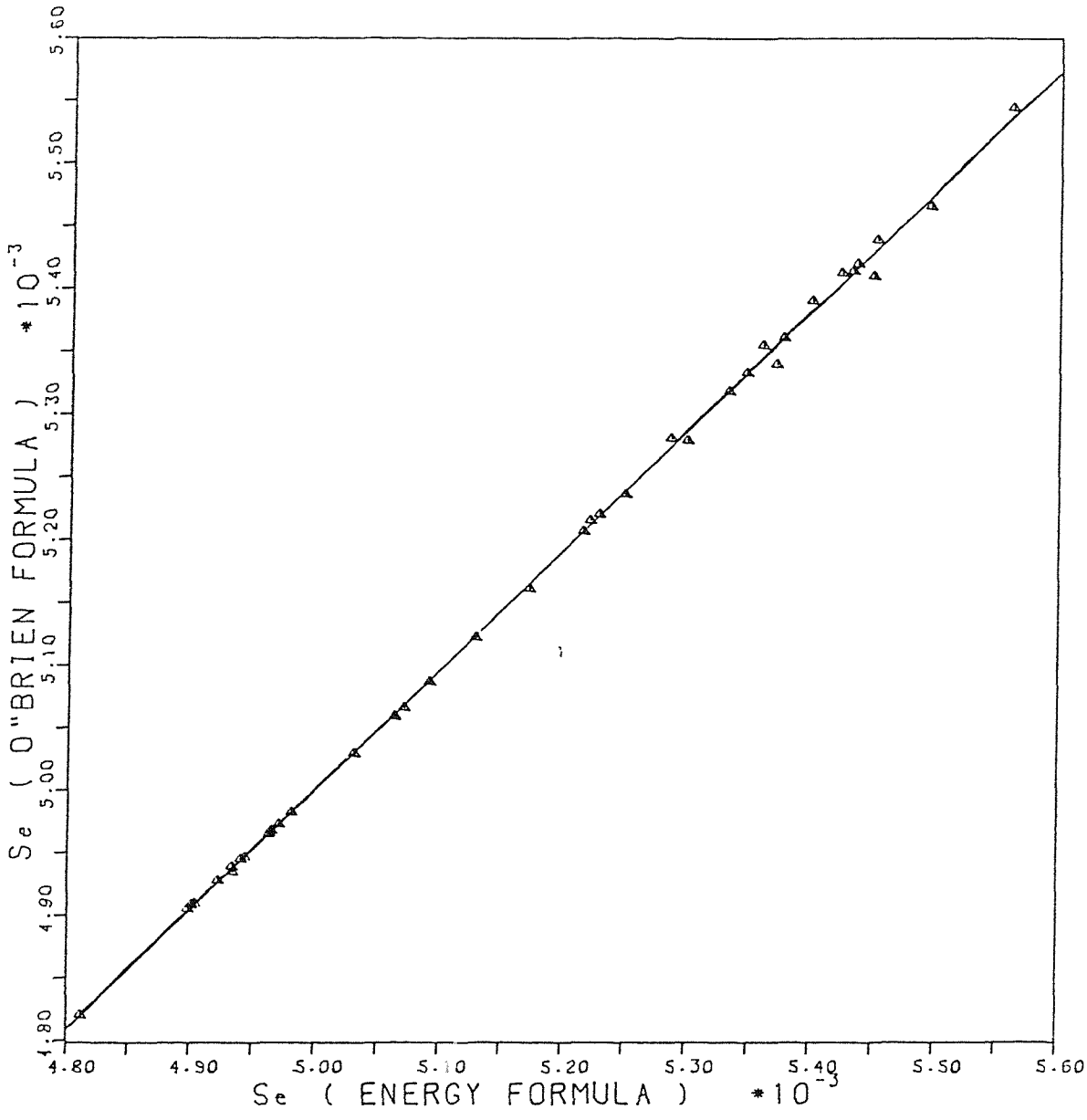

FIG.5-12: COMPARISON OF ENERGY SLOPE Se USING TWO DIFFERENT APPROACHES

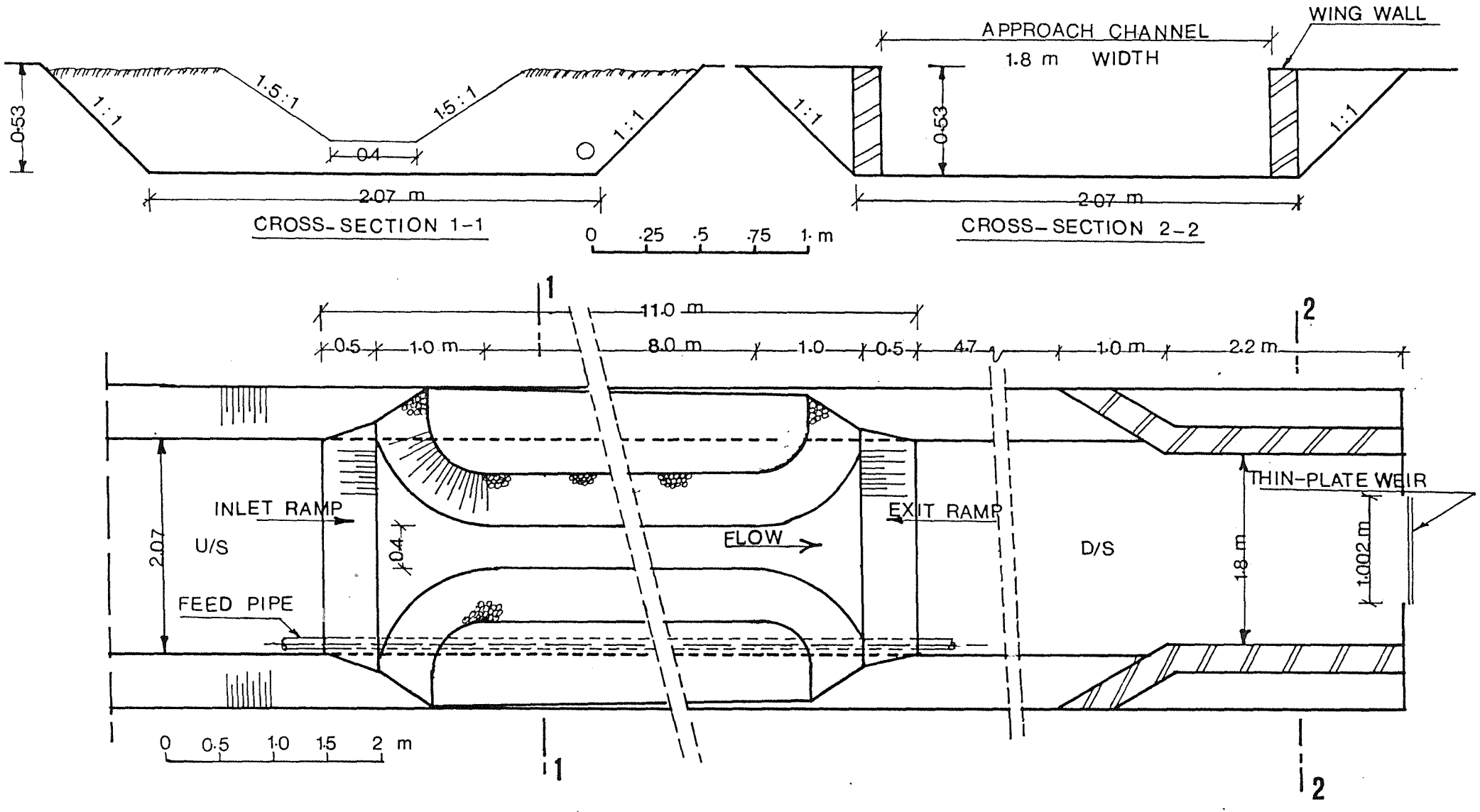

FIG. 5-13: GENERAL LAYOUT OF THE MODELS CONSTRUCTED IN THE CONCRETE FLUME

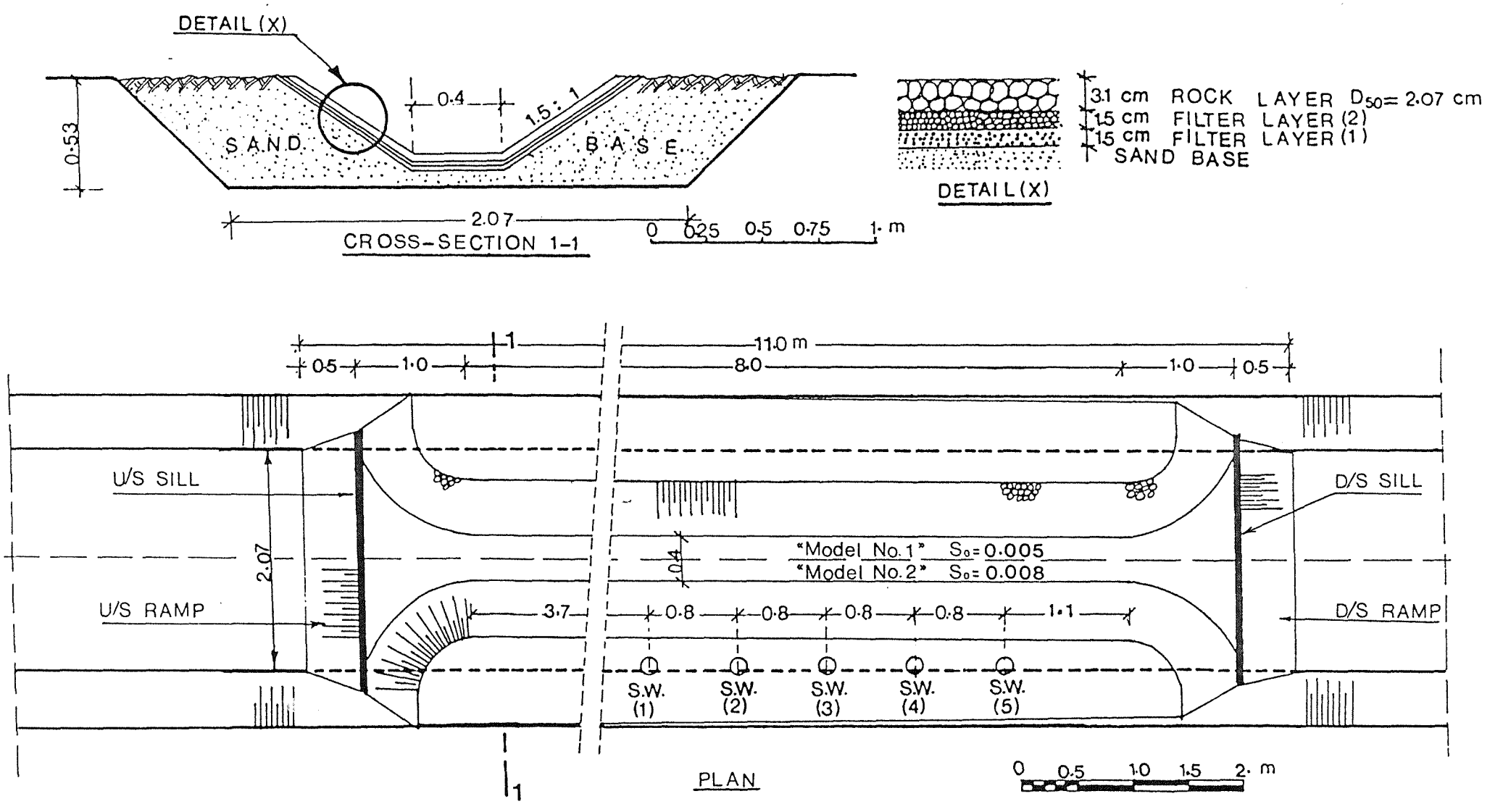

FIG.5-14 : DETAILS OF THE MODEL NOs. 1&2

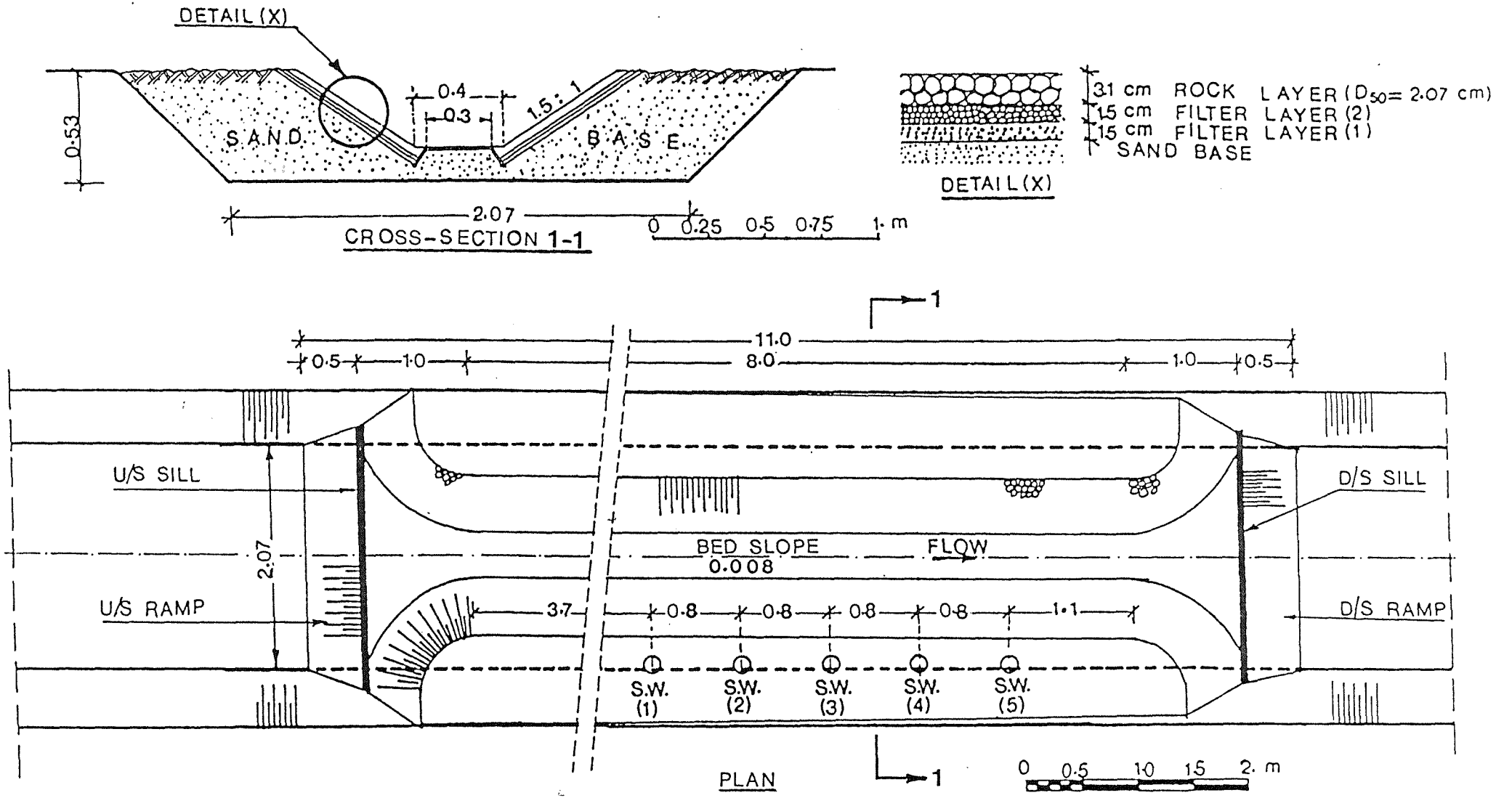

FIG. 5-15: DETAILS OF THE MODEL NO. 3

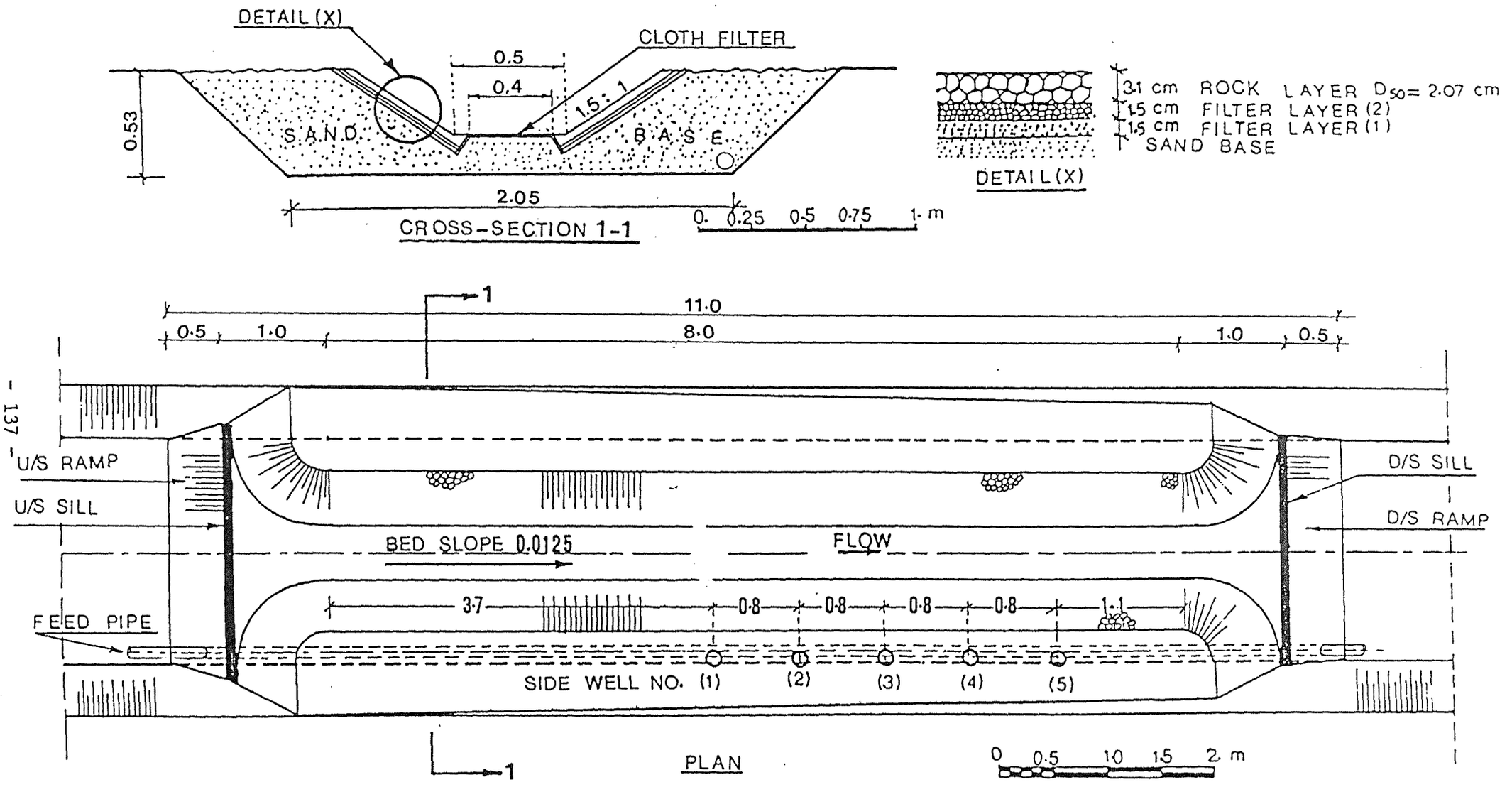

FIG. 5-16 : DETAILS OF THE MODEL NO. 4

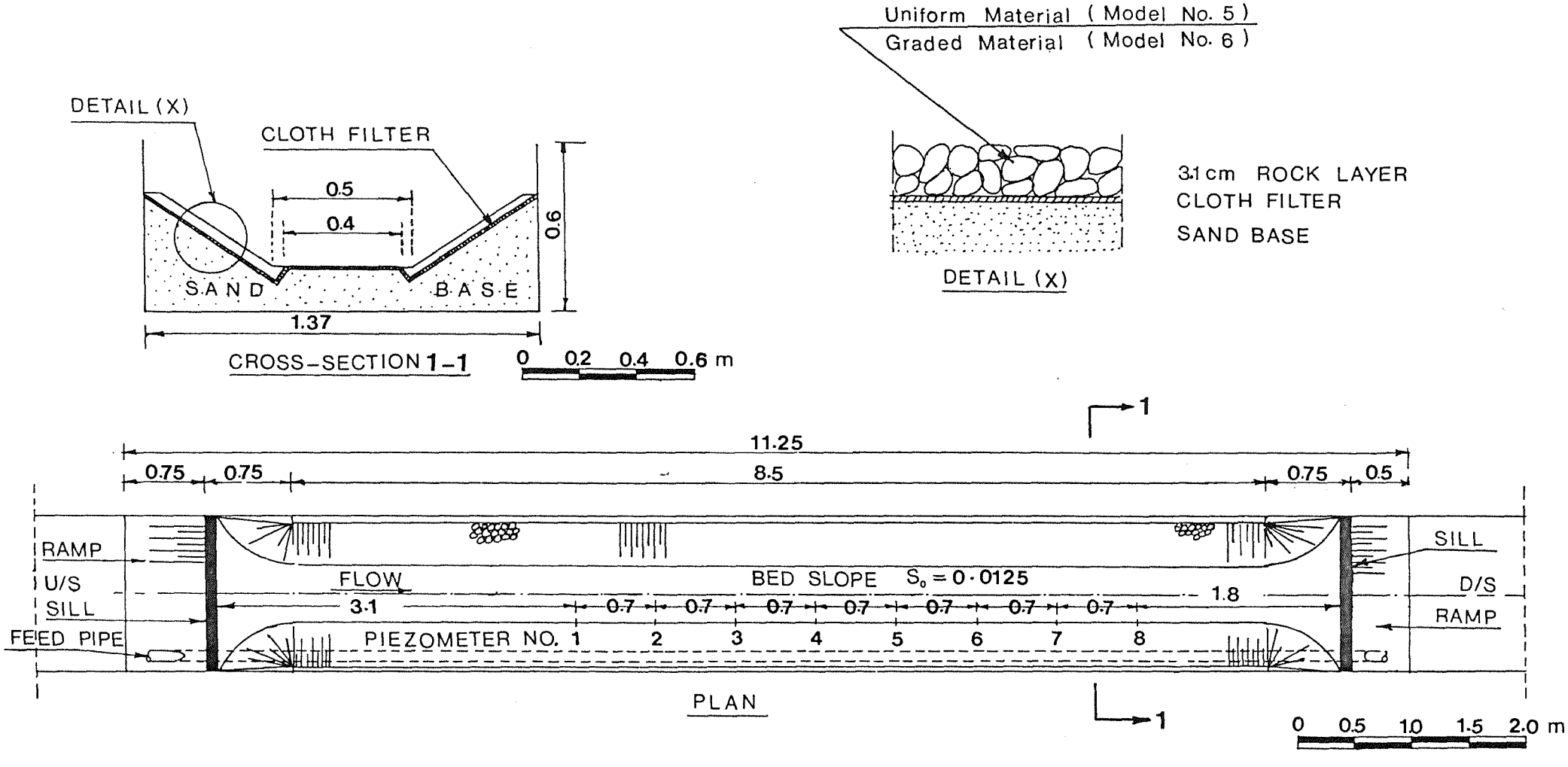

FIG. 5-17 : DETAILS OF THE MODEL NOs. 5&6

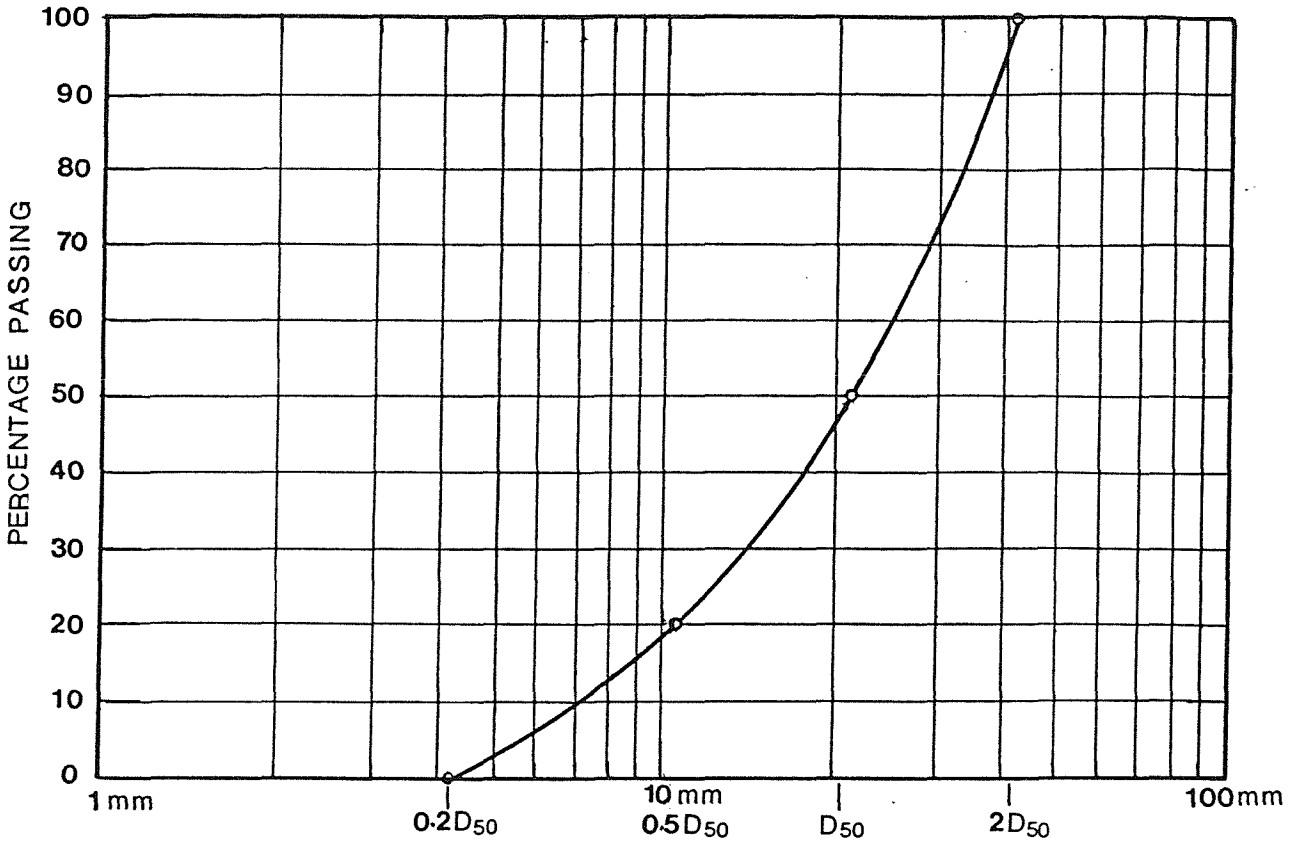

FIG. 5-18: SIMONS' GRADATION CURVE FOR RIPRAP

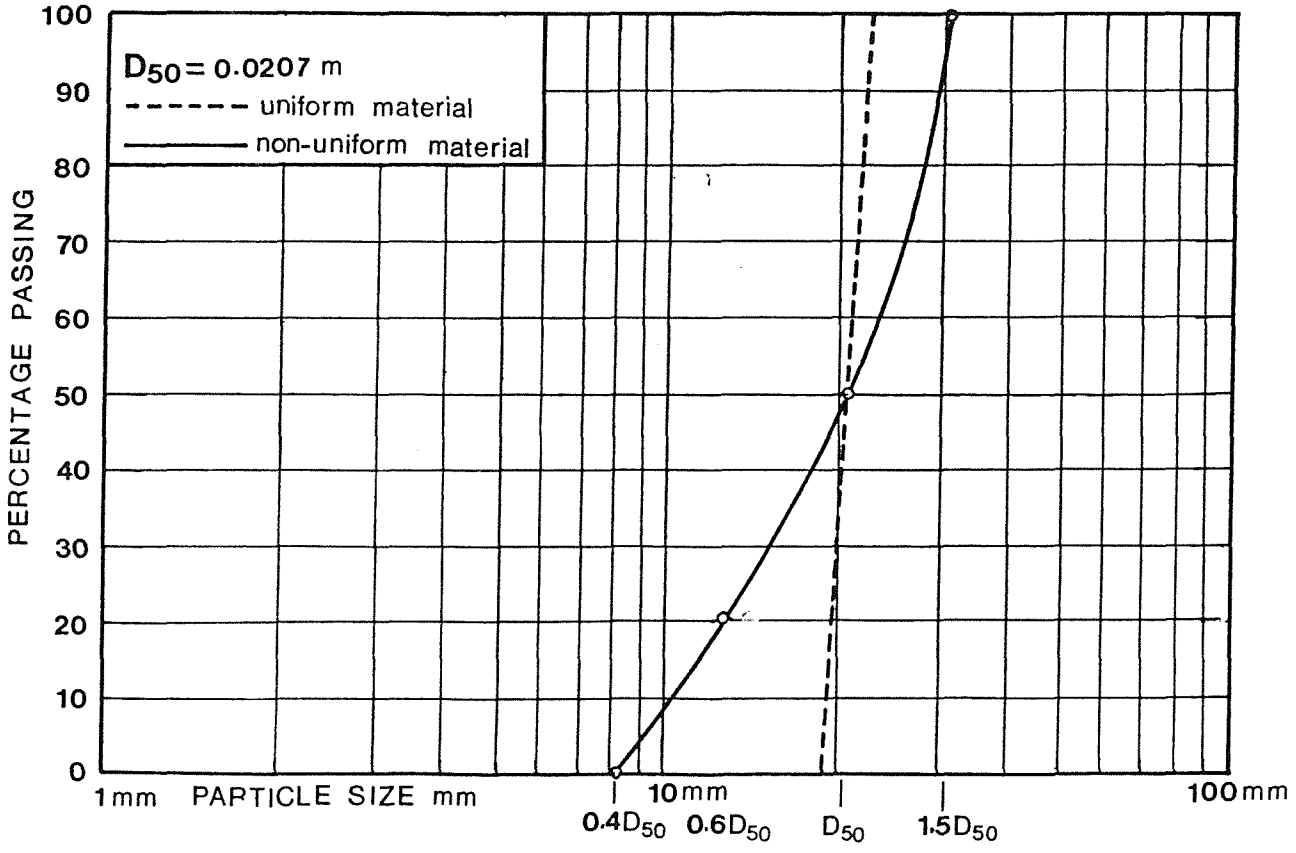

FIG. 5-19 : GRADATION CURVES OF MATERIALS USED IN THE CURRENT STUDY

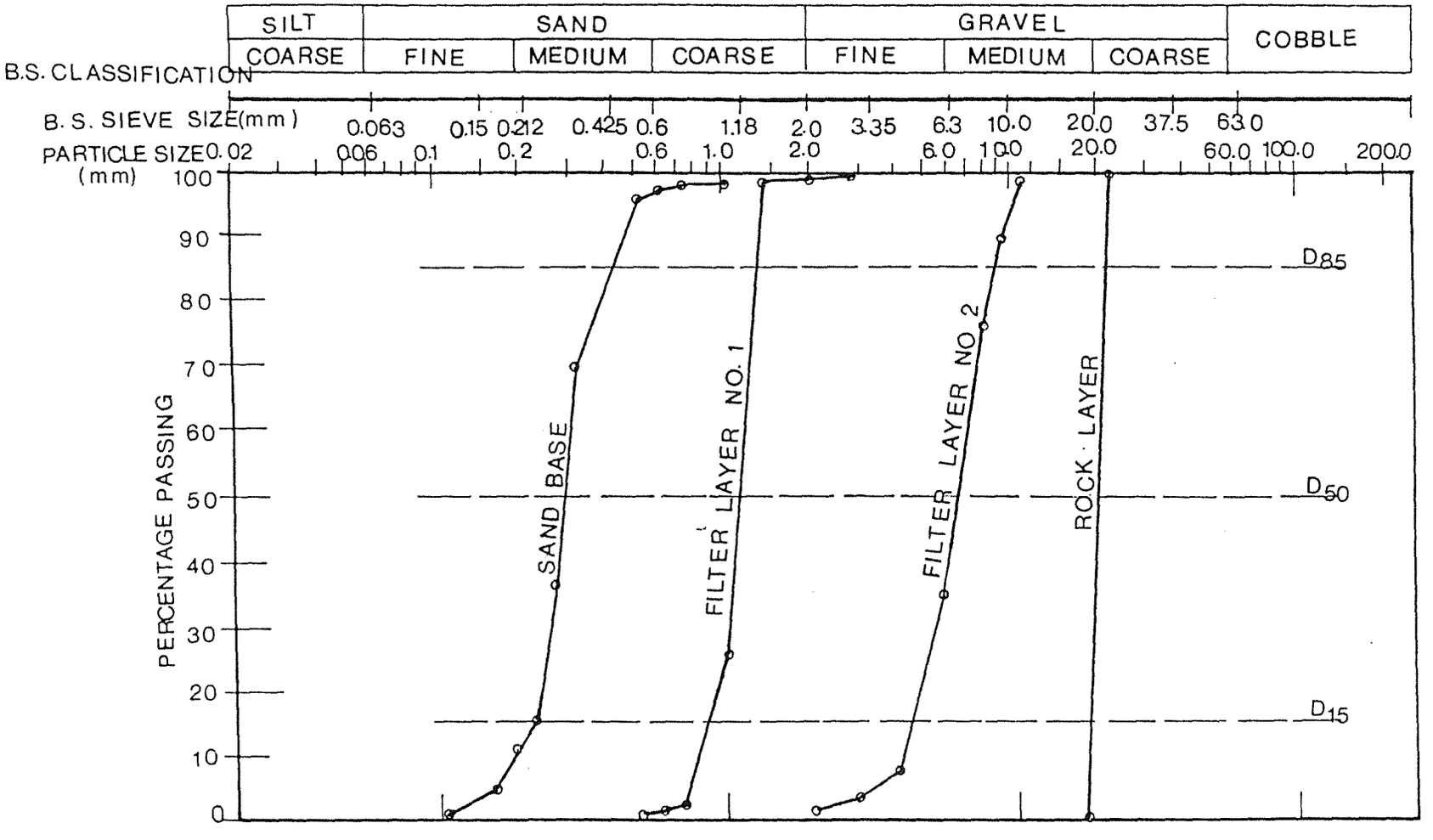

FIG. 5-20 : GRADING CURVES FOR FILTER MATERIALS USED IN MODEL NOS. 1, 2, 3 & 4

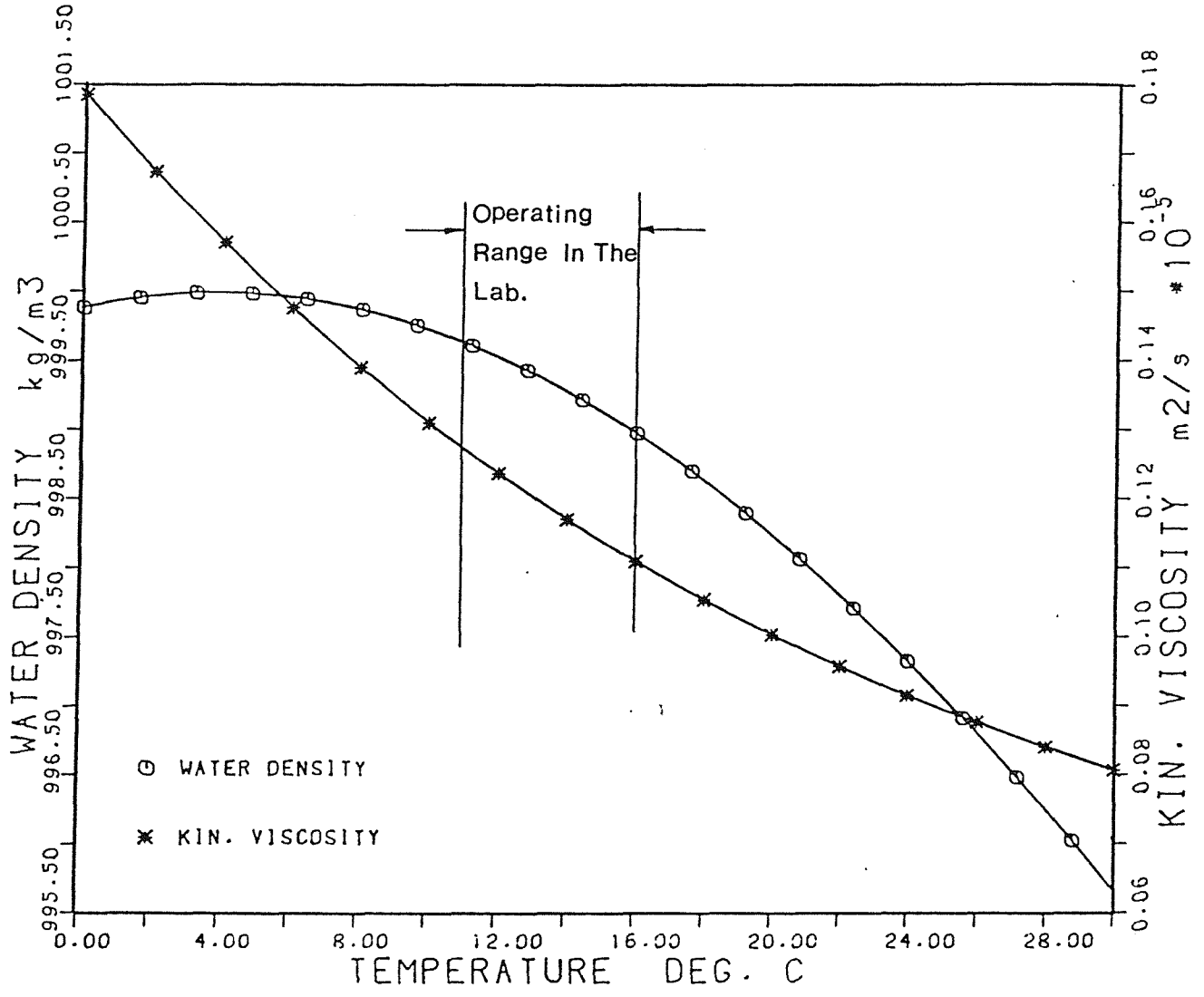

FIG.5—21:VARIATION OF WATER DENSITY AND KINEMATIC VISCOSITY WITH TEMPERATURE

(H.S.R.I. TABLES 1961)

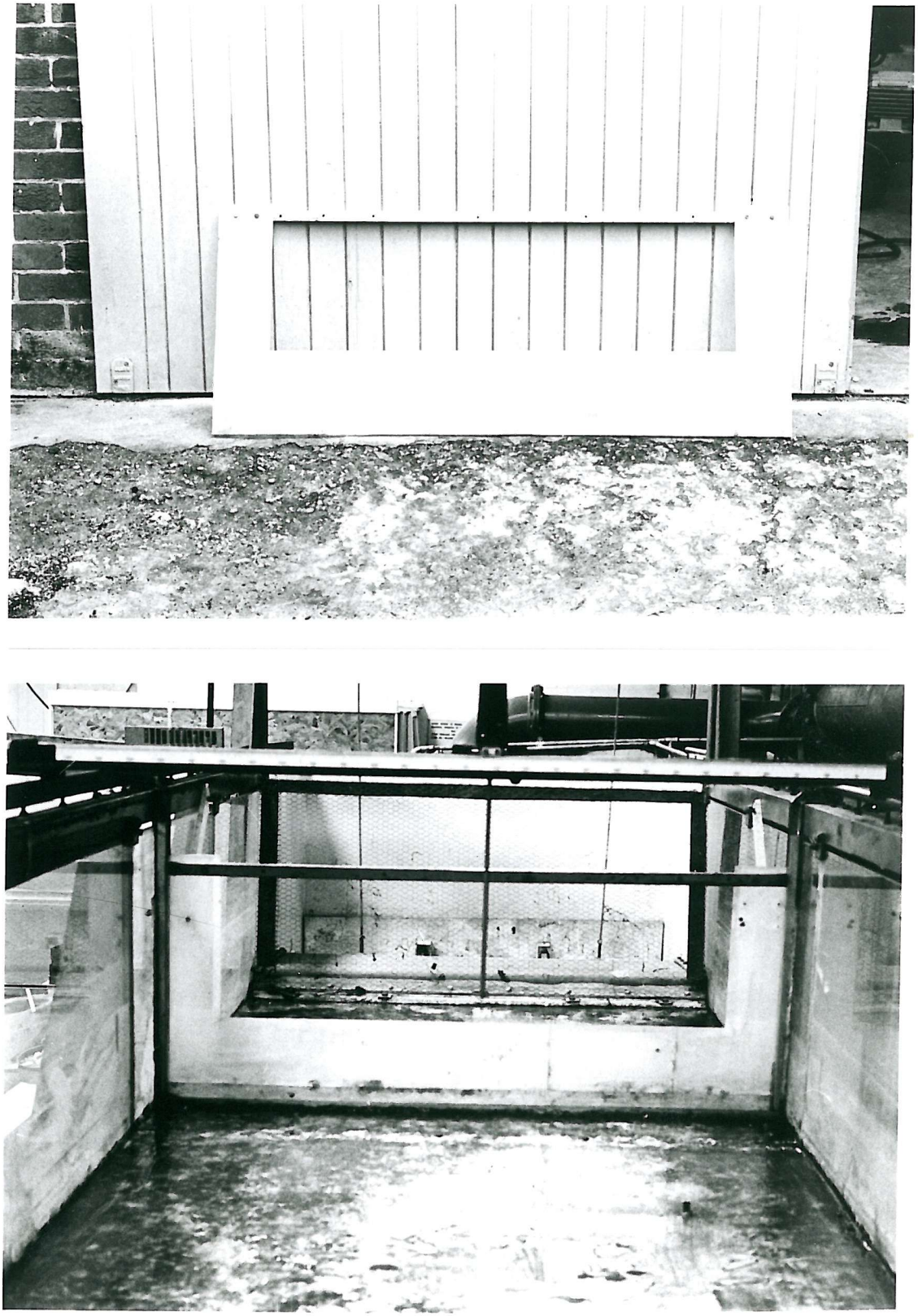

Plate (5-1) The thin plate weir inserted in the large flume

Plate (5-2) The side well stations

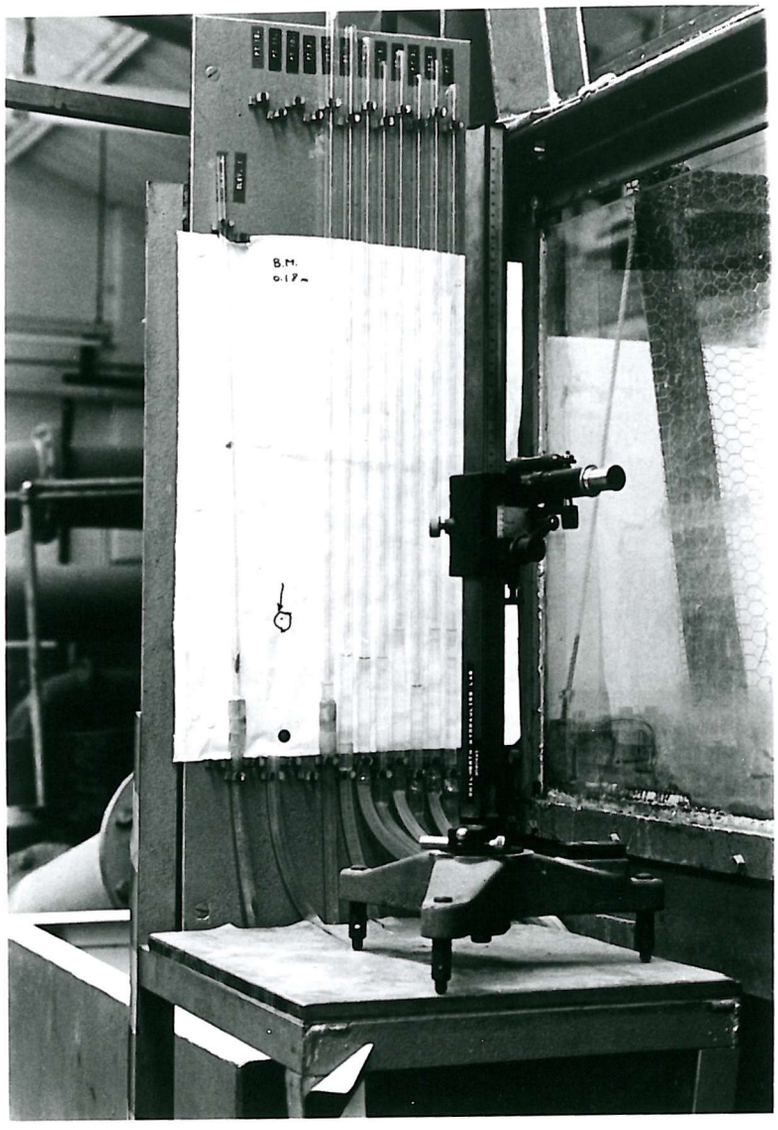

Plate (5-3) The piezometer glass tubes and cathetometer

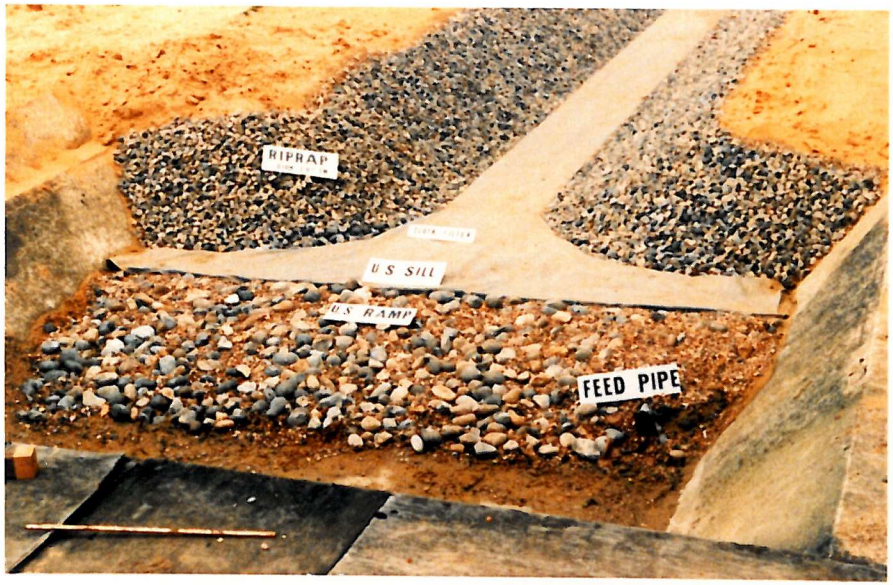

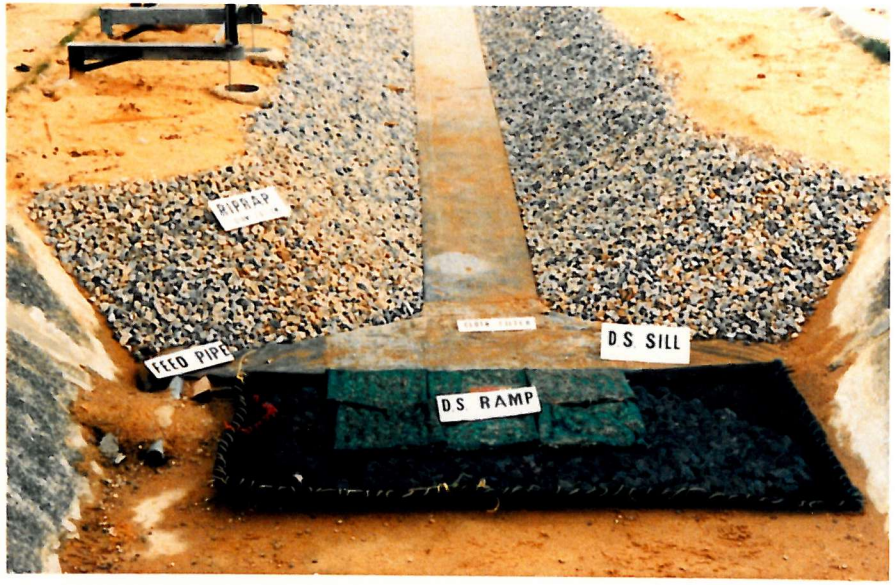

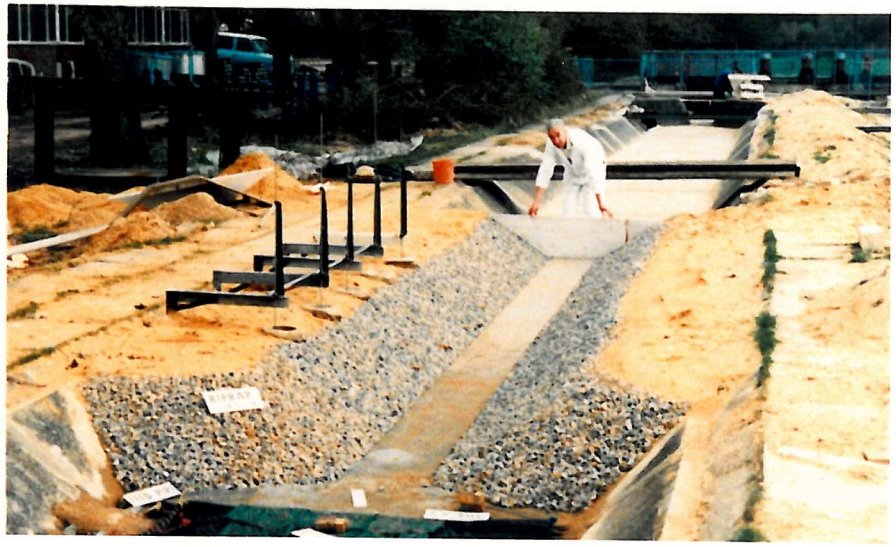

Plate (5-4) Model no.(4) before operation

Plate (5-5)

Model no.(4) during the experimental tests

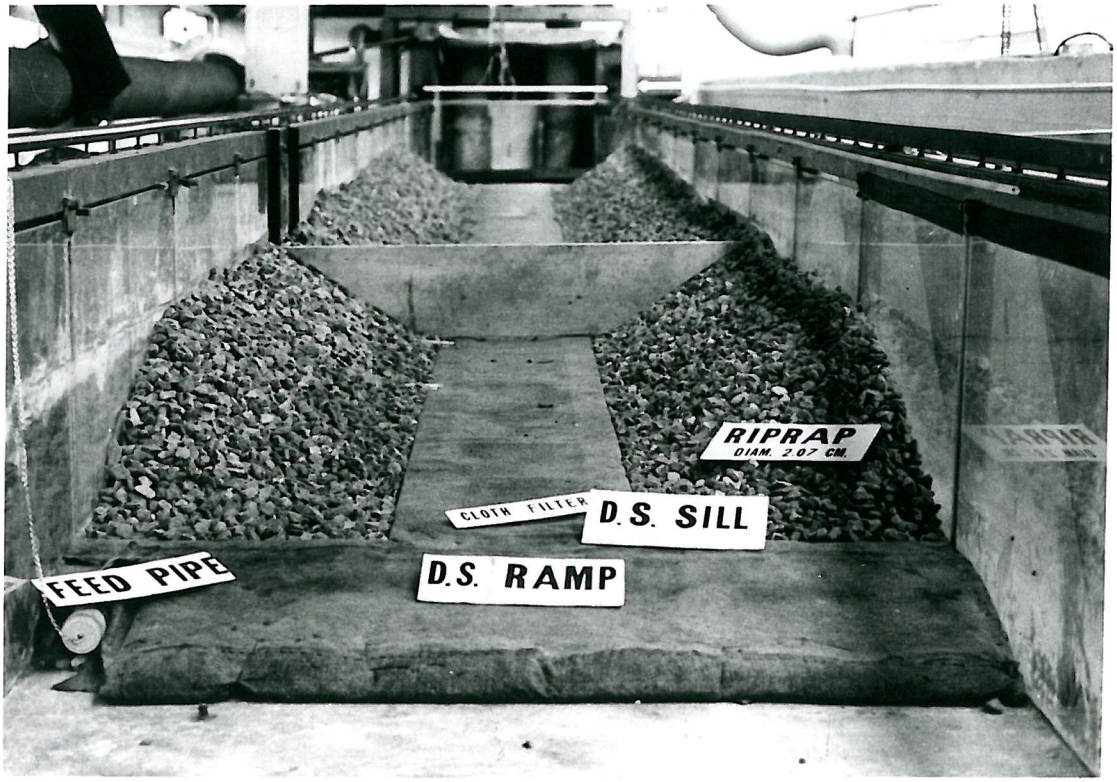

Plate (5-6) General views of Model no.(5) before operation

Plate (5-7) The uniform and graded materials employed during the investigation

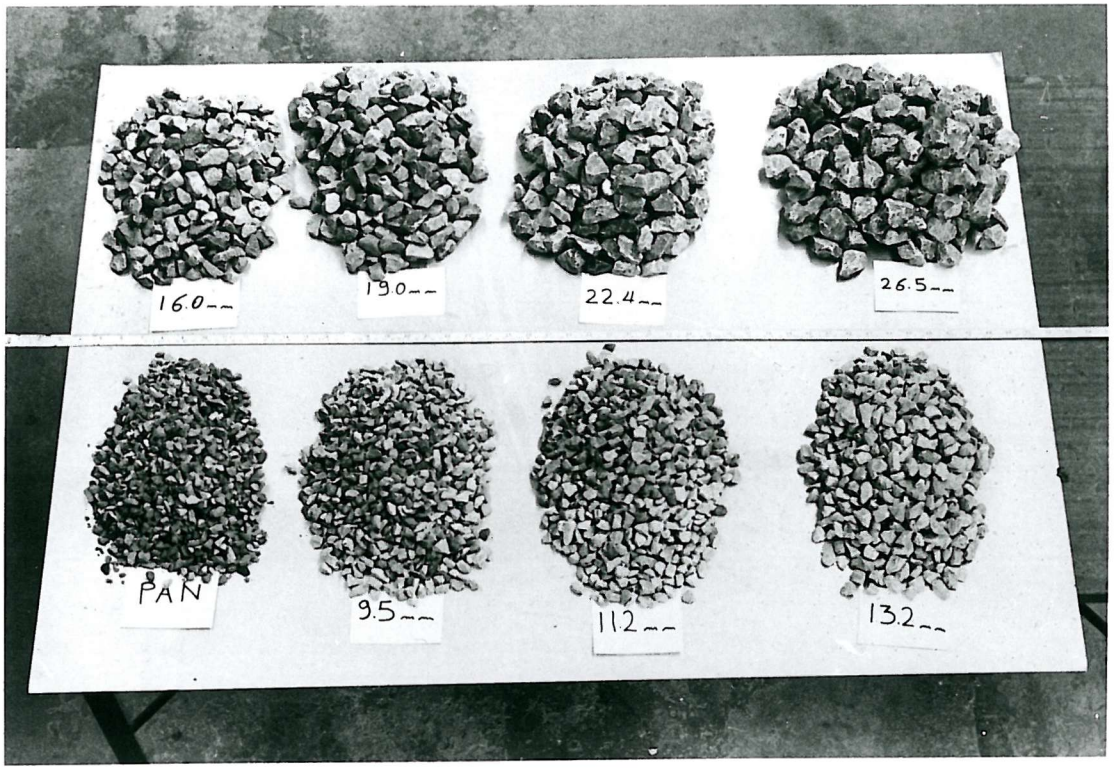

Plate (5-8) The rock sizes used in the graded riprap material

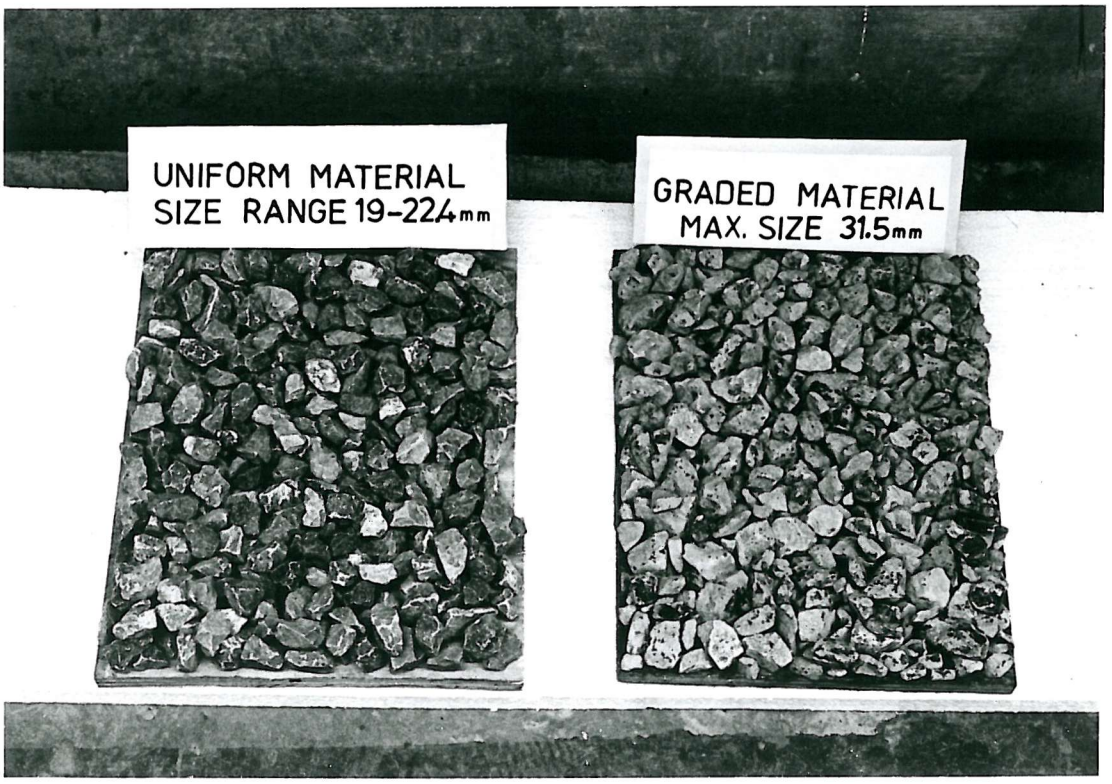

Plate (5-9) The roughened boards used to determine ϕ

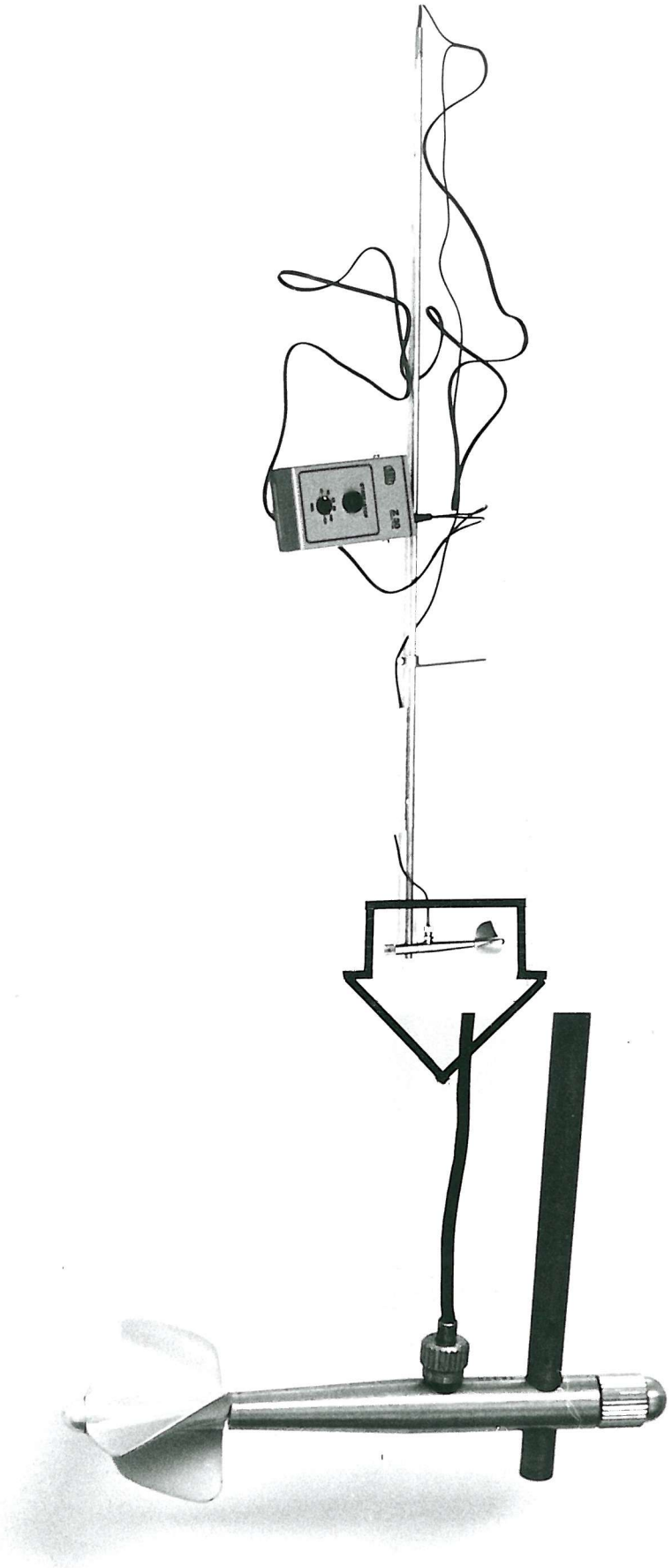

Plate (5-10) The laboratory current meter (Ott)

CHAPTER SIX

FORCE MEASURING CONCEPT

6.1 INTRODUCTION

With reference to the stability criteria discussed in Chapter Two, one may conclude that the major forces that affect the stability of a single particle and consequently the side slope stability are the gravity force and the hydrodynamic lift and drag forces. The gravity force can be evaluated as the resultant of the particle weight acting downward, and the effective lift pressure due to its submergence in water which acts vertically upwards. So this force can be equated with the submerged weight of the particle. Therefore, the current investigation was planned to measure the effective hydrodynamic lift and drag forces simultaneously.

Many mechanical and electrical designs have been proposed for the acquisition of these measurements, but due to the fluctuating nature of these forces as well as their expected magnitudes, a new design was developed. In this design, sensitive strain gauges were fabricated and attached to a thin beam so as to enable the forces to be measured simultaneously as will be explained in this chapter.

Since the protective layer usually consists of fragment particles without any cementing agent, the resistance of the whole layer will consequently be dependent on the stability of individual particles. Accordingly it was decided that measurement of the hydrodynamic forces acting on a representative particle would obviously be the first step to establish the stability criterion for the whole protective layer. To achieve this goal, comprehensive theoretical and experimental studies were employed to enable measurement of the lift and drag forces acting on a specially instrumented particle. These studies were:

1) Location of the maximum wall shear stress.
2) Determination of the best size of the instrumented spherical particle.
3) Establishing a suitable means of converting the measured signals into lift and drag forces.
4) Establishing the best design for acquiring the measured forces accurately.

In addition, in order to assess the applicability of employing a spherical particle during these measurements, an attempt was made to measure the hydrodynamic forces acting on four different wooden blocks simulating real particle shapes. The measuring equipment, calibration procedure and the basic techniques for the aforementioned studies are the subject of the present chapter.

6.2 LOCATION OF THE MAXIMUM WALL SHEAR

As there was some correlation between the side slope shear stress distribution and the resultant forces that attack the protective layer, it was suggested that the proposed hydrodynamic force measurements should be carried out at a certain location where the boundary stress is a maximum. Therefore, the principle of the shear measurement is discussed and an appropriate technique for locating the point of maximum wall shear is developed.

6.2.1 Shear Measurement

Preston, J.H. (1954) developed a very simple method for determining the skin friction in the turbulent boundary layer by means of a round pitot tube resting on the surface; it has been widely used and is generally recognized as the most convenient and reliable method for measuring shear distribution. This method depends upon the assumption that close to the wall in turbulent shear flow, there exists a region in which conditions are a function only of the skin friction and relevant properties of the fluid, and are independent of the pressure gradient and surface curvature.

Preston's calibration curve, as determined in a pipe using four geometrically similar round pitot tubes, implied that with a symmetrical bore for round Preston tubes the ratio of inside to outside diameter has a negligible effect on the calibration.

In 1955, Hsu, E.Y. confirmed the accuracy of Preston's method. In his experiments to establish an analytical relationship for shear, the boundary layer velocity profiles were measured in both zero and adverse pressure gradients. The skin friction values obtained by Hsu were found to be in excellent agreement with those given by Preston's method.

On the other hand, the National Physical Laboratory (1958) provided experimental evidence as to the uncertainties of Preston's assumption. Their experiments also indicated, however, that the Preston tubes underestimated the skin friction by some 14%.

But subsequently the experiments performed by Head, M. and Rechanberg, I. (1962) have provided convincing evidence for the correctness of Preston's original calibration curve. Their method for testing was to determine for each type of flow, the static and Preston tube readings corresponding to different rates of flow. They used pitot tubes of different diameters which showed that the results agreed very closely.

Ippen, A.T. and Drinker, P.A. (1962) modified the original relationship between the dynamic pressure and local shear for application in free surface flows. Assuming the Karman-Prandtl velocity distribution, Hwang, L.S. and Laursen, E.M. (1963) performed a relatively simple method to extend Preston's technique to be applied to the fully rough flow regime. They developed an analytical relationship between the dynamic pressures acting on the pitot tube in contact with the rough surface and the local shear.

Later, Patel, V.C. (1965) conducted a comprehensive calibration of several Preston tubes in three different pipes and presented a calibration curve that could be approximated by three analytical expressions valid in three regions of the curve. Recently, Head, M.R. and Vesanta, V.R. (1971) have tried to assess

the accuracy of Preston tube calibrations carried out by Patal, and two alternative parameters have been suggested. Ghosh, S.N. and Roy, N. (1970) were among the first to demonstrate the applicability of Preston's technique in fully rough open channels. They used a shear-pressure relationship derived from an experimentally determined resistance equation to compute the local shear by Preston's technique. In order to assess the relative efficacy of the shear distributions obtained, the local shear stresses were calculated by two other methods which indicated that all estimates of the total boundary shear per unit length of the channel were in close agreement with each other.

Kartha, V.C. and Leutheusser, H.J. (1970), performed some measurements of the actual shear distribution in a hydrodynamically smooth rectangular channel with the aid of Preston tubes. The tubes were calibrated indirectly using the logarithmic form of velocity distribution. The distribution determined was compared with the computed laminar distributions which were shown to be entirely dissimilar in all of the tests carried out.

Bertelrud, A. (1974) reported an investigation into the sensitivity of the Preston tube with respect to the pressures and pressure drops found in pipe flow calibrations. In addition, the effects of Preston tube diameter and relative length were tested. In this study, an estimate of the velocity profile and the mean velocity was obtained simultaneously by means of a 13-tube rake which was used to obtain an independent measurement of skin friction.

On the basis of the experimental results just described, one may conclude that so far the foregoing investigations have confirmed the applicability of Preston's technique as a simple, accurate method for measuring the local turbulent skin friction either in pipes or open channel flows. Therefore, it was decided to employ the Preston tube to locate the point of maximum wall stress for different flow conditions.

The following instrumentation was employed in the experiments.

1 - Preston tube
2 - Pressure transducer
3 - Transducer converter
4 - Digital integrator

and their use is explained in the following sections.

6.2.2 The Preston Tube

For the purpose of identifying the positions where the shear stress is a maximum, the calibration of the Preston tube has to be studied first. In fact, many attempts have been tried to establish the pressure-shear relationship either for smooth or fully rough boundaries which may be introduced as follows:

6.2.2.1 Smooth boundaries

Preston's method of measuring skin friction, which makes use of a circular pitot tube resting on the surface (the so-called Preston tube), depends upon the assumption that, within a limited portion of the boundary layer, the velocity distribution past a smooth surface may be expressed as:

$$\frac{u}{u_*} = f_1 \left(\frac{u_* y}{\nu}\right) \tag{6.1}$$

in which

$$u = \sqrt{2(P_t - P_o)/\rho} \tag{6.2}$$

$$u_* = \sqrt{\tau_o / \rho} \tag{6.3}$$

where

u is the local velocity;

y is the normal distance from the wall to the geometric centre of a small pitot tube;

ρ is the fluid density;

ν is the kinematic viscosity;

P_t is the total pressure (dynamic pressure) recorded by the pitot tube on the surface and is a function dependent only on ρ , ν , y, and τ_o;

P_o is the static pressure at the wall;

τ_o is the wall shear stress;

and u_* is the friction velocity.

By dimensional analysis, Eq. (6.1), may be regrouped as

$$\frac{(P_t - P_o)y^2}{\rho\nu^2} = f_2 \left(\frac{\tau_o y^2}{\rho\nu^2}\right) \tag{6.4}$$

If the pitot tube is placed on the surface, then y/d = constant, where d is the diameter of the tube, and Eq. (6.4), may be written as

$$\frac{(P_t - P_o)d^2}{\rho\nu^2} = f_3 \left(\frac{\tau_o d^2}{\rho\nu^2}\right) \tag{6.5}$$

In turbulent incompressible flow past a smooth boundary two flow regimes exist. Close to the wall, in the viscous sub-layer for the range $0 < u_* y/\nu < 11$ the velocity profile may be considered linear, and Eq. (6.1), takes the form

$$\frac{u}{u_*} = \frac{u_* y}{\nu} \tag{6.6}$$

Further out, the flow becomes turbulent and Eq. (6.1) can be approximated by the relation

$$\frac{u}{u_*} = 5.5 \log \frac{u_* y}{\nu} + 5.8 \tag{6.7}$$

or another approximation is

$$\frac{u}{u_*} = 8.67 \left(\frac{u_* y}{\nu}\right)^{1/7} \tag{6.8}$$

For the range $11 < \frac{u_* y}{\nu} < 500 - 700$.

To avoid the effect of laminar sublayer, Preston utilized a pitot tube with a diameter much greater than the thickness of laminar sublayer, then Eq. (6.1) can be expressed as a logarithmic or power function as in Eqs. (6.7) and (6.8) respectively. For the turbulent boundary layer, Preston obtained the following empirical relationship:-

$$y^* = -1.396 + 7/8\ x^* \tag{6.9}$$

when $4.5 < x^* < 6.5$

in which

$$x^* = \log \frac{(P_t - P_o)d^2}{4\rho\nu^2} \tag{6.10}$$

$$y^* = \log \frac{\tau_o\ d^2}{4\rho\nu^2} \tag{6.11}$$

Whereas the result obtained for viscous flow is

$$y^* = 0.15051 + 0.5\ x^* \tag{6.12}$$

when $x^* < 4.0$

Patel, V.C. (1965) concluded that the calibration relationship has to be a curve and not a straight line as suggested by Preston. His calibration curve which was found to fit the experimental calibration within ± 1% of τ_o was

$$x^* = y^* + 2 \log (1.95y^* + 4.1) \tag{6.13}$$

in the range of $3.5 < y^* < 5.3$

The calibration was presented by the empirical relation

$$y^* = 0.8287 - 0.1381x^* + 0.1437x^{*2} - 0.006x^{*3} \tag{6.14}$$

to within ± 1.5% of τ_o when $1.5 < y^* < 3.5$

In the region where $y^* < 1.5$ the calibration results fall on a straight line

$$y^* = 0.037 + 0.5x^* \qquad (6.15)$$

On the other hand, Patel concluded that the ratio of inside to outside diameter has a negligible effect on the calibration.

Bertelrud, A. (1976), presented his experimental results obtained from eight different Preston tubes in terms of, $(P_t-P_o)/\tau_o$, and, d^*, where, $d^* = u_* d/\nu$ and, $u_* = \sqrt{\tau_o/\rho}$; the results can be presented as

$$\frac{P_t - P_o}{\tau_o} = 14.15 - 54.01 \log d^* + 60.69 \ (\log d^*)^2 \qquad (6.16)$$

which is valid for, $d^* < 50$, and for the range, $50 < d^* < 1000$, the relation is

$$\frac{P_t - P_o}{\tau_o} = -51.93 + 87.77 \log d^* \qquad (6.17)$$

or

$$\frac{P_t - P_o}{\tau_o} = -111.92 + 38.85 \log \frac{(P_t - P_o)d^2}{\rho\nu^2} \qquad (6.18)$$

which is valid for

$$2.5 \times 10^5 < \frac{(P_t - P_o)d^2}{\rho\nu^2} < 2.1 \times 10^8$$

In addition, Bertelrud concluded that the relative length of the Preston tube ℓ/d is unimportant in the tested region $6.6 < \ell/d < 1.5$ in which ℓ is the Preston tube length.

6.2.2.2 Rough boundaries

For flow past a hydrodynamically rough surface the velocity distribution is independent of the Reynolds number, $u_* y/\nu$, and may be expressed as

$$\frac{u}{u_*} = f_4\left(\frac{y}{k}\right) \tag{6.19}$$

where k is the height of the roughness protrusions. Preston suggested the possibility of determining the corresponding calibration function for a pitot tube on a rough surface by a method analogous to the development of Eq. (6.5) to obtain

$$\frac{P_t - P_o}{\tau_o} = f_5\left(\frac{d}{k}\right) \tag{6.20}$$

The major difficulty of applying Eq. (6.20) is that, the pitot tube must always be placed in the same position with respect to the zero datum. Moreover, in the case of flow in open channels where the roughness distribution is not uniform, not only the problem of determination of zero datum remains, but in addition the selection of a suitable parameter that characterizes the rough boundary surface. However, few attempts have been made to overcome the aforementioned difficulties as well as to identify the shear distribution in the rough boundaries which can be summarized as follows:

Hwang, L. and Laursen, M. (1963), conducted a series of pipe experiments in the transitional rough boundary ($5 < u_*k_s/\nu < 70$), where k_s is Nikuradse's sand grain roughness, and only a few measurements in the fully rough region where $u_*k_s/\nu > 70$. Assuming that

$$A(P_t - P_o) = \int_A \frac{\rho u^2}{2}\, dA \tag{6.21}$$

where A is the frontal area of the Preston tube;

dA is an elemental area;

and u is given by the Karman-Prandtl equation

$$\frac{u}{u_*} = 5.75 \log \frac{30y}{k_s} \tag{6.22}$$

where y is the normal distance from the datum plane for the rough boundary.

Hwang and Laursen developed the following expression:

$$\frac{P-P_o}{\tau_o} = 16.531\ [E^2 - \ell n(E).B + \ell n^2 C] \qquad (6.23)$$

where

$$E = \log \frac{30h}{k_s}$$

$$B = 0.25\ (\frac{a}{h})^2 + 0.0833\ (\frac{a}{h})^4 + 0.00704\ (\frac{a}{h})^6 + \ldots$$

$$C = 0.25\ (\frac{a}{h})^2 + 0.1146\ (\frac{a}{h})^4 + 0.0586\ (\frac{a}{h})^6 + \ldots$$

in which

h is the height of centre of stagnation tube from zero datum;

and a is the inner radius of the stagnation tube.

This equation can be used for the fully rough flow regime to estimate the ratio of the dynamic pressure reading to the local wall shear as a function of the size of the tube and the roughness element. But in the Author's opinion, there are still certain difficulties which remain in placing the Preston tube in the same position with respect to zero velocity datum. Moreover, uncertain stress readings could also possibly result from a tube being sited in the wake of a large particle.

In (1970), Ghosh, S.N. and Roy, N. attempted to establish another shear-pressure relationship analytically which closely follows that proposed by Hwang and Laursen. In his study, the boundary roughness was artificially simulated by spherical leads in three different symmetrical roughnesses; then the resistance equation was derived, in which the characteristics of the rough surface were described in terms of the artificial roughness geometry. The resulting pressure-shear relations was

$$\frac{P_t - P}{\tau_o} = 16.531\ [x^2 - \ell n\ x\ .(Y) + \ell n^2(w)] \qquad (6.24)$$

in which

$$x = \log \frac{R}{\lambda . h}$$

$$Y = 0.25 \left(\frac{r}{J}\right)^2 + 0.0625 \left(\frac{r}{J}\right)^4 + 0.026 \left(\frac{r}{J}\right)^6 + \ldots$$

$$w = 0.25 \left(\frac{r}{J}\right)^2 + 0.1146 \left(\frac{r}{J}\right)^4 + 0.0594 \left(\frac{r}{J}\right)^6 + \ldots$$

$$J = r + t + z$$

$$\lambda = h\ w/Se$$

$$\frac{R}{\lambda h} = \text{Relative roughness}$$

where

- r is the inner radius of the stagnation tube;
- J is the location of the centre of the stagnation tube from the zero datum;
- z is the location of the bottom of the stagnation tube above datum;
- t is the thickness of the stagnation tube;
- h is the height of roughness elements used in the tests;
- λ is the ratio of roughness projection to area of channel boundary;
- w is the depth of roughness elements;
- S is the longitudinal spacing of roughness elements;
- e is the transverse spacing of roughness elements;

and R is the hydraulic radius.

Hallick, M. (1976) presented an investigation into the possibility of using the Preston tube technique on sand roughened boundaries. In his study, the results were satisfactory in smooth pipes whereas the uncertain stress readings obtained in the sand roughened pipe were thought to be due to variations in positioning the Preston tube relative to the zero velocity datum.

In conclusion, it would appear that Preston's shear measurement technique can be used successfully in smooth boundaries

where still certain difficulties remain in extending its range of utility in rough wall conditions. This was due to the difficulty of predicting the effective surface roughness as well as the uncertainty of positioning the Preston tube which must always be placed in the same position with respect to the rough boundary. Therefore, due to the fact that the aim of this preliminary qualitative study was limited to locating the point of maximum shear stress rather than its value, it followed that the only possible way to overcome the previously described difficulties was by utilizing an artificially roughened surface to simulate the side slope boundary roughness similar to that presented by Ghosh and Roy. But due to the fact that it was unnecessary to determine the wall shear stress quantititatively, Eq. (6.24) was simplified as

$$\frac{P_t - P}{\tau_o} = f\left(\frac{r}{J}, \frac{R}{\lambda h}\right) \qquad (6.25)$$

So as the terms included in the right hand side of the Eq. (6.25), were constant during each flow case, then Eq. (6.25) may be written as

$$\tau_o = f\,(P_t - P) \qquad (6.26)$$

which implies that for each run, the stress exerted on the roughened surface would only be a function of the mesured pressure difference between total and static pressure of the Preston tube. Therefore, Eq. (6.26), was used to locate the depth of maximum wall shear for different flow conditions.

6.2.3 Shear Measuring Equipment

6.2.3.1 Preston tube

The Preston tube employed in this study was manufactured in the laboratory according to the design recommended by Ippen, A.T. and Drinker, P.A. (1962), as shown in Fig. (6.1). The static tube is positioned above the total head tube in order to minimize the effects of the total pressure gradient near the boundary on the measured static pressure. Both total head and static tubes were made of stainless steel. The static holes were drilled nominally

three diameters back from the hemispherical tip. To strengthen the stem against the high velocities of the flow, both tubes were soldered together at many points and another tube of greater diameter was slipped over the other two tubes. The stem length which was in contact with the flow was ovoid shaped in an attempt to reduce the effect of the large tube.

The stem was attached to a point gauge for the measurement of the vertical movement. The whole system was supported by a movable rail carriage to facilitate horizontal movement along the side slope. Clear plastic tubing was used to connect the static and total head tubes with a differential pressure transducer. A rubber tube with a funnel in the top end was joined to the plastic tubing via T-shaped junctions for evacuating air bubbles. The transducer was connected to both the transducer converter and the digital integrator for the purpose of converting the pressure difference into voltage. Using the calibration curve of the transducer, values of pressure head difference between the total and static pressure were obtained.

6.2.3.2 Pressure transducer

A differential pressure transducer, type No. SE1150/D5964 manufactured by SE laboratories (EMI) Ltd and shown in Plate (6.1), was used as a quick, simple and suitable device for measuring the pressure difference between its two tappings. It was connected to the Preston tube by a system of clear plastic tubes, and firmly attached to a metal base which was secured to the base carrying the Preston tube so it could move together as one unit. The pressure transducer was calibrated for a maximum head difference of 20 cms. According to the specification, the pressure transducer had an accuracy of ± 0.3% with the natural frequency of 3.2 kHz.

6.2.3.3 Transducer converter

For the purpose of measuring the pressure head difference

accurately, a transducer converter type SE 905/2/1 which is shown in Plate (6.2), was used to convert the pressure difference into voltage. It was a compact portable self-contained 2 channel system. The system was contained in a cabinet which also contained a 24V D.C. rectifier, a stabilised 3 kHz and D.C. stabiliser. The transducer converter was connected to the pressure transducer to receive signals as input. The transducer converter was employed to amplify the input signal to produce an electrical signal proportional to the mechanical signal applied to the transducer.

6.2.3.4 Digital integrator

The digital integrator used in the current study was type 100EP manufactured by Time Electronics Ltd. The signal is received from the transducer converter and, within integration linearity of 0.1%, the resulting sum of the integral units can easily be read at the end of a selected period through a 6 digital magnetic counter. The measurement set-up used during this study is shown diagrammatically in Fig. (6.2).

6.2.4 Calibration of Pressure Transducer

In order to establish the relationship between the applied water head difference and the transducer output, the following procedure was carried out:

Two long glass manometer tubes, 1 cm in diameter and open to air, were attached to a vertical wooden board. Two rubber tubes with funnels at the upper ends were attached on the same board and parallel to the manometer tubes for the purpose of introducing various pressure differences across the transducer by changing the water elevations in the manometer tubes as well as evacuating all air bubbles trapped in the tubing system. Each of the manometer and rubber tubes was connected at its lower end by a tube then branched into another two tubes; one of each was connected together whilst the other one was then connected to one side of the transducer via rubber tubes as shown in Fig. (6.3). The transducer was fixed on a horizontal base plate via two screws to prevent any possible movement.

The water head differences were measured by means of a cathetometer reading to 0.01 mm. The pressure transducer was connected to the transducer converter and the digital integrator in series. The calibration was started by filling the tubes with water then evacuating all the air from the tubing system. This was done while the valve in the by-pass rubber tubes, which connects the lower ends of the manometer and rubber tubes, was being opened. When the water levels in both manometer tubes were brought to the same reading in the cathetometer, both the converter and digital integrator were adjusted to give zero readings. The by-pass rubber tubes were then closed and the pressure head difference between both the tubes was applied to its maximum and by draining some of the water in the higher level; the difference head decreased gradually in steps. At each step the pressure head difference and the corresponding totalized digit display were recorded. When the pressure head difference reached zero value, it was then increased gradually in steps by adding some water into the funnel until it reached the maximum operating value and during each step the readings were recorded as before.

The transducer was calibrated for maximum head of 20 cms which produced the following calibration equation:

$$H_w = 0.02719 + 0.01975\ V \qquad (6.27)$$

in which

H_w is the water head difference in cm;
and V is the displayed voltage.

The calibration curve which is shown in Fig. (6.4) was obtained with correlation coefficient of, 0.9994, and standard error of estimate of 0.1872.

6.2.5 The Experimental Procedure

As mentioned earlier, the present investigation was directed to finding the depth of maximum wall shear qualitatively and was

similar to the method developed by Ghosh, S.N. and Roy, N. (1970), since this was best suited to the purpose of the study. The technique adopted in this study was to modify a limited portion of each side slope by replacing the protective layer with artifically roughened surfaces as follows:

The rock protective layers within 0.6m length of the both side slopes at 2.5m upstream from the end of the channel were removed. Then the exposed areas were replaced with two symmetrical artificially roughened surfaces. Each roughened surface consisted of a 19.0mm thick timber board 0.9m length and 0.6m width which was artificially roughened with an orderly pattern of screw bolt heads of 11.3mm diameter and 4.0mm height. Each board was drilled, then the bolts were firmly inserted in the drilled holes. The longitudinal spacing of the roughness element used in this study was 50.0mm, whilst the transverse spacing was 40.0mm.

The roughness pattern used in this test is shown in Fig. (6.5) whereas Plate (6.3) shows the roughened surfaces and the modified side slopes before the investigation.

To carry out these measurements, the model was set at an arbitrarily chosen low discharge, and uniform flow was established by suitably adjusting the tail water gate, then using the point gauge fixed upstream of the tail water gate, the flow rate was measured. The Preston tube was mounted vertically with the total head tube aligned parallel to the downstream direction then lowered to the bottom end of the artificially roughened side slope with the tip resting on the boundary.

By taking into account the fact that the Preston tube should be placed ir the same position with respect to the boundary, it was then moved carefully in steps along the side slope. For each step, beginning from the foot of the side slope, the cumulative total digital display of the integrating voltmeter was recorded three times with integration period of 60 sec. In each case the average value was computed.

Using the calibration curve (see Fig. (6.4)) the value of the pressure difference between the total and static pressure was obtained for each step. Accordingly, the position of the maximum wall shear stress was obtained at the Preston tube location at which the recorded value of pressure difference between total and static pressure was the maximum.

6.2.6 Results and Discussion

In order to develop a relationship between the flow rate and the located depth of maximum shear, the technique established previously was applied for eight runs which covered a wide range of flow rates. During each run, flow depth and discharge were measured, then the depth of maximum shear was defined and recorded. The results obtained from this study are listed in Table (6.1), which indicates that the location of maximum wall shear for different flow rates was mostly found at a vertical distance of 0.29 y to 0.35 y above the channel bed where y is the water flow depth.

It is worth mentioning that utilizing analytical and finite-difference methods, Lane, E.W. (1955) found that for normal trapezoidal channels the maximum wall shear was found to be at a vertical distance of 0.2 y to 0.3 y above the channel bed. It would therefore seem that the results obtained in this study differ very little from those estimated by Lane with an order of maximum difference being within an acceptable range. Moreover, the experimental results confirm the results obtained from the failure tests in which most of the particles were moved mainly from within the lower part of the side slope.

In order to produce a general relationship between the located depth of maximum wall shear and the flow depth, the following simple formula was developed with standard deviation of 0.0178.

$$y_m = 0.313\ y \qquad (6.28)$$

in which

y_m is the depth of the maximum wall shear;
and y is the flow depth.

Therefore, as a result of this study, one may conclude that the planned hydrodynamic force measurements, for different flow conditions, should be conducted at a certain vertical distance above the channel bed. This distance could be obtained by applying Eq. (6.28). The results obtained in this study are depicted in Fig. (6.6).

6.3 PARTICLE SIZE MODELLING

Particle size is one of the most important factors in the evaluation of the hydrodynamic forces that act on the protective rock layer. As indicated in Chapter Five, the value of D_{50} used in the previous experimental work was 20.7 mm, and was obtained by sieving. A large number (500) of particles were examined volumetrically giving a mean value diamater of 21.7 mm. As the particle to be used for the force measurements was spherical, a representative spherical diameter was required.

The literature contains many methods for the determination of particle size. The most comprehensive review has been prepared by the Task Committee on Preparation of Sedimentation Manual (1969), in which the determination of particle size by direct and indirect measurements was briefly explained. However, the specified indirect methods are commonly applicable for particle size less than 2.0 mm. But during this study, the spherical diameter was accomplished hydraulically by sedimentation technique taking account of the configuration of the stones used in the experiments as follows:

6.3.1 Basis of Approach

The present study is based on the assumption that if an irregularly shaped particle is allowed to settle in a liquid, its terminal velocity may be compared with the terminal velocity of a sphere of the same density settling under similar conditions. The particle size is then equated to the diameter of the sphere. Details of the methods available can be found in Allen, T. (1981).

Assuming an individual particle is released in still water, it will accelerate until the resistance to motion offered by the fluid F_r is just equal to the gravitational force F_g, represented by the submerged weight of the particle. Therefore, the settling velocity can be obtained by equating F_r with F_g.

Assuming a spherical particle with diameter D and density ρ_s, therefore

$$F_r = C_D \tfrac{1}{2} \rho_w V_w^2 \tfrac{\pi}{4} D^2 \qquad (6.29)$$

$$F_g = \frac{\pi}{6} D^3 (\rho_s - \rho_w) g \qquad (6.30)$$

in which

C_D is the drag coefficient
g is the acceleration due to gravity
ρ_w is the fluid density
and V_w is the fall velocity

Equating Eqs. (6.29 and 6.30) to obtain

$$\frac{\pi}{6} D^3 (\rho_s - \rho_w) g = C_D \tfrac{1}{2} \rho_w V_w^2 \tfrac{\pi}{4} D^2 \qquad (6.31)$$

or

$$V_w^2 = \frac{4}{3} g \frac{D}{C_D} \Delta \qquad (6.32)$$

in which

Δ is the relative density of the particle and is equal to $\frac{\rho_s - \rho_w}{\rho_w}$

Assuming the settling process is not obstructed by other particles (hindered settling), it is found that for a perfect sphere in the laminar range ($R_e<1$), the drag coefficient C_D can be given by the following equation:

$$C_D = 24/R_e \tag{6.33}$$

in which

$$R_e = \frac{V_w D}{\nu} \tag{6.34}$$

where

R_e is the particle Reynolds number
ν is the kinematic viscosity
and D is the spherical particle diameter

So that Eq. (6.32) can be rewritten as

$$V_w = \frac{\Delta g D^2}{18\nu} \tag{6.35}$$

This equation is called Stokes Law and is only applicable in case of low Reynolds number, where the flow around the particle is essentially viscous and F_r is directly proportional to the fall velocity V_w.

For large Reynolds numbers, as in the case under investigation, the flow around the particle is turbulent and F_r is proportional to V_w^2. To determine the relationship between R_e and C_D, Fig. (6.7) developed by Albertson, M.L. (1953) was utilized to obtain the required relationship for different particle shape factors.

6.3.2 Experimental Procedure

A random sample of one hundred of the test particles was taken. Using a micrometer the three mutually perpendicular axes for each particle were measured to determine its shape factor as

$$SF = c/\sqrt{a\,b} \qquad (6.36)$$

in which

a is the major axis
b is the intermediate axis
and c is the minor axis.

The representative shape factor was taken as the mean value of the obtained shape factors.

To investigate the settling velocity, a glass sedimentation column, with a height of 1.73m and an inner diameter of 0.14m, was used. The column was filled with water, and two marks denoted as A and B were made on the column wall to fix the timing distance. To remove air bubbles adsorbed on the rock particle, which could possibly affect the particle velocity during the settling process, the particle was immersed for a short time then released to fall freely.

The particle motion was observed and timed between the marks A and B. The settling velocity was then determined by dividing the distance AB by the recorded time. To record the variation in the kinematic viscosity, the temperature of the water was recorded during each test.

Knowing the representative shape factor SF and the average fall velocity V_w, the following procedure was applied to determine the representative spherical diameter D of the particle.

- By assuming a value of D, R_e can be calculated from Eq. (6.34)
- Knowing the shape factor SF, C_D can be obtained from Fig. (6.7)
- Substituting the values V_w, g, Δ and C_D in Eq. (6.32) gives another value of D.
- The procedure was repeated until sufficient accuracy was obtained.

6.3.4 Results and Discussion

The results from the measurements can be summarized as follows:

The representative shape factor	=	0.558
The average fall velocity V_w	=	0.536 m/s
The average value of V_w/ν	=	528032 m^{-1}
Specific gravity of the particle S_s	=	2.6636
The relative density Δ	=	1.6636

By applying the procedure described, the representative diameter was determined as 20.1mm.

This result means that a spherical particle of 20.1mm diameter can be utilized to represent the particles used in the previous experimental work.

From comparison of this result with other methods one may conclude that the diameter from the sedimentation technique is very close to that determined by sieving.

6.4 FORCE MEASURING SYSTEM

As the previous part of this chapter was mainly directed to investigating auxiliary studies to permit the acquisition of the needed measurements, consideration is now given to illustrate the design used to obtain these measurements. In addition, in order to shed light on the system used, consideration will be in turn given to present the measuring devices as well as the instrumented particles utilized in this study. Therefore, the force measuring set up can be divided into the following parts:

- Basis of approach
- The load cell
- The instrumented particles
- The movable roughened board
- The embedded cavity
- Measuring equipment

6.4.1 Basis of Approach

Several methods were considered to determine the lift and drag forces on an individual particle in the side slope protective layer. To simplify the measurement procedure, a specially designed load beam cell was introduced as shown schematically in Fig. (6.8A), in which strain gauges were employed in a manner that will be discussed in the following section.

In this part of the study, consideration is directed to establishing relationships between the hydrodynamic forces acting on the instrumented load cell and the output signals obtained from the strain gauges. These relationships will be introduced theoretically on the basis of the combined action of the lift and drag forces on the thin beam contained within the load cell.

Assume a beam, both ends fixed (encastre), and having span L. The beam is subjected at the middle of its span, to lift force F, and moment M, as shown in Fig. (6.8B). In this case, the resulting bending moment due to the combined action of the applied loads can be obtained as the algebraic sum of that due to force F and moment M individually as depicted in Fig. (6.8C), and the resulting bending moments can be worked out separately as shown in Fig. (6.8D).

Suppose two similar strain gauges were firmly bonded on both sides of the beam so as to be at equal distance X from the mid span. These points are denoted as A and B in the given figure. The moment resulting at these points can be obtained as:

$$M_A = M_{AF} + M_{AM} \tag{6.37}$$

$$M_B = M_{BF} - M_{BM} \tag{6.38}$$

in which

M_A and M_B are the total resultant moments at points A and B, respectively;

M_{AF} and M_{BF} are the resultant moments due to force F at points A and B, respectively;

and M_{AM} and M_{BM} are the resultant moments due to moment M at points A and B, respectively.

In addition, it is obvious from Fig. (6.8D) that:

$$M_{AF} = M_{BF} \tag{6.39}$$

$$M_{AM} = -M_{BM} \tag{6.40}$$

Therefore, the external forces F and M can be evaluated as:

$$F = f_1 (M_A + M_B) = f_1 (M_{AF} + M_{BF}) \tag{6.41}$$

$$M = f_2 (M_A - M_B) = f_2 (M_{AM} + M_{BM}) \tag{6.42}$$

In which

f_1 and f_2 are functions which can be obtained by calibration.

On the other hand, for the case of homogeneous beam with rectangular cross-section, as that in the case under consideration, the resultant bending moment at any point along the beam was reported by Reeve, A. (1975) as

$$M_C = Z E \epsilon \tag{6.43}$$

in which

ϵ is the applied strain (the strain gauge reading);

E is the modulus of elasticity;

and Z is the elastic modulus of the cross-section which is equal to $\frac{bh^2}{6}$ for rectangular section of b width and h thickness.

Therefore, applying Eq. (6.43) at points A and B respectively, yields:

$$M_A = \frac{bh^2}{6} E\varepsilon_A \qquad (6.44)$$

$$M_B = \frac{bh^2}{6} E\varepsilon_B \qquad (6.45)$$

in which

ε_A and ε_B are the strain developed at points A and B respectively.

Substituting Eqs. (6.44) and (6.45) into Eqs. (6.41) and (6.42) respectively, one can obtain:

$$F = f_3 (\varepsilon_A + \varepsilon_B) \qquad (6.46)$$

$$M = f_4 (\varepsilon_A - \varepsilon_B) \qquad (6.47)$$

Eqs. (6.46) and (6.47) represent the final formulae which should be utilized to determine F and M values. In those equations, the terms ε_A and ε_B are the strain gauges readings obtained at points A and B respectively, where the functions f_3 and f_4 can be easily evaluated through the calibration process.

Since the load cell is composed of a very thin beam and column, the increase in lateral force, which represents the drag, causes a small deflection of the column. Therefore, the resulting moment induced from the axial force will reduce the effective moment due to drag force. Consequently the elastic response of the device becomes non-linear and the relationship between the stresses and the applied drag force are also non-linear, whilst the opposite is true in the case of lift force, which in other words means that the relationship between the lift force F and the corresponding stresses, will be linear.

6.4.2 The Load Cell

This device represents the measuring unit which is an electro-mechanical device employed to convert a mechanical input to an electrical output. Since this device is intended for measuring force and load, it is usually called a force transducer or load cell.

The load cell consisted of a simple beam, (116x12x 0.12mm), made of flexible phosphor bronze to work as a spring and nill-corroded under water. This beam was clamped at both sides, as shown in Fig. (6.9), by four stainless steel (s.s.) blocks, (50x12x12mm) each of which was attached firmly to a (140x50x3.2mm) s.s. plate. A s.s. rod 1.54mm diameter and 100.7mm length was then soldered at the mid point of the metallic beam and with a right angle through a base plate (12x12x1mm). The other end of the rod was soldered into a threaded nipple which can be used to set either of the spherical or non-spherical roughness elements.

Two similar load cells were designed to enable simultaneous left and right signals to be recorded which would be in turn converted into simultaneous lift and drag forces. Each load cell, as shown schematically in Fig. (6.10), consisted of a bridge of four (FLA-6-17) type strain gauges; two of them were fixed into a dummy gauge holder; whereas the other two were firmly soldered into an upper and lower face of the beam with an equal distance from its mid span. The dummy gauge holder was screwed into the s.s. plate. Then to protect the strain gauges as well as the wiring system against any damage, which might possibly take place due to the submergency in water, a non-corrosive silicon rubber was used to coat these units.

It is also worth mentioning that the two load cell bridges were designed in such way as not to alter the zero reading due to a variation in the water temperature (see Norton, H.N. (1969)). This in other words means that as long as the four strain gauges contained within one bridge were kept in the same water temperature, this temperature would not have any effect on the zero reading.

To prepare the load beam for measuring, it was secured into two s.s. angles (83 x 48 x 3.2mm), which were attached into a movable roughened unit. Some photographs included the load cell beam are shown in Plate (6.4).

6.4.3 The Instrumented Particles

In order to assess the applicability of using non-spherical particles during the current measurements, two types of particle shapes were utilized as follows:

6.4.3.1 Spherical particle

A spherical particle 20.1mm diameter, which was determined experimentally, was designed and manufactured to permit measuring the hydrodynamic forces. To prevent any lateral twisting moment on the thin beam, which may possibly take place if the submerged weight of the instrumented sphere was significant, it was designed in such way as to reduce its bulk specific gravity to unity which consequently makes its submerged weight equal to zero. This design was accomplished by drilling a few holes in the sphere to extract some timber material then the holes were sealed.

On the other hand, to simulate the roughness of the rock surface, the sphere was coated with a preservative liquid then a thin layer of find sand. To enable screwing the sphere into the threaded nipple, a screw was partially fitted into the sphere.

6.4.3.2 Non-spherical particles

Four wooden particles with different shapes were made for measuring the hydrodynamic forces. The particl shapes were randomly selected similar to four real rock particles used in the investigation. To make it possible to fit those particles into the threaded nipple, each particle was attached with a screw similar to that used in the spherical particle. The four real and simulated particles are shown in Plate (6.5).

6.4.4 The Movable Roughened Board

This unit was designed and manufactured to simulate part of the side slope containing the instrumented particle and the load cell. This consisted of a roughened plywood board (300x200x20mm), which could be adjusted easily at right angles to the flow direction in such way as to position the instrumented particle at the required level of maximum shear stress for each flow case. The board was screwed into the two load beam angles to work as one unit. To simulate the roughness of the protective layer, the upper face of the board was roughened with a rock layer 31mm thick. Then either the instrumented spherical or non-spherical particle, developed for measuring the instantaneous lift and drag forces, was screwed into the threaded nipple via a circular hole in the roughened board and adjusted to have the same height as the rock protective layer elsewhere. In this way the instrumented particle was allowed to move freely under the applied hydrodynamic forces.

In addition, to make it possible to cover the gap between the movable roughened board and the channel bed, different roughened slices with various widths were prepared as shown in Plate (6.6). Those slices were roughened in the same manner as the movable board. Plate (6.7) shows the movable unit during the investigation.

6.4.5 The Embedded Cavity

This unit was designed and manufactured by the Author to work as a part of the channel side slope as well as to accommodate the movable board as follows:

The side slope materials at 2.6m to 3.3m upstream from the channel end were removed. Two wooden wings were fitted 52.5cm apart in both sides of the cavity to work as retaining walls between the side slope base on each side U/S and D/S, and the cavity. To accommodate the roughened board, a hollow wooden construction conforming exactly to the side slope was manufactured separately with the dimensions indicated in Fig. (6.11). This was designed in

such way as to restrict any flow through it. Therefore, the hydrodynamic forces acting on the instrumented particle, were transferred to the load beam via the stainless steel rod, and would be the only force applied to the load beam cells.

The wooden construction was provided with two supports which could be used to hold the movable board firmly at a required level. This construction was then inserted into the cavity and screwed into both the retaining walls; finally a rock layer of 31mm was glued on to the side sloping face to simulate the roughness of the protective layer elsewhere. Plate (6.8) shows some construction stages of the embedded cavity.

Consideration is now given to select a suitable site for accommodating the various units of the force measuring set up. This location was designated on the basis of the results obtained from the velocity measurements and failure tests.

As shown in Figs. (6.12 to 6.14), the velocity distribution at three different flow rates and at various locations (L) from the channel inlet indicated the flow establishment within 5.5m long upstream of the channel end. In addition, it was noticed through the tests that the failure apparently occurs within 4.0m from the downstream end of the channel. Obviously these results were expected due to the boundary layer development which was likely to reach its complete establishment within these portions. Therefore, as a result of this, the instrumented roughened element was located on the right side slope, at 2.95m upstream of the channel end as shown in Fig. (6.15).

6.4.6 Force Measuring Equipment

Details of the system configurations used during the force measurements are schematically depicted in Fig. (6.16), in which the following instruments were utilized.

6.4.6.1 Signal conditioner

For the purpose of converting the generated output signals of the left and right load cell bridges into readable voltage units, a

conditioning system type SE1050, manufactured by Thorn EMI Datatech Ltd, was utilized for the force measurements. It is a single rack system comprising of a master rack fitted with a monitor module type SE1051 and four AC conditioning modules type SE1053. The system used in this study is shown in Plate (6.9).

To check the signals, a 20 MHz oscilloscope type D1011 shown in Plate (6.10), was used to compare the input and output signals to and from the conditioner.

6.4.6.2 The amplifier

The amplification of weak signals into stronger signals is of fundamental importance in almost any electronic system. Since the attainable signals from the load beam cells were very weak and the computer was not provided with an amplification system, it was decided to use an amplifier to ensure that the signal information would not be lost in noise.

The amplifier was designed and manufactured in the electronic workshop of The Civil Engineering Department for the purpose of increasing the level of the signals by 10 or 20 times. The amplifer was connected to receive its input signals from the signal conditioner through two channels, then it was fed as output to the data logger connected to the computer system as shown in Fig. (6.16). The circuit diagram of the amplifer is shown in Fig. (6.17).

6.4.6.3 The computer system

In order to record the fluctuations of the signals obtained from the load cells, a Cromemco-Z2 microcomputer system with a Cromemco D+7A Analogue/Digital Interface was used. Seven channels were available for receiving the data from the signal source. The interface is a high performance module and gives seven channels of 8-bit analogue to digital conversion with a fast conversion time of 5.5 microseconds; it has an input voltage range from -2.56 to +2.54

voltage. The system has two disk drives and is linked to a VDU terminal as shown in Plate (6.11). The computer system and the terminal were kept beside the flume ready for operation. Wiring of two channels was installed to the test site close to the signal source. Two channels of the computer system were used to receive the output signals from the amplifier.

6.5 LOAD BEAM CALIBRATION

As mentioned previously, the instrumented load beam is mainly designed to allow working under water to enable simultaneous left and right signals. These would be in turn converted mathematically, by applying the formulae established given by Eqs. (6.46 and 6.47), into simultaneous values of lift and drag forces. To achieve this goal, a special calibration procedure was conducted, in which the following conditions were taken into consideration.

1) The calibration process should be carried out by applying simultaneous lift and drag forces.

2) Simulating the working condition by submerging the load beam into water during the calibration process, the water must be still with almost the same temperature as that expected during the experimental work.

3) The calibration should cover the range of forces that could possibly be applied during the course of the measurements.

The calibration process was conducted in steps which can be summarized as follows:

6.5.1 The Helical Springs

For the purpose of calibrating the load beam accurately, it was decided to use calibrated helical springs to apply forces representing lift and drag forces. As a result of this, two stainless steel helical springs denoted as spring 1 and 2, and shown in Plate (6.12) were employed. These springs were as follows:

Spring No.	Length (mm)	Diameter (mm)	Wire Diameter (mm)
1	138.9	7.15	0.045
2	165.9	7.62	0.045

In order to introduce the relationship between the static force acting on the helical springs and the elongation of each, the following procedure was applied:

Both springs were hung on a vertical wooden board by means of two fixed nails. As the first spring would be used to apply static force in the lift direction, it was left free vertically then a load carrier was attached to its lower end. The second one, which would be utilized to apply drag force, was laid horizontally on a smooth piece of perspex which was screwed on the wooden board. In this case the load carrier was attached to the spring via a smooth pulley which was fixed against the wooden board at the same level as the spring centre line as shown in Fig. (6.18). To evaluate the elongation of the springs, a cathetometer reading to 0.01mm was used for the vertical spring, whereas a vernier reading to 0.02mm was employed for the horizontal one.

The calibration of each spring was then carried out according to the following procedure:

The calibration process started by recording the spring length, then the smallest load was applied as a static force and the spring length was also recorded to work out the elongation due to the applied force as the difference between each reading. The same procedure was applied for the various static forces. Then a relationship between the static force and the corresponding elongation, for both springs, was worked out and two separate equations of the following form were fitted to the recorded data.

$$F = T + S.\ \Delta L \qquad (6.48)$$

in which

F is the applied static force;

S is the calibration constant and represented by the line slope;

T is the intercept of Y axis;

and ΔL is the spring elongation (cm).

In this equation, knowing T and S, the applied force for any value of ΔL can be easily determined.

The results obtained from this study are shown in Fig. (6.19), and may be written in the following table:

Spring No.	Int. of Y axis (N)	Line Slope	Correlation Coefficient	Standard Error of Estimation	Equation No.
1	-0.00011	0.054	0.9998	0.0004	(6.49)
2	0.00014	0.041	0.9998	0.0003	(6.50)

In ideal conditions, the intercept on y axis should be equal to zero, but due to some reading error a very small value has been found.

6.5.2 Load Beam Calibration Set Up

To fulfil the mentioned three conditions during the load beam calibration process, the calibration set up shown in Fig. (6.20) was used, which may be explained as follows:

An open-ended wooden box (300x200x158mm) was manufactured and a plastic container, containing still water, was installed inside it. The movable board, including the attached load beam, was laid horizontally on the box in such a way as to submerge the load beam cells in the still water. Two aluminium channel cross-sections each 552 and 395mm long were screwed into the movable board as follows:

The first one was fitted vertically to enable the application of a static lift force through an attached vertical spring, whilst the second channel was fixed horizontally so as to allow the application of a static drag force through an attached horizontal spring.

During the calibration process, the instrumented particle was replaced with a long male thread which was secured vertically into the threaded nipple.

Two ends of the helical springs were tied up into two smooth rods 38mm length which were screwed to both ends of the aluminium channels with right angles as shown in Fig. (6.20). The other spring ends were then attached tightly to the male thread via two small drilled holes. The horizontal spring was laid on a smooth piece of perspex which was glued on the horizontal channel. To monitor the water temperature, a thermometer was utilized. The two load beam cells denoted as left and right were connected to the signal conditioner via two channels to measure the left and right strain due to the applied external forces. In this way, the calibration process was modified to establish the relationship between the displayed output of the signal conditioner and the applied lift and drag forces. Plate (6.13) shows the load beam set up during the calibration process.

6.5.3 Calibration of the Load Beam

The load beam was specially designed to measure the simultaneous lift and drag forces indirectly. Therefore the calibration process should be conducted in the same manner as in the working condition. This was carried out by applying combinations of simultaneous static forces which simulate drag and lift forces.

It was concluded from the theoretical study presented in section (6.4.1), that the resulting left and right strain in the load beam due to the effect of the horizontal (drag) force, would be dependent on the applied value of vertical (lift) force whereas the opposite is not true.

To prove this, a preliminary study was experimentally conducted by applying various values of drag force with various values of lift force and the results obtained were predictably independent of the drag values. Therefore, as a result of this study, it was decided to calibrate the load beam cells firstly with respect to the lift force, then with respect to the drag force during which various lift forces would be applied simultaneously as follows:

6.5.3.1 Lift force

Applying the developed formula for lift force as

$$F = S(\varepsilon_A + \varepsilon_B) \tag{6.51}$$

in which

F is the applied lift force (N);

ε_A and ε_B are the left and right readings displayed on the signal conditioner, respectively;

and S is a constant which can be determined through the calibration process.

Therefore, to determine the value of S in Eq. (6.51), the calibrated spring No.(1) was hung vertically between the smooth rod and the long thread which replaced the instrumented particle. Then, taking into account all the mentioned conditions, the calibration process was carried out according to the following procedure:

The left and right output readings were recorded before applying any force on the load beam. A small external force was applied by using the vertical spring. To achieve this, the upper end of the spring was extended in the upward direction and attached to the smooth rod. As the steady state was reached, the signal conditioner output was recorded and the spring elongation was worked out. Therefore, knowing the calibration of the spring, the applied lift force was determined which could be utilized, together with

the derived absolute values of the amplified output, to determine the value of S in Eq. (6.51). This procedure was carried out by increasing the applied lift force gradually in steps up to 1(N) then decreased gradually in steps, and in each step the amplified output readings were obtained, before and after applying the external force, and the spring elongation was measured.

Using the least square error technique, the variation of the applied static force with the total signal conditioner output was evaluated and the calibration equation was found expressed as

$$F = 0.00042 + 0.00623\ (\varepsilon_A + \varepsilon_B) \qquad (6.52)$$

This equation was obtained with correlation coefficient of 0.9997 and plotted in Fig. (6.21).

6.5.3.2 Drag force

To establish the relationship between the applied drag force and the corresponding amplified output readings, the calibration procedure utilized previously was applied with the following variation:

- The two springs were used simultaneously to apply instantaneous static lift and drag forces.
- The vertical spring was utilized to apply a constant force which gradually increased from zero to 1(N) with an increment 0.1(N) in each step.
- For each applied lift force in increments, the magnitude of the amplified voltage difference between left and right readings was carried out for all possible value of drag force up to about 0.4(N).
- For each increment the formula developed in Section (6.4.1) was used namely:

$$M = C(\varepsilon_A - \varepsilon_B) \qquad (6.53)$$

The results obtained from this calibration proved that C had no constant value because the relationship between the applied moment and the displayed output difference was found, as discussed before to be a curved relationship as shown in Fig. (6.22).

Therefore, to convert the simultaneous absolute values of the amplified left and right output ε_A and ε_B, respectively into corresponding lift and drag forces, the following procedure should be carried out:

1) Determine the two conjugate values $(\varepsilon_A + \varepsilon_B)$ and $(\varepsilon_A - \varepsilon_B)$.
2) Applying Eq. (6.52) the applied lift force can be obtained.
3) Using the $(\varepsilon_A - \varepsilon_B)$ value and the determined value of lift force, the corresponding value of the drag force can be interpolated.

To establish a relationship between the signal conditioner output and the computer output, the measuring system was connected as shown in Fig. (6.16); then a combination of forces on the load beam was applied, the outputs were recorded and the relationship was found to be expressed as:

$$Y = -16.981 + 0.875X \qquad (6.54)$$

in which

Y is the computer output;
and X is the amplified signal conditioner output.

Eq. (6.54) was obtained with correlation coefficient 0.99994 and plotted as shown in Fig. (6.23).

6.6 THE MEASURING TECHNIQUE

Many attempts were tried during the course of the measurements to establish the best technique for the acquisition of the data needed. A suitable technique was developed which can be summarized as follows:

- The flow rate was arbitrarily adjusted and the discharge measured at the thin plate weir.

- Using the tail gate, the flow could be adjusted to obtain uniform flow. Then using the cathetometer, flow uniformity was checked and the flow depth established.

- Applying Eq. (6.28) the depth of the maximum shear stress could be calculated.

- Using the point gauge, the movable roughened board was adjusted and fixed firmly on the embedded cavity as shown in Plate (6.7). This was done in such a way as to position the instrumented particle at its specified level which was calculated previously.

- The space between the channel bed and the roughened board was filled with suitable roughened slices shown in Plate (6.6).

- In order to obtain accurate measurements, the time interval between setting the zero datum of the signal conditioner and the data acquisition, should be kept to a minimum. To achieve this condition, a wooden construction shown in Plate (6.14) was designed and manufactured by the Author to cover the roughened board during zero setting to keep this portion as a dead flow zone.

- The zero datum was obtained by the computer as the average of 1000 readings for both left and right load cells separately; they were fed into the main computer programme then the wooden construction was removed and within 5 to 10 seconds, the measuring course was started by the computer to record the acquired data.

TABLE 6-1: RESULTS OBTAIBED FROM THE

SHEAR MEASUREMENTS

RUN NO	FLOW RATE Q (m3/s)	FLOW DEPTH d (m)	DEPTH* OF MAX. WALL SHEAR y (m)	RATIO (y/d)
1	0.0726	0.113	0.040	0.353
2	0.0962	0.134	0.042	0.314
3	0.1073	0.142	0.043	0.302
4	0.1271	0.156	0.050	0.320
5	0.1360	0.162	0.052	0.321
6	0.1501	0.172	0.053	0.309
7	0.1570	0.176	0.051	0.290
8	0.1691	0.184	0.055	0.299

* DEPTH IS VERTICAL HEIGHT ABOVE BED.

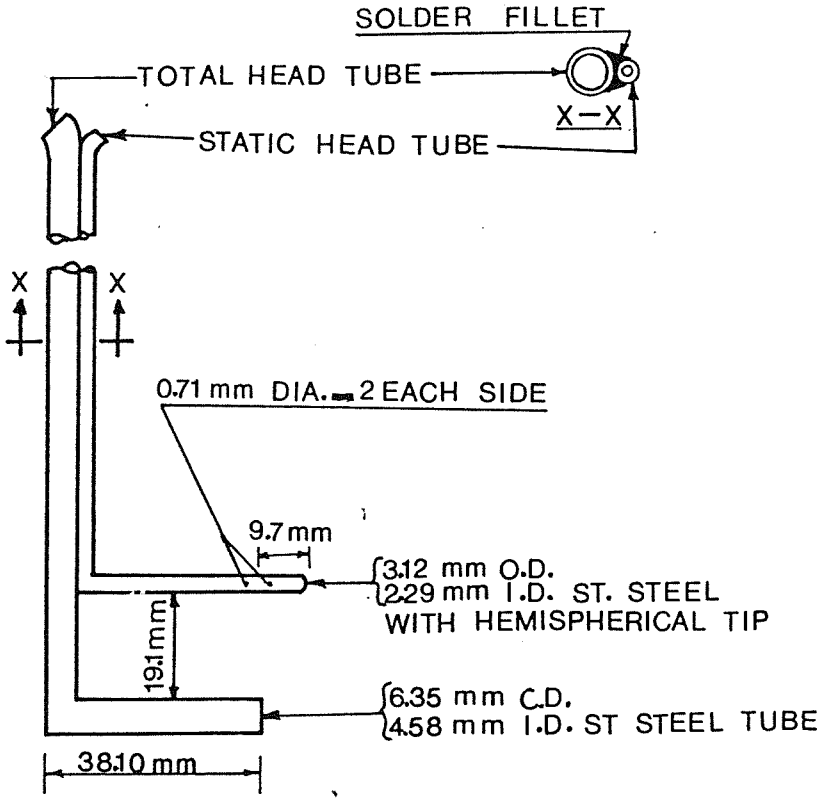

FIG.6-1: THE PRESTON TUBE

(IPPEN 1960)

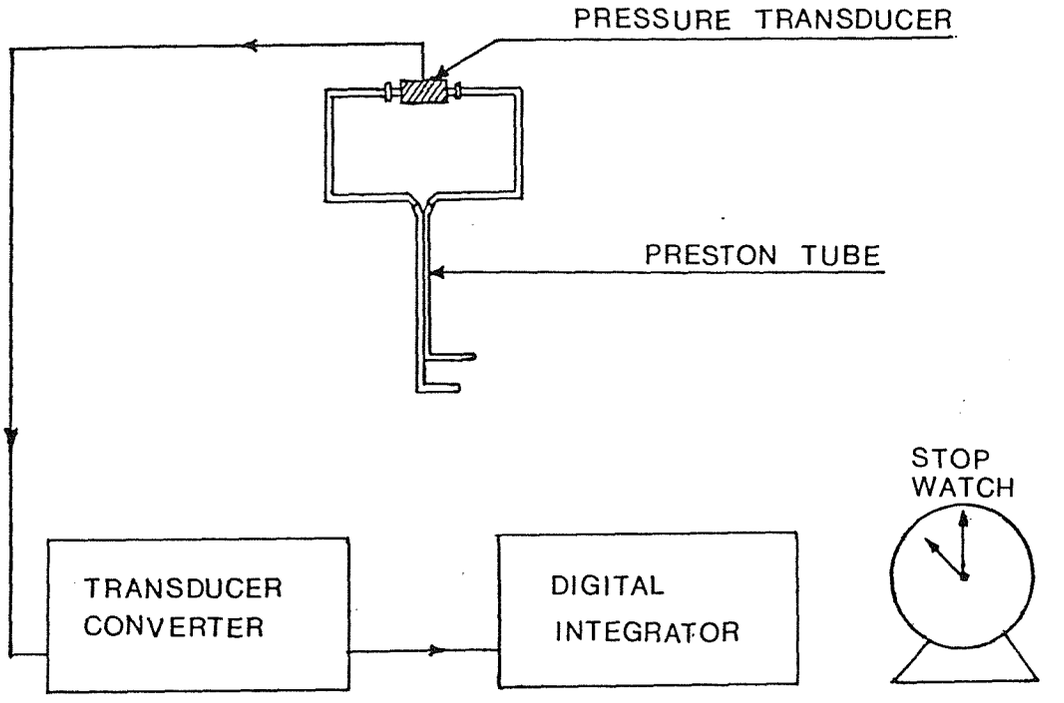

FIG.6-2 : SHEAR STRESS MEASUREMENT SET-UP

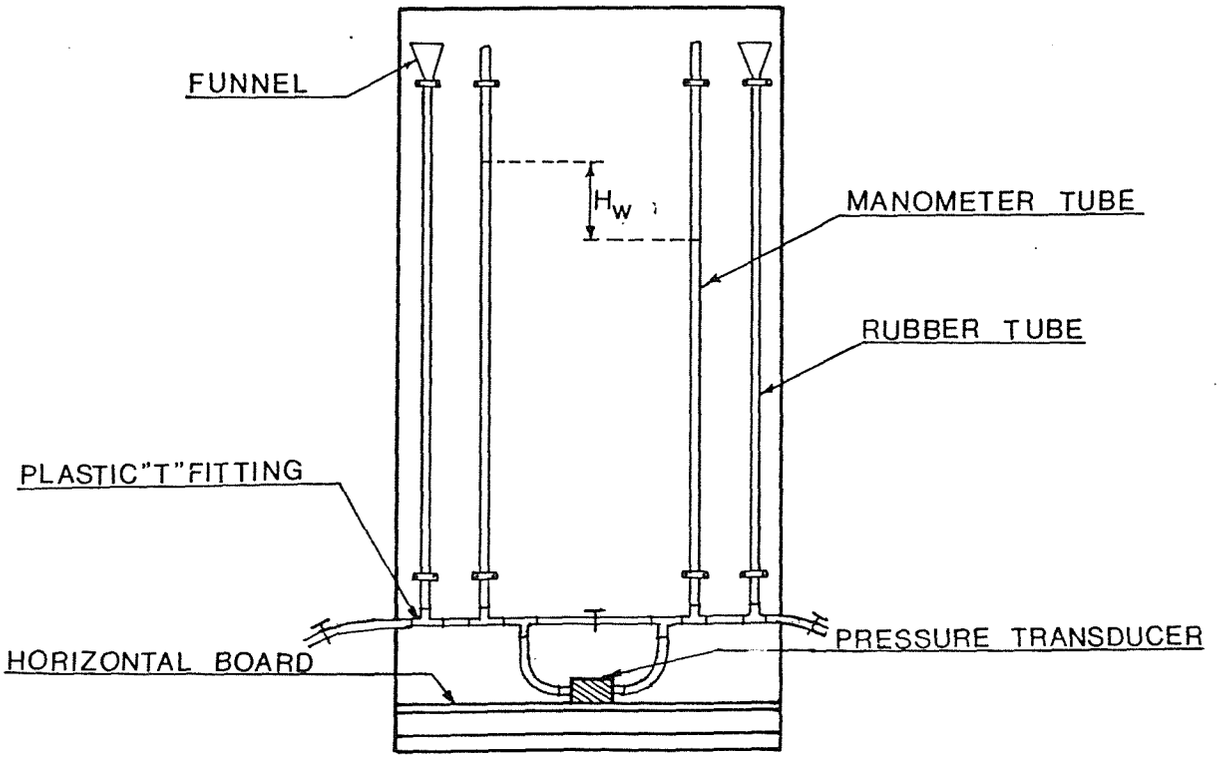

FIG.6-3:PRESSURE TRANSDUCER CALIBRATION BOARD

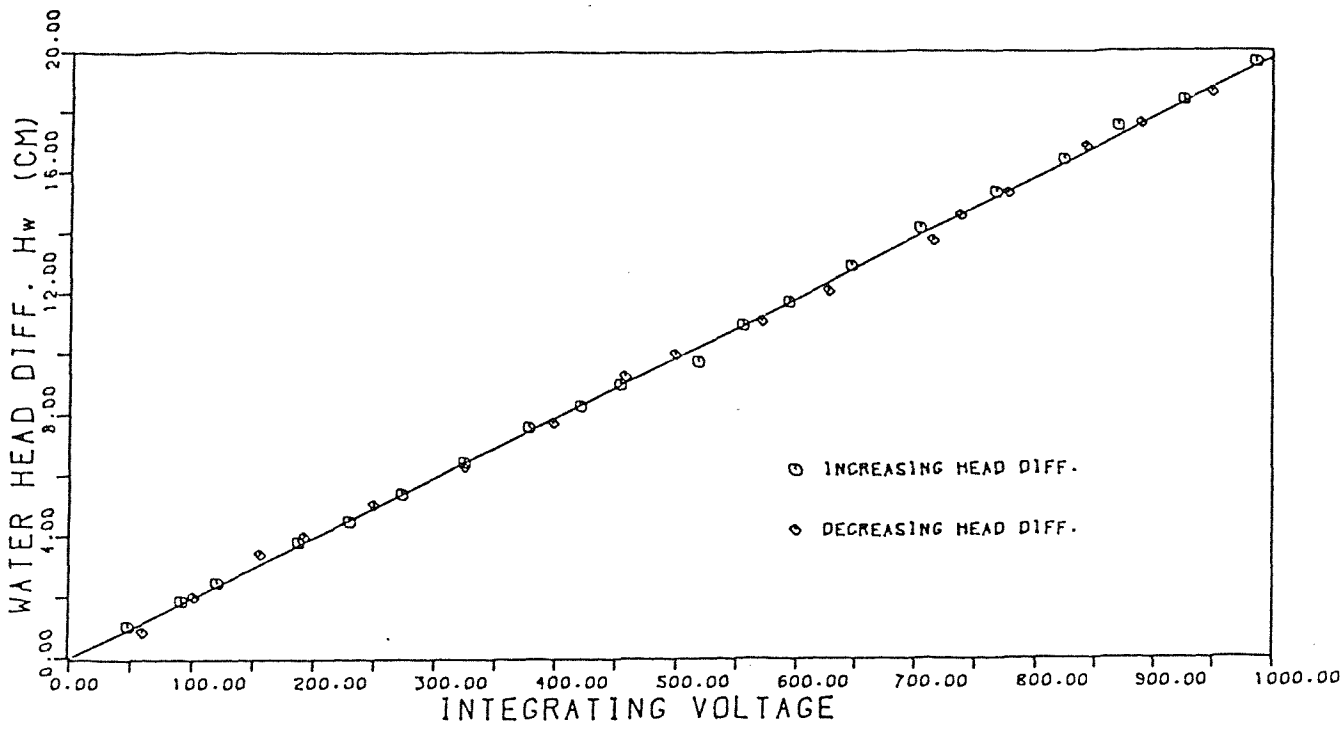

FIG.6-4 : PRESSURE TRANSDUCER CALIBRATION CURVE FOR MAX. DIFFERENCE HEAD OF 20 CMS

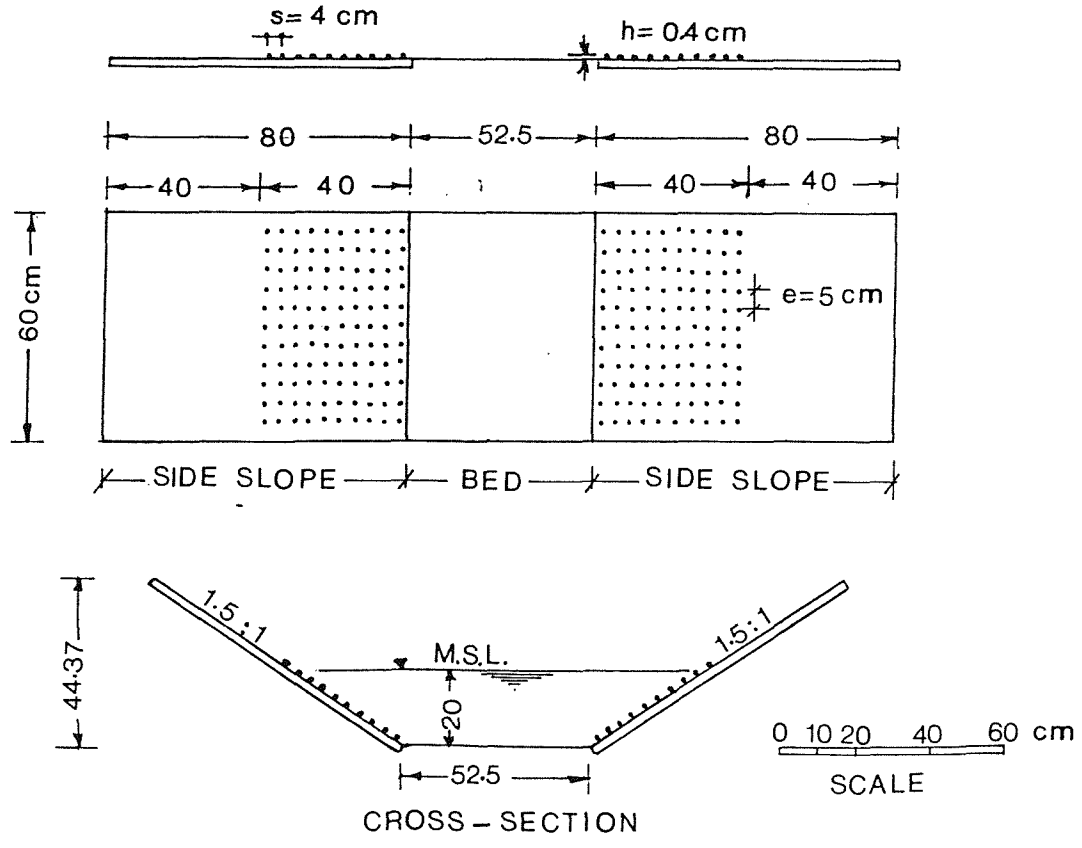

FIG.6-5: ROUGHNESS PATTERN USED IN THE TESTS

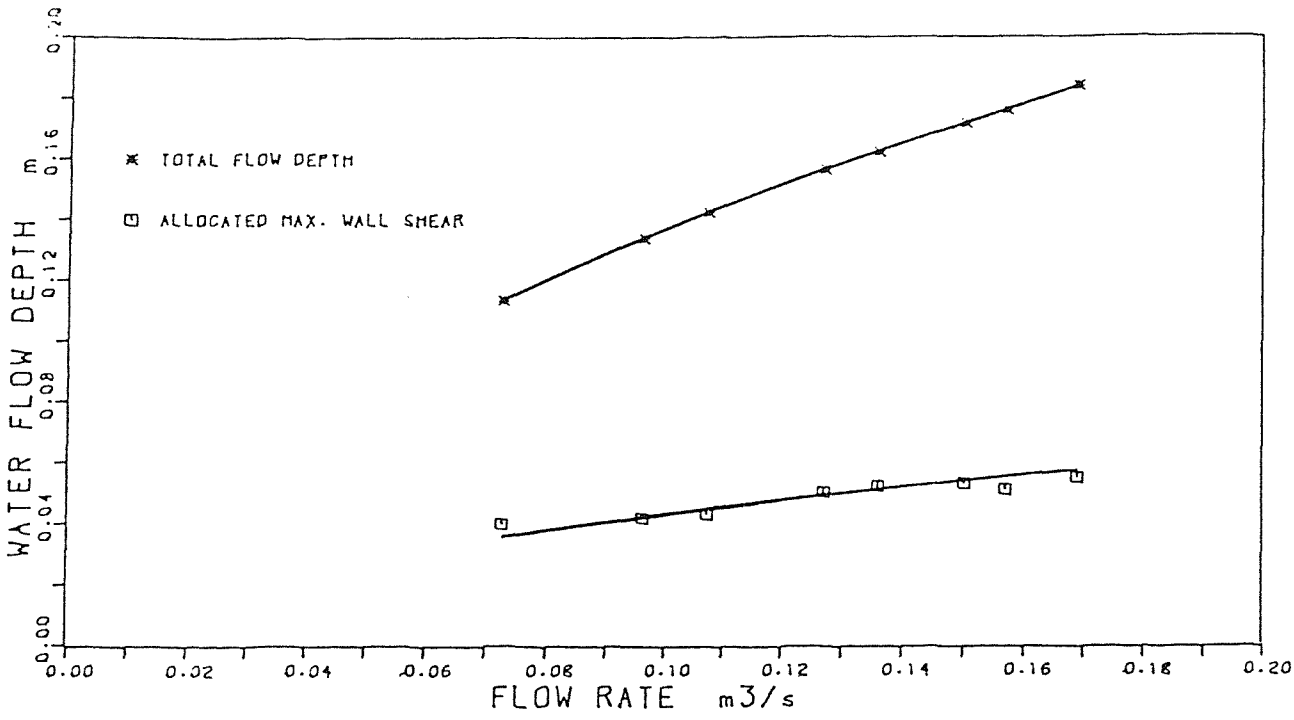

FIG. 6-6: VARIATION OF THE MAX. WALL SHEAR DEPTH FOR DIFFERENT FLOW RATES

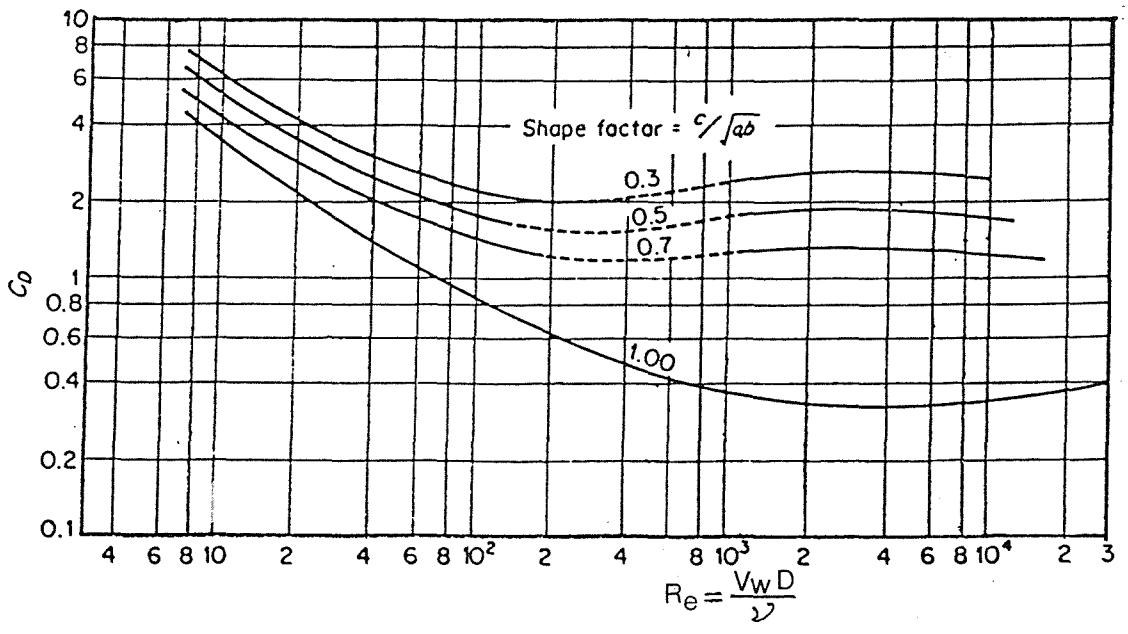

Fig. 6–7 : Drag coefficient vs. Reynolds number for different shape factors.

[*After* ALBERTSON (*1953*).]

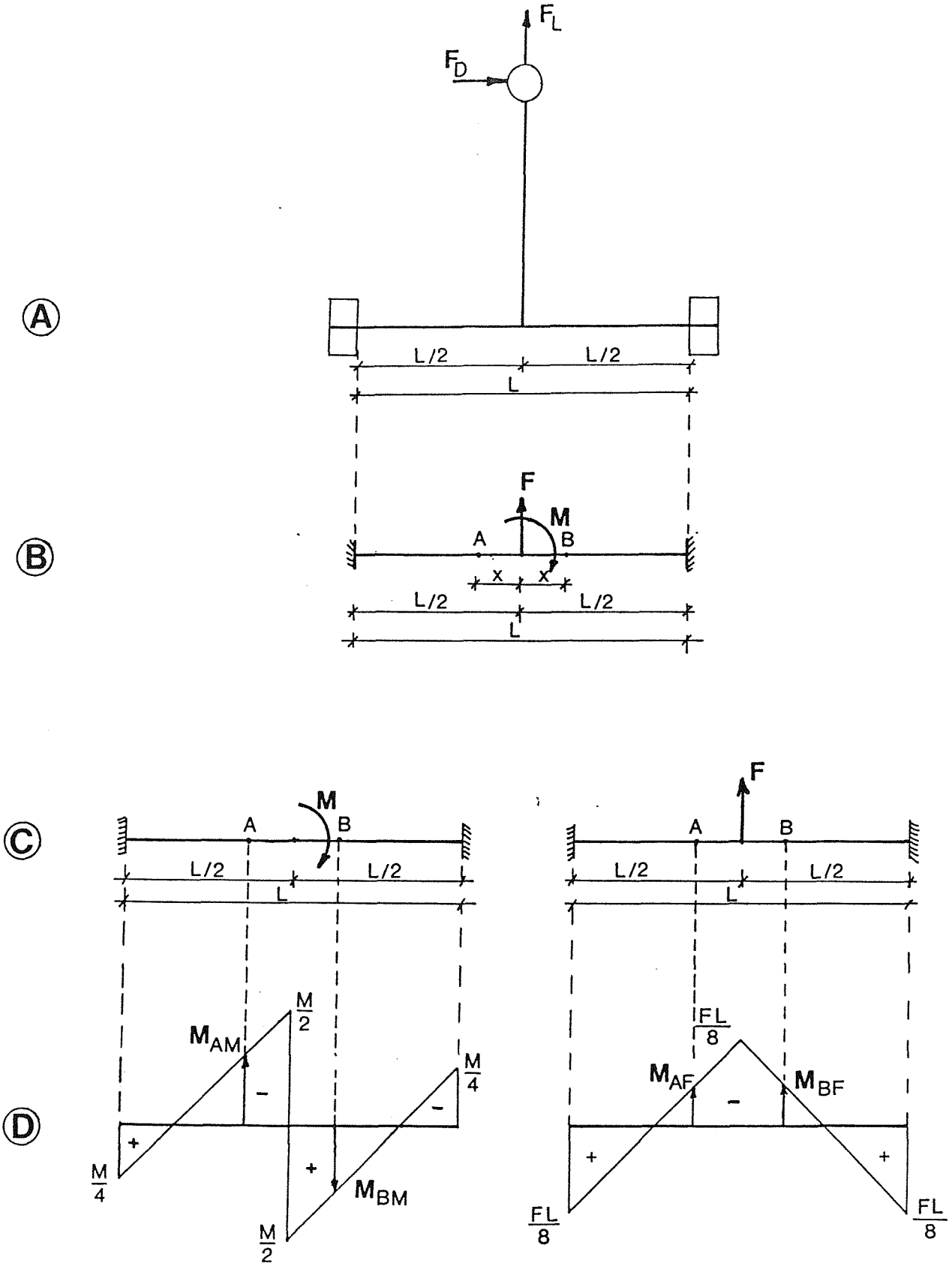

FIG. 6-8: B.M. DISTRIBUTIONS OF THE LOAD BEAM

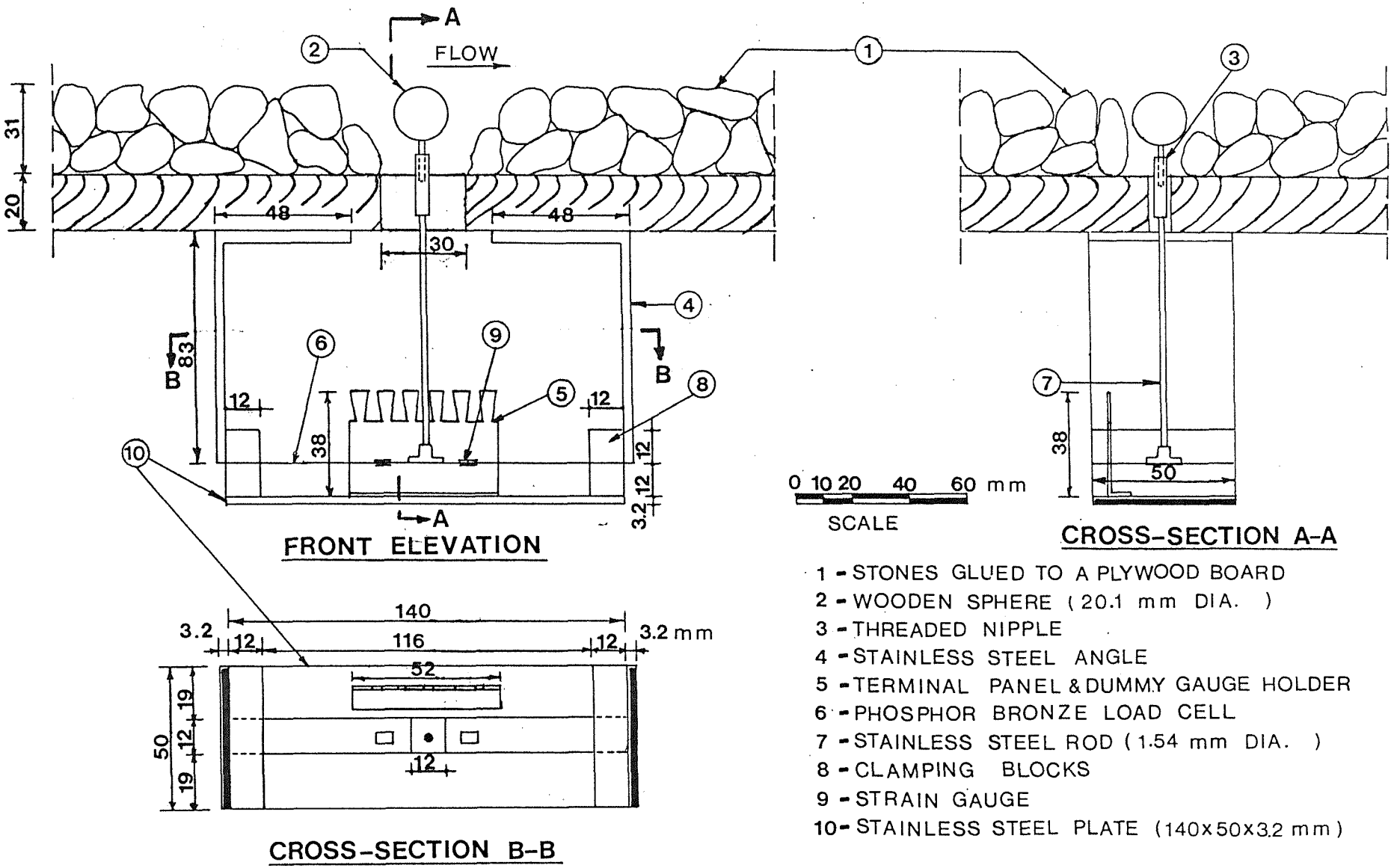

FIG. 6-9 : DETAILS OF THE LOAD BEAM ASSEMBLY

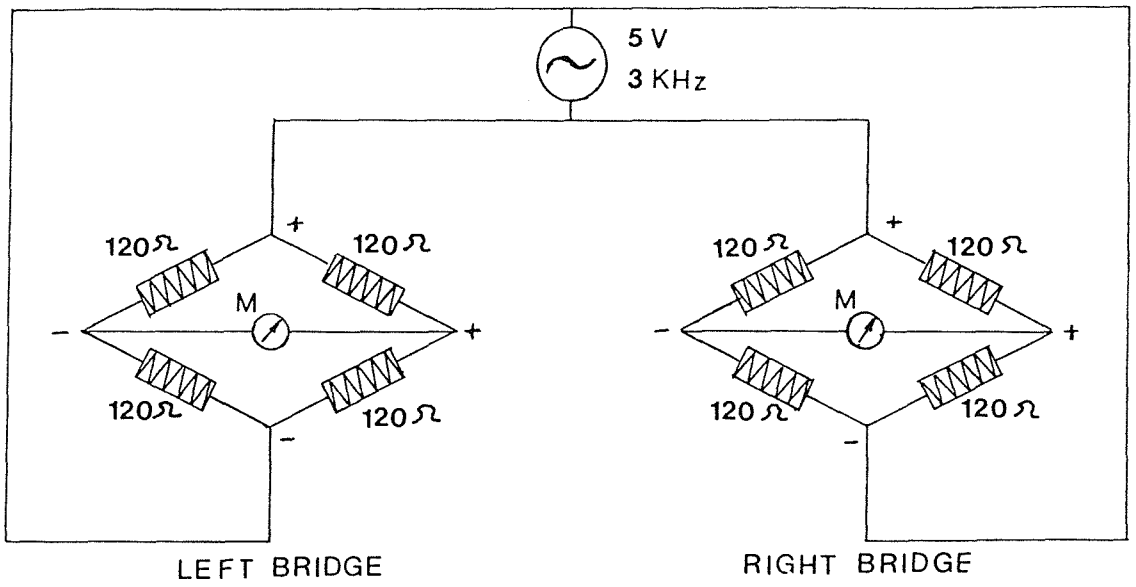

FIG.6-10:CIRCUIT DIAGRAM OF THE LOAD CELL

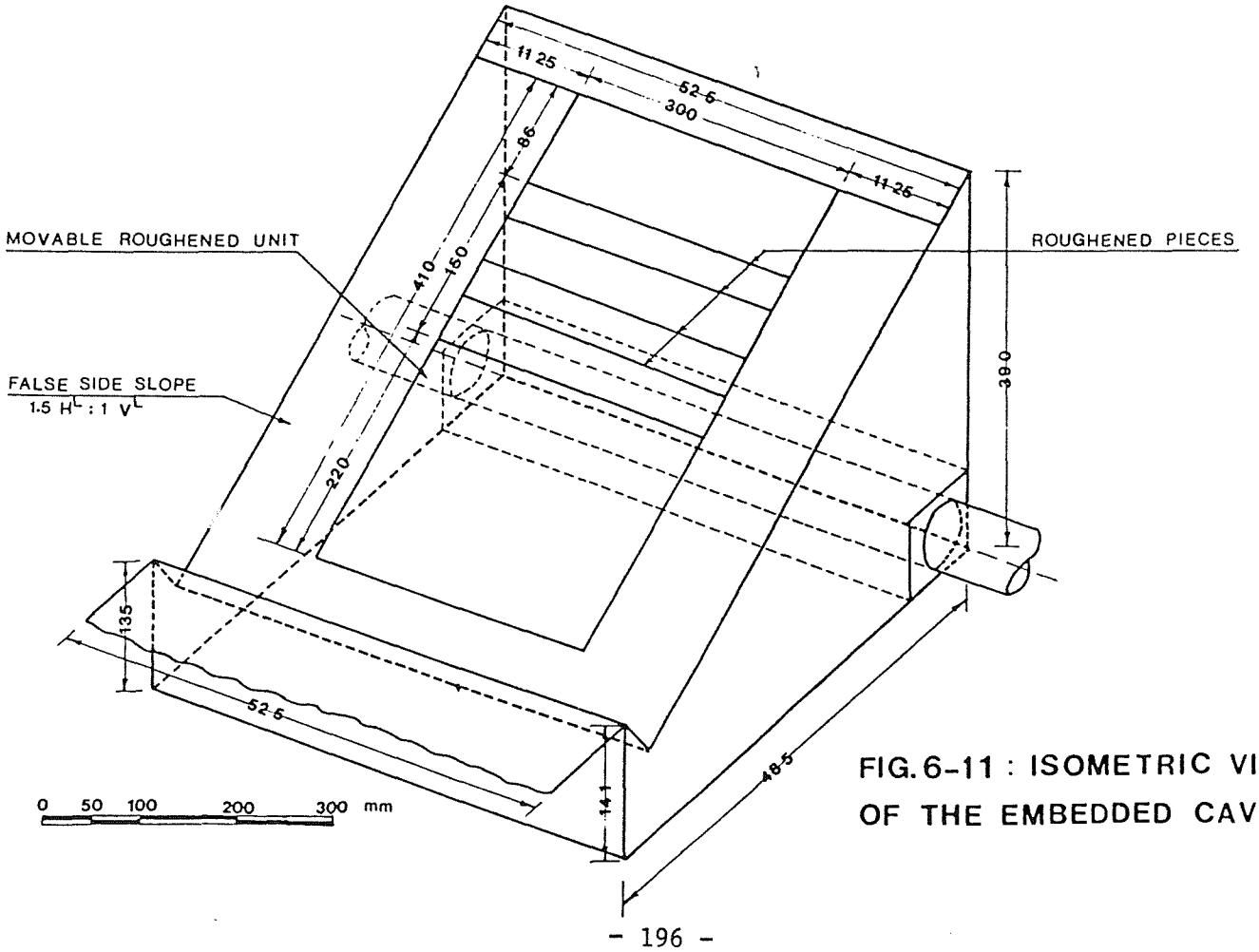

FIG. 6-11 : ISOMETRIC VIEW OF THE EMBEDDED CAVITY

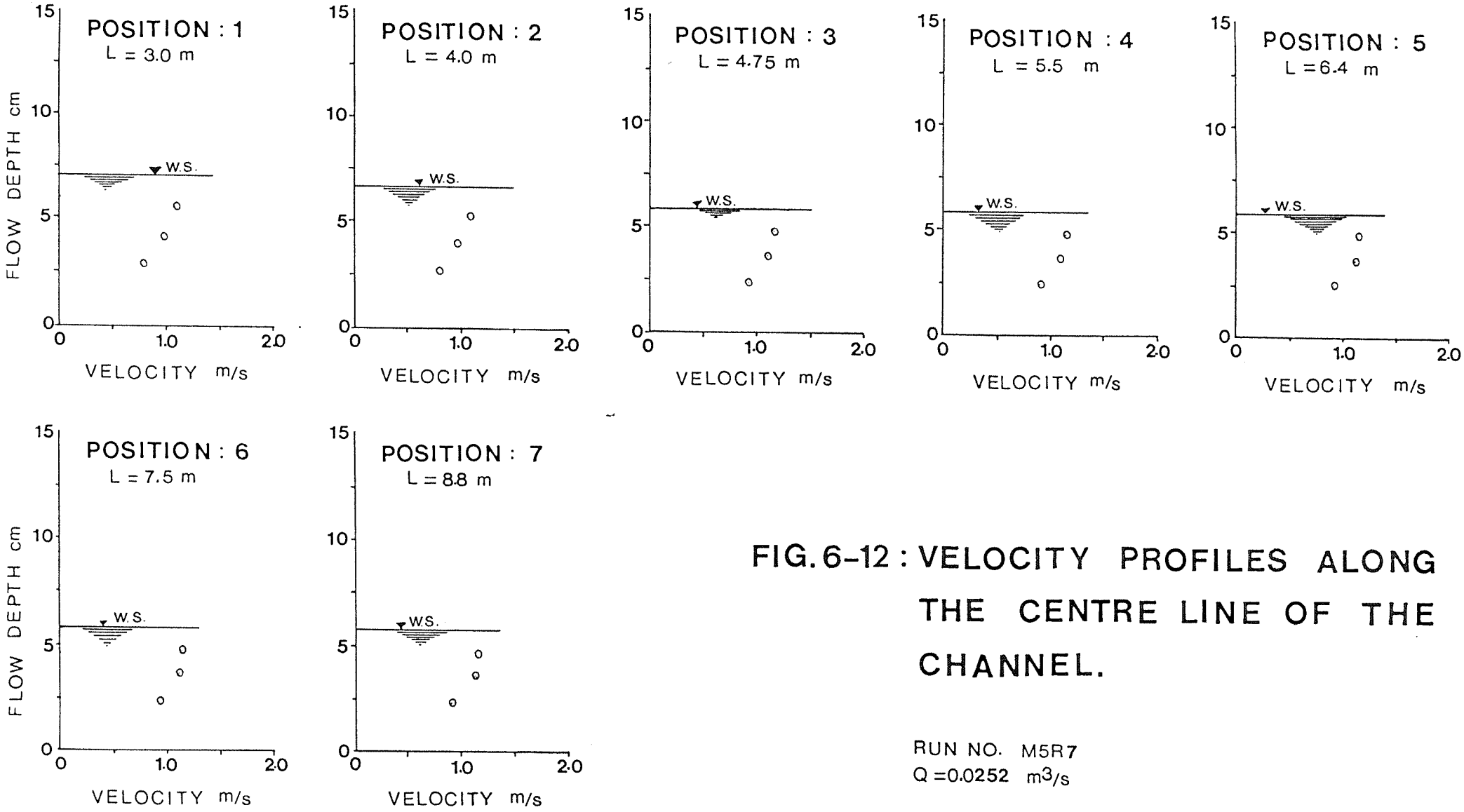

FIG. 6-12 : VELOCITY PROFILES ALONG THE CENTRE LINE OF THE CHANNEL.

RUN NO. M5R7
Q = 0.0252 m^3/s

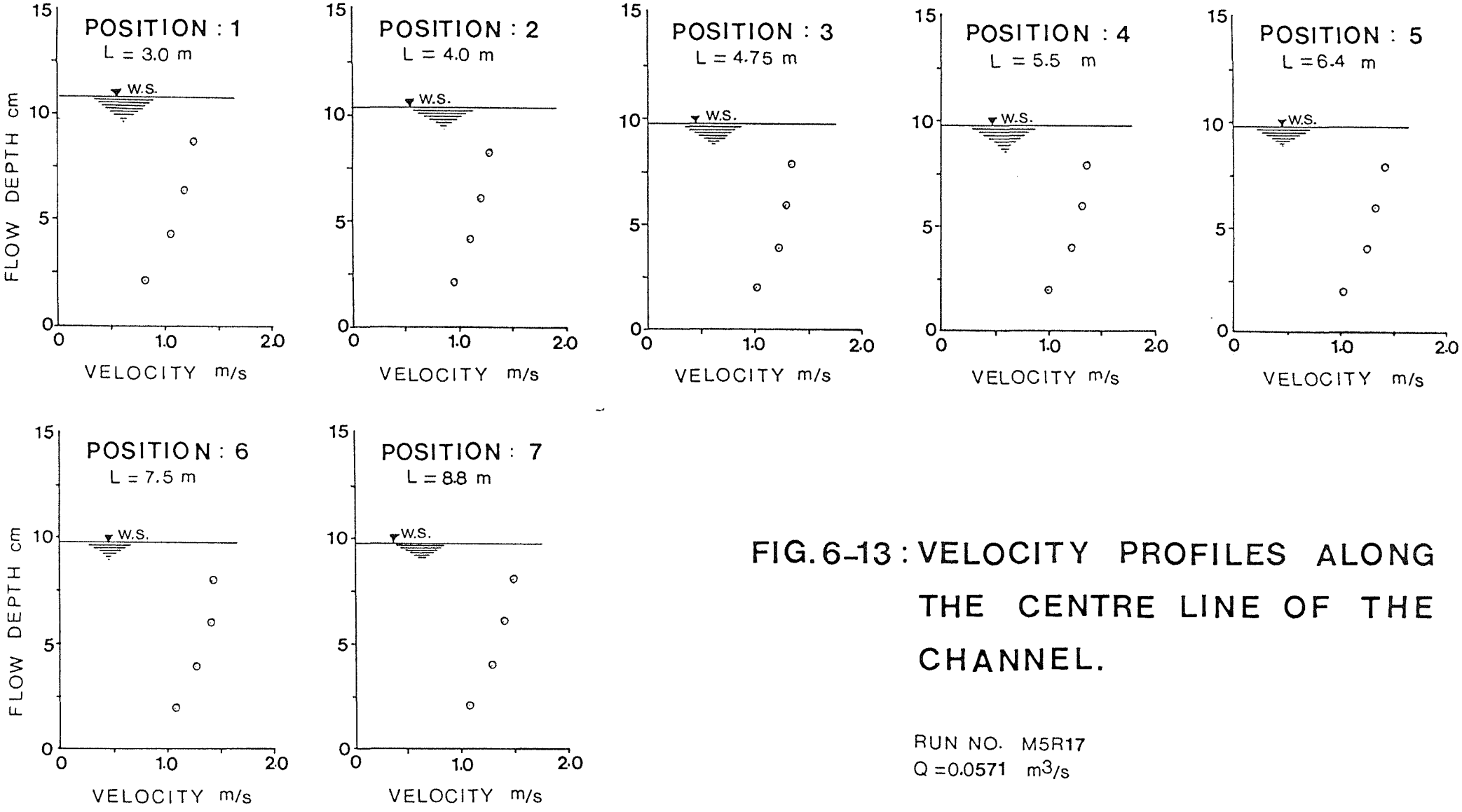

FIG. 6-13 : VELOCITY PROFILES ALONG THE CENTRE LINE OF THE CHANNEL.

RUN NO. M5R17
Q = 0.0571 m^3/s

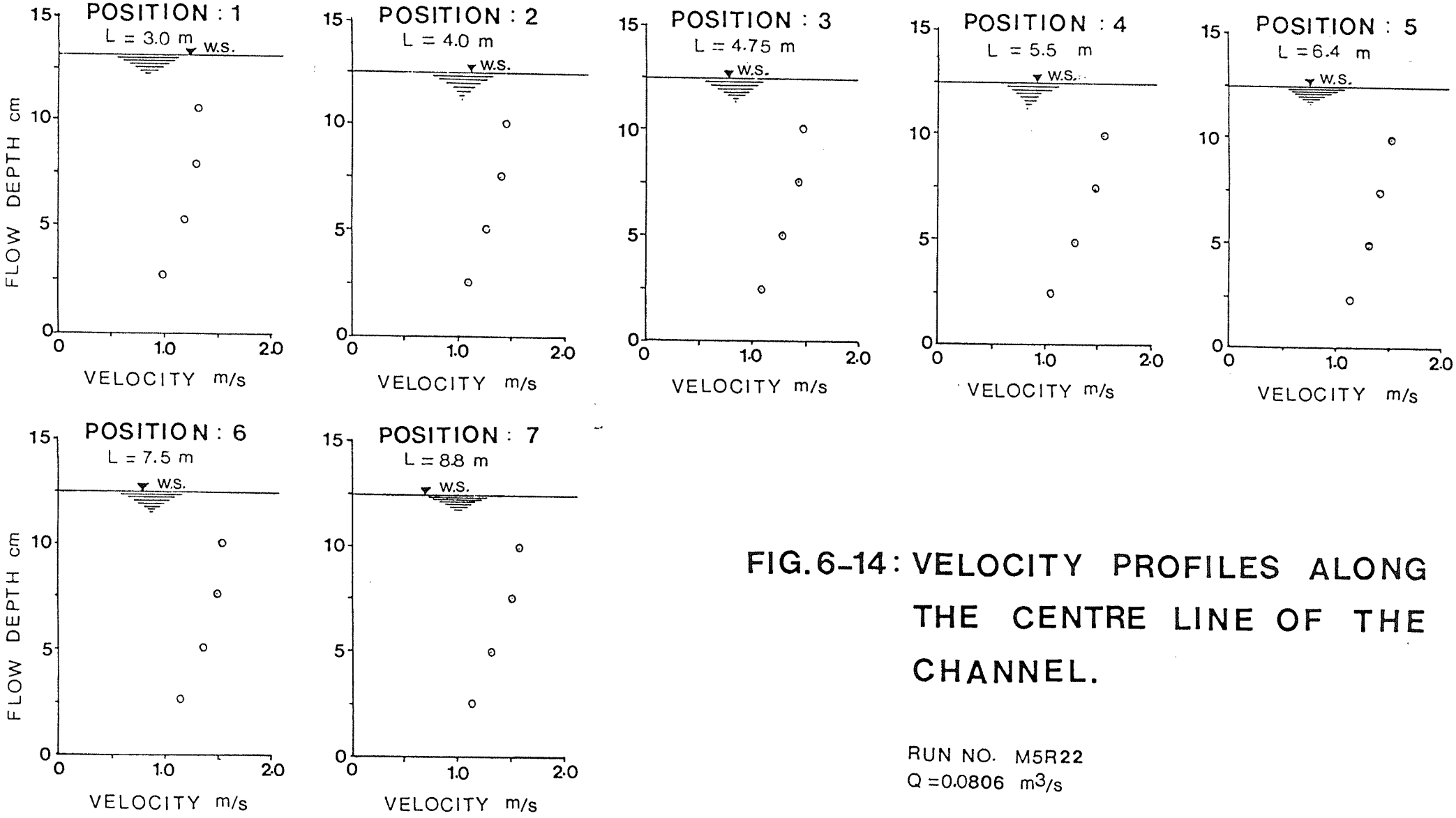

FIG. 6-14: VELOCITY PROFILES ALONG THE CENTRE LINE OF THE CHANNEL.

RUN NO. M5R22
Q = 0.0806 m^3/s

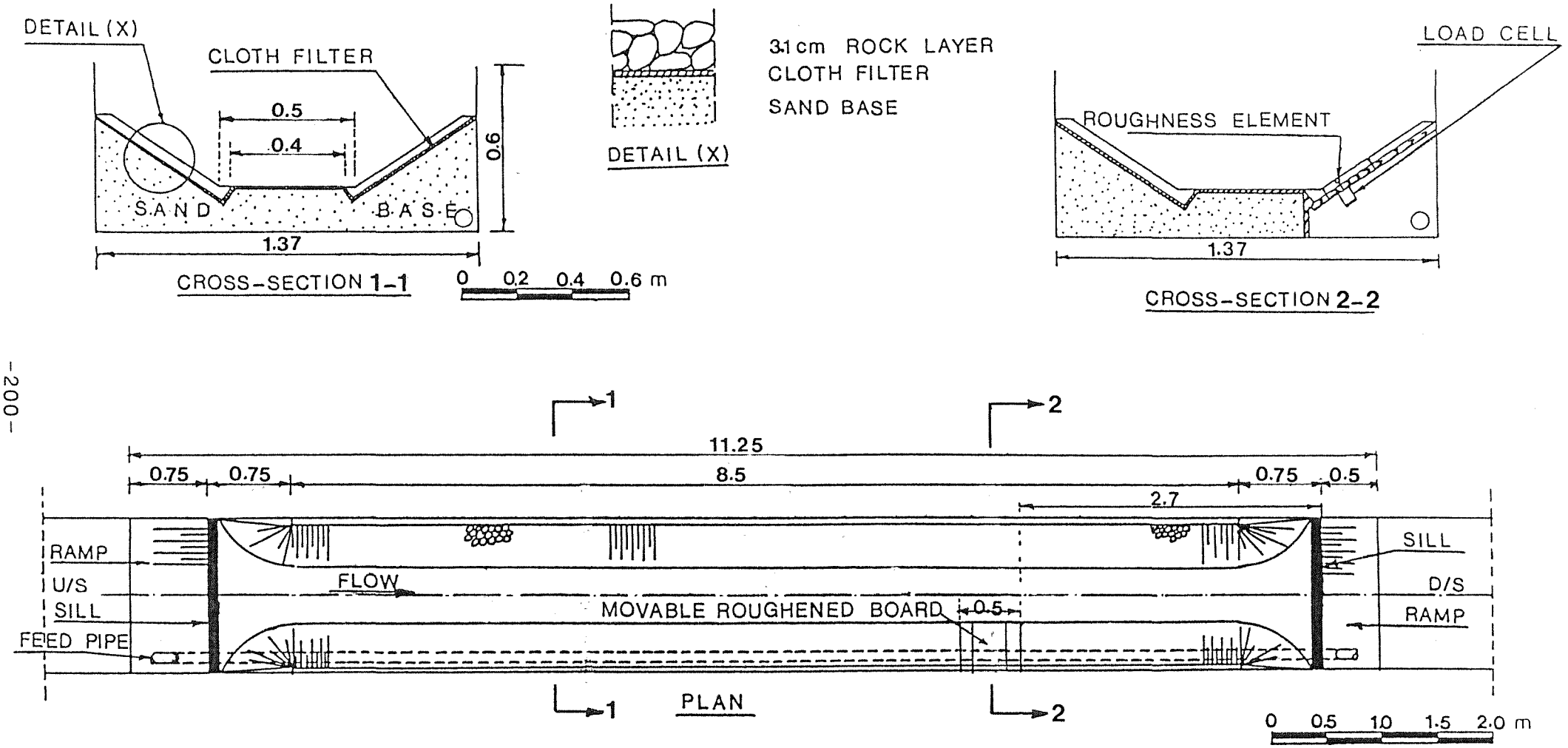

FIG. 6-15: MODEL ALIGNMENT DURING FORCE MEASUREMENTS

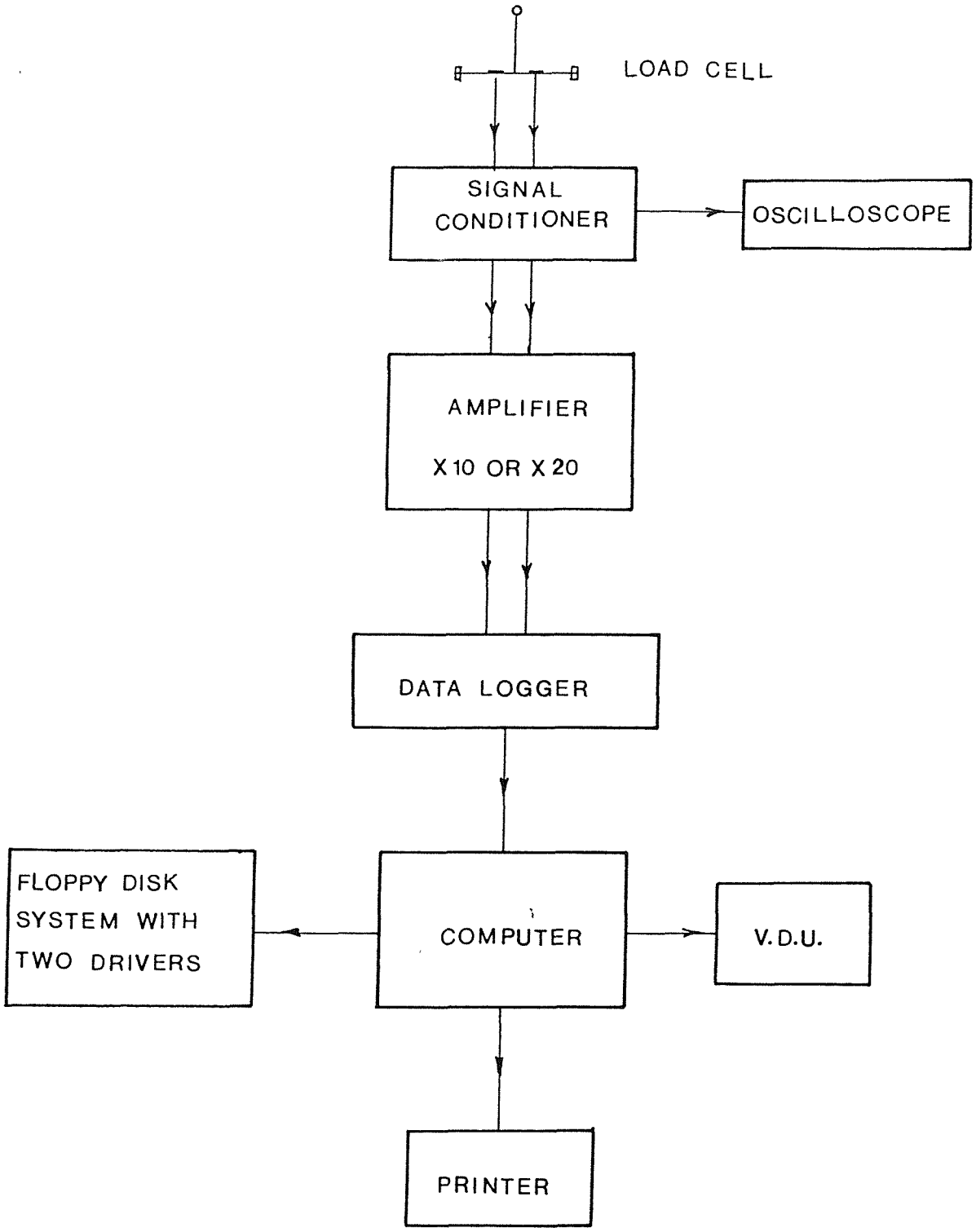

FIG.6-16: SCHEMATIC DIAGRAM OF THE DATA ACQUISITION SYSTEM

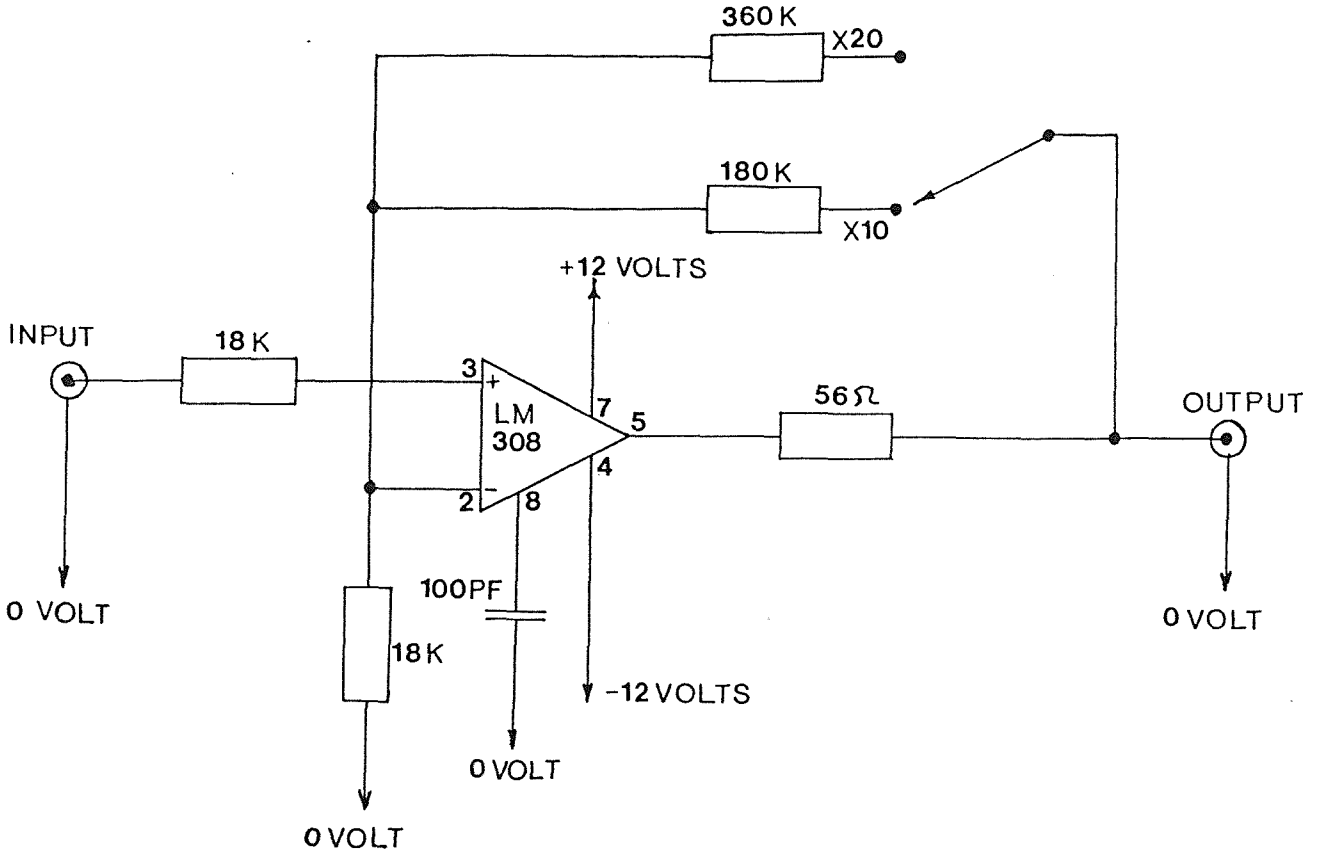

FIG.6-17:CIRCUIT DIAGRAM OF THE AMPLIFIER

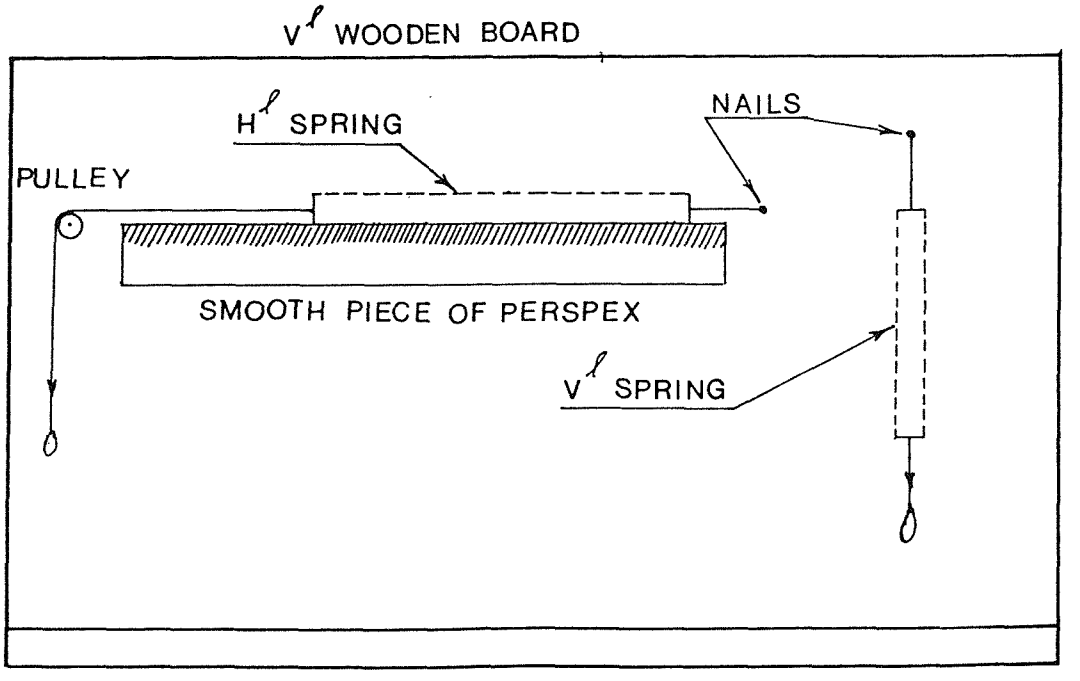

FIG.6-18: SCHEMATIC SKETCH OF THE SPRINGS CALIBRATION

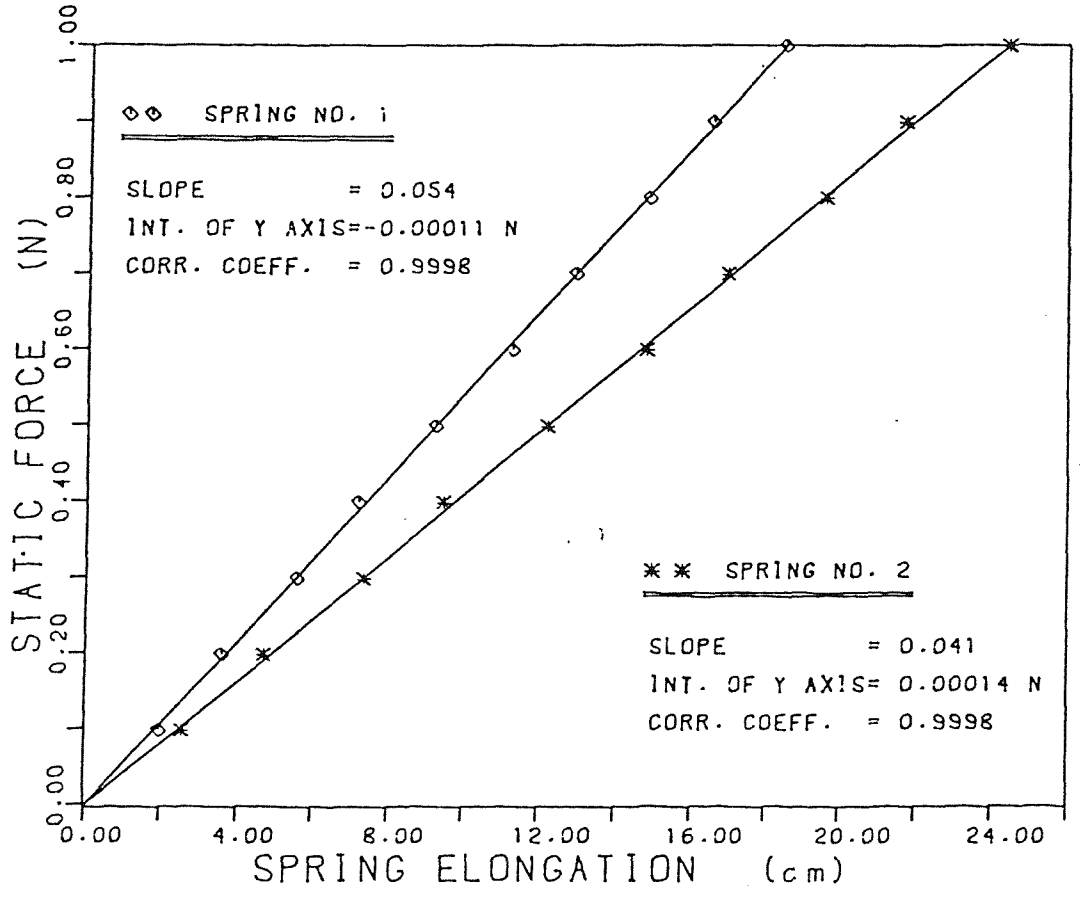

FIG. 6-19 : CALIBRATION OF THE HELICAL SPRINGS

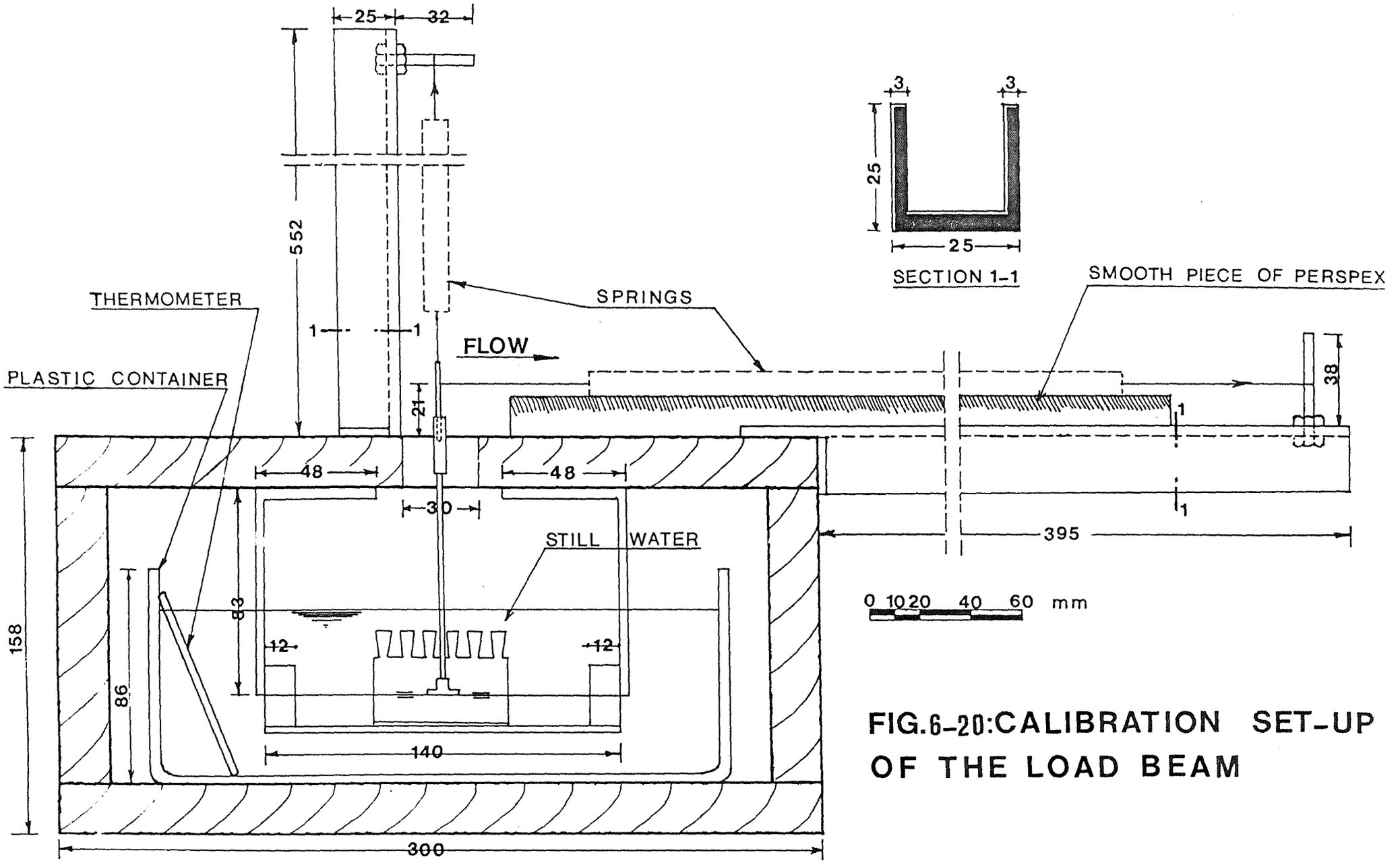

FIG.6-20:CALIBRATION SET-UP OF THE LOAD BEAM

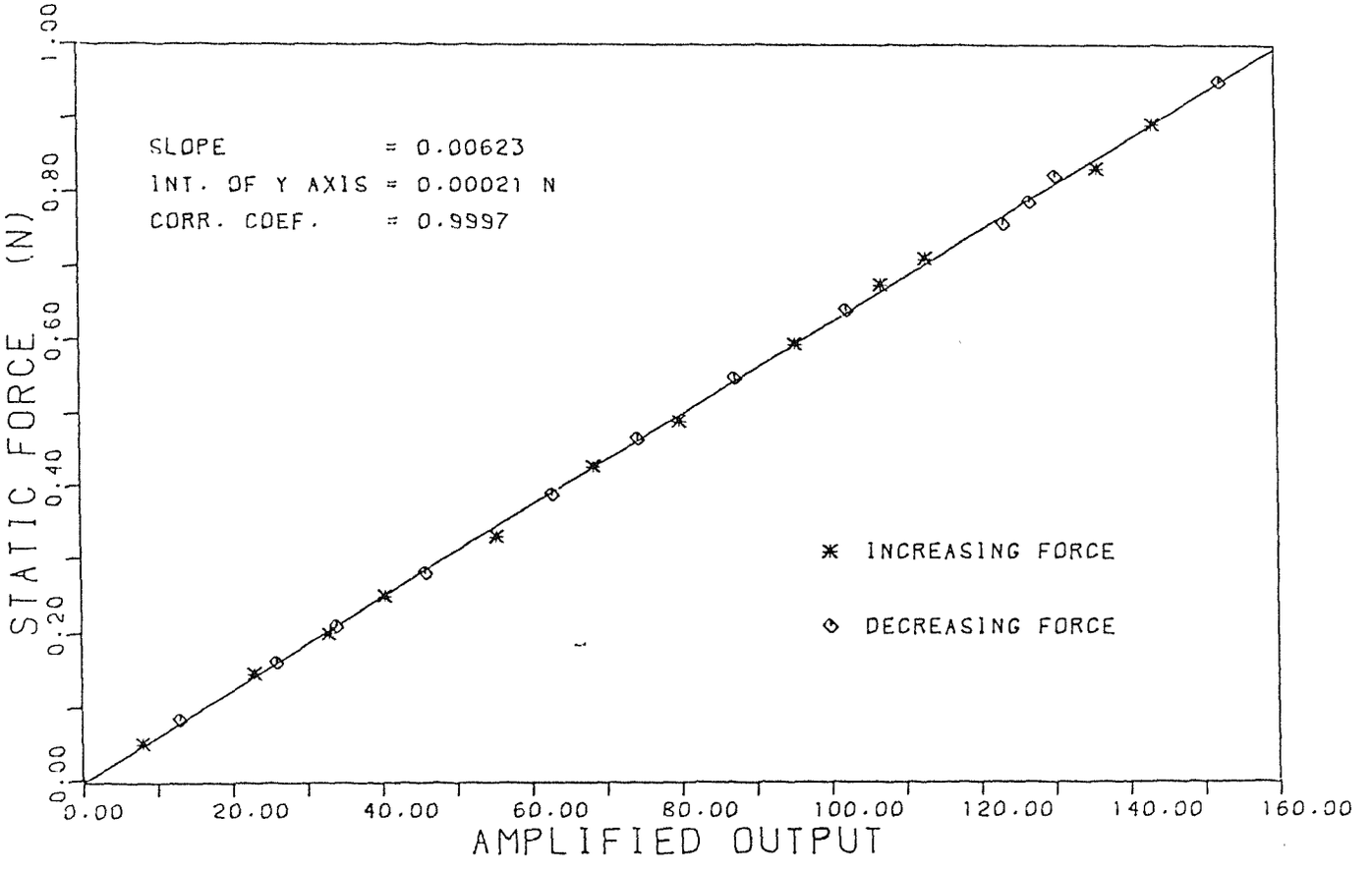

FIG.6-21:LOAD BEAM CALIBRATION CURVE WITH RESPECT TO LIFT FORCE

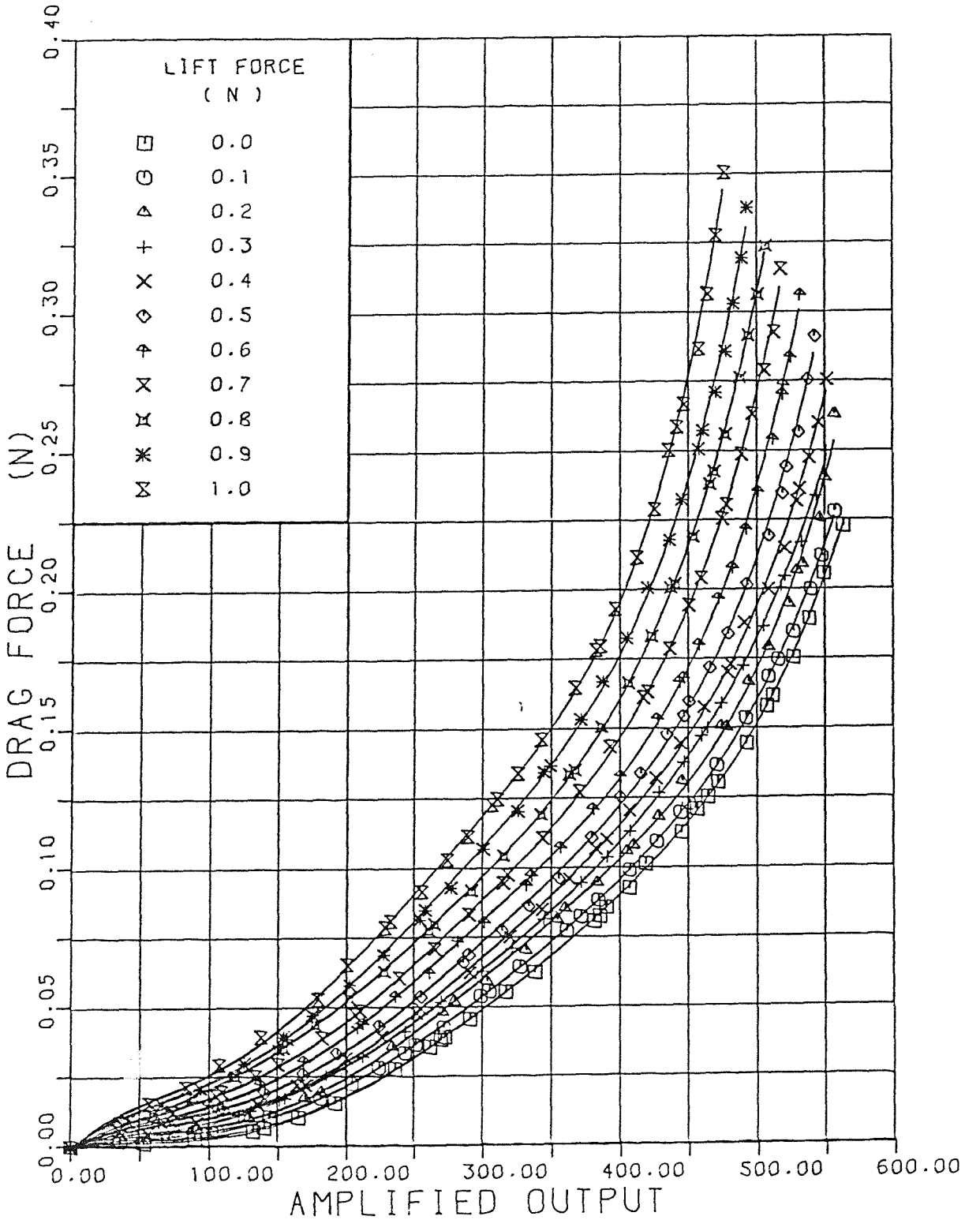

FIG.6-22:LOAD BEAM CALIBRATION CURVES

WITH RESPECT TO DRAG FORCE

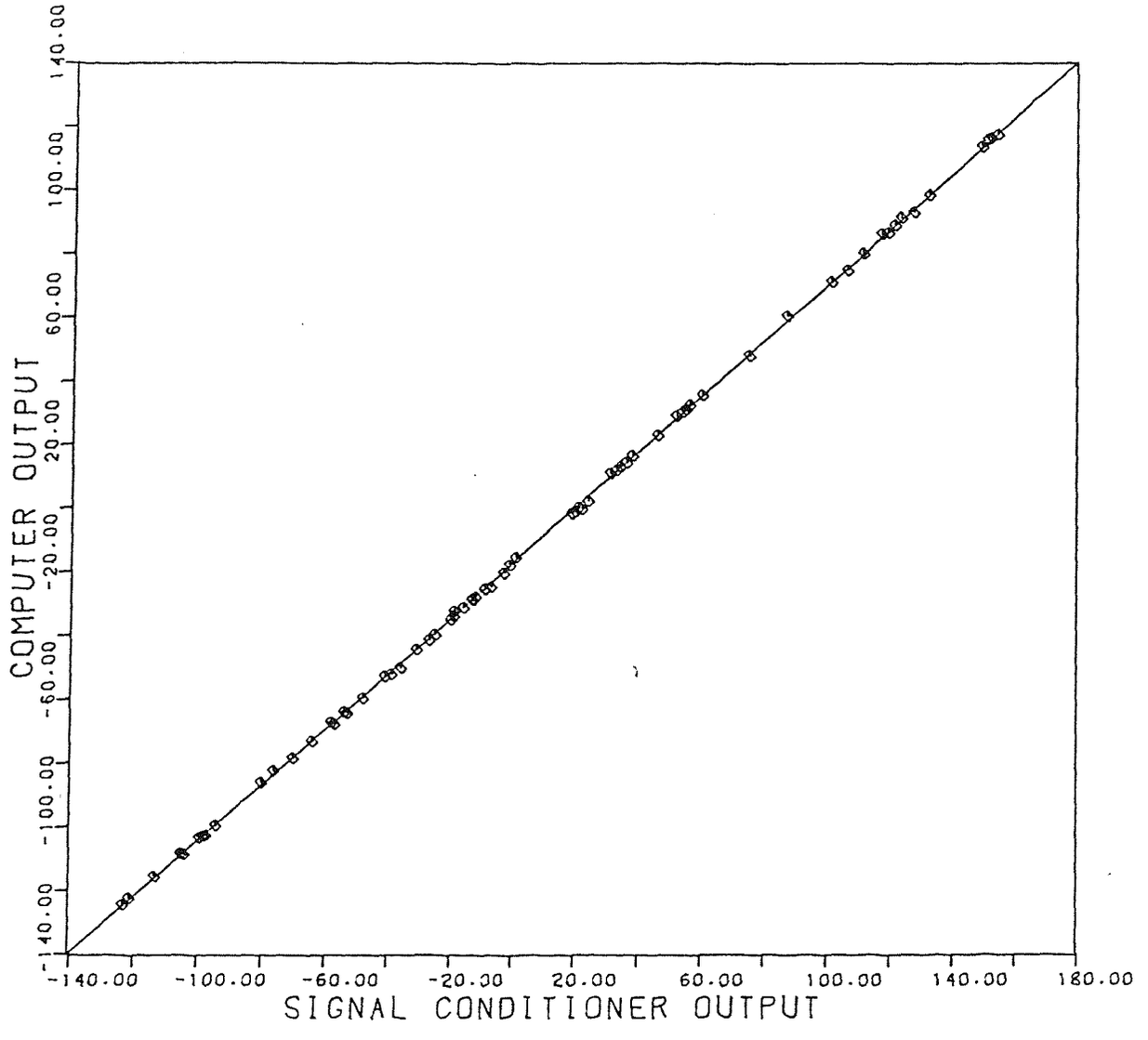

FIG.6-23:RELATIONSHIP BETWEEN SIGNAL CONDITIONER AND COMPUTER OUTPUT

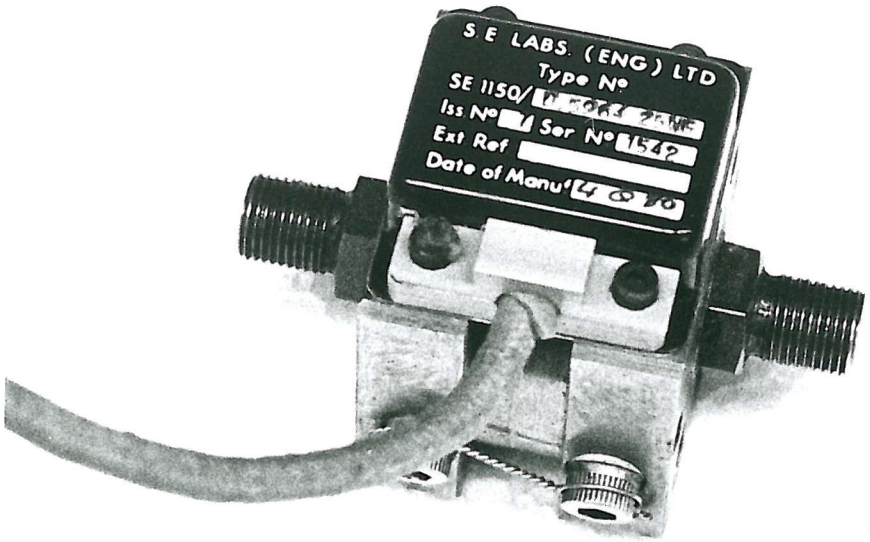

Plate (6-1) The differential pressure transducer

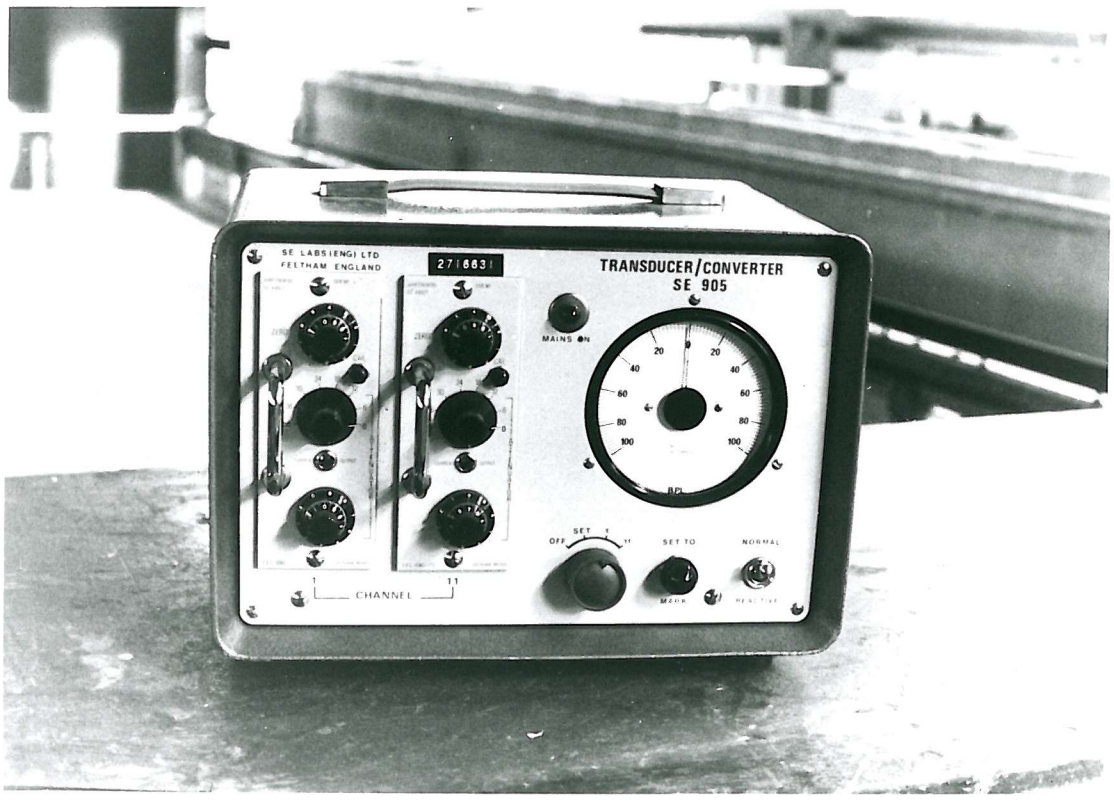

Plate (6-2) The transducer converter

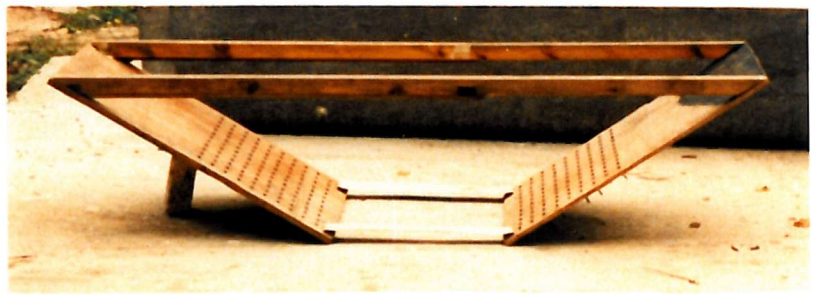

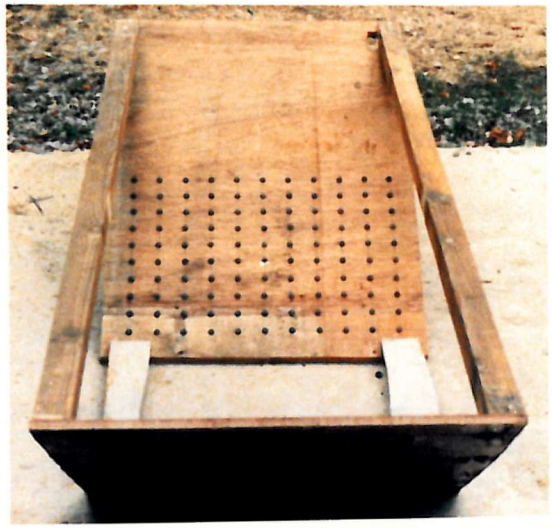

Plate (6-3) The artificially roughened walls used to locate point of maximum shear stress

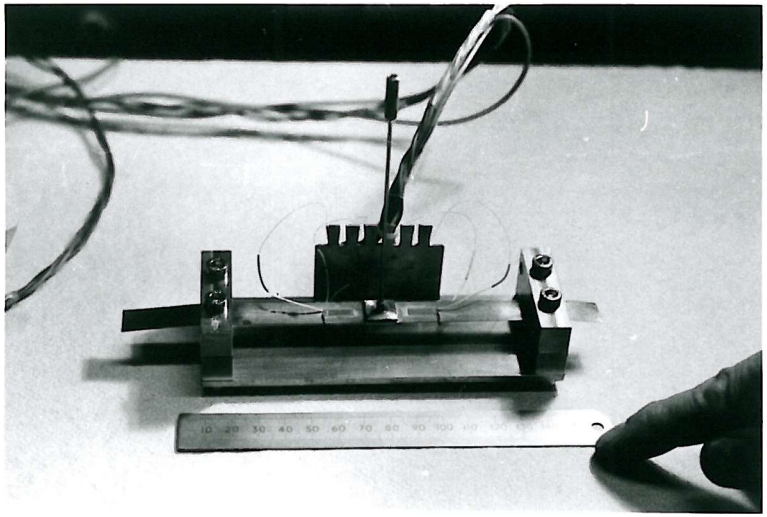

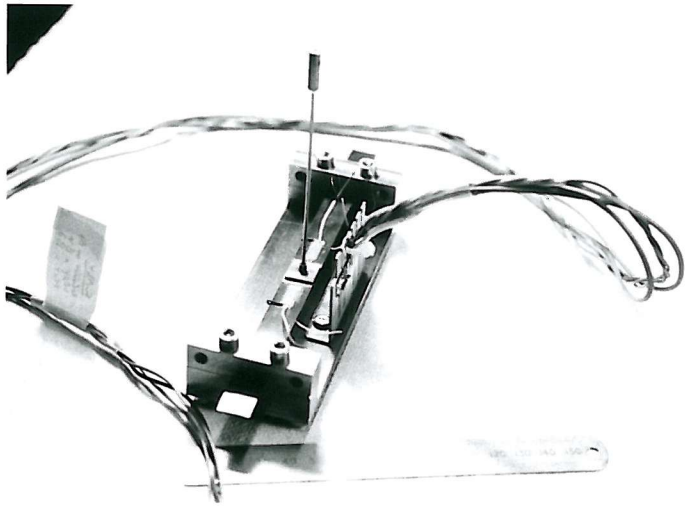

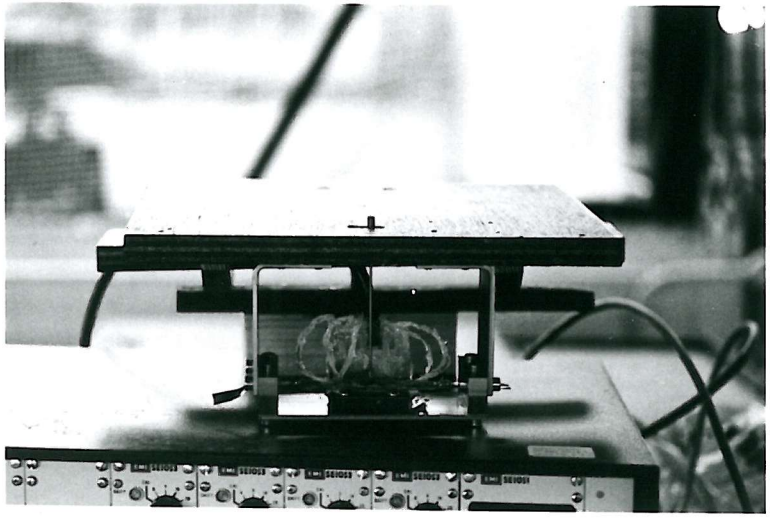

Plate (6-4) Different stages of manufacturing the load beam cell

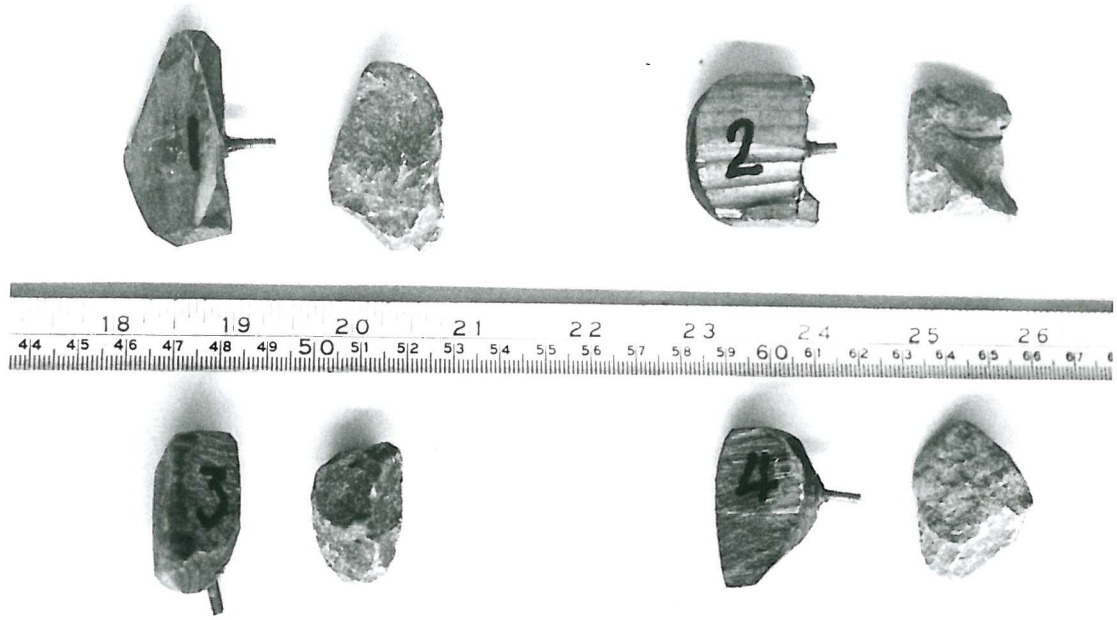

Plate (6-5) Real and simulated non-spherical particles employed for force measurements

Plate (6-6) The roughened slices

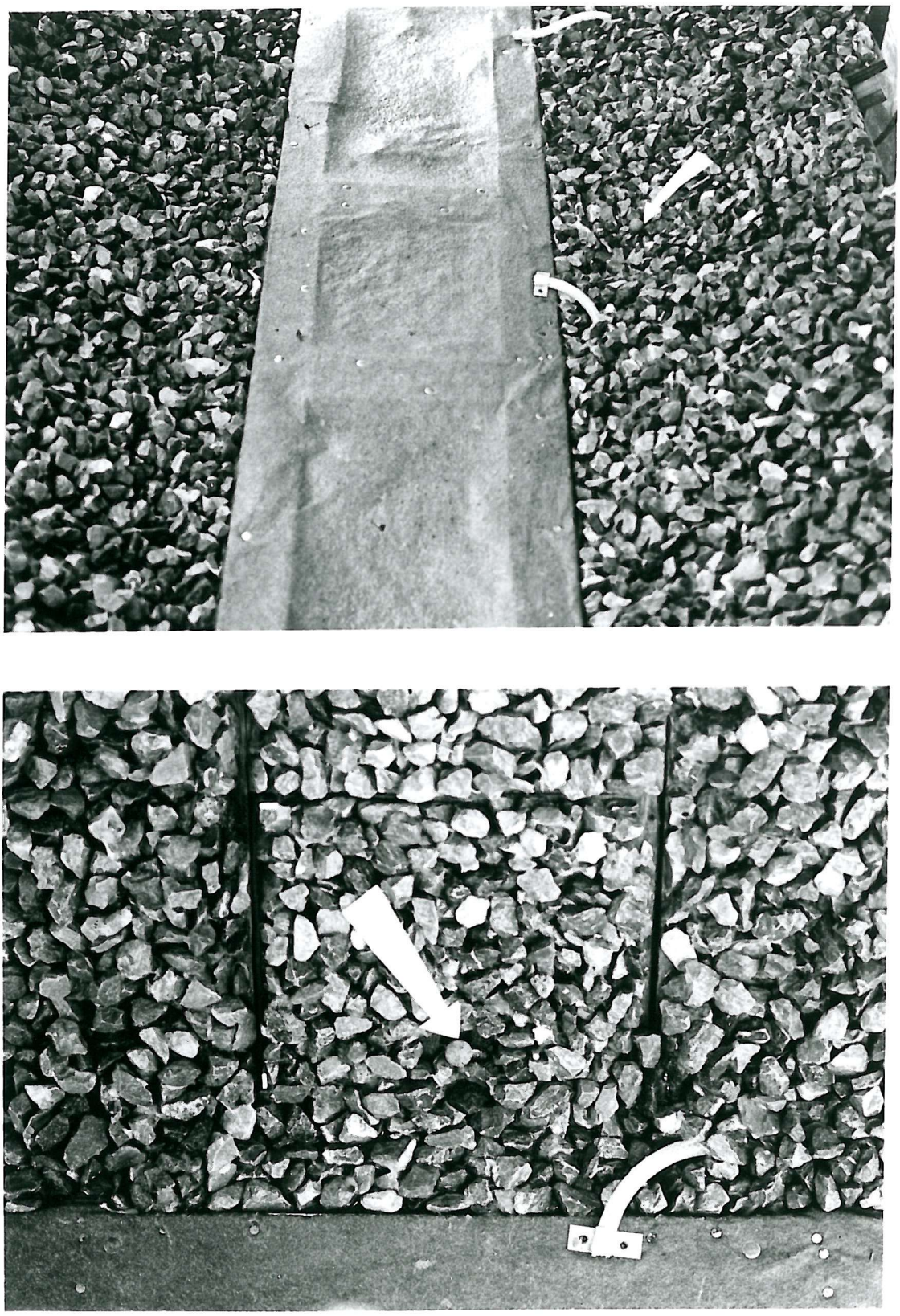

Plate (6-7) The movable roughened board in position

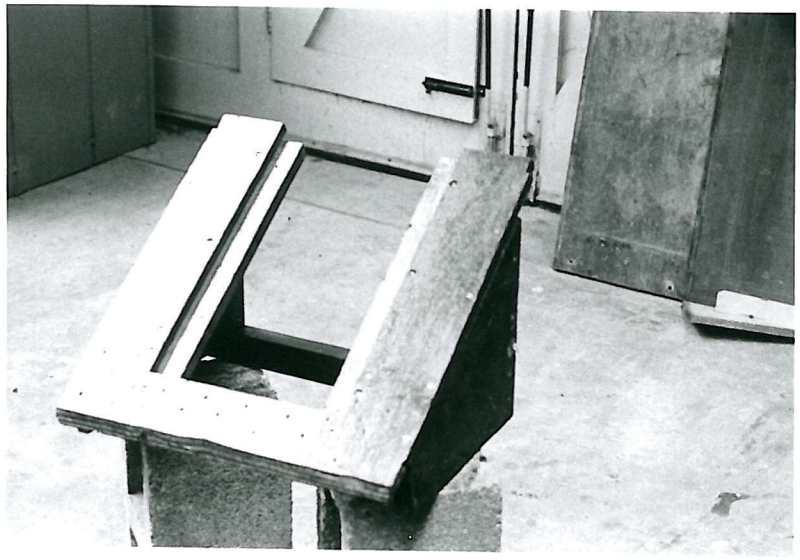

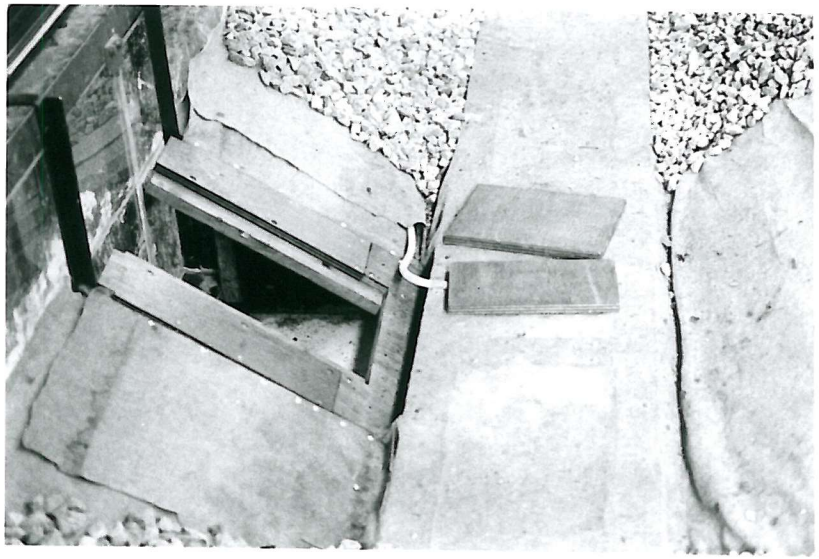

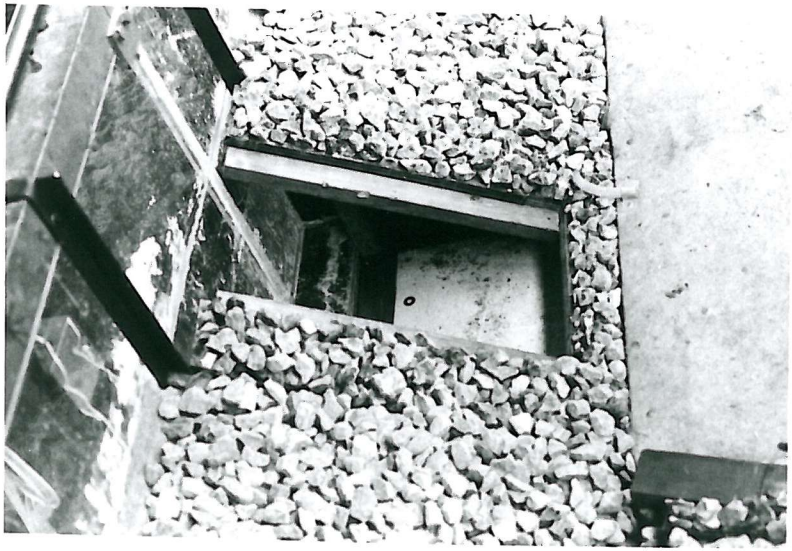

Plate (6-8) Different stages of installation of the embedded cavity

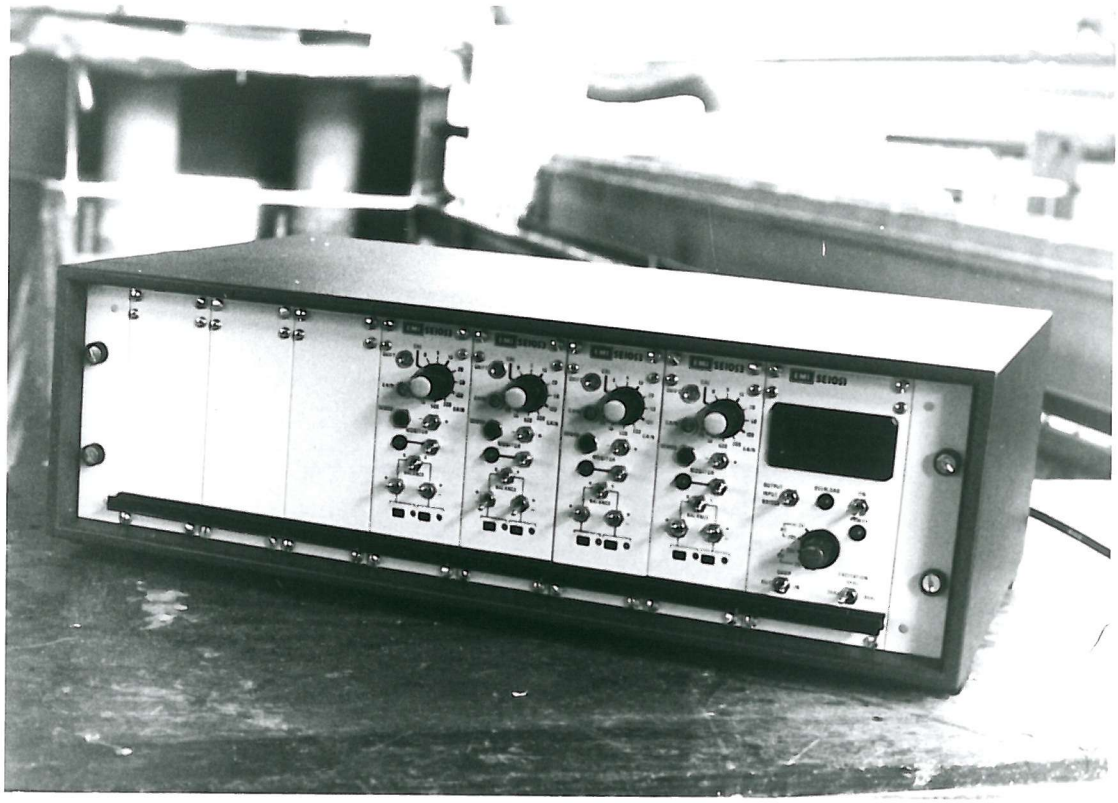

Plate (6-9) The signal conditioner

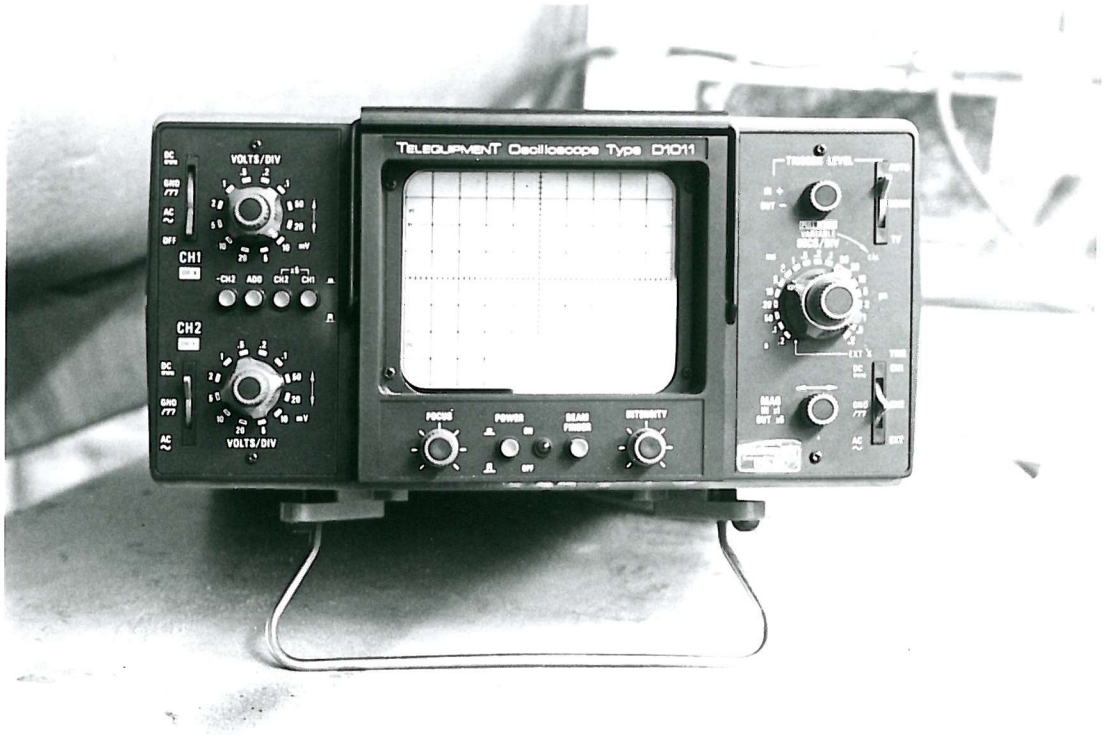

Plate (6-10) The oscilloscope

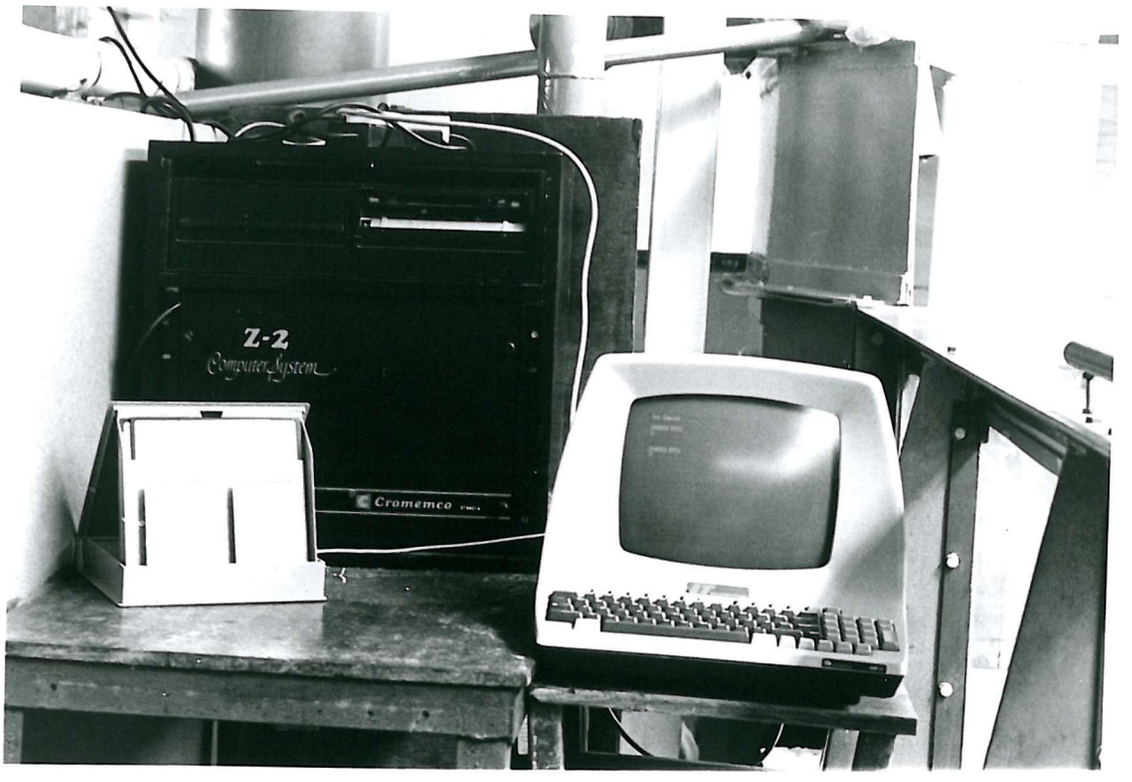

Plate (6-11) The computer system during operation

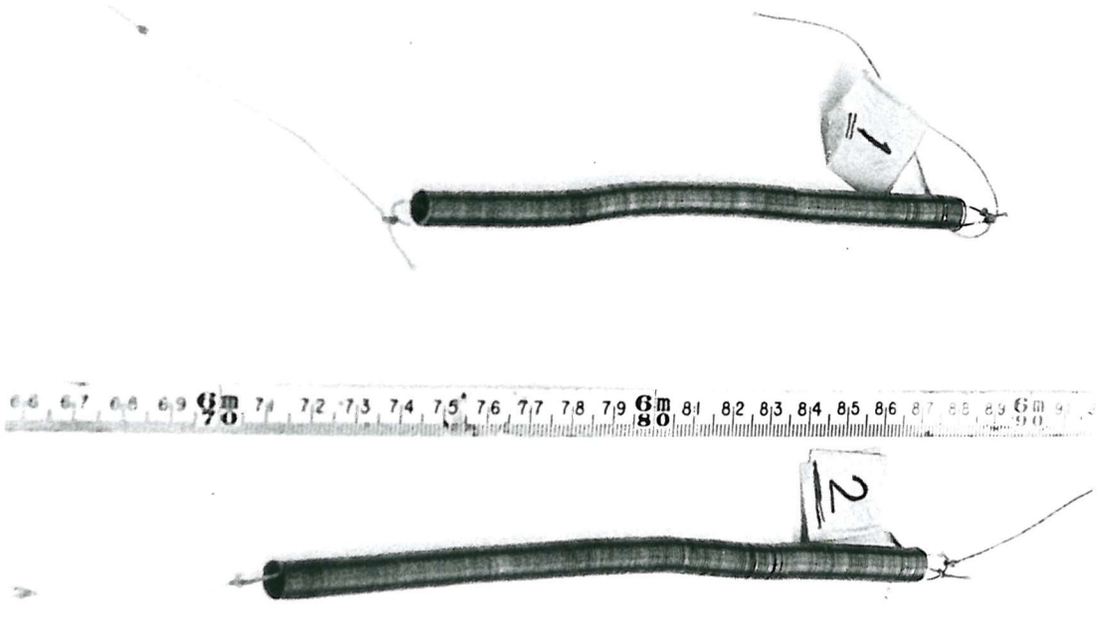

Plate (6-12) The helical springs

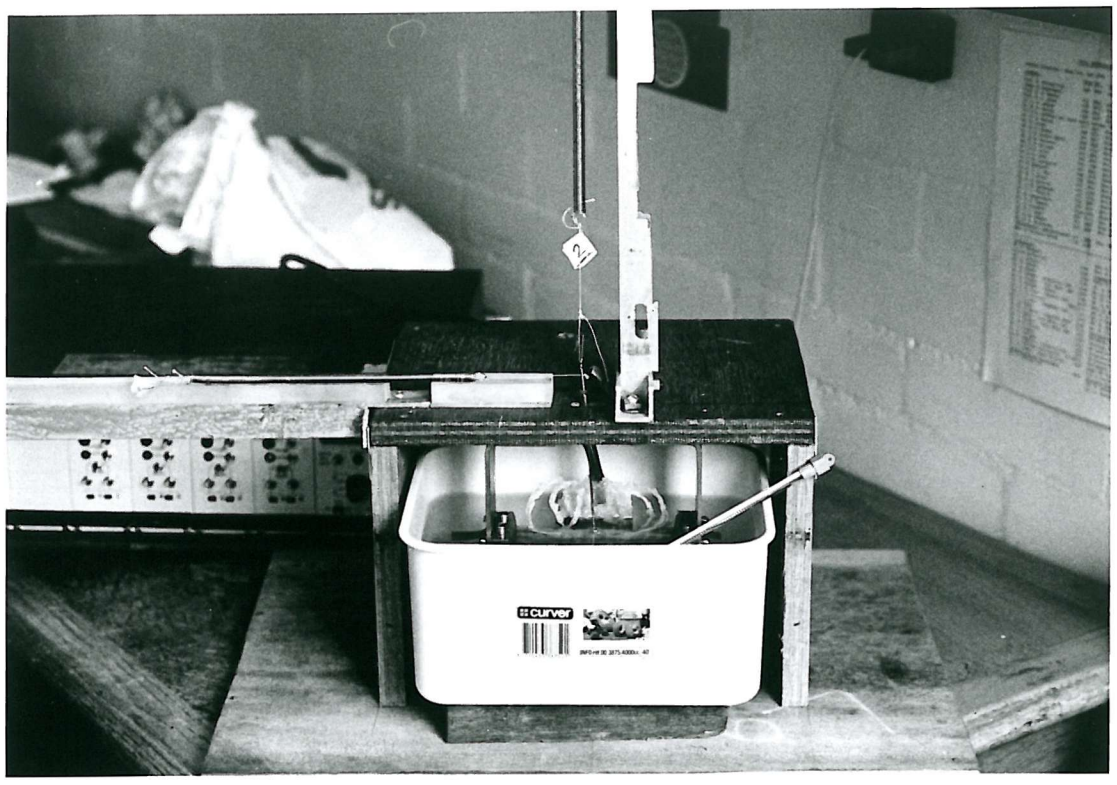

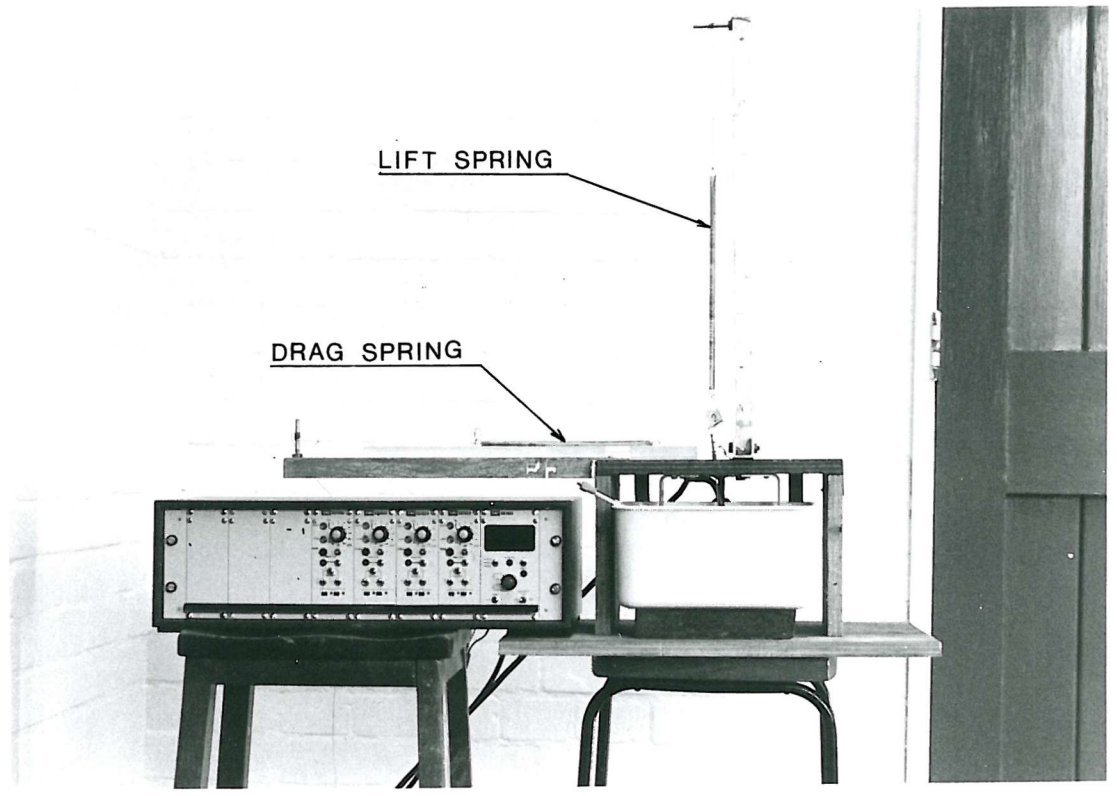

Plate (6-13) The load beam cell during calibration

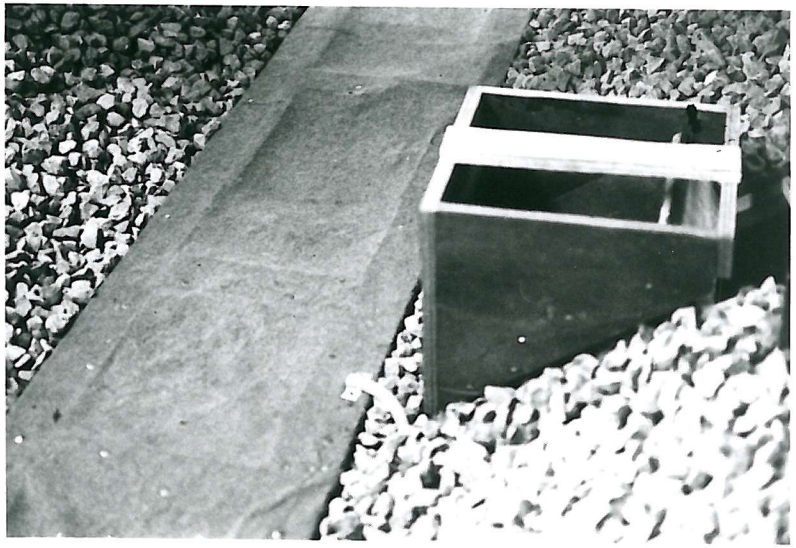

Plate (6-14) The wooden construction

CHAPTER SEVEN

RESULTS OF THE FAILURE TESTS

7.1 INTRODUCTION

Bearing in mind that the deterministic and probabilistic approaches discussed in Chapter Three were theoretically developed on the basis of stability of a single particle, and that movement of a single particle does not usually cause failure of the whole protective layer, the current investigation was planned to establish the conditions that promote failure as well as to predict the effect of some major factors influencing it. To achieve these goals, six modelled channels, protected with a layer consisting of free particles, were designed, constructed and tested (see Chapter Five).

In this chapter, the results obtained from different tests will be set forth, then the available deterministic and probabilistic approaches will be clarified with a numerically solved example by utilizing data obtained from one of the achieved runs. In addition, to obtain most of the experimental measurement benefits as well as to assess the applicability of the aforementioned approaches for sizing riprap, the side slope safety factor and probability of adequacy will be worked out for each run of all the tests; then the results obtained will be demonstrated separately for each model. Finally, the detailed criteria developed for the flow characteristics and flow resistance equations, which were found necessary for defining the guidelines for the rest of the study, will be presented.

7.2 TEST RESULTS

The models tested in this study may be classified, with respect to their purposes, into the following two series:-

Series No. (1): The tests were conducted to investigate the failure mode and to identify the hydraulic parameters at the threshold and

failure flow conditions as well as to study the flow resistance of the rough channels. Four models were constructed and tested during this series.

Series No. (2): The tests were mainly conducted to investigate the effect of utilizing sheet cloth filter and graded material on the side slope riprap stability, and also to investigate the failure process quantitatively. Two modelled channels were designed, constructed and tested during this series.

During all the aforementioned tests, the stone movements were observed and the failure recorded. Each run was started by passing a small flow rate which gradually increased in steps until the threshold and failure conditions were reached. In addition, it is worth noting that each run lasted at least for one hour, whilst at the final stages of every test, which can be distinguished by the particle movements, each run was extended as long as the movement took place, until all movement had ceased.

The results obtained from all the experimental tests may be summarised as follows:

7.2.1 Model Nos. (1,2 and 3)

In the case of these three models, the flume was run at various flow rate steps up to 0.22 m^3/s, (see Table 5.1). In spite of the fact that the maximum discharge was applied for a day and night, no failure was observed. This simply signifies that at the maximum attainable flow rate, the effective shear force acting at the top of the protective layer had not yet reached its critical value.

On the other hand, at relatively low flow rates, some particles, due to their unbalanced initial position, were displaced to some other stable place in the downstream direction. In fact, this phenomenon was expected as a result of the distinctive degree of exposure of the particles to the fluid forces; these were

entirely dependent on the relative shape and orientation of the particles comprising the top layer of the riprap blanket. This restricted movement may be said to be particle rearrangement rather than actual movement due to the applied hydrodynamic forces.

7.2.2 Model Nos. (4 and 5)

These models were dimensionally similar to each other, but the only difference was that a properly designed conventional filter was employed in the case of Model No. (4), whilst a cloth sheet filter was applied in the case of Model No. (5). These modelled channels, with 0.0125 bed slope and 10.0m length were of trapezoidal cross-section, 0.5m bed width and side slopes 1.5H:1.0V. A riprap blanket equivalent to 1.5 particle diameter thick consisting of uniform material with mean size 0.0207m was utilized in both models.

The mode of failure as well as the behaviour of particle movements will be discussed firstly, then the results obtained will be summarized separately.

During these tests, it was noticed that at relatively low flow rates some of the less well supported particles were individually displaced downstream to a second, more stable, position so as to rearrange these particles. As the rate of flow gradually increased, the aforementioned stage was followed by some particles, mainly from the top protective layer at the lower part of the side slope blanket, tending to vibrate under the effect of the hydrodynamic forces. When the flow was progressively increased, occasional particles were observed to move. Despite the particles being moved from the side slopes during the three previous stages, the riprap blanket was working efficiently and withstood the applied forces.

As the flow rate was progressively increased, another stage was reached at which movement of one particle would expose some shielded particles, within the same spot, to the flow currents. As a result of this a new force system was established which caused some less well supported particles to move. This distinctive stage, which was reached at run No. M4R25 in the case of Model No. (4), and

at M5R32 in the case of Model No. (5), was defined as the threshold stage and its flow rate was called the threshold flow.

Thereafter, as the flow increased, the rate of particle removals was found to be approximately proportional to the increment obtained in flow rate. A final stage was reached when the particles comprising the protective layer began to move at a rate which endangered the side slope stability. At this stage, the failure was identified when at some places in the lower part of the side slopes the stones covering were removed. Consequently, due to the unbalanced forces developed by the removal of the protective layer within these areas, the riprap blanket, within the upper part of the side slope above the failure spots collapsed. This stage was reached at run No. M4R33 in the case of Model No. (4), and M5R36 in the case of Model No. (5). Some photos for the failure are shown in Plates (7.1 and 7.2), for the case of Model No. (4), and Plate (7.3), for the case of Model No. (5).

In order to confirm the results obtained in both models as well as to determine the mode of failure in more detail, three more failure tests were performed on each of the modelled channels. Each test was started from the original condition which consequently means that before each confirmation test the sand base and filter layer materials were firstly checked, then the protective layer was carefully applied with the designed thickness and finally the channel cross-section was checked to conform to the original design.

During these tests, the aforementioned experimental procedure was applied and the corresponding failure flows were as follows:

Test No.	Failure Flow (m^3/s)	
	Model No. (4)	Model No. (5)
1	0.1794	0.1424
2	0.1825	0.1384
3	0.1853	0.1446
4	0.1769	0.1362

7.2.3 Model No. (6)

A factor of considerable importance in the design of riprap lined channels is the effect of the riprap gradation on the stability of the riprap blanket. To establish this effect, the model was constructed similar to that of Model No. (5), except that a protective layer consisting of graded material was used. This graded riprap mixture, with its gradation curve shown in Fig. (5.19), was designed in such a way to have the same value of D_{50} as that of the uniform riprap material used in the previous models.

It is obvious that in the case of a graded mixture, the particles are separated from each other by a lesser distance than for uniform material. On the other hand the interstices of the larger particles in the mixture are usually filled by the smaller, and when the layer is greater than one diameter thick, the particles tend to overlap and to close the internal spaces through which the side slope may have been exposed to direct flow currents.

Considering the tests conducted on the graded riprap lined channel, performed on Model No. (6), the behaviour of particle removals and consequently the failure processes were practically the same as that observed during the previous models. But on the other hand, it was noticed that when the rearrangement process was taking place, some small particles, particularly those which were not shielded by the larger particles, were directly washed out to the downstream end of the channel. In addition, at higher flow rates, where the hydrodynamic forces were capable of dislodging the medium size particles, the particle movements were consequently causing many smaller surrounding particles to move. This situation permitted the threshold and failure conditions to occur faster than in the case of uniform riprap particles.

As a result of the tests conducted on Model No. (6), failure was attained at run No. M6R22, at flow rate 0.1296 m^3/s. Plate (7.4) shows the exposed area of the riprap blanket after the failure.

7.2.4 The Quantitative Study

In order to define the failure of the protective layer quantitatively, another study was simultaneously conducted on Model No. (6). In this study, the protective layer was marked with eight different coloured compartments as illustrated in Section (5.6.2). So knowing the protective layer weight in each coloured area, the particles removed within those compartments could be detected.

Bearing in mind that the principal failure was developed at a distance upstream of the coloured compartments, and that the failure occurring at the areas under consideration was only partially established, the following results were obtained:

To establish a relationship between the riprap material transported during the failure test and the original contents of each compartment, the percentage of the particles transported was worked out for each area separately, which in upstream direction can be given as

D/S

6%	20%	30%	2.1%
11.4%	25%	19.7%	6.4%

U/S

Bed level

Obviously, the maximum percentage transport occurred at the upper part of the protective blanket which collapsed due to the particle movements within the lower part of the side slope.

Consideration is now directed to explaining the movement behaviour and the manner in which the particles were transported from within the riprap blanket. Undoubtedly, this manner is dependent on the force system that governs the process which is a complex function of time, space and properties of the particle under consideration. In these circumstances, establishing the applied forces on a representative particle is essential.

For any particle situated on the side slope, the dominant forces that regulate the beginning of motion were explained in Chapter Two. But as the incipient motion takes place, particle movement is governed by another system of forces. According to the previous investigations discussed in Chapter Two (see Section 2.6), Chepil, W.S. (1961), concluded that the lift force was at its greatest only when the roughness element is on the bed surface and diminishes rapidly with height and ceases to be measurable at a short distance above the bed surface. Furthermore, a similar conclusion, with respect to seepage force, was reported by Martin, C.S. (1970). Therefore, the only forces controlling the particle, immediately after the initial movement, are the submerged weight and drag force. But obviously the drag force exerted at this instant would be magnified due to the flow velocity which in turn increases rapidly with distance from the boundary. This explains the coloured particles scattered on the side slope as shown in Plates (7.5) and (7.6).

In addition, to clarify this phenomenon, the coloured particles displaced from each compartment were located within the neighbouring portions, then the angle between the scattered particles and the vertical were roughly determined at between 26 and 48 degrees. Bearing in mind the wide range of particle sizes contained in the riprap material, this result corroborates the previous conclusion and indicates the large forces acting on the riprap particles just after the initial motion had started.

7.3 DISCUSSION OF THE FAILURE TESTS

1 - According to the results obtained for different failure tests, the most efficient design may be defined as that permitting maximum flow rates before the complete failure. Comparing the attainable failure flow rates in the three tests, it is obvious that a riprap blanket consisting of uniform material with a conventional filter beneath it, as adopted in Model No. (4), is the optimum design for the riprap lined channel. As a matter of fact, this result was expected due to the following reasons:

A - The properly designed conventional filter, which consisted of a graded mixture, provided a rough foundation to the riprap blanket which consequently enabled the protective layer to withstand the applied hydrodynamic forces. On the other hand, the failure tests performed on Model Nos. (5 and 6), where a cloth filter was utilized, revealed the tendency of particles to move immediately after the incipient motion had taken place. This action reduced the time interval between the threshold of movement and failure as well as inducing failure earlier.

B - In the case of the riprap blanket comprising graded material, the larger particles provided shelter for the smaller ones. As a result, the ability of smaller particles to resist the hydrodynamic forces increased, whilst the opposite is true for the case of larger ones. Accordingly the resistance of the whole mixture would be less than that of the uniform material having the same mean size.

2 - The durability of filter cloth has not yet been established because it is only a recent product. In fact, the technical properties of the filter used, which was selected to suit the sand base grading satisfying both piping and permeability requirements, have not changed through the course of the experiment work. But on the other hand the relative roughness of the filter cloth material, which is necessary for the side slopes, was changed by the flow effect and became less than previously. This variation may have caused another type of failure which is likely to take place along the whole side slope.

In fact, this type of failure occurred during the tests conducted on Model No. (6) in which failure rapidly established itself along about 4.0m of the left side slope as shown in Plate (7.7). It is obvious that this failure was developed due to the filter sliding on the side slope sand base.

3 - During all the preceding failure tests, the particle movement started within the lower part of the side slope. This was obviously due to the shear stress exerted which, as experimentally concluded, is a maximum at this part of the side slopes.

7.4 COMPARISON OF THE EXPERIMENTAL RESULTS

It was suggested that to obtain the most advantage from the experiments as well as to apply the deterministic and probabilistic approaches, which were discussed in Chapter Three, the results obtained from the preceding investigation should be compared with those obtained by applying the various approaches.

In the Author's opinion, the comparison test would be accomplished by determining the side slope safety factor and probability of adequacy for a given flow condition in each run of the conducted tests, then as a result of this, the appropriate approach would be identified. But in order to set forth these approaches in greater detail, the procedure used for determining the mean safety factor and the probability of adequacy for one of the observed runs will be presented numerically. Then the results obtained for all the tests will be as follows:

7.4.1 The Deterministic Approach

In this study, judgement of riprap stability will be considered from the standpoint of the eight approaches discussed in Section (3.3), namely:

Method No. (1): USBR, Lane, E.W. (1953)
Method No. (2): Stevens, M.A. and Simons, D.B. (1971)
Method No. (3): Stevens, M.A. and Simons, D.B. (1976)
Method No. (4): Stevens, M.A. and Simons, D.B. (1976)
Method No. (5): Ruh-Ming, L. et al. (1976)
Method No. (6): Ruh-Ming, L. and Simons, D.B. (1979)
Method No. (7): Samad, M.A. (1978)
Method No. (8): Samad, M.A. (1978).

To illustrate the aforementioned approaches, a sample of calculation is numerically provided by utilizing the data obtained from Model No. (1), Run No. M1R25. This data may be summarised as follows:

A - Water properties

Density	$\rho = 999.276$ (Kg/m^3)
Kinematic viscosity	$\nu = 0.117 \times 10^{-5}$ (m^2/sec)
Water temperature	$T = 14.0\ ^{o}C$

B - Channel cross-section

Bed width	$B_o = 0.4$ (m)
Bed slope	$S_o = 0.005$
Side slope	1.5H : 1V
Side slope angle	$\theta = 33.69^{o}$

C - Rock properties

D_m	$= 0.02177$ (m)
D_{50}	$= 0.0207$ (m)
D_{75}	$= 0.02155$ (m)
Specific gravity	$S_s = 2.66$
Angle of repose	$\phi = 36.5^{o}$

D - Flow condition

Flow rate	$Q = 0.1281$ (m^3/s)
Average water depth	$y_o = 0.22$ (m)
Water surface slope	$S_w = 0.00488$
Energy slope (Eq.5.9)	$S_e = 0.00493$
Water depth correction	$\Delta y = 0.013$ (m)
Bed width correction	$\Delta B = 0.008$ (m)
Actual water depth	$y = y_o + \Delta y = 0.233$ (m)
Actual bed width	$B = B_o + \Delta B = 0.408$ (m)

E - Hydraulic results

Cross-section area	A	$= 0.1768$	(m^2)
Wetted perimeter	P	$= 1.249$	(m)
Hydraulic radius	$R = \frac{A}{P}$	$= 0.1416$	(m)
Average velocity	$\overline{u} = \frac{Q}{A}$	$= 0.724$	(m/s)
Shear velocity	$u* = \sqrt{gRS_e}$	$= 0.0827$	(m/s)
Reynolds number	$R_e = \frac{4Ru}{\nu}$	$= 350453.7$	
Froude number	$F_r = \frac{u}{\sqrt{gR}}$	$= 0.6148$	

7.4.1.1 Calculation procedure

The following procedure was used to determine the side slope safety factor for all the available approaches by using the symbols mentioned in Chapter Three.

7.4.1.1.1 Method No. (1)

In this method, Eqs. (3.11 to 3.15) should be utilized to obtain

Eq. (3.13)	$\tau_s = 17.22$	(N/m^2)	
Eq. (3.14)	$K = 0.361$		
Eq. (3.15)	$\tau_{sB} = 6.217$	(N/m^2)	
	$B/y = 1.75$		
	$C_T = 0.729$	(Fig. 3.5)	
Eq. (3.11)	$\tau_{oB} = 8.213$	(N/m^2)	
	$SF = \tau_{sB}/\tau_{oB} = 0.757$		

7.4.1.1.2 Method No. (2)

In this method Eqs. (3.21 to 3.25) should be utilized as follows:

Eq. (3.23)	$\eta = 0.3017$
Eq. (3.25)	$\beta = 11.4^{o}$
Eq. (3.24)	$\delta = 78.6^{o}$
Eq. (3.22)	$\eta' = 0.1806$
Eq. (3.21)	SF = 0.9088

7.4.1.1.3 Method No. (3)

Equations (3.41 to 3.48) should be applied to obtain the following:

Eq. (3.41)	$u_r = 0.556$ (m/sec)
Eq. (3.45)	$\eta = 0.2749$
Eq. (3.48)	$\alpha = 10.39^{o}$
Eq. (3.47)	$\eta' = 0.162$
Eq. (3.42)	SF = 0.9249

7.4.1.1.4 Method No. (4)

In this method Eqs. (3.31 to 3.37) should be utilized as follows:

Eq. (3.33)	$S_m = 1.1099$
Eq. (3.37)	$K = 0.361$
Eq. (3.36)	$\tau_s = 6.83$ (N/m^2)
Eq. (3.35)	$\tau_s' = 2.4692$ (N/m^2)
Eq. (3.34)	$\eta = 0.1536$
Eq. (3.32)	$\xi = 0.2049$
Eq. (3.31)	SF = 1.002

7.4.1.1.5 Method No. (5)

The following equations should be used:

Eq. (3.51)	$W = 0.088$ (N)
	$\beta = 0.85$
Eq. (3.52)	$\delta = 2.168 \times 10\text{-}3$ (m^2)
Eq. (3.50)	$\tau = 4.2814$ (N/m^2)
Eq. (3.49)	SF = 0.973

7.4.1.1.6 Method No. (6)

The following equations should be used:

Eq. (3.51)	$W = 0.088$ (N)
	$\beta = 2.85$
Eq. (3.54)	$\delta = 9.709 \times 10^{-4}$ (m^2)
Eq. (3.50)	$\tau = 4.2814$ (N/m^2)
Eq. (3.49)	$SF = 0.927$

7.4.1.1.7 Method No. (7)

The following equations should be used:

Eq. (3.56)	$A_L = 3.37 \times 10^{-4}$ (m^2)
Eq. (3.59)	$u_* = 0.065$ (m/sec)
Eq. (3.58)	$u_{35} = 0.386$ (m/sec)
Eq. (3.61)	$R_* = 1157.6$
	$\beta = 2.414$ (Fig. 3.10)
Eq. (3.51)	$W = 0.088$ (N)
Eq. (3.57)	$P_L = 13.26$ (N/m^2)
Eq. (3.55)	$SF = 1.042$

7.4.1.1.8 Method No. (8)

The following equations should be utilized:

Eq. (3.51)	$W = 0.088$ (N)
Eq. (3.59)	$u_* = 0.065$ (m/sec)
Eq. (3.61)	$R_* = 1157.6$
	$\beta = 2.414$ (Fig. 3.10)
Eq. (3.54)	$\delta = 1.08 \times 10^{-3}$ (m^2)
Eq. (3.50)	$\tau = 4.281$ (N/m^2)
Eq. (3.49)	$SF = 0.936$

7.4.1.2 Results

Since the calculation procedure for each method has been demonstrated, consideration is now directed to the comparison test in which the side slope safety factor is derived by all the available deterministic approaches for each run of the experimental tests. The values predicted for the safety factor are listed in Tables (7.1) to (7.6), and plotted in Figs. (7.1) to (7.24).

7.4.1.3 Discussion

As a result of the comparison test conducted in this study one may conclude that:

1 - Bearing in mind that no failure was established during the first three model tests, and the protective layers were working efficiently in spite of running the test continuously overnight with maximum attainable flow, the side slope safety factors predicted by all the methods were less than unity. This principally revealed that in the viewpoint of all these methods, failure should have occurred. On the other hand, the only result in accordance with the experiments was that obtained by Method No. (7), developed by Samad (1978). In this method the predicted safety factor for Model No. (1) in the case of maximum flow rates was equal to 1.022, whilst in the case of Model Nos. (2 and 3), the safety factors predicted by the same method were less than unity as shown in Tables (7.1) to (7.3), and Figs. (7.1) to (7.12).

2 - In the case of the other three models, failure was finally established at the last run in all the tests. But, the results obtained by all the applied approaches indicated that failure should occur at lower discharges than those registered in the experiments. Moreover, in the case of run No. (1), most of the safety factor predictions were much less than unity. This accordingly implied that the failure should be established immediately at the beginning of each test, which contradicts the experimental results.

3 - It was also realized from this test that the results predicted by Method No. (4), developed by Stevens and Simons (1976), and No. (7), developed by Samad (1978), were close to that obtained from the experimental tests. Applying these two approaches, the side slope safety factors predicted for the last run of all the models were as follows:

Model No.	(1)	(2)	(3)	(4)	(5)	(6)
Method 4	0.970	0.889	0.911	0.878	0.900	0.909
Method 7	1.022	0.994	0.986	0.936	0.941	0.979

4 - In addition, to obtain more benefit from the results as well as to examine these approaches, another comparison test was conducted. In this test the flow conditions, at threshold and failure stages for Model Nos. (4),(5) and (6), were utilized as input data for all the available deterministic approaches. This mathematical test was carried out for a wide range of particle size which was varied from 0.01m to 0.40m with increment 0.002m, then the side slope safety factor corresponding to every particle size was determined. The results obtained from this test are depicted in Figs. (7.25) to (7.30) which revealed that:

A - Only Method Nos. (1),(2),(4) and (7) listed overleaf embraced the line at which the factor of safety is equal to unity. This implied that the other Method Nos. (3),(5),(6) and (8), always predict failure whatever the particle size, which contradicts the experimental results.

B - In order to determine the recommended particle size, by the Method Nos. (1),(2),(4) and (7), at which the movement should be established, the particle size at which the corresponding factor of safety is equal to one was determined as follows:

Method	Mean Particle Size D_{50}(m)					
	Model No. (4)		Model No. (5)		Model No. (6)	
	Threshold	Failure	Threshold	Failure	Threshold	Failure
1	0.052	0.060	0.049	0.051	0.035	0.039
2	0.228	0.245	0.216	0.236	0.105	0.121
4	0.043	0.047	0.041	0.042	0.029	0.033
7	0.070	0.080	0.068	0.079	0.021	0.025

Therefore, bearing in mind that the riprap material used during the experimental work was D_{50} equal to 0.207m, one may conclude that the recommended particle sizes by the four methods, for the given flow conditions at the theshold and failure flows, are always greater than that used in the experimental tests.

This wide variation in the mean particle size predicted by various methods reflects the manner in which these approaches were developed, which are principally based on theoretical considerations and have not been tested with real measurements. It is also revealed that these methods are too conservative and not economic.

7.4.2 The Probabilistic Approach

In this study, side slope stability was considered from the viewpoint of four probabilistic approaches discussed in Chapter Three which can be listed as

Method No. (1) Ruh-Ming, L. et al. (1976)
Method No. (2) Ruh-Ming, L. and Simons, D.B. (1979)
Method No. (3) Samad, M.A. (1978)
Method No. (4) Samad, M.A. (1978)

Along with the preceding example presented in Section (7.4.1) for the deterministic approach, the same data given in this section will be used to illustrate the utilized probability methods.

7.4.2.1 Calculation procedure

The following procedure was used to determine the side slope probability of adequacy by using the symbols mentioned in Chapter Three.

7.4.2.1.1 Method No. (1)

The following set of equations are utilized:

	β	= 0.85	
Eq. (3.66)	δ	= 0.023	ft^2
Eq. (3.68)	A_1	= 6.602E-3	lb
Eq. (3.69)	A_2	= 0.604	lb
Eq. (3.70)	A_3	= 0.071	
Eq. (3.71)	τ_c	= 0.0631	lb/ft^2
Eq. (3.59)	$u*$	= 0.2145	ft/sec
Eq. (3.72)	f	= 0.0652	
Eq. (3.73)	$\sigma/\bar{\tau}$	= 2.076	
Eq. (3.74)	$\bar{\tau}$	= 0.089	lb/ft^2
Eq. (3.75)	σ_n	= 2.3039	
Eq. (3.76)	μ_n	= -2.53	
Eq. (3.77)	q_n	= -0.099	
Eq. (3.78)	P	= 0.4606	

7.4.2.1.2 Method No. (2)

The following equations would be used

	β	= 2.85	
Eq. (3.79)	δ	= 2.74E-4	ft^2
Eq. (3.81)	A_1	= 0.022	lb
Eq. (3.82)	A_2	= -3.447	lb
Eq. (3.83)	A_3	= 0.0714	
Eq. (3.84)	F_c	= 4.87	lb/ft^2
Eq. (3.85)	$u*$	= 0.2145	ft/sec
Eq. (3.86)	μ_d	= 9.45 E-4	
Eq. (3.87)	σ_d	= 3.487E-4	
Eq. (3.88)	q_n	= -1.313	
Eq. (3.89)	P	= 0.0955	

7.4.2.1.3 Method No. (3)

During this method, the following equations would be utilized:

Eq. (3.85)	u_* =	0.0654	m/sec
Eq. (3.101)	R_* =	1157.59	
	β =	2.41	(Fig. 3.10)
Eq. (3.56)	A_L =	3.367E-4	m^2
Eq. (3.91)	P_1 =	0.6866	
Eq. (3.92)	P_2 =	0.1883	
Eq. (3.90)	P_c =	18.24	N/m^2
Eq. (3.58)	u_{35} =	0.386	m/sec
Eq. (3.57)	P_L =	13.235	N/m^2
Eq. (3.93)	σ =	4.764	
Eq. (3.94)	q_n =	1.0505	
Eq. (3.95)	P =	0.853	

7.4.2.1.4 Method No. (4)

The following equations should be used:

Eq. (3.103)	δ =	1.082E-3	m^2
Eq. (3.104)	$\overline{\tau}$ =	4.272	N/m^2
Eq. (3.106)	$\overline{P_L}$ =	33.151	N/m^2
Eq. (3.97)	C_1 =	0.083	N
Eq. (3.98)	C_2 =	-2.193	
Eq. (3.99)	C_3 =	0.0714	
Eq. (3.96)	τ_c' =	2.350	N/m^2
Eq. (3.107)	P_c =	18.24	N/m^2
Eq. (3.108)	σ =	11.93	
Eq. (3.109)	q_n =	-1.249	
Eq. (3.110)	P =	0.106	

7.4.2.2 Results

The procedure applied previously was used to compare the experimental and predicted results. In this test, the data obtained

from each run of all the tests were utilized to predict the probability of adequacy by the four methods. The values obtained in this test are listed in Tables (7.7) to (7.12) and plotted in Figs. (7.31) to (7.36).

7.4.2.3 Discussion

As a result of the comparison test conducted in this study, one may conclude that

1 - The predictions obtained by both Method Nos. (2) and (4), were approximately the same and very close to the zero for all the six models. This implied that their predictions were in the same order regardless of whether the failure was not established, as in the case of the first three models, or it did occur, as in the case of the last three models.

2 - The values predicted by Method No. (3), were in agreement with the experimental results only in the case of Model No. (1), whilst in the case of Model Nos. (2) and (3), the probability of adequacy at the maximum flow were 0.3081 and 0.2558, respectively. Moreover, the same method predicted the failure occurrence at the very beginning of the tests conducted on the last three models which contradicts the experimental results.

3 - The probability of adequacy predicted by Method No. (1) can be said to be approximately following the same trend. In other words for all six models, the prediction at the beginning of each test was more than 0.6 and rapidly decreased, as the flow rate increased, up to the range of 0.38 to 0.46 in the case of the maximum rate.

4 - Since the first two methods were only applicable in (fps) system, therefore the given data for each run was converted to permit the exact solution.

7.5 HYDRAULIC RESISTANCE

Regarding the models constructed during the current investigation, two distinctive types of channel roughness were utilized;

1 - A wetted perimeter covered with a homogeneous roughness, as in Model Nos. (1) and (2). In these models, the entire cross-section was protected with a uniform free rock layer equivalent to 1.5 times the mean rock diameter thickness. The only difference was the bed slope, which was 0.005 in the case of Model No. (1) and 0.008 in the case of Model No. (2).

2 - A wetted perimeter covered with a non-homogeneous roughness, as in Model Nos. (3) to (6). In these models, the side slopes were protected similar to those in the first two models, whereas the bed was covered with a sheet cloth filter.

Therefore, due to the principal distinction between the two types, it was decided to study the flow resistance of each type separately.

Also to identify the flow characteristics along with the flow resistance formulae in more detail, each of the resistance coefficientsand the controlling hydraulic parameters were worked out separately for each run of the models tested. These results are listed in Tables (7.13) to (7.18), in which

Q is the flow rate (m^3/sec);
Y is the flow depth (m);
S_o is the bed slope;
S_w is the observed water surface slope;
S_e is the energy slope;
R_e is the Reynolds number;
F_r is the Froude number;
n is the Manning resistance coefficient ($sec/m^{1/3}$)
f is the Darcy-Weisbach friction factor;
and C is the Chezy coefficient ($m^{\frac{1}{2}}$/sec).

The flow characteristics and hydraulic resistance formulae developed during the current investigation can be summarized as follows:

7.5.1 Manning and Chezy Resistance Coefficients

As mentioned by Chow, V.T. (1959), there are many important formulae for the determination of either Manning or Chezy resistance factors. But, for the case in hand, the following equations were utilized

$$n = A R^{2/3} S_e^{\frac{1}{2}}/Q \qquad (7.1)$$

$$C = Q/ (A \sqrt{RS_e}) \qquad (7.2)$$

in which

A is the effective cross-section area;
and R is the hydraulic radius.

Since both the resistance coefficients were determined over a wide range of flows, accordingly the results obtained also varied successively with the flow variation. Therefore, the technique developed by Overton, D.E. (1967), for flow resistance analysis was adopted, because his technique is applicable to all types of boundary conditions of prismatic channels.

According to this technique, to determine Manning coefficient in Eq. (7.1), the flow rate Q, should be plotted against $AR^{2/3} S_e^{\frac{1}{2}}$, then the value 1/n, would be determined as the slope of the line. Also the same procedure can be applied to obtain the value C by plotting Q against $A(RS_e)^{\frac{1}{2}}$. Using a linear least square technique, the results obtained for Manning n and Chezy C are depicted in Figs. (7.37 to 7.42), which may be summarized as follows:

No	Fig.	Model No.	n ($sec/m^{1/3}$)	Corr. Coeff.	Intercept of Y axis	Standard error	Eq. No.
1	(7.37)	(1)&(2)	0.0276	0.9915	-0.0031	0.0078	(7.3)
2	(7.39)	(3)	0.0284	0.998	0.0054	0.0034	(7.4)
3	(7.41)	(4),(5)&(6)	0.0254	0.9995	0.0033	0.00138	(7.5)

No	Fig.	Model No.	C ($m^{\frac{1}{2}}/s$)	Corr. Coeff.	Intercept of Y axis	Standard error	Eq. No.
1	(7.38)	(1)&(2)	27.49	0.9898	-0.0092	0.00858	(7.6)
2	(7.40)	(3)	26.74	0.998	-0.0026	0.00343	(7.7)
3	(7.42)	(4),(5)&(6)	28.37	0.9994	-0.0018	0.00156	(7.8)

7.5.2 Darcy-Weisbach Resistance Factor

It was found during the investigation conducted in Chapter Four that the Darcy-Weisbach resistance factor is widely used for measuring the resistance to flow in open channels. Also through the dimensional analysis presented in Section (4.2), the resistance to flow formula was found to be well defined as

$$1/\sqrt{f} = \phi\,(R/D_{50}) \qquad (7.9)$$

in which

R/D_{50} is the relative roughness parameter.

In addition, it was shown that when a fully developed turbulent flow takes place over rough boundaries, as the case in hand, the friction factor parameter, $1/\sqrt{f}$, would be directly related to

the relative roughness parameter, R/D_{50}. In this case the resistance equation may be expressed by a power (monomial) type equation

$$1/\sqrt{f} = G(R/D_{50})^{m} \qquad (7.10)$$

in which G and m are parameters that may be determined for each particular case.

As a matter of fact, many attempts have been made to develop a resistance formula in the semi-logarithmic form. But the best fitting was determined by the power type formula which for Model Nos. (1)and (2)was developed as

$$1/\sqrt{f} = 1.259\ (R/D_{50})^{0.4457} \qquad (7.11)$$

Equation (7.11), is plotted in Fig. (7.43)

Taking into account that

$$\sqrt{8/f} = u/u_{*} = C/\sqrt{g} \qquad (7.12)$$

Eq. (7.11) can be written as

$$u/u_{*} = 3.561\ (R/D_{50})^{0.4457} \qquad (7.13)$$

or

$$C/\sqrt{g} = 3.561\ (R/D_{50})^{0.4457} \qquad (7.14)$$

In addition, the resistance formula developed for the case of Model Nos. (4), (5) and (6) was:

$$1/\sqrt{f} = 2.096\ (R/D_{50})^{0.03043} \qquad (7.15)$$

This equation, which is plotted in Fig. (7.44) can also be written as

$$u/u_{*} = 8.4742\ (R/D_{50})^{0.03043} \qquad (7.16)$$

or

$$C/\sqrt{g} = 8.4742\ (R/D_{50})^{0.03043} \qquad (7.17)$$

7.5.3 Discussion

In this part of the study, the models tested were divided, with respect to roughness distribution, into two main divisions, then the friction factors as well as the resistance equations developed for each division were presented. Therefore the main conclusion can be summarized as follows:

1 - It is worth mentioning that the results obtained for Model Nos. (3) to (6), were not comparable. This is principally due to the difference in roughness of the channel side slope and the bed. Therefore, the comparison will be limited to the results obtained for the first two models.

2 - Due to the technique utilized for determination of Manning and Chezy resistance coefficients, the results obtained were, in the Author's opinion, excellent fits and highly correlated with an acceptable small intercept.

3 - In the case of Model Nos. (1) and (2), the value obtained from Manning's n was found in agreement with the values listed by Chow, V.T. (1959), for rough streams, and the value obtained, which is given by Eq. (7.3), can be written in the form

$$n = (D_{50})^{1/6} / 18.98 \qquad (7.18)$$

in which D_{50} is the mean particle size in (m).

4 - It was found during the investigation that both Manning's n and Chezy's C are independent of the slope of the channel bed.

TABLE 7 – 1 : SUMMARY OF THE PREDICTED SIDE SLOPE

SAFETY FACTORS FOR MODEL NO.(1)

RUN NO	FLOW RATE (m3/s)	WATER DEPTH (m)	CALCULATED SIDE SLOPE SAFETY FACTOR							
			METHOD (1)	METHOD (2)	METHOD (3)	METHOD (4)	METHOD (5)	METHOD (6)	METHOD (7)	METHOD (8)
M1R 1	0.017	0.098	1.727	1.057	1.060	1.054	1.079	1.064	1.093	1.071
M1R 2	0.021	0.107	1.465	1.043	1.046	1.045	1.069	1.051	1.088	1.059
M1R 3	0.027	0.115	1.377	1.027	1.032	1.042	1.059	1.038	1.083	1.046
M1R 4	0.033	0.124	1.252	1.010	1.016	1.036	1.048	1.022	1.077	1.030
M1R 5	0.035	0.132	1.186	1.014	1.020	1.033	1.051	1.027	1.079	1.035
M1R 6	0.039	0.137	1.135	1.005	1.012	1.030	1.045	1.019	1.076	1.027
M1R 7	0.045	0.146	1.047	0.997	1.005	1.025	1.039	1.011	1.073	1.020
M1R 8	0.048	0.153	1.062	0.998	1.006	1.027	1.041	1.013	1.073	1.021
M1R 9	0.056	0.160	0.979	0.977	0.987	1.021	1.026	0.993	1.066	1.002
M1R10	0.061	0.165	0.987	0.971	0.981	1.022	1.021	0.987	1.064	0.996
M1R11	0.064	0.168	0.947	0.962	0.973	1.019	1.014	0.979	1.061	0.988
M1R12	0.067	0.174	0.917	0.965	0.976	1.016	1.017	0.982	1.062	0.991
M1R13	0.072	0.179	0.898	0.957	0.968	1.015	1.011	0.974	1.059	0.983
M1R14	0.076	0.187	0.844	0.962	0.973	1.010	1.015	0.979	1.061	0.988
M1R15	0.081	0.191	0.859	0.953	0.965	1.012	1.008	0.971	1.058	0.980
M1R16	0.085	0.196	0.908	0.949	0.962	1.017	1.005	0.967	1.056	0.976
M1R17	0.089	0.200	0.861	0.950	0.962	1.013	1.006	0.968	1.057	0.977
M1R18	0.092	0.204	0.845	0.945	0.958	1.012	1.002	0.963	1.055	0.972
M1R19	0.098	0.209	0.829	0.939	0.952	1.010	0.997	0.957	1.053	0.966
M1R20	0.106	0.216	0.763	0.929	0.943	1.002	0.989	0.947	1.049	0.956
M1R21	0.109	0.219	0.770	0.929	0.943	1.003	0.989	0.947	1.049	0.956
M1R22	0.113	0.221	0.716	0.923	0.938	0.996	0.985	0.941	1.047	0.950
M1R23	0.119	0.227	0.779	0.919	0.934	1.005	0.982	0.938	1.046	0.947
M1R24	0.124	0.232	0.738	0.916	0.932	0.999	0.979	0.935	1.044	0.944
M1R25	0.128	0.233	0.756	0.909	0.925	1.002	0.973	0.927	1.042	0.936
M1R26	0.134	0.238	0.724	0.903	0.920	0.998	0.968	0.921	1.039	0.930
M1R27	0.139	0.242	0.734	0.903	0.919	0.999	0.968	0.921	1.039	0.930
M1R28	0.144	0.247	0.703	0.902	0.919	0.995	0.968	0.921	1.039	0.929
M1R29	0.148	0.253	0.699	0.904	0.921	0.995	0.969	0.923	1.040	0.932
M1R30	0.155	0.258	0.660	0.897	0.915	0.989	0.964	0.916	1.037	0.925
M1R31	0.160	0.262	0.673	0.897	0.915	0.991	0.964	0.916	1.037	0.925
M1R32	0.167	0.265	0.629	0.889	0.907	0.983	0.956	0.907	1.034	0.916
M1R33	0.172	0.268	0.649	0.885	0.903	0.987	0.953	0.903	1.033	0.912
M1R34	0.177	0.273	0.638	0.884	0.902	0.985	0.952	0.902	1.032	0.910
M1R35	0.184	0.277	0.645	0.880	0.898	0.987	0.948	0.897	1.030	0.906
M1R36	0.189	0.281	0.640	0.880	0.898	0.986	0.948	0.897	1.030	0.906
M1R37	0.194	0.286	0.624	0.878	0.897	0.984	0.947	0.895	1.030	0.904
M1R38	0.202	0.291	0.615	0.875	0.895	0.982	0.945	0.893	1.029	0.901
M1R39	0.214	0.294	0.557	0.859	0.880	0.970	0.930	0.875	1.022	0.884
M1R40	0.219	0.298	0.557	0.858	0.879	0.970	0.929	0.874	1.022	0.883

TABLE 7-2 : SUMMARY OF THE PREDICTED SIDE SLOPE SAFETY FACTORS FOR MODEL NO.(2)

RUN NO	FLOW RATE (m3/s)	WATER DEPTH (m)	CALCULATED SIDE SLOPE SAFETY FACTOR							
			METHOD (1)	METHOD (2)	METHOD (3)	METHOD (4)	METHOD (5)	METHOD (6)	METHOD (7)	METHOD (8)
M2R 1	0.057	0.146	0.733	0.934	0.946	0.991	0.991	0.950	1.050	0.960
M2R 2	0.072	0.163	0.645	0.909	0.923	0.978	0.972	0.925	1.041	0.935
M2R 3	0.074	0.163	0.681	0.906	0.920	0.984	0.969	0.922	1.040	0.932
M2R 4	0.094	0.184	0.570	0.885	0.901	0.965	0.951	0.900	1.032	0.910
M2R 5	0.111	0.199	0.525	0.863	0.881	0.956	0.931	0.877	1.023	0.887
M2R 6	0.119	0.208	0.504	0.865	0.884	0.951	0.934	0.880	1.024	0.890
M2R 7	0.137	0.221	0.467	0.846	0.866	0.940	0.916	0.859	1.016	0.868
M2R 8	0.143	0.226	0.456	0.842	0.863	0.937	0.913	0.855	1.015	0.864
M2R 9	0.146	0.229	0.461	0.845	0.865	0.939	0.915	0.858	1.016	0.868
M2R10	0.156	0.237	0.372	0.838	0.859	0.903	0.909	0.851	1.013	0.860
M2R11	0.162	0.239	0.462	0.828	0.850	0.940	0.899	0.839	1.009	0.848
M2R12	0.167	0.244	0.374	0.829	0.850	0.904	0.900	0.840	1.009	0.849
M2R13	0.177	0.249	0.389	0.817	0.839	0.912	0.888	0.825	1.004	0.834
M2R14	0.184	0.256	0.393	0.819	0.841	0.914	0.890	0.828	1.005	0.837
M2R15	0.194	0.262	0.405	0.815	0.837	0.920	0.886	0.823	1.003	0.832
M2R16	0.199	0.266	0.398	0.814	0.836	0.917	0.885	0.822	1.003	0.831
M2R17	0.206	0.271	0.395	0.813	0.836	0.916	0.884	0.821	1.002	0.831
M2R18	0.215	0.291	0.428	0.848	0.869	0.931	0.919	0.862	1.017	0.872
M2R19	0.213	0.278	0.371	0.819	0.842	0.906	0.891	0.829	1.005	0.838
M2R20	0.217	0.274	0.340	0.794	0.818	0.889	0.865	0.799	0.994	0.807
M2R21	0.216	0.273	0.339	0.795	0.819	0.889	0.865	0.800	0.994	0.808

TABLE 7 - 3 : SUMMARY OF THE PREDICTED SIDE SLOPE SAFETY FACTORS FOR MODEL NO.(3)

RUN NO	FLOW RATE (m3/s)	WATER DEPTH (m)	CALCULATED SIDE SLOPE SAFETY FACTOR							
			METHOD (1)	METHOD (2)	METHOD (3)	METHOD (4)	METHOD (5)	METHOD (6)	METHOD (7)	METHOD (8)
M3R 1	0.043	0.108	0.886	0.901	0.913	1.004	0.962	0.914	1.036	0.925
M3R 2	0.055	0.125	0.768	0.891	0.905	0.991	0.955	0.905	1.033	0.916
M3R 3	0.063	0.134	0.772	0.870	0.887	0.993	0.937	0.884	1.025	0.895
M3R 4	0.079	0.153	0.653	0.862	0.880	0.976	0.930	0.876	1.022	0.887
M3R 5	0.085	0.162	0.616	0.866	0.884	0.970	0.935	0.881	1.024	0.892
M3R 6	0.092	0.166	0.617	0.847	0.867	0.971	0.917	0.860	1.016	0.871
M3R 7	0.098	0.171	0.574	0.844	0.865	0.962	0.915	0.857	1.016	0.869
M3R 8	0.107	0.180	0.570	0.834	0.855	0.962	0.905	0.846	1.011	0.858
M3R 9	0.114	0.188	0.556	0.836	0.857	0.960	0.907	0.848	1.012	0.860
M3R10	0.128	0.197	0.530	0.819	0.842	0.954	0.891	0.829	1.005	0.840
M3R11	0.135	0.203	0.497	0.816	0.839	0.946	0.888	0.826	1.004	0.837
M3R12	0.139	0.210	0.470	0.827	0.850	0.938	0.899	0.839	1.009	0.851
M3R13	0.142	0.212	0.466	0.825	0.848	0.937	0.897	0.836	1.008	0.848
M3R14	0.151	0.219	0.461	0.818	0.841	0.936	0.890	0.828	1.005	0.840
M3R15	0.161	0.223	0.458	0.802	0.827	0.936	0.874	0.810	0.998	0.821
M3R16	0.171	0.233	0.435	0.806	0.831	0.928	0.879	0.815	1.000	0.826
M3R17	0.178	0.237	0.428	0.800	0.825	0.926	0.872	0.807	0.997	0.818
M3R18	0.192	0.248	0.408	0.799	0.824	0.918	0.872	0.807	0.997	0.818
M3R19	0.196	0.253	0.392	0.805	0.830	0.912	0.878	0.814	1.000	0.826
M3R20	0.211	0.257	0.362	0.780	0.807	0.898	0.852	0.784	0.988	0.795
M3R21	0.216	0.260	0.392	0.778	0.805	0.912	0.849	0.781	0.987	0.792
M3R22	0.222	0.263	0.389	0.775	0.801	0.911	0.846	0.777	0.986	0.787

TABLE 7-4 : SUMMARY OF THE PREDICTED SIDE SLOPE SAFETY FACTORS FOR MODEL NO.(4)

RUN NO	FLOW RATE (m3/s)	WATER DEPTH (m)	CALCULATED SIDE SLOPE SAFETY FACTOR							
			METHOD (1)	METHOD (2)	METHOD (3)	METHOD (4)	METHOD (5)	METHOD (6)	METHOD (7)	METHOD (8)
M4R 1	0.061	0.102	0.655	0.774	0.795	0.962	0.838	0.768	0.983	0.777
M4R 2	0.063	0.103	0.644	0.766	0.787	0.960	0.829	0.758	0.979	0.766
M4R 3	0.065	0.107	0.620	0.779	0.800	0.956	0.845	0.775	0.985	0.784
M4R 4	0.066	0.109	0.610	0.775	0.798	0.954	0.841	0.772	0.984	0.781
M4R 5	0.073	0.112	0.597	0.747	0.771	0.952	0.810	0.735	0.970	0.743
M4R 6	0.077	0.116	0.573	0.747	0.772	0.947	0.810	0.736	0.971	0.744
M4R 7	0.080	0.119	0.560	0.745	0.771	0.944	0.809	0.735	0.970	0.743
M4R 8	0.081	0.122	0.548	0.752	0.778	0.941	0.817	0.744	0.974	0.752
M4R 9	0.084	0.125	0.535	0.754	0.780	0.938	0.820	0.747	0.975	0.756
M4R10	0.090	0.127	0.527	0.728	0.756	0.936	0.790	0.713	0.962	0.720
M4R11	0.091	0.129	0.517	0.737	0.765	0.934	0.802	0.726	0.967	0.734
M4R12	0.096	0.134	0.498	0.736	0.764	0.929	0.801	0.725	0.967	0.733
M4R13	0.102	0.137	0.488	0.719	0.749	0.927	0.781	0.703	0.958	0.710
M4R14	0.103	0.142	0.474	0.743	0.772	0.922	0.810	0.736	0.971	0.744
M4R15	0.104	0.139	0.482	0.718	0.747	0.925	0.780	0.701	0.958	0.708
M4R16	0.110	0.146	0.459	0.730	0.759	0.918	0.795	0.718	0.964	0.726
M4R17	0.116	0.150	0.447	0.724	0.754	0.914	0.789	0.711	0.961	0.719
M4R18	0.121	0.153	0.439	0.712	0.743	0.911	0.774	0.695	0.955	0.702
M4R19	0.125	0.156	0.432	0.710	0.742	0.909	0.773	0.693	0.955	0.700
M4R20	0.132	0.159	0.423	0.694	0.726	0.906	0.752	0.669	0.946	0.676
M4R21	0.135	0.161	0.417	0.692	0.725	0.904	0.751	0.668	0.945	0.674
M4R22	0.142	0.165	0.410	0.681	0.715	0.901	0.737	0.652	0.939	0.658
M4R23	0.144	0.167	0.403	0.687	0.721	0.898	0.745	0.661	0.943	0.667
M4R24	0.148	0.170	0.396	0.688	0.722	0.896	0.746	0.662	0.943	0.669
M4R25	0.149	0.172	0.393	0.690	0.724	0.895	0.749	0.666	0.945	0.672
M4R26	0.153	0.172	0.393	0.677	0.711	0.895	0.732	0.646	0.937	0.652
M4R27	0.153	0.174	0.389	0.683	0.717	0.893	0.739	0.655	0.940	0.661
M4R28	0.156	0.175	0.386	0.676	0.711	0.892	0.731	0.645	0.937	0.651
M4R29	0.158	0.177	0.383	0.678	0.712	0.890	0.733	0.647	0.938	0.653
M4R30	0.161	0.179	0.377	0.679	0.714	0.888	0.735	0.650	0.939	0.656
M4R31	0.168	0.184	0.368	0.681	0.716	0.884	0.738	0.653	0.940	0.659
M4R32	0.176	0.189	0.359	0.674	0.709	0.880	0.729	0.643	0.936	0.649
M4R33	0.179	0.191	0.355	0.673	0.709	0.878	0.729	0.642	0.936	0.648

TABLE 7-5 : SUMMARY OF THE PREDICTED SIDE SLOPE SAFETY FACTORS FOR MODEL NO.(5)

RUN NO	FLOW RATE (m3/s)	WATER DEPTH (m)	CALCULATED SIDE SLOPE SAFETY FACTOR							
			METHOD (1)	METHOD (2)	METHOD (3)	METHOD (4)	METHOD (5)	METHOD (6)	METHOD (7)	METHOD (8)
M5R 1	0.012	0.035	1.894	0.891	0.870	1.048	0.920	0.863	1.018	0.871
M5R 2	0.013	0.037	1.790	0.893	0.874	1.045	0.925	0.869	1.020	0.877
M5R 3	0.019	0.050	1.329	0.874	0.869	1.026	0.919	0.862	1.018	0.870
M5R 4	0.022	0.054	1.242	0.861	0.859	1.021	0.909	0.851	1.013	0.858
M5R 5	0.023	0.056	1.200	0.854	0.854	1.018	0.903	0.844	1.011	0.851
M5R 6	0.024	0.057	1.165	0.844	0.845	1.016	0.894	0.833	1.007	0.840
M5R 7	0.025	0.058	1.146	0.839	0.841	1.015	0.890	0.828	1.005	0.835
M5R 8	0.029	0.064	1.036	0.829	0.834	1.007	0.882	0.819	1.002	0.826
M5R 9	0.036	0.074	0.903	0.825	0.836	0.995	0.884	0.821	1.002	0.828
M5R10	0.037	0.076	0.883	0.815	0.827	0.993	0.874	0.810	0.998	0.816
M5R11	0.043	0.081	0.823	0.796	0.810	0.986	0.856	0.788	0.990	0.795
M5R12	0.044	0.083	0.801	0.797	0.812	0.983	0.858	0.790	0.991	0.797
M5R13	0.045	0.084	0.792	0.794	0.810	0.982	0.855	0.788	0.990	0.794
M5R14	0.047	0.085	0.782	0.782	0.798	0.981	0.842	0.772	0.984	0.778
M5R15	0.051	0.091	0.731	0.788	0.806	0.974	0.851	0.783	0.988	0.789
M5R16	0.054	0.094	0.710	0.779	0.798	0.971	0.842	0.772	0.984	0.778
M5R17	0.057	0.099	0.676	0.784	0.804	0.966	0.848	0.780	0.987	0.786
M5R18	0.060	0.100	0.671	0.764	0.785	0.965	0.826	0.755	0.978	0.760
M5R19	0.066	0.108	0.618	0.771	0.794	0.956	0.837	0.766	0.982	0.772
M5R20	0.069	0.110	0.605	0.763	0.786	0.953	0.828	0.756	0.978	0.761
M5R21	0.077	0.118	0.563	0.763	0.788	0.945	0.830	0.759	0.979	0.764
M5R22	0.081	0.120	0.555	0.748	0.773	0.943	0.812	0.738	0.972	0.743
M5R23	0.084	0.125	0.533	0.754	0.780	0.938	0.821	0.748	0.975	0.753
M5R24	0.088	0.127	0.527	0.740	0.767	0.936	0.804	0.729	0.968	0.733
M5R25	0.094	0.131	0.508	0.734	0.762	0.932	0.797	0.721	0.965	0.726
M5R26	0.099	0.136	0.491	0.730	0.759	0.927	0.794	0.717	0.964	0.722
M5R27	0.106	0.142	0.470	0.727	0.756	0.921	0.791	0.714	0.963	0.718
M5R28	0.112	0.146	0.458	0.723	0.753	0.917	0.787	0.709	0.961	0.713
M5R29	0.117	0.151	0.444	0.720	0.751	0.913	0.785	0.706	0.960	0.710
M5R30	0.122	0.153	0.438	0.711	0.743	0.911	0.774	0.694	0.955	0.698
M5R31	0.126	0.157	0.429	0.707	0.739	0.908	0.769	0.688	0.953	0.692
M5R32	0.130	0.159	0.424	0.703	0.735	0.906	0.764	0.683	0.951	0.686
M5R33	0.133	0.160	0.421	0.695	0.728	0.905	0.754	0.671	0.947	0.674
M5R34	0.136	0.162	0.415	0.694	0.727	0.903	0.752	0.670	0.946	0.673
M5R35	0.140	0.164	0.412	0.684	0.718	0.902	0.740	0.656	0.941	0.658
M5R36	0.142	0.165	0.408	0.683	0.717	0.900	0.739	0.654	0.941	0.657

TABLE 7- 6 : SUMMARY OF THE PREDICTED SIDE SLOPE SAFETY FACTORS FOR MODEL NO.(6)

RUN NO	FLOW RATE (m3/s)	WATER DEPTH (m)	CALCULATED SIDE SLOPE SAFETY FACTOR							
			METHOD (1)	METHOD (2)	METHOD (3)	METHOD (4)	METHOD (5)	METHOD (6)	METHOD (7)	METHOD (8)
M6R 1	0.011	0.036	2.291	0.973	0.953	1.095	1.011	0.961	1.048	0.767
M6R 2	0.014	0.041	2.008	0.938	0.922	1.085	0.981	0.926	1.036	0.729
M6R 3	0.019	0.051	1.620	0.924	0.919	1.066	0.978	0.922	1.045	0.758
M6R 4	0.023	0.057	1.445	0.908	0.908	1.054	0.967	0.910	1.044	0.753
M6R 5	0.027	0.064	1.297	0.895	0.900	1.043	0.959	0.900	1.043	0.750
M6R 6	0.035	0.072	1.133	0.852	0.862	1.027	0.918	0.854	1.025	0.693
M6R 7	0.047	0.087	0.948	0.824	0.841	1.005	0.894	0.826	1.018	0.670
M6R 8	0.063	0.106	0.776	0.814	0.838	0.976	0.890	0.822	1.021	0.680
M6R 9	0.069	0.108	0.760	0.775	0.801	0.973	0.846	0.772	1.000	0.610
M6R10	0.073	0.116	0.706	0.800	0.826	0.962	0.877	0.807	1.017	0.666
M6R11	0.080	0.121	0.675	0.784	0.812	0.954	0.859	0.787	1.009	0.641
M6R12	0.083	0.122	0.671	0.766	0.795	0.953	0.838	0.763	0.999	0.607
M6R13	0.087	0.127	0.645	0.776	0.805	0.947	0.851	0.777	1.006	0.631
M6R14	0.093	0.133	0.615	0.775	0.805	0.939	0.851	0.778	1.007	0.634
M6R15	0.100	0.138	0.594	0.759	0.791	0.933	0.833	0.757	0.999	0.608
M6R16	0.104	0.140	0.587	0.748	0.780	0.931	0.819	0.742	0.993	0.588
M6R17	0.107	0.144	0.574	0.750	0.783	0.927	0.823	0.746	0.995	0.595
M6R18	0.110	0.146	0.563	0.754	0.786	0.923	0.827	0.751	0.997	0.603
M6R19	0.115	0.148	0.557	0.735	0.768	0.921	0.804	0.725	0.987	0.568
M6R20	0.119	0.153	0.540	0.743	0.776	0.915	0.815	0.737	0.992	0.586
M6R21	0.124	0.156	0.530	0.738	0.772	0.911	0.809	0.730	0.990	0.579
M6R22	0.130	0.158	0.523	0.719	0.754	0.909	0.786	0.704	0.979	0.544

TABLE 7-7 : SUMMARY OF SIDE SLOPE PROBABILITY

OF ADEQUACY PREDICTED FOR MODEL NO.(1)

RUN NO	FLOW RATE (m3/s)	WATER DEPTH (m)	PREDICTED PROBABILITY OF ADEQUACY			
			METHOD (1)	METHOD (2)	METHOD (3)	METHOD (4)
M1R 1	0.0167	0.0979	0.7468	0.9976	1.0000	0.9999
M1R 2	0.0215	0.1066	0.7160	0.9451	1.0000	0.9888
M1R 3	0.0268	0.1155	0.6869	0.7874	1.0000	0.8999
M1R 4	0.0331	0.1243	0.6585	0.5708	1.0000	0.6984
M1R 5	0.0354	0.1321	0.6473	0.6282	1.0000	0.7585
M1R 6	0.0392	0.1371	0.6332	0.5259	1.0000	0.6486
M1R 7	0.0449	0.1461	0.6133	0.4428	1.0000	0.5511
M1R 8	0.0480	0.1533	0.6033	0.4591	1.0000	0.5707
M1R 9	0.0564	0.1604	0.5805	0.2988	0.9993	0.3697
M1R10	0.0607	0.1653	0.5698	0.2607	0.9979	0.3200
M1R11	0.0642	0.1679	0.5614	0.2204	0.9941	0.2672
M1R12	0.0673	0.1745	0.5544	0.2361	0.9961	0.2878
M1R13	0.0722	0.1789	0.5441	0.2014	0.9903	0.2423
M1R14	0.0760	0.1870	0.5369	0.2224	0.9943	0.2697
M1R15	0.0811	0.1912	0.5274	0.1908	0.9872	0.2283
M1R16	0.0853	0.1956	0.5200	0.1775	0.9819	0.2110
M1R17	0.0885	0.2005	0.5148	0.1795	0.9828	0.2136
M1R18	0.0925	0.2038	0.5084	0.1646	0.9748	0.1941
M1R19	0.0985	0.2095	0.4992	0.1490	0.9624	0.1738
M1R20	0.1065	0.2157	0.4876	0.1274	0.9346	0.1460
M1R21	0.1092	0.2191	0.4841	0.1273	0.9345	0.1459
M1R22	0.1127	0.2210	0.4793	0.1166	0.9139	0.1322
M1R23	0.1188	0.2268	0.4718	0.1106	0.8999	0.1247
M1R24	0.1239	0.2316	0.4658	0.1063	0.8882	0.1193
M1R25	0.1281	0.2333	0.4606	0.0955	0.8533	0.1058
M1R26	0.1344	0.2379	0.4535	0.0883	0.8239	0.0968
M1R27	0.1386	0.2423	0.4494	0.0882	0.8233	0.0966
M1R28	0.1437	0.2475	0.4445	0.0875	0.8204	0.0958
M1R29	0.1478	0.2525	0.4412	0.0900	0.8311	0.0989
M1R30	0.1555	0.2576	0.4338	0.0825	0.7964	0.0897
M1R31	0.1601	0.2622	0.4300	0.0824	0.7960	0.0896
M1R32	0.1667	0.2650	0.4237	0.0742	0.7497	0.0795
M1R33	0.1715	0.2681	0.4195	0.0709	0.7283	0.0755
M1R34	0.1771	0.2728	0.4153	0.0699	0.7219	0.0744
M1R35	0.1840	0.2774	0.4099	0.0665	0.6977	0.0703
M1R36	0.1886	0.2814	0.4069	0.0666	0.6979	0.0704
M1R37	0.1942	0.2856	0.4030	0.0652	0.6880	0.0688
M1R38	0.2020	0.2914	0.3978	0.0636	0.6750	0.0668
M1R39	0.2136	0.2945	0.3886	0.0535	0.5861	0.0549
M1R40	0.2191	0.2984	0.3853	0.0529	0.5799	0.0542

TABLE 7-8 : SUMMARY OF SIDE SLOPE PROBABILITY

OF ADEQUACY PREDICTED FOR MODEL NO.(2)

RUN NO	FLOW RATE (m3/s)	WATER DEPTH (m)	PREDICTED PROBABILITY OF ADEQUACY			
			METHOD (1)	METHOD (2)	METHOD (3)	METHOD (4)
M2R 1	0.0572	0.1463	0.5810	0.1326	0.9425	0.1554
M2R 2	0.0725	0.1630	0.5441	0.0933	0.8441	0.1046
M2R 3	0.0735	0.1635	0.5420	0.0892	0.8274	0.0995
M2R 4	0.0938	0.1844	0.5040	0.0689	0.7139	0.0742
M2R 5	0.1114	0.1988	0.4775	0.0543	0.5931	0.0566
M2R 6	0.1191	0.2080	0.4677	0.0559	0.6082	0.0585
M2R 7	0.1369	0.2208	0.4465	0.0463	0.5093	0.0472
M2R 8	0.1431	0.2258	0.4400	0.0448	0.4928	0.0456
M2R 9	0.1459	0.2294	0.4373	0.0460	0.5060	0.0469
M2R10	0.1558	0.2367	0.4277	0.0433	0.4749	0.0438
M2R11	0.1619	0.2391	0.4216	0.0396	0.4299	0.0396
M2R12	0.1669	0.2437	0.4175	0.0398	0.4321	0.0398
M2R13	0.1771	0.2488	0.4084	0.0359	0.3823	0.0354
M2R14	0.1843	0.2556	0.4031	0.0367	0.3919	0.0362
M2R15	0.1943	0.2625	0.3957	0.0354	0.3757	0.0349
M2R16	0.1987	0.2657	0.3926	0.0352	0.3723	0.0346
M2R17	0.2062	0.2714	0.3877	0.0350	0.3698	0.0344
M2R18	0.2146	0.2905	0.3864	0.0475	0.5232	0.0487
M2R19	0.2125	0.2785	0.3843	0.0368	0.3935	0.0364
M2R20	0.2174	0.2740	0.3790	0.0303	0.3054	0.0292
M2R21	0.2157	0.2730	0.3801	0.0305	0.3081	0.0294

TABLE 7-9 : SUMMARY OF SIDE SLOPE PROBABILITY OF ADEQUACY PREDICTED FOR MODEL NO.(3)

RUN NO	FLOW RATE (m3/s)	WATER DEPTH (m)	PREDICTED PROBABILITY OF ADEQUACY			
			METHOD (1)	METHOD (2)	METHOD (3)	METHOD (4)
M3R 1	0.0429	0.1082	0.6434	0.0804	0.7837	0.0906
M3R 2	0.0547	0.1255	0.5991	0.0723	0.7359	0.0803
M3R 3	0.0634	0.1340	0.5749	0.0579	0.6255	0.0623
M3R 4	0.0788	0.1530	0.5369	0.0536	0.5854	0.0571
M3R 5	0.0849	0.1618	0.5240	0.0563	0.6115	0.0604
M3R 6	0.0924	0.1661	0.5107	0.0466	0.5122	0.0486
M3R 7	0.0975	0.1715	0.5018	0.0456	0.5014	0.0475
M3R 8	0.1070	0.1795	0.4869	0.0417	0.4554	0.0429
M3R 9	0.1145	0.1879	0.4760	0.0425	0.4641	0.0437
M3R10	0.1275	0.1969	0.4590	0.0368	0.3931	0.0371
M3R11	0.1347	0.2032	0.4504	0.0360	0.3830	0.0362
M3R12	0.1389	0.2102	0.4461	0.0396	0.4292	0.0404
M3R13	0.1417	0.2122	0.4430	0.0388	0.4191	0.0395
M3R14	0.1509	0.2188	0.4334	0.0367	0.3916	0.0370
M3R15	0.1606	0.2230	0.4236	0.0325	0.3347	0.0321
M3R16	0.1714	0.2335	0.4143	0.0335	0.3497	0.0334
M3R17	0.1778	0.2369	0.4087	0.0319	0.3273	0.0315
M3R18	0.1919	0.2483	0.3979	0.0319	0.3269	0.0315
M3R19	0.1958	0.2532	0.3957	0.0334	0.3477	0.0332
M3R20	0.2108	0.2571	0.3837	0.0279	0.2706	0.0270
M3R21	0.2158	0.2602	0.3804	0.0275	0.2649	0.0266
M3R22	0.2216	0.2633	0.3765	0.0268	0.2558	0.0259

TABLE 7-10 : SUMMARY OF SIDE SLOPE PROBABILITY OF ADEQUACY PREDICTED FOR MODEL NO.(4)

RUN NO	FLOW RATE (m3/s)	WATER DEPTH (m)	PREDICTED PROBABILITY OF ADEQUACY			
			METHOD (1)	METHOD (2)	METHOD (3)	METHOD (4)
M4R 1	0.0610	0.1021	0.6159	0.0257	0.2400	0.0244
M4R 2	0.0631	0.1034	0.6099	0.0244	0.2210	0.0229
M4R 3	0.0647	0.1071	0.6019	0.0266	0.2535	0.0254
M4R 4	0.0664	0.1087	0.5967	0.0261	0.2464	0.0248
M4R 5	0.0729	0.1119	0.5814	0.0220	0.1877	0.0204
M4R 6	0.0771	0.1164	0.5693	0.0221	0.1889	0.0205
M4R 7	0.0799	0.1192	0.5618	0.0219	0.1869	0.0204
M4R 8	0.0815	0.1218	0.5567	0.0229	0.2000	0.0214
M4R 9	0.0839	0.1247	0.5501	0.0232	0.2045	0.0217
M4R10	0.0898	0.1267	0.5395	0.0201	0.1606	0.0184
M4R11	0.0905	0.1289	0.5366	0.0212	0.1760	0.0196
M4R12	0.0961	0.1341	0.5247	0.0211	0.1747	0.0195
M4R13	0.1016	0.1367	0.5152	0.0193	0.1504	0.0176
M4R14	0.1026	0.1416	0.5109	0.0221	0.1890	0.0205
M4R15	0.1038	0.1385	0.5110	0.0192	0.1485	0.0175
M4R16	0.1099	0.1460	0.4987	0.0205	0.1668	0.0189
M4R17	0.1158	0.1504	0.4891	0.0199	0.1589	0.0183
M4R18	0.1210	0.1528	0.4816	0.0188	0.1428	0.0171
M4R19	0.1246	0.1557	0.4760	0.0186	0.1410	0.0169
M4R20	0.1319	0.1588	0.4665	0.0172	0.1220	0.0155
M4R21	0.1354	0.1615	0.4616	0.0171	0.1208	0.0154
M4R22	0.1420	0.1647	0.4534	0.0163	0.1100	0.0145
M4R23	0.1439	0.1672	0.4507	0.0167	0.1159	0.0150
M4R24	0.1475	0.1703	0.4461	0.0168	0.1170	0.0151
M4R25	0.1488	0.1717	0.4445	0.0170	0.1196	0.0153
M4R26	0.1528	0.1723	0.4402	0.0160	0.1065	0.0143
M4R27	0.1535	0.1738	0.4392	0.0164	0.1119	0.0147
M4R28	0.1564	0.1748	0.4361	0.0160	0.1061	0.0142
M4R29	0.1585	0.1766	0.4337	0.0161	0.1074	0.0143
M4R30	0.1614	0.1791	0.4304	0.0162	0.1088	0.0144
M4R31	0.1636	0.1840	0.4237	0.0163	0.1107	0.0146
M4R32	0.1760	0.1886	0.4155	0.0158	0.1045	0.0141
M4R33	0.1794	0.1909	0.4122	0.0158	0.1043	0.0141

TABLE 7-11: SUMMARY OF SIDE SLOPE PROBABILITY OF ADEQUACY PREDICTED FOR MODEL NO.(5)

RUN NO	FLOW RATE (m3/s)	WATER DEPTH (m)	PREDICTED PROBABILITY OF ADEQUACY			
			METHOD (1)	METHOD (2)	METHOD (3)	METHOD (4)
M5R 1	0.0117	0.0353	0.9505	0.0480	0.5301	0.0484
M5R 2	0.0125	0.0373	0.9389	0.0506	0.5568	0.0512
M5R 3	0.0191	0.0501	0.8596	0.0477	0.5262	0.0480
M5R 4	0.0215	0.0536	0.8377	0.0433	0.4754	0.0430
M5R 5	0.0229	0.0556	0.8254	0.0410	0.4485	0.0405
M5R 6	0.0244	0.0573	0.8148	0.0379	0.4093	0.0370
M5R 7	0.0252	0.0582	0.8088	0.0365	0.3911	0.0355
M5R 8	0.0293	0.0643	0.7754	0.0345	0.3640	0.0333
M5R 9	0.0355	0.0738	0.7296	0.0349	0.3699	0.0338
M5R10	0.0374	0.0755	0.7205	0.0324	0.3354	0.0310
M5R11	0.0427	0.0811	0.6938	0.0286	0.2817	0.0269
M5R12	0.0442	0.0833	0.6853	0.0289	0.2865	0.0273
M5R13	0.0451	0.0843	0.6811	0.0284	0.2800	0.0268
M5R14	0.0470	0.0853	0.6747	0.0262	0.2475	0.0244
M5R15	0.0510	0.0913	0.6540	0.0277	0.2691	0.0260
M5R16	0.0539	0.0940	0.6430	0.0262	0.2477	0.0244
M5R17	0.0571	0.0986	0.6287	0.0273	0.2634	0.0256
M5R18	0.0600	0.0996	0.6217	0.0240	0.2166	0.0221
M5R19	0.0664	0.1080	0.5976	0.0254	0.2372	0.0236
M5R20	0.0694	0.1103	0.5895	0.0242	0.2192	0.0223
M5R21	0.0766	0.1184	0.5679	0.0245	0.2234	0.0226
M5R22	0.0806	0.1203	0.5597	0.0223	0.1921	0.0204
M5R23	0.0844	0.1253	0.5490	0.0233	0.2062	0.0214
M5R24	0.0880	0.1267	0.5422	0.0214	0.1797	0.0195
M5R25	0.0936	0.1313	0.5302	0.0208	0.1708	0.0188
M5R26	0.0989	0.1358	0.5195	0.0204	0.1662	0.0185
M5R27	0.1063	0.1423	0.5054	0.0202	0.1624	0.0182
M5R28	0.1115	0.1464	0.4964	0.0198	0.1571	0.0178
M5R29	0.1173	0.1512	0.4868	0.0196	0.1545	0.0176
M5R30	0.1216	0.1533	0.4806	0.0187	0.1424	0.0167
M5R31	0.1263	0.1565	0.4738	0.0183	0.1374	0.0164
M5R32	0.1295	0.1585	0.4693	0.0180	0.1326	0.0160
M5R33	0.1329	0.1599	0.4649	0.0173	0.1237	0.0153
M5R34	0.1362	0.1623	0.4605	0.0172	0.1225	0.0153
M5R35	0.1400	0.1636	0.4559	0.0165	0.1127	0.0145
M5R36	0.1424	0.1653	0.4528	0.0164	0.1120	0.0145

TABLE 7-12 : SUMMARY OF SIDE SLOPE PROBABILITY

OF ADEQUACY PREDICTED FOR MODEL NO.(6)

RUN NO	FLOW RATE (m3/s)	WATER DEPTH (m)	PREDICTED PROBABILITY OF ADEQUACY			
			METHOD (1)	METHOD (2)	METHOD (3)	METHOD (4)
M6R 1	0.0107	0.0358	0.9491	0.0784	0.8470	0.0704
M6R 2	0.0139	0.0409	0.9175	0.0560	0.6997	0.0491
M6R 3	0.0189	0.0506	0.8577	0.0541	0.6860	0.0477
M6R 4	0.0226	0.0567	0.8213	0.0489	0.6342	0.0429
M6R 5	0.0271	0.0636	0.7830	0.0453	0.5940	0.0396
M6R 6	0.0350	0.0725	0.7349	0.0334	0.4305	0.0286
M6R 7	0.0468	0.0866	0.6723	0.0288	0.3564	0.0244
M6R 8	0.0626	0.1058	0.6074	0.0281	0.3470	0.0239
M6R 9	0.0687	0.1079	0.5938	0.0225	0.2485	0.0188
M6R10	0.0731	0.1162	0.5761	0.0261	0.3134	0.0221
M6R11	0.0799	0.1214	0.5596	0.0240	0.2755	0.0202
M6R12	0.0832	0.1223	0.5534	0.0217	0.2353	0.0181
M6R13	0.0866	0.1272	0.5439	0.0230	0.2585	0.0193
M6R14	0.0926	0.1332	0.5304	0.0230	0.2589	0.0193
M6R15	0.1000	0.1380	0.5166	0.0212	0.2274	0.0177
M6R16	0.1038	0.1399	0.5101	0.0201	0.2073	0.0167
M6R17	0.1073	0.1436	0.5033	0.0204	0.2122	0.0170
M6R18	0.1098	0.1464	0.4986	0.0207	0.2191	0.0173
M6R19	0.1150	0.1481	0.4911	0.0189	0.1874	0.0157
M6R20	0.1192	0.1530	0.4837	0.0197	0.2011	0.0164
M6R21	0.1235	0.1560	0.4773	0.0193	0.1936	0.0160
M6R22	0.1296	0.1580	0.4694	0.0177	0.1663	0.0146

TABLE 7-13: SUMMARY OF RESULTS OBTAINED FROM MODEL NO.(1)

RUN NO	Q (m3/s)	Y (m)	So x10^3	Sw x10^3	Se x10^3	Re x10^6	F_r	n (s/m$^{1/3}$)	f	C (m$^{1/2}$/s)
M1R 1	0.017	0.098	5.00	4.93	4.94	0.075	0.368	0.039	0.292	16.40
M1R 2	0.021	0.107	5.00	5.43	5.36	0.093	0.410	0.037	0.255	17.55
M1R 3	0.027	0.115	5.00	5.35	5.28	0.111	0.448	0.034	0.211	19.30
M1R 4	0.033	0.124	5.00	5.54	5.41	0.132	0.487	0.032	0.183	20.71
M1R 5	0.035	0.122	5.00	5.50	5.39	0.137	0.469	0.034	0.196	20.00
M1R 6	0.039	0.137	5.00	5.58	5.44	0.148	0.487	0.033	0.183	20.68
M1R 7	0.045	0.146	5.00	5.73	5.54	0.164	0.500	0.032	0.177	21.04
M1R 8	0.048	0.153	5.00	5.28	5.22	0.171	0.491	0.032	0.173	21.31
M1R 9	0.056	0.160	5.00	5.59	5.42	0.195	0.532	0.030	0.153	22.65
M1R10	0.061	0.165	5.00	5.31	5.22	0.206	0.544	0.029	0.141	23.56
M1R11	0.064	0.168	5.00	5.53	5.36	0.217	0.560	0.029	0.137	23.94
M1R12	0.067	0.174	5.00	5.48	5.33	0.222	0.548	0.030	0.142	23.50
M1R13	0.072	0.179	5.00	5.47	5.32	0.234	0.562	0.029	0.135	24.14
M1R14	0.076	0.187	5.00	5.59	5.41	0.240	0.547	0.030	0.145	23.26
M1R15	0.081	0.191	5.00	5.30	5.21	0.253	0.560	0.029	0.133	24.32
M1R16	0.085	0.196	5.00	4.74	4.82	0.262	0.565	0.028	0.121	25.50
M1R17	0.089	0.200	5.00	4.95	4.97	0.268	0.561	0.028	0.126	24.95
M1R18	0.092	0.204	5.00	4.96	4.97	0.276	0.569	0.028	0.123	25.26
M1R19	0.098	0.209	5.00	4.92	4.95	0.289	0.576	0.028	0.119	25.67
M1R20	0.106	0.216	5.00	5.36	5.24	0.307	0.591	0.028	0.120	25.56
M1R21	0.109	0.219	5.00	5.19	5.12	0.312	0.589	0.028	0.118	25.76
M1R22	0.113	0.221	5.00	5.72	5.47	0.320	0.598	0.028	0.122	25.33
M1R23	0.119	0.227	5.00	4.86	4.91	0.331	0.601	0.027	0.109	26.85
M1R24	0.124	0.232	5.00	5.14	5.09	0.341	0.603	0.027	0.112	26.47
M1R25	0.128	0.233	5.00	4.89	4.93	0.350	0.615	0.026	0.104	27.43
M1R26	0.134	0.238	5.00	5.10	5.06	0.363	0.622	0.026	0.105	27.39
M1R27	0.139	0.242	5.00	4.85	4.91	0.369	0.620	0.026	0.102	27.72
M1R28	0.144	0.247	5.00	5.05	5.03	0.378	0.618	0.027	0.105	27.29
M1R29	0.148	0.253	5.00	4.95	4.97	0.383	0.612	0.027	0.106	27.19
M1R30	0.155	0.258	5.00	5.26	5.16	0.397	0.620	0.027	0.107	27.03
M1R31	0.160	0.262	5.00	4.97	4.98	0.404	0.618	0.027	0.10	27.41
M1R32	0.167	0.265	5.00	5.46	5.28	0.418	0.630	0.027	0.106	27.15
M1R33	0.172	0.268	5.00	5.10	5.06	0.426	0.634	0.026	0.101	27.93
M1R34	0.177	0.273	5.00	5.11	5.07	0.435	0.634	0.026	0.101	27.88
M1R35	0.184	0.277	5.00	4.90	4.94	0.447	0.638	0.026	0.097	28.44
M1R36	0.189	0.281	5.00	4.85	4.91	0.453	0.636	0.026	0.097	28.43
M1R37	0.194	0.286	5.00	4.95	4.97	0.462	0.637	0.026	0.098	28.29
M1R38	0.202	0.291	5.00	4.91	4.95	0.473	0.637	0.026	0.097	28.39
M1R39	0.214	0.294	5.00	5.73	5.41	0.497	0.661	0.026	0.099	28.13
M1R40	0.219	0.298	5.00	5.60	5.34	0.505	0.660	0.026	0.098	28.30

TABLE 7-14: SUMMARY OF RESULTS OBTAINED FROM MODEL NO.(2)

RUN NO	Q (m3/s)	Y (m)	So x10^3	Sw x10^3	Se x10^3	Re x10^6	F_r	n (S/ m$^{1/3}$)	f	C (m$^{1/2}$/s)
M2R 1	0.057	0.146	8.00	7.84	7.90	0.198	0.635	0.030	0.157	22.36
M2R 2	0.072	0.163	8.00	8.18	8.10	0.235	0.666	0.030	0.146	23.18
M2R 3	0.074	0.163	8.00	7.36	7.65	0.238	0.672	0.029	0.136	24.05
M2R 4	0.094	0.184	8.00	8.24	8.13	0.283	0.692	0.029	0.136	24.03
M2R 5	0.111	0.199	8.00	8.42	8.20	0.320	0.717	0.029	0.128	24.80
M2R 6	0.119	0.208	8.00	8.38	8.19	0.332	0.706	0.029	0.132	24.43
M2R 7	0.137	0.221	8.00	8.83	8.39	0.368	0.728	0.029	0.127	24.88
M2R 8	0.143	0.226	8.00	8.88	8.41	0.379	0.730	0.029	0.126	24.92
M2R 9	0.146	0.229	8.00	8.45	8.22	0.382	0.723	0.029	0.126	24.98
M2R10	0.156	0.237	8.00	12.03	9.89	0.400	0.728	0.032	0.149	22.93
M2R11	0.162	0.239	8.00	7.78	7.90	0.412	0.742	0.028	0.115	26.16
M2R12	0.167	0.244	8.00	11.50	9.59	0.419	0.739	0.031	0.141	23.62
M2R13	0.177	0.249	8.00	10.40	9.04	0.439	0.754	0.029	0.127	24.85
M2R14	0.184	0.256	8.00	9.66	8.74	0.448	0.746	0.029	0.126	24.99
M2R15	0.194	0.262	8.00	8.59	8.26	0.464	0.748	0.028	0.118	25.77
M2R16	0.199	0.266	8.00	8.72	8.32	0.470	0.747	0.029	0.119	25.66
M2R17	0.206	0.271	8.00	8.52	8.23	0.481	0.745	0.029	0.119	25.71
M2R18	0.215	0.291	8.00	6.37	7.13	0.477	0.681	0.029	0.123	25.26
M2R19	0.213	0.278	8.00	9.16	8.54	0.487	0.731	0.030	0.128	24.78
M2R20	0.217	0.274	8.00	11.62	9.46	0.504	0.772	0.030	0.127	24.85
M2R21	0.216	0.273	8.00	11.77	9.53	0.501	0.771	0.030	0.128	24.74

TABLE 7-15: SUMMARY OF RESULTS OBTAINED FROM MODEL NO.(3)

RUN NO	Q (m3/s)	Y (m)	So $x10^3$	Sw $x10^3$	Se $x10^3$	Re $x10^6$	F_r	n ($s/m^{1/3}$)	f	C ($m^{1/2}/s$)
M3R 1	0.043	0.108	8.00	9.57	8.71	0.152	0.741	0.026	0.127	24.87
M3R 2	0.055	0.125	8.00	9.56	8.72	0.180	0.736	0.027	0.129	24.70
M3R 3	0.063	0.134	8.00	8.33	8.14	0.202	0.762	0.025	0.112	26.47
M3R 4	0.079	0.153	8.00	9.11	8.48	0.234	0.755	0.027	0.119	25.70
M3R 5	0.085	0.162	8.00	9.13	8.52	0.244	0.738	0.028	0.125	25.06
M3R 6	0.092	0.166	8.00	8.69	8.28	0.262	0.767	0.026	0.113	26.39
M3R 7	0.098	0.171	8.00	9.52	8.63	0.271	0.766	0.027	0.118	25.82
M3R 8	0.107	0.180	8.00	8.82	8.33	0.290	0.775	0.026	0.111	26.59
M3R 9	0.114	0.188	8.00	8.40	8.17	0.302	0.764	0.027	0.112	26.49
M3R10	0.128	0.197	8.00	8.47	8.18	0.327	0.784	0.026	0.106	27.15
M3R11	0.135	0.203	8.00	9.21	8.47	0.339	0.783	0.027	0.111	26.65
M3R12	0.139	0.210	8.00	9.55	8.66	0.342	0.759	0.028	0.120	25.56
M3R13	0.142	0.212	8.00	9.55	8.65	0.347	0.761	0.028	0.119	25.64
M3R14	0.151	0.219	8.00	9.18	8.49	0.362	0.767	0.028	0.115	26.08
M3R15	0.161	0.223	8.00	9.04	8.39	0.381	0.788	0.027	0.108	26.95
M3R16	0.171	0.233	8.00	9.17	8.47	0.395	0.774	0.027	0.113	26.34
M3R17	0.178	0.237	8.00	9.30	8.50	0.405	0.782	0.027	0.111	26.55
M3R18	0.192	0.248	8.00	9.42	8.57	0.424	0.774	0.028	0.114	26.18
M3R19	0.196	0.253	8.00	9.80	8.76	0.427	0.761	0.029	0.121	25.48
M3R20	0.211	0.257	8.00	11.67	9.34	0.455	0.796	0.028	0.118	25.80
M3R21	0.216	0.260	8.00	9.51	8.55	0.462	0.798	0.027	0.108	27.02
M3R22	0.222	0.263	8.00	9.43	8.51	0.471	0.801	0.027	0.106	27.18

TABLE 7-16: SUMMARY OF RESULTS OBTAINED FROM MODEL NO.(4)

RUN NO	Q (m^3/s)	Y (m)	So $\times 10^3$	Sw $\times 10^3$	Se $\times 10^3$	Re $\times 10^6$	F_r	n ($s/m^{1/3}$)	f	C ($m^{1/2}/s$)
M4R 1	0.061	0.102	12.50	12.17	12.48	0.210	0.975	0.024	0.105	27.34
M4R 2	0.063	0.103	12.50	13.41	12.52	0.216	0.988	0.024	0.103	27.65
M4R 3	0.065	0.107	12.50	13.19	12.56	0.218	0.956	0.025	0.110	26.72
M4R 4	0.066	0.109	12.50	13.70	12.60	0.222	0.959	0.025	0.110	26.75
M4R 5	0.073	0.112	12.50	13.10	12.50	0.241	1.002	0.024	0.099	28.09
M4R 6	0.077	0.116	12.50	13.04	12.51	0.251	0.994	0.024	0.101	27.83
M4R 7	0.080	0.119	12.50	12.79	12.51	0.257	0.991	0.024	0.102	27.75
M4R 8	0.081	0.122	12.50	12.67	12.51	0.260	0.974	0.025	0.105	27.28
M4R 9	0.084	0.125	12.50	12.53	12.50	0.265	0.966	0.025	0.107	27.05
M4R10	0.090	0.127	12.50	12.34	12.50	0.281	1.007	0.024	0.099	28.20
M4R11	0.091	0.129	12.50	12.93	12.51	0.281	0.986	0.024	0.103	27.62
M4R12	0.096	0.134	12.50	12.50	12.50	0.293	0.980	0.025	0.104	27.45
M4R13	0.102	0.137	12.50	12.51	12.50	0.307	1.003	0.024	0.099	28.11
M4R14	0.103	0.142	12.50	12.10	12.46	0.305	0.955	0.026	0.109	26.79
M4R15	0.104	0.139	12.50	12.48	12.50	0.312	1.003	0.024	0.099	28.10
M4R16	0.110	0.146	12.50	12.25	12.49	0.322	0.971	0.025	0.106	27.22
M4R17	0.116	0.150	12.50	12.12	12.48	0.334	0.974	0.025	0.105	27.31
M4R18	0.121	0.153	12.50	12.53	12.50	0.346	0.990	0.025	0.102	27.74
M4R19	0.125	0.156	12.50	12.08	12.49	0.353	0.989	0.025	0.102	27.71
M4R20	0.132	0.159	12.50	11.94	12.51	0.370	1.012	0.024	0.098	28.33
M4R21	0.135	0.161	12.50	12.64	12.50	0.377	1.010	0.025	0.098	28.30
M4R22	0.142	0.165	12.50	13.01	12.48	0.391	1.024	0.024	0.095	28.71
M4R23	0.144	0.167	12.50	11.93	12.51	0.393	1.011	0.025	0.098	28.30
M4R24	0.148	0.170	12.50	12.43	12.50	0.399	1.005	0.025	0.099	28.15
M4R25	0.149	0.172	12.50	12.95	12.50	0.401	0.999	0.025	0.100	27.99
M4R26	0.153	0.172	12.50	13.32	12.47	0.411	1.021	0.024	0.096	28.63
M4R27	0.153	0.174	12.50	13.07	12.49	0.411	1.009	0.025	0.098	28.28
M4R28	0.156	0.175	12.50	12.51	12.50	0.418	1.018	0.025	0.096	28.52
M4R29	0.158	0.177	12.50	12.61	12.50	0.421	1.014	0.025	0.097	28.40
M4R30	0.161	0.179	12.50	12.35	12.50	0.425	1.008	0.025	0.098	28.24
M4R31	0.168	0.184	12.50	12.60	12.50	0.435	0.999	0.025	0.100	27.99
M4R32	0.176	0.189	12.50	12.45	12.50	0.451	1.005	0.025	0.099	28.15
M4R33	0.179	0.191	12.50	12.47	12.50	0.456	1.003	0.025	0.099	28.09

TABLE 7–17: SUMMARY OF RESULTS OBTAINED FROM MODEL NO.(5)

RUN NO	Q (m3/s)	Y (m)	So x10^3	Sw x10^3	Se x10^3	Re x10^{-6}	F_r	n (s/m$^{1/3}$)	f	C (m$^{1/2}$/s)
M5R 1	0.012	0.035	12.50	12.80	12.50	0.061	0.999	0.020	0.100	27.99
M5R 2	0.013	0.037	12.50	12.66	12.51	0.065	0.980	0.021	0.104	27.44
M5R 3	0.019	0.050	12.50	12.94	12.54	0.092	0.948	0.022	0.112	26.51
M5R 4	0.022	0.054	12.50	13.03	12.54	0.102	0.959	0.022	0.109	26.82
M5R 5	0.023	0.056	12.50	12.67	12.51	0.108	0.965	0.022	0.107	27.03
M5R 6	0.024	0.057	12.50	12.71	12.51	0.114	0.979	0.022	0.104	27.41
M5R 7	0.025	0.058	12.50	12.61	12.50	0.117	0.985	0.022	0.103	27.60
M5R 8	0.029	0.064	12.50	13.27	12.53	0.132	0.982	0.022	0.104	27.49
M5R 9	0.036	0.074	12.50	12.71	12.52	0.153	0.955	0.023	0.110	26.73
M5R10	0.037	0.076	12.50	12.68	12.51	0.160	0.969	0.023	0.106	27.15
M5R11	0.043	0.081	12.50	12.69	12.50	0.179	0.989	0.023	0.102	27.71
M5R12	0.044	0.083	12.50	12.63	12.50	0.183	0.981	0.023	0.104	27.48
M5R13	0.045	0.084	12.50	12.59	12.50	0.186	0.983	0.023	0.103	27.55
M5R14	0.047	0.085	12.50	12.60	12.50	0.193	1.004	0.023	0.099	28.13
M5R15	0.051	0.091	12.50	12.70	12.51	0.204	0.976	0.024	0.105	27.33
M5R16	0.054	0.094	12.50	12.66	12.50	0.214	0.986	0.023	0.103	27.61
M5R17	0.057	0.099	12.50	12.70	12.51	0.222	0.965	0.024	0.107	27.02
M5R18	0.060	0.100	12.50	12.74	12.50	0.233	0.999	0.023	0.100	28.00
M5R19	0.066	0.108	12.50	12.60	12.51	0.249	0.967	0.024	0.107	27.08
M5R20	0.069	0.110	12.50	12.61	12.50	0.258	0.977	0.024	0.105	27.38
M5R21	0.077	0.118	12.50	12.67	12.51	0.276	0.960	0.025	0.109	26.89
M5R22	0.081	0.120	12.50	12.71	12.51	0.288	0.984	0.024	0.103	27.57
M5R23	0.084	0.125	12.50	12.65	12.51	0.297	0.964	0.025	0.108	26.99
M5R24	0.088	0.127	12.50	12.61	12.50	0.308	0.986	0.024	0.103	27.63
M5R25	0.094	0.131	12.50	12.59	12.50	0.322	0.988	0.024	0.102	27.69
M5R26	0.099	0.136	12.50	12.65	12.50	0.335	0.987	0.025	0.103	27.64
M5R27	0.106	0.142	12.50	12.61	12.50	0.352	0.982	0.025	0.104	27.49
M5R28	0.112	0.146	12.50	12.60	12.50	0.364	0.992	0.025	0.104	27.50
M5R29	0.117	0.151	12.50	12.57	12.50	0.377	0.978	0.025	0.104	27.41
M5R30	0.122	0.153	12.50	12.50	12.50	0.388	0.990	0.025	0.102	27.75
M5R31	0.126	0.157	12.50	12.64	12.50	0.399	0.993	0.025	0.101	27.81
M5R32	0.130	0.159	12.50	12.80	12.50	0.407	0.997	0.025	0.101	27.92
M5R33	0.133	0.160	12.50	12.63	12.50	0.415	1.008	0.025	0.098	28.24
M5R34	0.136	0.162	12.50	12.54	12.50	0.422	1.007	0.025	0.099	28.20
M5R35	0.140	0.164	12.50	12.56	12.50	0.432	1.021	0.024	0.096	28.60
M5R36	0.142	0.165	12.50	12.65	12.49	0.437	1.020	0.024	0.096	28.58

TABLE 7-18: SUMMARY OF RESULTS OBTAINED FROM MODEL NO.(6)

RUN NO	Q (m3/s)	Y (m)	So_3 X10^3	Sw_3 X10^3	Se_3 X10^3	Re_{-6} X10^{-6}	F_r	n ($s/m^{1/3}$)	f	C ($m^{1/2}/s$)
M6R 1	0.011	0.036	12.50	12.62	12.52	0.055	0.907	0.022	0.122	25.39
M6R 2	0.014	0.041	12.50	12.41	12.49	0.069	0.956	0.021	0.109	26.78
M6R 3	0.019	0.051	12.50	12.59	12.51	0.089	0.931	0.023	0.116	26.06
M6R 4	0.023	0.057	12.50	12.65	12.52	0.104	0.934	0.023	0.115	26.15
M6R 5	0.027	0.064	12.50	11.93	12.42	0.120	0.932	0.023	0.114	26.18
M6R 6	0.035	0.072	12.50	12.35	12.49	0.149	0.981	0.023	0.104	27.48
M6R 7	0.047	0.087	12.50	11.83	12.48	0.188	0.987	0.023	0.103	27.66
M6R 8	0.063	0.106	12.50	12.32	12.48	0.232	0.955	0.025	0.110	26.77
M6R 9	0.069	0.108	12.50	11.99	12.52	0.253	1.014	0.023	0.097	28.40
M6R10	0.073	0.116	12.50	12.53	12.50	0.261	0.957	0.025	0.109	26.79
M6R11	0.080	0.121	12.50	12.76	12.52	0.279	0.972	0.025	0.106	27.22
M6R12	0.083	0.122	12.50	12.83	12.50	0.290	1.000	0.024	0.100	28.01
M6R13	0.087	0.127	12.50	12.31	12.49	0.296	0.975	0.025	0.105	27.32
M6R14	0.093	0.133	12.50	12.90	12.53	0.310	0.966	0.025	0.107	27.02
M6R15	0.100	0.138	12.50	13.06	12.52	0.329	0.982	0.025	0.104	27.50
M6R16	0.104	0.140	12.50	12.60	12.50	0.340	0.997	0.024	0.101	27.92
M6R17	0.107	0.144	12.50	11.89	12.48	0.347	0.987	0.025	0.102	27.67
M6R18	0.110	0.146	12.50	12.36	12.49	0.352	0.978	0.025	0.105	27.39
M6R19	0.115	0.148	12.50	12.56	12.50	0.366	1.004	0.024	0.099	28.12
M6R20	0.119	0.153	12.50	11.96	12.48	0.373	0.984	0.025	0.103	27.59
M6R21	0.124	0.156	12.50	12.53	12.50	0.383	0.987	0.025	0.103	27.66
M6R22	0.130	0.158	12.50	12.33	12.50	0.399	1.013	0.024	0.098	28.36

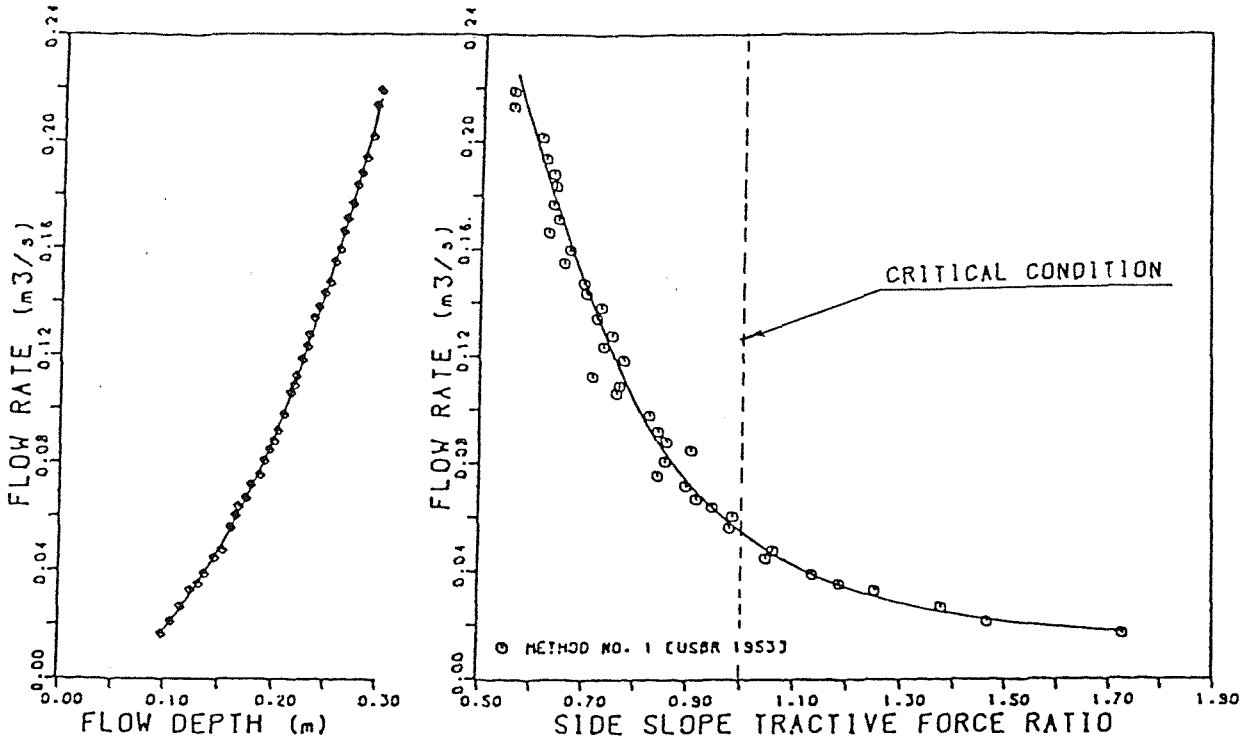

FIG.7-1 : CALCULATED TRACTIVE FORCE RATIO USING U.S.B.R. APPROACH FOR MODEL NO. 1 [BED SLOPE = 0.005]

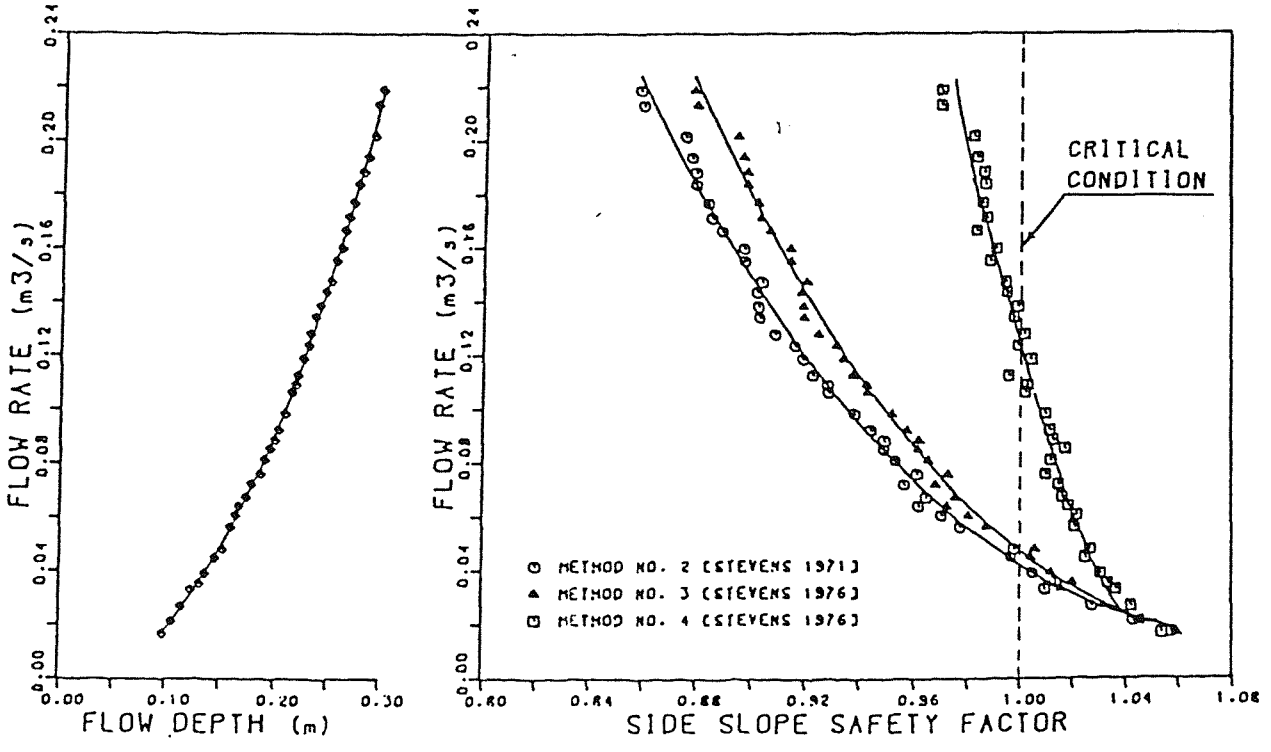

FIG.7-2 : CALCULATED SAFETY FACTOR USING STEVENS & SIMONS APPROACHES FOR MODEL NO. 1 [BED SLOPE = 0.005]

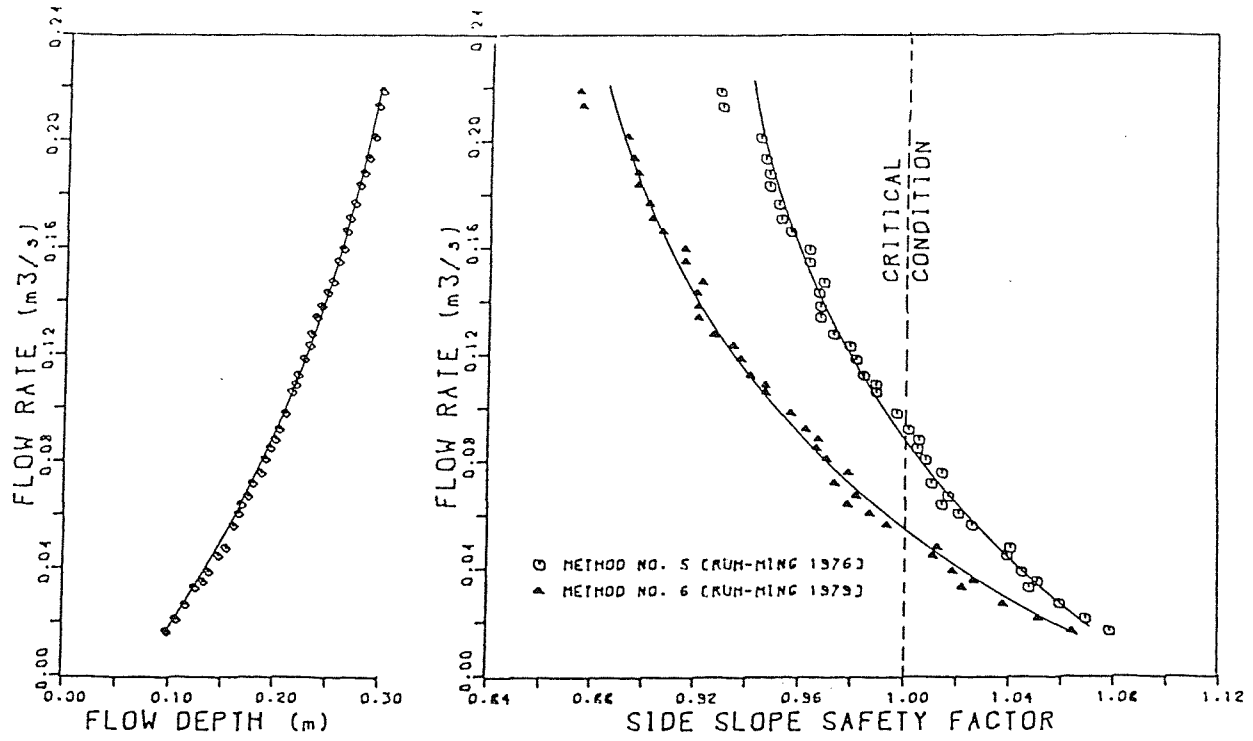

FIG. 7-3: CALCULATED SAFETY FACTOR USING RUH-MING et. al. APPROACHES FOR MODEL NO. 1 [BED SLOPE = 0.005]

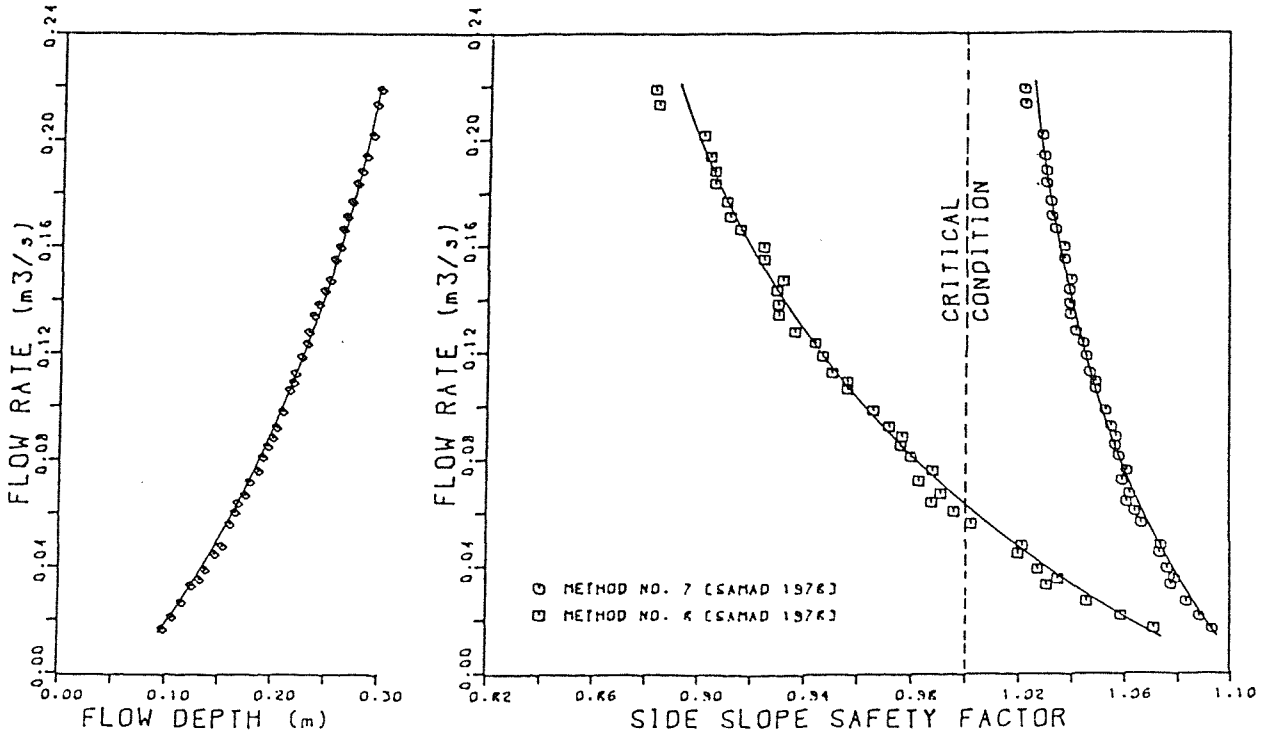

FIG. 7-4 : CALCULATED SAFETY FACTOR USING SAMAD APPROACHES FOR MODEL NO. 1 [BED SLOPE = 0.005]

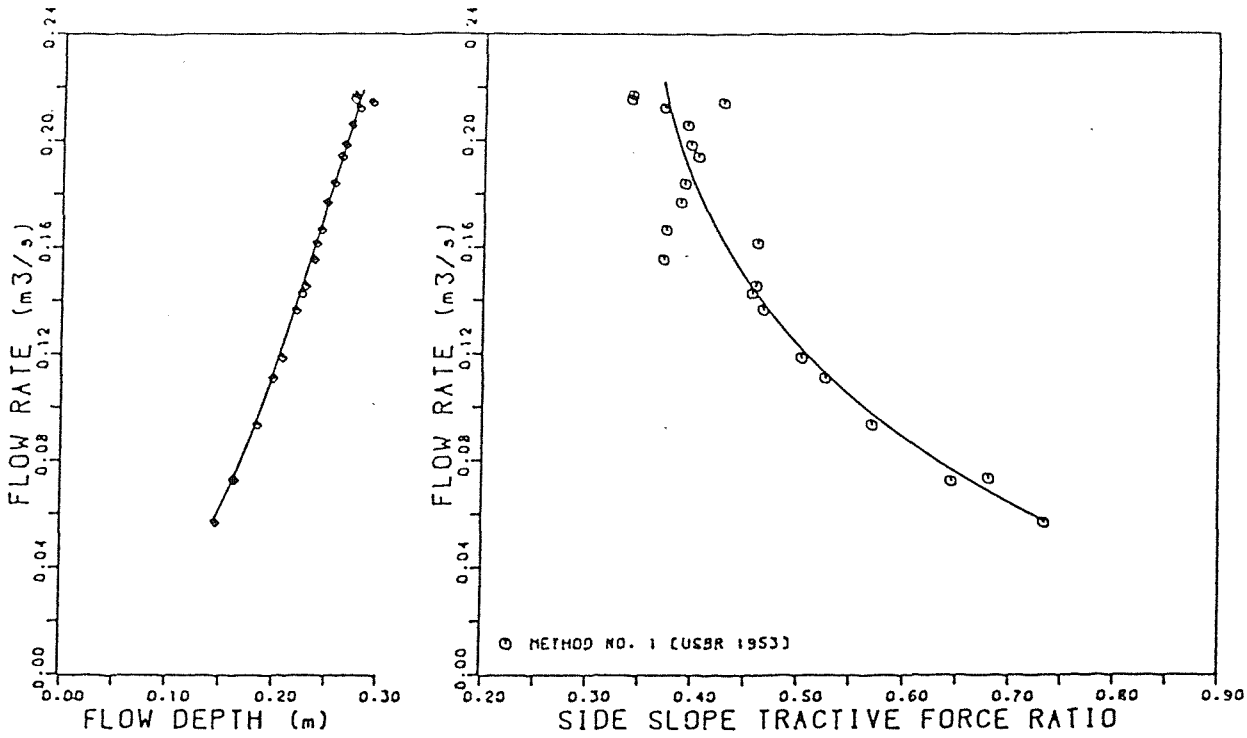

FIG. 7-5 : CALCULATED TRACTIVE FORCE RATIO USING U.S.B.R. APPROACH FOR MODEL NO. 2 [BED SLOPE = 0.008]

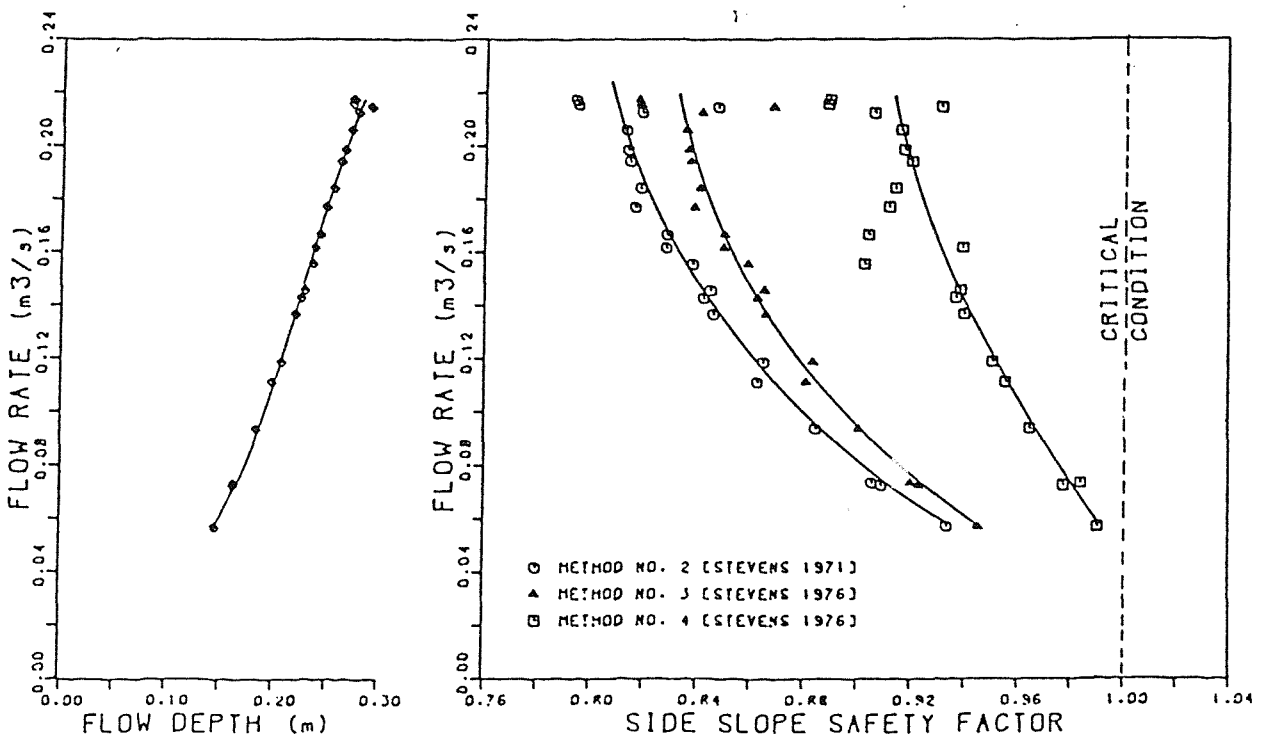

FIG. 7-6 : CALCULATED SAFETY FACTOR USING STEVENS & SIMONS APPROACHES FOR MODEL NO. 2 [BED SLOPE = 0.008]

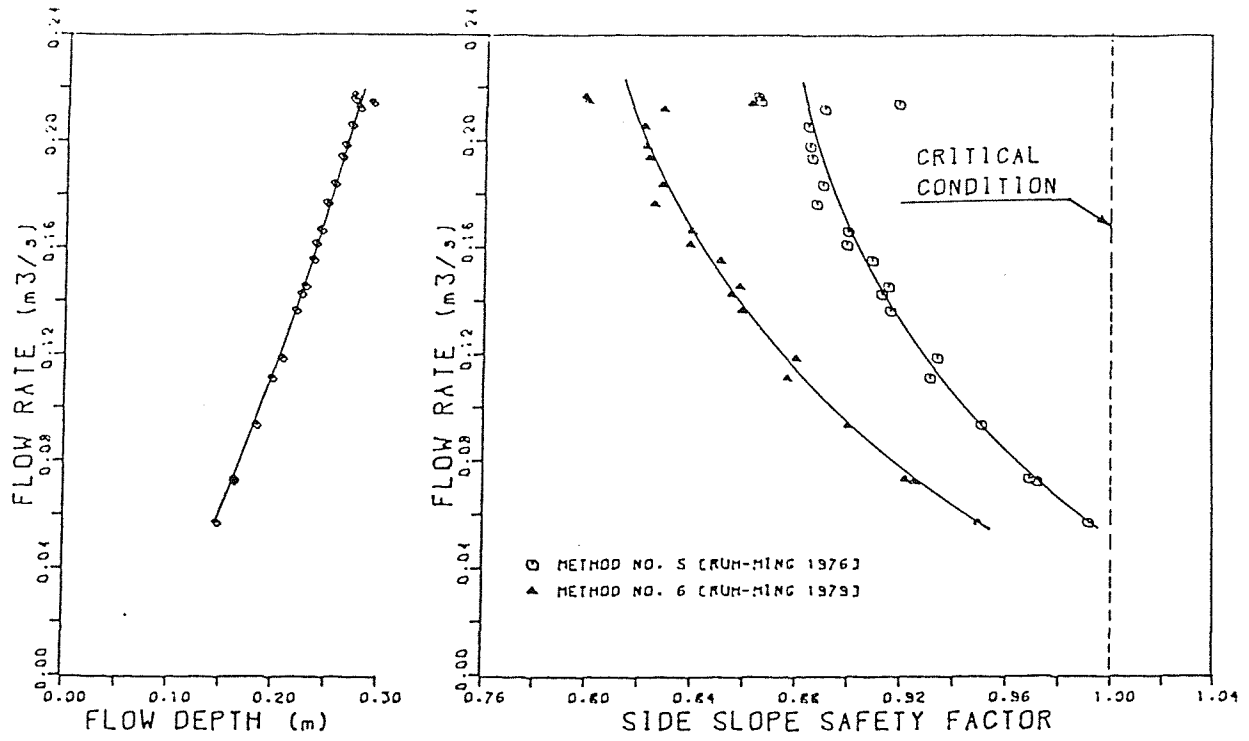

FIG. 7-7 : CALCULATED SAFETY FACTOR USING RUH-MING et. al. APPROACHES FOR MODEL NO. 2 [BED SLOPE = 0.008]

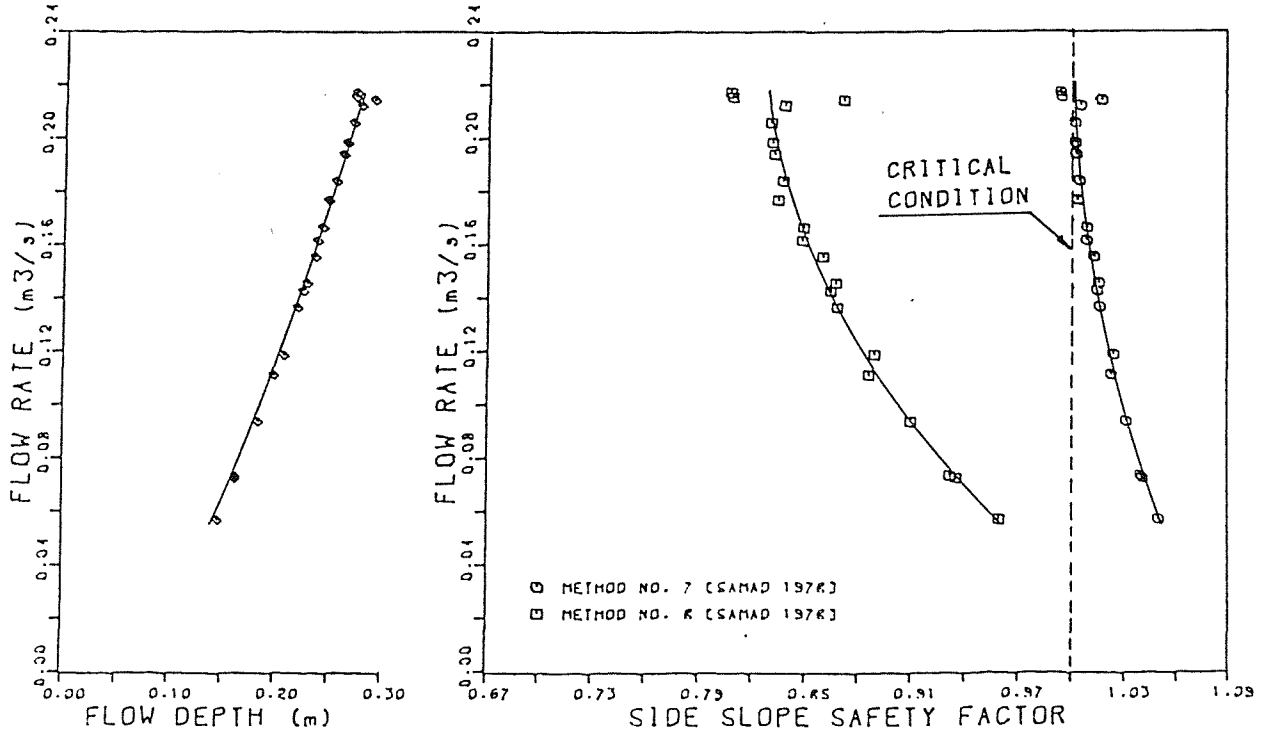

FIG. 7-8 : CALCULATED SAFETY FACTOR USING SAMAD APPROACHES FOR MODEL NO. 2 [BED SLOPE = 0.008]

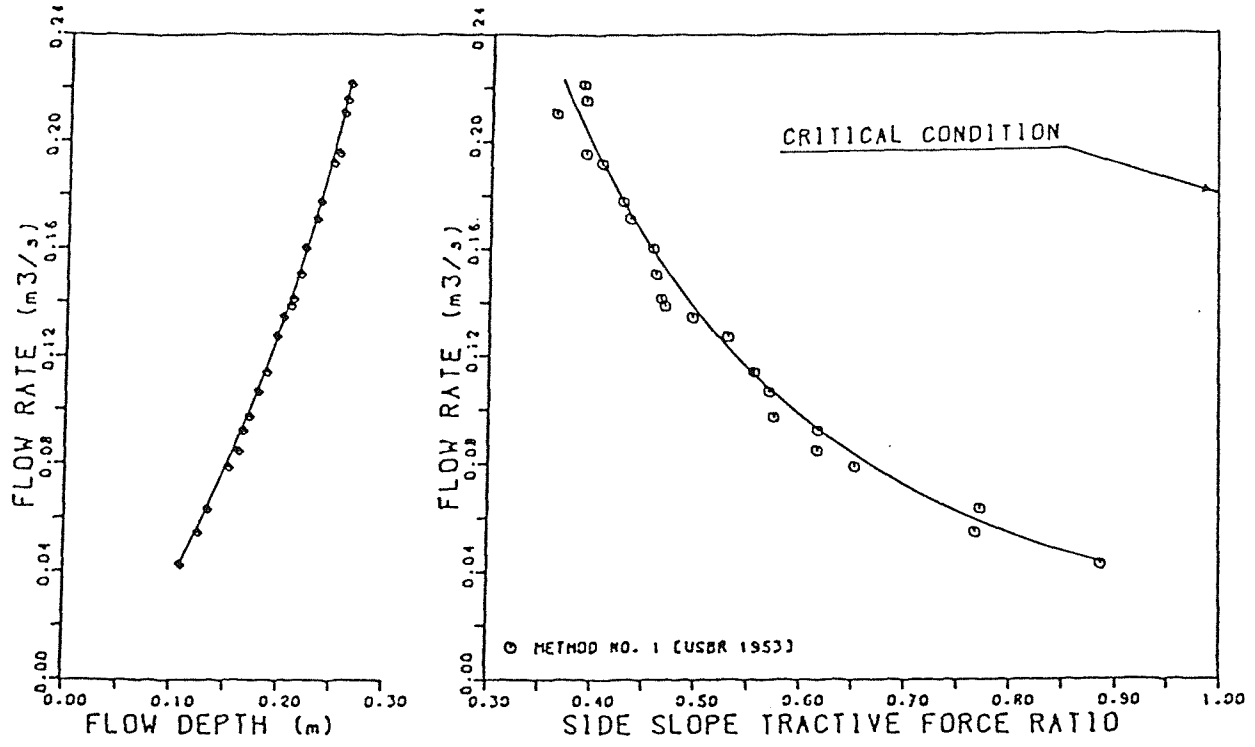

FIG.7-9 : CALCULATED TRACTIVE FORCE RATIO
USING U.S.B.R. APPROACH FOR MODEL NO. 3
[BED SLOPE = 0.008]

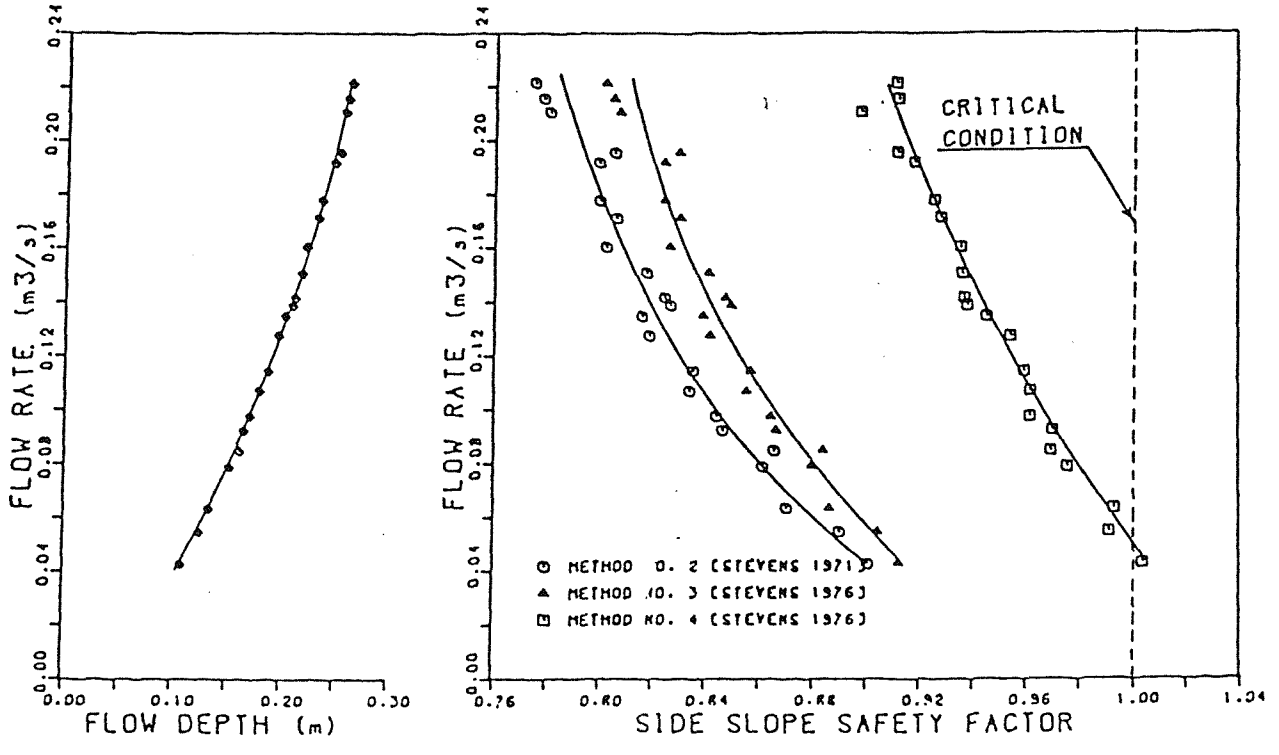

FIG.7-10 : CALCULATED SAFETY FACTOR USING
STEVENS & SIMONS APPROACHES FOR MODEL NO. 3
[BED SLOPE = 0.008]

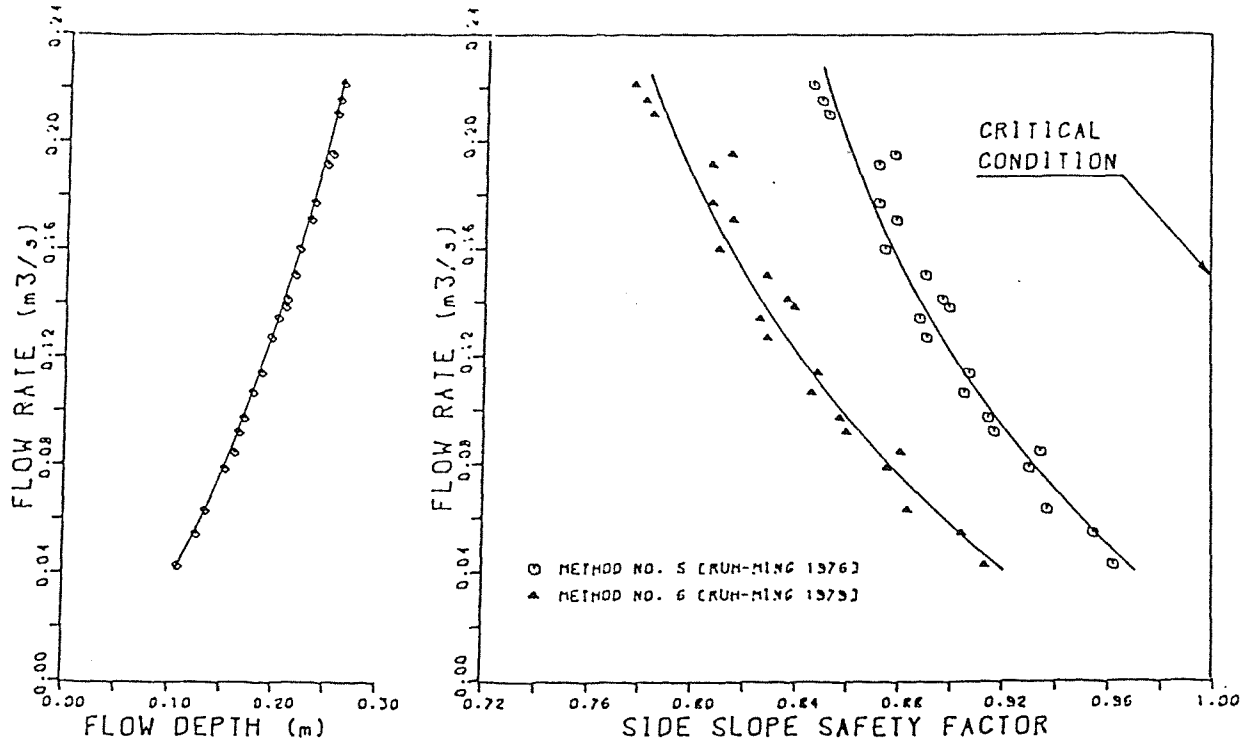

FIG.7–11 : CALCULATED SAFETY FACTOR USING
RUH-MING et. al. APPROACHES FOR MODEL NO. 3
[BED SLOPE = 0.008]

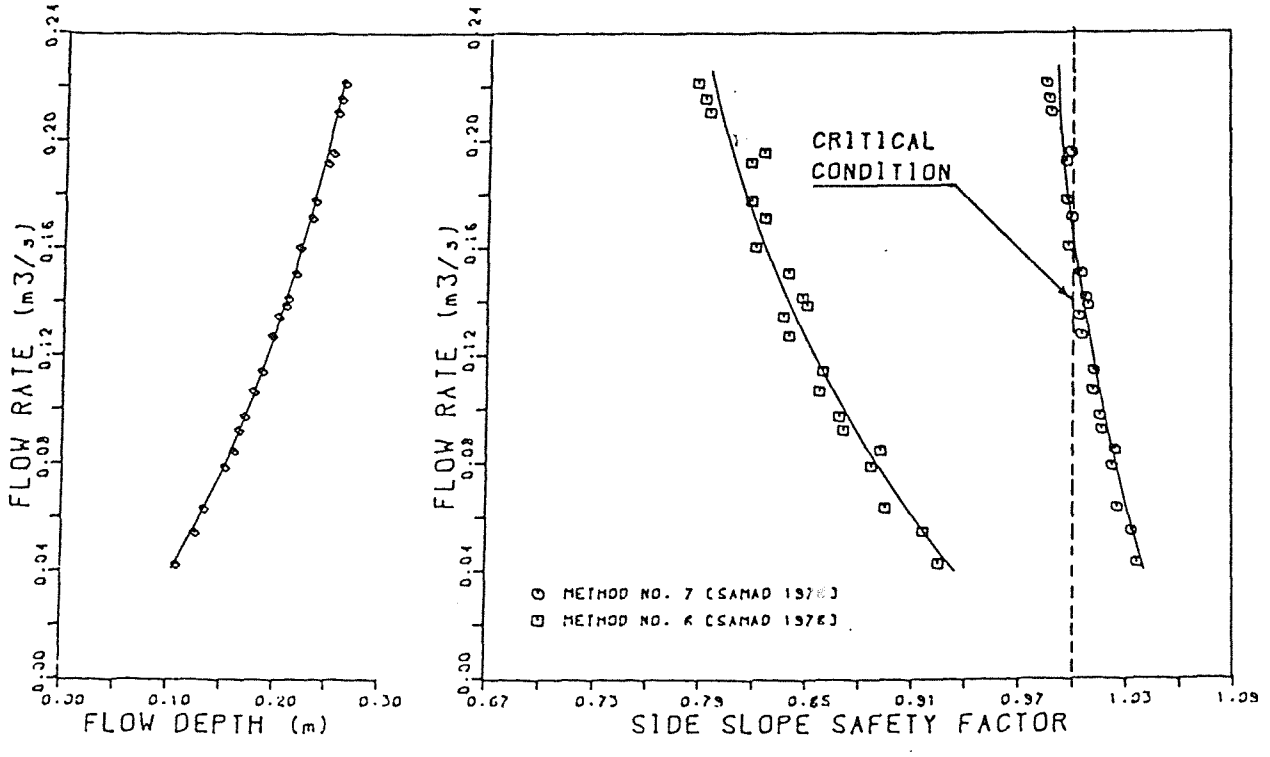

FIG.7–12 : CALCULATED SAFETY FACTOR USING
SAMAD APPROACHES FOR MODEL NO. 3
[BED SLOPE = 0.008]

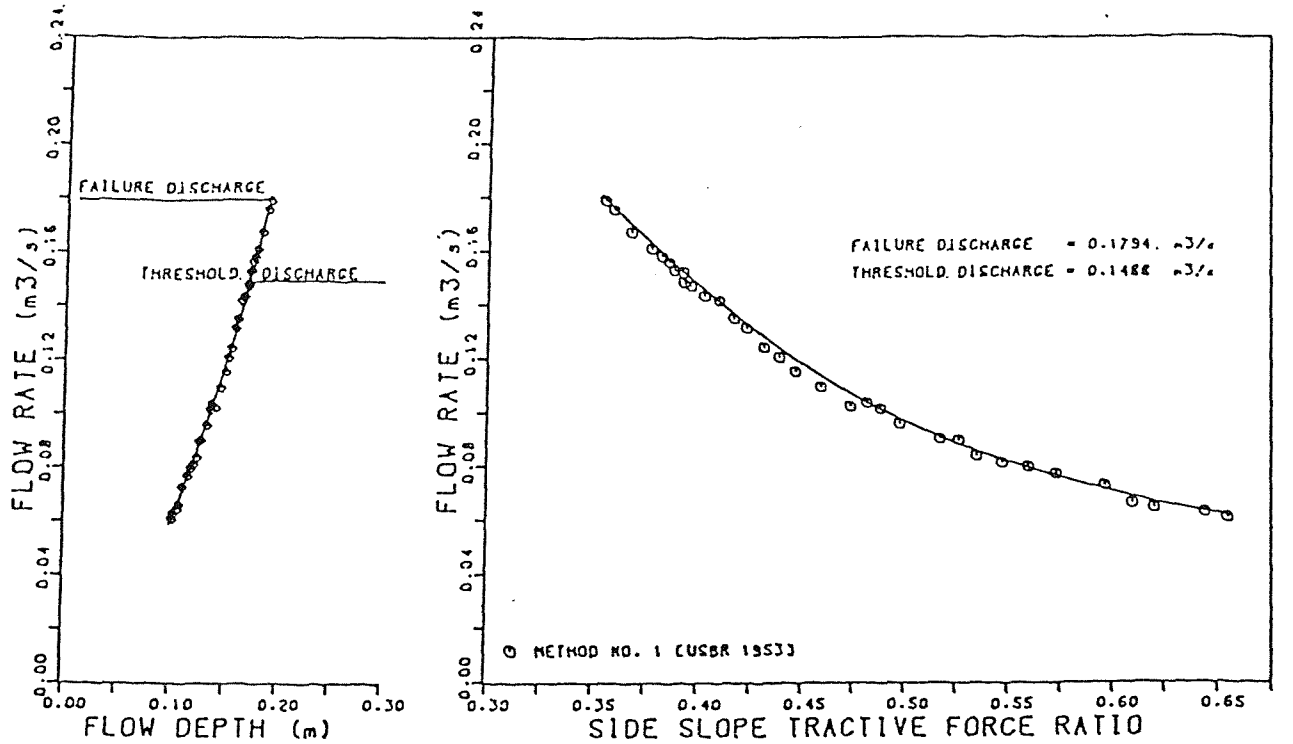

FIG.7-13: CALCULATED TRACTIVE FORCE RATIO USING U.S.B.R. APPROACH FOR MODEL NO. 4 [BED SLOPE = 0.0125]

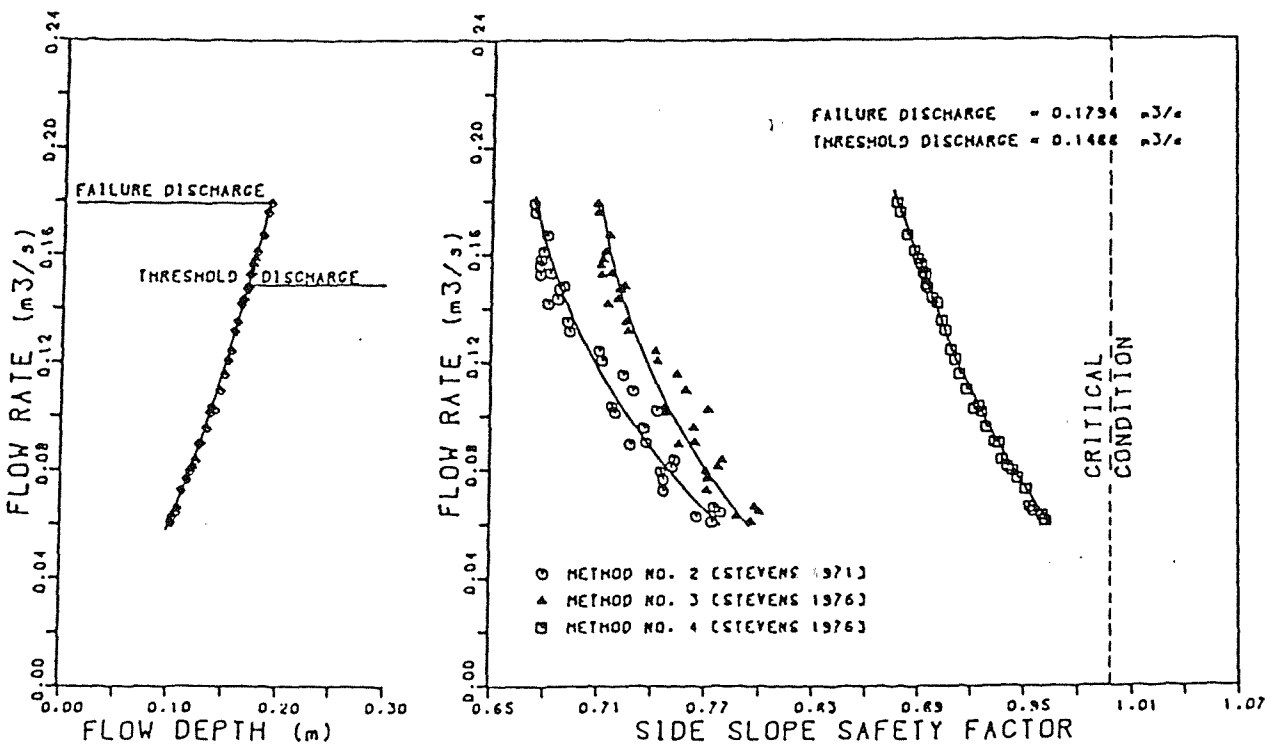

FIG.7-14: CALCULATED SAFETY FACTOR USING STEVENS & SIMONS APPROACHES FOR MODEL NO. 4 [BED SLOPE = 0.0125]

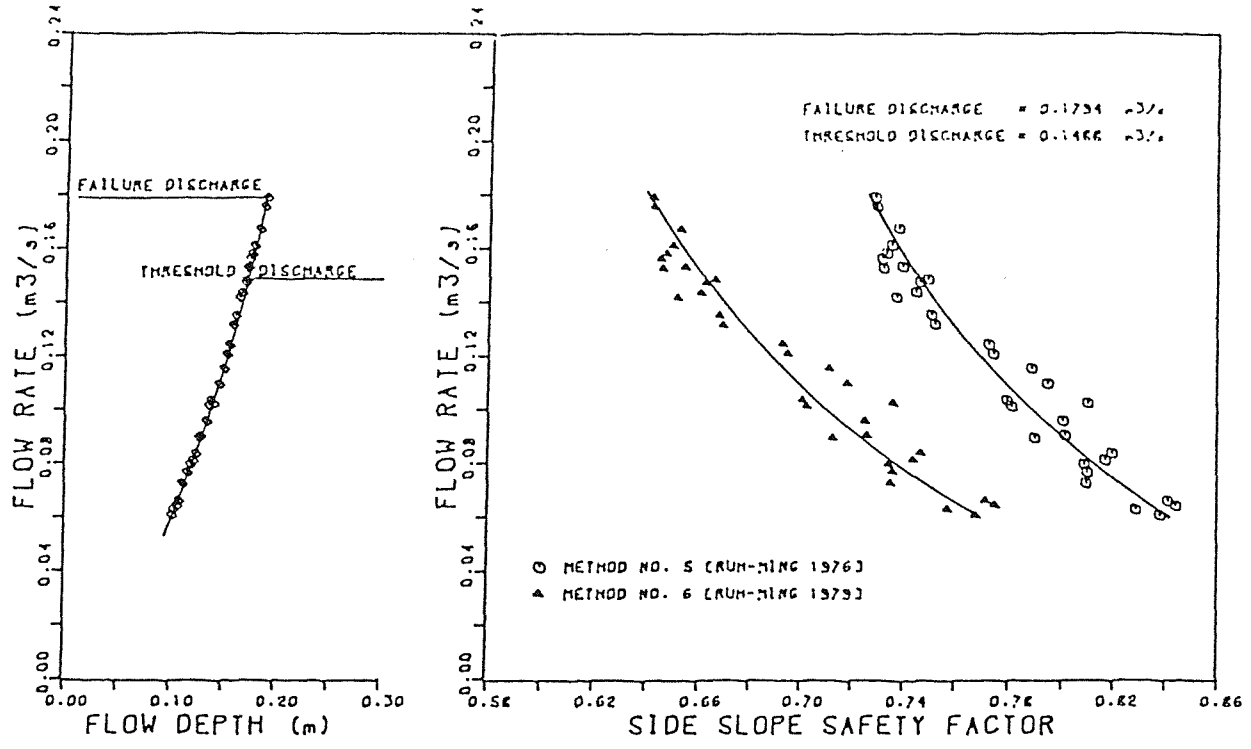

FIG. 7-15: CALCULATED SAFETY FACTOR USING RUH-MING et. al. APPROACHES FOR MODEL NO. 4 [BED SLOPE = 0.0125]

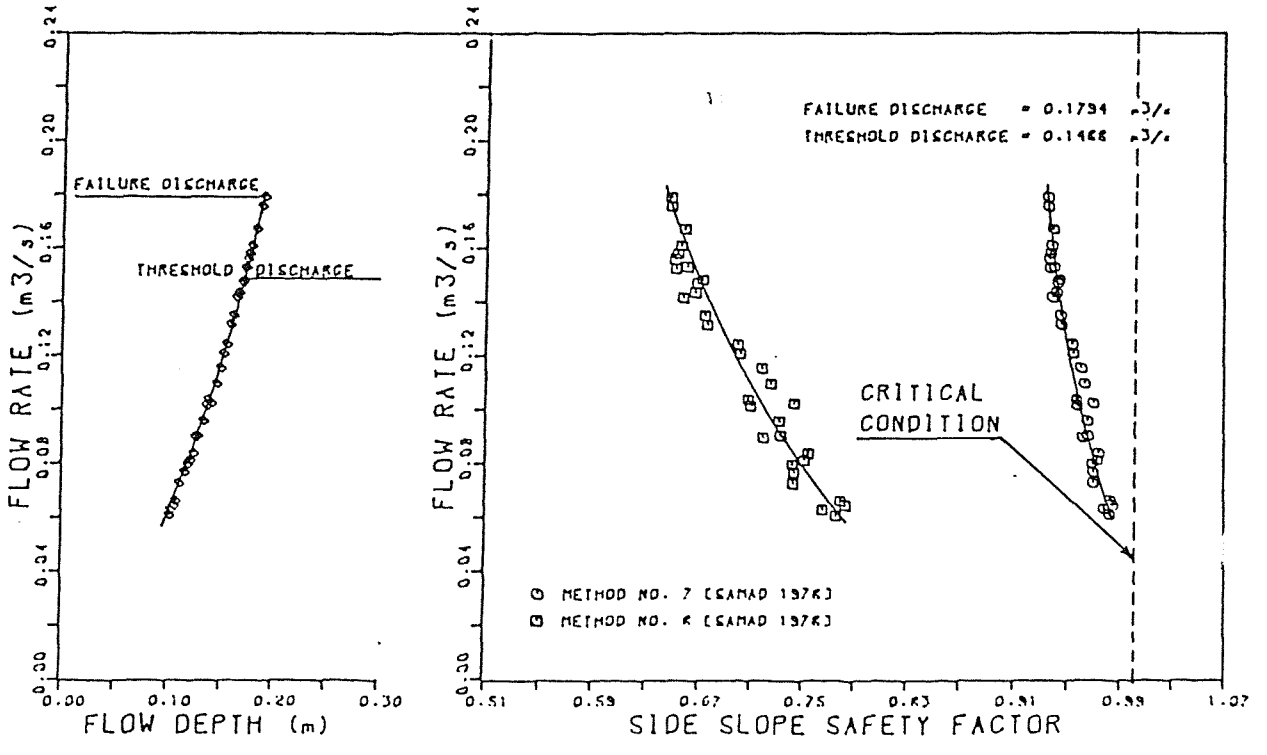

FIG. 7-16: CALCULATED SAFETY FACTOR USING SAMAD APPROACHES FOR MODEL NO. 4 [BED SLOPE = 0.0125]

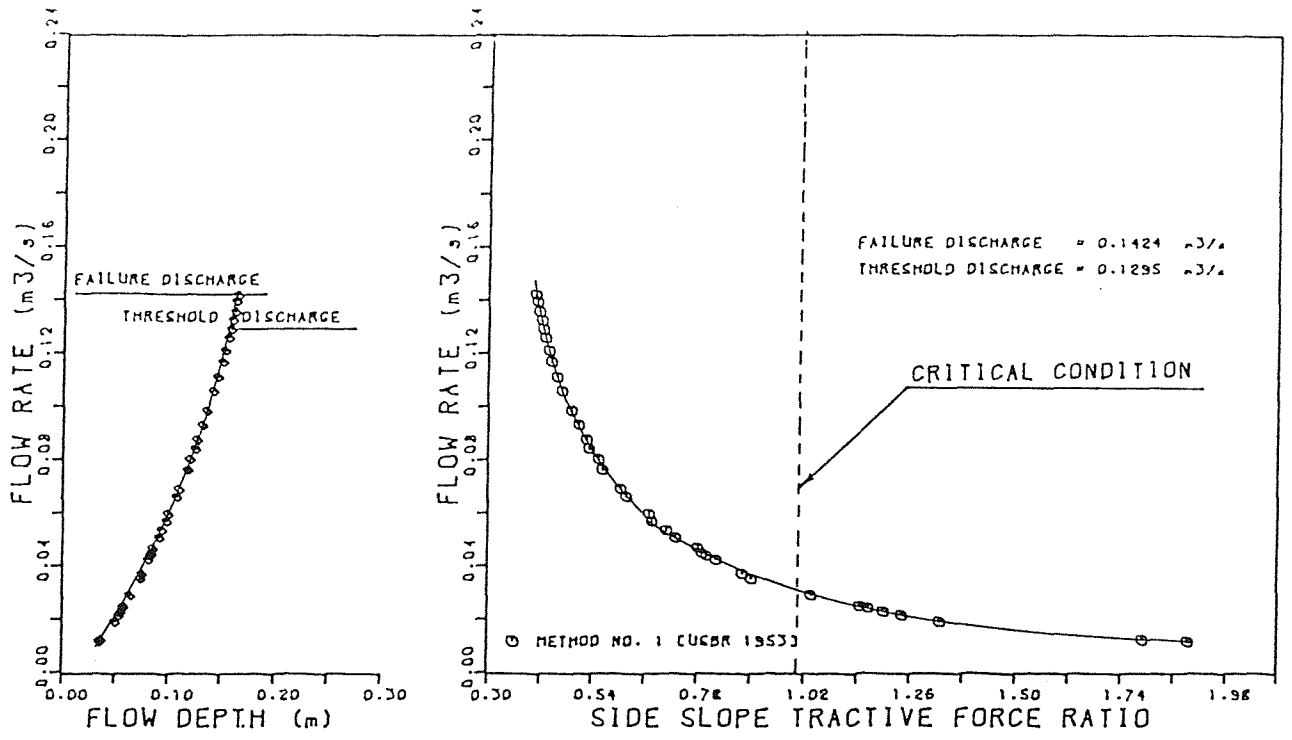

FIG.7-17: CALCULATED TRACTIVE FORCE RATIO USING U.S.B.R. APPROACH FOR MODEL NO. 5 [BED SLOPE = 0.0125]

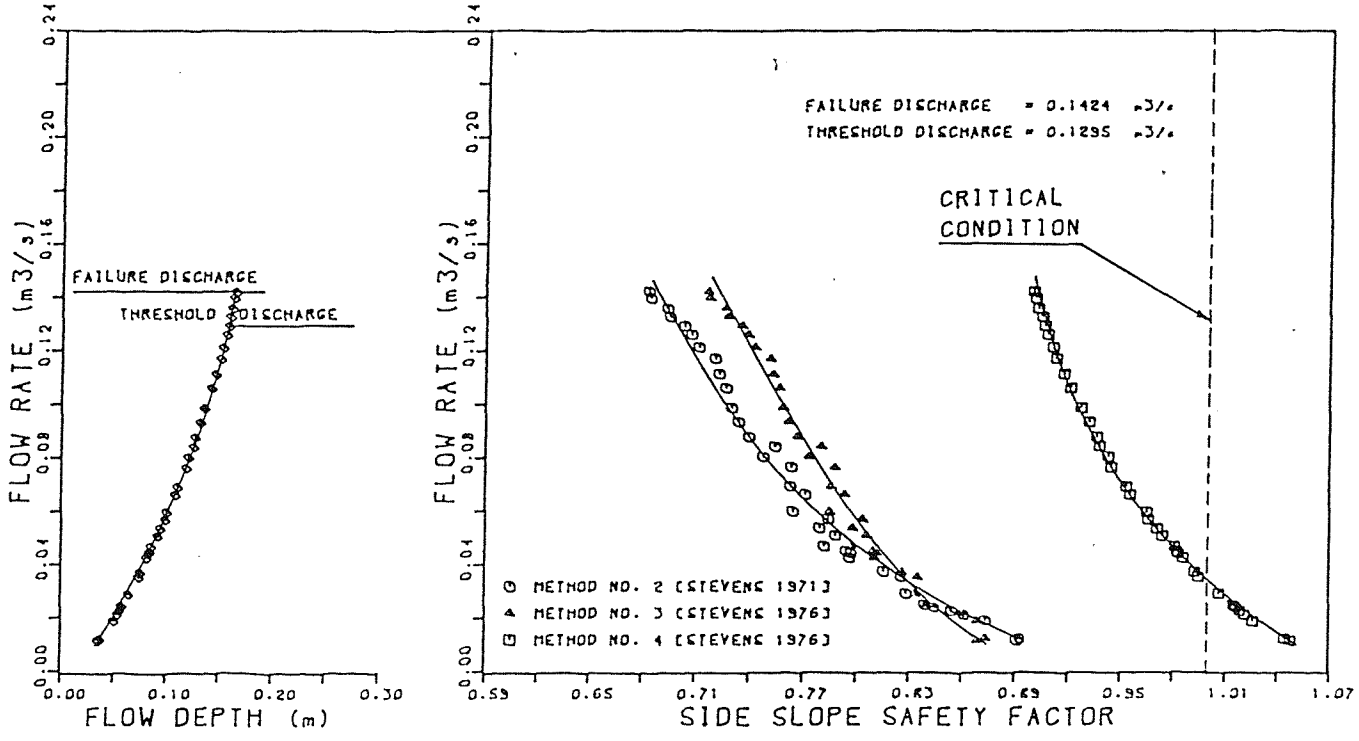

FIG.7-18: CALCULATED SAFETY FACTOR USING STEVENS & SIMONS APPROACHES FOR MODEL NO. 5 [BED SLOPE = 0.0125]

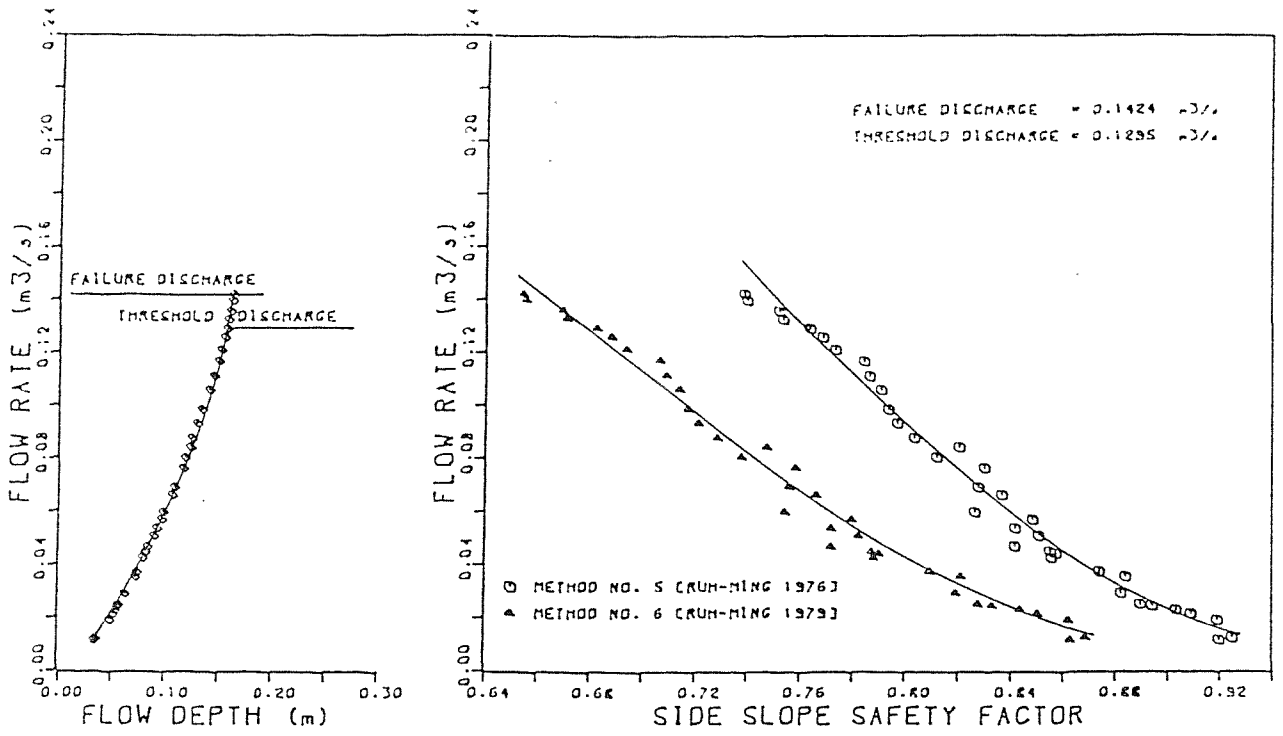

FIG.7-19: CALCULATED SAFETY FACTOR USING RUH-MING et. al. APPROACHES FOR MODEL NO. 5 [BED SLOPE = 0.0125]

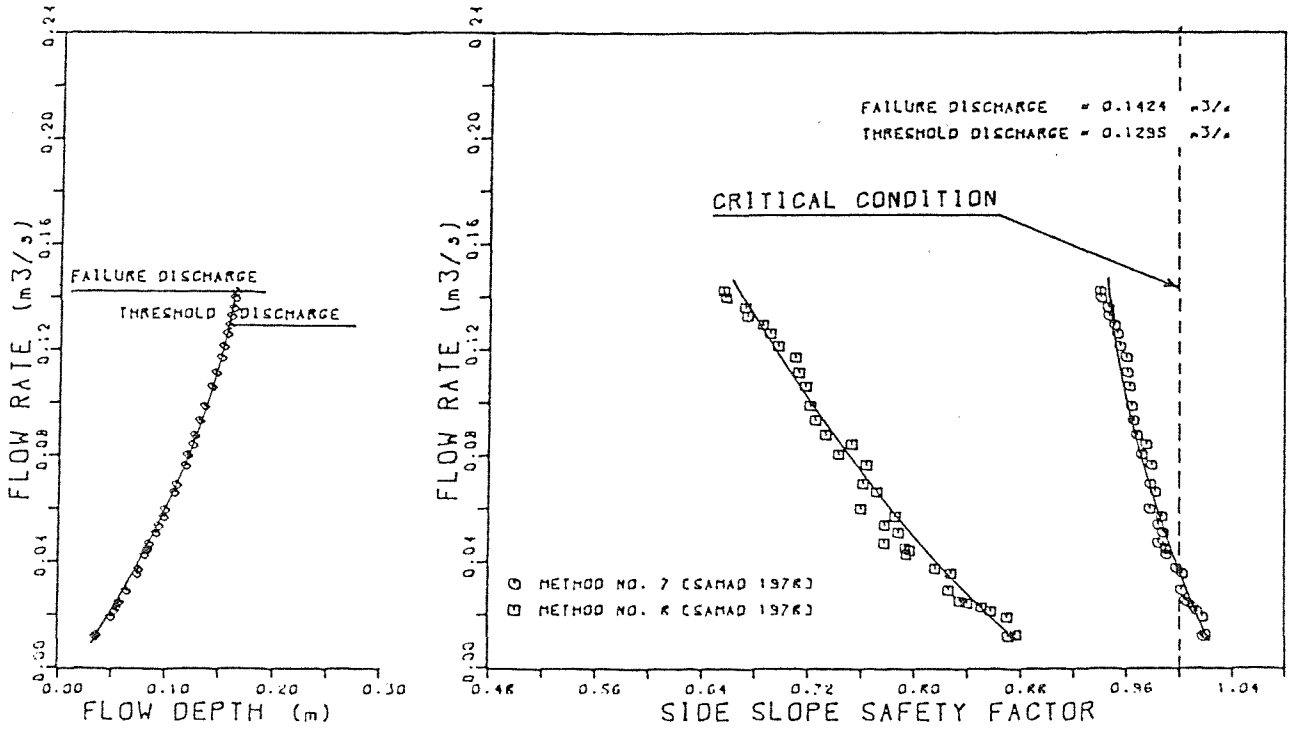

FIG.7-20: CALCULATED SAFETY FACTOR USING SAMAD APPROACHES FOR MODEL NO. 5 [BED SLOPE = 0.0125]

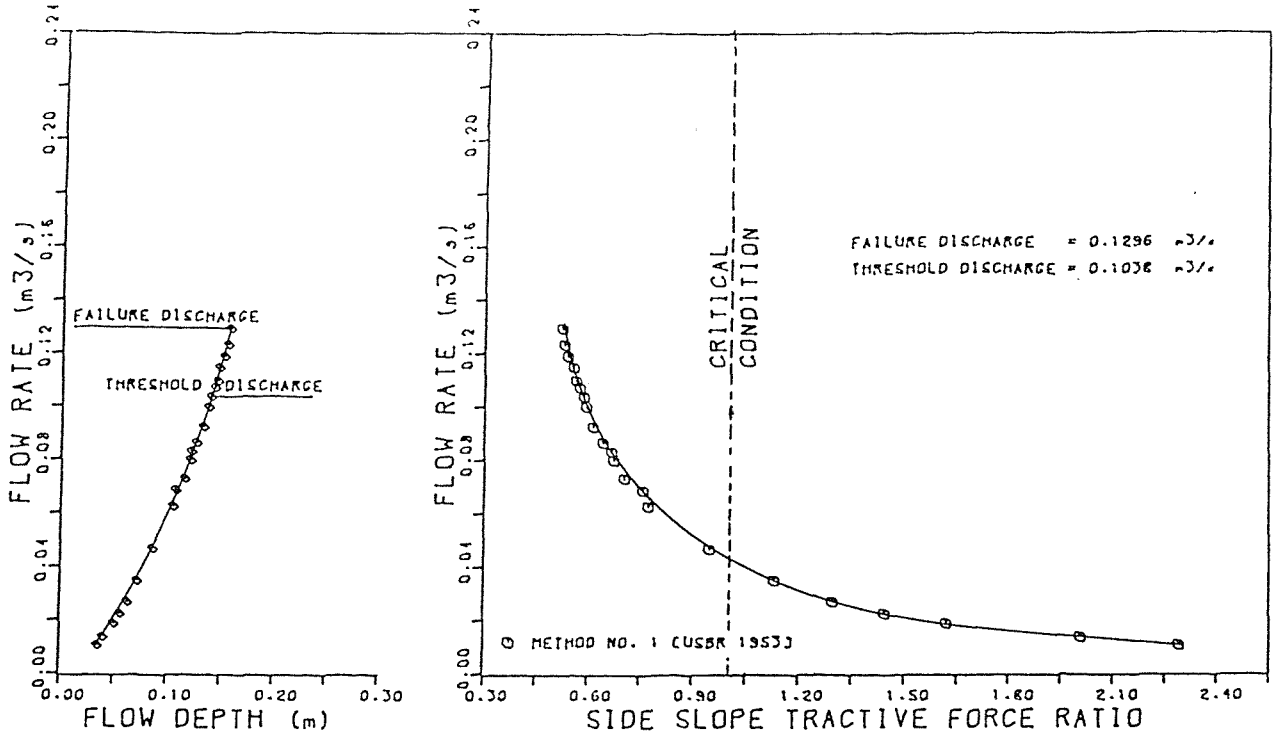

FIG.7-21: CALCULATED TRACTIVE FORCE RATIO USING U.S.B.R. APPROACH FOR MODEL NO. 6 [BED SLOPE = 0.0125]

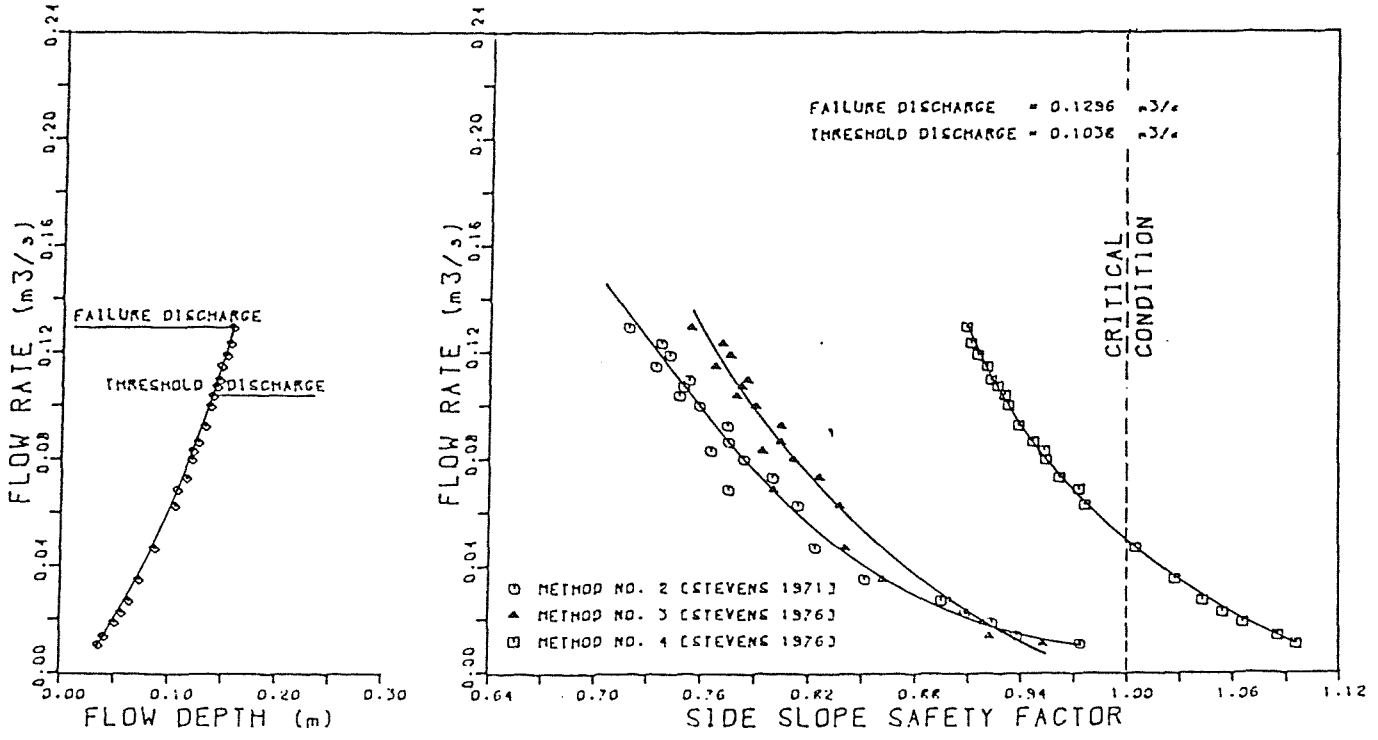

FIG.7-22: CALCULATED SAFETY FACTOR USING STEVENS & SIMONS APPROACHES FOR MODEL NO. 6 [BED SLOPE = 0.0125]

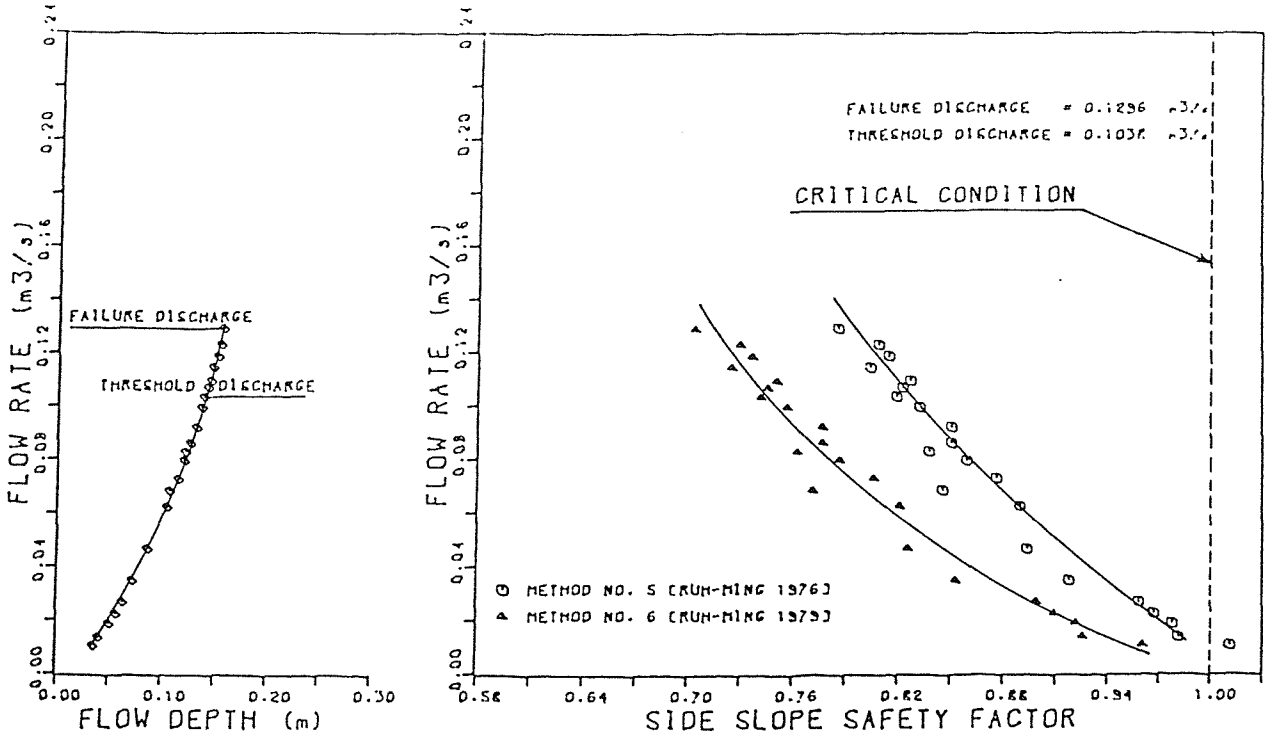

FIG.7-23 : CALCULATED SAFETY FACTOR USING RUH-MING et. al. APPROACHES FOR MODEL NO. 6 [BED SLOPE = 0.0125]

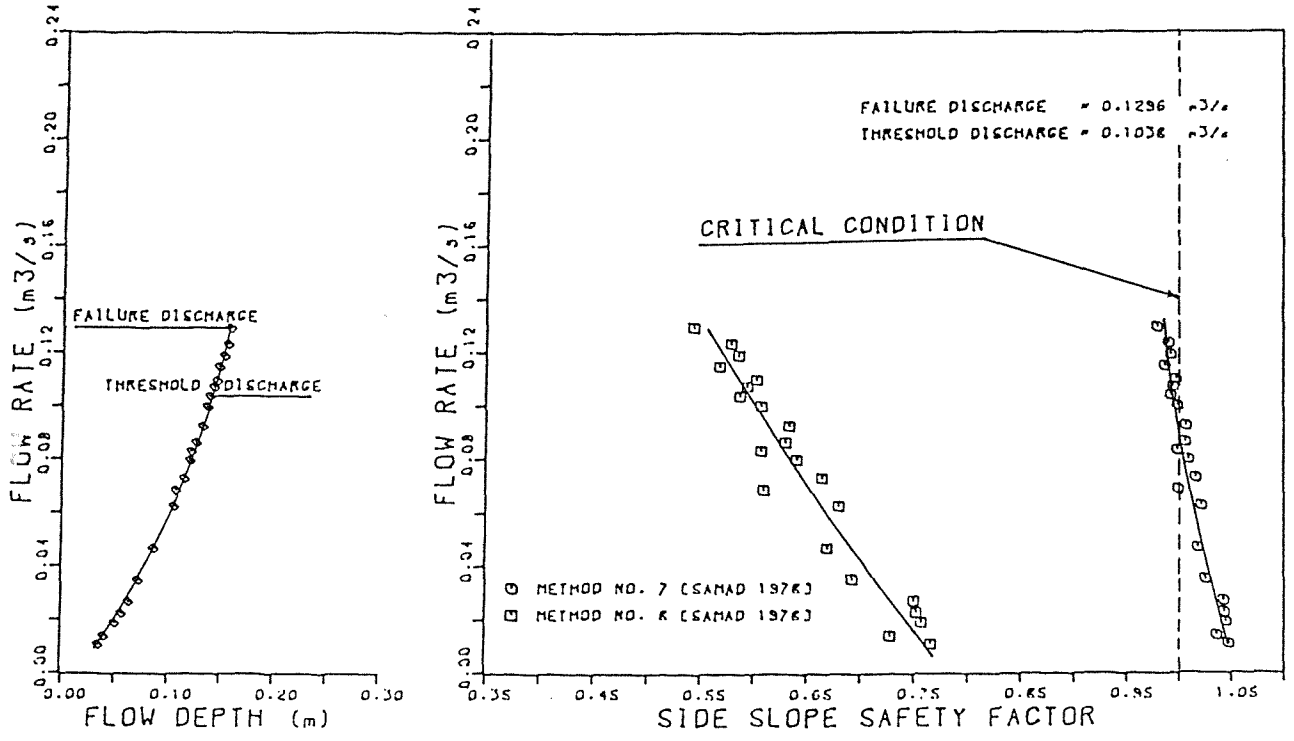

FIG.7-24 : CALCULATED SAFETY FACTOR USING SAMAD APPROACHES FOR MODEL NO. 6 [BED SLOPE = 0.0125]

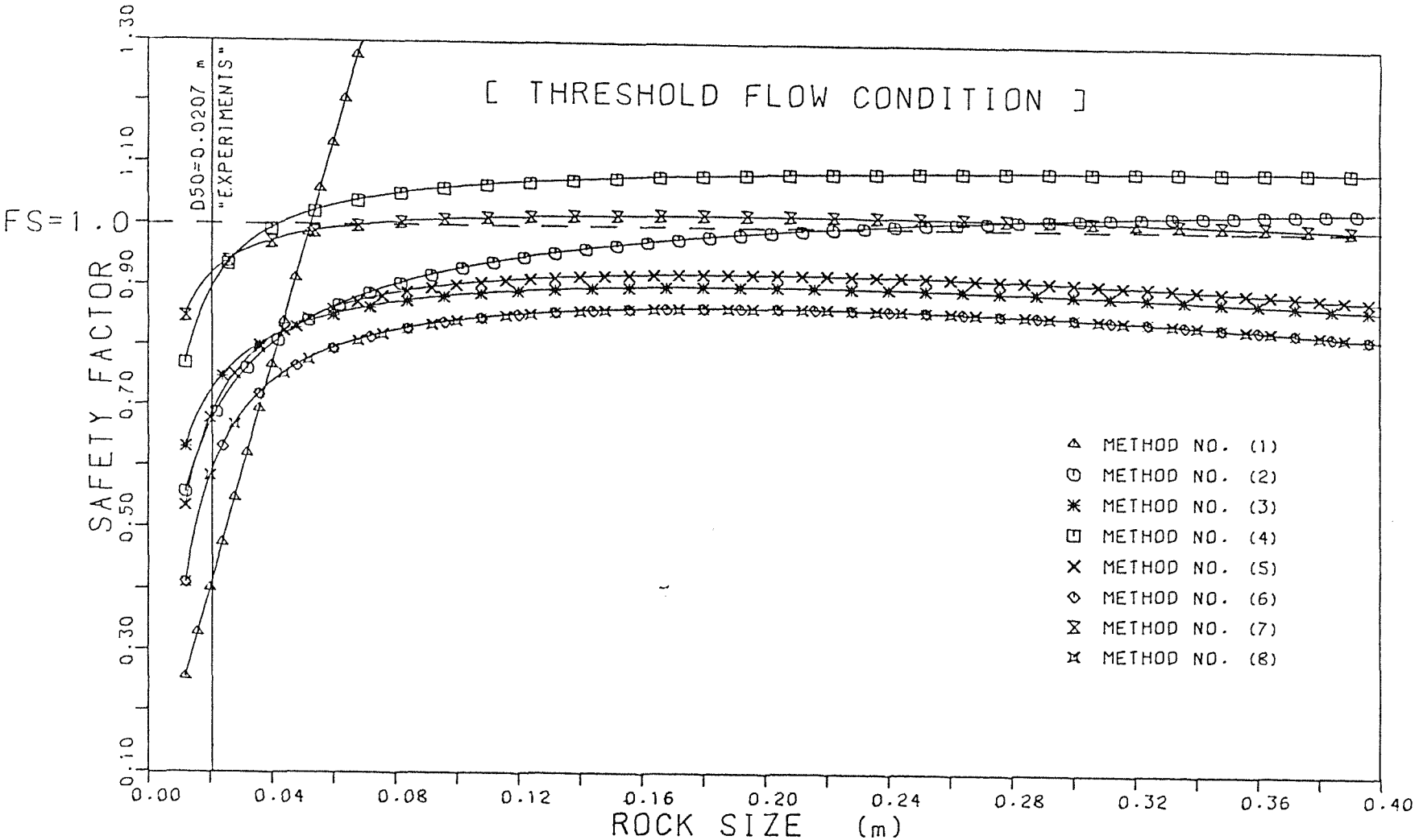

FIG.7-25:COMPARISON OF SAFETY FACTOR FOR DIFFERENT ROCK SIZES [MODEL NO. 4]

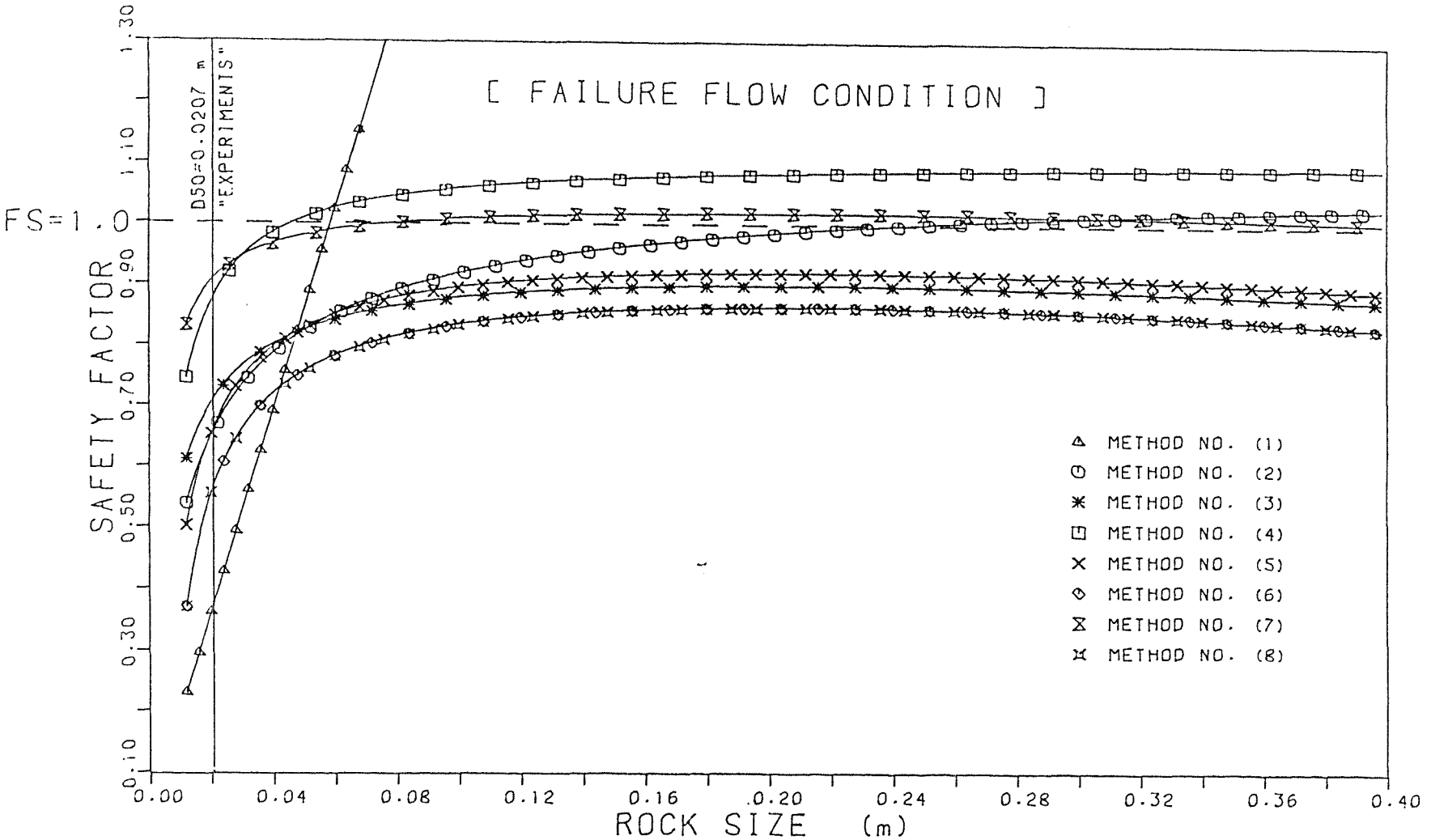

FIG.7-26:COMPARISON OF SAFETY FACTOR FOR DIFFERENT ROCK SIZES [MODEL NO. 4]

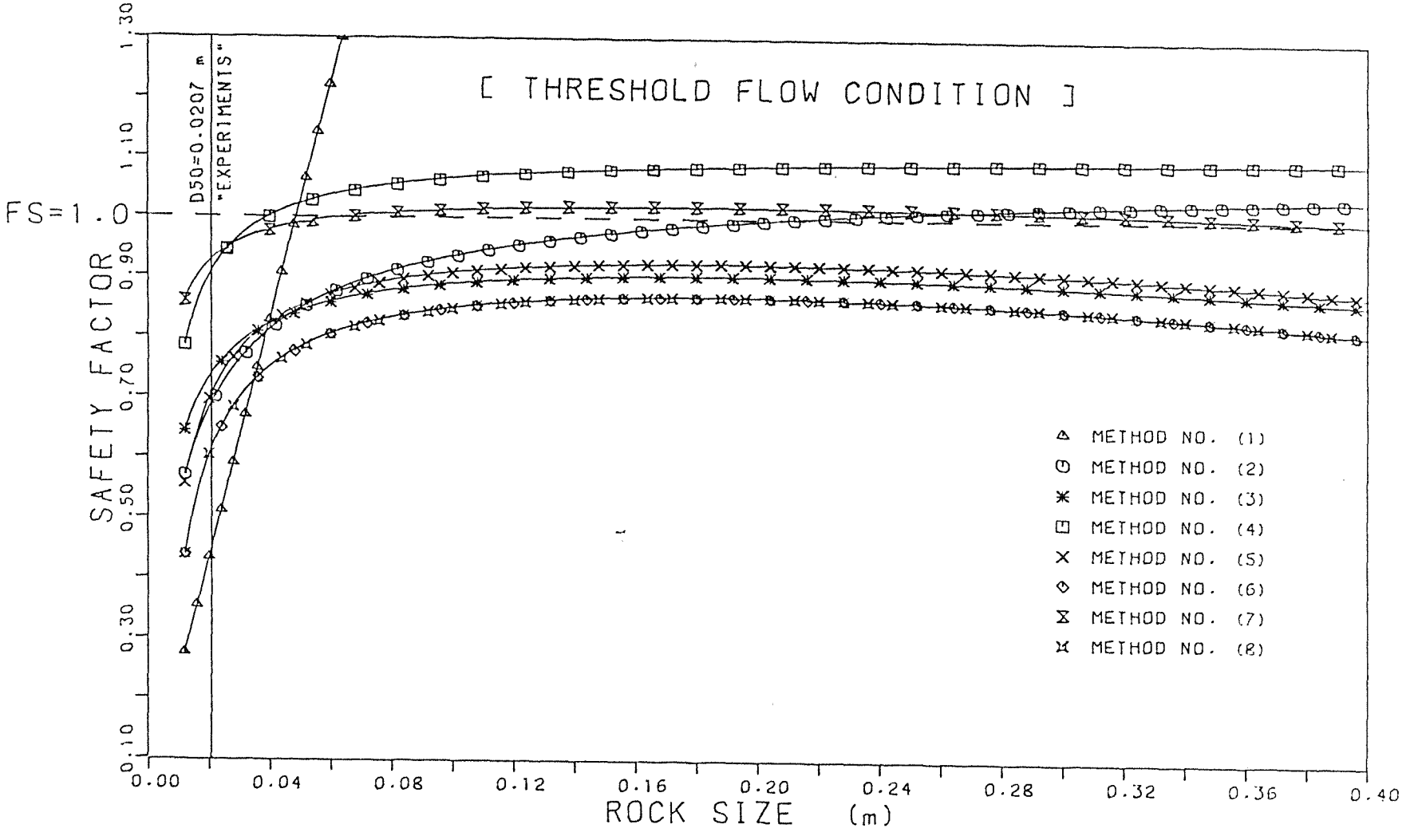

FIG.7-27: COMPARISON OF SAFETY FACTOR FOR DIFFERENT ROCK SIZES [MODEL NO. 5]

FIG.7-28:COMPARISON OF SAFETY FACTOR FOR DIFFERENT ROCK SIZES [MODEL NO. 5]

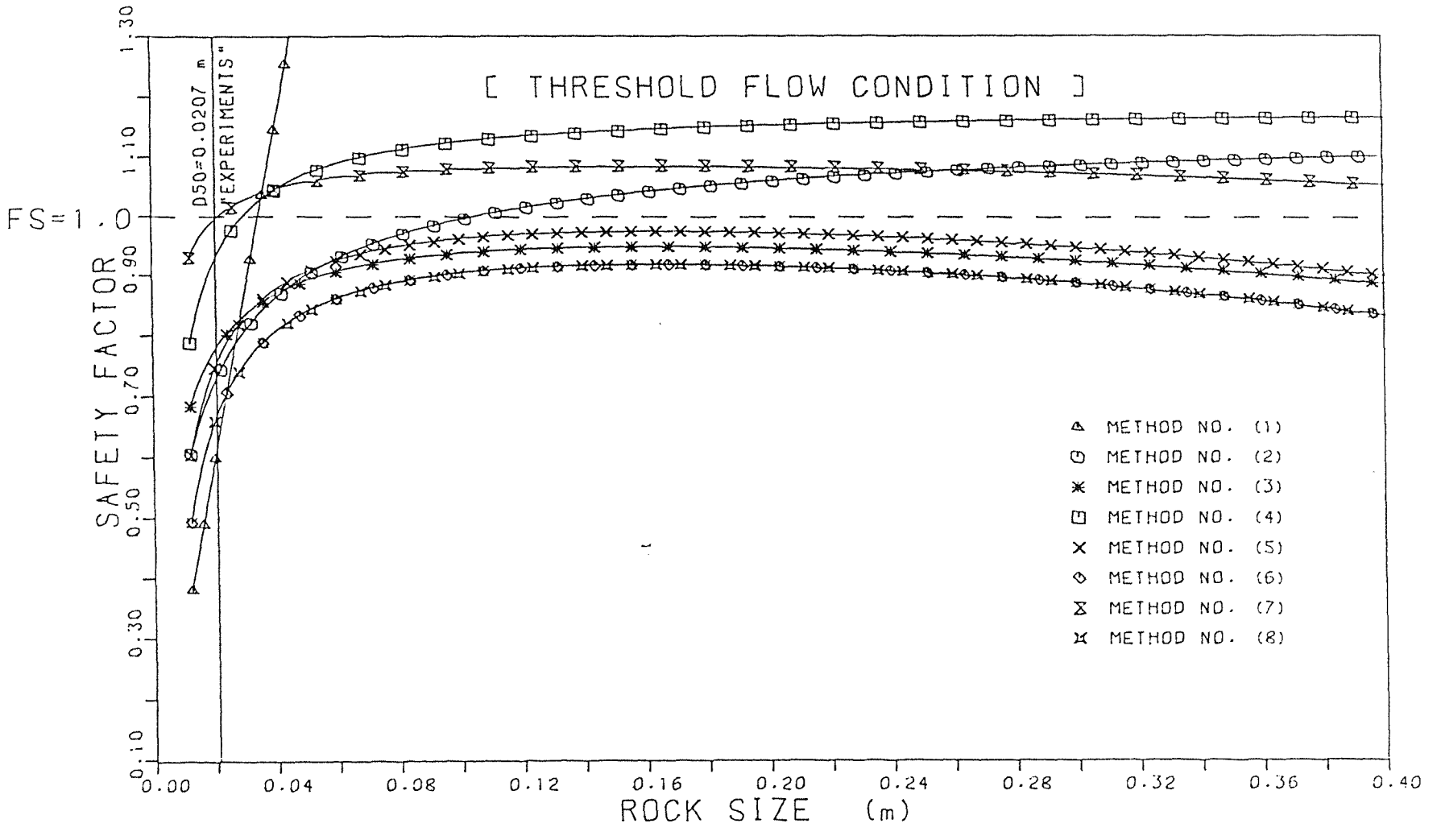

FIG.7-29:COMPARISON OF SAFETY FACTOR FOR DIFFERENT ROCK SIZES [MODEL NO. 6]

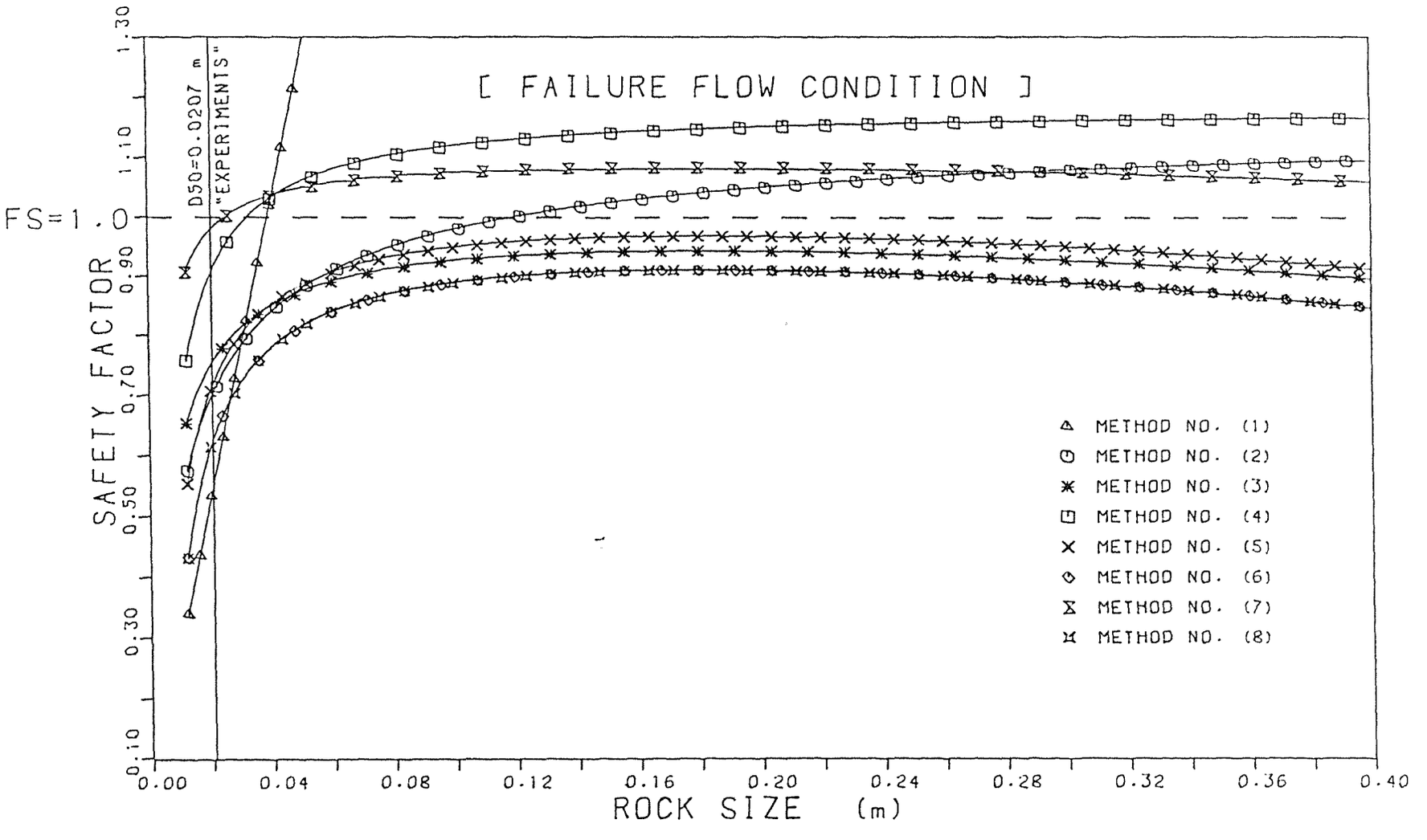

FIG.7-30: COMPARISON OF SAFETY FACTOR FOR DIFFERENT ROCK SIZES [MODEL NO. 6]

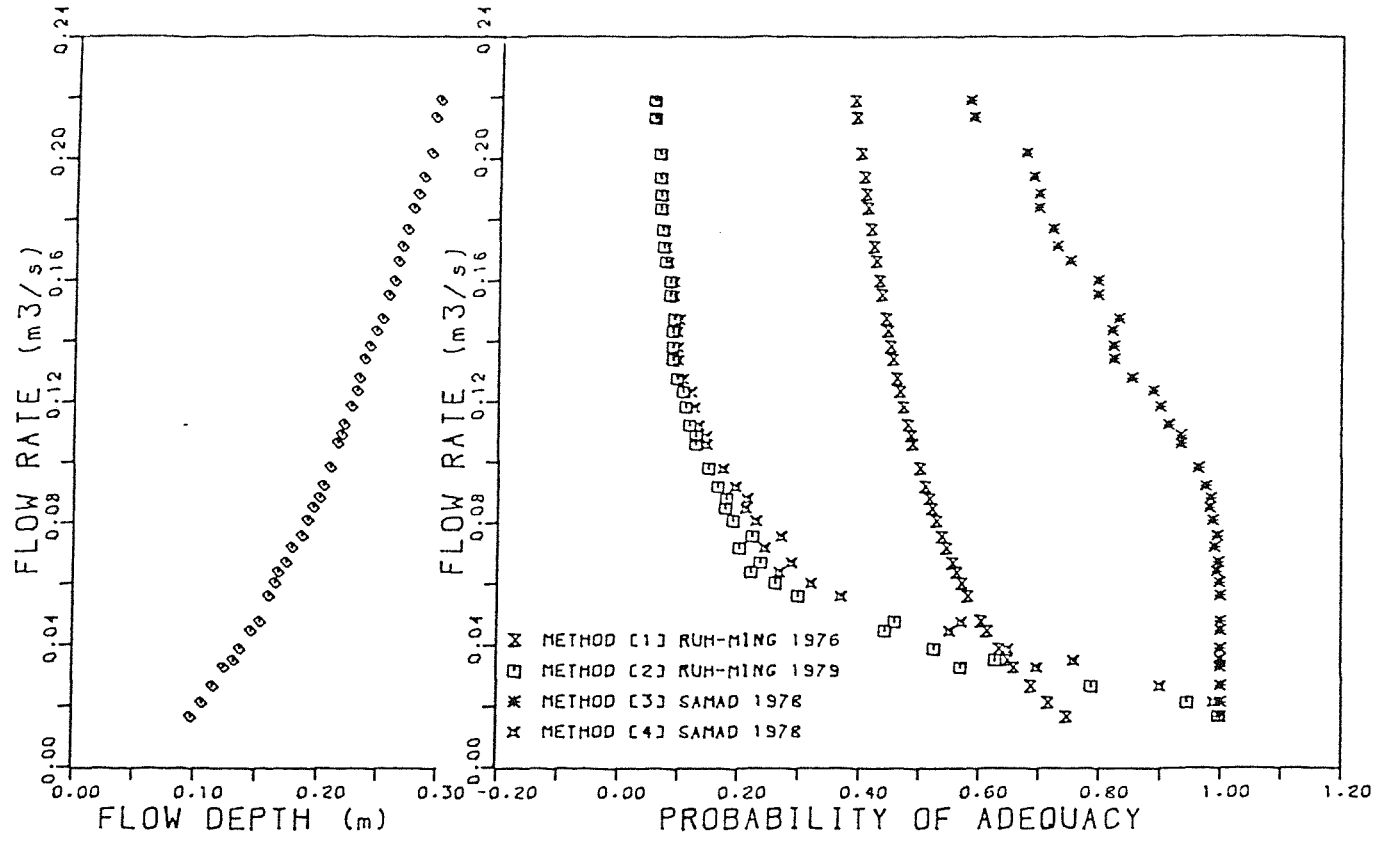

FIG.**7-31**: THE PROBABILITY OF SIDE SLOPE ADEQUACY PREDICTED FOR MODEL NO. (1) [S_o = 0.005]

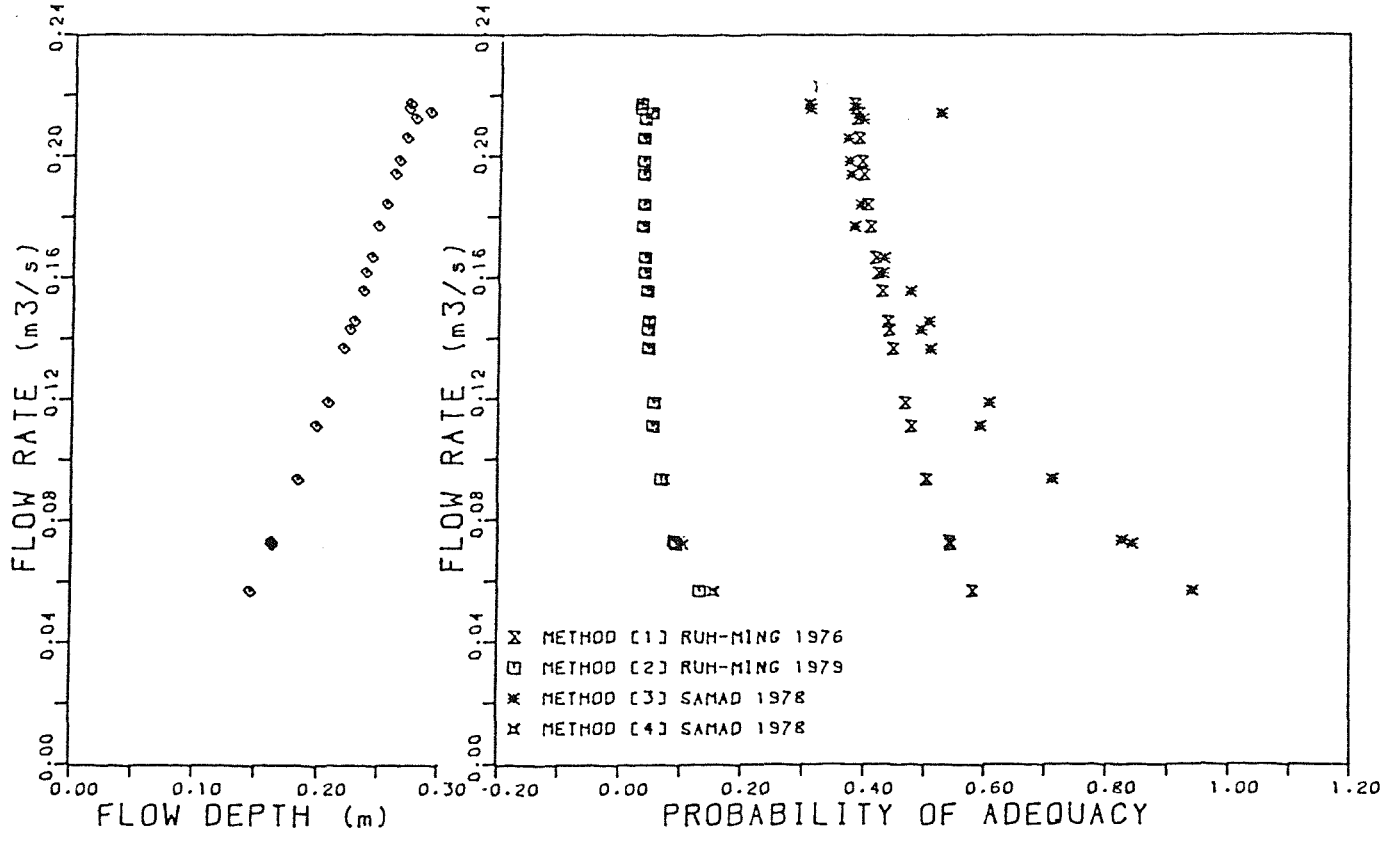

FIG.**7-32**: THE PROBABILITY OF SIDE SLOPE ADEQUACY PREDICTED FOR MODEL NO. (2) [S_o = 0.008]

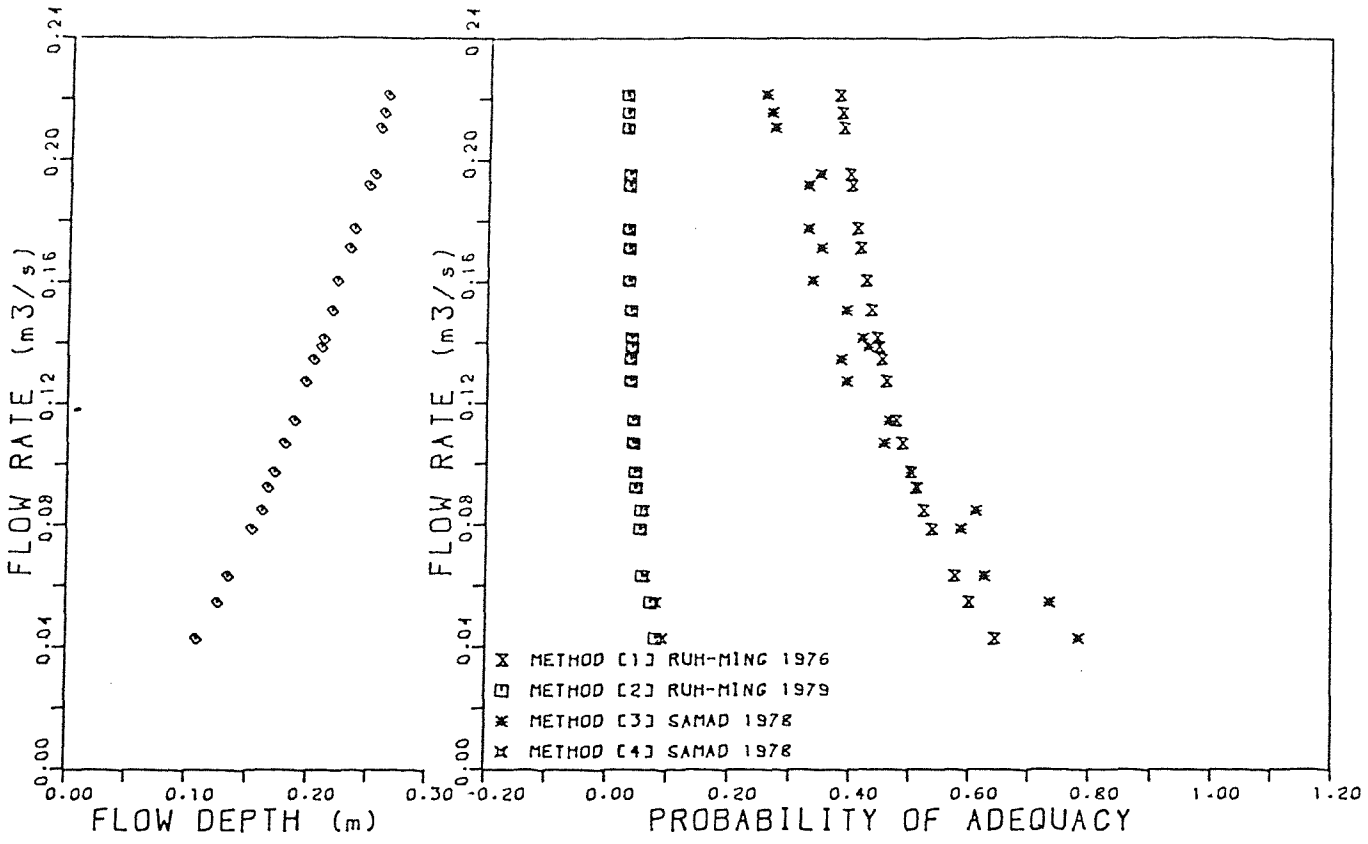

FIG.**7-33** : THE PROBABILITY OF SIDE SLOPE ADEQUACY PREDICTED FOR MODEL NO. (3) [S_o = 0.008]

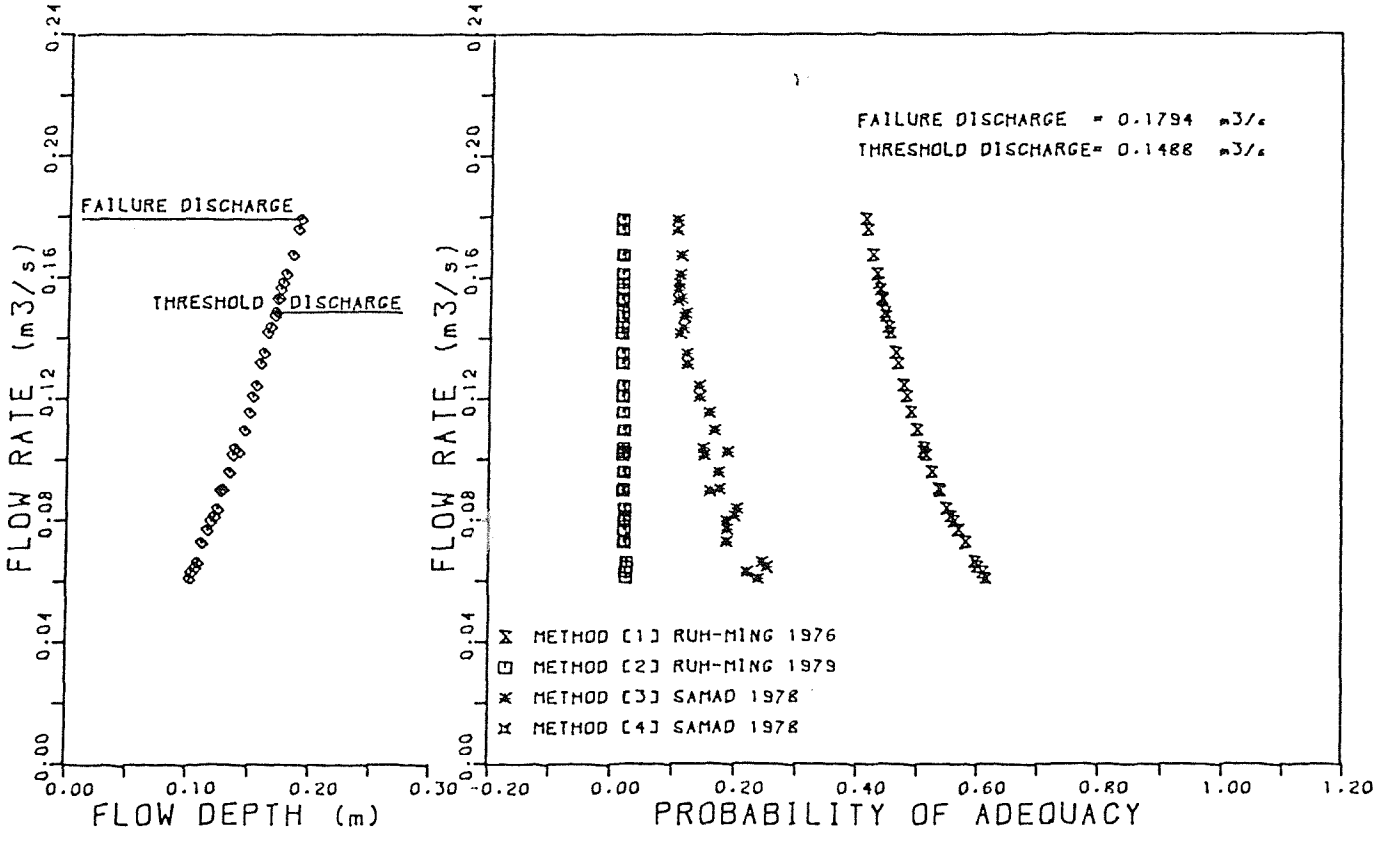

FIG.**7-34** : THE PROBABILITY OF SIDE SLOPE ADEQUACY PREDICTED FOR MODEL NO. (4) [S_o =0.0125]

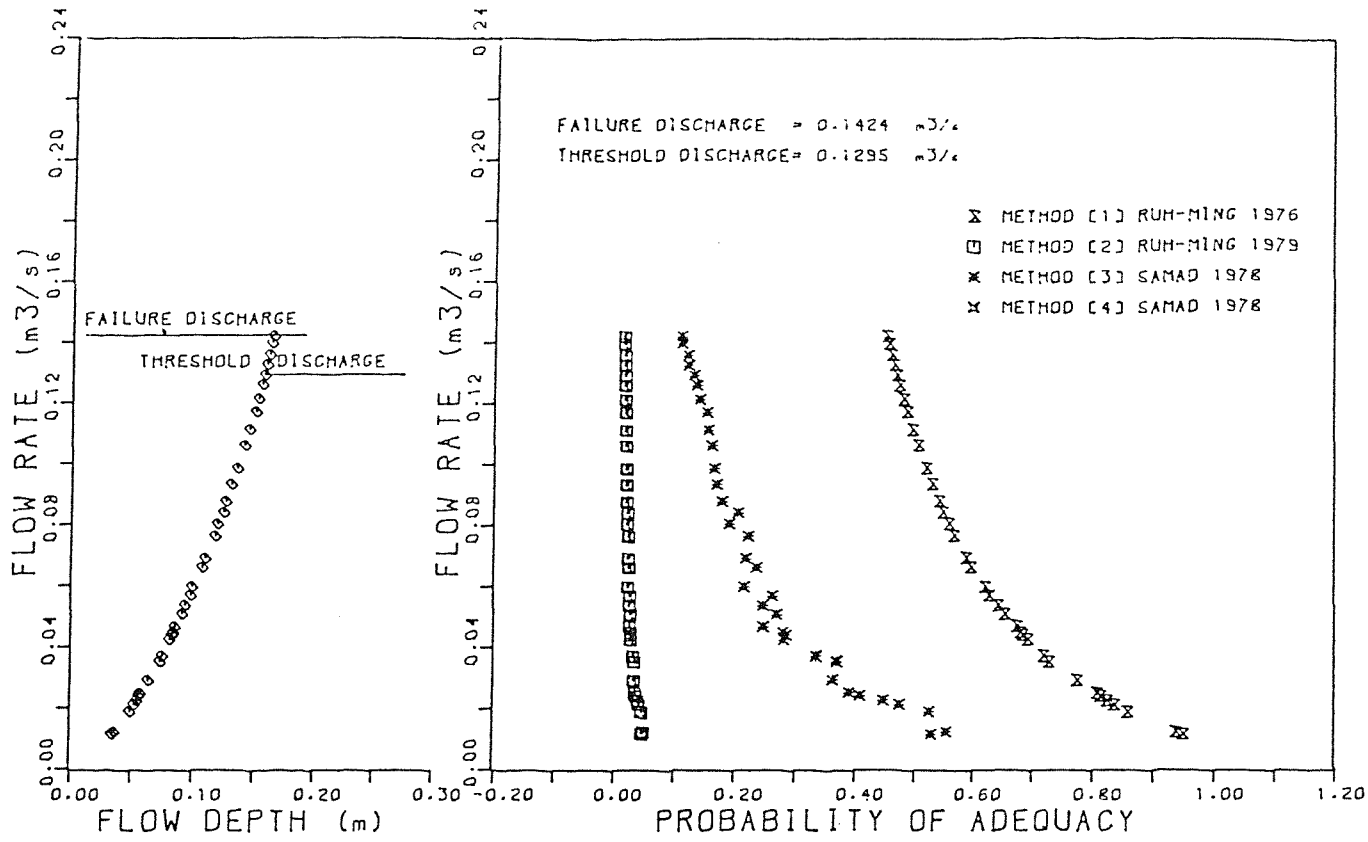

FIG.7-35 : THE PROBABILITY OF SIDE SLOPE ADEQUACY PREDICTED FOR MODEL NO. (5) [S_o = 0.0125]

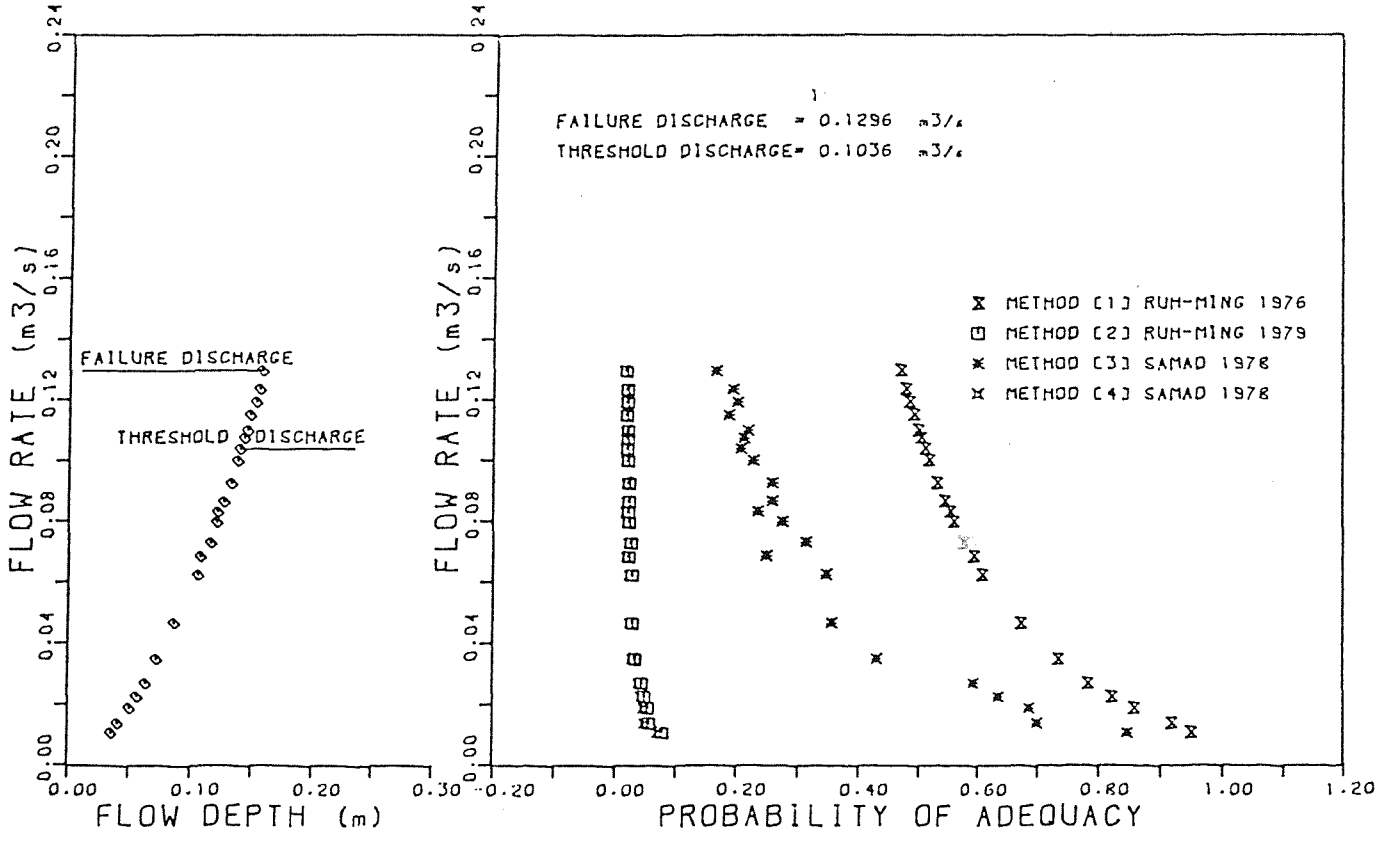

FIG.7-36 : THE PROBABILITY OF SIDE SLOPE ADEQUACY PREDICTED FOR MODEL NO. (6) [S_o = 0.0125]

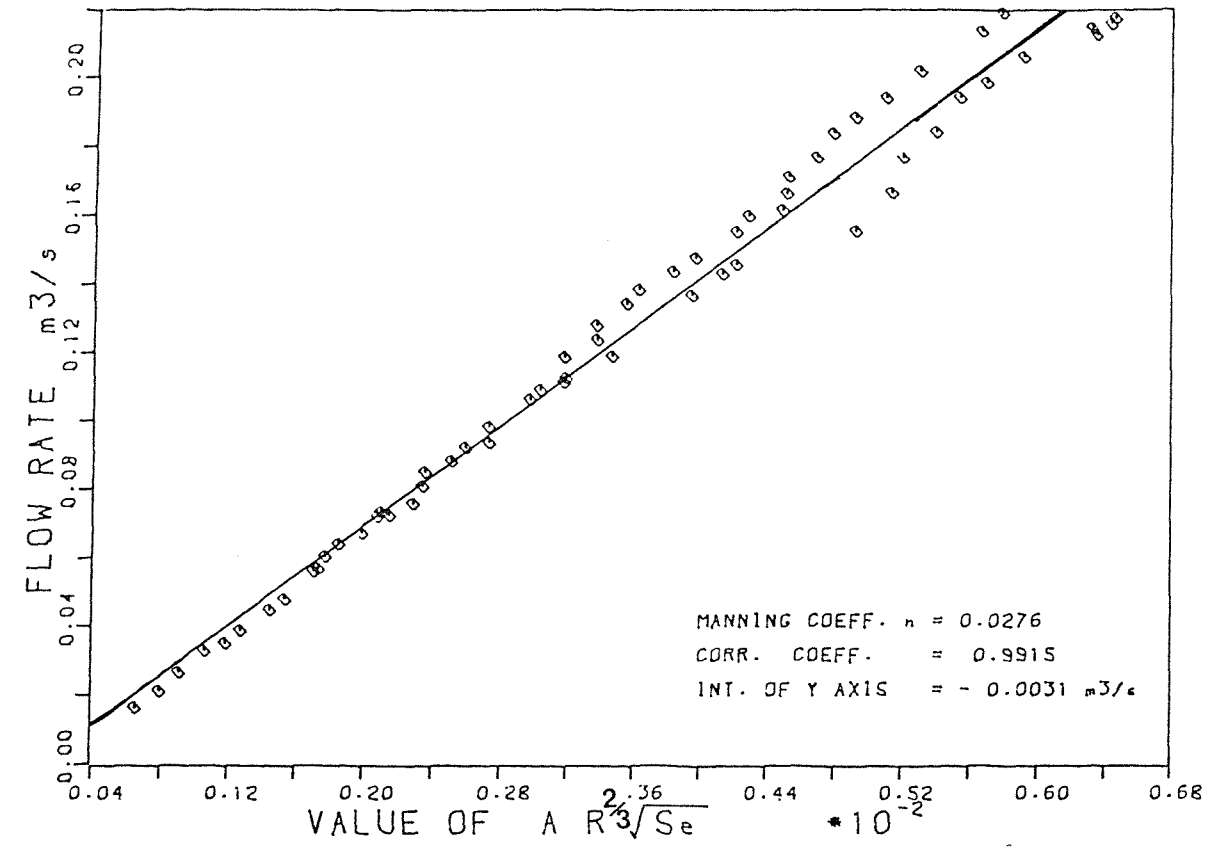

FIG.7-37: DETERMINATION OF MANNING COEFF. n

FOR MODELS 1 & 2

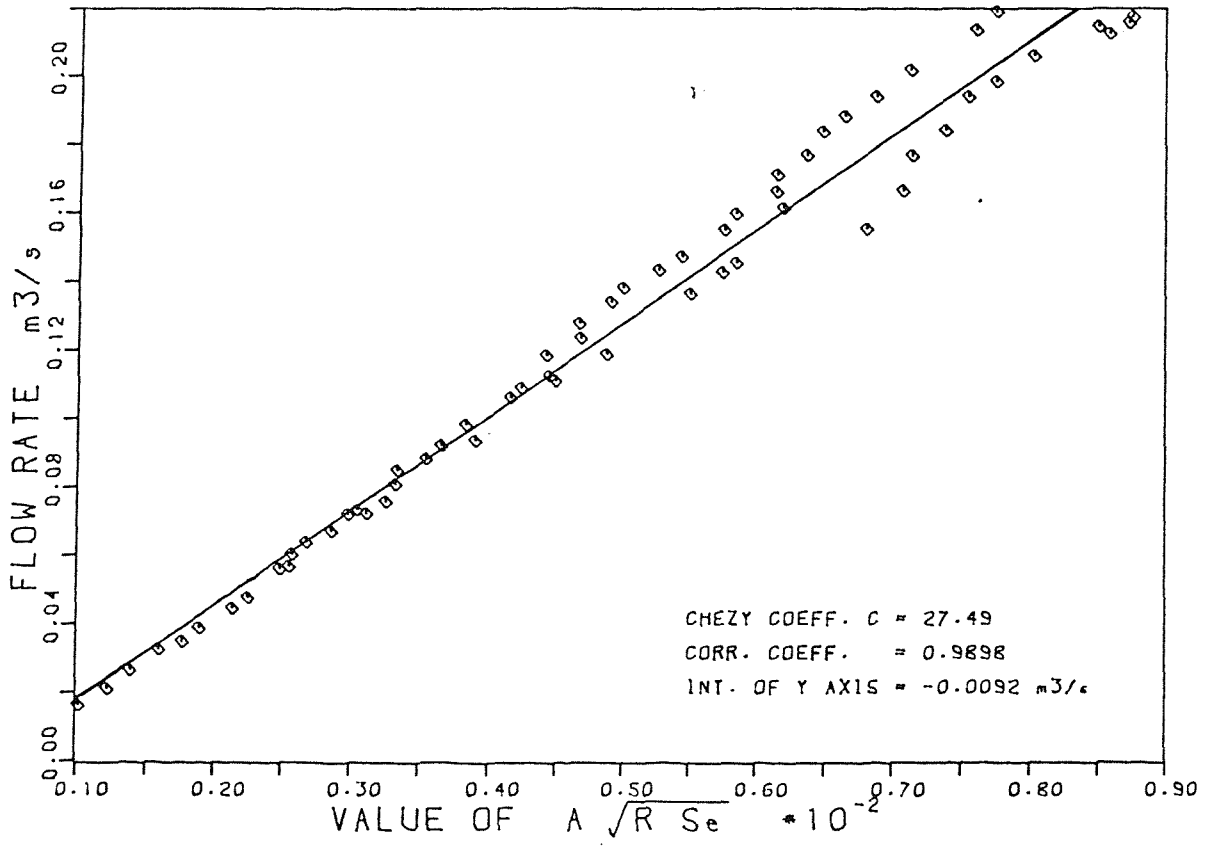

FIG.7-38: DETERMINATION OF CHEZY COEFF. C

FOR MODELS 1 & 2

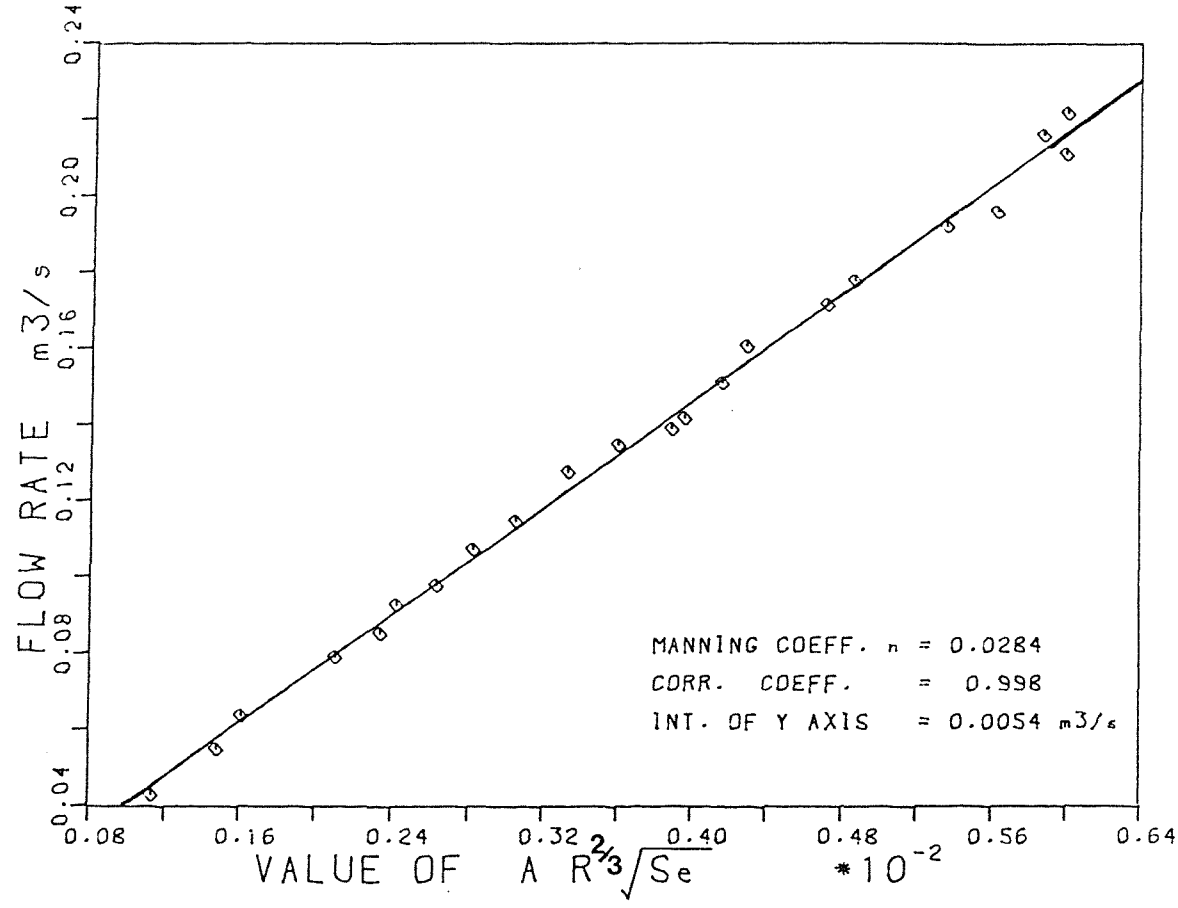

FIG.7-39: DETERMINATION OF THE EQUIVALENT MANNING COEFF. n FOR MODEL 3

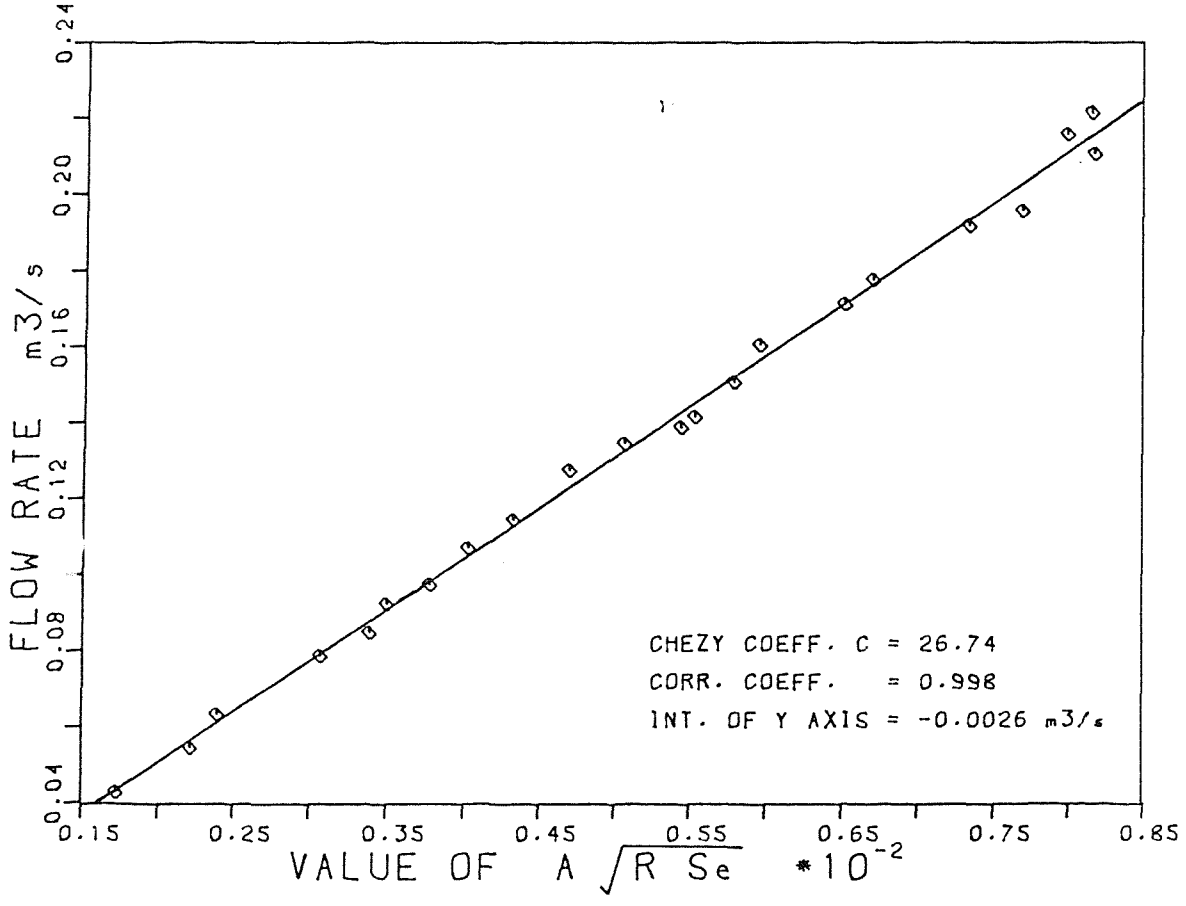

FIG.7-40: DETERMINATION OF THE EQUIVALENT CHEZY COEFF. C FOR MODEL 3

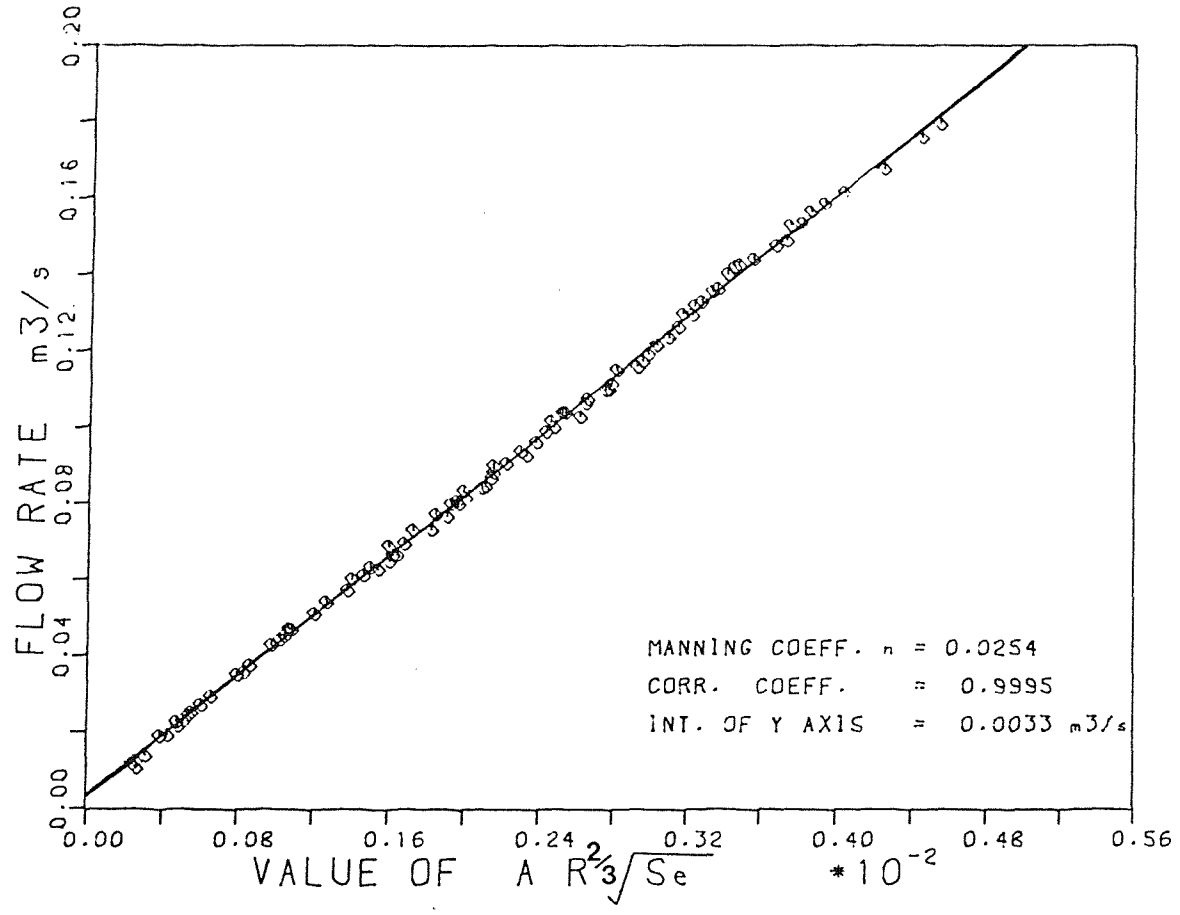

FIG.7-41: DETERMINATION OF THE EQUIVALENT MANNING COEFF. n FOR MODELS 4,5&6

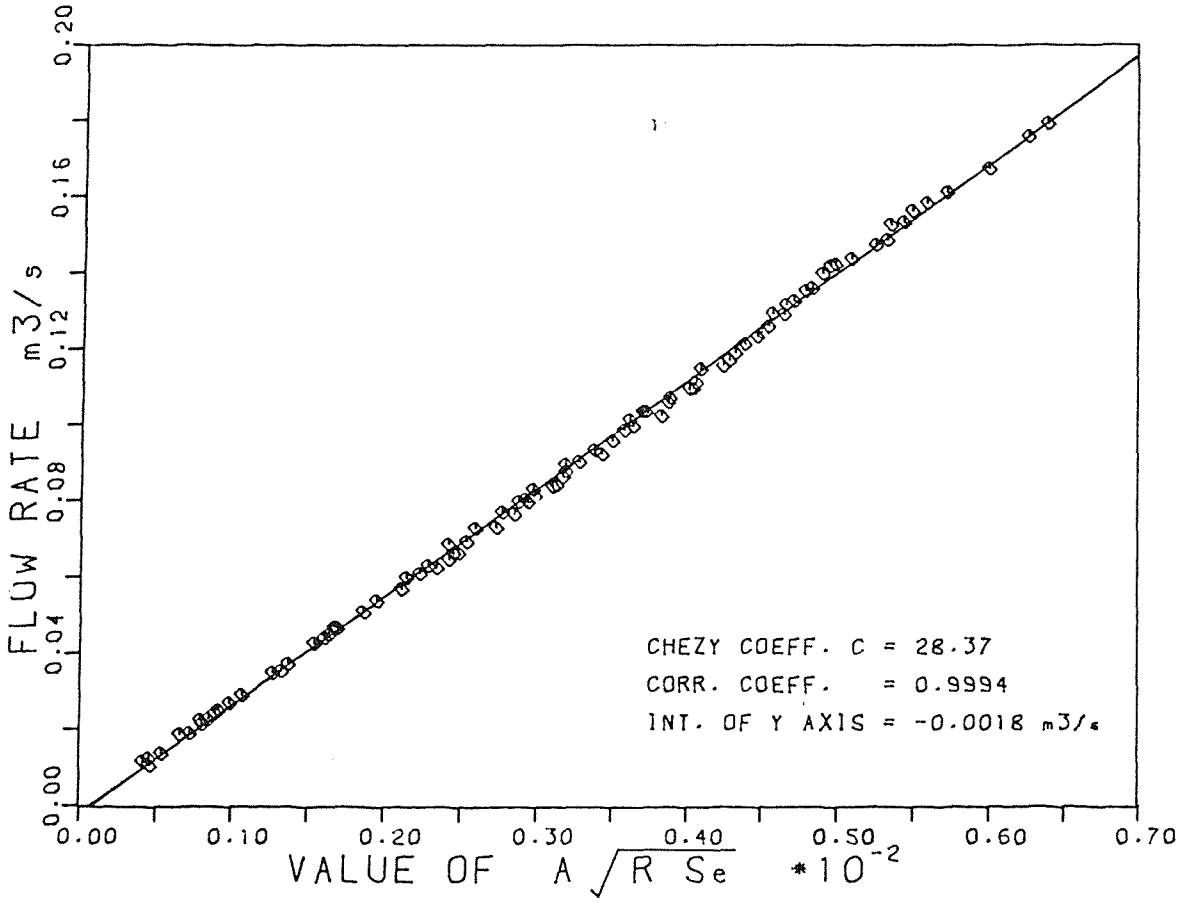

FIG.7-42: DETERMINATION OF THE EQUIVALENT CHEZY COEFF. C FOR MODELS 4,5&6

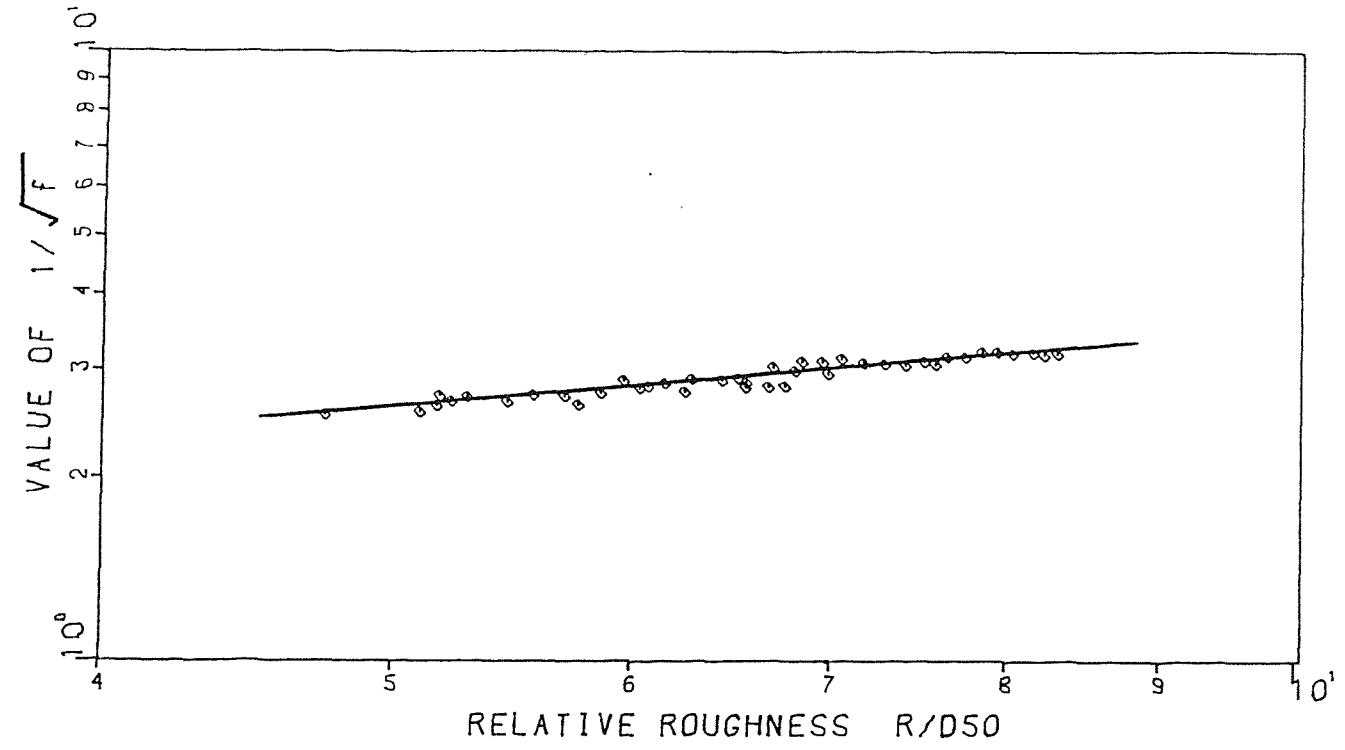

FIG.7-43: VARIATION OF $1/\sqrt{f}$ WITH R/D50
FOR MODELS 1 & 2

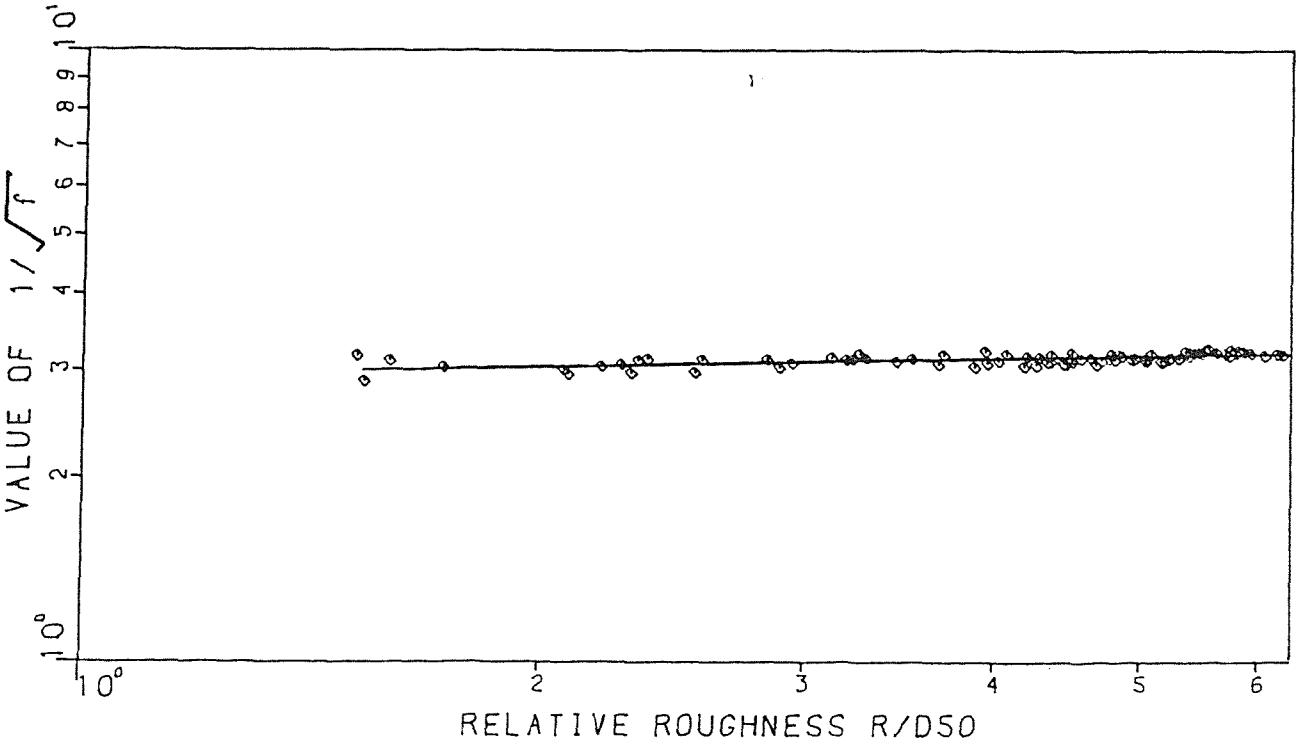

FIG.7-44: VARIATION OF $1/\sqrt{f}$ WITH R/D50
FOR MODELS 4 , 5 & 6

Plate (7-1) Some photos of the failures occurring in Model no.(4)

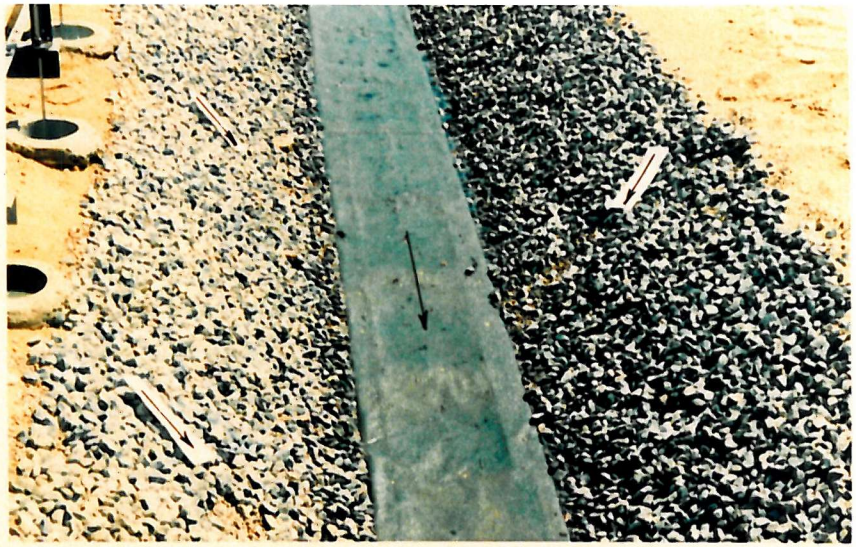

Plate (7-2) General views of the slope failure in Model no.(4)

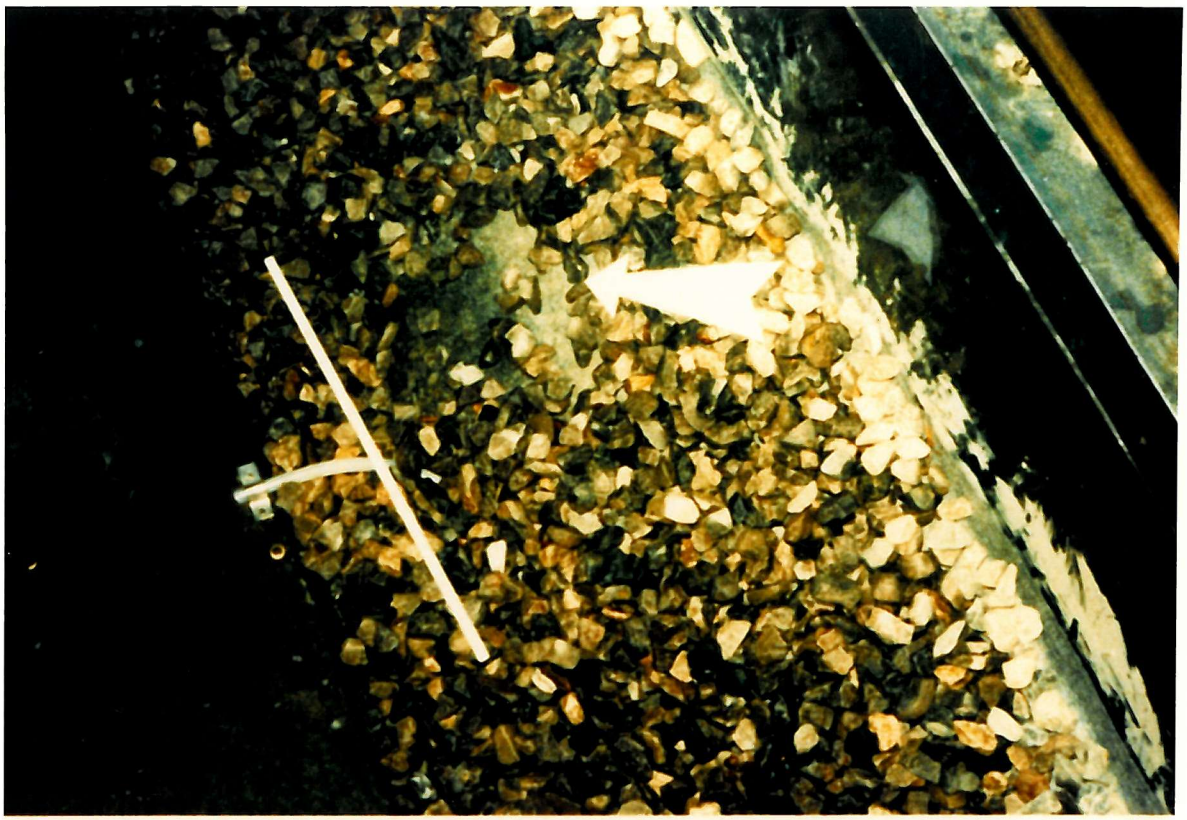

Plate (7-3) Slope failures in Model no.(5)

Plate (7-4) Slope failure in Model no.(6)

Plate (7-5) Failures within the coloured compartments

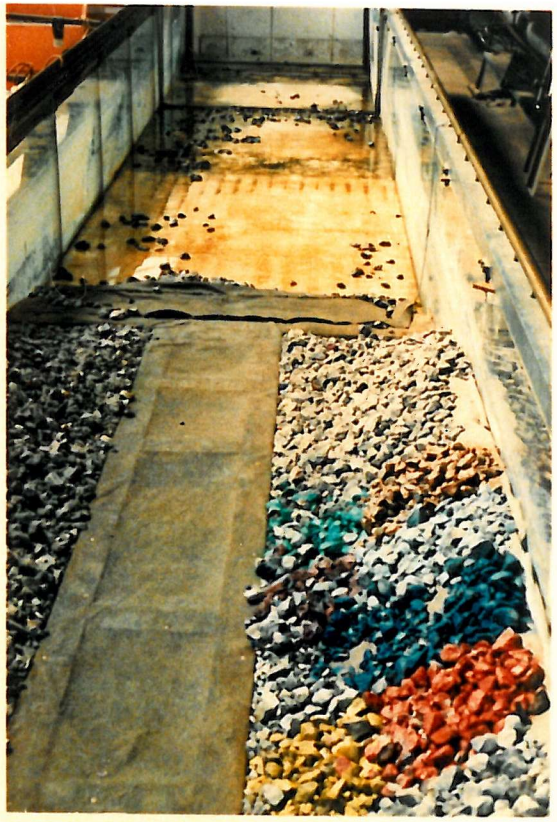

Plate (7-6) The coloured compartments before and after test

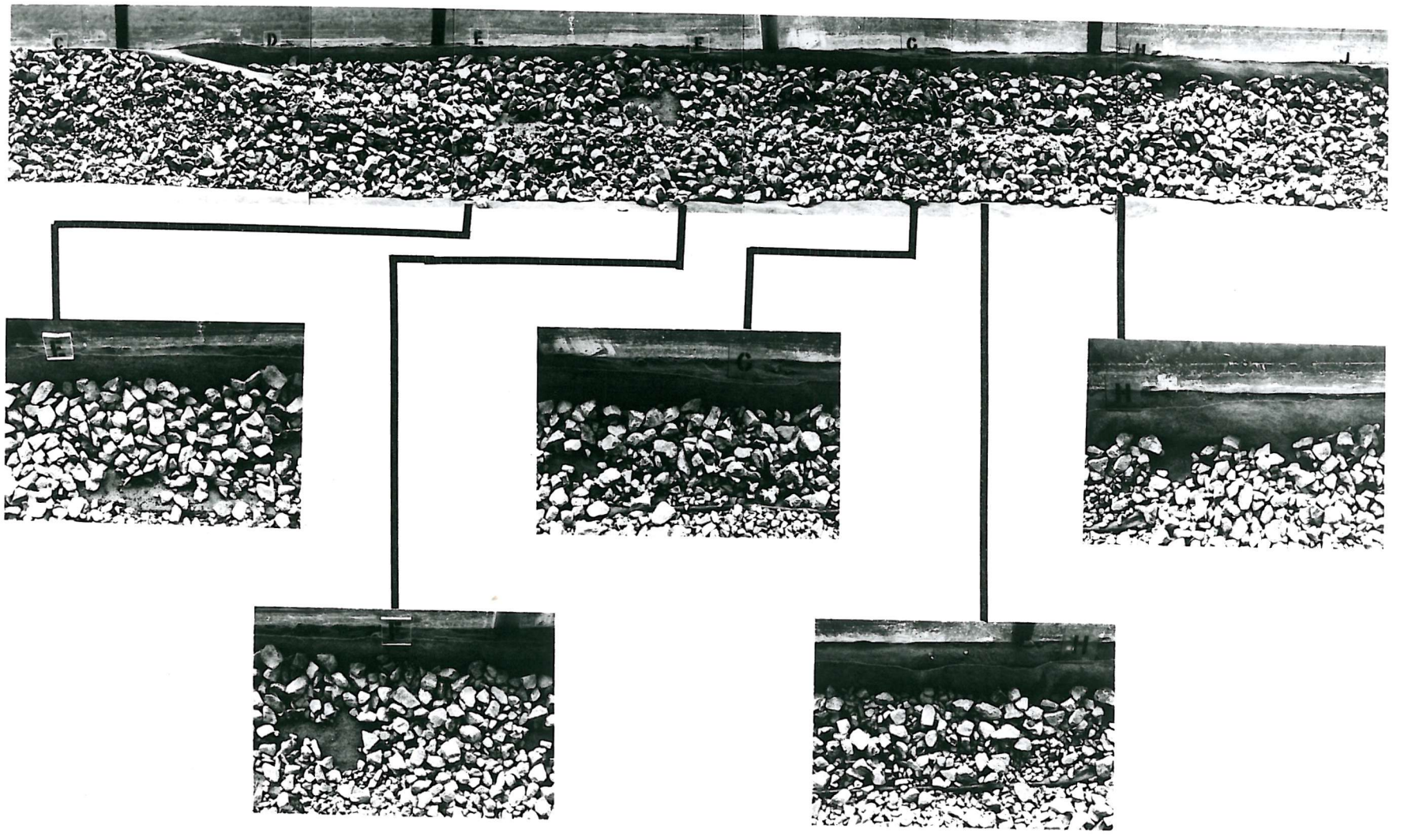

Plate (7-7) Local instability of filter cloth due to sliding in Model no.(6)

CHAPTER EIGHT

RESULTS OF THE FORCE MEASUREMENTS

8.1 INTRODUCTION

So far, it has been shown in the previous chapters that the side slope safety factor and probability of adequacy, predicted by various deterministic and probabilistic approaches, cannot be said to be in accordance with the results from the experimental measurements. This is mainly due to the basis on which these approaches have been established, and also due to the dubious assumptions in some of them. Additionally, to the best of the Author's knowledge, no method was based on laboratory or field measurements of the forces acting on the side slope protective layer.

Furthermore, according to the previous investigations reviewed in Chapter Two, it was proved that a particle, lying either on the bed or side slope of an open channel in turbulent flow, experiences several kinds of forces which are not constant, but varying with the time at frequencies of the same order as the turbulent velocity fluctuations. This principally means that replacement of any particle will depend not only on the temporal mean values of the local drag and lift forces, but also on their instantaneous values and their statistical distribution. In the light of these considerations as well as the need to develop a design method based on experimental work, the following procedures were adopted.

In order to make direct measurements of the instantaneous values of lift and drag forces, a special force measuring device was designed. The experime tal arrangement was devised as a result of the following studies:

1 - Location of the depth of maximum wall shear for various flow conditions.

2 - Determination of the best size of the instrumented spherical particle.

3 - Design of suitable instrumentation for accurately measuring the forces.

4 - The devising of a suitable means of converting the signals measured into lift and drag forces.

The preceding studies as well as the calibration of the load cell were discussed in Chapter Six, whilst the results obtained from force measurements on spherical and non-spherical particles are presented in this chapter.

8.2 ANALYSIS OF RANDOM SIGNALS

One of the most significant purposes in any study is to characterize the topic under investigation. Typically, there is no unique description and, as the investigations develop, alternatives appear that prove more useful in some applications. Data representing a random physical phenomenon cannot be described explicitly because each discrete observation will be unique. In other words, any given observation will represent only one of many possible results which might have occurred. Therefore to extract information from the measured hydrodynamic lift and drag forces that direct observation may not reveal, certain statistical parameters can be worked out such as; (1) the mean and mean square values to obtain the probabilistic description of the instantaneous values of the data; (2) the probability density function to define the relative frequency; (3) the correlation function to give information about the influence of physical data at any time and (4) the frequency spectrum which describes the frequency composition of the data. These functions may be estimated as follows:-

8.2.1 Mean and Mean Square Values

For any finite set of stationary random signals x(i) where i = 1,2,3,...,N, the properties of the phenomenon can be hypothetically described by computing the mean value which is simply

the average of all values. In equation form, the mean value μ_x can be obtained as

$$\mu_x = \frac{1}{N} \sum_{i=1}^{N} x(i) \qquad (8.1)$$

the mean square value can be given as

$$\sigma_x^2 = \frac{1}{N} \sum_{i=1}^{N} x^2(i) \qquad (8.2)$$

Eq (8.2) , gives indication about the average energy of the signal. Substitute the mean value for the data set and apply the previous procedure, the signal variance can be obtained as:

$$\sigma_x^2 = \frac{1}{N} \sum_{i=1}^{N} (x(i) - \mu_x)^2 \qquad (8.3)$$

For a large number of observations (N>30), the variance can be defined with (N-1), replacing N, and Eq. (8.4) can be written as

$$\sigma_x^2 = \frac{1}{N-1} \sum_{i=1}^{N} (x(i) - \mu_x)^2 \qquad (8.4)$$

The square root of the signal variance is called the standard deviation which represents the average of the signal fluctuations around the mean.

8.2.2 Probability Density Function

The probability density function for random data describes the probability that the data will assume a value within some definite range at any instant of time, in other words, the probability density function provides information concerning the properties of the data in the amplitude domain.

Following Bendat, J.S. and Piersol, A.G. (1966), the probability that the instantaneous value x(t) assumes a value within the range between x and $(x+\Delta x)$ may be obtained by taking the ratio of T_x/T, where T_x is the total amount of time that x(t) falls inside the range $(x,x+\Delta x)$ during an observation time T.

In addition, to establish the frequency distribution for any observations, the data range can be distributed into equal class intervals and the number of observations within each class can be determined; then the relative frequency of any class would be equal to the frequency of the class divided by the total frequencies of all classes. Thereby, to determine the probability at any class interval, the corresponding cumulative frequency should be divided by the total number of observations.

On the practical side, it is usually required to know whether the observed frequencies differ significantly from the expected. In this case a measure of discrepancy existing between observed and expected frequencies may be established by applying the Chi-Squared test as

$$\chi^2 = \sum_{i=1}^{i=N} \frac{(O_i - e_i)^2}{e_i} \tag{8.5}$$

in which

$O_1, O_2, O_3, \ldots O_N$ are the observed frequencies
$e_1, e_2, e_3, \ldots e_N$ are the corresponding expected frequencies

where, if the total frequency is equal to K,

$$\Sigma O_i = \Sigma e_i = K \tag{8.6}$$

As a result of this test, if $\chi^2 = 0$, it means that both observed and theoretical frequencies are exactly in agreement, while the opposite is true if $\chi^2 > 0$.

Therefore, applying Eq. (8.5), the observed frequency distribution can be tested versus all the standard distributions and the larger the value of χ^2, the greater is the discrepancy between observed and expected. This, in other words, means that the frequency distribution fitted to the observed data will be that which gives minimum value of χ^2.

8.2.3 Correlation Functions

Considering two different sets of random signals x(i) and y(i), the dependence of value at any time on the value at another time can be described by the autocorrelation function, whilst the cross-correlation function describes the dependency of the values of one set of data on the other. These functions can be summarized as follows:

8.2.3.1 Autocorrelation function

For a given set of random data x(i), where i = 1,2,3,...N, the mathematical expression for the autocorrelation function can be written as

$$R_x(t) = \frac{1}{N-t} \sum_{i=1}^{N-t} x(i).\ x(i+t) \qquad (8.7)$$

in which $t = 0,1,2,\ldots,M,$

$i = 1,3,3,\ldots,N;$

and M is the number of lag times.

The normalized autocorrelation function may be defined as

$$RN(t) = R_x(t)/R_x(0) \qquad (8.8)$$

8.2.3.2 Cross-correlation function

Considering two sets of random signals x(i) and y(i), the mathematical expression for the cross-correlation function $R_{xy}(t)$ may be expressed as

$$R_{xy}(t) = \frac{1}{N-t} \sum_{i=1}^{N-t} x(i).y(i+t) \qquad (8.9)$$

The normalized cross-correlation function RNxy(t) may then be defined as

$$RN_{xy}(t) = \frac{R_{xy}(t)}{(R_x(0))^{\frac{1}{2}}.(R_y(0))^{\frac{1}{2}}} \qquad (8.10)$$

Eq. (8.10) satisfies all values of t including t = 0, and also the condition

$$-1 \leqslant RN_{xy}(t) \leqslant +1 \qquad (8.11)$$

When $RN_{xy}(t) = 0$, it means there is no dependency between x(i) and y(i). But when $RN_{yx}(t) = 1$, it means both sets are completely related and these roles are also applicable in the case of RN(t) given by Eq. (8.8).

8.2.4 Frequency Spectrum

To establish the frequency composition of the data, the Fourier Transform should be computed, which converts the data from time domain to the frequency domain. The finite range, discrete time, Fourier Transform X(K); for the Kth frequency; for real time histories x(i) is

$$X(K) = T \sum_{i=1}^{N-1} x(i) \exp^{(-j.2\pi iK/N)} \qquad (8.12)$$

in which

K = 0,1,2, ... , N/2 for N even
K = 0,1,2, ... , (N-1)/2 for N odd

and the corresponding frequency is

$$f_K = K/(N.T) = K/P \qquad (8.13)$$

where

T is the sampling interval;
j is the square root of (-1);
N is the number of x data values;
and P is the record length.

The Fourier Transform at specific frequency is a complex number and is often described in terms of polar coordinates as:

$$|X(K)| = [R_o^2 (X(K)) + I_m^2 (X(K))]^{\frac{1}{2}} \qquad (8.14)$$

where $R_o(X(K))$ and $I_m(X(K))$ are the real and imaginary parts of the Fourier Transform respectively and can be defined as:

$$R_o(X(K)) = T \sum_{i=1}^{N-1} x(i) \cos (2\pi iK/N) \qquad (8.15)$$

$$I_m(X(K)) = -T \sum_{i=1}^{N-1} x(i) \sin (2\pi iK/N) \qquad (8.16)$$

To establish the frequency spectrum of the data measured, a computer programme was developed which included a Fast Fourier Transform Subroutine written by Otnes, R.K. and Enochson, L.D. (1978).

8.3 DATA SAMPLING

A major consideration in any data analysis is the extraction of the maximum amount of information from the minimum amount of data. In other words, selection of an appropriate sampling scheme can usually decrease the volume of data required to define the parameter of interest with the desired precision.

On the practical side, two vital factors should be determined before carrying out any measurements, and these are the record length and sampling interval. In fact, both parameters are influenced by numerous factors, obviously the major ones being the amount of statistical information desired and the limited storage capacity of the available computer system.

8.3.1 Record Length

To establish the record length, a preliminary run was made, in which the lift and drag forces were recorded for thirty seconds at a rate of 250 readings per second. Then the data was analysed from the beginning of the record for different record lengths. For each case, the mean and standard deviation were determined and found nearly constant.

These results revealed that the process is stationary random and accordingly a sample period of 7 seconds was successfully recorded for each run of the measurements. This means for each run a record length of 1750 data values for both lift and drag forces was acquired.

8.3.2 Sampling Interval

Sampling for the digital data is usually performed at equally spaced intervals f_c. The problem then is to determine the appropriate sampling interval. Sampling at points which are too close will yield correlated and highly redundant data and thus an unnecessary increase in the computation time. Also sampling at points which are too far apart will lead to confusion between the low and high frequency components in the original data, called "aliasing".

In order to select the appropriate sampling interval, the frequency spectrum of the preceding test run was established which showed the concentration of the signal power in the low frequency range between 0 and 20 Hz. For reasons of safety, a cut off frequency of 125 Hz was found sufficient to prevent the aliasing error and also to satisfy the condition reported by Bendat, J.S., and Piersal, A.G. (1966), as

$$F_s = 1/(2.f_c) \qquad (8.17)$$

in which

F_s is the cutoff frequency equal to 125 Hz.

Applying Eq. (8.17), it is obvious that a sampling interval f_c equal to 0.004 seconds is satisfactory. The speed of the data recording (the sampling rate) was regulated by means of a calibrated time delay loop which was included within a specially written subroutine for acquiring the force measurements.

8.4 CALIBRATION TESTS

The load beam was calibrated in the manner described in Section (6.5), and both the record length and sampling interval discussed previously were adopted. The following tests were carried out to examine the whole system.

8.4.1 In Still Water

To examine the measuring system as well as the computer programme, the flume was partially filled with water, then both ends of the flume were blocked so as to maintain still water conditions. The movable board containing the instrumented particle was fixed on the embedded cavity so as to submerge the instrumented spherical particle in the still water. The measuring technique summarized in Section (6.6) was then carried out.

The mean values of lift and drag forces obtained from this test were almost zero. This result revealed that the computer programme was working successfully and also the zero datum readings obtained from the signal conditioner did not alter during the course of the measuring.

8.4.2 Under Steady Flow Conditions

The hydrodynamic forces acting on any particle, regardless either of its position or orientation, are entirely dependent on the flow condition, so that the forces acting on any one particle will follow a certain behaviour as long as no movement occurs and there is no change in the flow condition. This was employed to specify the characteristics of the measured forces in more detail as follows:

An arbitrary run was obtained, then the flow uniformity established. Three samples were recorded for the forces at a sampling rate of 250 readings per second for a period of two seconds at an interval of ten minutes between one record and another.

The data recorded are plotted in Fig. (8.1), which shows that both lift and drag forces signals are randomly fluctuating around a mean value. Also the mean was the same for the three data sets which indicated that the fluctuation process was stationary random.

8.5 THE TESTING PROCEDURE

Twelve runs covering a wide range of flows and named MF1 to MF12, were performed. For each run the hydrodynamic lift and drag forces acting on a simulated spherical particle were recorded, as explained in Section (6.6). During the experimental work, for all runs, the drag and lift forces as well as the necessary information of the flow condition were recorded on a floppy disk and the statistical parameters were calculated and displayed on the VDU screen and also recorded on the disk. These data were transferred, via the BBC computer system, to the mainframe (VAX) computer at the Civil Engineering Department, for carrying out the necessary evaluation and analysis.

In order to ascertain the effect of particle shape and orientation, the drag and lift forces were measured on each of the four non-spherical particles as described in Section (6.4.3.2). Since the test was principally established for the purpose of comparison, the investigation was conducted, for all particles, only in one flow condition. In each case the instantaneous values of lift and drag forces were simultaneously recorded for four seconds.

8.6 DATA ANALYSIS AND RESULTS

8.6.1 Spherical Particle

8.6.1.1 Statistical parameters

For all runs, the mean, standard deviation (SD), skewness coefficient and the coefficient of variation (intensity), which is equal to SD/mean, for both lift and drag forces were determined. Then in order to carry out a frequency analysis, the data acquired

were regrouped into histogram class intervals and the technique explained in Section (8.2.2), was applied in order to estimate the theoretical density function that was appropriate to the observations.

Using the aforementioned technique, it was concluded that for all runs, the probability densities of the fluctuating lift and drag forces in this investigation were normally distributed. The fluctuations and the probability distributions of the forces acquired are shown in Figs. (8.2) to (8.13), whilst a summary of the results obtained for all runs is listed in Table (8.1).

8.6.1.2 Correlation functions and frequency spectrum

Applying the procedure explained in Section (8.2.3), the correlation coefficients for lift and drag and between both of them were calculated and plotted for all runs as shown in Figs. (8.14) to (8.25).

All the autocorrelation plots show a rapid decline from unity at zero time lag to zero at a delay time about a value of 0.15 seconds in the case of drag forces, and 0.01 in the case of lift forces, then a periodic oscillation about the line of zero correlation. This result proves that the signals are randomly fluctuating with low correlation.

Similarly, the cross-correlation plots indicated that the correlation coefficient between lift and drag at zero time lag was almost zero for all runs, then oscillated periodically within a range of ±0.05. This reveals that the cross-correlation was not significant and could be ignored hich leads to the conclusion that the drag and lift signals are uncorrelated and they are statistically independent.

In order to establish the frequency composition of the data acquired, the frequency spectrum for all runs was evaluated by using the procedure explained in Section (8.2.4). The results obtained were depicted on a decibel scale against the frequency in Hz (CPS) for all runs in Figs. (8.26) to (8.31). It can be seen from these figures that the frequency displays the same characteristics as the autocorrelation function. Where there is high content of energy in the low frequency range 0 up to about 20 Hz, the contribution to the total energy of frequencies higher than 20 Hz is small and becomes almost negligible.

8.6.1.3 Drag and lift coefficients

According to the prior investigation presented in Section (2.2), the hydrodynamic drag and lift forces acting on a typical particle were expressed as:

$$\overline{F_D} = C_D \rho u^2 D^2/2 \qquad (8.18)$$

$$\overline{F_L} = C_L \rho u^2 D^2/2 \qquad (8.19)$$

in which

$\overline{F_D}$ and $\overline{F_L}$ are the mean drag and lift forces, respectively;
C_D and C_L are the drag and lift coefficients, respectively;
u is some characteristic velocity;
D is the representative diameter of the particle;
and ρ is the mass density of the water.

Since the present force measurements were conducted on a side slope particle located at various levels which were dependent on the flow depth, and because of the irregularity of the particles comprising the riprap layer, it was concluded that none of the local velocities at any location above the particle could be adequately used as a characteristic velocity in Eqs. (8.18) and (8.19). So this value was evaluated for each run from the measured discharge and water cross-section area.

It is also worth mentioning that Noori, B.M. (1985) in his study of the stability of block protected weirs, reached the same conclusion and used the average flow velocity as a characteristic velocity throughout his study.

As a result of the preceding discussion, u in Eqs. (8.18) and (8.19) will be replaced by the mean flow velocity $\overline{u}$ to obtain:

$$\overline{F_D} = C_D \rho \overline{u}^2 D^2/2 \qquad (8.20)$$

$$\overline{F_L} = C_L \rho \overline{u}^2 D^2/2 \qquad (8.21)$$

The above equations were used to determine the drag coefficient (C_D), and lift coefficient (C_L) for the experimental measurements in all runs.

In order to derive the relationships required for the stability analysis, the variation of C_D and C_L with the relative depth (R/D_{50}), and Reynolds number (R_e), was studied. The results obtained are shown in Figs. (8.32) to (8.35), and found to be defined by a simple power equation of the following form:

$$C_D = 0.01074 \, (R/D_{50})^{-0.268} \qquad (8.22)$$

with correlation coefficient of 0.964 and standard error of estimate of 0.0067, and

$$C_L = 0.063 \, (R/D_{50})^{-0.557} \qquad (8.23)$$

with correlation coefficient of 0.996 and standard error of estimate of 0.0045, and

$$C_D = 0.0624 \, (R_e)^{-0.171} \qquad (8.24)$$

with correlation coefficient of 0.970 and standard error of estimate of 0.0061, and

$$C_L = 2.3816 \, (R_e)^{-0.355} \qquad (8.25)$$

with correlation coefficient of 0.998 and standard error of estimate of 0.0035.

8.6.1.4 Lift to drag ratio

As can be concluded from Eqs. (8.20) and (8.21), the lift and drag forces are dependent on the same variables; therefore, the ratio of the mean values of these two forces should also be dependent on the same variables. This yields,

$$\beta = \overline{F_L}/\overline{F_D} = C_L/C_D \tag{8.26}$$

$$\beta = f_1 (R/D_{50}) = f_2 (R_e) \tag{8.27}$$

in which β is the ratio of mean lift to mean drag.

Actually, as it has been shown through Chapter Two, many attempts have been made to establish this ratio to be used in the sizing approaches. Ruh-Ming, L. et al. (1976) recommended the use of a constant value of $\beta = 0.85$ for the design of riprap for bank protection. Later Ruh-Ming, L. and Simons, D.B. (1979), recommended the use of $\beta = 2.85$ for the design of riprap. This value was based on the analysis presented by Samad, M.A. (1978), in which the curve shown in Fig. (3.10), for the approximate relation between the ratio and the boundary Reynolds number was developed.

Using the results obtained of lift and drag measurements, the ratio β was plotted against (R/D_{50}) and (R_e), as shown in Fig. (8.36). These relations yield:

$$\beta = 5.861 (R/D_{50})^{-0.289} \tag{8.28}$$

with correlation coefficient 0.992 and standard error of estimate of 0.0033, and

$$\beta = 38.19 (R_e)^{-0.183} \tag{8.29}$$

with correlation coefficient of 0.990 and standard error of estimate of 0.0038.

In addition, the ratio of lift to drag for each run was determined separately and listed within Table (8.1). Therefore, according to the preceding results, one may conclude that recommending a constant value for this ratio for various flow conditions was not in agreement with the results obtained from the current study.

8.6.1.5 Drag and lift relative intensities

During the course of the investigation, the standard deviation of the force fluctuations, σ , was calculated as a measure of variability of the hydrodynamic force in the turbulent flow. But, in order to represent the force characteristics in more detail, another dimensionless term was formulated as the relative intensity of lift or drag defined as:

$$DI = \sigma_D / \bar{F}_D \qquad (8.30)$$

$$LI = \sigma_L / \bar{F}_L \qquad (8.31)$$

where

DI and LI are the drag and lift intensities, respectively;
and σ_D and σ_L are the drag and lift standard deviation, respectively.

The two preceding equations were applied to obtain DI and LI for all runs, and the results achieved are listed in Table (8.1). In order to study the variation of these intensities with (R/D_{50}) and (R_e), the experimental results were plotted in Figs. (8.37) and (8.38). These figures show that the relative intensity of the lift and drag forces are independent of the relative roughness and the flow Reynolds number, and can be determined as constant values.

In fact, these are in accordance with the findings of results which have been confirmed by some investigators. As a result of the laboratory studies of hydrodynamic forces on a rough wall conducted by Einstein, H.A. and El Samni, E.A. (1949), the lift intensity was found to be of constant value equal to 0.37. Also the relative intensity of the lift force was studied by Cheng, E.D. and Clyde, C.G. (1972), and found to be independent of depth of flow and slope of channel bed, and had a constant value equal to 0.18.

To determine DI and LI, the standard deviation for all runs was plotted against the corresponding mean values. Then the relative intensity was determined as the slope of the fitted line. This test was conducted separately for the drag and lift forces as indicated in Fig. (8.39), and the results obtained yield:

$$DI = 0.168 \tag{8.32}$$

with correlation coefficient of 0.922 and standard error of estimate of 0.126E-4, and

$$LI = 0.554 \tag{8.33}$$

with correlation coefficient of 0.9522 and standard error of estimate of 0.986E-4.

8.6.2 Non-Spherical Particles

Furthermore, in order to assess the desirability of employing a spherical particle for measuring the acting hydrodynamic forces, four non-spherical particles with different shapes were made as explained in Section (6.4.2.2). Applying the measuring technique used previously with the spherical particle, the forces acting on all of these particles were recorded.

In fact this study was also planned to investigate the effect of the particle shape and orientation on the measured lift and drag forces. For this reason, the study was conducted in only one run (i.e. one discharge) for all the particles, in which the data forces were acquired for four seconds with the same sampling interval used previously.

The results obtained from these measurements, which are shown in Fig. (8.40), reveal the diversity of the results, which is undoubtedly due to the difference between the projection area of the particle subjected to drag and that subjected to lift force. Additionally, to establish more specifically the difference between the acquired results, the projected areas to the lift and drag were assumed equal and equivalent to that of the representative spherical particle. Then the various parameters determined previously were worked out for all the particles as listed in Table (8.1).

8.7 DISCUSSION

The detailed experimental work performed on the spherical particle suggests the following:

1 - It is obvious from Fig. (8.1) that the hydrodynamic lift and drag forces are randomly fluctuating around mean values.

2 - The probability distributions of the fluctuating forces in this study are found to be approximately normal distributions as shown in Figs. (8.2) to (8.13).

3 - The cross-correlation analysis for the measured lift and drag instantaneous values, as shown in Figs. (8.14) to (8.25), reveal that they are not correlated. This means each force is randomly fluctuating without being dependent on the other.

4 - The relationships developed either for the variation of the lift and drag coefficients or the ratio of lift to drag, as depicted in Figs. (8.32) to (8.36), proved the correlation between these coefficients and the values of both (R/D_{50}) and (R_e) which are represented by Eqs. (8.22) to (8.29).

5 - The relative intensity of the lift and drag forces as defined in this study by Eqs. (8.30) and (8.31), were found to be independent of (R/D_{50}) and (R_e) as shown in Figs. (8.37) and (8.38), and had constant values which from Fig. (8.39) are seen to be equal to 0.168 in the case of drag and 0.554 in the case of lift force.

For the case of non-spherical particles, one may conclude the following:

1 - The comparison between the results obtained for all particles for the same flow condition revealed that the magnitude of the forces exerted by the flow is entirely dependent on the projected area of the particle. Accordingly, the stability of any particle will be dependent on the particle shape and orientation which varied widely from one particle to another.

2 - In the Author's opinion, using non-spherical particle for measuring the acting hydrodynamic forces, is inappropriate. This is obviously due to the difference between the projected areas of the particle in perpendicular directions to the lift and drag forces.

3 - Using non-spherical particles for deriving stability criteria, will be misleading. This is simply because the approach applied can only represent one of the particle shapes.

TABLE 8-1:SUMMARY OF RESULTS OBTAINED FROM

THE FORCE MEASUREMENTS

RUN NO	FLOW RATE (m3/s)	FLOW DEPTH (m)	TEMP. °C	DRAG FORCE FD				LIFT FORCE FL				FL/FD RATIO
				MEAN (N) X 10^3	ST. DV. (N) X 10^3	INT. %	COEFF. X 10^3	MEAN (N) X 10^3	ST. DV. (N) X 10^3	INT. %	COEFF. X 10^2	
MF 1	0.036	0.073	13.20	0.979	0.229	23.38	8.016	4.218	2.140	50.74	3.452	4.31
MF 2	0.050	0.090	13.80	1.092	0.215	19.69	7.706	4.537	2.290	50.48	3.202	4.16
MF 3	0.058	0.099	13.20	1.148	0.239	20.82	7.544	4.629	2.500	54.01	3.042	4.03
MF 4	0.065	0.107	12.70	1.209	0.229	18.95	7.494	4.793	2.460	51.33	2.972	3.97
MF 5	0.070	0.111	13.20	1.269	0.247	19.46	7.630	4.910	2.620	53.36	2.952	3.87
MF 6	0.078	0.119	13.50	1.289	0.260	20.17	7.305	4.947	2.520	50.94	2.803	3.84
MF 7	0.089	0.128	14.10	1.353	0.274	20.26	7.186	5.123	2.890	56.41	2.722	3.79
MF 8	0.100	0.137	14.30	1.421	0.296	20.84	7.066	5.292	2.620	49.51	2.632	3.73
MF 9	0.107	0.143	13.70	1.471	0.286	19.44	7.016	5.459	2.790	51.11	2.603	3.71
MF10	0.120	0.152	14.10	1.495	0.303	20.26	6.683	5.531	2.890	52.25	2.472	3.70
MF11	0.132	0.159	14.10	1.622	0.359	22.14	6.865	5.815	3.090	53.14	2.462	3.59
MF12	0.143	0.167	13.50	1.683	0.257	15.27	6.814	5.965	3.150	52.81	2.414	3.54

TABLE 8-2:RESULTS OF FORCE MEASUREMENTS

ON NON-SPHERICAL PARTICLES

	DESCRIPTION	PARTICLE NO. (1)	(2)	(3)	(4)
DRAG FORCE	MEAN FD ,(N X 10^3)	2.647	2.069	1.754	1.835
	STANDARD DEVIATION X 10^3	0.443	0.359	0.226	0.214
	DRAG INTENSITY (DI) ,%	16.76	17.35	12.91	11.67
	FD(NON-SPHERE) / FD(SPHERE)	2.181	1.705	1.445	1.512
LIFT FORCE	MEAN FL ,(N X 10^3)	6.794	4.067	4.423	5.272
	STANDARD DEVIATION X 10^3	2.910	2.390	2.570	2.600
	LIFT INTENSITY (LI) ,%	42.80	58.71	58.19	49.35
	FL(NON-SPHERE) / FL(SPHERE)	1.422	0.851	0.926	1.103
X	LIFT TO DRAG RATIO	2.56	1.96	2.52	2.87

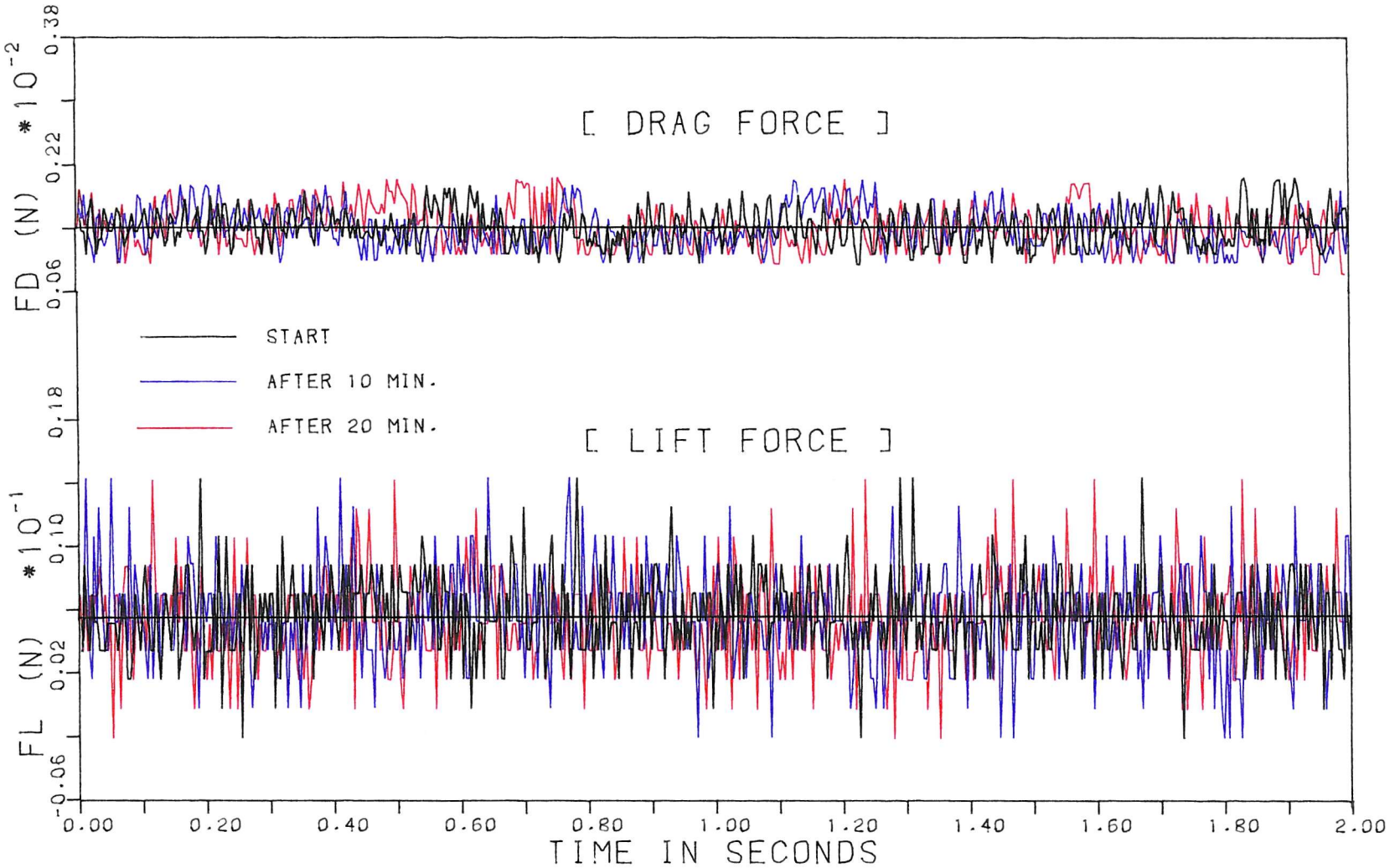

FIG. 8-1: TEST RESULTS UNDER STEADY FLOW CONDITIONS

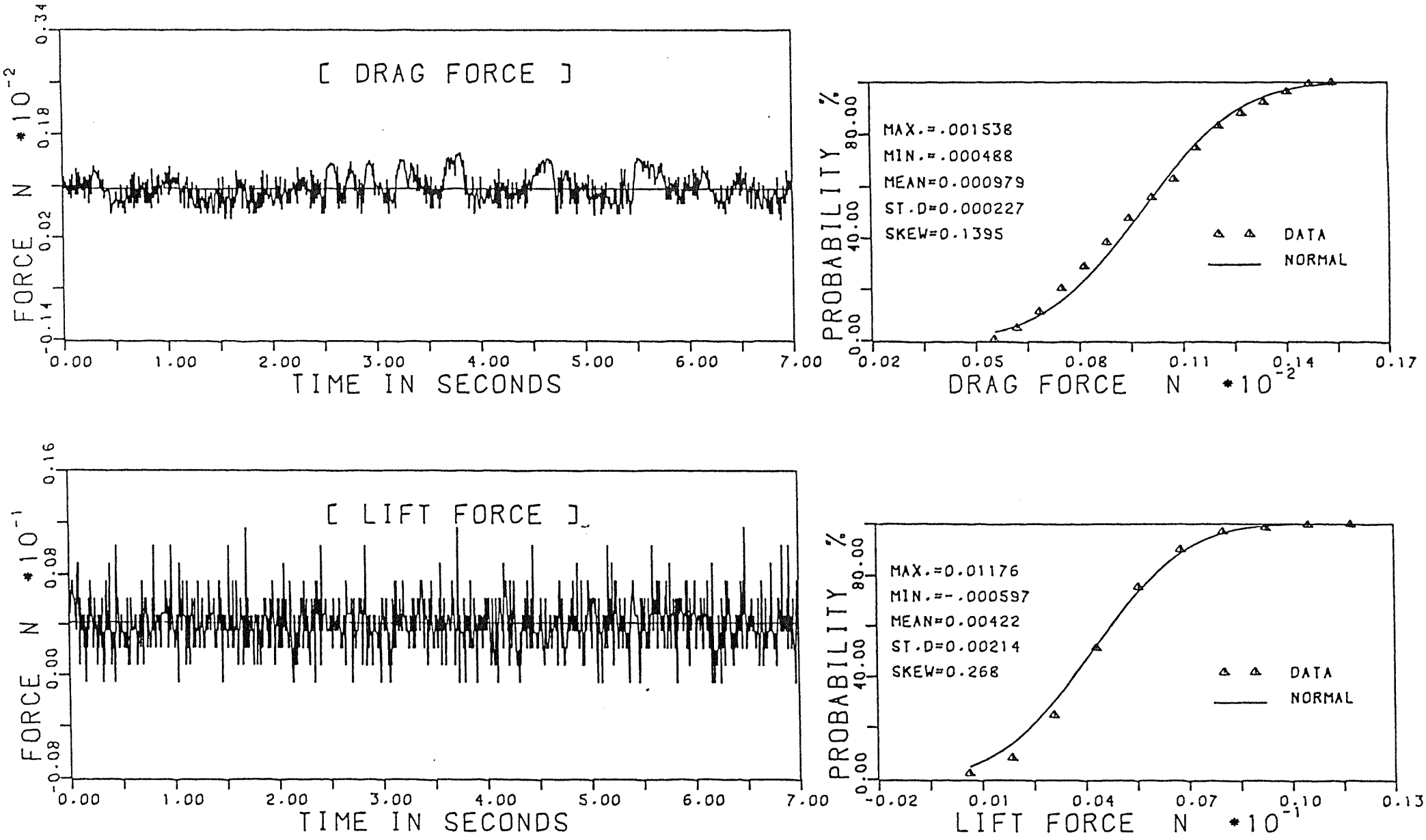

FIG. **8-2**: FLUCTUATION & PROBABILITY DISTRIBUTIONS OF MEASURED FORCES.

[RUN NO. 1]

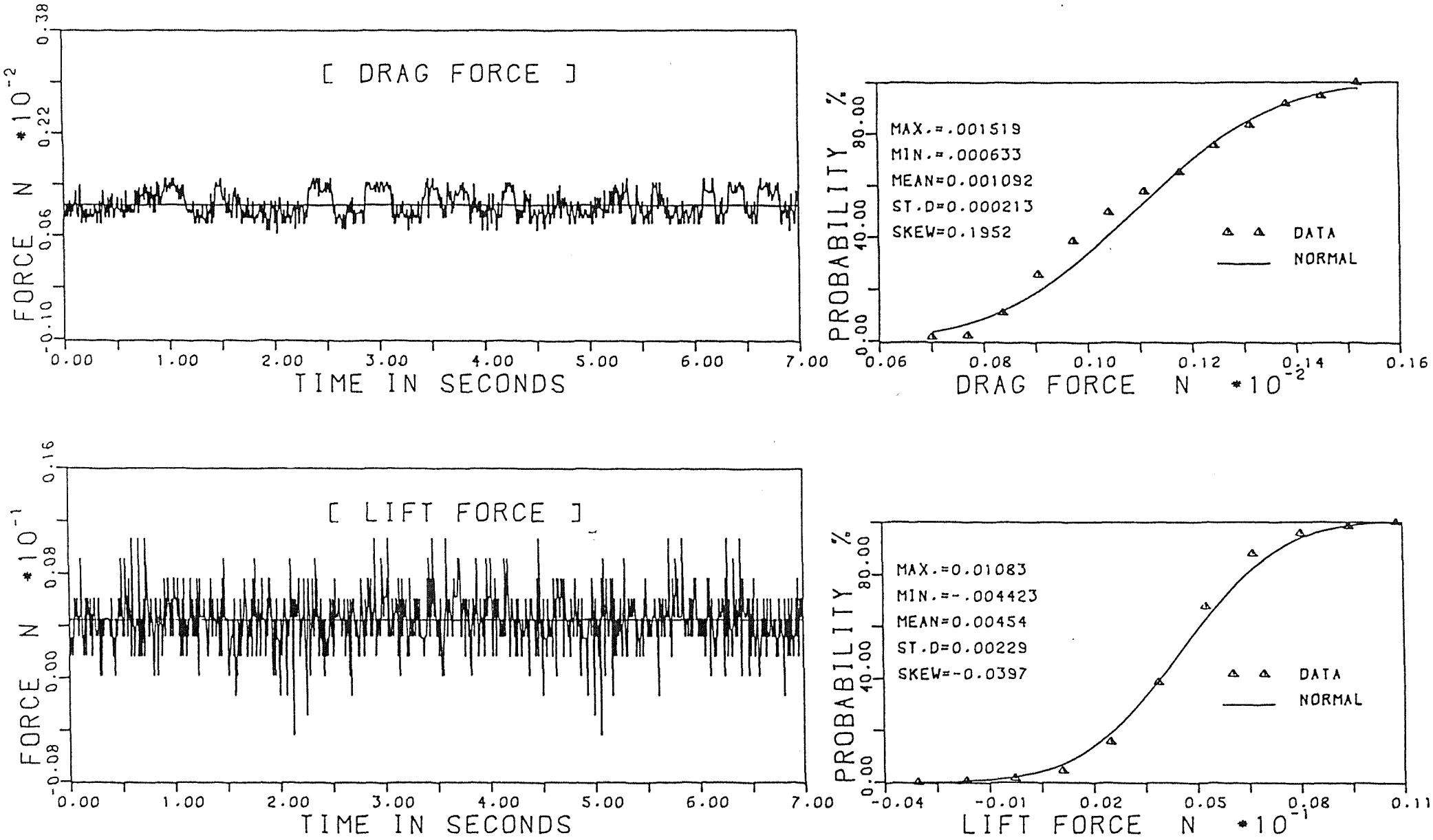

FIG. **8-3**: FLUCTUATION & PROBABILITY DISTRIBUTIONS OF MEASURED FORCES.

[RUN NO. 2]

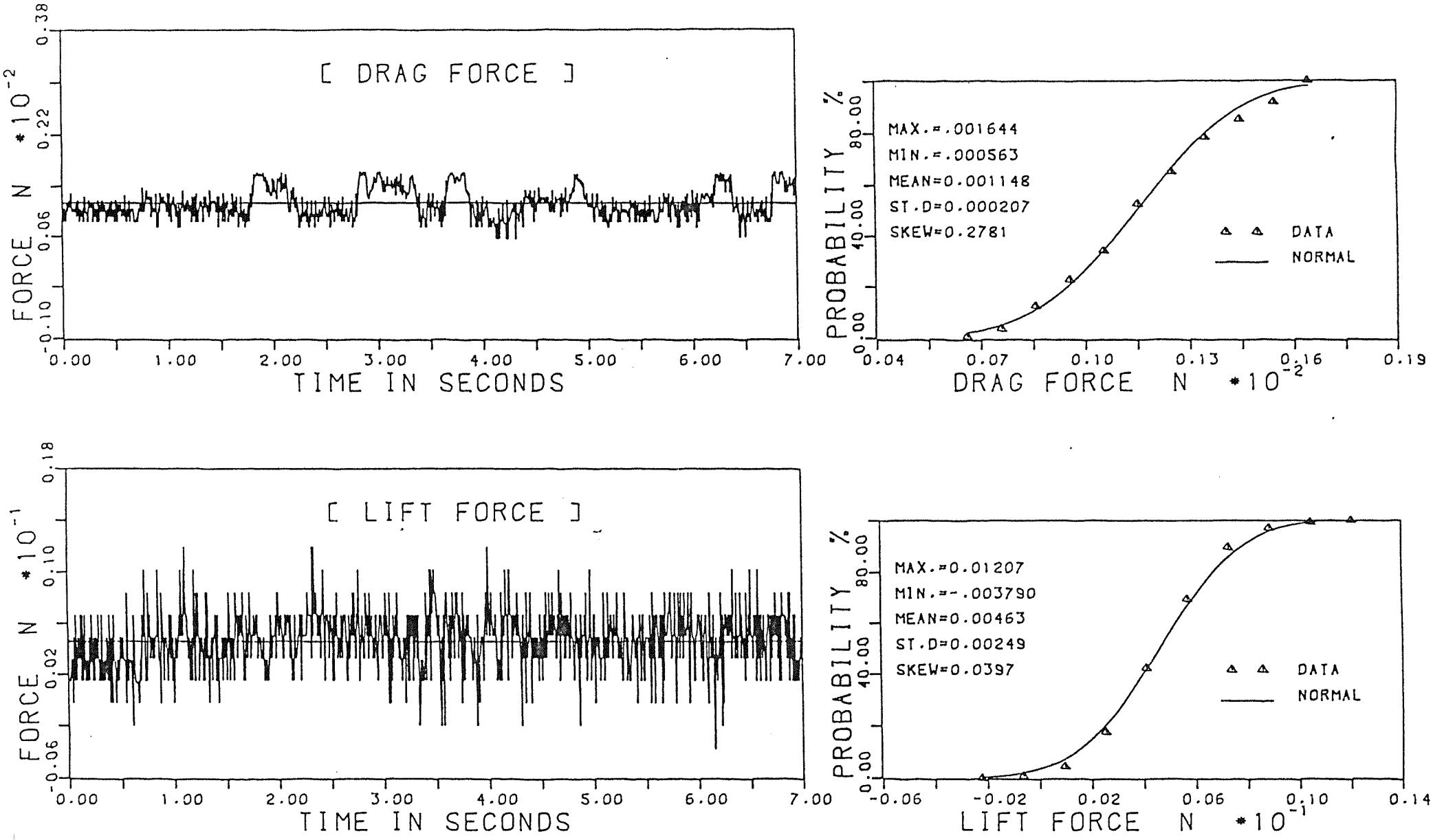

FIG.8-4:FLUCTUATION & PROBABILITY DISTRIBUTIONS OF MEASURED FORCES.

[RUN NO. 3]

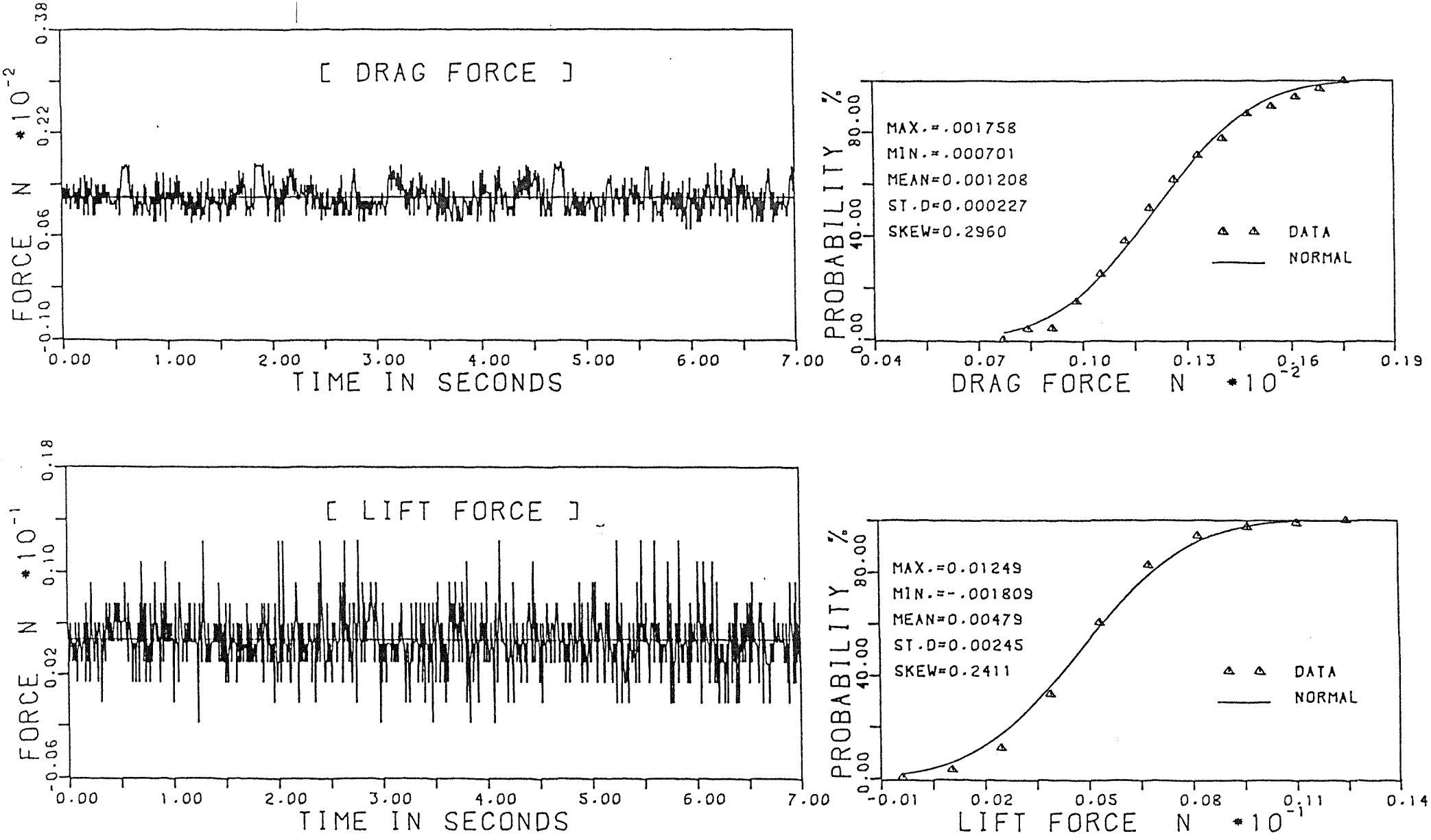

FIG. **8-5**: FLUCTUATION & PROBABILITY DISTRIBUTIONS OF MEASURED FORCES.

[RUN NO. 4]

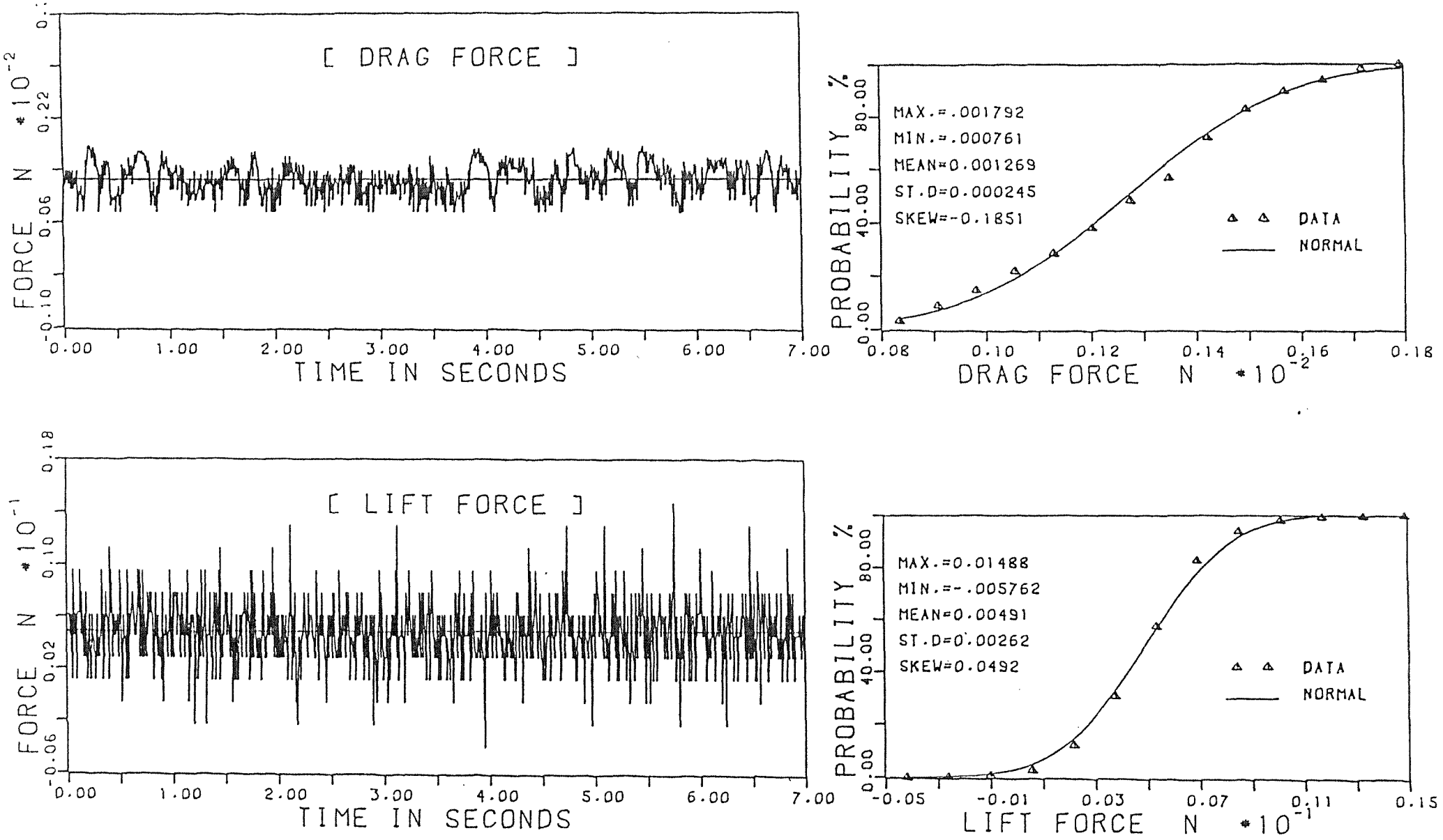

FIG.**8-6**:FLUCTUATION & PROBABILITY DISTRIBUTIONS OF MEASURED FORCES.

[RUN NO. 5]

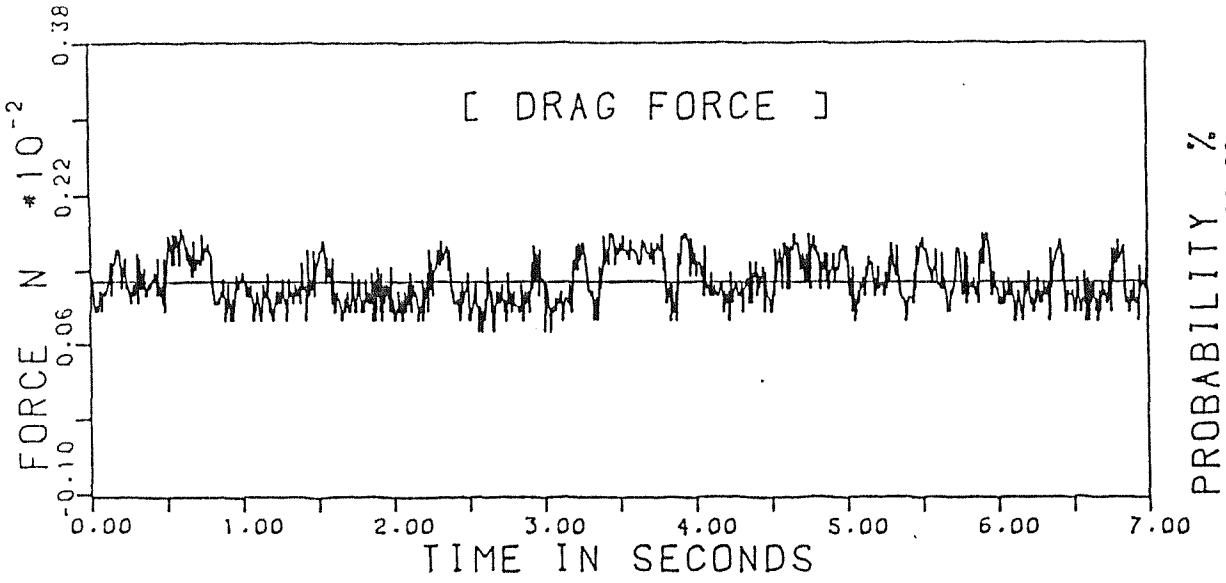

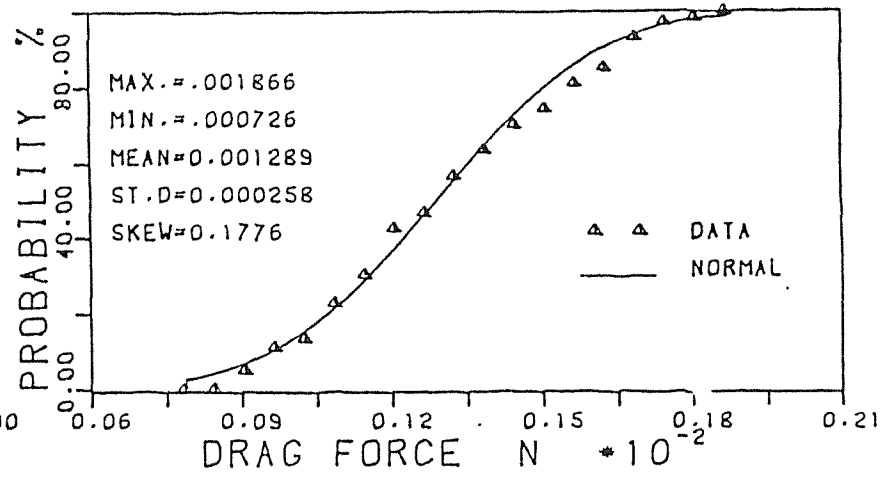

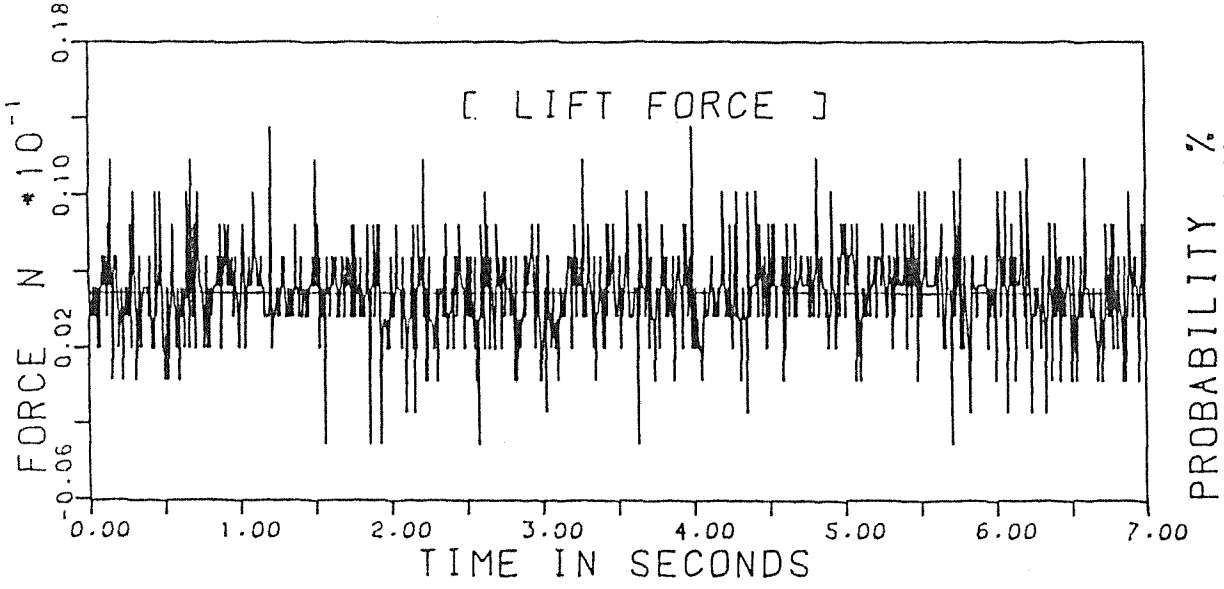

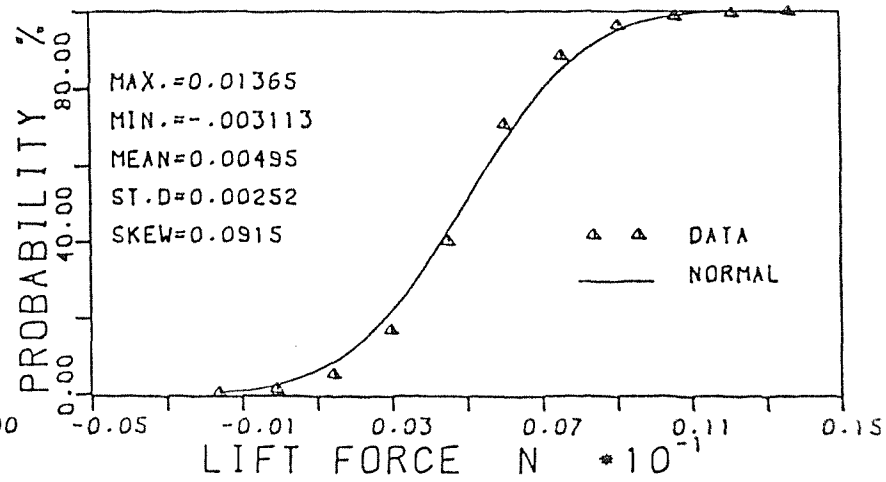

FIG.8-7:FLUCTUATION & PROBABILITY DISTRIBUTIONS OF MEASURED FORCES.

[RUN NO. 6]

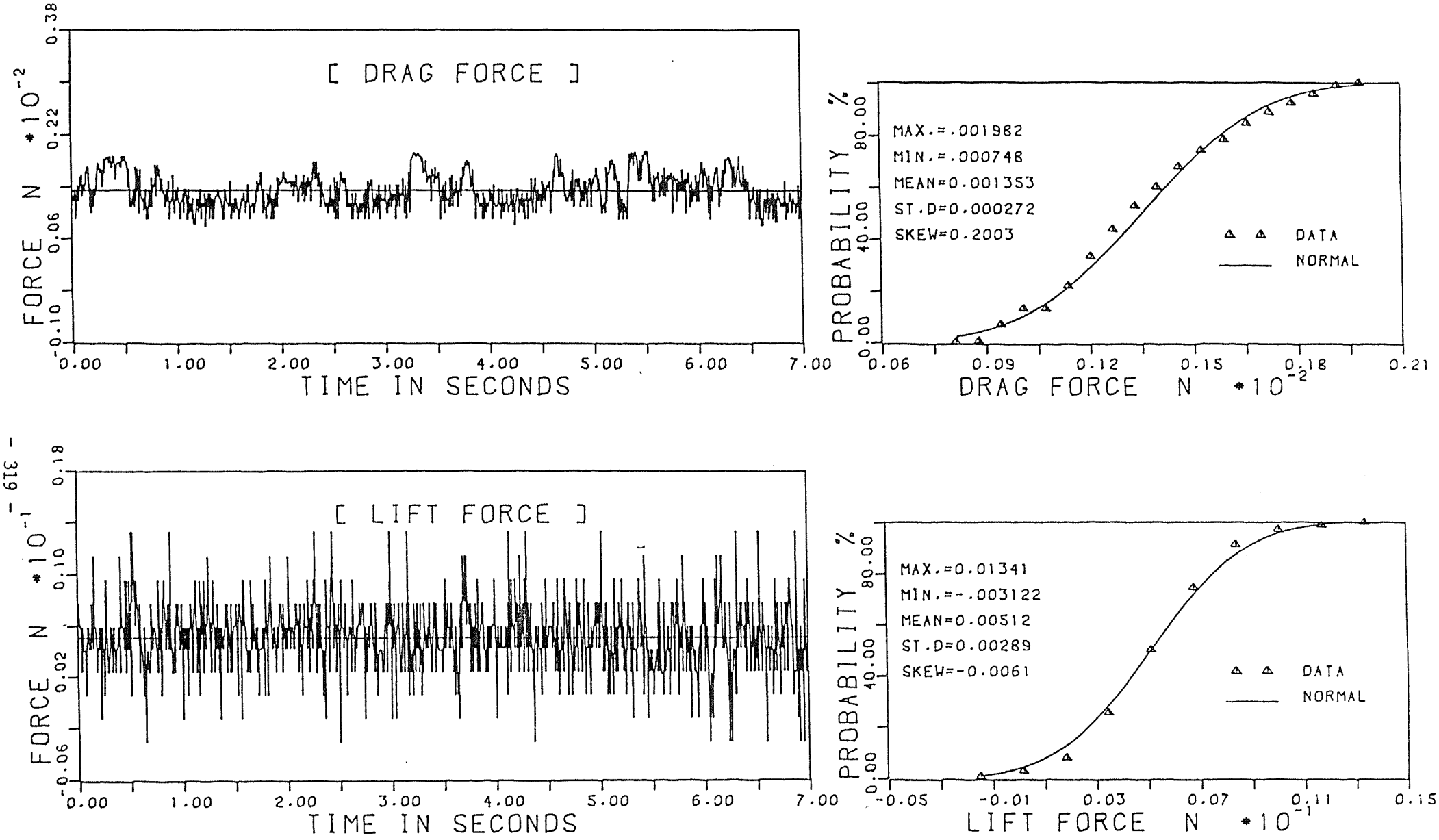

FIG.**8-8**:FLUCTUATION & PROBABILITY DISTRIBUTIONS OF MEASURED FORCES.

[RUN NO. 7]

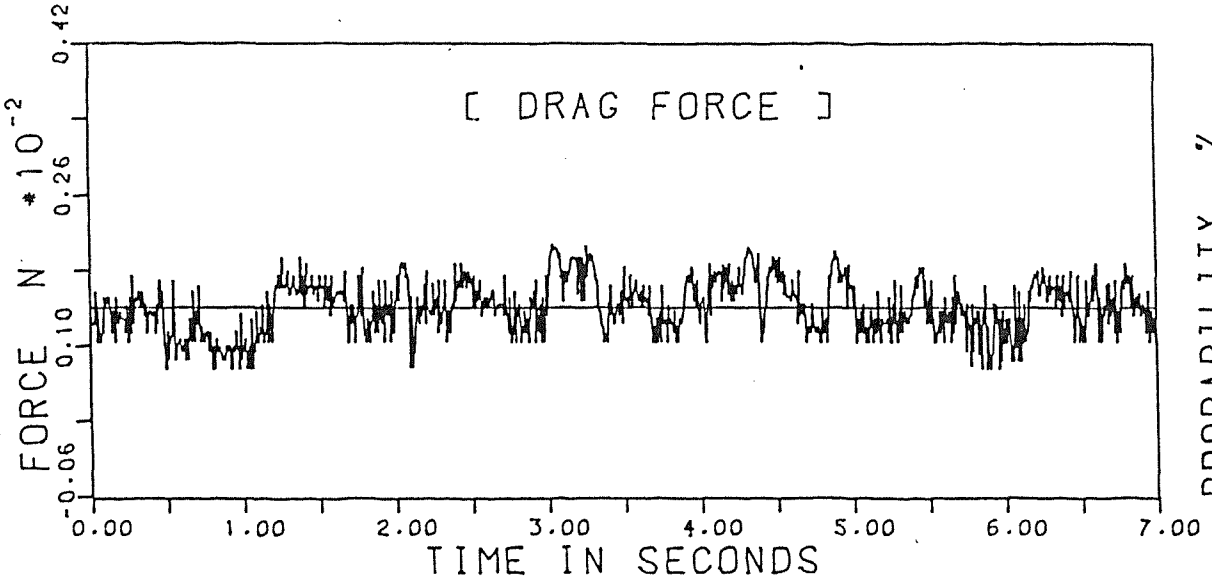

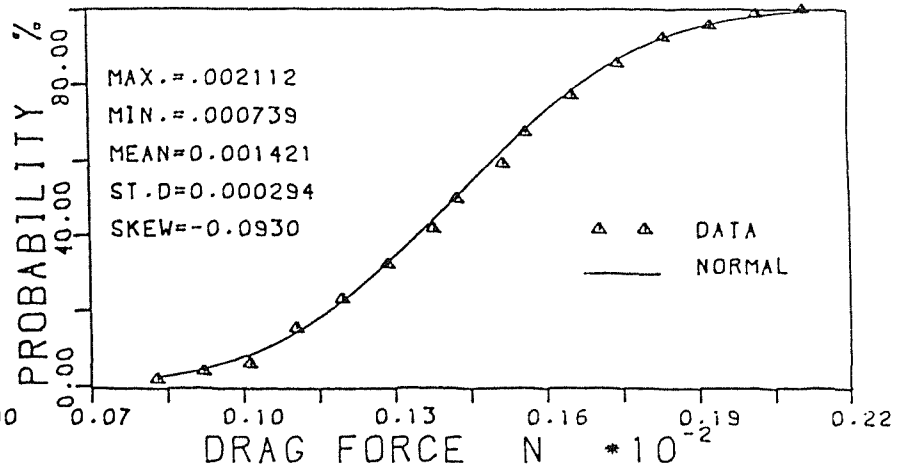

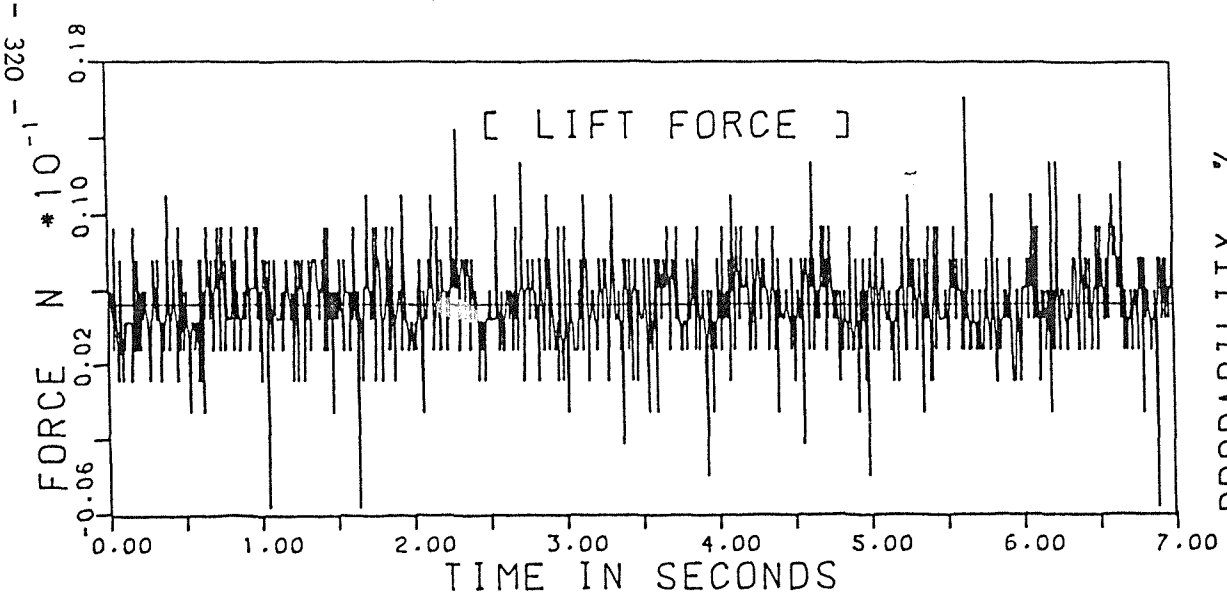

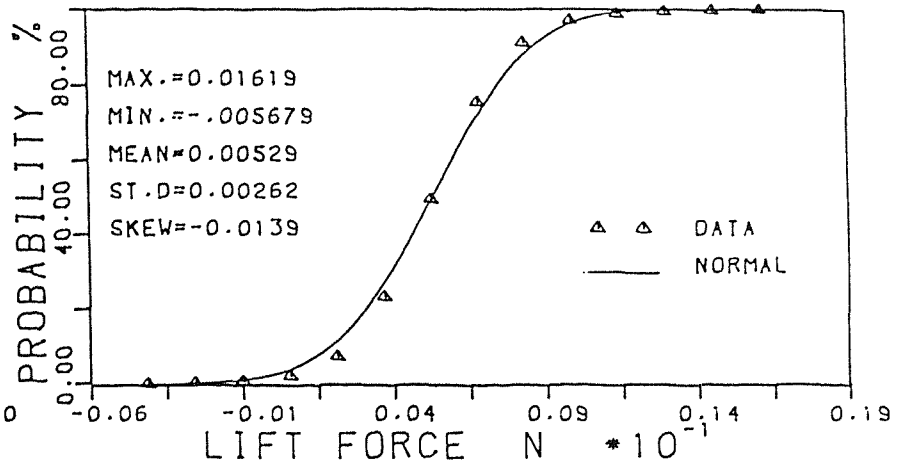

FIG.**8-9**:FLUCTUATION & PROBABILITY DISTRIBUTIONS OF MEASURED FORCES.

[RUN NO. 8]

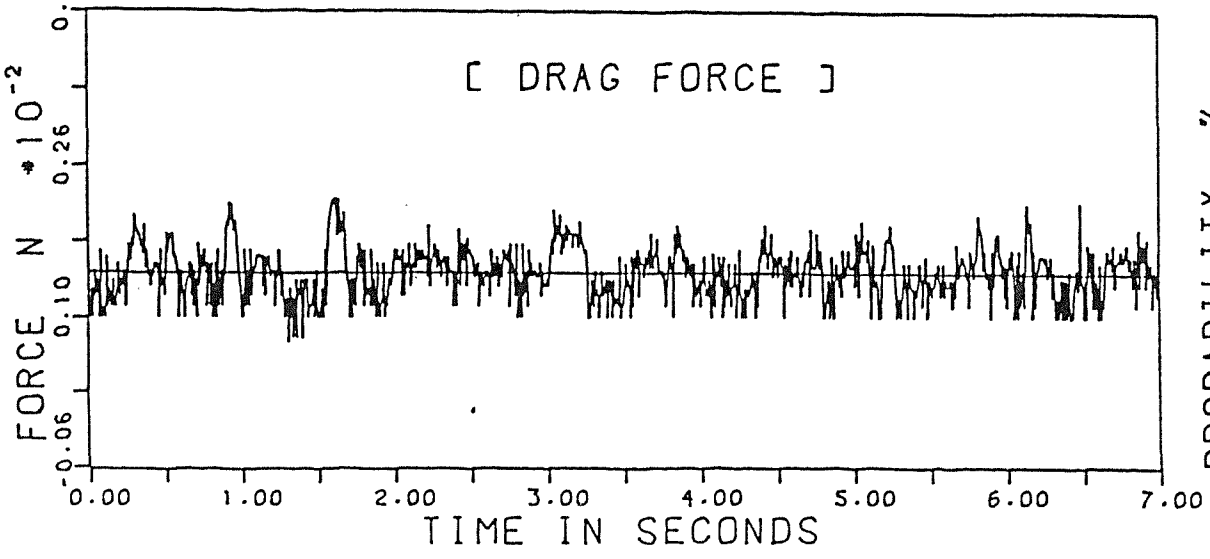

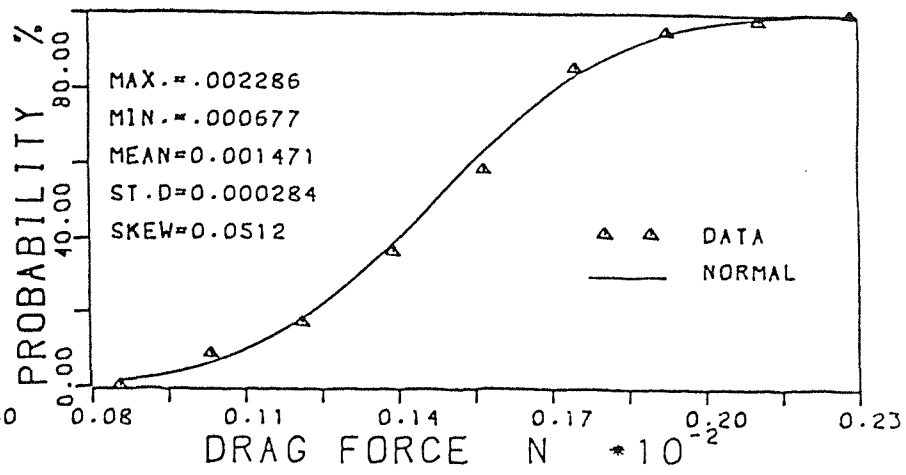

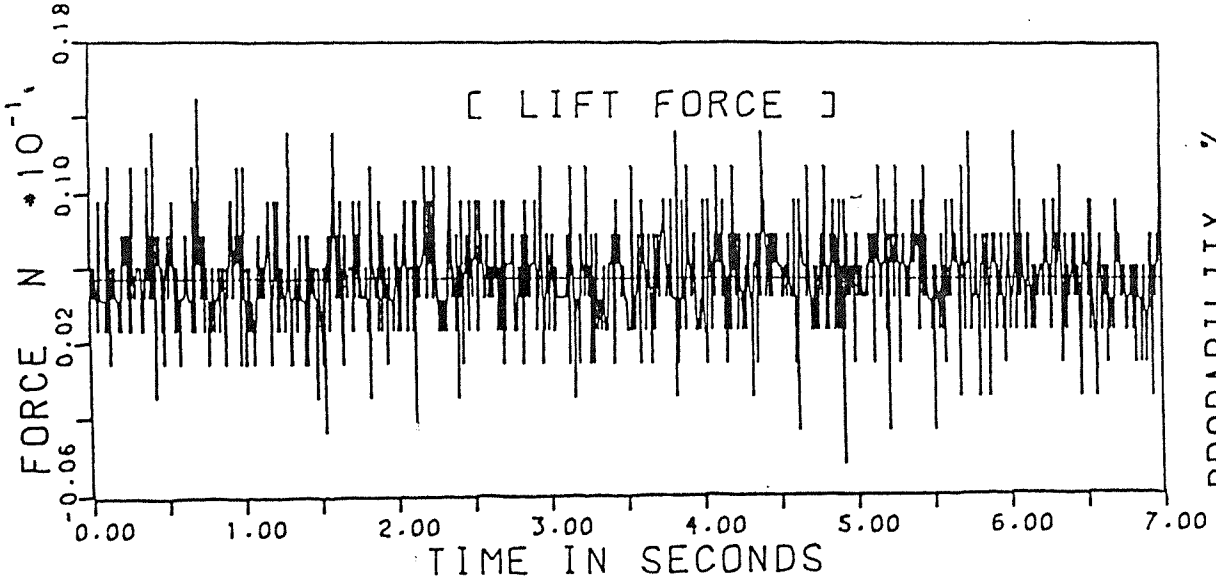

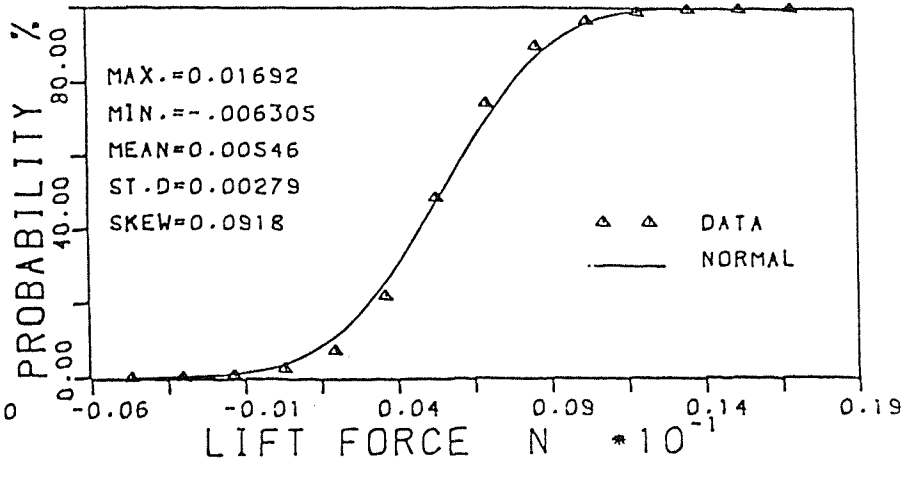

FIG.8-10:FLUCTUATION & PROBABILITY DISTRIBUTIONS OF MEASURED FORCES.

[RUN NO. 9]

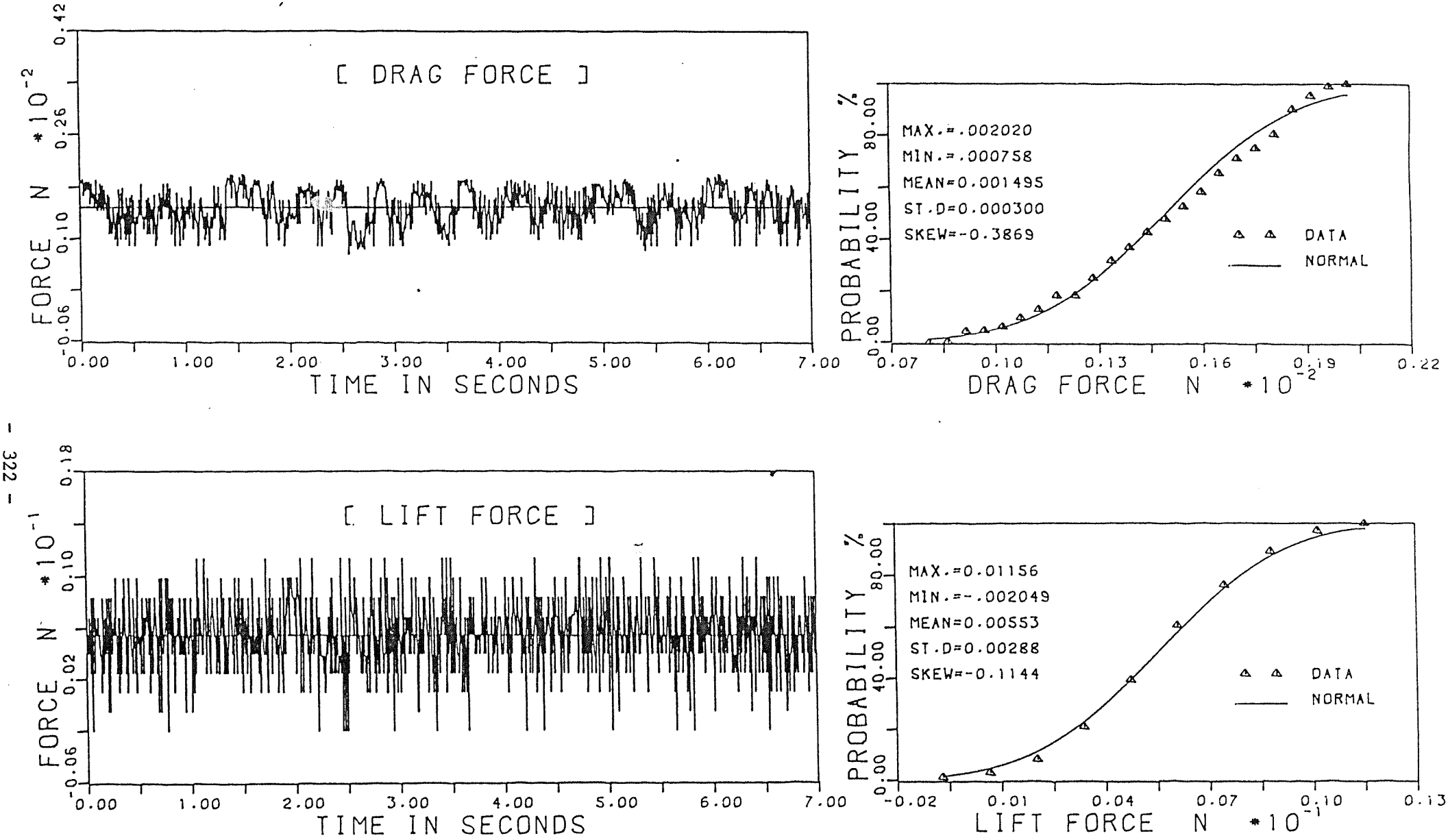

FIG.**8-11:**FLUCTUATION & PROBABILITY DISTRIBUTIONS OF MEASURED FORCES.

[RUN NO. 10]

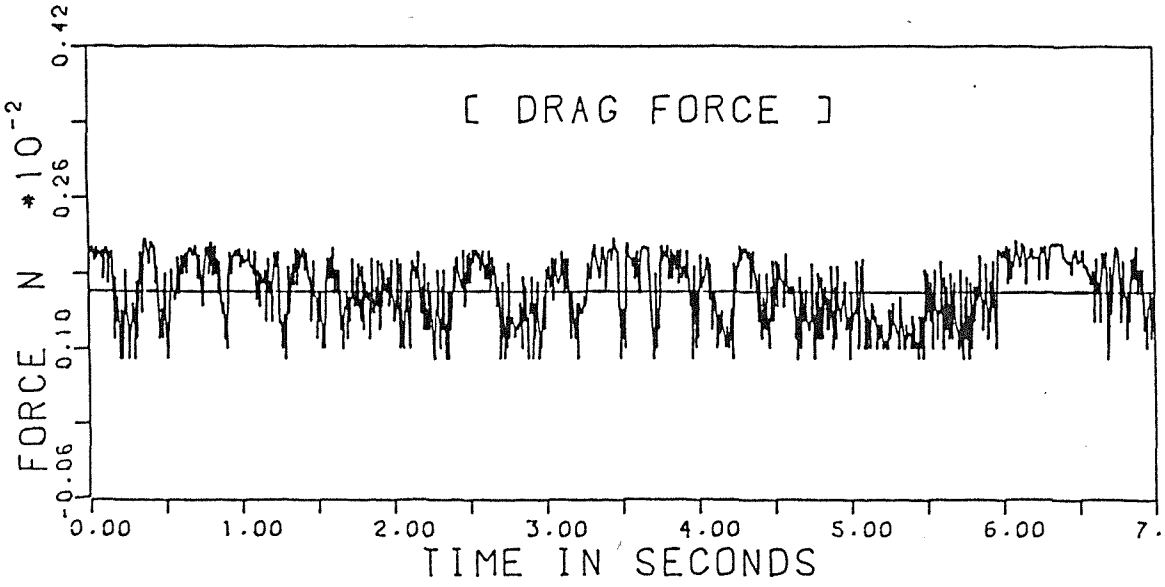

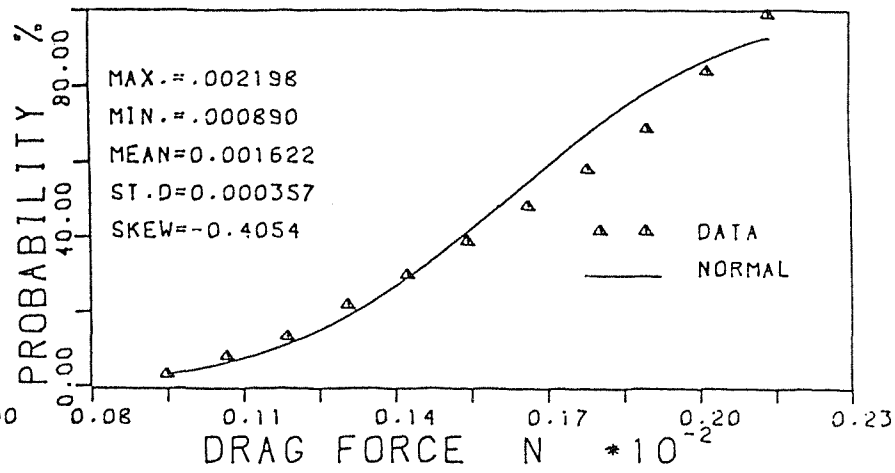

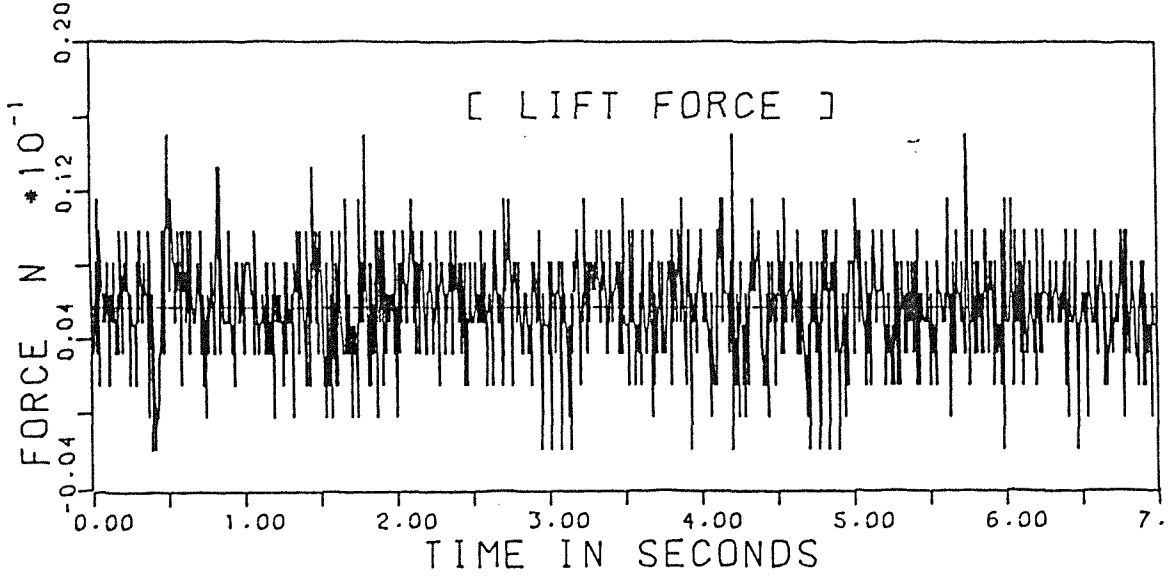

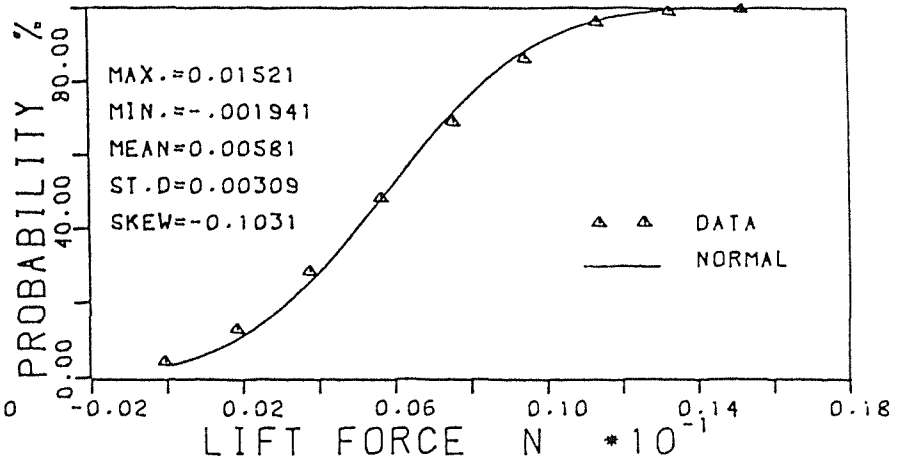

FIG.**8-12**:FLUCTUATION & PROBABILITY DISTRIBUTIONS OF MEASURED FORCES.

[RUN NO. 11]

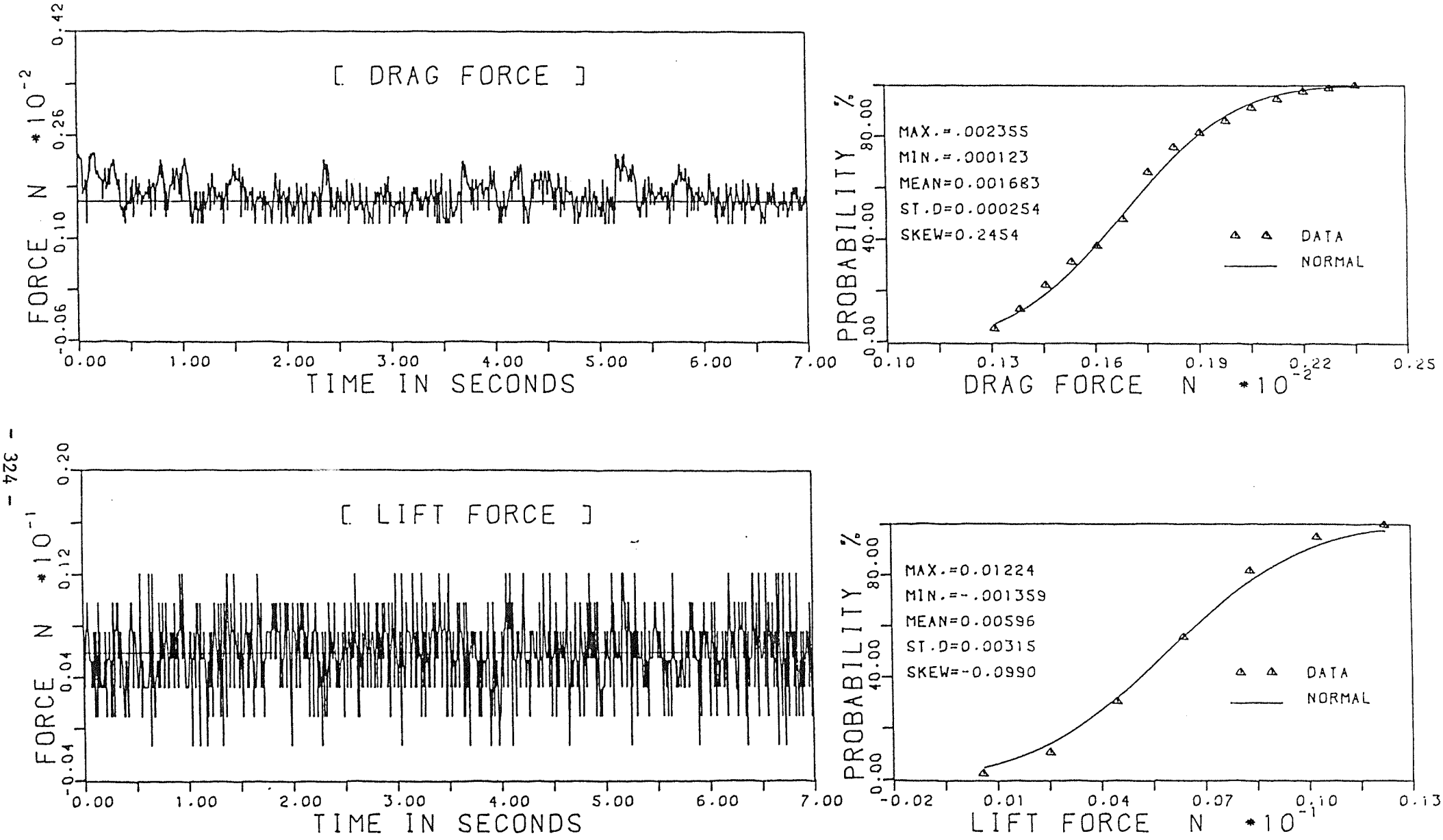

FIG.**8-13**:FLUCTUATION & PROBABILITY DISTRIBUTIONS OF MEASURED FORCES.

[RUN NO. 12]

[RUN NO. 1]

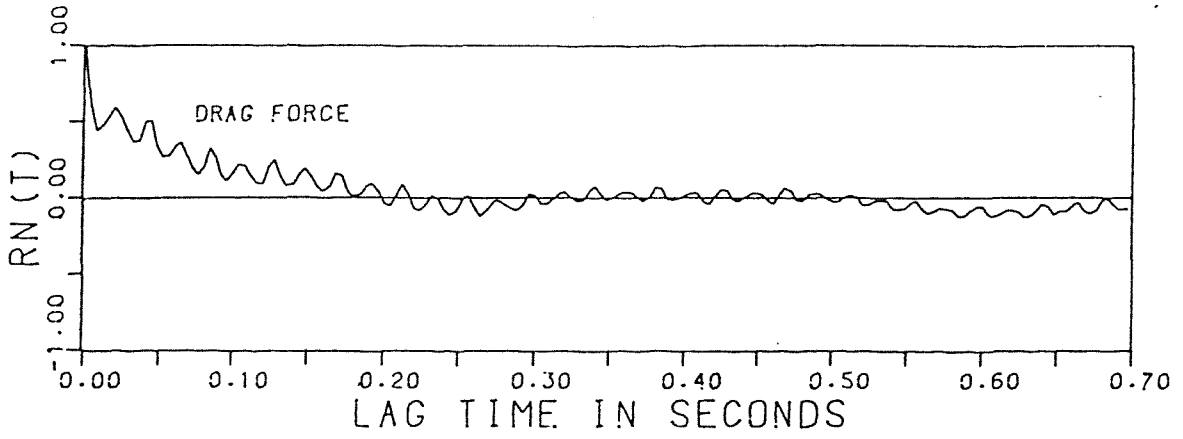

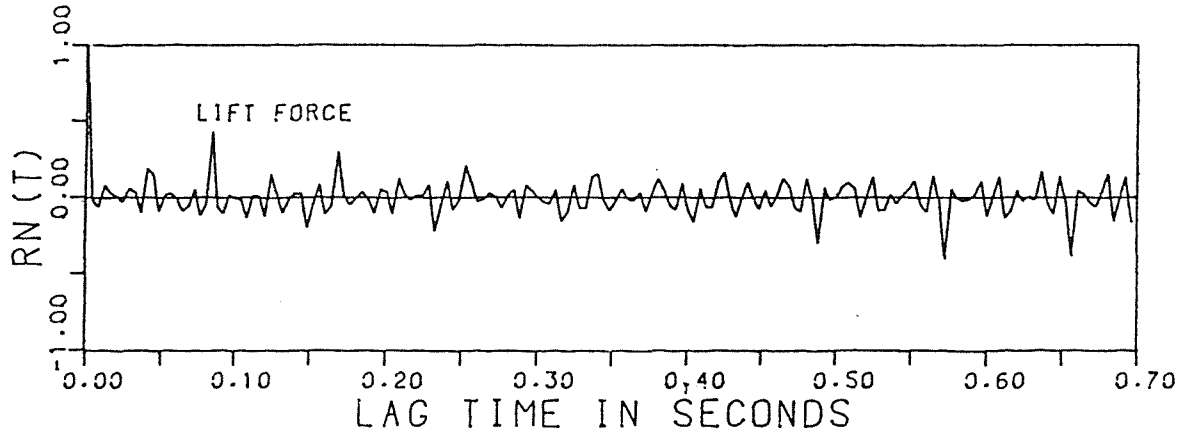

FIG. **8-14A**: AUTOCORRELATION COEF. FOR THE FLUCTUATING FORCES

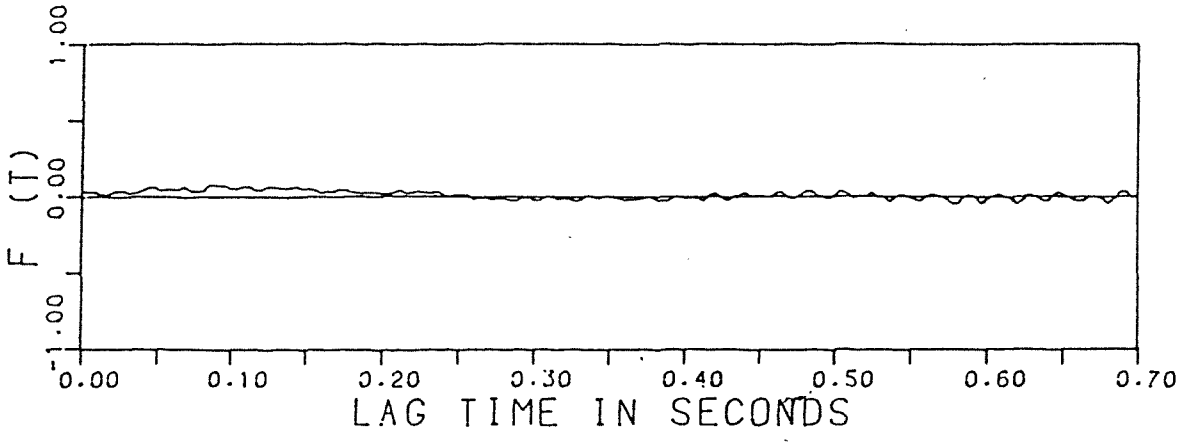

FIG. **8-14B**: CROSS CORRELATION COEF. FOR THE DRAG AND LIFT FORCES

[RUN NO. 2]

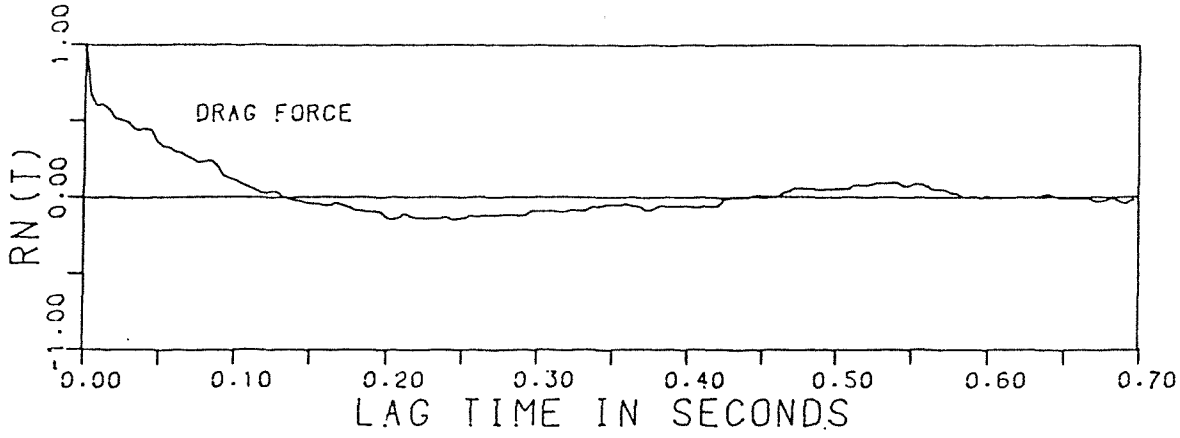

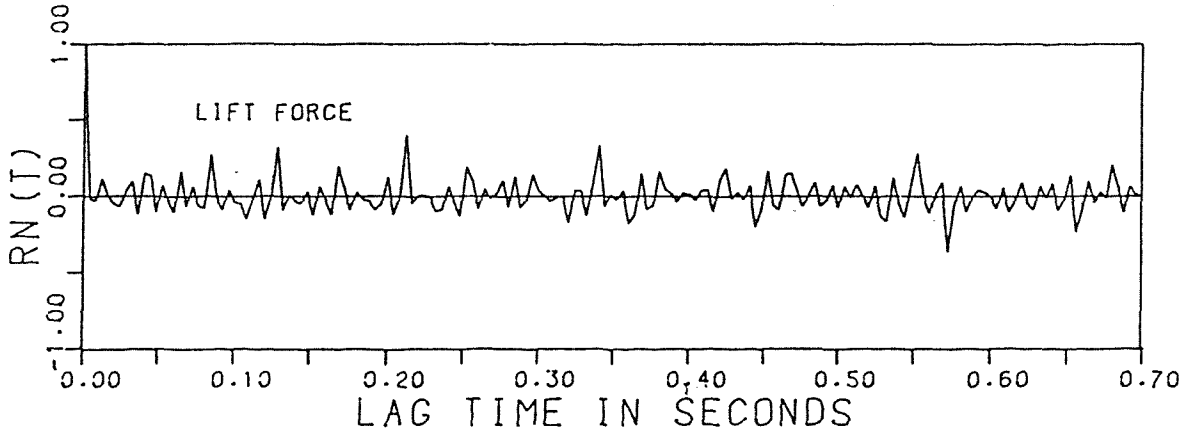

FIG. **8-15A**: AUTOCORRELATION COEF. FOR THE FLUCTUATING FORCES

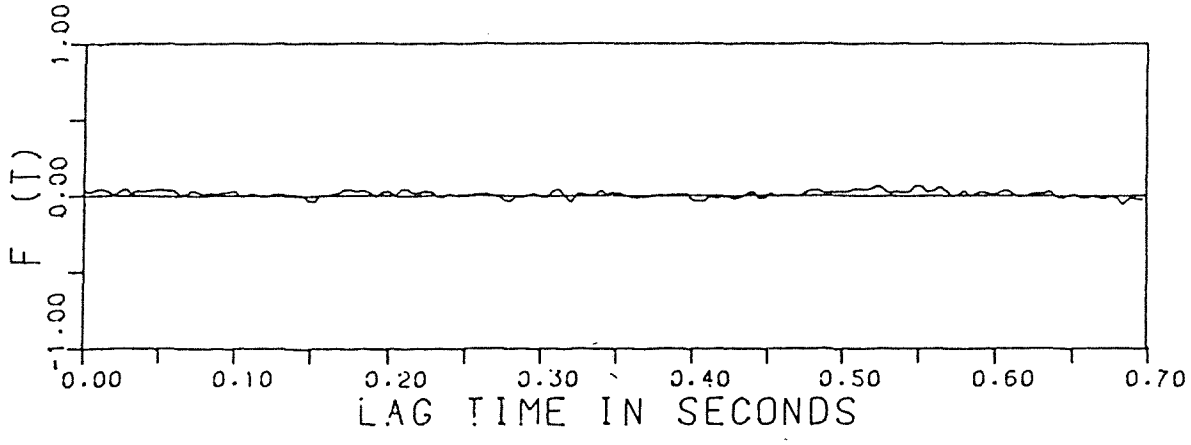

FIG. **8-15B**: CROSS CORRELATION COEF. FOR THE DRAG AND LIFT FORCES

[RUN NO. 3]

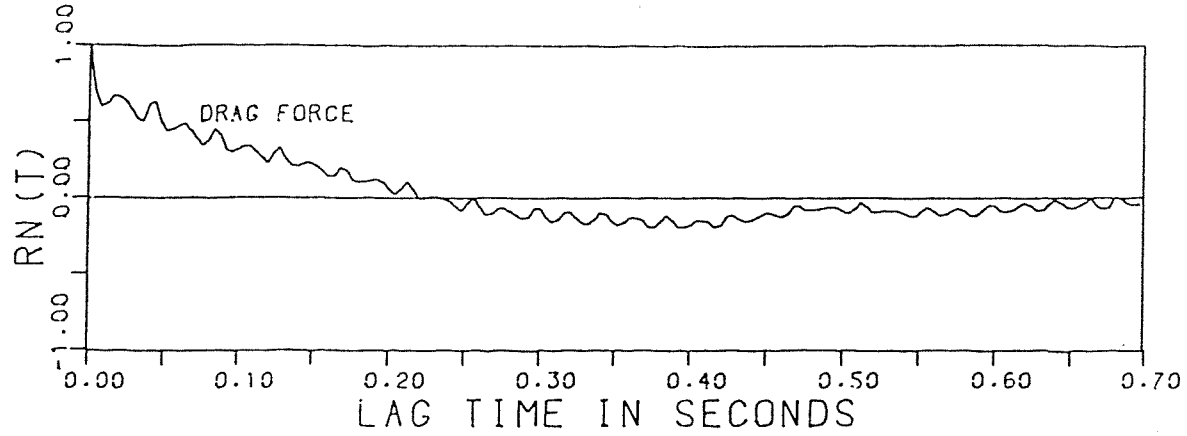

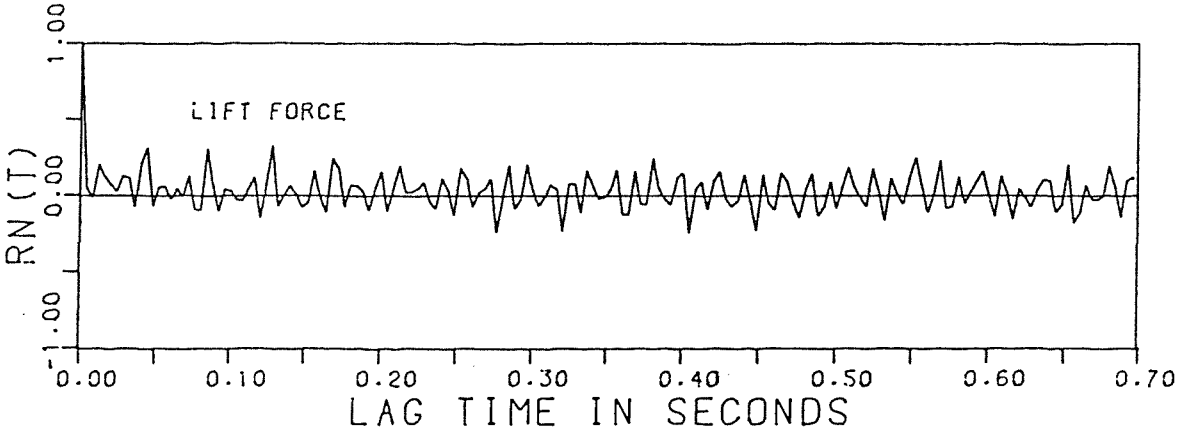

FIG.**8-16A**: AUTOCORRELATION COEF. FOR THE FLUCTUATING FORCES

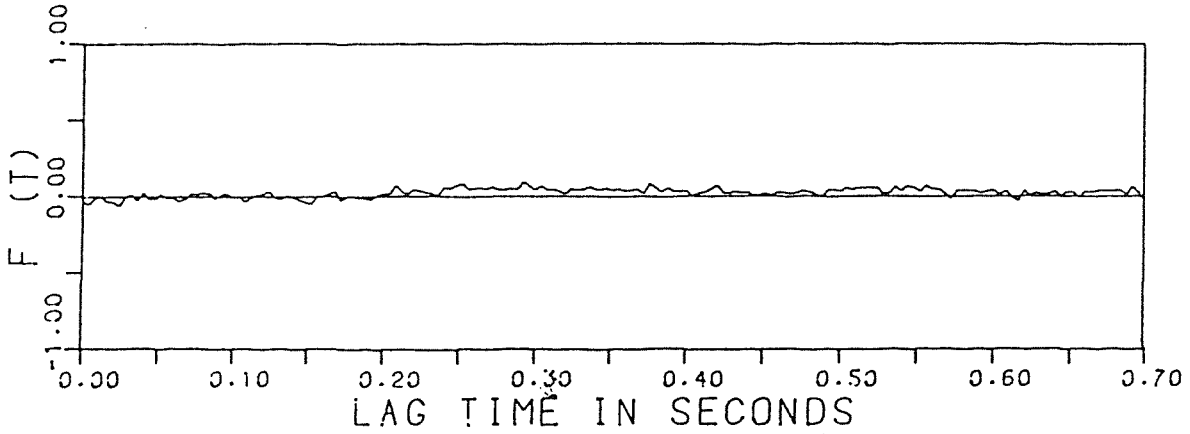

FIG.**8-16B**: CROSS CORRELATION COEF. FOR THE DRAG AND LIFT FORCES

[RUN NO. 4]

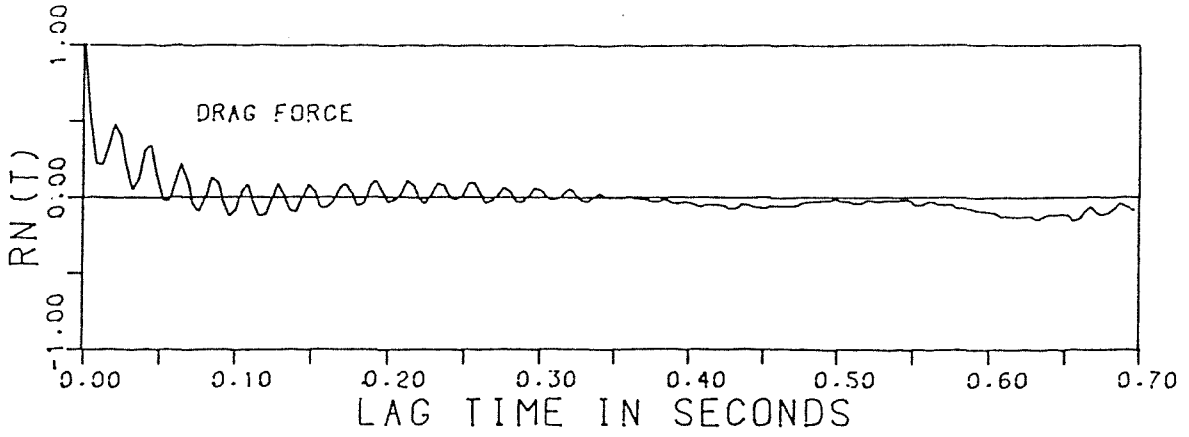

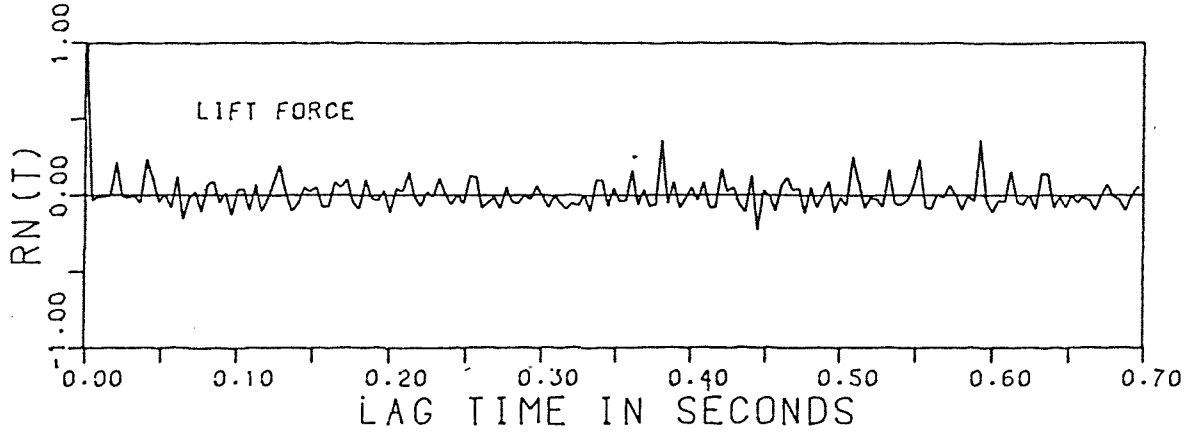

FIG.**8-17A**: AUTOCORRELATION COEF. FOR THE FLUCTUATING FORCES

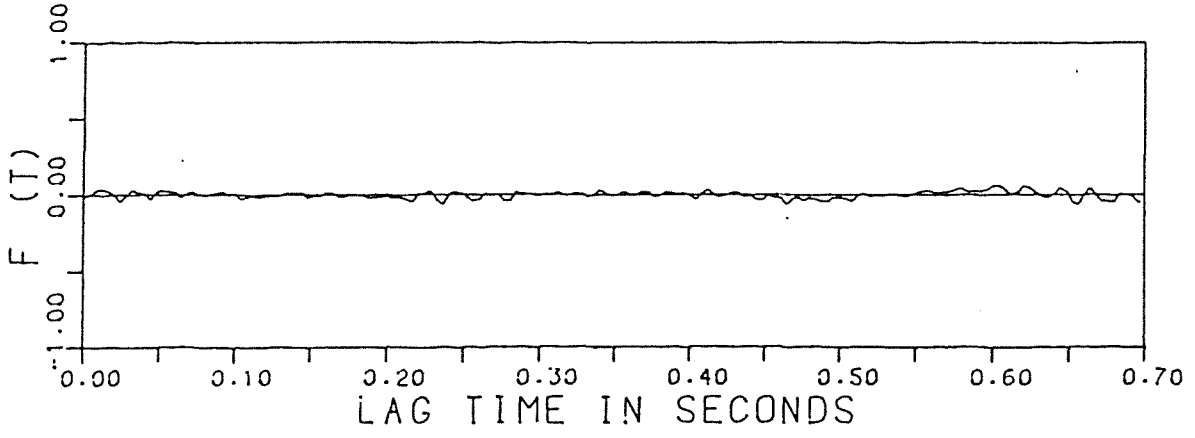

FIG.**8-17B**: CROSS CORRELATION COEF. FOR THE DRAG AND LIFT FORCES

[RUN NO. 5]

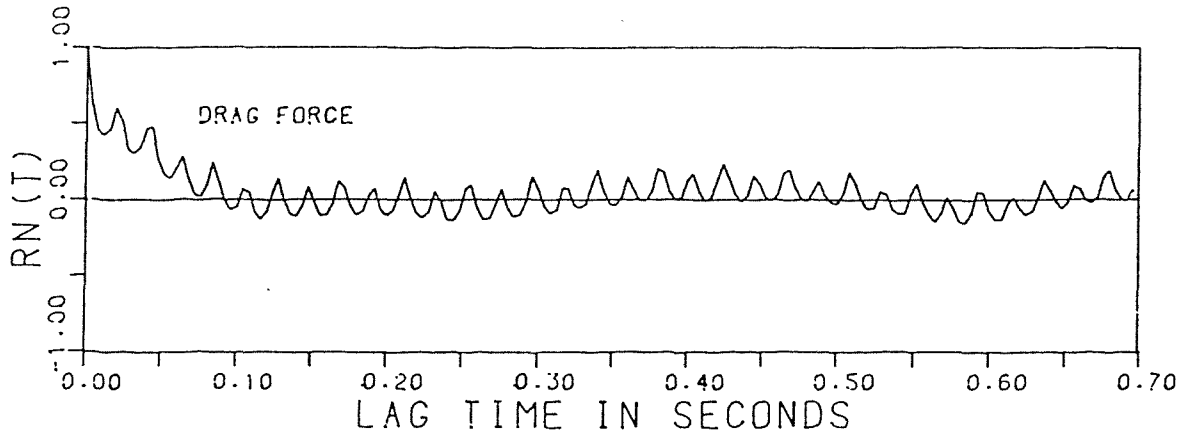

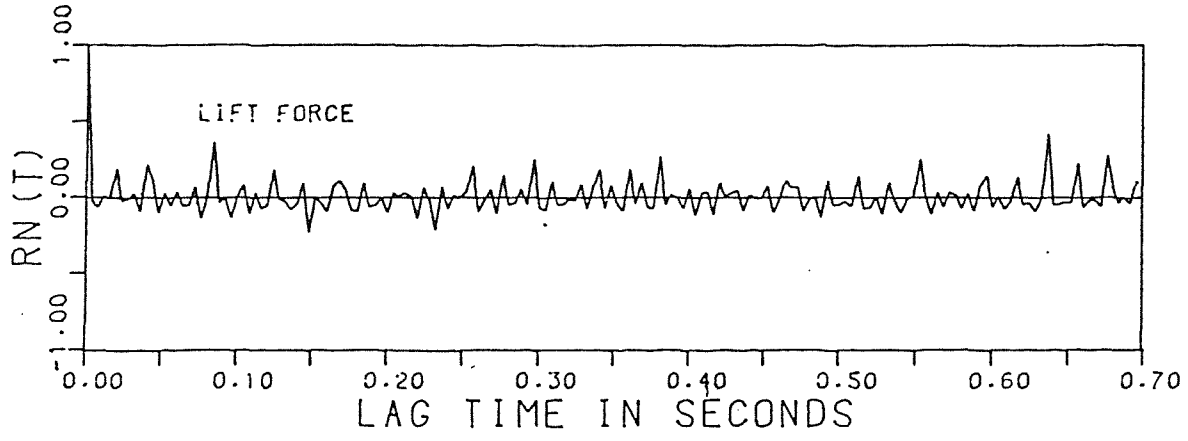

FIG. **8-18A**: AUTOCORRELATION COEF. FOR THE FLUCTUATING FORCES

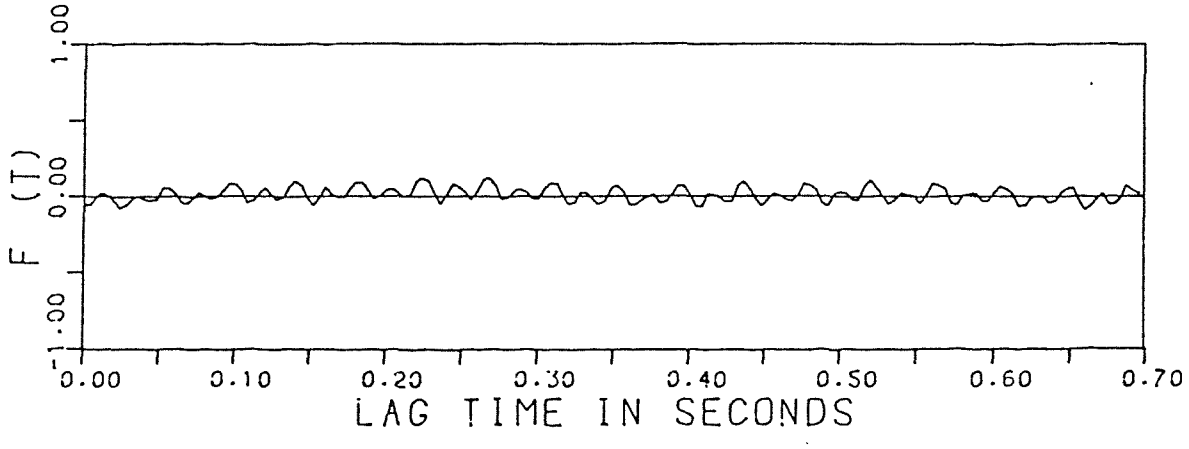

FIG. **8-18B**: CROSS CORRELATION COEF. FOR THE DRAG AND LIFT FORCES

[RUN NO. 6]

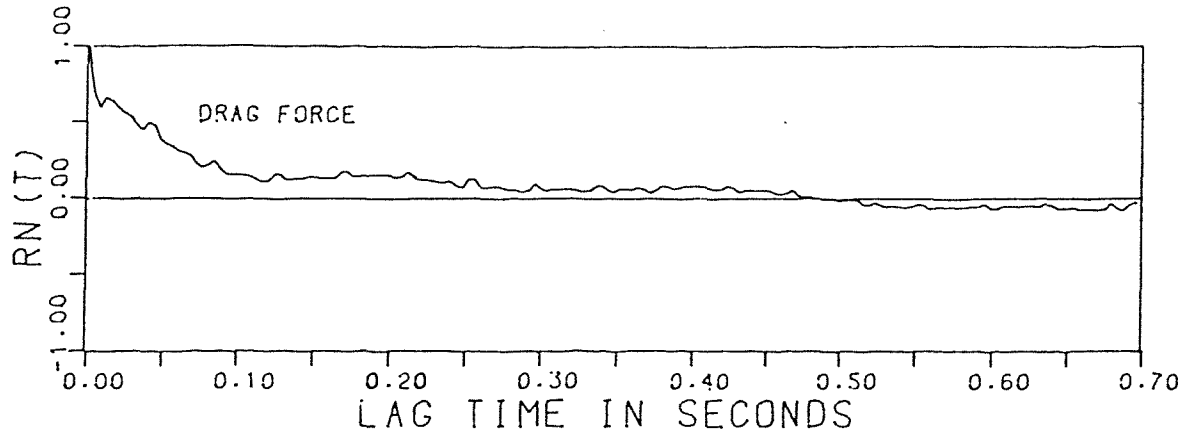

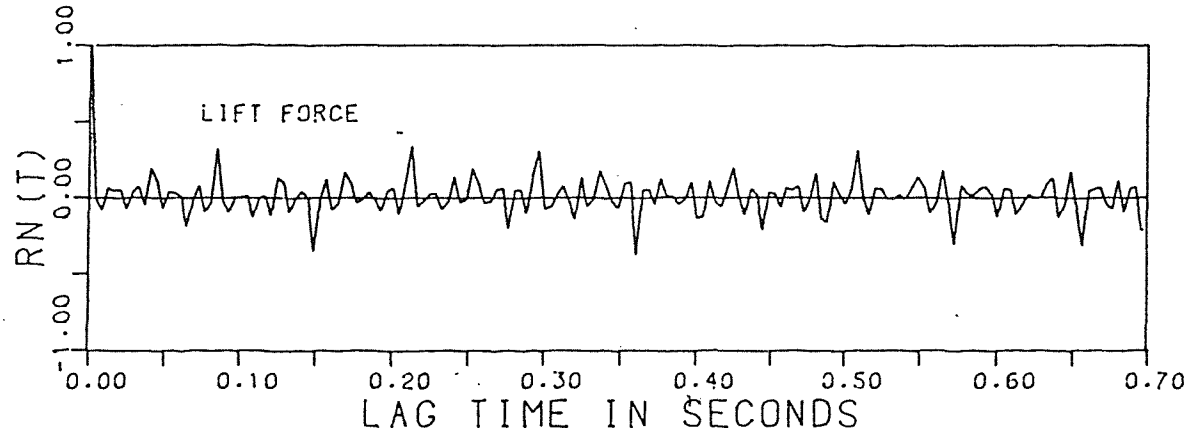

FIG. **8-19A:** AUTOCORRELATION COEF. FOR THE FLUCTUATING FORCES

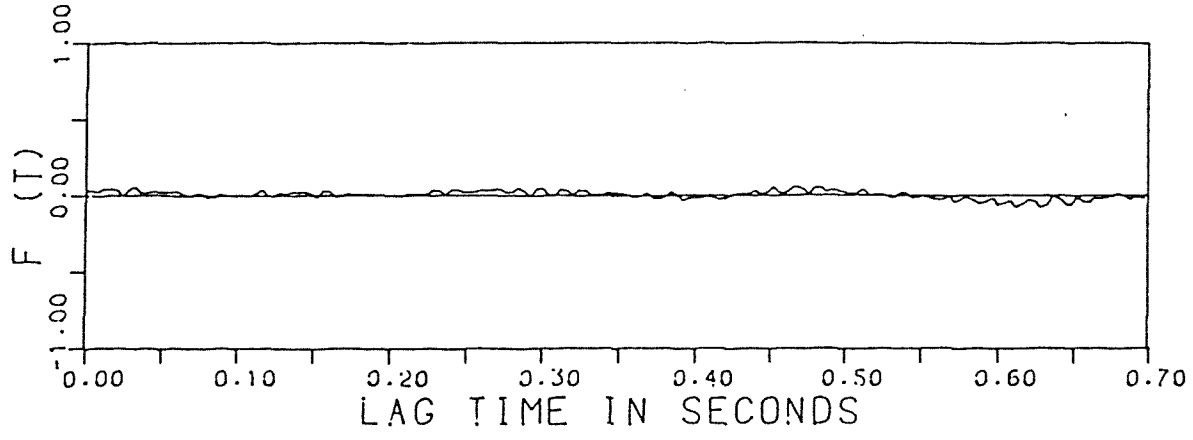

FIG. **8-19B:** CROSS CORRELATION COEF. FOR THE DRAG AND LIFT FORCES

[RUN NO. 7]

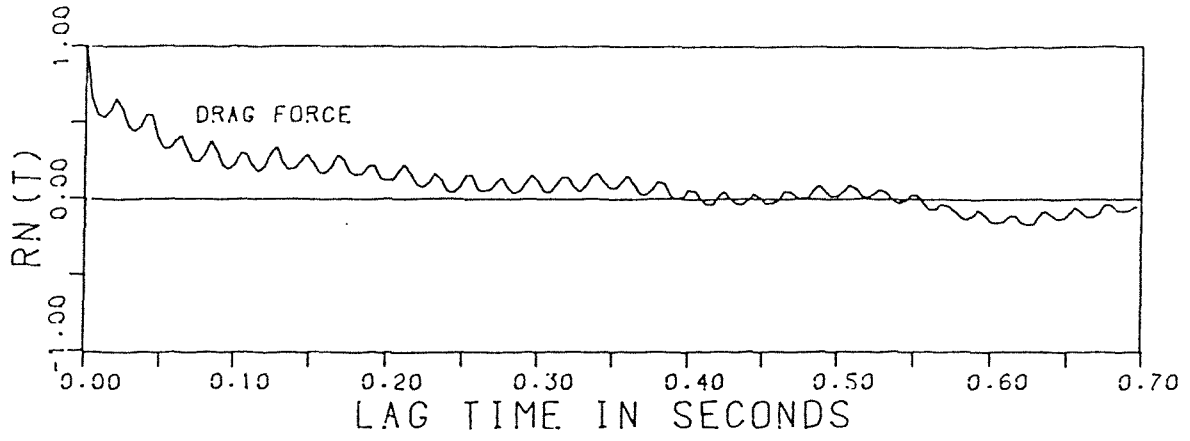

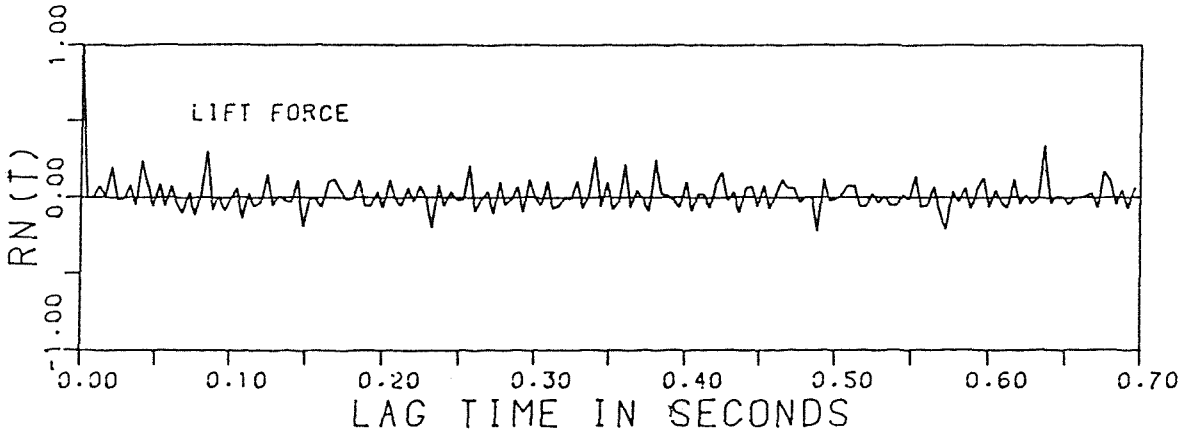

FIG.**8-20A**: AUTOCORRELATION COEF. FOR THE FLUCTUATING FORCES

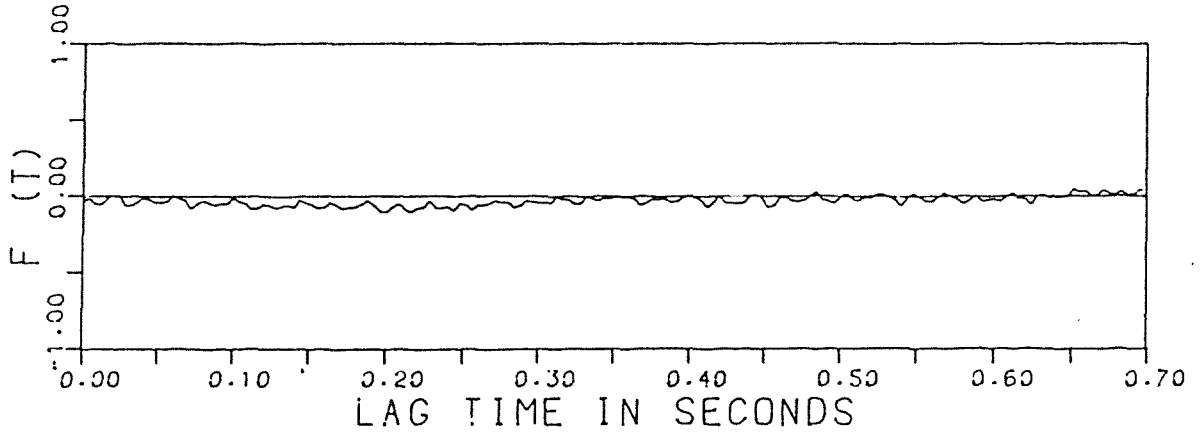

FIG.**8-20B**: CROSS CORRELATION COEF. FOR THE DRAG AND LIFT FORCES

[RUN NO. 8]

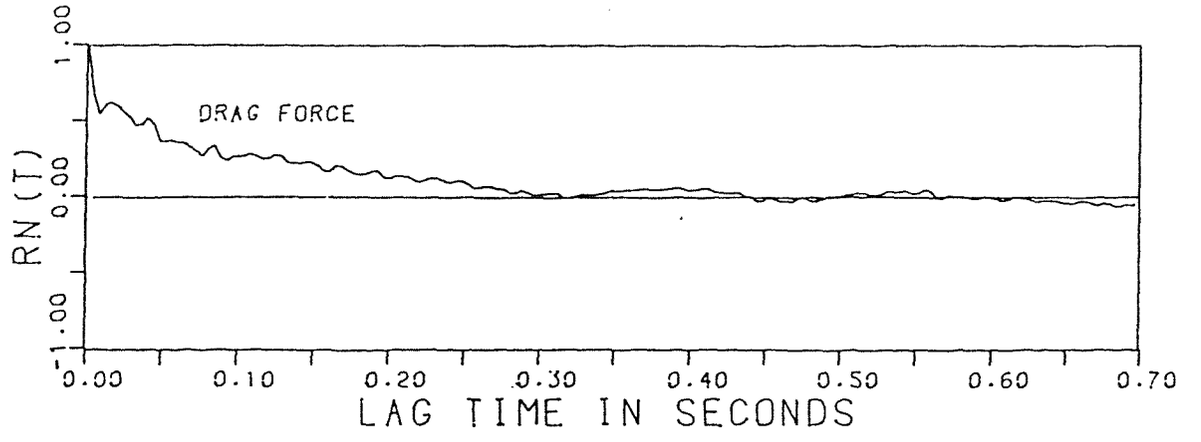

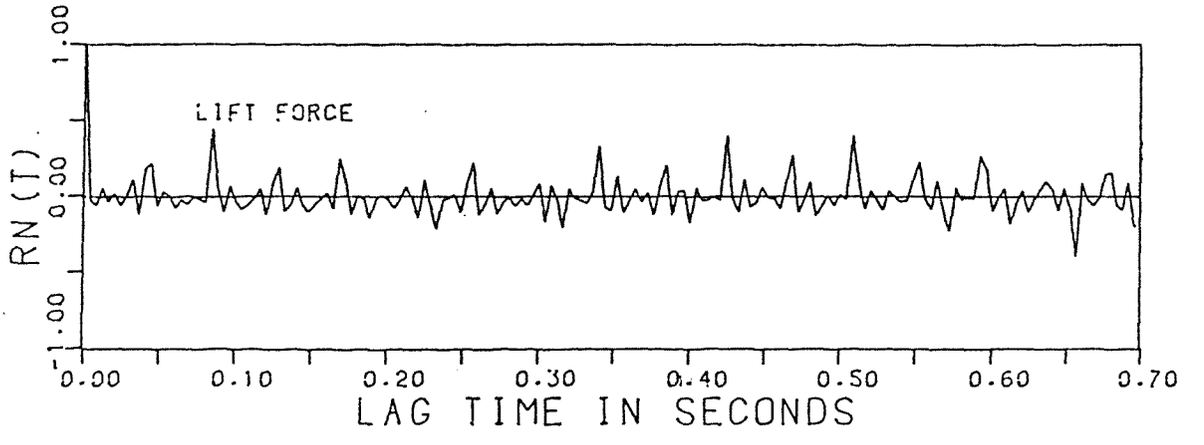

FIG. **8-21A**: AUTOCORRELATION COEF. FOR THE FLUCTUATING FORCES

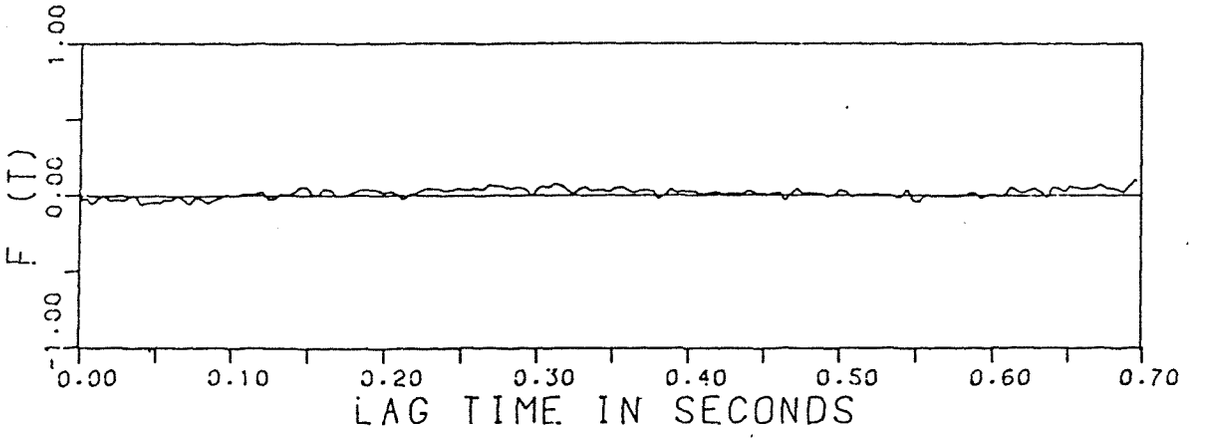

FIG. **8-21B**: CROSS CORRELATION COEF. FOR THE DRAG AND LIFT FORCES

[RUN NO. 9]

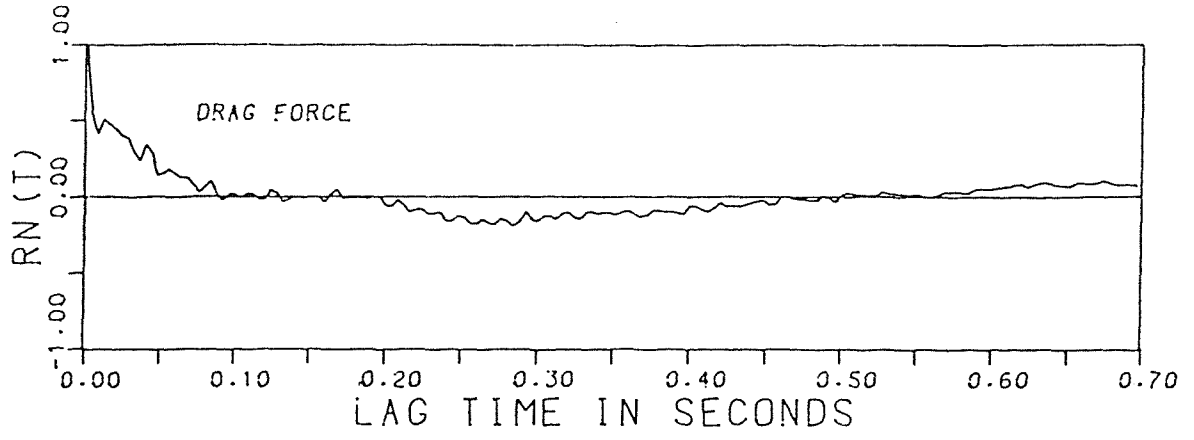

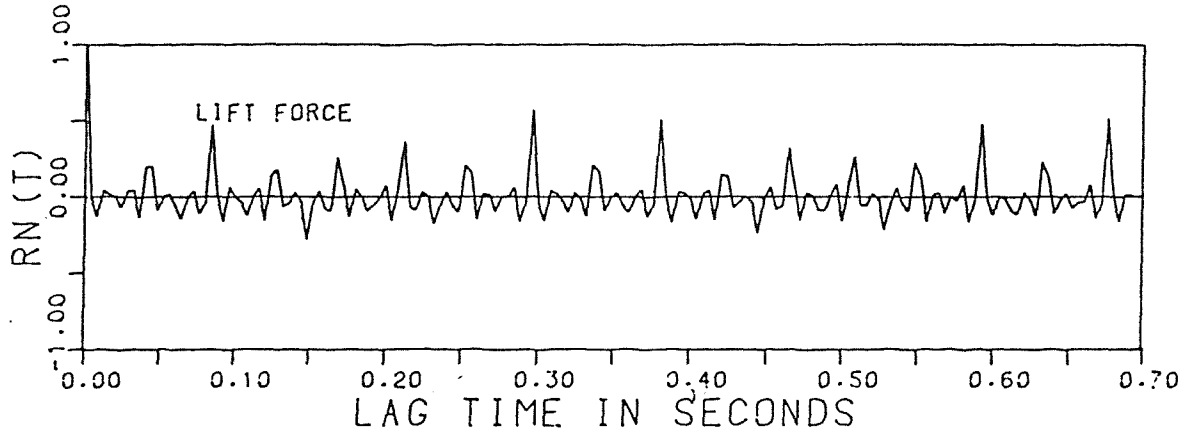

FIG.**8-22A**: AUTOCORRELATION COEF. FOR THE FLUCTUATING FORCES

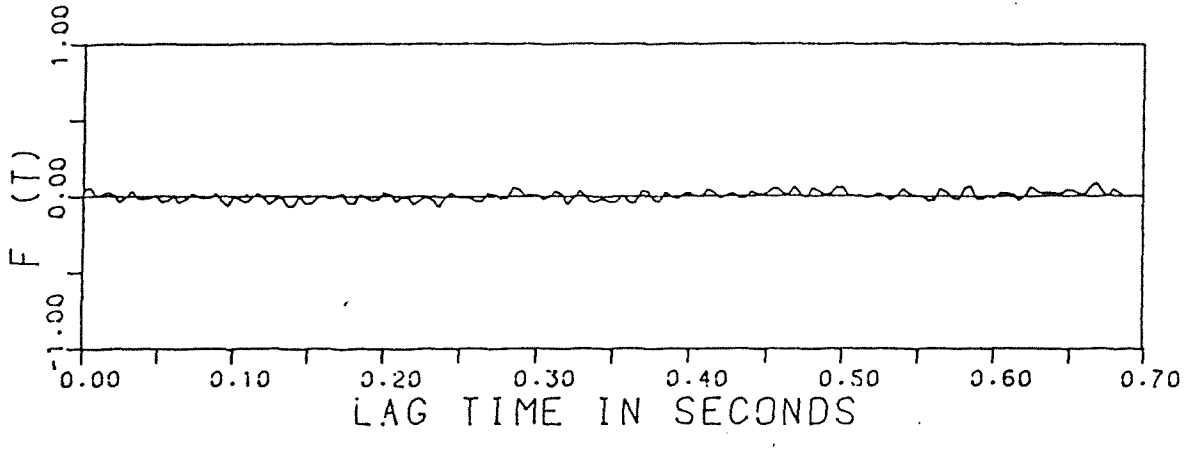

FIG.**8-22B**: CROSS CORRELATION COEF. FOR THE DRAG AND LIFT FORCES

[RUN NO. 10]

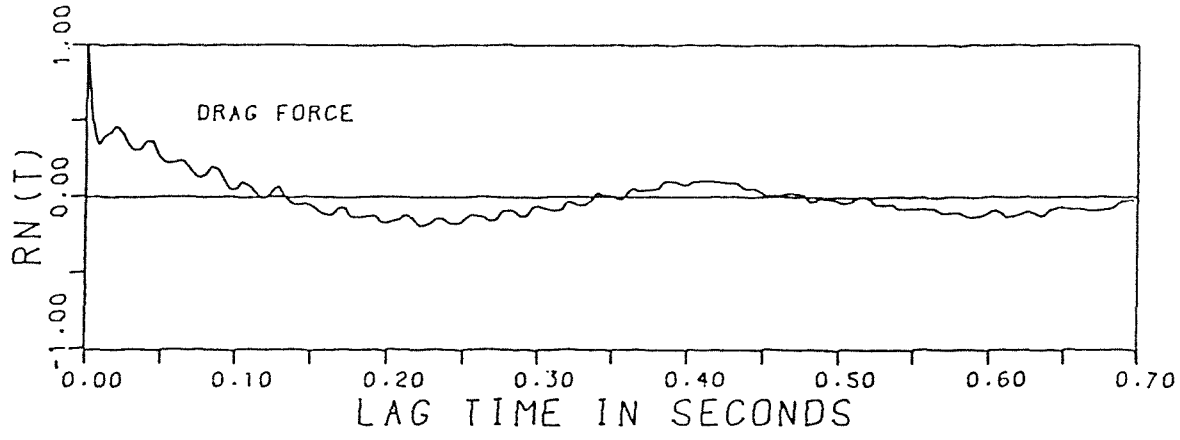

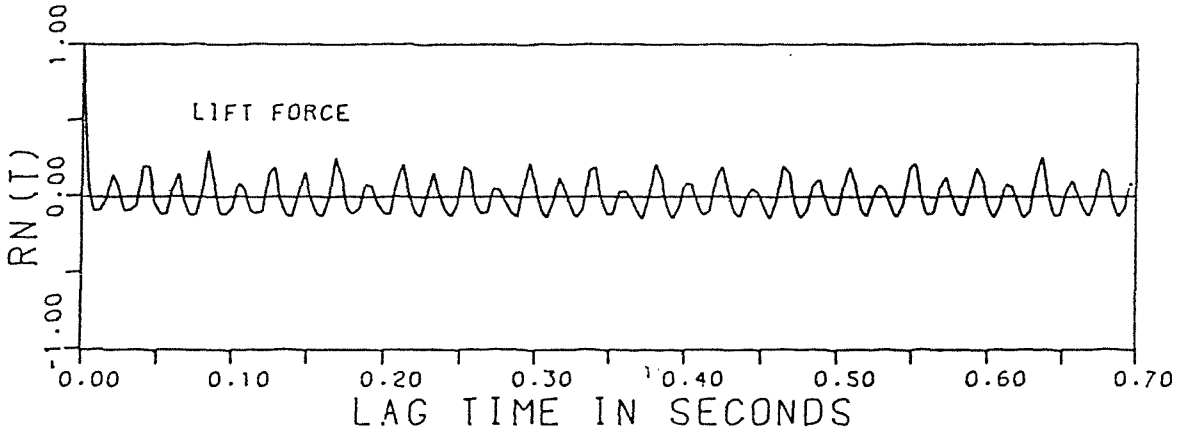

FIG. **8-23A**: AUTOCORRELATION COEF. FOR THE FLUCTUATING FORCES

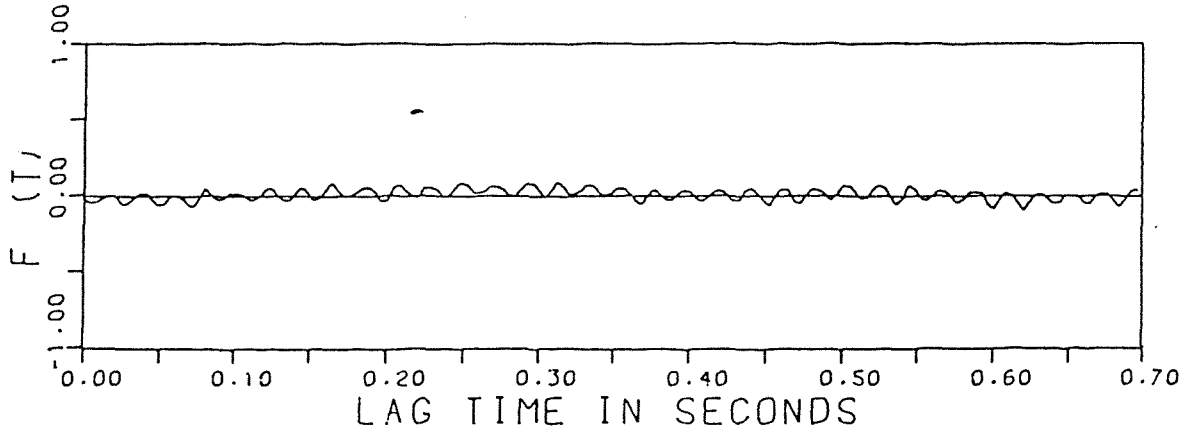

FIG. **8-23B**: CROSS CORRELATION COEF. FOR THE DRAG AND LIFT FORCES

[RUN NO. 11]

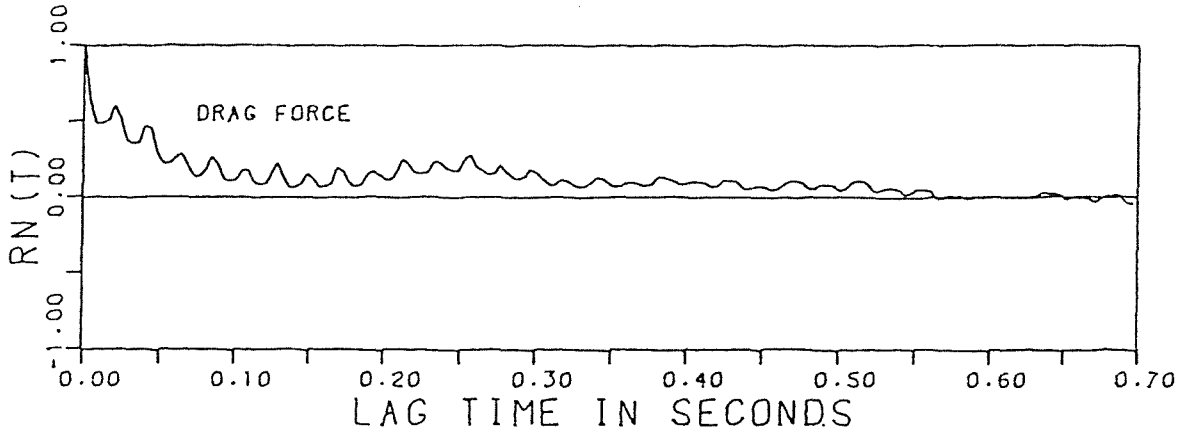

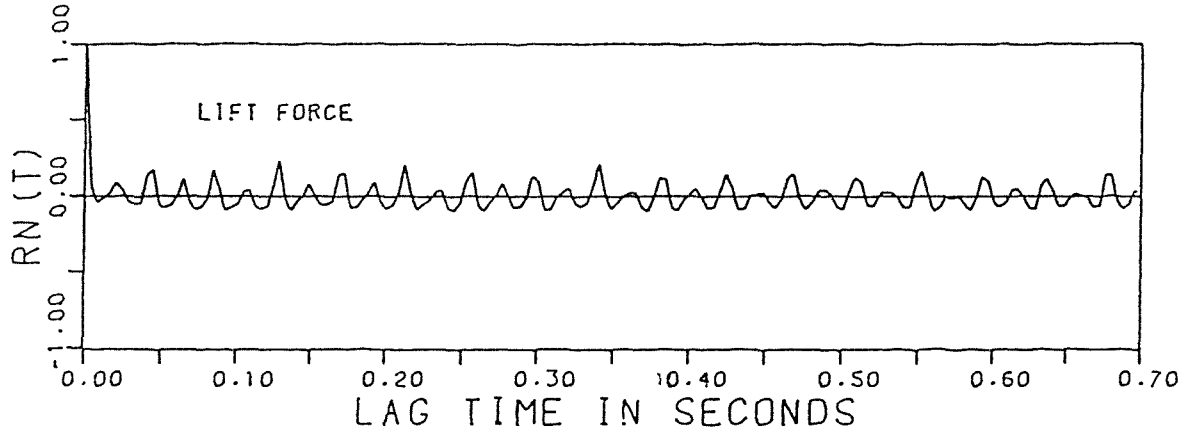

FIG. **8-24A**: AUTOCORRELATION COEF. FOR THE FLUCTUATING FORCES

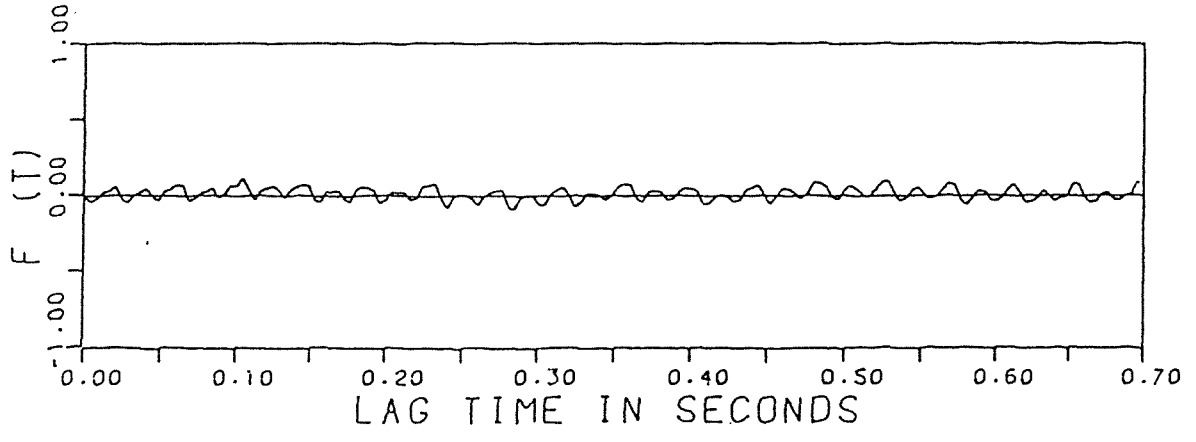

FIG. **8-24B**: CROSS CORRELATION COEF. FOR THE DRAG AND LIFT FORCES

[RUN NO. 12]

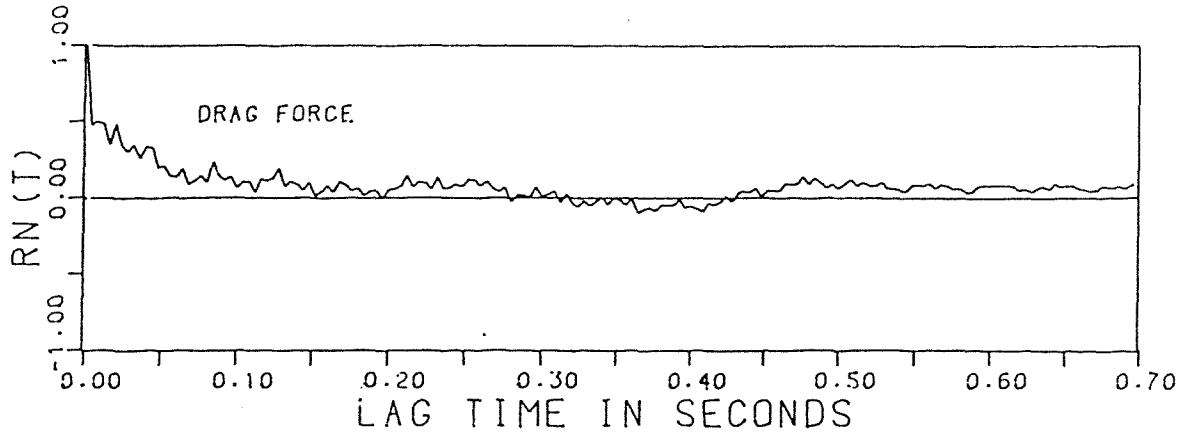

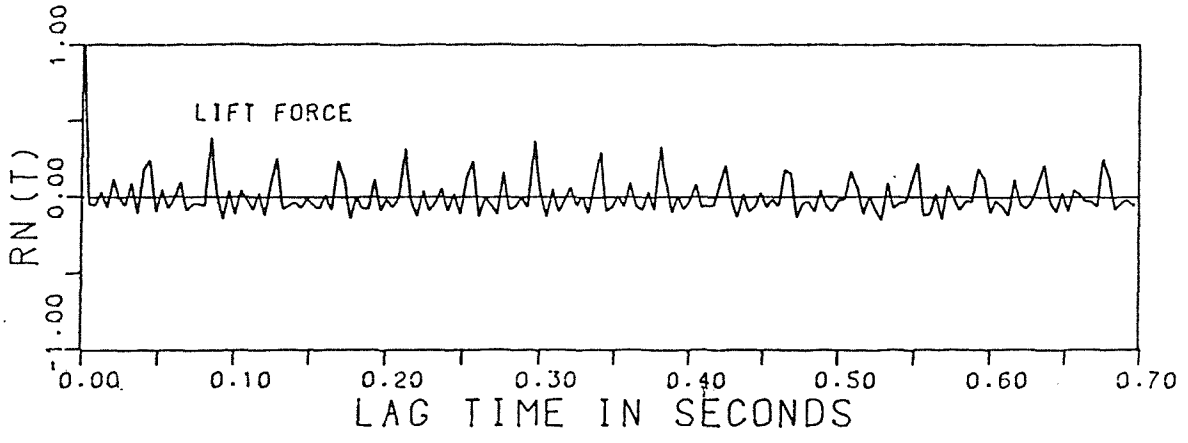

FIG. **8-25A**: AUTOCORRELATION COEF. FOR THE FLUCTUATING FORCES

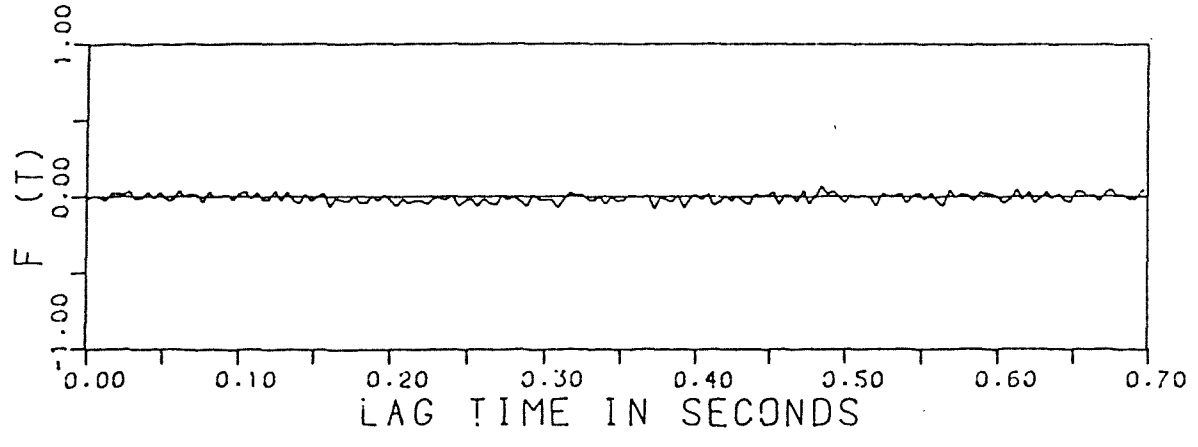

FIG. **8-25B**: CROSS CORRELATION COEF. FOR THE DRAG AND LIFT FORCES

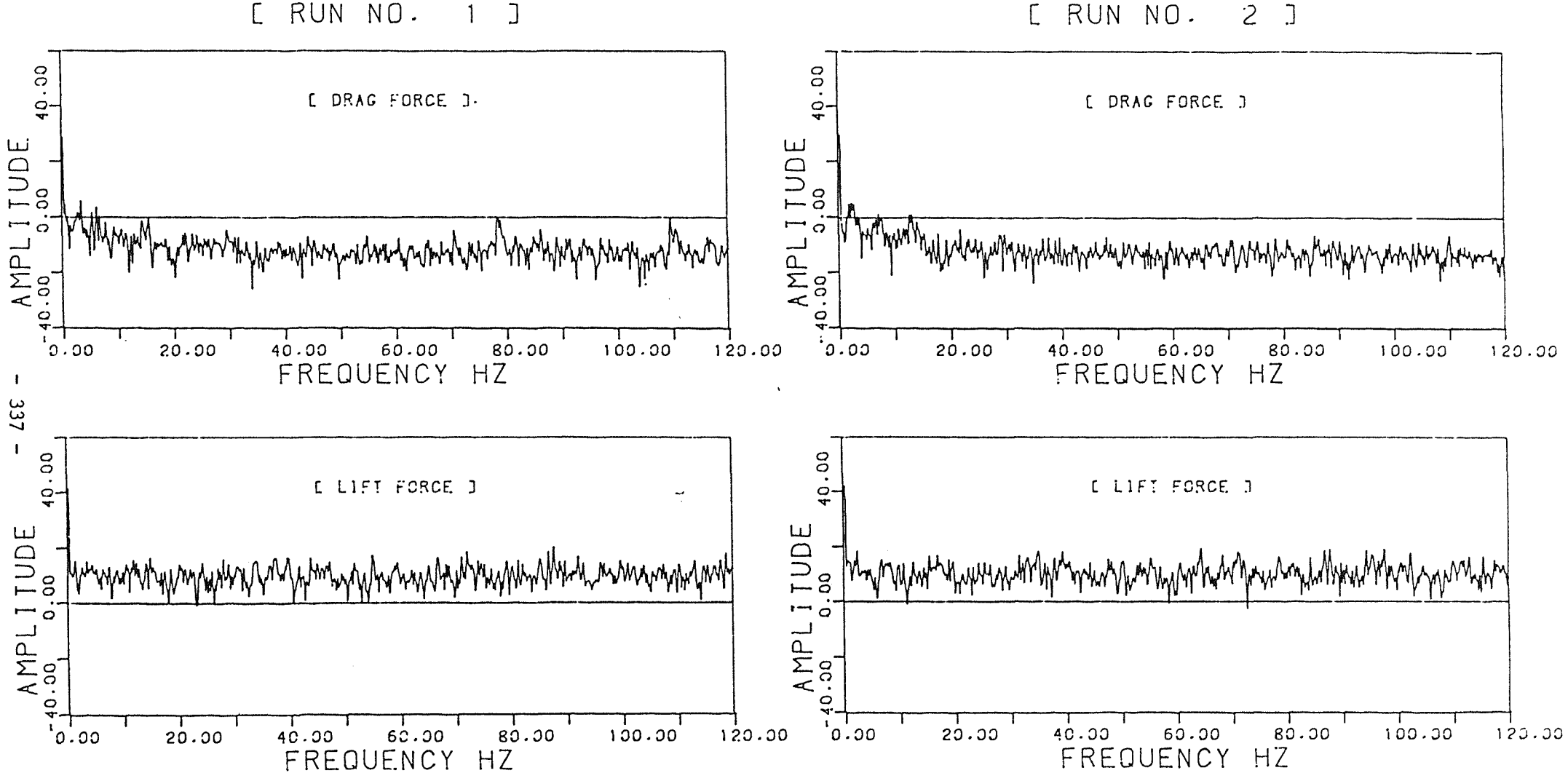

FIG. **8-26** : FREQUENCY SPECTRUM FOR THE RECORDED LIFT & DRAG FORCES

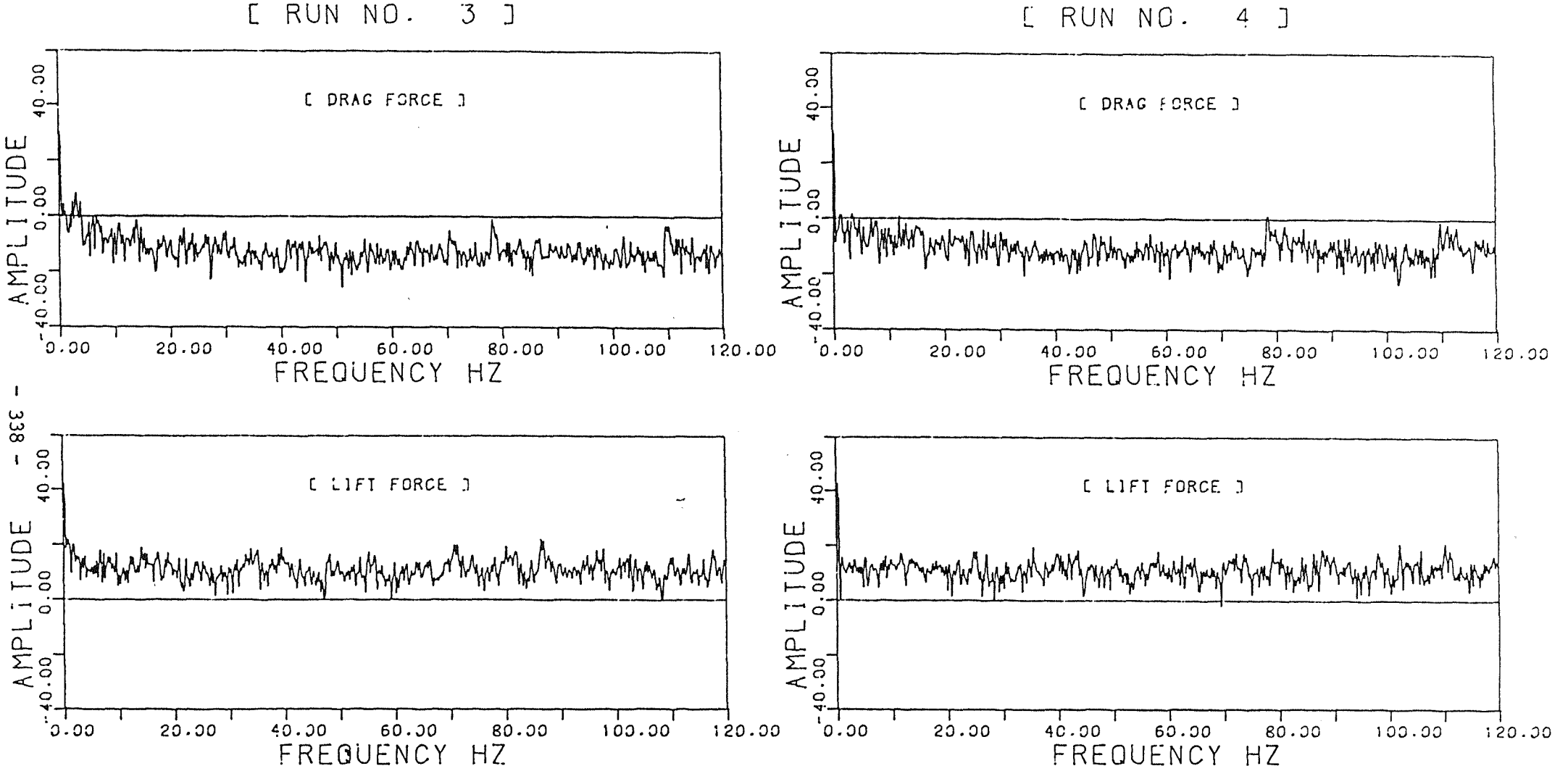

FIG.**8-27**: FREQUENCY SPECTRUM FOR THE RECORDED LIFT & DRAG FORCES

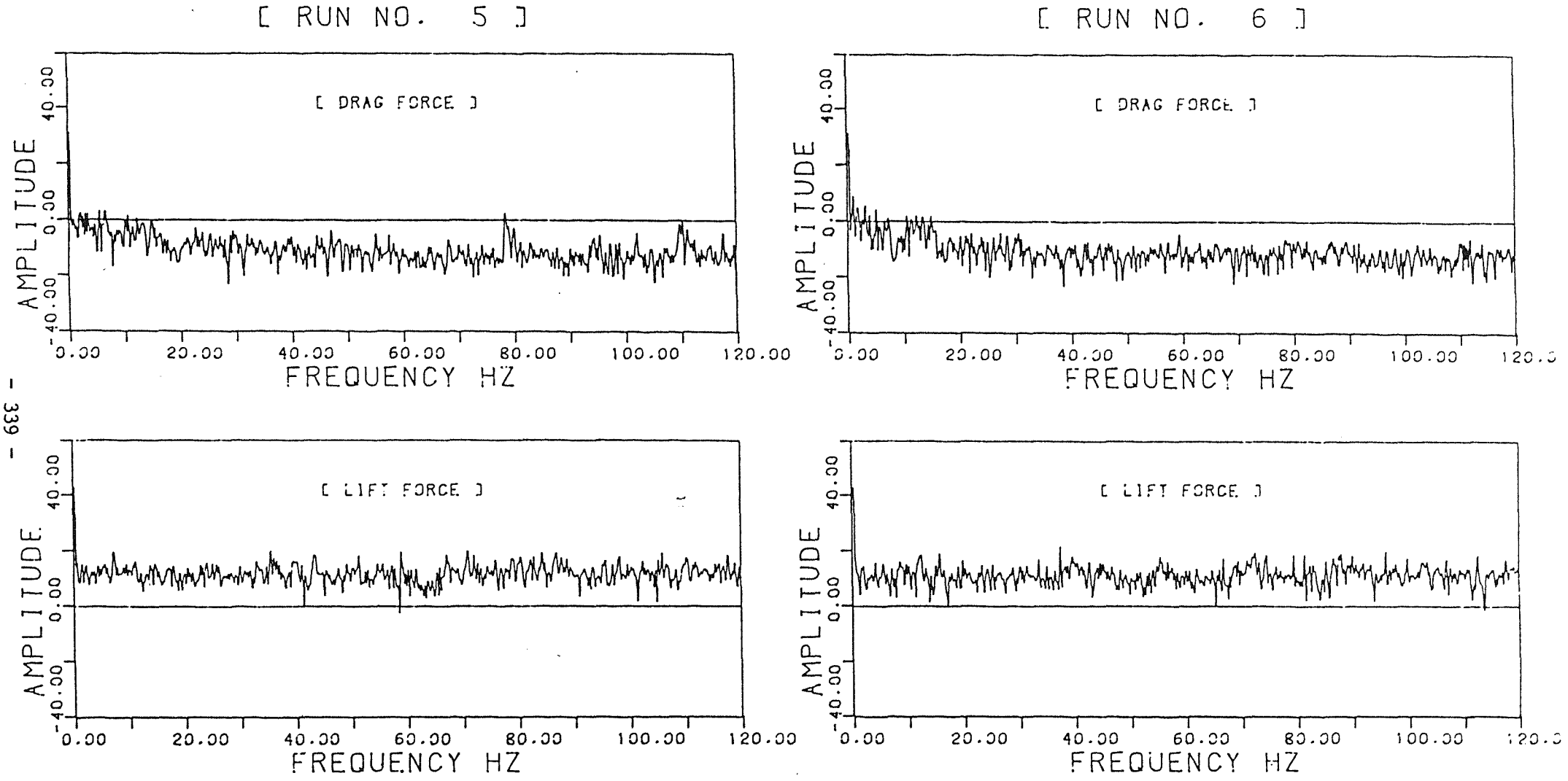

FIG. **8-28**: FREQUENCY SPECTRUM FOR THE RECORDED LIFT & DRAG FORCES

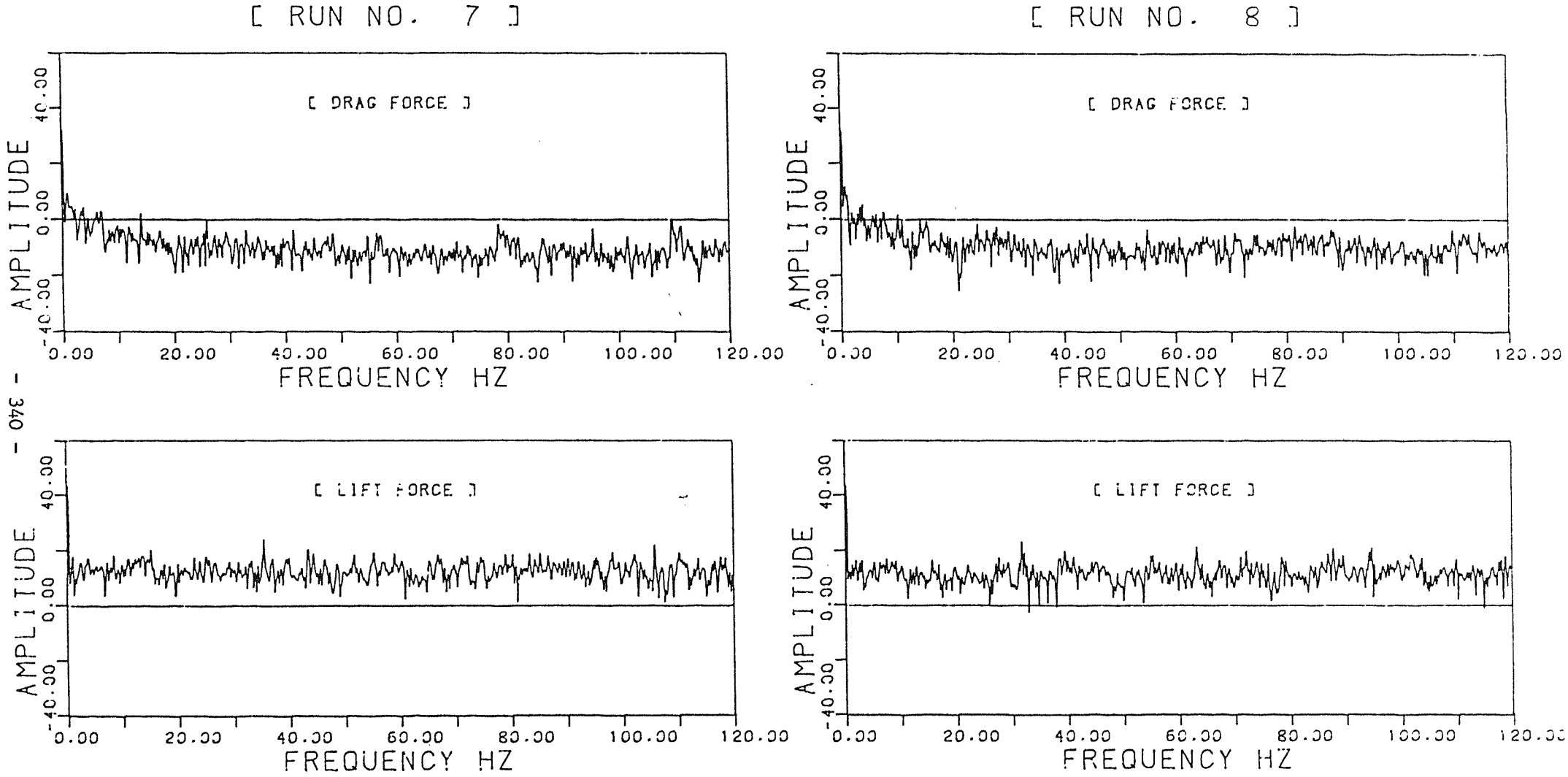

FIG.**8-29** : FREQUENCY SPECTRUM FOR THE RECORDED LIFT & DRAG FORCES

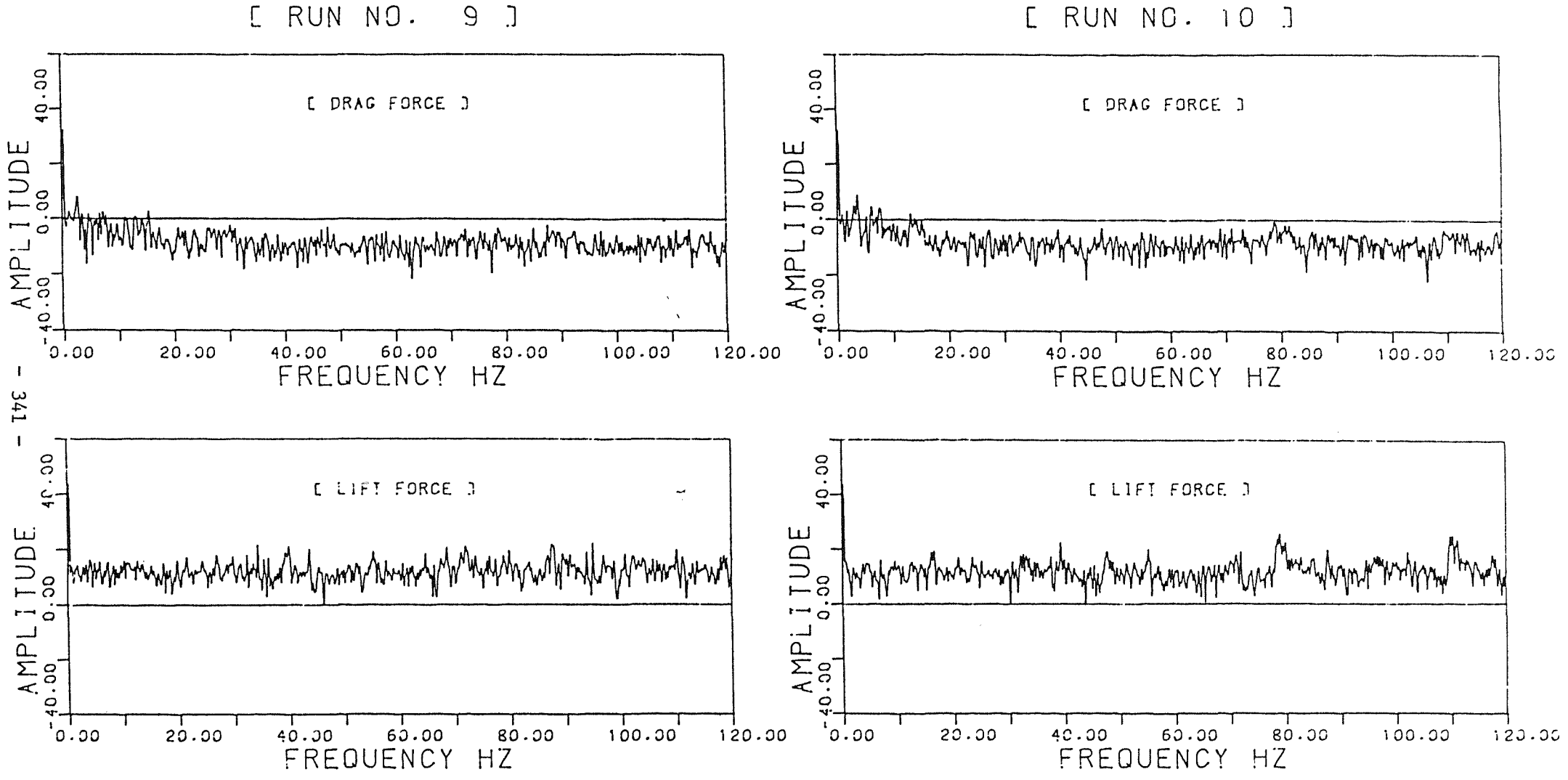

FIG. **8-30** : FREQUENCY SPECTRUM FOR THE RECORDED LIFT & DRAG FORCES

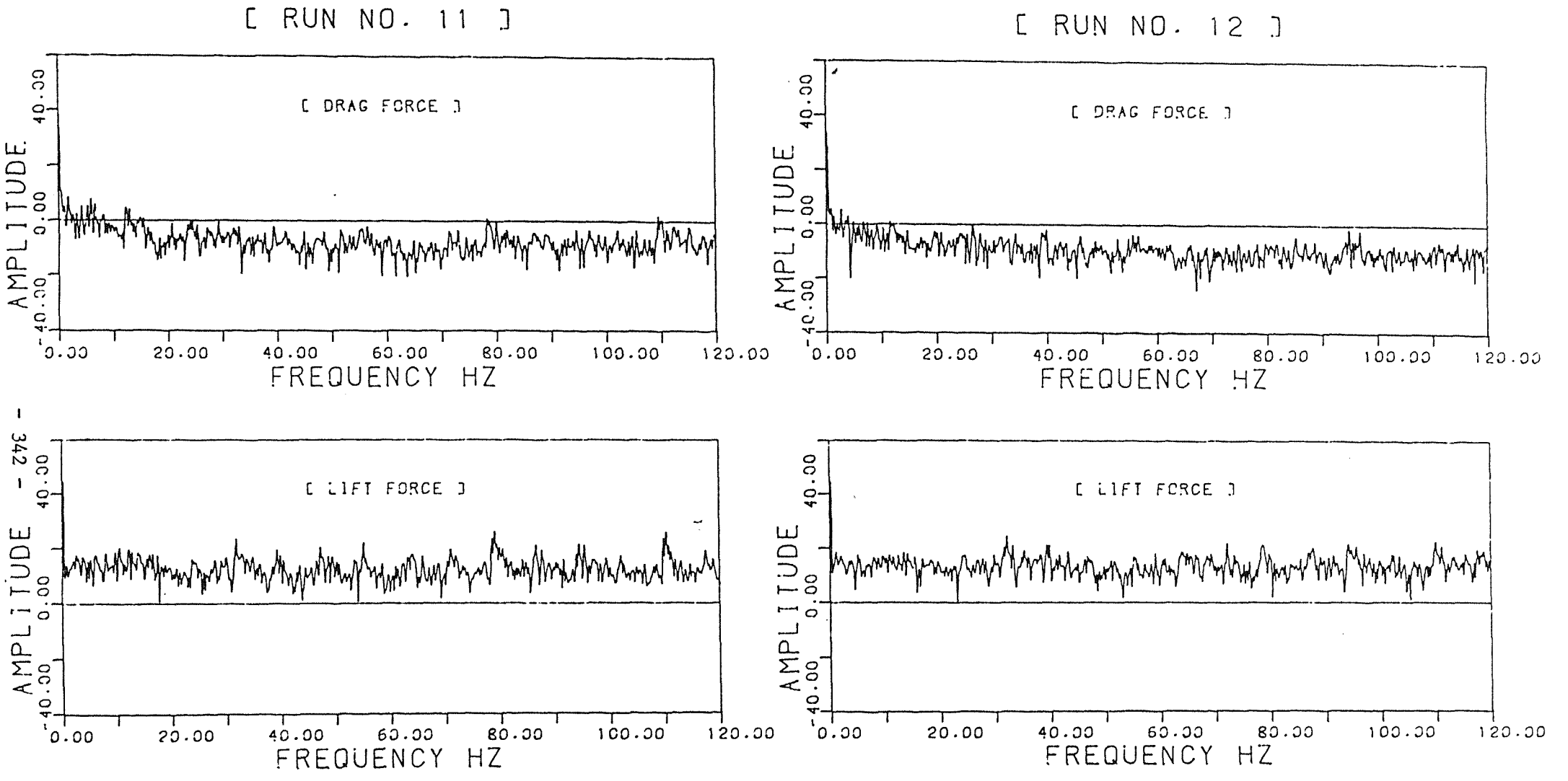

FIG. **8-31**: FREQUENCY SPECTRUM FOR THE RECORDED LIFT & DRAG FORCES

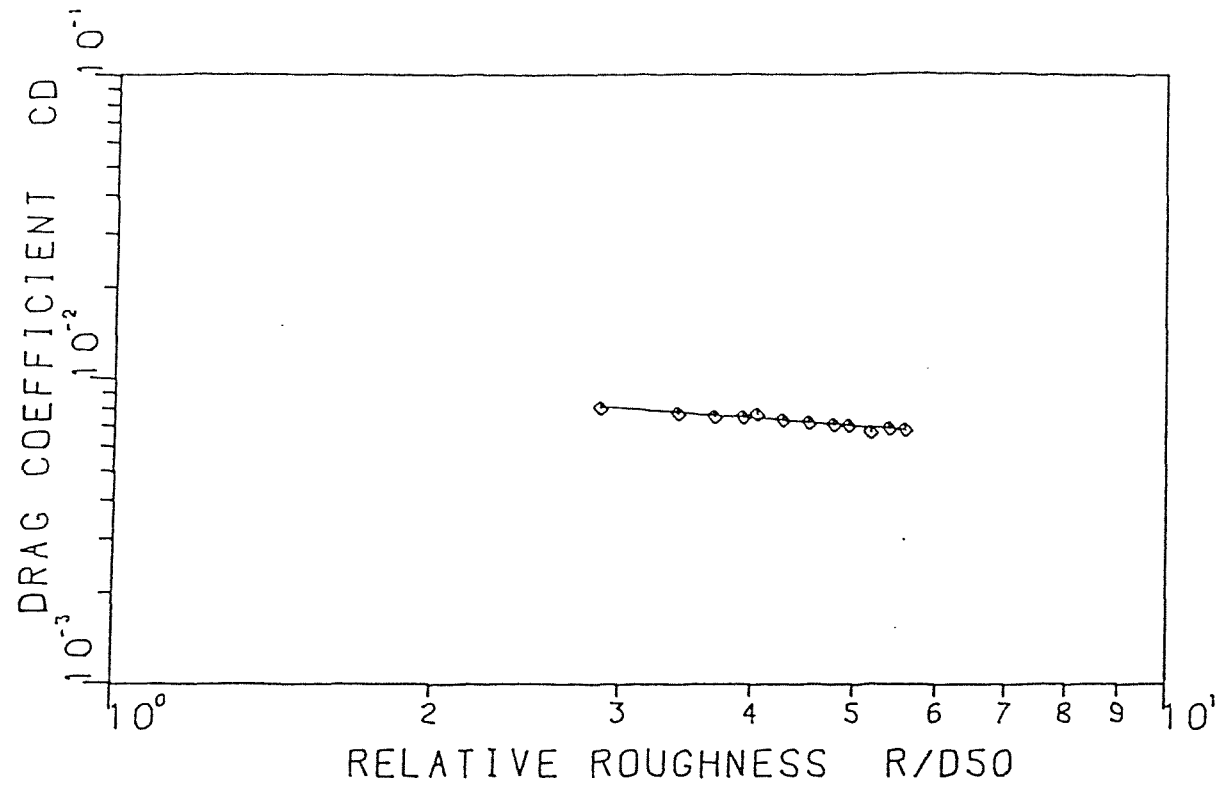

FIG.**8-32** : VARIATION OF CD WITH R/D50

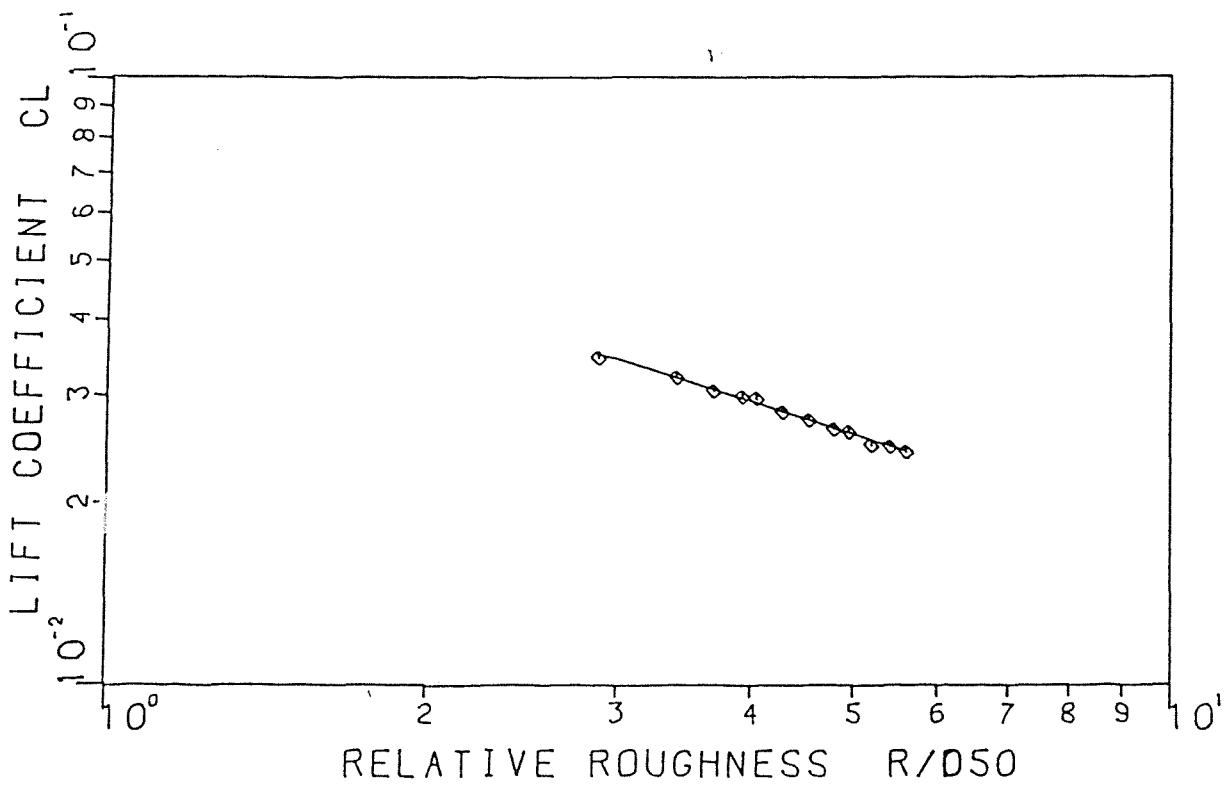

FIG.**8-33** : VARIATION OF CL WITH R/D50

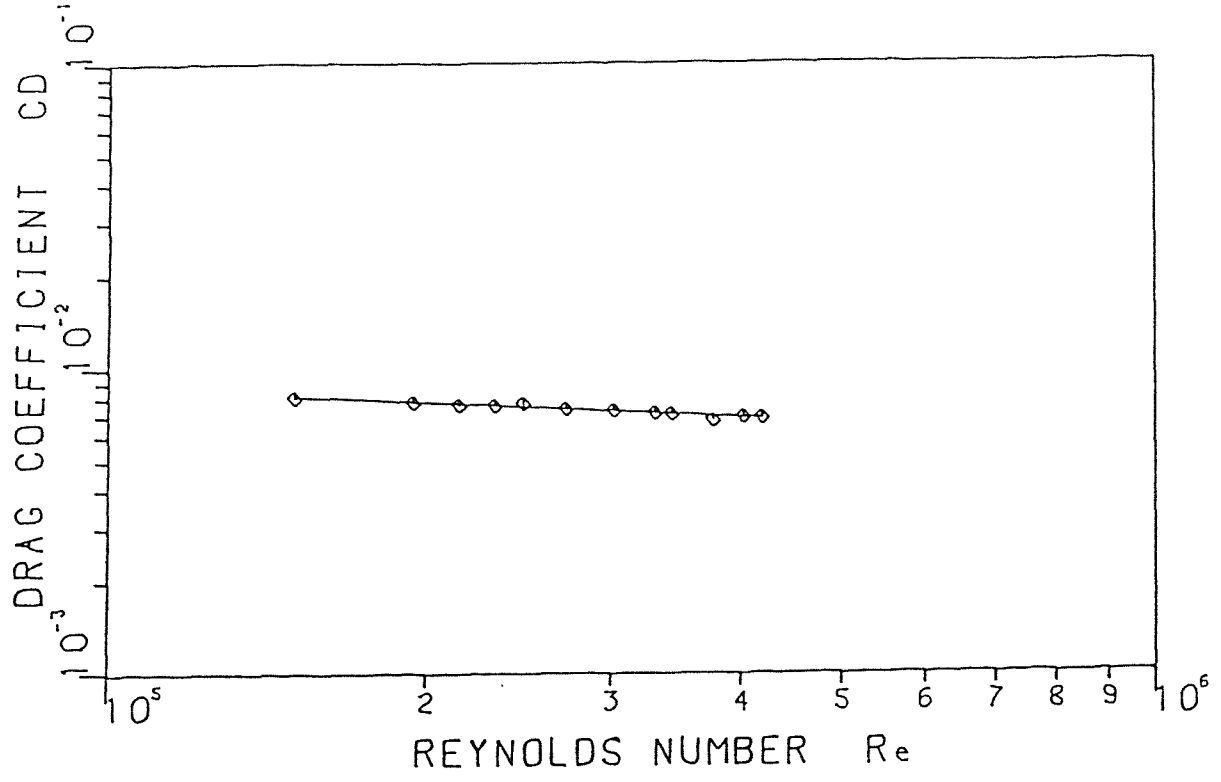

FIG. **8-34** : VARIATION OF CD WITH Re

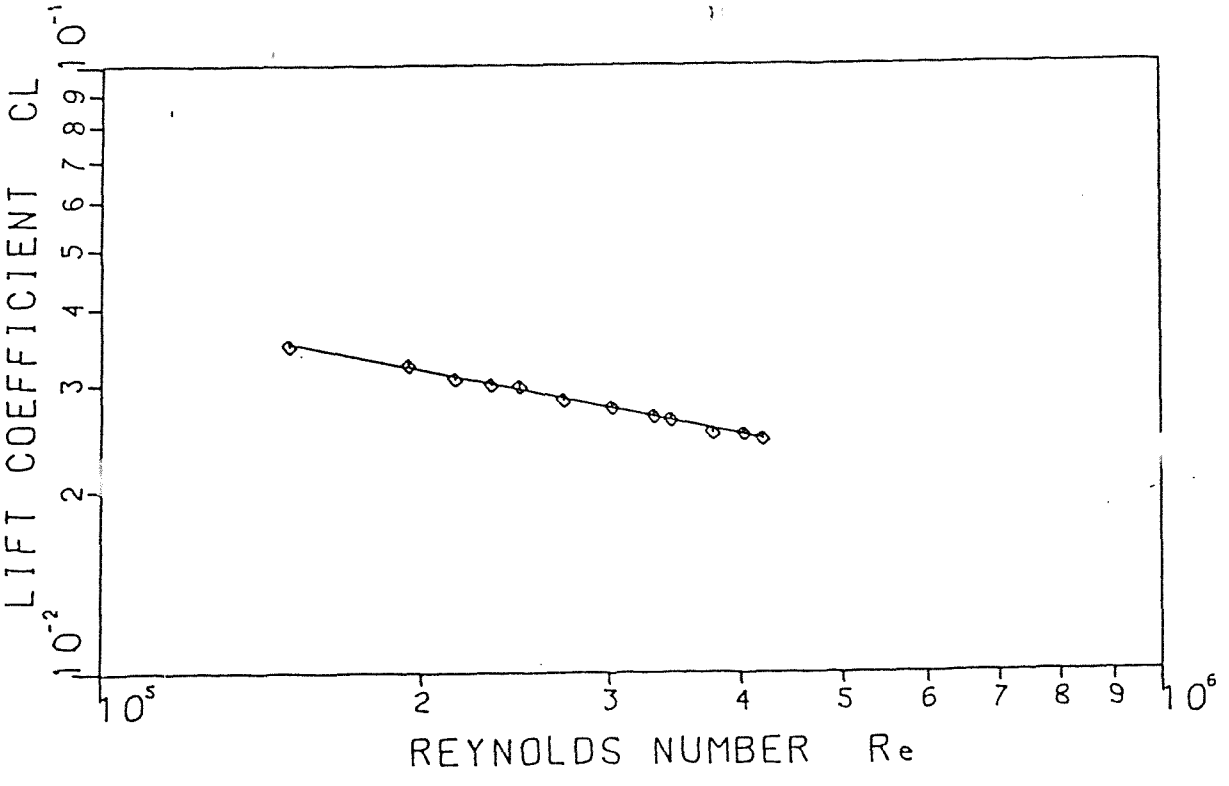

FIG. **8-35** : VARIATION OF CL WITH Re

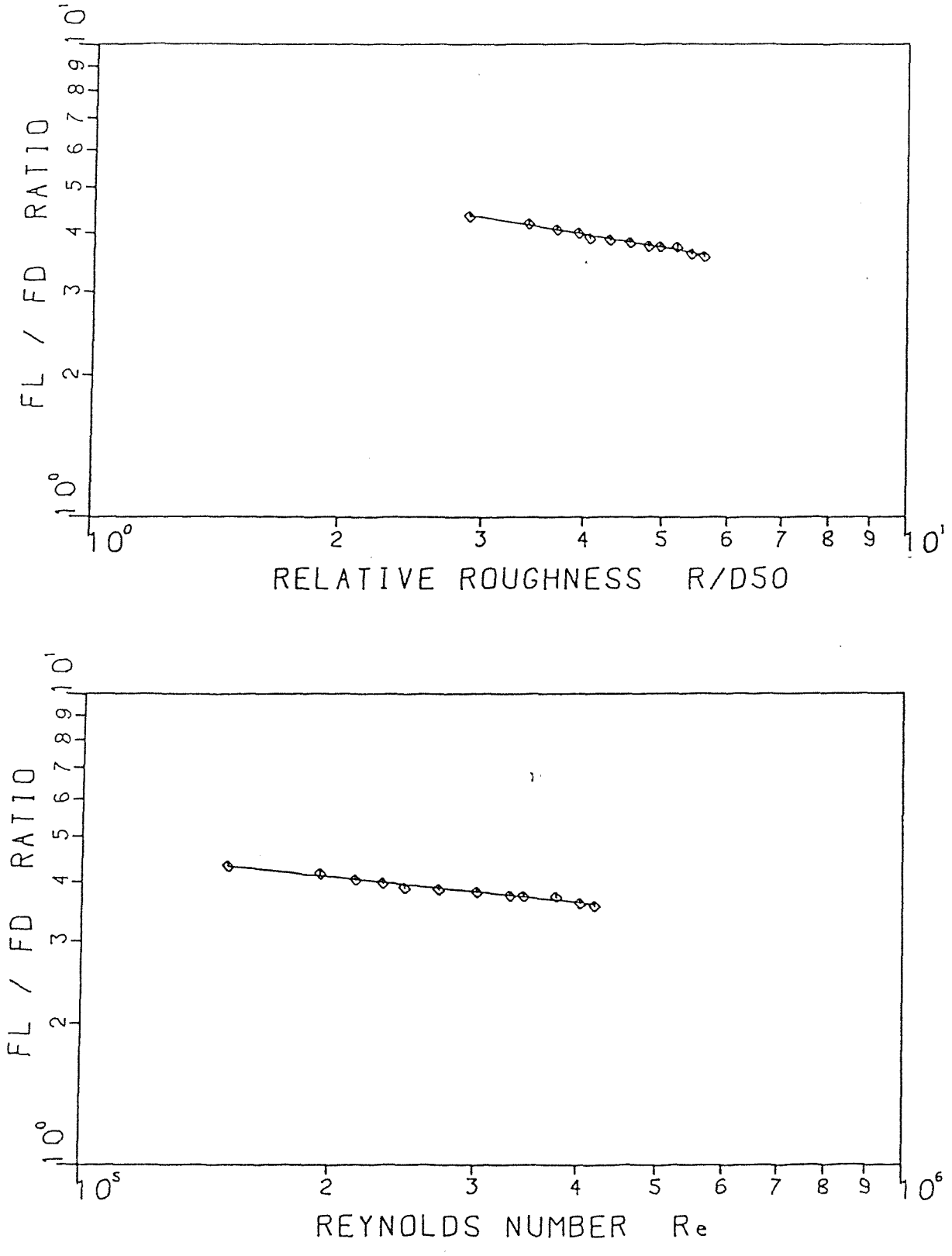

FIG.8-36:VARIATION OF (FL/FD) RATIO WITH (R/D50) AND Re

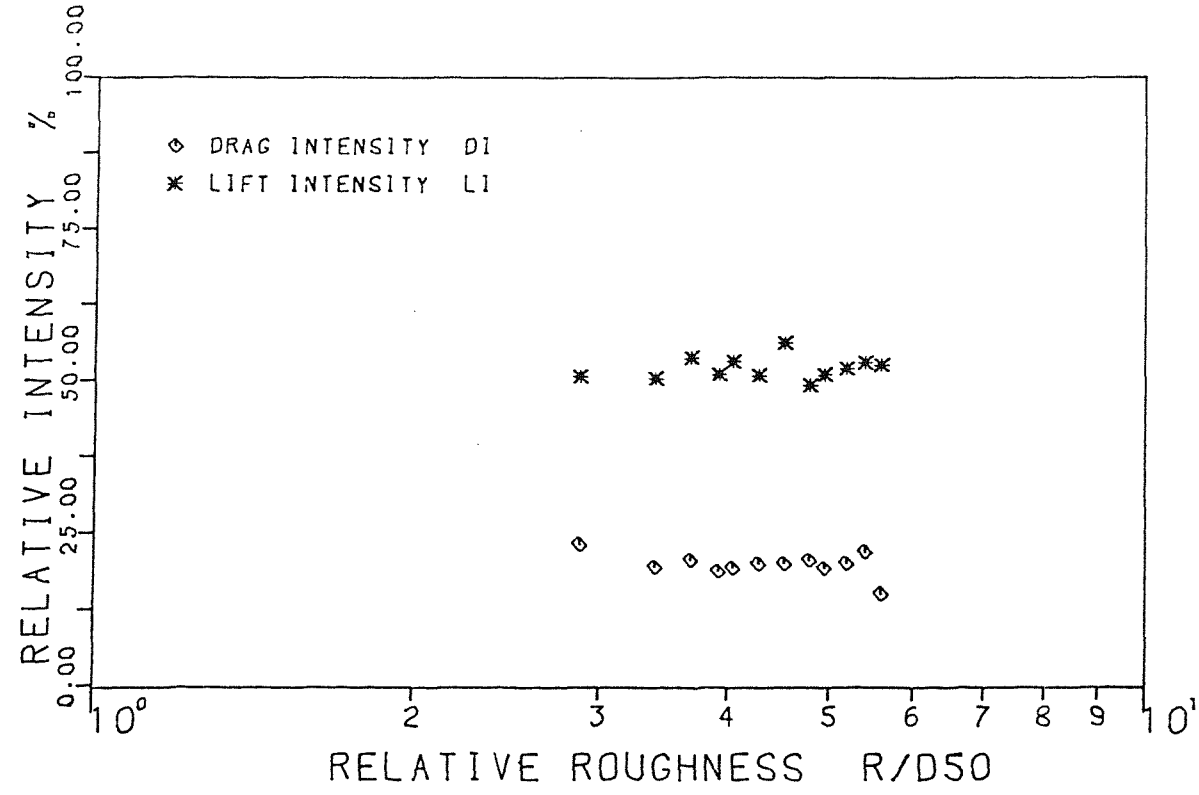

FIG.8-37: VARIATION OF DI & LI WITH R/D50

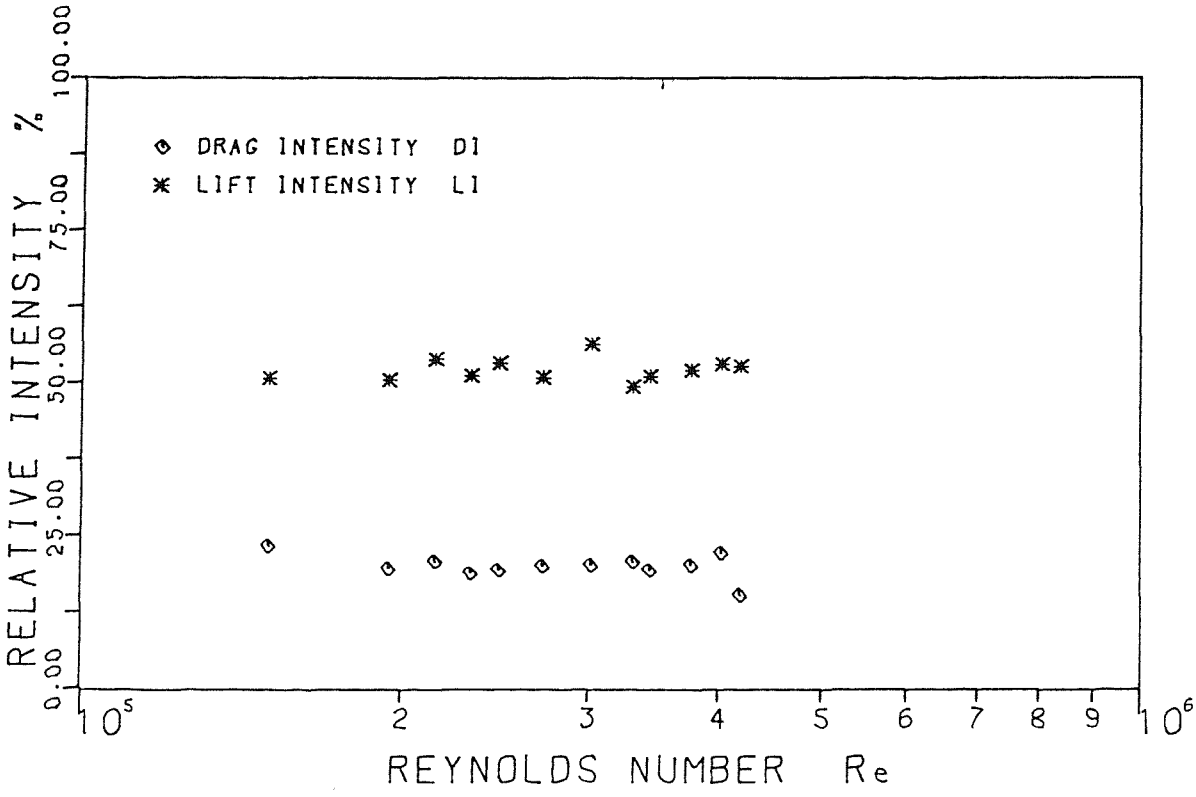

FIG.8-38: VARIATION OF DI & LI WITH Re

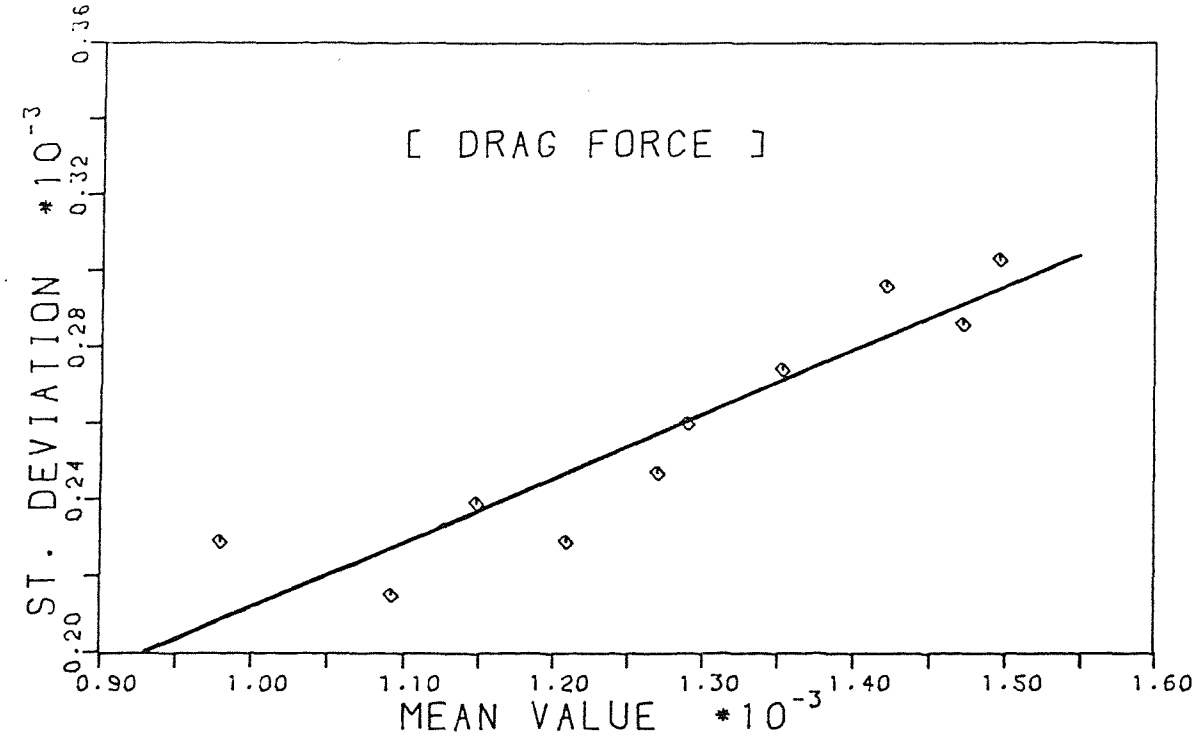

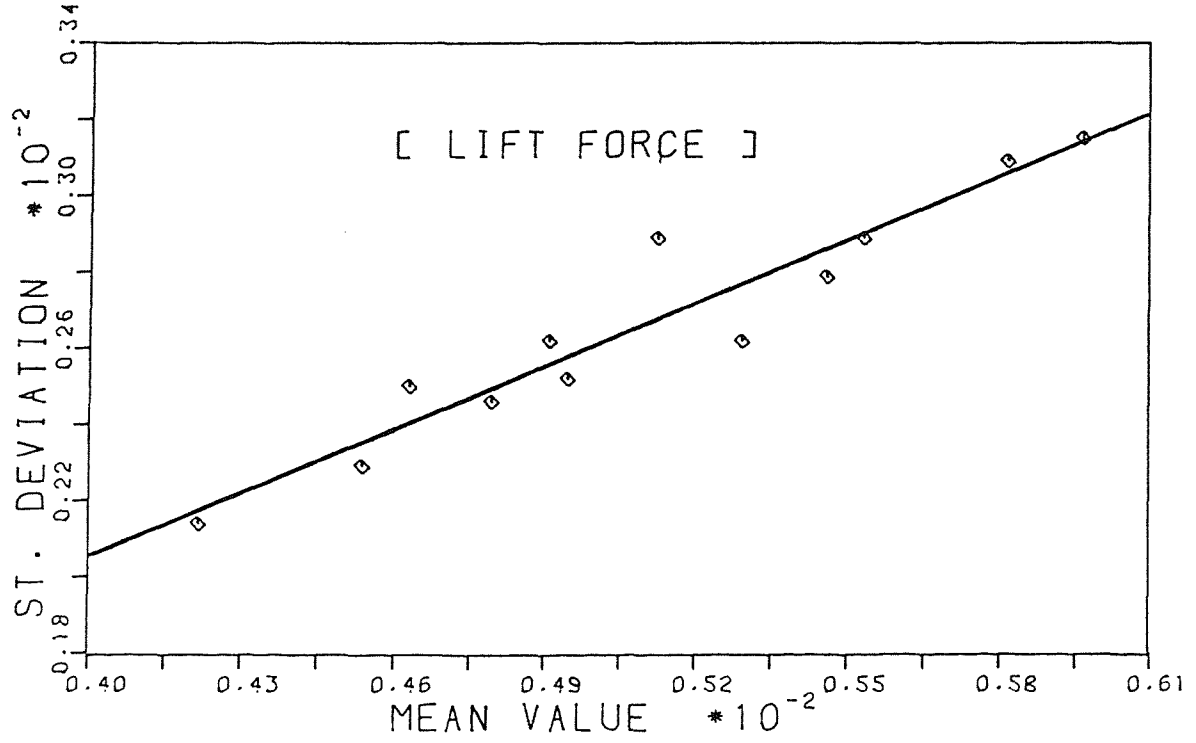

FIG.8-39: VARIATION OF DRAG AND LIFT FORCE INTENSITIES

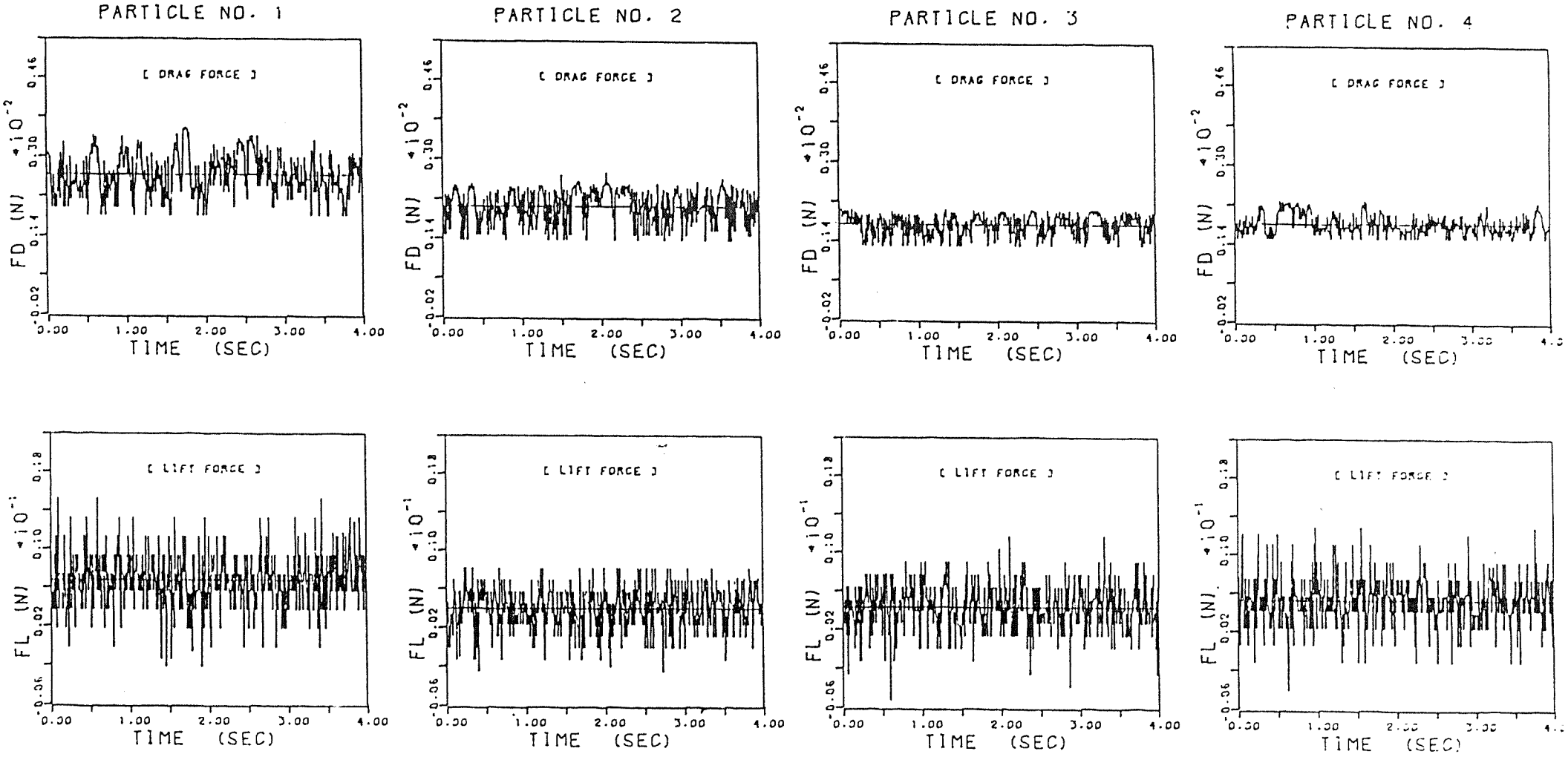

FIG.8-40:COMPARISON OF THE MEASURED HYDRODYNAMIC FORCES USING DIFFERENT ROCK SHAPES

CHAPTER NINE

STABILITY ANALYSIS AND RESULTS

9.1 INTRODUCTION

It was concluded through the comparison analysis conducted in Chapter Seven, that neither the deterministic methods nor the probabilistic methods predicted the side slope stability in accordance with that obtained during the experimental tests. In the Author's opinion, this discrepancy was mainly due to the lack of experimental measurements as a basis for the analytical stability criteria.

Although the rock protection usually consists of some thickness of fragment particles, its stability and accordingly that of the whole structure, must be ultimately dependent on the stability of an individual particle. However, the experiments conducted during the current study revealed that movement of one particle does not usually cause the failure. This contradiction made it necessary to differentiate between two kinds of particle movement:

1 - Movement due to the initial unbalanced position of the particles, which usually occurs at low rates of flow to some of the less well supported particles and limited in such a way as not to cause failure. This movement is not only due to the acting hydrodynamic forces but also due to a particle's local unstable position.

2 - Movement due to the applied hydrodynamic forces, which usually increase rapidly in proportion to the increase in the flow rate, and accordingly cause progressive failure.

As a result of the preceding clarification, one may conclude that the derivation of a design criterion on the basis of the stability of a single particle can be achieved as long as the result is confirmed experimentally.

The relationships derived in the previous chapter will be utilized to formulate two different approaches for sizing riprap. These approaches can be summarized as:

1 - Deterministic approach to predict the mean safety factor by considering the mean values of lift and drag forces.

2 - Probabilistic approach to predict the chance of movement of an individual particle of the side slope which accordingly enables the designer to establish the stability of the whole riprap layer.

In addition, to establish the applicability of each approach, the side slope safety factor and probability of adequacy will be predicted utilizing the available laboratory data, and a sensitivity analysis will be established between the various deterministic and probabilistic approaches reviewed in Chapter Three, and the new methods developed in this study.

9.2 STABILITY HYPOTHESIS

Referring to the detailed discussion presented in Chapters Two, Three and Seven, and the results of the force measurements presented in Chapter Eight, a physical model of various forces acting on an individual particle of side slope is shown in Fig. (9.1) as

1 - The resultant of the hydrodynamic drag force F_D which acts parallel to the flow direction.

2 - The resultant of the hydrodynamic lift force F_L, which acts perpendicular to the side slope plane.

3 - The submerged weight of the particle W, acting vertically downwards.

Resolving these forces into their components, parallel to the flow motion and perpendicular to the side slope plane, and calculating the resultant forces in both directions, a stability hypothesis can be established by considering a single particle on the side slope which is subjected to two groups of forces:

1 - Forces tending to dislodge the particle from its position, which may be termed as driving force

2 - Forces resisting the movement of the particle, which may be termed as resisting force.

The driving force F_{DR} may be expressed as

$$F_{DR} = (W^2 \sin^2 \theta + F_D^2)^{\frac{1}{2}} \qquad (9.1)$$

where

$$W = \frac{\pi}{6} D^3 \rho g (S_s - 1) \qquad (9.2)$$

in which

F_D is the drag force (N);
W is the submerged weight of the particle (N);
θ is the angle of side slope of the channel;
g is the gravitational accelation (m/sec^2);
ρ is the water density (Kg/m^3);
S_s is the particle specific gravity;
and D is the representative diameter (m).

The resisting force F_{RE} is given by

$$F_{RE} = (W\cos\theta - F_L)\tan\phi \qquad (9.3)$$

in which

F_L is the lift force (N);

and ϕ is the angle of repose in degrees.

Therefore, the factor of safety against movement of a particle may be defined as the ratio of the resisting force, F_{RE} to the driving force, F_{DR} on a representative particle size of the riprap blanket. According to this definition, the factor of safety FS of a riprap blanket can be expressed as

$$SF = F_{RE}/F_{DR} \tag{9.4}$$

Substituting F_{RE} and F_{DR} values into Eq. (9.4), the factor of safety can be obtained as

$$SF = \frac{(W\cos\theta - F_L)\tan\phi}{(W^2\sin^2\theta + F_D^2)^{\frac{1}{2}}} \tag{9.5}$$

When $SF > 1$, the particle is considered stable. If $SF = 1$ the particle is considered in the state of incipient motion or at the critical condition, and if $SF < 1$, failure may be expected.

9.3 DETERMINISTIC APPROACH

The mean value of the safety factor given by Eq. (9.5), can be obtained by considering the mean value of drag and lift forces given in Eqs. (9.1 and 9.3), as $\overline{F}_D$ and $\overline{F}_L$. Thus the mean or conventional safety factor is defined as

$$\overline{SF} = \frac{(W\cos\theta - \overline{F}_L)\tan\phi}{(W^2\sin^2\theta + \overline{F}_D^2)^{\frac{1}{2}}} \tag{9.6}$$

When $\overline{SF} = 1$, the rock protection is considered to be at the critical condition, and when $\overline{SF} > 1$, the rock protection is safe, and if $\overline{SF} < 1$, the rock protection is considered unsafe and failure may be established.

Consideration is now given to formulating a deterministic method for establishing the conventional safety factor of the side slope.

For the given values of D, R, ϕ , θ , S_e, ρ and S_s

where

R is the hydraulic radius (m);

and S_e is the energy slope.

The following procedure is recommended:

Step 1: Use Eq. (9.2) to determine W

Step 2: Using the following equation, the shear velocity is determined:

$$u_* = \sqrt{gRS_e} \tag{9.7}$$

Step 3: Eq.(7.16) is used to obtain the mean flow velocity $\overline{u}$ from

$$\overline{u}/u_* = 8.4742\ (R/D)^{0.0304} \tag{9.8}$$

Step 4: Use Eqs. (8.22) and (8.20) to determine the value of $\overline{F}_D$ from

$$C_D = 0.01074\ (R/D)^{-0.268} \tag{9.9}$$

$$\overline{F}_D = C_D \rho \overline{u}^2 D^2/2 \tag{9.10}$$

Step 5: Using Eqs. (8.23)and (8.21)

Value of $\overline{F}_L$ is determined from:

$$C_L = 0.063(R/D)^{-0.557} \tag{9.11}$$

$$\overline{F}_L = C_L \rho \overline{u}^2 D^2/2 \tag{9.12}$$

Step 6: Applying Eq. (9.6), the side slope safety factor may be obtained.

9.4 PROBABILISTIC HYPOTHESIS

As mentioned earlier in Chapters Two and Three, and according to the detailed measurements and results presented in Chapter Eight, both lift and drag forces acting on a side slope particle were found to be randomly fluctuating as a function of time as shown in Figs. (8.1) to (8.13), and both processes were also found to be stationary random. Thus, the probability of adequacy of a riprap protection can be determined as

$$P_a = \text{probability } [F_{RE} > F_{DR}] \tag{9.13}$$

$$P_a = P[F_{RE} > F_{DR}] \tag{9.14}$$

$$= f(FS) \tag{9.15}$$

in which P[.] is the probability of the specified event.

According to the assumption established by Smith, K.V.H. (1986), the drag force F_D was considered to be proportional to the boundary shear stress τ, and the lift force F_L was considered to be related to drag force F_D, i.e.

$$F_D = \delta\tau \tag{9.16}$$

and

$$F_L = \beta F_D = \delta\beta\tau \tag{9.17}$$

where

δ is the proportionality parameter and has units L^2

and β is the ratio lift to drag.

Therefore, the conventional safety factor given by Eq. (9.5) can be derived utilizing Eqs. (9.16) and (9.17), to obtain

$$SF = \frac{(W\cos\theta - \beta\delta\tau)\tan\phi}{(W^2\sin^2\theta + \delta^2\tau^2)^{\frac{1}{2}}} \tag{9.18}$$

In order to evaluate the proportionality constant δ, the expression

$$\tau = \rho u_*^2 \tag{9.19}$$

is utilised. Then, from Eqs. (9.10) and (9.16) we obtain

$$F_D = \delta\tau = \delta\rho u_*^2 = C_D\rho u^2 D^2/2 \tag{9.20}$$

Eq. (9.20) can be regrouped into the following dimensionless form:

$$\frac{\delta}{D^2} = \left(\frac{u}{u_*}\right)^2 \cdot \left(\frac{C_D}{2}\right) \tag{9.21}$$

The right hand side of Eq. (9.21) can be obtained by utilising Eqs. (9.8) and (9.9) to develop another simple formula in the form

$$\frac{\delta}{D^2} = f\,(R/D) \tag{9.22}$$

To establish this relation, the term (δ/D^2), was plotted against (R/D), for all runs as shown in Fig. (9.2), and the result obtained was

$$\delta = 0.3858\, D^2\, (R/D)^{-0.2071} \tag{9.23}$$

This formula indicates that δ, does not have a constant value as suggested by Ruh-Ming, L. et al. (1976), and Ruh-Ming, L. and Simons, D.B. (1979).

For an existing riprap structure, the rock size and accordingly the submerged weight of a particle is known. Thus, the critical shear stress for the failure can be determined by utilizing Eq. (9.18) with $\tau = \tau_c$ when SF = 1, to obtain:

$$(W\cos\theta - \beta\delta\tau_c)\tan\phi = (W^2\sin^2\theta + \delta^2\tau_c^2)^{\frac{1}{2}} \qquad (9.24)$$

in which τ_c is the critical shear stress.

Eq. (9.24) is a quadratic equation, and its solution in the form quoted by Ruh-Ming, L. et al. (1976) is

$$\tau_c = \frac{(A_1^2 + W^2A_2A_3)^{\frac{1}{2}} - A_1}{\delta \cdot A_2} \qquad (9.25)$$

in which

$$A_1 = \beta W\cos\theta \tan^2\phi \qquad (9.26)$$

$$A_2 = 1 + \beta^2\tan^2\phi \qquad (9.27)$$

$$A_3 = \cos^2\theta \tan^2\phi - \sin^2\theta \qquad (9.28)$$

Due to the proportionality between the boundary shear stress and the drag and lift forces, the value of SF in Eq. (9.18) will be less than or equal to 1.0 when τ is greater or equal to τ_c. Thus, the probability of adequacy of riprap structure can be expressed as:

$$P_a = \text{probability } [\tau_c \geqslant \tau] \qquad (9.29)$$

$$P_a = P[\tau_c \geqslant \tau] \qquad (9.30)$$

$$P_a = f(\tau_c) \qquad (9.31)$$

In order to derive relationships between shear stress and the applied hydrodynamic forces, Eqs. (9.16) and (9.17) were utilized to establish the following equations:

$$\overline{F_D} = \delta\bar{\tau} \qquad (9.32)$$

$$\overline{F_L} = \delta\beta\bar{\tau} \qquad (9.33)$$

$$F_{CD} = \delta\tau_c \tag{9.34}$$

$$F_{CL} = \delta\beta\tau_c \tag{9.35}$$

in which

F_{CD} and F_{CL} are the drag and lift forces respectively at the case of the critical shear stress.

Therefore, as the lift and drag forces are perpendicular to each other, the mean and critical resultant can be obtained as

$$\overline{F} = \sqrt{\overline{F_L}^2 + \overline{F_D}^2} = \delta\overline{\tau}\sqrt{\beta^2 + 1} \tag{9.36}$$

$$F_C = \sqrt{F_{CL}^2 + F_{CD}^2} = \delta\tau_c\sqrt{\beta^2 + 1} \tag{9.37}$$

in which

$\overline{F}$ is the mean resultant force;
and F_C is the critical resultant force.

As a result of the current invetigation, it was concluded from Eq. (8.33) that the lift force is normally distributed with relative intensity equal to

$$LI = \frac{\sigma_L}{\overline{F_L}} = 0.554 \tag{9.38}$$

in which

σ_L is the standard deviation of the lift force.

Substituting for $\overline{F_L}$ into Eq. (9.38) the σ_L value becomes:

$$\sigma_L = 0.554\ C_L\ \rho\overline{u}^2 D^2/2 \tag{9.39}$$

Therefore, one can evaluate the quantile point q_n as

$$q_n = \frac{F_c - \overline{F}}{\sigma_L} \tag{9.40}$$

and

$$f(F_c) = f(\tau_c) = \phi(q_n) \tag{9.41}$$

in which $\phi(.)$ is the cumulative distribution function for the normalised distribution curve, and then the probability of adequacy is

$$P_a = \phi(q_n) \tag{9.42}$$

9.5 PROBABILISTIC APPROACH

All the parameters necessary to establish the probability of adequacy were derived in the previous chapter. It is thus possible to determine the side slope probability of adequacy as follows:

For the given values of $D, R, \phi, \theta, S_e, \rho$ and S_e, the following procedure should be utilized.

Step 1: From Eq. (9.2) particle submerged weight W is determined.

Step 2: The value of β is evaluated from Eq. (8.28) as

$$\beta = 5.861\ (R/D)^{-0.289} \tag{9.43}$$

Step 3: δ is determined from Eq. (9.23)

Step 4: τ_c is determined from Eq. (9.25)

Step 5: τ is determined from Eq. (9.19)

Step 6: $\overline{F}$ is determined from Eq. (9.36)

Step 7: F_c is determined from Eq. (9.37)

Step 8: C_L is determined from Eq. (9.11)

Step 9: σ_L is determined from Eq. (9.39)

Step 10: q_n is determined from Eq. (9.40)

Step 11: The probability of adequacy $\phi(q_n)$ is expressed as a cumulative distribution function for the normalised distribution curve which can be obtained from a standard normal table.

In this case, if P_a = 50%, it means that $\overline{F} = F_c$ and the particle can then be considered in the state of incipient motion or at the critical condition. If P_a > 50%, the particle is said to be stable, and if P_a < 50% the particle will be displaced.

9.6 VERIFICATION

To establish the applicability of the two approaches developed in this study, four different tests were established by utilizing the results obtained in the laboratory experiments. Also a comparison between each approach and the approaches of other Authors was made. These analyses may be summarized as follows:

9.6.1 First Test

Despite the predictions obtained by various methods indicating that the failure should occur in the first three models, the laboratory tests conducted on these models revealed no significant movement and accordingly no failure resulted. Using the flow condition obtained for the three models as input data, the predictions for side slope safety factor and probability of adequacy were evaluated for all runs and the results are plotted in Fig. (9.3), which revealed the following predictions at the maximum attainable flow rates:

Model No.	1	2	3
FS	1.056	1.038	1.033
P_a	98.0%	79.7%	78.3%

This principally confirms the results from the laboratory investigations, in which despite the fact that the maximum discharge for a day and night was applied, in the case of the three models, no failure was observed. This means that up to the maximum flow rates the effective shear force acting at the top of the protective layer had not yet reached its critical value.

9.6.2 Second Test

In this test, the two developed approaches were utilized to predict the failure discharge for the case of Model 4, and the corresponding probability of adequacy of the results obtained from the failure tests, the results being as follows:

Test No.	Actual failure flow (m^3/s)	Predicted failure flow (m^3/s)	P_a %
1	0.1794	0.1815	50.2
2	0.1825	0.1815	49.9
3	0.1853	0.1815	49.64
4	0.1769	0.1815	50.43

These results are in accord with the failure discharge in the laboratory tests, and confirm the applicability of the developed models.

9.6.3 Third Test

To achieve greater benefit from the current study as well as to test the developed approaches, a comparison between these approaches and all the aforementioned approaches was made utilizing the available data of Model 4. This mathematical test was conducted by considering the flow to be uniform with both energy and bed slopes equal to 0.0125. The results of this test are plotted in Figs. (9.4) and (9.5), whilst the variation of conventional safety factor with the probability of adequacy is shown in Fig. (9.6).

The results obtained from this test allow a comparison to be made between the predictions obtained by the new approaches and that of all the aforementioned approaches. In addition, for a better appreciation of the comparison, the root mean deviation RMS was determined as

$$S = \sqrt{\frac{\Sigma(x_1 - x_2)^2}{(N-1)}} \qquad (9.44)$$

in which

x_1 is the prediction obtained by the new approaches;

and x_2 is the prediction obtained by any of the aforementioned approaches.

This test was applied for each of the deterministic and probabilistic approaches and the results obtained were as follows:

A: The deterministic approaches

Method No.	1	2	3	4	5	6	7	8
S	0.501	0.302	0.261	0.098	0.290	0.378	0.080	0.373

B: The probabilistic approaches

Method No.	1	2	3	4
S	0.086	0.653	0.432	0.662

These results revealed that in the case of the deterministic approaches, Method Nos. 4 and 7 give the closest results to the new approach, whilst Method No. 1 gives the nearest results in the case of the probabilistic approaches, and also these results are in agreement with those concluded in Chapter 8.

9.6.4 Fourth Test

During this test, the side slope factor of safety and probabibility of adequacy were determined for various rock sizes which varied in steps from 0.005m to 0.03m. Applying the flow conditions obtained in Model 4, the results are plotted in Fig. (9.7). These graphs indicate the relationship between the particle size and the values predicted for all the flow cases. Clearly as the particle size is increased, the protective layer should be more stable.

In addition, the safety factors predicted for all particle sizes are plotted against the corresponding probability of adequacy as shown in Fig. (9.8). For the critical condition in both deterministic and probabilistic approaches, the factor of safety is one and the probability of adequacy is 50%.

9.7 DISCUSSION

Two methods for sizing riprap were developed on the grounds of the relationships developed throughout the previous chapter. The deterministic method of riprap design was developed on the basis of stability of a single particle by considering the mean value of lift and drag forces, and the alternative probabilistic approach which takes into account the randomness of the forces acting on the riprap to enable the designer to interpret the likelihood of adequacy under a certain deterministic design condition.

A sensitivity analysis of the developed models was made in which the available laboratory data was utilized, and the results were very close to that obtained in the experimental work. Also a similar analysis was conducted to justify the applicability of the new approaches in comparison to the others, and the test showed that all the other methods were a little more conservative than the approaches developed in this study. This in fact leads to the conclusion that the Author's approaches are practical and more economic than the other methods.

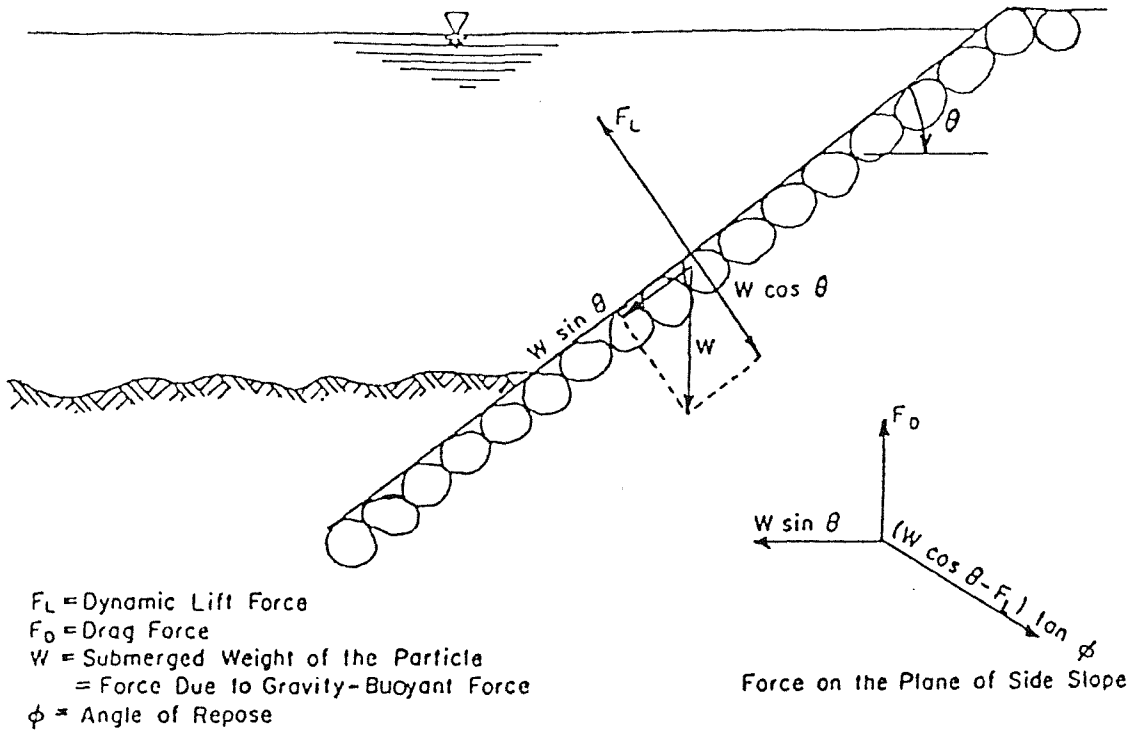

FIG. 9-1: FORCES ACTING ON SIDE SLOPE PARTICLE

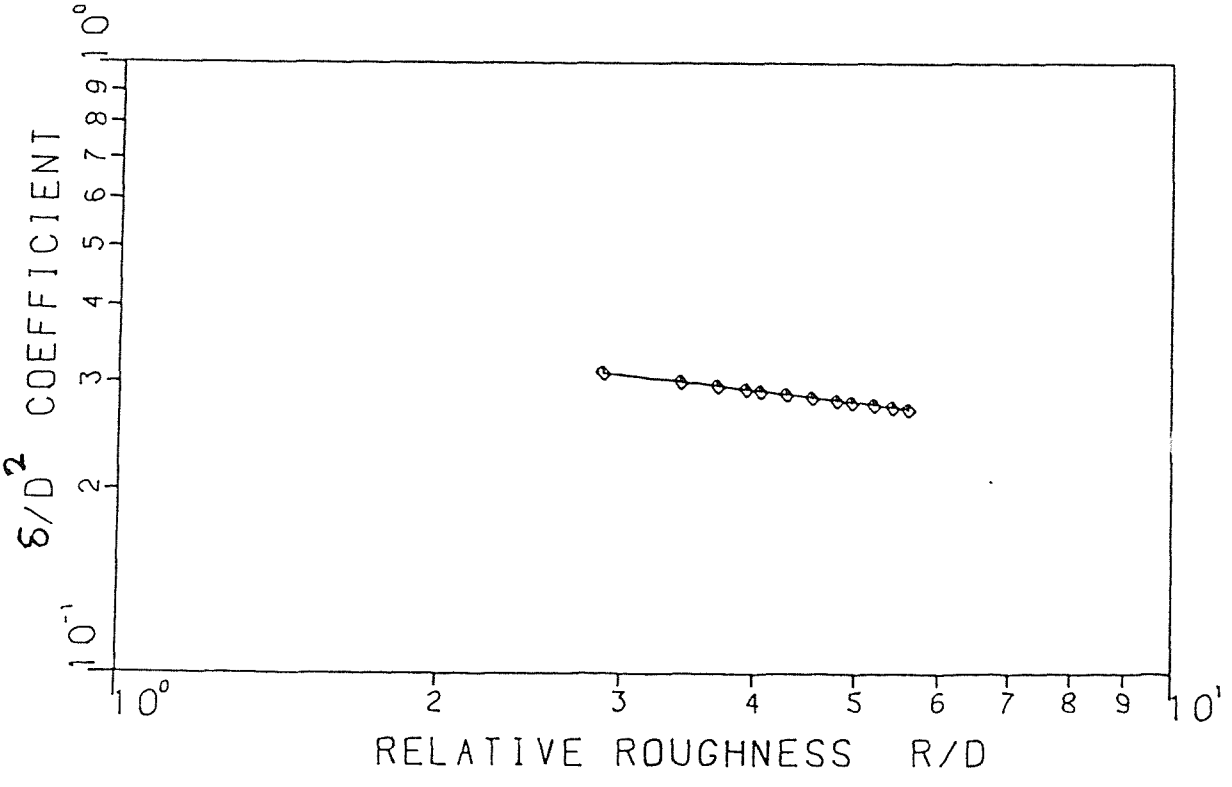

FIG. 9 - 2: VARIATION OF δ/D^2 WITH R/D

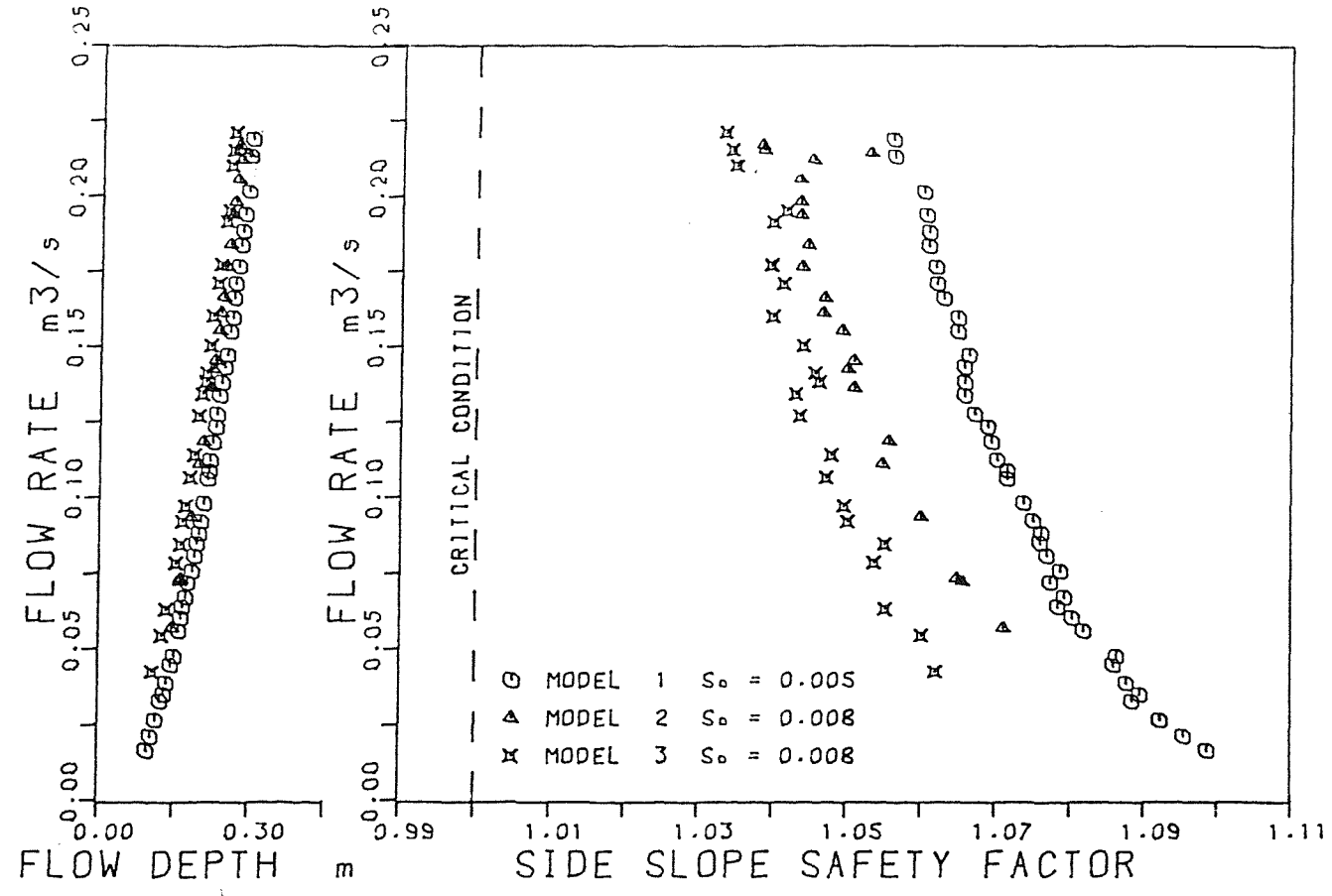

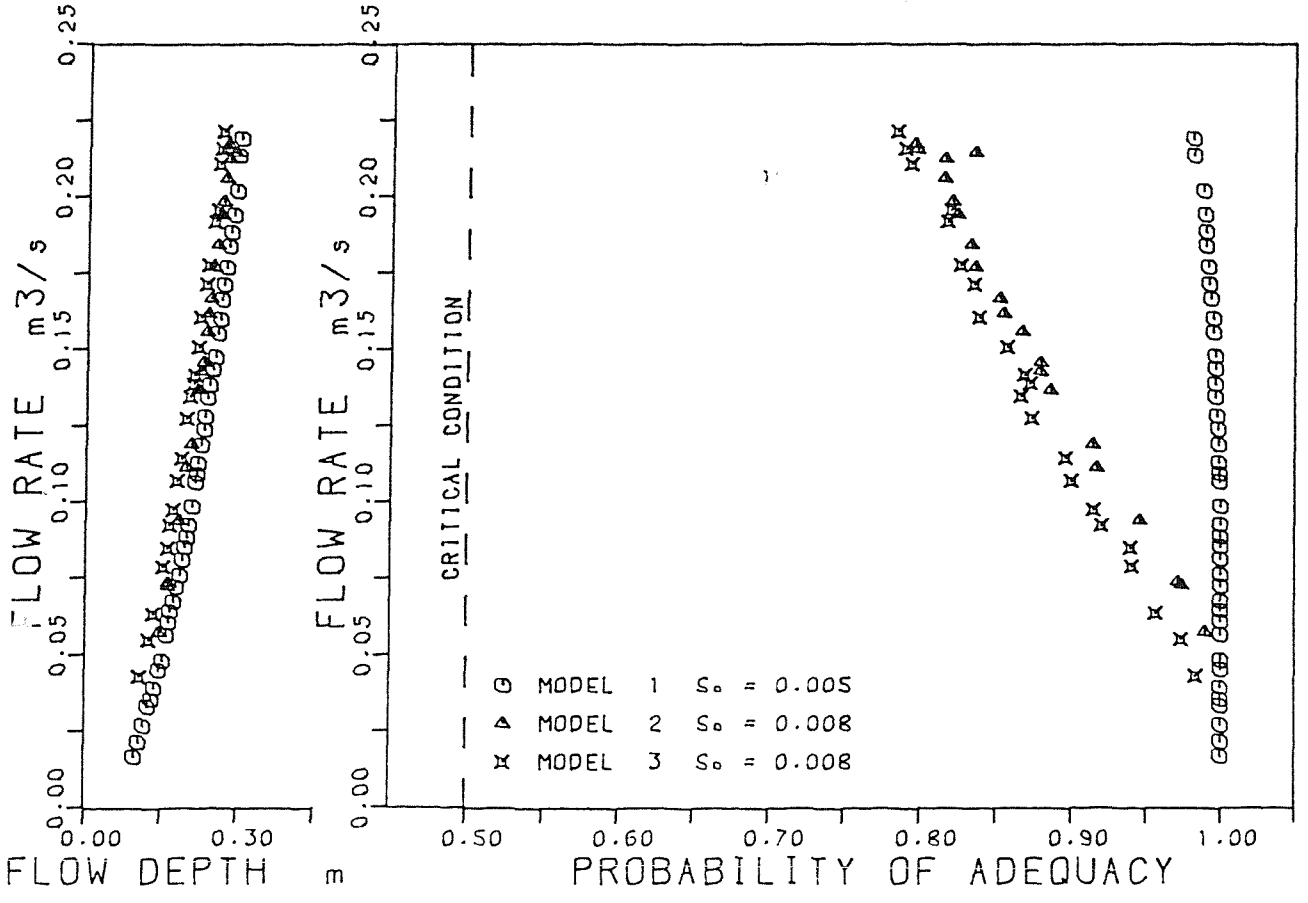

FIG.9-3: SIDE SLOPE SAFETY FACTOR & PROBABILITY OF ADEQUACY FOR MODELS 1 , 2 & 3

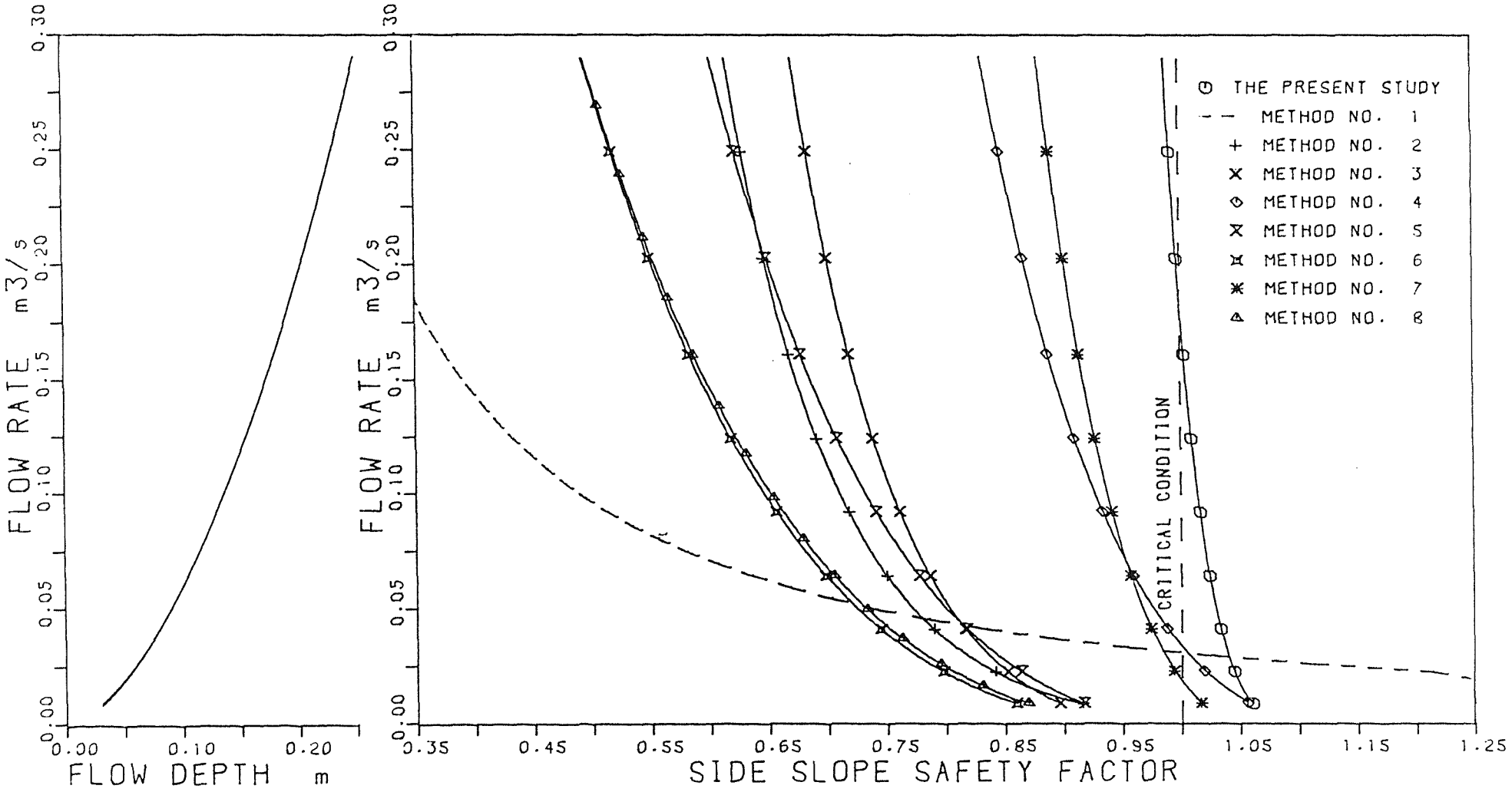

FIG.9-4: COMPARISON OF CONVENTIONAL SAFETY FACTOR WITH VARIOUS METHODS

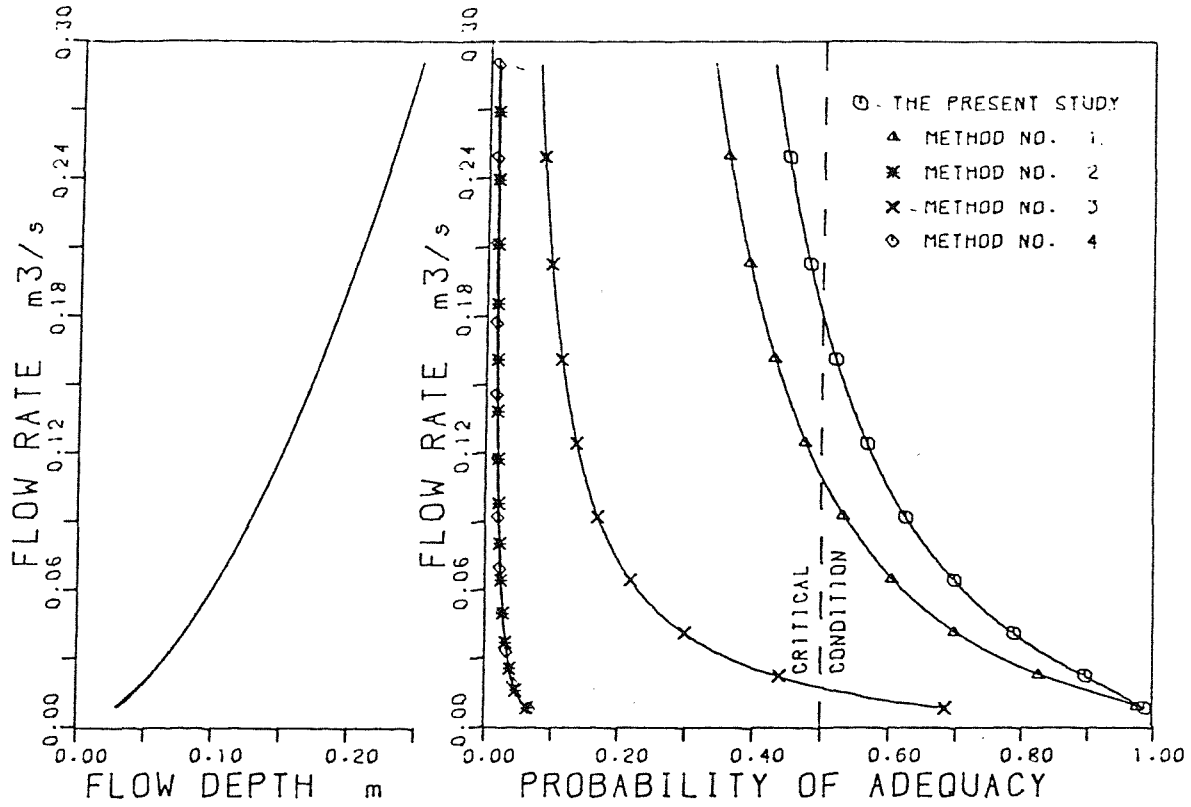

FIG.9-5:COMPARISON OF THE PROBABILITY OF ADEQUACY WITH VARIOUS METHODS

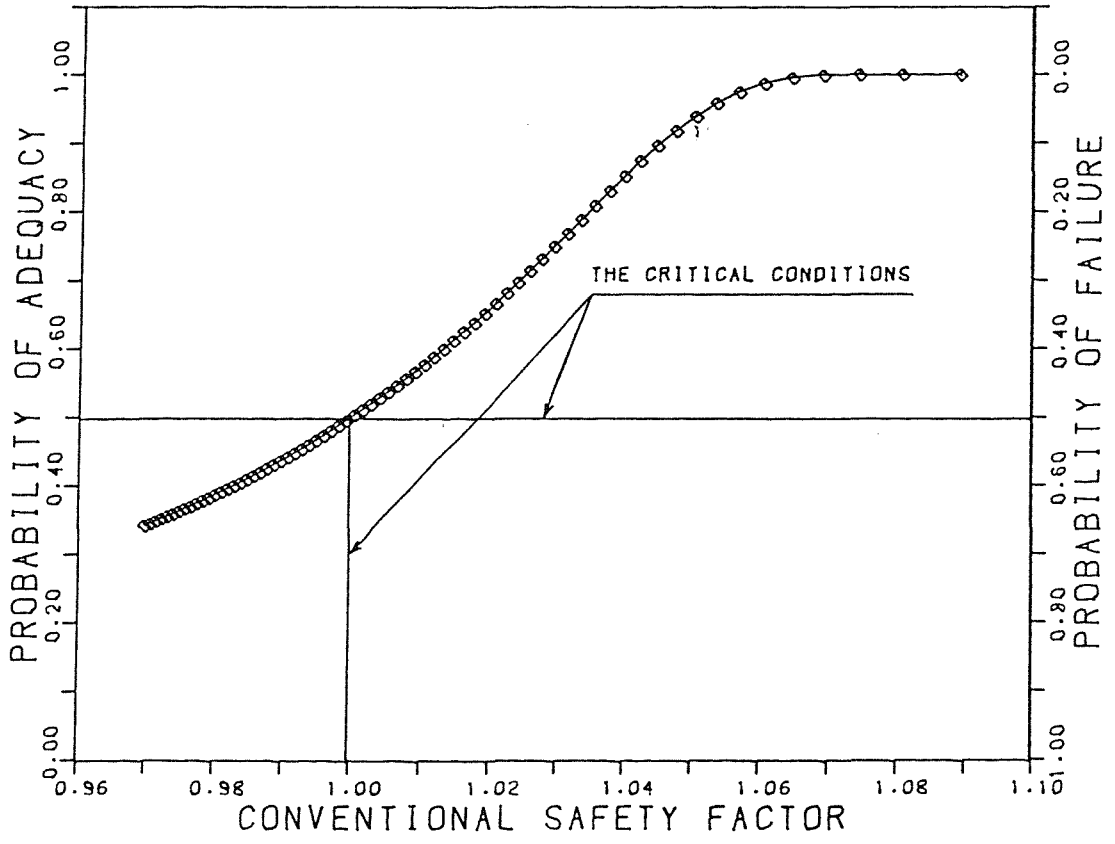

FIG.9-6:VARIATION OF CONVENTIONAL SAFETY FACTOR WITH PROBABILITY OF ADEQUACY

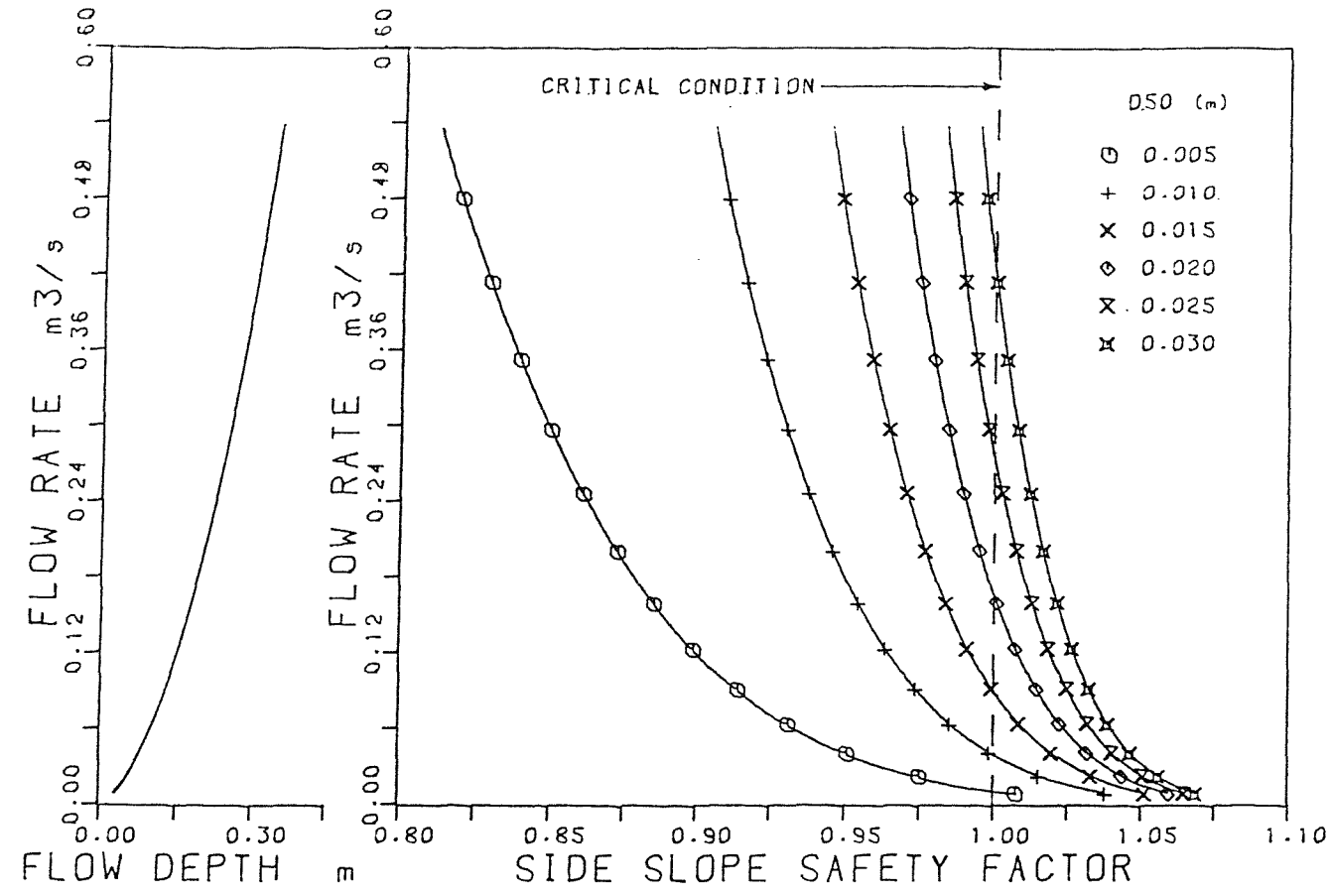

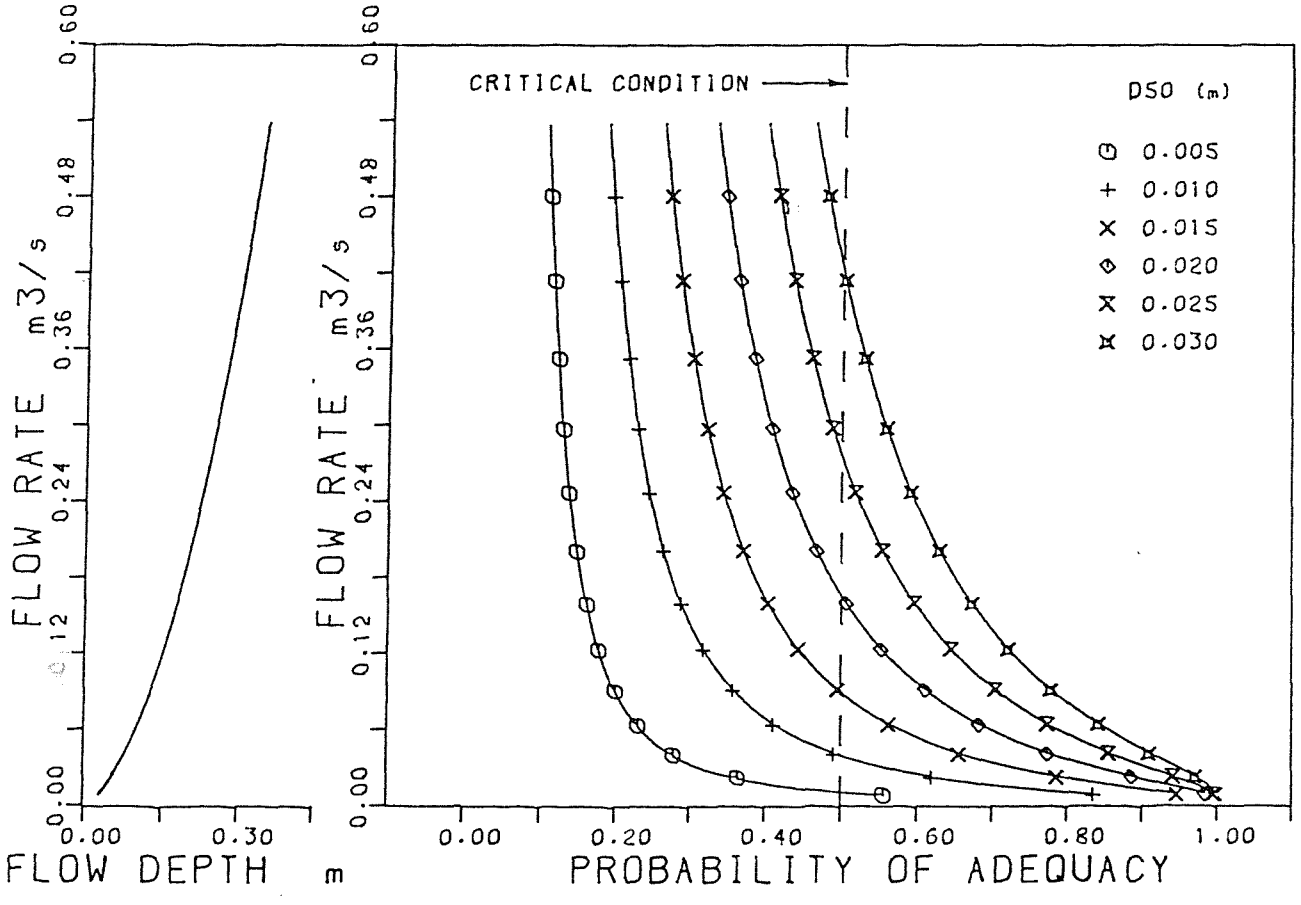

FIG.9-7: SIDE SLOPE SAFETY FACTOR & PROBABILITY OF ADEQUACY FOR DIFFERENT ROCK SIZES

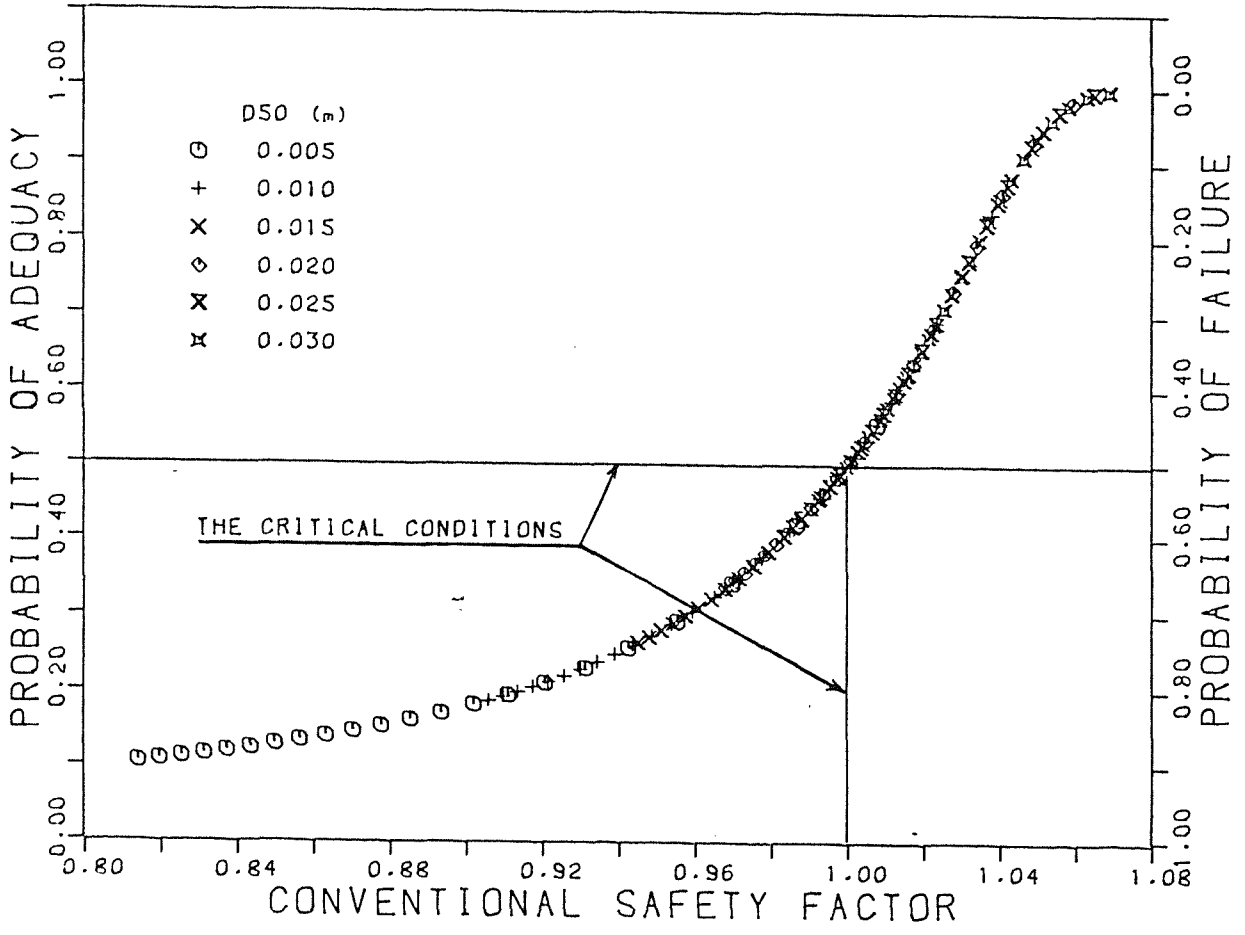

FIG.9-8:PROBABILITY OF ADEQUACY Vs CONVENTIONAL SAFETY FACTOR FOR DIFFERENT ROCK SIZES

CHAPTER TEN

CONCLUSIONS AND RECOMMENDATIONS

10.1 CONCLUSIONS

The aim of this research was to obtain a greater insight into the problem of the stability of riprap protected side slopes in open channel flow, and more especially to establish a better understanding of the failure process, the hydrodynamic forces acting on the rock particles, the hydraulic resistance and flow characteristics of large scale rough channels.

For the above purpose, six modelled channels, with side slopes protected with a layer of rock armour have been designed, constructed and tested in an outdoor flume and in an indoor tilting flume, as explained in Chapter Five. Then for the purpose of measuring the hydrodynamic forces acting on an individual representative spherical particle as well as on four non-spherical particles, Model No. (5) was modified as explained in Chapter Six.

In the previous chapters there has been detailed discussion of the various findings and the main conclusions are set out below:

A - Riprap stability

In the case of the first three models, the flume was operated with various flow rate steps up to 0.22 m^3/s, as shown in Table (5.1). But although the maximum discharge was applied for a day and night, and that most methods of sizing riprap predicted failure, in fact no failure was observed. The implications are as follows:

1 - The effective shear force acting at the top of the protective layer, at the maximum attainable flow rate, had not reached its critical value.

2 - The deterministic and probabilistic methods for sizing riprap are too conservative, and thus tend to be uneconomic. This is obviously due to the manner in which these approaches have been developed, namely very largely on the basis of theoretical considerations and without the benefit of verification by actual measurements.

In the case of the last three models, in which both uniform and graded riprap materials, as well as both a conventional filter and a sheet filter cloth were tested, increasing discharges were applied in steps until failure occurred. The mode of failure was assessed and, in one case, a more detailed examination was made with the aid of coloured rock particles. From the results of the tests on these models, the following conclusion can be drawn:

1 - The visualization study of the failure process revealed that no flow stage exists at which the riprap layer suddenly collapses since movement of individual particles takes place progressively over a wide range of applied shear stress, as the flow velocity increases.

2 - In describing the manner in which failure occurred in these models, the following stages of failure can be identified:

a - Rearrangement movement

This movement usually occurs at relatively low flow velocities to some of the less well supported particles and limited in such a way as not to cause failure. It is worth mentioning that this rearranging process is taking place not only due to the acting hydrodynamic forces, but also due to a particle's local unstable position.

b - Occasional movement

As the flow rate is increased, some particles, mainly from the top protective layer at the lower part of the side slope blanket, tend to vibrate under the effect of the fluctuating hydrodynamic forces. The vibration leads to a new stage in which occasional movement to some particles was observed. It

was noticed during this stage that despite the particles being moved on the side slopes, the protective layer as a whole was working efficiently and withstood the applied forces.

c - Threshold stage

This stage was characterised by a displacement of one particle, which at the same place, would expose some previously shielded particles to the flow current. As a result of this, a new system was established which caused some less well supported particles to move.

d - Failure stage

This last stage was reached when the rate of particle removal was found to be approximately proportional to the increase in flow rate; finally, the rate of removal became such that the stability of the side slope, in some portions, was endangered. Failure was deemed to occur when the riprap lining was removed from small areas of the lower part of the side slope. Generally, this resulted in a collapse of the upper part of the side slope due to the removal of the support afforded by the lower portions.

3 - It was observed in all of the tests of failure that particle movement originated in the lower part of the side slope. This was obviously due to the location of maximum shear which, as experimentally found, had a peak value within that part of the side slope.

4 - The stability of a side slope is influenced by the type of filter layer. This is exemplified by the results of the tests on Model Nos. (4) and (5) each having the same riprap lining. The failure discharge in the case of Model No. (4), where there was a conventional filter consisting of two aggregate layers 1.5 cm thick each, was 1.29 times that in Model No. (5) where there was a synthetic filter layer.

This result was expected because unlike the properly designed

conventional filter, which provides a rough foundation to the riprap blanket and consequently enables the protective layer to withstand the applied hydrodynamic forces, the filter cloth has the tendency to facilitate the particle movement immediately after the incipient motion has taken place. This action reduces the time interval between the threshold of movement and failure as well as inducing failure earlier.

5 - The effect of rock grading on stability is illustrated by the results of tests on Model Nos. (5) and (6). Model No. (5) was protected with uniform rock particles of D_{50} = 20.7 mm (Table 5.1) having a layer thickness of 1.5 x D_{50}, whilst Model No. (6) had a graded material with D_{50} the same as in Model No. (5) and with layer thickess (see Fig. 5.19) similar to that in Model No. (5). Failure occurred in Model No. (6) at a flow rate of 92% of that in Model No. (5).

This may be explained by the fact that, in the case of a riprap blanket comprising a graded material, the large particles provide shelter for the smaller ones. Thus the resistance of the smaller particles to the applied forces is enhanced whereas the resistance of the larger particles is diminished. Overall, the effect is that a graded material will provide less stability than a uniform material of the same median grain size.

6 - There is currently some debate concerning the relative merits of filter cloths and granular filters. The filter cloth is more economical since, being less labour demanding, it is quick and easy to install; it is normally resistant to puncturing, but as it is a fairly recent innovation its durability is not yet proved.

Certainly, it can be said that there was no indication of any deterioration in the physical properties of the filter cloth utilised in Model Nos. (5) and (6), although, of course, their exposure to flow conditions was very short relative to that which might be expected in a field installation.

On the other hand, the relative roughness of the cloth, which is necessary for stability on a side slope, was changed by the exposure to the flow and became less than previously. This reduction in resistance may be conducive to a particular type of failure affecting the whole side slope, as occurred during the tests conducted on Model No. (6). In this test, as shown in Plate (7.7), the failure rapidly established itself along the side slope which was obviously due to the filter cloth sliding on the side slope face of the sand base.

This experience leads to the conclusion that a filter cloth should be installed as far as the upper end of the side slope, then steel rods or any available heavy materials could be used as weights securing the filter along its upper edge.

7 - Considering the quantitative study conducted on Model No. (6), in which a more detailed examination was made with the aid of coloured rock particles, the observations confirmed that the maximum percentage transport occurred within the upper part of the protective blanket. This was obviously due to the slump induced within the upper part as a result of the particles removed from the lower part of the side slope.

Moreover, from observations on the particle behaviour during their displacement it was concluded that they were being subjected to increasing drag force associated with the increase in velocity with distance from the boundary.

B - Channel roughness and hydraulic resistance

Investigation of the hydraulic resistance and flow characteristics of the large scale rough channels conducted in this study revealed the following:

1 - Tables (7.13) to (7.18) and Figs. (7.38), (7.40) and (7.42) confirm that the Chezy resistance coefficient C is independent of the slope of the channel bed, and increases with the increase in flow rate.

2 - Manning's n was also confirmed to be independent of the slope of the channel bed and decreased with the increase in flow rate as shown in Tables (7.13) to (7.18) and Figs. (7.37), (7.39) and (7.41).

3 - According to the Eqs. (7.11) to (7.17) developed in this study, it was concluded that the Darcy-Weisbach friction factor parameter ($1/\sqrt{f}$) is directly correlated with the relative roughness parameter (R/D_{50}) by a power (monomial) type formula as shown in Figs. (7.43) and (7.44).

C - Applicability of existing sizing methods

An investigation of the applicability of the approaches developed for sizing riprap either deterministically or probabilistically has been comprehensively conducted in the light of the results obtained from all the experimental tests. It was found that the results differed materially from those predicted by the various approaches, and that the predictions themselves covered a wide range for all the experimental tests as demonstrated in Figs. (7.1) to (7.24).

In addition, as shown in Chapter Seven, the comparison test conducted for various deterministic approaches and for a wide range of particle sizes showed that some of these methods always predict failure results whatever the particle size as depicted in Figs. (7.25) to (7.30), whilst the particle sizes recommended by the remaining methods for the given flow conditions, are always greater than these used in the experimental tests, in other words are too conservative.

This wide variation in the prediction obtained by various methods reflects the manner in which these approaches were developed, that is to say principally based on theoretical considerations and unconfirmed by real measurements.

D - Location of maximum wall shear

It was found, from the experimental study conducted to locate the point of maximum shear stress along the side slope for various flow conditions, that the maximum wall shear, as shown in Table (6.1) and Fig. (6.6), was located at between 0.29y and 0.35y, where y is vertical height above the channel bed, which is in accordance with the results obtained by Lane, E.W. (1955).

E - Lift and drag properties

For the purpose of formulating stability criteria for side slopes, a specially fabricated measuring device was employed to acquire simultaneous values of lift and drag forces for various flow conditions. It comprised a spherical particle of diameter equal to 20.1 mm which has been determined experimentally. From the results obtained, the main conclusions can be summarized as follows:

1 - The probability densities of the fluctuating lift and drag forces in this investigation were found to be approximately normal distributions, as shown in Figs. (8.2) to (8.13).

2 - The cross-correlation analysis for the measured lift and drag instantaneous values, as shown in Figs. (8.14) to (8.25), revealed that they were not correlated. This means each force is randomly fluctuating and is independent, one of another.

3 - The relationships developed either for the variation of the lift and drag coefficients, and the ratio of lift to drag, as depicted in Figs. (8.32) to (8.36), confirmed the correlation between these coefficients and the values of both the relative roughness parameter (R/D_{50}) and Reynolds number (R_e), as represented by Eqs. (8.22) to (8.29).

4 - The relative intensities of the lift and drag forces, as defined in this study by Eqs. (8.30) and (8.31), were found to be independent of (R/D_{50}) and (R_e) as shown in Figs. (8.37) and (8.38), and had constant values which from Fig.

(8.39) are seen to be equal to 0.168 in the case of drag force and 0.554 in the case of lift force.

F - Particle shape and orientation

Effect of particle shape and orientation was investigated experimentally by measuring the forces acting on four different shaped non-spherical particles as well as on the spherical particle. This study revealed that the magnitude of the measured forces is dependent on the projected area of the particle. Accordingly, the stability of any particle will not only be influenced by the hydrodynamic forces acting on it, but also is dependent on the particle shape and orientation which may vary widely from one particle to another.

G - Modified methods for sizing riprap

A sensitivity analysis of both the deterministic methods for sizing riprap and the other auxiliary probabilistic methods derived in this study was made, and the results were very close to those obtained in the experimental work as shown in Figs. (9.3) to (9.8). Also, a similar analysis was conducted to justify the applicability of the new approaches in comparison to the others, and it was shown that all the other methods are a little more conservative than the approaches developed in this study as shown in Figs. (9.4) to (9.6). This in fact leads to the conclusion that the approaches developed in this study are practical and more economic than the other methods, although it must be acknowledged that they are only based on a limited range of conditions.

10.2 RECOMMENDATIONS FOR FUTURE INVESTIGATION

The experiments, although on models of fairly large dimensions, of the order of 0.4 and 0.5m bed width and side slope 1V:1.5H, were necessarily somewhat limited in scope, bearing in mind the many factors influencing the stability of channel side slopes. A greater variety of channel geometry needs to be considered - ratio bed width to flow depth, longitudinal bed slope, steepness of side slope, and the variation in plan form, such as the effect of bends.

The performance of different types of riprap lining merit further investigation, for instance the effect of different gradings, thicknesses and packing factors (consolidation levels in loose tipping and purposeful placing). For instance, it might be beneficial to armour to a higher standard for the lower portion of the side slope than the upper. Also, the nature of the bed must have an effect on side slope stability and this requires further study.

Filter design is an important issue. A great variety of synthetic fabrics are available and their relative merits as well as their comparison with conventional filter layers, require experimental study.

The mechanics of the threshold of movement and subsequent failure need to be investigated more intensively. Experiments aimed at establishing in detail the sequence of events could be beneficial. Tests could be conducted to establish the lift and drag on different shaped particles in various environments, for example in different locations on a side slope and with different arrangements of neighbouring particles.

In the present study, a channel core consisting of medium sand having D_{50} = 0.27 was adopted. But in some circumstances, as in the case of the River Nile in Egypt, the banks usually comprise either silt or silty clay materials having certain characteristics different from that of sand. Therefore, it would be interesting to investigate the effect, on the riprap stability, of using silt as a channel core. It is expected, in this case, that the filter design will be a dominant factor in the stability of the riprap layer.

The modified approach to riprap sizing proposed by the Author requires further vertification in the light of the various influencing factors outlined above. The results of laboratory and field trials on the lines indicated will give a much greater confidence to the engineer when faced with the important design problem of protecting the banks of rivers and artificial channels.

It is understood that a very large riprap test facility has recently been constructed at the U.S. Army Engineers of Waterways Experiment Station - Vicksburg, and an extensive programme is planned with the aim of improving design methods for sizing riprap.

REFERENCES

AKSOY, S. (1973). "Fluid Force Acting on a Sphere Near a Solid Boundary", Proc. 15th. Congress IAHR, Vol.1, pp. 217-224.

ALBERTSON, M.L. (1953). "Effect of Shape on the Fall Velocity of Gravel Particles", Proc. of 5th. Iowa Hyd. Conf., Iowa City, Iowa.

ALLEN, T. (1981). "Particle Size Measurement", Chapman and Hall, London, Third Edition.

ANDERSON, A.G. et al. (1970). "Tentative Design Procedure of Riprap Lined Channels", Project Report No. 96, St. Antony Falls Hyd. Lab., Minneapolis, Minnesota.

----------(1948). "Review of Slope Protection Methods", ASCE Sub-Committee on Slope Protection, Trans. of ASCE, Vol.74, pp. 845-866.

----------(1963). "Friction Factors in Open Channels", ASCE Progress Report of the Task Committee on Friction Factors in Open Channels, Proc. Hyd. Div., ASCE, Vol.89, No.HY2, pp.97-143.

----------(1969). "Sediment Measurement Techniques :F. Laboratory Procedures", ASCE Task Committee on Preparation of Sedimentation Manual, Proc. Hyd. Div., ASCE, Vol.95, No. HY5, pp.1515-1543.

----------(1972). "Sediment Control Methods: B. Stream Channels", ASCE Task Committee on Sedimentation Manual, Proc. Hyd. Div., ASCE, Vol.98, No. HY7, pp.1295-1326.

BATHURST, J.C. (1978). "Flow Resistance of Large-Scale Roughness", Proc. Hyd. Div., ASCE, Vol.104, No. HY12, pp.1587-1603.

BATHURST, J.C. et al. (1981). "Resistance Equation for Large-Scale Roughness", Proc. Hyd. Div., ASCE, Vol. 107, No. HY12, pp.1593-1613.

BAUER, W.J. (1954). "Turbulent Boundary Layer on Steep Slopes", Trans. ASCE, Vol. 119, pp.1212-1233.

BAYAZIT, M. (1976). "Free Surface Flow in a Channel of Large Relative Roughness", Jour. of Hyd. Research, IAHR, Vol.14, No. 2, pp.115-125.

BENDAT, J.S. and PIERSOL, A.G. (1966). "Measurement and Analysis of Random Data", 10 Ed., John Wiley and Sons, Inc. New York.

BENDICT, B.A. and CHRISTENSEN, B.A. (1972). "Hydrodynamic Lift on a Stream Bed", Chapter 5 in SHEN, H.W. (Ed.),"Sedimentation", Water Resources, Fort Collins, Colorado. pp.5.1-5.17.

BERTELRUD, A. (1974). "Pipe Flow Calibration of Preston Tubes of Different Diameters and Relative Lengths Including Recommendations on Data Presentation for Best Accuracy", Aero. Res. Inst., Sweden (FFA), Report No. 125, Stockholm.

BERTELRUD, A. (1976). "Preston Tube Calibration Accuracy", AIAA Journal, Vol. 14, No. 1, pp.98-100.

BLINCO, P.H. and SIMONS, D.B. (1974). "Characteristics of Turbulent Boundary Shear Stress", Proc. Eng. Mech. Div., ASCE, Vol. 100, No. EM2, pp.203-220.

BRAY, D.I. (1979). "Estimating Average Velocity in Gravel-Bed Rivers", Proc. Hyd. Div., ASCE, Vol. 105, No. HY9, pp.1103-1122.

----------(1975). "Methods of Test for Soil for Civil Engineering Purposes", B.S. No. 1377, British Standards Institution, London.

———————— (1981). "Thin-Plate Weirs", B.S. No. 3680, Part 4A, British Standards Institution, London.

BURKHAM, D.E. and DAWDY, D.R. (1976). "Resistance Equation for Alluvial-Channel Flow", Proc. Hyd. Div., ASCE, Vol. 102, No. HY10, pp.1479-1489.

CAMPBELL, F.B. (1966). "Hydraulic Design of Rock Riprap", Misc. Paper No. 2-777, Office of Chief of Engineers, U.S. Army, Waterways Experiment Station, Vicksburg, Mississippi.

CHENG, E.D.H. and CLYDE, C.G. (1972). "Instantaneous Hydrodynamic Lift and Drag Forces on Large Roughness Elements in Turbulent Open Channel Flow", Chapter 3 in SHEN, H.W. (Ed.), "Sedimentation", Water Resources, Fort Collins, Colorado.

CHEPIL, W.S. (1958). "The Use of Evenly Spaced Hemispheres to Evaluate Aerodynamic Forces on a Soil Surface", Trans. American Geophysical Union, Vol.39, No. 3, pp.397-404.

CHEPIL, W.S. (1961). "The Use of Spheres to Measure Lift and Drag on Wind-Eroded Soil Grains", Proc., Soil Science Soc. of America, Vol. 25, No. 5, pp.343-345.

CHIEN, N. (1954). "The Present Status of Research on Sediment Transport", Proc. Hyd. Div., ASCE., Vol. 80.

CHOW, V.T. (1959). "Open Channel Hydraulics", McGraw-Hill, New York, N.Y.

COLEBROOK, C.F. and WHITE, C.M. (1937). "Experiments with Fluid Friction in Roughened Pipes", Proc. of the Royal Society of London, Series A, Vol.161, pp.367-387.

COLEMAN, N.L. (1967). "A Theoretical and Experimental Study of Drag and Lift Forces Acting on a Sphere Resting on a Hypothetical Streambed", Proc. of the 12th Congress of IAHR, Vol.3, Fort Collins, pp. c22.1-c22.8.

COX, R.G. (1973). "Effective Hydraulic Roughness for Channels Having Bed Roughness Different from Bank Roughness", U.S. Army Engineers, Waterways Experiment Station, Vicksburg, Mississippi.

DAVIES, T.R.H. and SAMAD, M.F.A. (1978). "Fluid Dynamic Lift on a Bed Particle", Proc. Hyd. Div., ASCE, Vol.104, No. HY8, pp.1171-1182.

DELLEUR, J.W. (1957). "The Boundary Layer Development in Open Channels", Proc. Eng. Mechanics Div., ASCE, Vol.83, No.EM1, pp.1138.1-1138.24.

EINSTEIN, H.A. and BANKS, R.B. (1950). "Fluid Resistance of Composite Roughness", Trans. American Geophysical Union, Vol.31, No.4, pp.603-610.

EINSTEIN, H.A. and EL-SAMNI, E.A. (1949). "Hydrodynamic Forces on a Rough Wall", Review of Modern Physics, Vol.21, No.3, pp.520-524.

GESSLER, J.B. (1965). "The Beginning of Bedload Movement of Mixtures Investigated as Natural Armouring in Channels", W.M. Keck Lab. of Hydraulics and Water Resources, Calif. Inst. of Technology, Pasadena.

GESSLER, J.B. (1971). "Beginning and Causing of Sediment Motion", River Mechanics, Vol.1, Edited by H.W. SHEN, Chapter 7, Fort Collins, Colorado, pp.7.1-7.21.

GHOSH, S.N. and ROY, N. (1970). "Boundary Shear Distribution in Open Channel Flow", Proc. Hyd. Div., ASCE, Vol.96, No.HY4, pp.967-994.

GLANVILLE, W.H. (1951). "Soil Mechanics for Road Engineers", Road Research Laboratory, Harmondsworth, Middlesex.

GRASS, A.J. (1970). "Initial Instability of Fine Bed Sand", Proc. Hyd. Div., ASCE, Vol.96, No.HY3, pp.619-632.

GRIFFITHS, G.A. (1981). "Flow Resistance in Coarse Gravel Bed Rivers", Proc. Hyd. Div., ASCE, Vol. 107, No.HY7, pp.899-918.

HEAD, M.R. and RECHENBERG, I. (1962). "The Preston Tube as a Means of Measuring Skin Friction", Jour. of Fluid Mech., Vol.14, Part 4, pp.1-17.

HEAD, M.R. and VASANTA, R.V. (1971). "Simplified Presentation of Preston Tube Calibration", Aeronautical Quarterly, Vol.22, Part 3, pp.295-300.

HERMAN, J.K. (1984). "Scour Due to Riprap and Improper Filters", Proc. Hyd. Div., ASCE, Vol. 110, No. HY10, pp.1315-1324.

HEY, R.D. (1979). "Flow Resistance in Gravel-Bed Rivers", Proc. Hyd. Div., ASCE, Vol.105, No. HY4, pp.365-379.

HOARE, D.J. (1982). "Synthetic Fabrics as Soil Filters: A Review", Proc. Geotechnical Eng. Div., ASCE, Vol. 108, No. GT10, pp.1230-1245.

HOLLICK, M. (1976). "Boundary Shear Stress Measurement by Preston Tube", Technical Notes, Proc. Hyd. Div., ASCE, Vol. 102, No. HY7, pp.1053-1057.

HSU, E.Y. (1955). "The Measurement of Local Turbulent Skin Friction by Means of Surface Pitot Tubes", Report No. 957, U.S. Dept. of the Navy, David W. Taylor model Basin.

HWANG, L.S. and LAURSEN, E.M. (1963). "Shear Measurement Technique for Rough Surfaces", Proc. Hyd. Div., ASCE. Vol.89, No.HY2, pp.19-37.

----------(1966). "Tables for Irrigation and Hydraulic Laboratory Practice", Hyd. and Sediment Research Inst., Delta Barrages, Egypt.

IPPEN, A.T. and DRINKER, P.A. (1962). "Boundary Shear Stresses in Curved Trapezoidal Channels", Proc. Hyd. Div., ASCE, Vol.88, No.HY5, pp.143-179.

JEFFREYS, H. (1929). "On the Transport of Sediments by Streams", Proc. Cambridge Phil. Soc. Vol. 25, pp.272-277.

KARTHA, V.C. and LEUTHEUSSER, H.J. (1970). "Distribution of Tractive Force in Open Channels", Proc. Hyd. Div., ASCE, Vol.96, No.HY7, pp.1469-1483.

KAZEMIPOUR, A.K. and APELT, C.J. (1979). "Shape Effects on Resistance to Uniform Flow in Open Channels", Jour. of Hyd. Research, Vol.17, No.2, pp.129-147.

KELLERHALS, R. (1970). "Stable Channels With Gravel-Paved Beds", Proc. Waterways and Harbour Div., ASCE, Vol.93, No. WW1, pp.63-84.

KEULEGAN, G.H. (1938). "Laws of the Turbulent Flow in Open Channels", Jour. of Research of the National Bureau of Standards, Vol.21, pp.707-741.

KRAMER, H. (1935). "Sand Mixtures and Sand Movement in Fluvial Models", Trans. ASCE, Vol.100, pp.798-878.

LANE, E.W. (1952). "Progress Report on Results of Studies on the Design of Stable Channels", USBR, Hydraulic Laboratory Report No. HYD-352, Denver, Colorado.

LANE, E.W. and CARLSON, E.J. (1953). "Some Factors Affecting the Stability of Canals Constructed in Coarse Granular Materials", Proc. of the Minnesota Int. Hyd. Convention, Sep. 1-4, Joint Meeting of IAHR and Hyd. Div. of ASCE, pp.37-48.

LANE, E.W. (1955). "Design of Stable Channels", Trans. ASCE, Vol. 120, pp.1234-1260.

LEOPOLD, L.B. et al. (1964). "Fluvial Processes in Geomorphology", W.H. Freeman, San Francisco, California.

LIMERINOS, J.T. (1970). "Determination of the Manning Coefficient From Measured Bed Roughness in Natural Channels", Water Supply Paper 1898-B, U.S. Geological Survey, Washington, D.C.

LIU, H.K. and HWANG, S.Y. (1959). "Discharge Formula for Straight Alluvial Channels", Proc. Hyd. Div., ASCE, Vol.85, No. HY11, pp.65-97.

MARTIN, C.S. (1966). "The Effect of a Permeable Bed on Sediment Motion - Phase 1: Seepage Force on Bed Particles", Water Resources Center, Georgia Inst. of Technology, Atlanta, Georgia.

MARTIN, C.S. (1970). "Effect of a Porous Sand Bed on Incipient Sediment Motion", Water Resources Research, Vol. 6, No. 4, pp.1162-1174.

MARTIN, C.S. (1971). "Seepage Force on Interfacial Bed Particles", Proc. Hyd. Div., ASCE, Vol.97, No. HY7, pp.1081-1100.

MEYER-PETER, E. and MULLER, R. (1948). "Formulas for Bed-Load Transport", Report on Second Meeting of the int. Ass. for Hyd. Structures Research, Stockholm, Sweden, Appendix 2, pp.39-64.

MILNE-THOMSON, L.M. (1968). "Theoretical Hydrodynamics", Macmillan & Co.Ltd. 5th Edition.

MIRAJGAOKER, A.G. and CHARLU, K.L.N. (1963). "Natural Roughness Effects in Rigid Open Channels", Proc. Hyd. Div., ASCE, Vol.89, No. HY5, pp.,29-44.

MURPHY, T.E. and GRACE, J.L. (1963). "Riprap Requirements for Overflow Embankments", Highway Research Board, Record No. 30, Washington D.C., pp.47-55.

NOORI, B.M. (1985). "Investigation of Stepped Blocks Protecting Weir Slopes", Ph.D. Thesis, Department of Civil Eng., University of Southampton, U.K.

NORTON, H.N. (1969). "Handbook of Transducers for Electronic Measuring Systems", Prentice-Hall, Inc., Englewood Cliffs, N.J.

O'BRIEN, M.P. and HICKOX, G.H. (1937). "Applied Fluid Mechanics", McGraw-Hill Company, New York.

OLIVIER, H. (1967). "Through and Overflow Rockfill Dams - New Design Techniques", Proc. Inst. of Civ. Eng., pp.433-441.

OTNES, R.K. and ENOCHSON, L.D. (1978). "Applied Time Series Analysis : Volume 1 Basic Techniques", John Wiley and Sons, New York.

OVERTON, D.E. (1967). "Flow-Retardance Coefficients for Selected Prismatic Channels", Trans. of the ASAE, Vol.10, No.3, pp.327-329.

PATEL, V.C. (1965). "Calibration of the Preston Tube and Limitations on its Use in Pressure Gradients", Journ. of Fluid Mechanics, Vol.23, Part 1, pp.185-208.

POSEY, C.J. (1953). "Some Basic Requirements for Protection Against Erosion", Proc. IAHR and ASCE, St. Anthony Falls Hyd. Lab., Minneapolis, Minnesota, pp.85-88.

POSEY, C.J. (1957). "Flood-Erosion Protection for Highway Fills", Trans. ASCE, Vol. 122, pp.531-542.

POSEY, C.J. (1969). "Erosion Prevention Experiments", Proc. of the 13th. Congress of IAHR, Vol.2, Aug. 31-Sep. 5, pp.211-219.

POWELL, R.W. (1946). "Flow in a Channel of Definite Roughness", Trans., ASCE, Vol.111, pp.531-566.

POWELL, R.W. (1950). "Resistance to Flow in Rough Channels", Trans. American Geophysical Union, Vol.31, No. 4, pp.575-582.

PRESTON, J.H. (1954). "The Determination of Turbulent Skin Friction by Means of Pitot-Tubes", Jour. of Royal Aeronautical Society, Vol. 58, pp.109-121.

REEVE, A. (1975). "Transducers", Welwyn Strain Measurement Ltd. Basingstoke, England.

RUH-MING, L. et al. (1976). "Probabilistic Approach to Design of Riprap for River Bank Protection", Symposium on Inland Waterways for Navigation, Flood Control and Water Diversions, Vol.2, pp.1572-1591.

RUH-MING, L. and SIMONS, D.B. (1979). "Failure Probability of Riprap Structures", ASCE Convention and Exposition, Atlanta, pp.1-21.

SAFFMAN, P.G. (1965). "The Lift on a Small Sphere in a Slow Shear Flow", Jour. of Fluid Mechanics, Vol.22, Part 2, pp.385-400.

SAMAD, M.A. (1978). "Analysis of Riprap for Channel Stabilization", Ph.D. Dissertation, Colorado State Univ., Fort Collins, Colorado.

SCHOBER, W. and TEINDL, H. (1979). "Filter-Criteria for Geotextiles", Proc. of the 7th. European Conference on Soil Mech. and Foundation Engineering, Vol.2, pp.121-129.

SEARCY, J.K. (1967). "Use of Riprap for Bank Protection", Hyd. Eng. Circular No. 11, pp.11.1-11.43, Bureau of Public Roads, Washington, D.C.

SIMONS, D.B. and ALBERTSON, M.L. (1960). "Uniform Water Conveyance Channels in Alluvial Material", Proc. Hyd. Div., ASCE, Vol.86, No. HY5, pp.33-71.

SIMONS, D.B. and SENTURK, F. (1977). "Sediment Transport Technology", Water Resources Publications, Fort Collins, Colorado.

SMITH, K.V.H. (1986). "Probabilistic Approach to the Stability Analysis of Rock Protection for Earth Weirs", Proc. of Inst. of Civil Eng., Part 2, Vol.81, pp.243-253.

----------(1958). "On the Measurement of Local Surface Friction on a Flat Plate by Means of Preston Tubes", Staff of Aerodynamics Div., N.P.L., Aero. Res. Council, Reports and Memoranda No. 3185, London.

STEPHENSON, D. (1979). "Rockfill in Hydraulic Engineering", Elsevier Scientific Publishing Company, Netherlands.

STEVENS, M.A. and SIMONS, D.B., (1971). "Stability Analysis for Coarse Granular Material on Slopes", Chapter 17 in SHEN, H.W. (Ed.), "River Mechanics, Vol.1", Fort Collins, Colorado, pp.17.1-17.27.

STEVENS, M.A. AND SIMONS, D.B. (1976). "Safety Factors for Riprap Protection", Proc. Hyd. Div., ASCE, Vol. 102, No. HY5, pp.637-655.

SUMER, B.M. and OGUZ, B. (1978). "Particle Motions Near the Bottom in Turbulent Flow in an Open Channel", Jour. of Fluid Mechanics, London, Vol.86, No. 1, pp.109-127.

SUMER, B.M. and DEIGAARD, R. (1981). "Particle Motions Near the Bottom in Turbulent Flow in an Open Channel: Part 2", Jour. of Fluid Mechanics, London, Vol.109, pp.311-337.

SUMER, B.M. (1984). "Lift Forces on Moving Particles Near Boundaries", Proc. Hyd. Div., ASCE, Vol.110, No.HY9, pp.1272-1278.

TERZAGHI, K. and PECK, R. (1964). "Soil Mechanics in Engineering Practice", John Wiley and Sons, New York, Inc. 13th Print.

THANIKACHALAM, V. and SAKTHIVALIVEL, R. (1975). "Design of Filter Thickness Based on the Application of Queueing Theory", Jour. of Hyd. Research, Vol.13, No.2, pp.207-219.

THOMPSON, S.M. and CAMPBELL, P.L. (1979). "Hydraulics of Large Channel Paved With Boulders", Jour. of Hyd. Research, International Association of Hyd. Research, Vol.17, No.4, pp.341-354.

----------(1958). "Hydraulic Design of Stilling Basins and Energy Dissipators", U.S. Bureau of Reclamation, Engineering Monograph No.25, Denver, Colorado.

----------(1970). "Stone Stability - Velocity Vs Stone Diameter", U.S. Army Engineers, Waterways Exp. Station, Hyd. Design Criteria, Sheet 712-1.

----------(1970). "Open Channel Flow - Composite Roughness Effective Manning's n", U.S. Army Engineers, Waterways Exp. Station, Hyd. Design Criteria, Sheets 631-4 and 631-4/1.

VANONI, V.A. (1966). "Sediment Transportation Mechanics: Initiation of Motion", Proc. Hyd. Div., ASCE, Vol.92, No.HY2, pp.291-314.

VICKERS, B. (1978). "Laboratory Work in Civil Engineering-Soil Mechanics", Granada Publishing Limited, London.

WATTERS, G.Z. and RAO, M.V.P. (1971). "Hydrodynamic Effects of Seepage on Bed Particles", Proc. Hyd. Div., ASCE, Vol.97, No. HY3, pp.421-439.

WEBBER, N.B. (1971). "Fluid Mechanics for Civil Engineers", Chapman and Hall Ltd., London.

WHITE, C.M. (1939). "The Equilibrium of Grains on the Bed of a Stream", Proc. of Royal Society of London, Vol.174A, pp.322-334.

ZAGNI, A.F. and SMITH, K.V.H. (1976). "Channel Flow Over Permeable Beds of Graded Spheres", Proc. Hyd. Div., ASCE, Vol.102, No.HY2, pp.207-222.